THE UNIVERSITY OF SYDNEY

Developing Sustainable and Multifunctional Cementitious Composites by Repurposing FRP Composite Waste

Yunyun Tao

Supervisor: Dr. S. Ali Hadigheh

Submitted in fulfilment of the requirements for the degree of

Doctor of Philosophy

School of Civil Engineering

Faculty of Engineering

The University of Sydney

June 2025

Statement of Originality

This is to certify that the content of this thesis is my own work. This thesis has not been submitted for any other degree or purpose.

I certify that the intellectual content of this thesis is the product of my own work, and that all assistance received in preparing this thesis and all sources have been acknowledged.

Yunyun Tao

05 June 2025

Acknowledgements

First of all, I would like to express my deepest gratitude to my supervisor, Dr. S. Ali Hadigheh, for his unwavering support and guidance throughout my PhD journey. I had the privilege of getting to know him during my master's capstone project, and it was through his encouragement and the opportunity to participate in the Vacation Research Internship Program that I discovered my passion for this research topic. Over the past three and a half years, he has been a kind and encouraging mentor, always providing the necessary resources and support for my research.

I would also like to thank the Progress Evaluation Meeting panel chair, Professor Gwenaelle Proust, and panel member, Dr Mike Bambach, for their guidance and feedback on my progress, as well as their research recommendations.

A heartfelt thanks to my family - my parents, grandparents, sister, and my beloved fur babies - for their endless love, patience, and company. Their understanding and unconditional support, both financial and affective, have been my source of strength and motivation throughout this journey.

During this journey, I am grateful to my colleagues, both within our research group and beyond, at the University of Sydney. Thanks to our research team members: Yaning Wei, Ziyuan Wang, Keyvan Aghabalaei Baghaei, Yang Yu, Songnan Li, Shuvashis Saha, and David Kim. Our frequent communication, mutual assistance, and shared moments have helped us maintain a positive and supportive environment. I would also like to give special thanks to my friends both in Shanghai and Sydney for their emotional support and the life lessons they have shared with me. Their encouragement and perspectives on life have taught me about the pursuit of goals and a positive attitude towards life.

I am also thankful to the dedicated lab manager and staff at the School of Civil Engineering for their invaluable technical support, which was crucial for the successful completion of my experiments. Special thanks to Garry Towell, Paul Busstra, Paul Burrell, and James Ryder for their kind assistance with my experiments.

I acknowledge this research was supported by the Australian Government through the Australian Research Council's Discovery Early Career Researcher Award (DECRA) fellowship scheme (Project DE200100406). Further acknowledgment is for the facilities and technical

assistance and training received from Sydney Microscopy and Microanalysis (SMM), Sydney Analytical (SA), and the Engineering Analytical Facility (EAF) at the University of Sydney.

During the preparation of this thesis, Copilot and ChatGPT were used for text enhancement. Where any text was modified by generative AI, the author then reviewed the resulting content for any errors, inaccuracies or biases, and modified it as required. The author takes full responsibility for the submitted thesis and ensures the work is their own and has used generative AI within the parameters of use.

Authorship Attribution Statement

I declare that all work presented in this thesis is my own, except where explicitly referenced or acknowledged. Below is a summary of my contributions, including published and submitted journal articles incorporated into this thesis.

Published Papers:

This paper is one of the works included in Chapter 2

1. Y. Tao, S.A. Hadigheh, Y. Wei, Recycling of glass fibre reinforced polymer (GFRP) composite wastes in concrete: A critical review and cost benefit analysis, Structures 53 (2023) 1540-1556.
   DOI: https://doi.org/10.1016/j.istruc.2023.05.018

Y. Tao: Writing – original draft, Visualization, Validation, Software, Methodology, Investigation, Formal analysis, Data curation. **S.A. Hadigheh:** Writing – review & editing, Visualization, Validation, Supervision, Resources, Project administration, Methodology, Funding acquisition, Data curation, Conceptualization. **Y. Wei:** Writing – original draft, Visualization, Validation, Resources, Methodology, Investigation, Formal analysis, Data curation.

These papers are the works included in Chapter 3

2. Y. Tao, S.A. Hadigheh, Z. Wang, Void geometry analysis and multifaceted characterisation of cementitious mortar reinforced with short carbon and glass fibres – A comparative study, J. Build. Eng. 89 (2024) 109283.
   DOI: https://doi.org/10.1016/j.jobe.2024.109283

Y. Tao: Writing – original draft, Visualization, Validation, Software, Methodology, Investigation, Formal analysis, Data curation, Conceptualization. **S.A. Hadigheh:** Writing – review & editing, Validation, Supervision, Resources, Project administration, Methodology, Visualization, Funding acquisition, Data curation, Conceptualization. **Z. Wang:** Writing – original draft, Visualization, Software, Investigation, Formal analysis.

3. Y. Tao, Z. Wang, S.A. Hadigheh, Enhancing X-ray micro-CT analysis for detecting voids and carbon fibre features in fibre-reinforced cementitious composites using advanced 3D Gaussian filtering, Measurement (2025) 117018.
   DOI: https://doi.org/10.1016/j.measurement.2025.117018

Y. Tao: Writing – original draft, Visualization, Validation, Methodology, Investigation, Formal analysis, Data curation. **Z. Wang:** Writing – original draft, Visualization, Validation, Software, Methodology, Investigation, Formal analysis, Data curation, Conceptualization. **S.A. Hadigheh:** Writing – review & editing, Visualization, Validation, Supervision, Resources, Project administration, Methodology, Funding acquisition, Data curation.

These two papers comprise Chapter 4

4. Y. Tao, S.A. Hadigheh, Bio-based cross-linking and esterification process for surface functionalisation of carbon fibres in fibre-reinforced cementitious composites, Compos. Part A Appl. Sci. Manuf. (2025) 109037.
   DOI: https://doi.org/10.1016/j.compositesa.2025.109037

Y. Tao: Writing – original draft, Visualization, Validation, Software, Methodology, Investigation, Formal analysis, Data curation. **S.A. Hadigheh:** Writing – review & editing, Visualization, Validation, Supervision, Resources, Project administration, Methodology, Funding acquisition, Data curation, Conceptualization.

5. Y. Tao, S.A. Hadigheh, D.J. Hayne, B. Newman, L.C. Henderson, Electrochemical grafting of hydroxyl and amine groups on carbon fibres for improved performance in cementitious composites, Constr. Build. Mater. 484 (2025) 141843.
   DOI: https://doi.org/10.1016/j.conbuildmat.2025.141843

Y. Tao: Writing – original draft, Visualization, Validation, Software, Methodology, Investigation, Formal analysis, Data curation. **S.A. Hadigheh:** Writing – review & editing, Visualization, Validation, Supervision, Resources, Project administration, Methodology, Funding acquisition, Data curation, Conceptualization. **D.J. Hayne:** Writing – review & editing, Methodology. **Ben Newman:** Writing – review & editing, Methodology. **L.C. Henderson:** Writing – review & editing, Visualization, Resources, Methodology.

This paper comprises Chapter 5

6. Y. Tao, S.A. Hadigheh, Enhancing the strength, microstructural integrity, and shrinkage performance of cement-based mortar using pulverised carbon and glass FRP composite waste, J. Build. Eng. 94 (2024) 110053.
   DOI: https://doi.org/10.1016/j.jobe.2024.110053

Y. Tao: Writing – original draft, Visualization, Validation, Software, Methodology, Investigation, Formal analysis, Data curation. **S.A. Hadigheh:** Writing – review & editing, Validation, Supervision, Resources, Project administration, Methodology, Investigation, Funding acquisition, Data curation, Conceptualization.

This paper is one of the works included in Chapter 6

7. Y. Tao, S.A. Hadigheh, S. Saha, Y. Wei, Pulverised CFRP waste and reclaimed carbon fibre for cement-based sensors: Investigating electrical resistivity and piezoresistivity under varying environmental conditions, Constr. Build. Mater. 470 (2025) 140516.
   DOI: https://doi.org/10.1016/j.conbuildmat.2025.140516

Y. Tao: Writing – original draft, Visualization, Validation, Software, Methodology, Investigation, Formal analysis, Data curation. **S.A. Hadigheh:** Writing – review & editing, Validation, Supervision, Resources, Project administration, Methodology, Visualization, Funding acquisition, Data curation, Conceptualization. **S. Saha:** Visualization, Validation, Software, Methodology, Investigation, Formal analysis, Data curation. **Y. Wei:** Software, Methodology, Investigation, Data curation.

The conference papers the candidate contributed to or presented are listed below:

1. Y. Tao, S.A. Hadigheh, S. Saha, Y. Wei, Smart Self-sensing Mortar with Recycled Fillers, Ninth Asia-Pacific Conference on FRP in Structures (APFIS 2024), Adelaide, Australia, 2024.

Y. Tao: Writing – original draft, Visualization, Validation, Software, Methodology, Investigation, Formal analysis, Data curation. **S.A. Hadigheh:** Writing – review & editing, Validation, Supervision, Resources, Project administration, Methodology, Visualization, Funding acquisition, Data curation, Conceptualization. **S. Saha:** Visualization, Validation, Software, Methodology, Investigation, Formal analysis, Data curation. **Y. Wei:** Software, Methodology, Investigation, Data curation.

2. Y. Tao, S.A. Hadigheh, Evaluation of the effect of FRP composite waste on mechanical and microstructural behaviour of cementitious mortar. The 8th Conference of the Combined Australian Materials Societies (CAMS 20224), Adelaide, Australia. 2024.
3. Y. Tao, S.A. Hadigheh, An Experimental Investigation on Mechanical Properties and Microstructures of Mortar Incorporated with Recycled Fibre-reinforced Polymer (rFRP) Composite Waste, in: A. Ilki, D. Çavunt, Y.S. Çavunt (Eds.) Building for the Future: Durable, Sustainable, Resilient, Springer Nature Switzerland, Cham, 2023, pp. 524-535.
4. Y. Tao, S.A. Hadigheh, Drying shrinkage, water absorption and electrical behaviour of mortar reinforced with polymer fibres, The 26th Australasian Conference on Mechanics of Structures and Materials (ACMSM26), Auckland, New Zealand, 2023.

For these three conference papers: **Y. Tao:** Writing – original draft, Visualization, Validation, Software, Methodology, Investigation, Formal analysis, Data curation. **S.A. Hadigheh:** Writing – review & editing, Visualization, Validation, Supervision, Resources, Project administration, Methodology, Funding acquisition, Data curation, Conceptualization.

5. Y. Tao, S.A. Hadigheh, David J. Hayne, B. Newman, L.C. Henderson, Eco-friendly surface modification of carbon fibres for application in cement-based composites, 21th European Conference on Composite Materials, Nantes, Paris, 2024.

Y. Tao: Writing – original draft, Visualization, Validation, Software, Methodology, Investigation, Formal analysis, Data curation. **S.A. Hadigheh:** Writing – review & editing, Visualization, Validation, Supervision, Resources, Project administration, Methodology, Funding acquisition, Data curation, Conceptualization. **D.J. Hayne:** Writing – review & editing, Methodology. **Ben Newman:** Writing – review & editing, Methodology. **L.C. Henderson:** Writing – review & editing, Visualization, Resources, Methodology.

6. Z. Huang, S.A. Hadigheh, Y. Tao, The development of sustainable and durable composite anodes for cathodic corrosion protection in bridges. Ninth Asia-Pacific Conference on FRP in Structures (APFIS 2024). Adelaide, Australia. 2024.

Y. Tao: Methodology, Writing – review & editing. **Z. Huang:** Writing – original draft, Visualization, Validation, Software, Methodology, Investigation, Formal analysis, Data curation. **S.A. Hadigheh:** Writing – review & editing, Visualization, Validation, Supervision, Resources, Project administration, Methodology, Funding acquisition, Data curation, Conceptualization.

In addition to the authorship attribution statements above, in cases where I am not the corresponding author of a published item, permission to include the published material has been granted by the corresponding author.

Yunyun Tao, 05 June 2025

As supervisor for the candidature upon which this thesis is based, I can confirm that the authorship attribution statements above are correct.

Dr S. Ali Hadigheh, 05 June 2025

Abstract

Fibre-reinforced polymer (FRP) composites are widely adopted across various industries due to their high strength-to-weight ratio, resistance to environmental degradation, and manufacturing flexibility. The growing demand for FRP composites from different sectors has generated significant waste streams over the past few decades, both from industrial manufacturing processes and end-of-life (EoL) products. FRP composites present substantial environmental challenges due to their non-biodegradable nature, complex composition, and highly crosslinked thermoset matrices, which make them inherently resistant to natural decomposition processes. Current major waste disposal practices for composites include incineration and landfill, both of which are not sustainable solutions. These methods release harmful emissions into the atmosphere, pollute soil and water sources, and contribute to the growing problem of waste accumulation. Consequently, there is a pressing need to develop sustainable recycling strategies to mitigate these adverse environmental impacts and enable efficient resource recovery, aligning with the principles of a circular economy.

The increasing awareness of environmental sustainability has led to extensive research into recycling FRP wastes in recent years. Recycling and repurposing thermoset FRP composites is primarily achieved through three main routes, which are mechanical, thermal, and chemical methods, which constitute the majority of current industrial practices. Although recycled fibres can be reclaimed through these recycling strategies and used in composite re-manufacturing, their degraded mechanical properties, reduced fibre length and high recycling costs limit their feasibility in high-performance applications. To address these challenges and offer an alternative solution, this research provides a viable strategy for large-scale waste management through the repurposing of FRP waste in cementitious composites (CCs) applications. The research projects presented in this thesis consist of experimental and numerical studies on incorporating carbon and glass fibre-reinforced polymer (CFRP & GFRP) composite wastes into cementitious matrices and developing innovative methods for characterising and enhancing the performance of fibre-reinforced cementitious composites (FRCC).

The thesis begins with a comprehensive literature review on the recycling and repurposing of FRP composite wastes, followed by chapters presenting the research work and findings. Two types of FRP composite waste that are repurposed into CC are fabric

reinforcement offcuts and industrial FRP composite waste. These recyclates undergo either mechanical or chemical recycling processes before their incorporation into CC. In the first part of this thesis, the effects of carbon and glass fibre (CF & GF) with different contents on the performance of CCs are studied through a comprehensive testing program that includes physical and mechanical testing, durability testing, and microstructural analysis. Void geometry analyses of these composites are conducted using micro-computed tomography (micro-CT), and their influences on the performance of the CCs are discussed. The examination of the internal microstructure of composites is crucial for understanding their performance. To enable the detection of CFs in cementitious matrices and address the current challenges of low phase contrast and image noise, novel image processing filters have been developed for micro-CT analysis, along with a comparative assessment using ultrasonic testing (UT). This investigation contributes to the advancement of non-destructive testing (NDT) methods for detecting and characterising multi-scale features in cementitious matrices.

To address industry challenges, specifically the hydrophobic surface of CFs that leads to increased CF agglomeration and weak interfacial bonding with the cementitious matrix, innovative CF surface modification strategies have been developed. These strategies include bio-based and electrochemical treatments, both aimed at improving the performance of FRCC in construction applications. The alternations of CFs before and after treatments are examined by a series of tests, including surface morphology analysis, chemical characterisations and tensile testing. The enhanced interfacial bonding properties and mechanical strength between functionalised CFs and the cementitious matrices are quantitatively investigated. The results demonstrate successful new strategies for sustainable and efficient CF surface modifications and their potential application in the construction industry.

The second part of this thesis transitions from focusing on CCs with fibres to developing new methods for recycling industrial composite waste in CCs. The viability of pulverising and repurposing FRP composite waste from electrical cross-arms and aerospace composite parts as a partial substitute for cement in cementitious is confirmed. The recycling method includes a two-step mechanical size reduction process for FRP waste without resin removal. Physical properties, mechanical properties, durability and electrical properties of the resulting CCs are evaluated. The inclusion of FRP recyclates resulted in a denser microstructure, a reduction in drying shrinkage, and a significant improvement in mechanical strength.

This research also investigates the self-sensing capacity of cement-based sensors incorporating mechanically recycled CFRP and CF, as well as chemically reclaimed CF waste,

for structural health monitoring (SHM). The electrical resistivity and piezoresistive performance of these composites are evaluated under various environmental conditions, including chloride-induced corrosion. During the corrosion process, electrochemical performance is monitored and analysed to assess the impact of chloride ingress and corrosion on the CCs embedded with steel mesh. The findings demonstrate the effectiveness of utilising recycled CFRP (rCFRP) to develop CCs that mitigate steel corrosion. The results also highlight the potential of rCFRP-based cementitious sensors for SHM applications, particularly in aggressive marine environments.

This work contributes to developing alternative strategies for managing FRP composite waste by integrating it into CCs, rather than the currently unsustainable waste disposal methods. Recycling and repurposing FRP composite waste into CCs presents an effective and eco-friendly approach to mitigate environmental impacts while transforming waste into valuable resources for construction applications. This process reduces the reliance on natural resource extraction and offers both economic and social benefits. In addition to improved mechanical and durability, the incorporation of recyclates also enhances the multifunctionality of CCs, expanding their potential applications. The findings of this research are expected to advance current FRP waste management strategies and promote the repurposing of recyclates in the construction industry, contributing to more sustainable, cost-effective and socially beneficial solutions.

Table of Contents

List of Figures

List of Tables

Chapter 1: Introduction

1.1 BACKGROUND AND MOTIVATION

Fibre-reinforced polymer (FRP) composites have been extensively utilised across various industries, including construction, aerospace, renewable energy, and marine sectors [1]. With their unique features of high strength-to-weight ratio, corrosion resistance and manufacturing flexibility, the demand for FRP composites is rapidly increasing [2, 3]. Specifically, due to the outstanding performance of carbon and glass fibre-reinforced polymer (CFRP & GFRP) composites, the market demand for these two types of FRP composites is increasing [2]. However, the high-volume production and utilisation of FRP materials have led to a significant increase in composite waste generation. The waste arises both during the manufacturing process (scraps) and from end-of-life (EoL) products. By 2050, the annual accumulation of CFRP waste from industries such as aerospace and renewable energy is projected to surge to 840,300 tonnes [4]. Moreover, waste carbon fibres (CFs) alone are estimated to reach 263,000 tonnes by 2030 [5]. Similarly, GFRP, a primary material used in wind turbine blades, is expected to generate approximately 100,000 tonnes of waste annually by 2030 [6]. The non-biodegradable nature of these composites presents a substantial environmental challenge, emphasising the urgent necessity for sustainable waste management and recycling practices to mitigate their negative impact. Current methods for managing FRP waste, such as incineration and landfill disposal, continue to pose considerable threats to the environment and ecosystem [7-9]. Consequently, developing effective solutions for FRP disposal is essential to address these challenges and promote resource recovery within a circular economy framework.

Over the last decade, increasing awareness of sustainability has driven researchers to focus on recycling and reusing FRP wastes. Promising methods for recycling thermoset FRP composites can be categorised into three primary approaches: mechanical, thermal, and chemical techniques, which collectively account for approximately 80% of the current recycling methods [8, 10]. Mechanical recycling provides an optimal capacity for waste disposal and a lower environmental impact, while it is constrained by the production of low-grade fibres [6]. Conversely, thermal and chemical recycling methods yield recycled fibres with superior mechanical performance. Hadigheh et al. [11] demonstrated an optimised pyrolysis process for recycling CF from CFRP composite waste through a controlled two-stage decomposition reaction. This effective method produces clean recycled CFs with minimal

surface damage, thereby preserving their mechanical properties and enhancing their potential for reuse. According to a review conducted by Rani et al. [12] on the recycling and reuse methods for CF/GF composite wastes from wind turbine blades, thermal recycling is not ideal for recovering GF due to the significant reduction in mechanical strength caused by heat treatment, even though it can be used for CF recovery. Additionally, GF is a low-cost material, making energy-intensive processes such as pyrolysis and fluidised bed techniques less economically viable for GF recovery. The chemical approach offers an alternative for reclaiming CF and GF from composites with an emphasis on sustainable and green chemistry. Ongoing research is focused on developing methods that operate at lower temperatures and pressures [13]. Furthermore, Wei and Hadigheh [14] developed an effective hybrid recycling approach for the recovery of CFRP waste, which incorporated a chemical method for pre-treatment prior to thermal degradation. This optimised method can retain up to 90.53% of the tensile strength of the virgin carbon fibres (vCFs), and the treatment was validated in real-world applications.

In addition to the strategies that recover fibres from the polymer matrix for reuse in the polymer industry, repurposing these wastes for alternative applications is also an efficient strategy for managing large-scale waste disposal. As an example, cement co-processing is a lower-emission and resource-efficient strategy where the mineral component of GFRP waste serves as clinker, while the organic polymer matrix is used as fuel. Although it is not the most cost-effective option, it is preferred over incineration and landfill [15]. Recently, there has been growing research on incorporating FRP waste in the construction field, which addresses environmental, economic, and performance challenges. Researchers have been actively developing various methods to repurpose industrial FRP wastes into CCs in different forms, including fillers, fibre reinforcement, and replacements for cement or aggregates [10, 16, 17]. Adopting the appropriate amount of FRP recyclates for incorporation into cementitious composites (CCs) can effectively enhance the performance of CCs, with improvements observed in compressive strength, splitting tensile strength, flexural properties, and other related characteristics [10, 18]. Meanwhile, this approach supports sustainable construction practices by reducing the need for raw material extraction and production. The use of either micro or macro fibre reinforcement has the potential to minimise the reliance on traditional rebars in steel-reinforced concrete (RC) structures. In this context, the incorporation of recycled FRP waste into CCs is anticipated to offer benefits similar to those observed in well-known fibre-reinforced cementitious composites (FRCCs), where discrete fibres provide a bridging

effect that limits crack formation, controls shrinkage and improves mechanical properties. Additionally, carbon-FRCCs are also utilised as cement-based sensors in structural health monitoring (SHM) by forming a conductive network within the composites [19-23].

1.2 RESEARCH GAP

Building on the background and motivation, despite there is growing interest in incorporating recycled FRP composite waste into CCs, certain research gaps remain in several key areas. The comprehensive review of FRP waste performance in CCs, including cost-benefit analysis and life cycle assessment remains underdeveloped. Current research is also limited regarding the durability of CCs containing short fibres, particularly in understanding microstructural and porosity changes. While non-destructive testing (NDT) methods can examine internal structures, both micro-computed tomography (micro-CT) and ultrasonic array (UA) imaging face significant challenges in distinguishing CFs and defects within the cement matrix. Furthermore, the presence of sizing agents on commercial CFs hampers their direct incorporation into cementitious materials, limiting their potential performance benefits. On the other hand, although some studies have explored recycling CFRP and GFRP waste in CCs, practical implementation remains limited. Contradictory results necessitate further detailed research on a case-by-case basis. In addition, exploring these CCs for multipurpose applications also remains an important area for future investigation. Additional investigation is needed regarding the chloride-corrosion resistance and self-sensing capabilities of steel-reinforced CCs incorporating CFRP waste.

1.3 RESEARCH SCOPE AND OBJECTIVES

The goal of this research is to comprehensively assess the feasibility and evaluate the influences of incorporating fabric reinforcement offcuts and industrial FRP composite waste into cementitious mortars. To advance this field, this research aims to optimise fibre-matrix interactions through innovative fibre surface modification techniques. Furthermore, enhanced NDT are being developed for accurate internal structure characterisation. This study also explores the multifunctional performance including self-sensing capacities and corrosion resistance of steel-reinforced CCs. The research is structured in stages, with the following specific objectives:

1. Chapter 2 –

- To provide a comprehensive literature review on the recycling and repurposing of both CFRP and GFRP composite wastes in CCs,
- To review the design, measurement and performance of cement-based sensors incorporating CF and CFRP wastes for SHM applications, and
- To review the current CF surface modification strategies for enhancing FRCC performance.

2. Chapter 3 –
    - To conduct a comprehensive investigation into the effects of incorporating short CF and GF into cementitious mortar on its multifaceted characterisation, including acid diffusion, water absorption, drying shrinkage and electrical resistivity measurement,
    - To conduct a void geometry analysis and examine its influence on FRCC multifaceted performance,
    - To develop and apply novel image processing filters for X-ray micro-CT analysis of carbon-FRCC, and
    - To compare and discuss the practical advantages and limitations of micro-CT scanning versus ultrasonic testing (UT).
3. Chapter 4 –
    - To develop effective CF surface modification methods to enhance interfacial fibre-matrix bond strength, and
    - To evaluate the effectiveness of these surface modifications, focusing on fibre-matrix interfacial bonding strength, and the fresh, physical, compressive, and flexural properties of the resulting composites.
4. Chapter 5 –
    - To develop sustainable waste recycling practices for the utility and aerospace sectors by incorporating mechanically recycled FRP into construction materials, and
    - To investigate the effects of incorporating CFRP and GFRP recyclates on the fresh, physical, mechanical and electrical properties of the resulting CCs.

5. Chapter 6 –

   - To investigate the viability of the self-sensing ability of CFRP waste-incorporated FRCCs,
   - To study the influence of CF & CFRP recyclates on the electrical resistivity and piezoresistivity of CCs under varying temperatures, humidity and chloride-induced corrosion, and
   - To examine the effects of repurposing CF & CFRP recyclates on the corrosion resistance and electrochemical properties of steel mesh-embedded CCs.

1.4 RESEARCH FRAMEWORK AND OUTLINE OF THE THESIS

This thesis consists of seven chapters. The current chapter (Chapter 1) provides the background, motivation and research gaps, and identifies the research objectives this study aims to address. The remaining chapters are organised as follows:

Chapter 2 presents the literature review, which primarily provides an overview of integrating FRP wastes, such as recycled CFRP/ GFRP (rCFRP/ rGFRP) and recycled CF/ GF (rCF/ rGF), into cementitious materials. Given that past research on the performance of recycled GFRP wastes into CCs has not been compiled, this chapter begins by providing a comprehensive investigation into the influences of GFRP waste incorporation on the properties of fresh concrete/mortar, mechanical properties, durability mechanisms, as well as environmental and financial aspects. Based on the existing review of utilising CFRP waste in CCs, this chapter then transitions to examining the incorporation of CFRP waste on the properties of concrete and mortar. Particular attention is given to their contribution to electrical properties for potential self-sensing ability and addressing durability concerns in relation to steel corrosion. This chapter also explores existing CF surface modification techniques for enhancing the performance of FRCCs. Different modification strategies are evaluated, and their effectiveness is examined.

Chapter 3 presents a comprehensive experimental investigation into the physical, durability, and electrical properties of FRCC. The study begins by evaluating the durability and internal microstructure of CCs incorporating short fibre offcuts, aiming to demonstrate their viability for construction applications. It also includes numerical studies on the acid diffusion process within these materials. The numerical studies in this chapter also cover the development and application of computational algorithms for micro-CT analysis. This chapter consists of

two major contributions: (i) Multifaceted characterisation of cementitious mortar with CFs and GFs, focusing on how the incorporation of additional fibres affects the void geometry distribution (e.g., elongation and eccentricity) within FRCC, and how these influences reflect on acid diffusion, water absorption, mechanical strength and drying shrinkage of FRCC; and (ii) Development and application of the Anisotropic Gaussian filtering in X-ray micro-CT analysis tailored for detecting CF features in the CC. To address the limitations and high costs of X-ray micro-CT, this chapter also investigates the application of the Total Focusing Method (TFM) ultrasonic technique, with post-processed TFM imaging results validated against advanced micro-CT analysis.

Chapter 4 builds upon the findings of Chapter 3 by addressing a critical challenge: the increased presence of elongated voids between CFs and the cementitious matrix, primarily due to the inherently hydrophobic nature of the CF surface. This characteristic results in a weak fibre-matrix interface and poor fibre dispersion, both of which significantly compromise the performance of FRCC. To address this issue, this chapter proposes two novel types of CF surface modifications (bio-based treatments and electrochemical grafting methods) to enhance fibre-matrix interfacial bonding strength, as well as the fresh, physical, compressive, and flexural properties of carbon-FRCC. To examine the successful application of these methods individually, chemical and physical surface characteristics of CFs are evaluated to elucidate the underlying alterations, including attached functional groups and increased surface roughness. Better fibre-matrix interaction is demonstrated by fibre pullout testing and microstructural examination. As a result, enhanced mechanical strengths (e.g., compressive and flexural strength) with denser microstructures are observed in all FRCC specimens with functionalised CFs using the proposed surface modification methods. Both surface modification methods demonstrate their distinct advantages in this field. Bio-based treatments provide a gentle and environmentally friendly alternative to conventional chemical treatments, making them a continuously active area of research interest. Meanwhile, in-situ electrochemical grafting techniques demonstrate their high efficacy for CF modification, leading to outstanding FRCC mechanical performance.

Chapter 5 extends this line of research into the realm of sustainability by introducing a strategy for incorporating recycled FRP (rFRP) wastes into cementitious materials. This approach demonstrates the repurposing of GFRP and CFRP composite waste from the utility and aerospace sectors through a two-step pulverisation process for size reduction. The chapter evaluates the mechanical, physical, durability, and electrical properties of CCs incorporating

these recycled FRPs. Additionally, a microstructural analysis was conducted to evaluate the physical and chemical alterations at varying dosages of CFRP/GFRP replacements in cement-based mortar. The findings offer valuable insights into the re-utilisation of waste materials from various industries in construction, contributing to sustainable development efforts.

Chapter 6 leverages both the recycled materials and electrical properties of CFs, as highlighted in the previous chapters, to explore the development of multifunctional cement-based sensors. These sensors incorporate pulverised CFRP waste and both mechanically and chemically reclaimed CFs. Firstly, this chapter discusses how these recyclates influence the corrosion resistance and electrochemical properties of stainless-steel mesh-embedded CCs when exposed to a simulated marine environment. The study then evaluates their effect on the electrical resistivity and piezoresistivity of CCs under varying conditions, including different temperatures, humidity, and chloride-induced corrosion exposure. The findings demonstrate the effectiveness of utilising rCFRP/rCF to develop CCs that mitigate steel corrosion and highlight the potential of rCFRP/rCF-based cementitious sensors for SHM applications, particularly in aggressive marine environments.

Chapter 7 summarises the major research findings and presents the key conclusions. Additionally, it provides recommendations for future research directions.

The thesis structure is briefly illustrated in Figure 1-1.

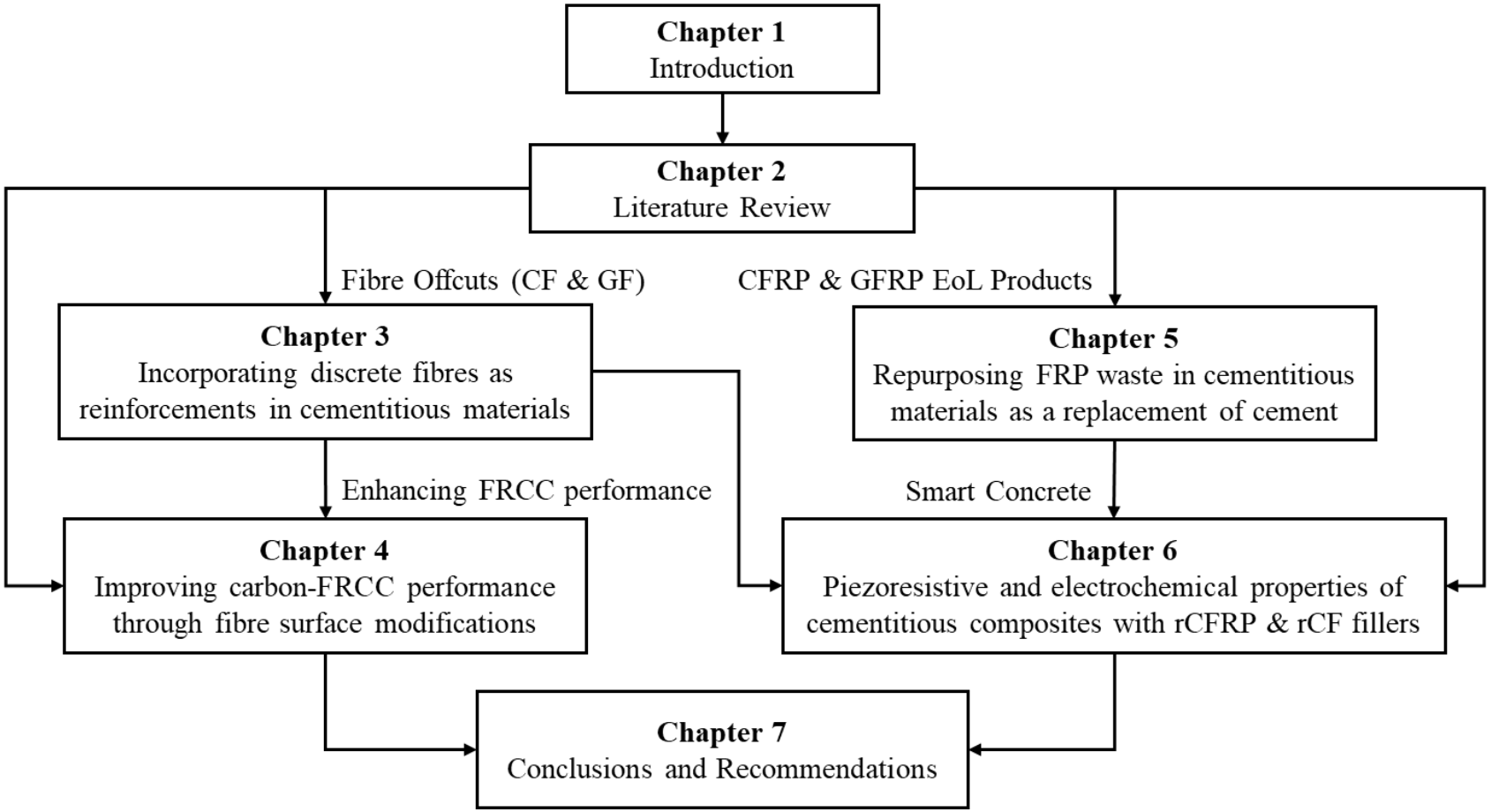

Figure 1-1. Outline of this thesis.

1.5 REFERENCES

[1] S.A. Hadigheh, F. Ke, S. Kashi, 3D acid diffusion model for FRP-strengthened reinforced concrete structures: Long-term durability prediction, Constr. Build. Mater. 261 (2020) 120548.

[2] S.K. Gopalraj, T. Kärki, A review on the recycling of waste carbon fibre/glass fibre-reinforced composites: fibre recovery, properties and life-cycle analysis, SN Appl. Sci. 2(3) (2020) 1-21.

[3] S.A. Hadigheh, S.S. Mahini, S. Setunge, S.A. Mahin, A preliminary case study of resilience and performance of rehabilitated buildings subjected to earthquakes, Earthq. Struct. 11(6) (2016) 967-982.

[4] The looming 840,000 tonne waste problem that isn't single-use plastics, 2023. https://www.sydney.edu.au/news-opinion/news/2023/07/03/-the-looming-840-000-tonne-waste-problem-that-isn-t-single-use-p.html#:~:text=The%20annual%20accumulation%20of%20CFRP,to%20landfill%20or%20is%20incinerated.

[5] Y. Wei, S.A. Hadigheh, Enhancing carbon fibre recovery through optimised thermal recycling: Kinetic analysis and operational parameter investigation, Materials Today Sustainability 25 (2024) 100661.

[6] Y. Wei, S.A. Hadigheh, Cost benefit and life cycle analysis of CFRP and GFRP waste treatment methods, Constr. Build. Mater. 348 (2022) 128654.

[7] J. Zhang, V.S. Chevali, H. Wang, C.-H. Wang, Current status of carbon fibre and carbon fibre composites recycling, Compos. B. Eng. 193 (2020) 108053.

[8] A.E. Krauklis, C.W. Karl, A.I. Gagani, J.K. Jørgensen, Composite material recycling technology—state-of-the-art and sustainable development for the 2020s, J. Compos. Sci. 5(1) (2021) 28.

[9] S. Hadigheh, Y. Wei, S. Kashi, Optimisation of CFRP composite recycling process based on energy consumption, kinetic behaviour and thermal degradation mechanism of recycled carbon fibre, J. Clean. Prod. 292 (2021) 125994.

[10] A. Danish, M.A. Mosaberpanah, M.U. Salim, M. Amran, R. Fediuk, T. Ozbakkaloglu, M.F. Rashid, Utilization of recycled carbon fiber reinforced polymer in cementitious composites: A critical review, J. Build. Eng. 53 (2022) 104583.

[11] S.A. Hadigheh, Y. Wei, S. Kashi, Optimisation of CFRP composite recycling process based on energy consumption, kinetic behaviour and thermal degradation mechanism of recycled carbon fibre, J. Clean. Prod. 292 (2021) 125994.

[12] M. Rani, P. Choudhary, V. Krishnan, S. Zafar, A review on recycling and reuse methods for carbon fiber/glass fiber composites waste from wind turbine blades, Compos. B. Eng. 215 (2021) 108768.

[13] O. Zabihi, M. Ahmadi, C. Liu, R. Mahmoodi, Q. Li, M.R. Ghandehari Ferdowsi, M. Naebe, A Sustainable Approach to the Low-Cost Recycling of Waste Glass Fibres Composites towards Circular Economy, Sustainability, 2020.

[14] Y. Wei, S.A. Hadigheh, Development of an innovative hybrid thermo-chemical recycling method for CFRP waste recovery, Compos. B. Eng. 260 (2023) 110786.

[15] D. Peter, J.N. Angela, G. Fergal, L. Heloisa, L.D. Emma, M.M. Jennifer, G. Conor, G.L. Paul, P.D. Niall, M. Gerard, End-of-Life alternatives for wind turbine blades: Sustainability Indices based on the UN sustainable development goals, Resour. Conserv. Recycl. 171 (2021) 105642.

[16] A. Yazdanbakhsh, L.C. Bank, A Critical Review of Research on Reuse of Mechanically Recycled FRP Production and End-of-Life Waste for Construction, 6(6) (2014) 1810-1826.

[17] C.-S. Cheng, Y.-B. Xu, C.-Y. Xiao, B. Fu, R.-F. Gao, Y.-D. Kuang, Behavior of confined concrete with recycled glass fiber-reinforced polymer needles as coarse aggregates under axial compression, J. Build. Eng. 71 (2023) 106453.

[18] B. Fu, K.C. Liu, J.F. Chen, J.G. Teng, Concrete reinforced with macro fibres recycled from waste GFRP, Constr. Build. Mater. 310 (2021) 125063.

[19] J. Donnini, T. Bellezze, V. Corinaldesi, Mechanical, electrical and self-sensing properties of cementitious mortars containing short carbon fibers, Journal of Building Engineering 20 (2018) 8-14.

[20] A. Belli, A. Mobili, T. Bellezze, F. Tittarelli, Commercial and recycled carbon/steel fibers for fiber-reinforced cement mortars with high electrical conductivity, Cem. Concr. Compos. 109 (2020) 103569.

[21] L. Wang, F. Aslani, Mechanical properties, electrical resistivity and piezoresistivity of carbon fibre-based self-sensing cementitious composites, Ceramics International 47(6) (2021) 7864-7879.

[22] B. Han, L. Zhang, C. Zhang, Y. Wang, X. Yu, J. Ou, Reinforcement effect and mechanism of carbon fibers to mechanical and electrically conductive properties of cement-based materials, Constr. Build. Mater. 125 (2016) 479-489.

[23] L. Deng, Y. Ma, J. Hu, S. Yin, X. Ouyang, J. Fu, A. Liu, Z. Zhang, Preparation and piezoresistive properties of carbon fiber-reinforced alkali-activated fly ash/slag mortar, Constr. Build. Mater. 222 (2019) 738-749.

Chapter 2: Literature Review

2.1 INTRODUCTION

CCs are widely recognised as the preferred construction material in civil engineering due to their excellent mechanical properties, durability, and cost-effectiveness. However, their continuous consumption and extensive use pose significant environmental challenges. Cement production contributes to over 7% of total global carbon emissions [1, 2]. Additionally, sand and gravel, which make up approximately 70% of CCs by volume, lead to the depletion of natural resources, negative impacts on ecosystems, and carbon dioxide emissions [3]. Concurrently, the growing production and use of thermoset composites, particularly CFRP and GFRP composites, from various industries also present environmental concerns. These advanced composites offer distinct advantages such as high strength-to-weight ratio and corrosion resistance. Nevertheless, their non-biodegradable nature and complex chemical structure complicate recycling and safe disposal. According to statistics, worldwide CFRP waste accumulation from the commercial aeronautical sector is projected to exceed 500 thousand tons by the year 2050 [4]. Wind turbine blades, predominantly manufactured from GFRP, will accumulate approximately 40 million tons of waste worldwide by 2050 [5].

To address these issues and promote sustainable development in construction, extensive research has been conducted into recycling and reusing FRP waste in cementitious materials as an alternative application. While economic considerations remain, the primary factor influencing the future of thermoset composite recycling, the key to making this process viable lies in developing cost-effective repurposing strategies and maximising the value potential of these recyclates [6]. The incorporation of FRP waste into CCs (concrete and mortar) represents a promising solution that not only addresses environmental and waste management challenges but also has the potential to enhance the performance of these materials, hence providing both environmental and economic benefits.

This chapter presents a literature review of existing FRP recycling strategies, with a focus on their repurposing in CCs. It discusses the separate incorporation of GFRP and CFRP into CCs to explore the effects on their properties. Furthermore, the chapter delves into the development of innovative cement-based sensors for structural health monitoring (SHM) that incorporate CFRP and CF recyclates. Different surface modification techniques for CFs are also introduced in this chapter as critical strategies to enhance the interfacial bonding between

fibres and cementitious matrices. This enhancement is essential for developing CCs with high mechanical performance for advanced structural applications. This chapter is organised into three main sections. Section 2.2 presents a published journal review paper on the topic of recycling GFRP composite wastes in concrete. Section 2.3 presents a comprehensive review of studies investigating the repurposing of CFRP composite wastes into CCs. Section 2.4 analyses the existing knowledge and literature on CF surface modification techniques that have been developed for enhanced FRCC.

2.2 RECYCLING OF GLASS FIBRE REINFORCED POLYMER (GFRP) COMPOSITE WASTES IN CONCRETE: A CRITICAL REVIEW AND COST BENEFIT ANALYSIS

Y. Tao[1], S.A. Hadigheh[1,*], Y. Wei[1]

[1]School of Civil Engineering, Faculty of Engineering, The University of Sydney, Sydney, New South Wales 2006, Australia

[*]Corresponding Author: Dr Ali Hadigheh

Structures, https://doi.org/10.1016/j.istruc.2023.05.018, Published in May 2023.

2.2.1 Abstract

The application of fibre reinforced polymer (FRP) composites has increased substantially in recent years as a result of need for lighter and stronger materials. Currently, the reuse and/or recycling of composite wastes is very limited while most of wastes are disposed of in landfill or incinerated. Recently, mechanical recycling, fluidised bed, and pyrolysis has been developed to recycle FRP composites, but yet to be fully commercialised. As an alternative recycling strategy, incorporating glass fibre reinforced polymer (GFRP) into concrete has shown a great potential from both economic and environmental perspectives. This paper systematically reviews the performance of recycling of GFRP wastes into concrete with respect to fresh properties, mechanical properties, durability, environmental and financial aspects. Results show that the effect of recycled glass fibre reinforced polymer (rGFRP) on concrete mechanical strength is associated with the content of waste material (fibre or resin rich) and physical properties (shape, density, hydrophilicity) of GFRP recyclates, as well as the amount of recyclates. For rGFRP powder, the filler effect combined with the pozzolanic reaction can improve interfacial transition zone strength, increasing mechanical strength. Recycled glass fibre has reinforcing effect to restraint cracks and can provide extra slip resistance to strengthen the bond, resulting in improvement of flexural strength. Recycling of GFRP waste in concrete reduces water absorption of the concrete, improving durability properties. Furthermore, this research presents outcomes of cost-benefit analysis and benefit-cost ratio on five common GFRP recycling methods. The results show that repurposing rGFRP in concrete can reduce the total required investment and increase net profit. Recommendations and future perspectives are also provided to allow a wider adoption of rGFRP repurposing from industrial waste and the development of a more sustainable life cycle.

Keywords: Glass fibre-reinforced polymer (GFRP); Concrete; Recycling; Durability; Cost-benefit analysis (CBA); Sustainability.

2.2.2 Introduction

Due to the advantageous characteristics of high strength-to-weight ratio, resistance to corrosion and unprecedented flexibility, fibre-reinforced polymer (FRP) composites have been utilised in more industries than ever before, such as transportation, aerospace, marine and construction industries [7]. As the market for FRP composites rapidly grows, a substantial amount of composite waste is generated through the high-volume production and consumption of FRP materials [8, 9]. More than two million metric tonnes of glass FRP (GFRP) wastes are projected to be created annually in the United States from both residues from the production process and end-of-life (EoL) products [10]. The United Nations (UN) has defined 17 Sustainable Development Goals (SDGs), with promoting sustainable construction industry activities being an essential component of Goal 11: Sustainable cities and human settlements. Recycling and repurposing waste in the building industry are directly related to this subject and could contribute to achieving the target by 2030, as planned in the agenda [11]. Therefore, developing strategies for recycling and repurposing FRP composites is crucial for mitigating the negative environmental and ecological consequences of landfilling and incineration. By implementing such strategies, the construction industry can move towards more sustainable practices, in line with the goals set out by the UN [12-14].

FRP composites are anisotropic materials, composed of a resin matrix and fibre reinforcement. Depending on the constituent materials, carbon, glass, aramid and basalt fibre reinforced polymer (CFRP, GFRP, AFRP, and BFRP) are recognised as four main FRP composites in the civil engineering industry. Due to the outstanding characteristics of GFRP and CFRP composites, the market demand for these two composite materials is remarkably high. GFRP composites dominate the composite market (a market share of over 95%), with glass fibres accounting for 65% of the profits produced by FRP material sales [13, 15]. Considering high mechanical and superior durability performance of CFRP, these composites are commonly used for high-performance applications in aerospace, automobiles and structural strengthening [16-19]. The significant growth of the global demand for CFRP has increased from 50 kilo tonnes in 2010 to more than 160 kilo tonnes in 2020 [20].

The need for composite recycling solutions has recently become more urgent in automotive, renewable energy and aerospace sectors. Instead of landfill and incineration, FRP

composites can be recycled through mechanical, thermal and chemical recycling techniques. Chemical and thermal recycling methods are mainly used to reclaim carbon fibre from the CFRP due to the higher price of virgin carbon fibre (vCF) [13, 14]. The amount of EoL wind turbine blades has continuously increased due to the designed service-life of 20 years and the growing demand for renewable energies [13]. Since GFRP is the major component of wind turbine blades and has non-biodegradable characteristics, it is critical to properly manage these composite wastes. In the case of GFRP recycling strategies, low-cost recycling methods are utilised due to the lower price of virgin glass fibres (vGF) [13, 15, 18]. Currently, mechanical recycling is a feasible approach to recycle GFRP composites with reduced energy consumption and cost, despite the recyclate is discontinuous and cannot be used as high-value products [8, 21, 22]. Thus, developing an alternative way to efficiently utilise GFRP composite wastes has attracted increasing interests worldwide.

A viable option to utilise mechanically recycled GFRP composites is to incorporate GFRP recyclates into concrete (named repurposing GFRP waste in concrete in this paper) in the forms of powder, fibre and aggregate [15, 21]. Recycled GFRP elements are mixed in concrete as a partial replacement of fine and coarse aggregate, or as a reinforcing element. This alternative repurposing approach has the potential to be a long-term and sustainable solution for managing the growing GFRP wastes by reducing environmental impacts of waste composites. There have been some efforts to commercialise rGFRP in concrete since the last decade. Currently, the commercially viable solutions include precast concrete blocks, manhole module, and railway sleepers [23-25].

The application of recycled fibre-reinforced polymer (rFRP) composites, which are made from recycled carbon fibre-reinforced polymer (CFRP) and glass fibre-reinforced polymer (GFRP) wastes, in the construction sector is an area of research that is expanding. Although recent investigations have been conducted on the effect of recycling GFRP waste in concrete, past research findings have not been compiled and systematically analysed. To the authors' knowledge, while there are reviews on the reuse of mechanically recycled FRP waste in cementitious materials for construction, no existing review articles have been published that specifically focus on the performance of repurposing GFRP composite waste in concrete, as well as the cost-benefit and life cycle analysis of recycling pathways. A systematic review that includes all key concrete characteristics, as well as the economic and environmental issues of repurposing rGFRP in concrete, is needed to fill this gap in the literature. Thus, a critical review of the literature will be especially valuable in synthesising research findings to provide robust

guidelines for waste treatment selection and market outlook of GFRP recycling. For this purpose, a review of current recycling methods of FRP composites is briefly presented in Section 2.2.3. Subsequently, the effect of incorporating GFRP waste in concrete with a focus on fresh properties, mechanical properties and durability aspects is discussed in Section 2.2.4. In Section 2.2.5, the cost-benefit analysis (CBA) approach is employed to assess the economic feasibility of five different recycling methods by taking into account the capital investment, operating costs, total benefit and net profit.

2.2.3 FRP composite recycling methods

Recycling of FRP composite at the end of its service life is a feasible alternative to landfilling and incineration, offering several financial and environmental benefits. This section primarily focuses on common FRP recycling methods including mechanical, thermal and chemical recycling techniques.

2.2.3.1 Mechanical recycling

Mechanical recycling is a method that breakdowns FRP wastes into smaller pieces for reuse in new composites or as a pre-recycling process for other techniques [8]. Recycled parts can be produced in various shapes and sizes using cyclones and sieves. Mechanical recycling is one of the most common techniques due to simplicity of the process and low investment requirements. However, loss of mechanical properties and geometrical shape and lower value of the final product affect the widespread use of this method [26]. Recycled fibre recovered by mechanical techniques, such as crushing or milling, cannot maintain high mechanical properties (e.g. 50% reduction in tensile capacity) and fibre integrity (i.e. crushed fibres), resulting in the lack of market competitiveness [27]. Currently, mechanical recycling is commonly employed for GFRP composite due to the lower value of vGF [8].

2.2.3.2 Thermal recycling

Pyrolysis is one of the thermal recycling methods, in which the bond between the matrix and the fibre is broke down in an oxygen-free environment. Compared with mechanical methods, pyrolysis could reclaim longer (around 6-60 mm) and clean fibres from wastes via thermal degradation process. The thermal process must be carefully designed in order to achieve high strength and clean recycled fibre. Hadigheh et al. [14]’s research showed that there is a risk of fibre surface damage due to the application of excessive heat during recycling process. The behaviour of recycled fibres highly depends on the setting of process variables, such as

heating rate, cap temperature, nitrogen (N_2) flow rate, and isothermal dwell time [14]. With accurately designed parameters setting, pyrolysis could achieve carbon fibre with strength up to 90% of virgin carbon fibre. As a result, these reclaimed fibres can be used for high structural elements such as facades, noise absorption walls and pipes [26, 28]. This technique has been commercialised in recent years. The main drawback of pyrolysis in practice is the high risk of uncontrolled chars on recycled fibre and toxic gas (e.g. CO) formation, therefore, additional treatments are required to remove the residues and capture toxic gases.

Fluidised bed (gasification) is also a thermal recycling method, which employs flow stream to transfer the heat to the composite waste placed on the silica sand bed for matrix thermal degradation. High temperature applied during this process can minimise the char formation and recover the energy that is released during combustion of the polymers [29]. In fluidised bed, the decomposition of FRP starts at around 400 °C and higher strength recycled carbon fibre could be obtained under continues or semi-continuous reaction medium flow. The procedure consists of four stages: placing waste composite in the reactor, pumping heated reaction medium to create semi-continuous or continuous flow, cooling product and filtering liquid wastes which passing through a pressure control valve [30]. During gasification, a chemical conversion takes place at the fibre surface, initiating conversion of hydroxyl groups to carbonyl and carboxylic groups [31]. The fibres reclaimed via gasification process have shown significant mechanical property reduction, for example, 33% tensile strength reduction was reported [31]. Similar to pyrolysis, fibres reclaimed via fluidised bed are fluffy with unstable dimensions, makes it difficult to reuse and remanufacture recycled composite [8]. Furthermore, strategies should be put in place to deal with the large amount of waste liquid generated after recycling that can hinder the use of this method in an industrial scale.

2.2.3.3 Chemical recycling

Solvolysis is a process for separating fibres from composites that uses a chemical solvent incorporating catalysts/additives to decompose the matrix bond at a certain pressure and temperature. Solvolysis can be carried out under low temperature and pressure (LTP) or high temperature and pressure (HTP) [32]. Solvolysis at LTP is usually carried out below 200 °C at the atmospheric pressure with reactive solvents such as nitric acid [33]. Although LTP requires longer reaction time and aggressive solvents in the process, it can lead to higher fibre quality after recycling [32]. On the other hand, HTP with super and sub-critical conditions is gaining more popularity since it is more environmentally friendly than the HTP method. According to

Amaral de Oliveira and Goettmann [34]'s research, the optimal design for recycling CFRP waste with the maximum resin degradation is to use acetic acid as the solvent and hydrochloric acid as the catalyst at 180°C under autogenous pressure. The solvolysis recycling for GFRP composite is currently being investigated on a small scale [35-37]. To recycle GFRP wind turbine blades, a two-step solvolysis method was adopted, which included heating GFRP waste at 270 °C in ethylene glycol for 16 hours, and subsequently heating at 330 °C in water/1-propanol/KOH for 3 hours [36]. Further research is needed to achieve the commercial status for solvolysis-based recycling of End-of-Life wind turbine blades.

2.2.4 Repurposing GFRP waste in cementitious materials

Repurposing GFRP waste in cementitious materials is considered as an alternative/end-use application of utilising recycled GFRP composite waste for purposes other than its original intended use. In the process of cement co-processing, the size of GFRP composite wastes is first reduced, then the mineral component of GFRP composite is used to make clinker while the organic polymer matrix is converted into fuel. Cement co-processing is regarded as a zero-emission strategy during which composite waste is reused as a raw material or a source of energy. Co-processing of FRP composites in cement kiln is beneficial for both energy recovery (around 33%) and material recovery (around 67%), becoming more widespread for composite waste management [13, 38, 39]. In this process, Cement kiln co-processing has shown low negative impact on the environment [38]. Although co-processing is not the most cost-effective choice when compared to other recycling options, it is still preferred over incineration and landfill [40].

FRP waste can be also used as an additive in brick manufacturing [41]. More recently, repurposing FRP wastes as supplementary cementitious materials have been the subject of research. Before being mixed into the concrete, FRP waste is mechanically recycled to a smaller size or a certain shape. Concrete consisting of rCFRP and rGFRP have shown the potential to enhance mechanical properties and long-term durability [42, 43]. Based on the quantity and length of the rGF, Ribeiro et al. [44] classified mechanically (shredding, milling and sieving) recycled GFRP waste into two types: the GFRP recyclate with greater fibrous content which primarily functions as reinforcing material in concrete, and GFRP waste with higher powdered fractions which mainly acts as filler. Both these two different types of recyclates have been found to improve the mechanical properties of polymer concrete materials. Moreover, incorporating both rCFRP and crumb rubber into concrete can substantially reduce CO_2 emissions with improved mechanical properties [45, 46]. However, the optimum size and

dosage of FRP composite wastes are still being researched. A number of research has been devoted to studying the viability of incorporating GFRP waste in concrete. Table A1 of Appendix 2-A summarises available data in the literature, provides information about GFRP waste source, mechanical recycling processes, recyclate dimensions, and incorporation content. Two main strategies have been adopted in the literature including replacement of fine and coarse aggregates with GFRP recyclates or the use of rGF as an internal reinforcing element, while just few studies have used rGFRP as a substitute for cement and filler. This section provides a comprehensive investigation on the influence of GFRP waste incorporation in concrete in relation to the properties of fresh concrete, mechanical properties, and durability mechanisms. Based on data in Table A1, the content of rGFRP in concrete was converted to a percentage of the total mass in the figures in this paper in order to make it possible to compare the effect of different rGFRP content.

2.2.4.1 Properties of fresh concrete

Fresh properties of concrete relate to the workability and fresh density, both of which are important for the material to be properly placed and cured. Since the fresh properties of concrete are also critical to its strength and durability, it is essential to evaluate the performance of fresh concrete when GFRP recyclates are incorporated into the mix.

Workability

Workability refers to the properties of raw concrete which determines its homogeneity and the ease of placing. There are several factors influencing workability of concrete, such as water-to-cement ratio (w/c), gradation, type of aggregates and mix proportion. Apart from these major factors, the workability of concrete also varies with the content, size and morphological characteristics of GFRP wastes. Slump flow diameter and w/c ratio are two measurements used to evaluate the workability of fresh mortar/concrete.

Experimental results have shown that higher dosage of GFRP fibrous recyclates decreases slump flow diameter (see Figure 2-1 (a)). This is attributed to the conglomeration of fibrous and granular recyclates, which increases water demand. On the other hand, GFRP waste has a high specific surface area, that increases water demand, resulting in reduction in workability [21, 47]. Moreover, the slump flow diameter of fresh mixtures was found proportionally reduced with both longer fibre length and higher fibre content. In most cases, limiting the recycled GFRP content to 2% can lead to an acceptable slump value [48, 49]. Patel et al. [50] reported that incorporation of rGF leads to higher workability than addition of virgin GF. vGF

exhibits greater hydrophilic behaviour requiring more water, while the resin coating on the surface of recycled fibre assists to reduce water demand, thus resulting in higher slump value [50]. The GFRP powdered particles are irregular with low roughness which fill the voids between fine aggregates, reducing the volume of water required. Figure 2-1 (a) also shows that GFRP composite waste used as a filler in mortar can positively affect the workability [15, 51]. For the mortars with the same w/c ratio, Farinha et al. [15] observed that replacing 20 wt% fine aggregates with GFRP waste (smaller than 63 μm) significantly increases the flow value. As a partial replacement of fine aggregate, GFRP particle absorbs less water than the fine aggregate it replaces, which is another contributor to lower the water demand. No significant influence on concrete workability was observed when GFRP composite is recycled into needle shape (e.g. with 6×6 mm2 cross-section and 100 mm length) and used to partially replace coarse aggregates. Compared to plain needles, the slump values of grooved needles are slightly lower, due to a larger surface area and a rougher surface of grooved needles [22].

The amount of mixing water has a direct relationship with the workability of fresh mortar. As shown in Figure 2-1 (b), w/c ratio decreases with lower rGFRP replacement and then slightly increases with higher rGFRP dosage [15, 52]. In these studies, the size of GFRP powder was found to be smaller than fine aggregates (refer to Figure 2-1 (d) [52]). This distinct behaviour is related to morphological characteristics and specific surface area of the GFRP. The round shape of rGFRP particles with low roughness improves workability, while the high specific surface area of rGFRP particles increases water consumption. The negative effect of high specific surface area becomes more evident as the dosage of rGFRP replacement increases. In contrast, Oliveira et al. [53] observed that the w/c ratio gradually increases with GFRP waste as replacement of sand. As indicated in Figure 2-1 (d) [53], the particle size distribution of GFRP powdered waste is within the acceptable limit of the fine aggregates used in mortar. The explanation for the increasing water demand may be the comparable size of GFRP powered waste with irregular dimensions.

Bulk density

The inclusion of GFRP waste into the concrete mix lowers the density of fresh concrete/mortar. Coppola et al. [54] explained that replacing 10% of fine aggregates by volume with GFRP powder results in a decrease in density of fresh mortar owing to air entrapment, as illustrated in Figure 2-1 (c). Correia et al. [52] have observed that when the GFRP powder for replacement of fine aggregates increases from 5% to 20% by volume, the density of fresh concrete gradually decreases up to 5.8%. The reason behind this is that GFRP has a lower

specific density (1840 kg m^{-3}) than the fine aggregates that were being replaced (2590 kg m^{-3}). This is consistent with the findings of Farinha et al. [15] where they investigated the density of mortars with 0% to 15% GFRP waste by volume as sand replacement. Nonetheless, when GFRP waste content was raised from 20% to 50%, a higher bulk density was observed (Figure 2-1 (c)). The filling effect is responsible for the increasing bulk density where GFRP particles fill the voids between aggregates, causing the mortar to become more compact.

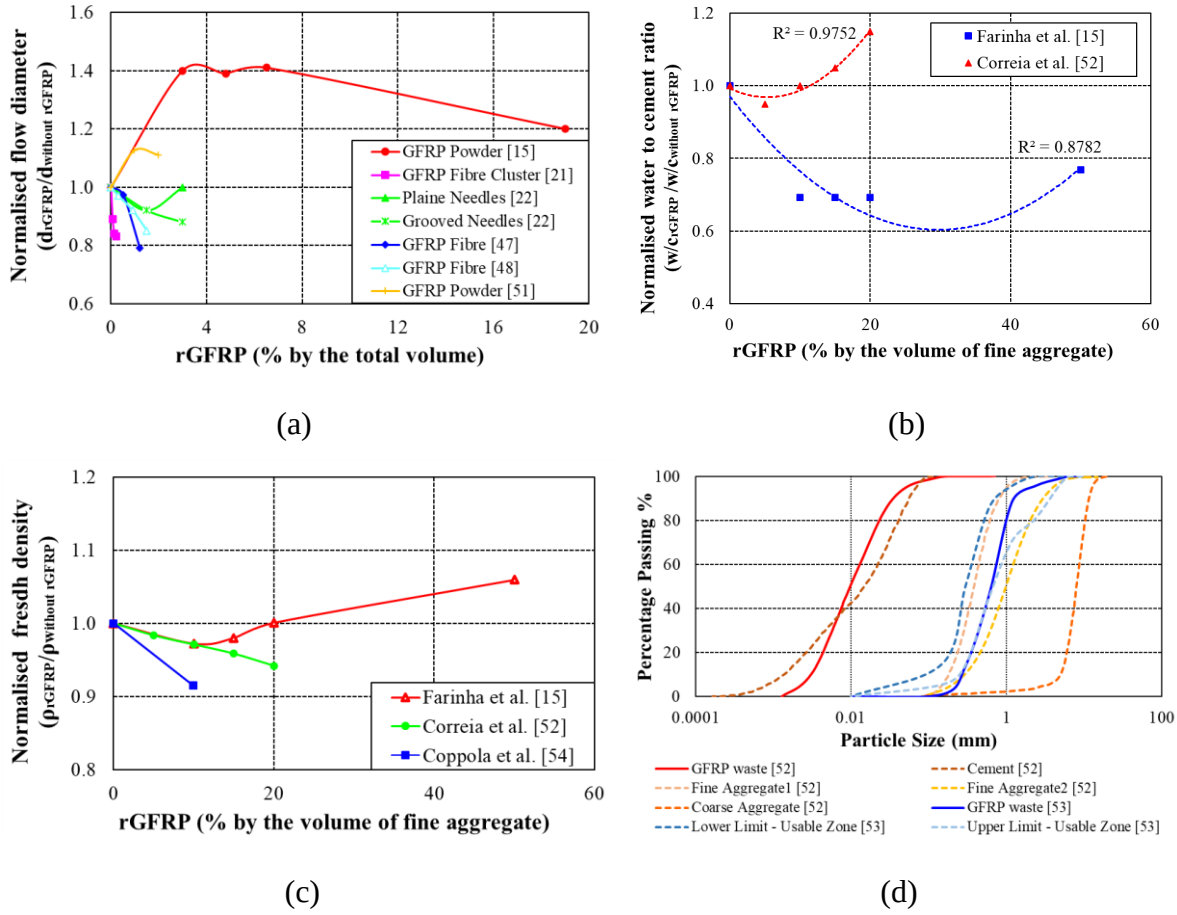

Figure 2-1. Effect of rGFRP on: (a) flow diameter, (b) w/c ratio, (c) bulk density of fresh mortar, and (d) Particle size distribution of GFRP waste in various studies [52, 53].

2.2.4.2 Mechanical properties

The following sections summarise the influence of incorporating different forms of rGFRP on the mechanical properties of concrete including compressive strength, flexural strength and splitting tensile strength, elastic modulus, toughness and impact resistance.

Compressive strength

Since various types and sizes of rGFRP have been reported in different research, a direct comparison may result in misleading conclusions about the influence of rGFRP on concrete compressive strength. Hence, we categorised rGFRP incorporation based on replacement methodology; fine aggregate replacement, coarse aggregate replacement, or rGF as supplementary material.

- **Fine aggregate replacement**

The influence of incorporating GFRP powdered waste as a partial replacement of fine aggregates on concrete compressive strength is presented in Figure 2-2 (a) Two distinct responses can be observed; some results show reduction and the others show increase in compressive strength of concrete/mortar due to partial replacement of fine aggregates with GFRP waste. The reduction in compressive strength can be attributed to a variety of factors [52, 53, 55, 56], including (i) lower compressive strength of rGFRP particles compared to natural sand, (ii) weaker interfacial bond between rGFRP particles and cement paste, due to the cylindrical shape of the rGFRP particles, polymer fractions of the rGFRP waste, and size of the rGFRP particles and (iii) the presence of voids and uneven distribution of GFRP waste in concrete. Rodin III et al. [57] found that smaller rGFRP particles can lead to a greater compressive strength reduction due to the need for higher binder content. Research has also reported the increase in compressive strength of concrete by using the GFRP waste powder [15, 44]. This is mainly due to the filler effect of fine rGFRP particle size that leads to reduction of the voids between the particles in the concrete. As the particle size distribution displayed in Figure 2-2 (c), compared to coarse waste (CW), fine waste (FW) works more as a filler extension for fine aggregates. Baturkin et al. [58] argued that the GFRP waste (without organic content) can contribute to a higher pozzolanic activity, which is mainly controlled by the silicate content as well as fineness (the particle size of GFRP waste is smaller than that of cement, as shown in Figure 2-2 (c)). When replacing 10 wt% cement, GFRP waste powder can maintain and enhance the compressive strength compared to plain concrete, especially at 90 days. The filler effect of glass particles accelerates the hydration rate through providing more hydration sites and exhibiting the pozzolanic activity due to the presence of silica in glass fibre [59].

In addition to GFRP waste powder, compressive strength can be improved by reinforcing effect when fibrous GFRP recyclates replaced 4% to 12% (weight content of total mass) of fine aggregates [44]. Ribeiro reported an optimum GFRP fibrous recyclates content of 8% of the total weight. Furthermore, an adhesion promoter such as silane coupling agent improved compressive strength by enhancing the interface bond between the resin matrix and particles.

García et al. [47] used an optimised mechanical treatment to reduce the amount of polymer particles in the GFRP waste before incorporating it into concrete. By introducing 1 wt% recycled glass fibre (rGF) recovered from this treatment, the mechanical performance of concrete enhanced by up to 22%, which is attributed to the better adhesion between fibres and cement matrix. In addition, Patel et al. [50] found that partially substituting fine aggregates with glass fibres (0.1 to 0.3 vol% of the mix) reclaimed from shredding machine can improve compressive strength by up to 22%, owing to the high concentration of calcium, silicon, and sulphur in rGF which promotes the calcium silicate hydrate (C-S-H) reaction within interface region. The better interfacial bonding between the recycled glass fibre and cementitious material can explain the positive effect on mechanical properties.

The effect of curing condition on the compressive strength of concrete/mortar containing rGFRP is shown in Figure 2-2 (b) The compressive strength of GFRP incorporated concrete is higher with dry curing condition (air and oven) than with water curing. Asokan et al. [60] and Tittarelli and Shah [61] reported a polymeric film can form at the surface of cement hydrates during the hydration process when air (T = 23 ± 2 °C, RH = 50 ± 5%) or oven curing (T = 50 ± 2 °C) is adopted. The polymeric film intermingles with cement hydrates and can help arrest cracks, thus improving the compressive strength of concrete. Moreover, Asokan et al. [62] stated that superplasticiser (SP) may promote the development of polymeric films, resulting in good bonding between GFRP waste and cementitious material.

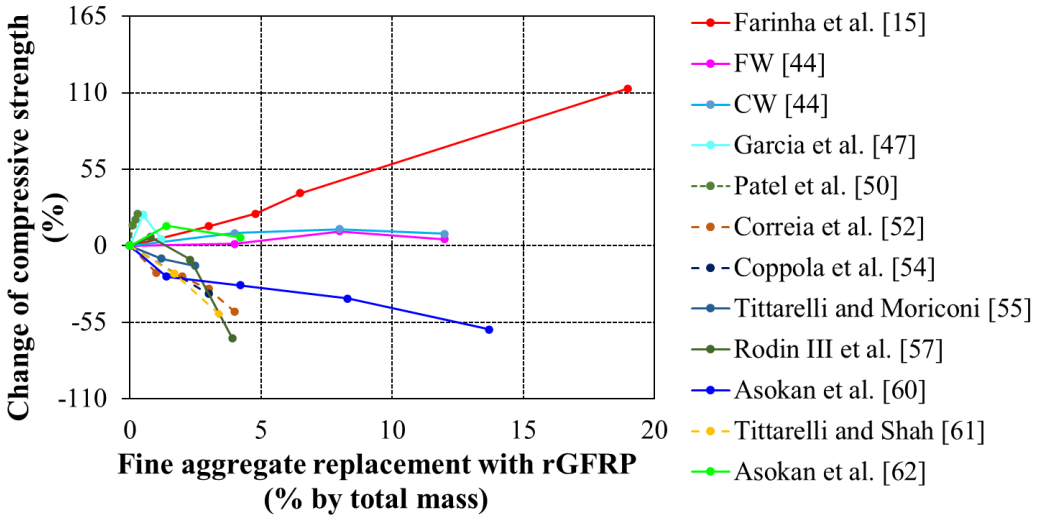

(a)

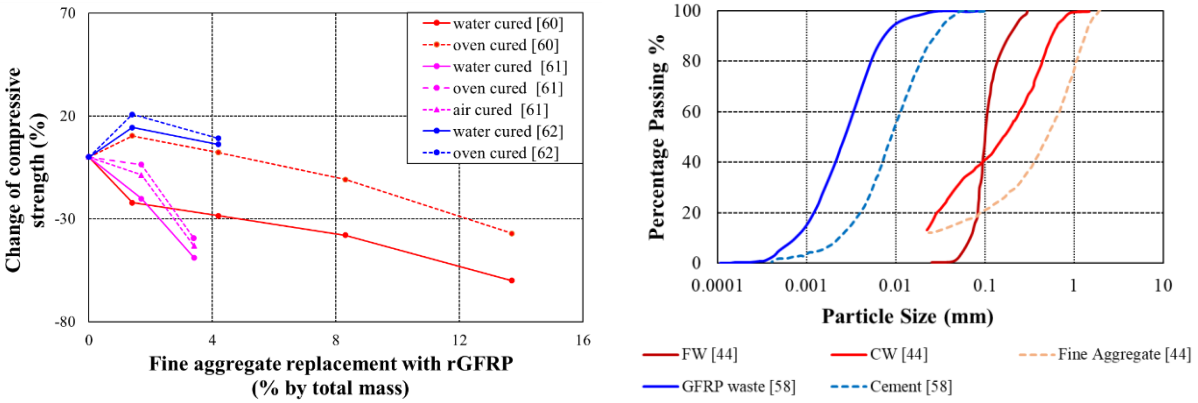

(b) (c)

Figure 2-2. Effect of (a) fine aggregate replacement, and (b) curing condition on compressive strength of rGFRP incorporated concrete/mortar; (c) Particle size distribution of GFRP recyclates, fine aggregates and cement in various studies [44, 58].

- **Coarse aggregate replacement**

Hofmeister [63] found that replacing coarse aggregates with 50 and 100 vol% GFRP cubes can dramatically reduce compressive strength. Recycled cubes (between 6 to12mm) were cut from GFRP composites. The flat surface of GFRP cubes has a negative impact on bonding performance and consequently compressive strength. This is supported by the finding of Yazdanbakhsh et al. [64] and Yazdanbakhsh et al. [65], where they found that replacing 40 and 100 vol% of coarse aggregates with GFRP rebar waste results in a 13% to 21% decrease in compressive strength, respectively. Due to the loss of angular form and lower roughness of the GFRP aggregates, a weaker physical bond between the GFRP aggregates and the cement paste leads to lower compressive strength. Furthermore, the orientation of the glass fibre in the recyclates plays an important role on compressive strength of concrete made of rGFRP. It has been shown that the GFRP needles with transverse glass fibres arrangement do not improve compressive strength of the concrete [22]. Hofmeister [63] added 3mm wide and 30mm long GFRP strips cut from wind turbine blades at 1 vol% of the mix. Since the GFRP strips were cut parallel to the unidirectional fibres, the compressive strength of concrete was increased by 13% after 7 days.

- **rGF as a supplementary material**

Research has shown that incorporating recycled glass fibre as a supplementary material can enhance compressive strength of concrete [21, 48]. Recycled GF works as a bridging component, transferring stress to the matrix and increasing the resistance of concrete against

cracking [48]. The addition of glass fibre (e.g. 0.5 to 2 vol% with 10 to 30 mm length) demonstrated that greater rGF contents combined with longer fibre lengths can enhance compressive strength by 45% [49]. Higher compressive strength can be attributable to a variety of factors: (i) the resin coated and rough surface of rGF can lead to a strong bond between rGF and matrix, (ii) lower proportion of large sized pores in mortar is desirable for strength gain, (iii) the formation of C-S-H gels on rGF can improve the adhesion of rGF to the matrix, (vi) the higher hydrophilicity of rGF may result in stronger bond to the matrix.

Flexural strength

Flexural strength of concrete with rGFRP shows trends similar to compressive strength. Flexural strength increases when GFRP is recycled as a replacement for fine aggregate or rGF is reused as a supplementary material in concrete (see Figure 2-3 (a)) [15, 21, 44, 47, 48, 50, 60]. 18% increase in flexural strength of polymer mortars with 8% (by the total mass) sand replacement with GFRP wastes (fibrous waste lengths ranging from a few micrometres to 25mm) is reported by Ribeiro et al. [44]. Farinha et al. [15] showed that the mortars containing GFRP waste has 155% higher flexural strength at 365 days compared to plain mortar. Nonetheless, the incorporation of rGFRP in the powdered form could lead to a decrease in flexural strength in some cases, similar to the compressive strength [54, 61]. The reduced mechanical strength was explained by the lower strength of rGFRP powder in comparison to silica sand and an increase in porosity.

The reinforcing effect of GFRP recyclates significantly improves flexural behaviour and inhibits crack propagation in concrete. In general, the addition of rGF results in improvement of flexural strength by 58% for 5wt% (of cement) addition [60], 14% for 4wt% fine aggregate replacement [44], and 22% for 0.3 vol% fine aggregate replacement [50]. The length of GF also affects flexural strength improvement. Mastali et al. [48] and Mastali et al. [49] observed that the flexural strength gradually increases with higher content and length of rGF. Zhou et al. [21] suggested that samples with 6 to 20mm long rGF show higher flexural strength with a length to width ratio greater than 6. Another factor that contributes to higher flexural strength is the resin coating and subsequently rough surface of the rGF. This enhances the bond between the fibre and the matrix, generating extra slipping resistance at the fibre-cement interfaces.

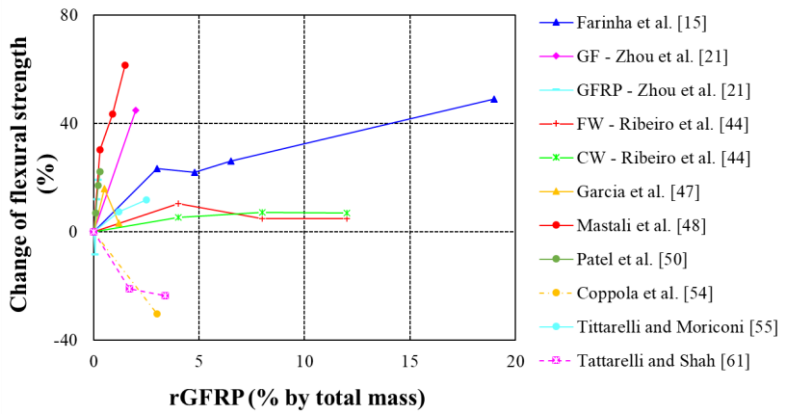

(a)

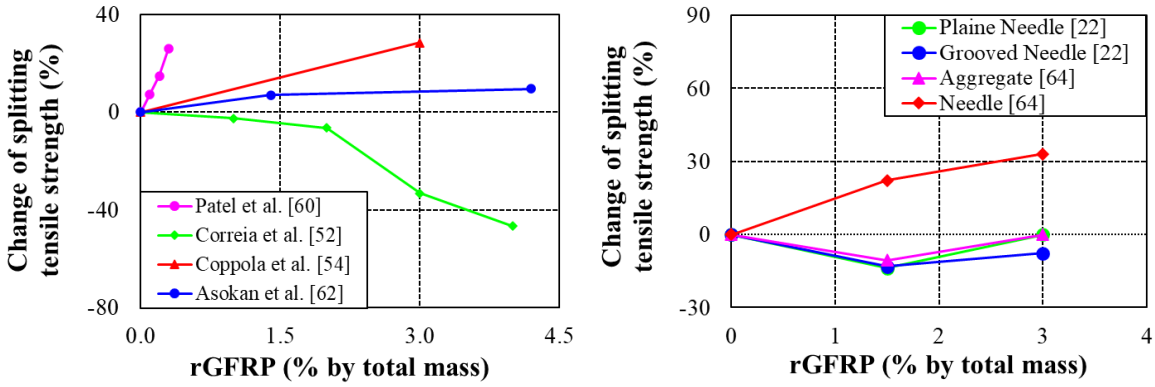

(b) (c)

Figure 2-3. The effect of rGFRP content on (a) flexural strength; (b) and (c) splitting tensile strength.

Tensile strength

The effect of partially replacing fine aggregates with rGFRP recyclates on the splitting tensile strength of concrete is shown in Figure 2-3 (b). The improvement of splitting tensile strength is attributed to the presence of rGF as a reinforcing material and the stronger bonding between rGFRP surface and matrix [50, 62]. Coppola et al. [54] reported that the tensile strength can be enhanced by about 30% when 10% of sand volume is replaced by GFRP powder. Nevertheless, Correia et al. [52] found that substituting 20 vol% of sand with rGFRP powder reduces splitting tensile strength by 47% due to the cylindrical shape of rGFRP particles, creating weaker bonds within the matrix.

Yazdanbakhsh et al. [64] reported that replacing 40 and 100 vol% of natural aggregates with round GFRP recyclates (produced from rebar) reduces concrete tensile strength by up to 35%. In contrast, Yazdanbakhsh et al. [65] found that using GFRP rod-shape needles (100 mm length) to replace 10 vol% coarse aggregates can improve concrete tensile strength by more

than 30%. This is because compared to the round GFRP recyclates, stronger connections between GFRP rod-shaped needles and concrete were observed. Nevertheless, incorporating GFRP plain and grooved needles negatively affected splitting tensile strength, which was related to the transversely-oriented glass fibres in the needles, and the small cross sections of the grooved needles [22].

Modulus of elasticity

Replacing 5 to 20 vol% of fine aggregates with rGFRP powder reduces 28 days elastic modulus by 3% to 50% [52, 66], while utilising low dosage (1.5 and 3% of the total mass) of rGFRP rod-shaped needles or aggregates shows no significant influence on the elastic modulus of concrete [65]. However, when 3% (by the total mass) grooved and plain needles were added to the concrete, the modulus of elasticity was increased by 12.5% [22].

Corinaldesi [67] conducted ultrasound pulse velocity (UPV) measurements and reported that the dynamic modulus of elasticity decreases with replacing limestone powder with rGFRP powder. Farinha et al. [15] investigated the deformability of the concrete with GFRP waste and found that lowering w/c ratio and increasing GFRP waste content can slightly increase modulus of elasticity. More compact mortar shows a higher elasticity modulus due to the filler effect. Mastali et al. [49] investigated the impact of the rGF content and fibre length on the porosity of the mixture using UPV measurements. They demonstrated that the velocity decreases as GFRP content and fibre length increase, indicating higher porosity of the mixture. This effect should be considered in combination with the bridging effect, which prevents crack propagation.

Toughness and impact resistance

Toughness is an indicator of the energy absorbed under stress, commonly calculated by the area under the load-deflection curves. Increasing the amount and size of rGFRP in concrete can improve the toughness. Mastali et al. [49] observed that increasing rGF from 0 to 2 vol% and fibre lengths from 10 to 30 mm gradually improves residual strength and absorbed energy. Rodin III et al. [57] reported the same trend and showed that the toughness of the concrete specimens with rGFRP was higher than the controlled samples. The toughness index of large-sized rGFRP was the highest, and higher rGFRP content led to greater toughness indices. Moreover, rGFRP needles had a significant influence on toughness despite most of the fibres in needles were transversely aligned [22]. The energy absorption by the concrete was increased from 1.2J (control concrete) to 33.3J (incorporating 10 % plain needles). Overall, the utilisation of GFRP recyclates in concrete/mortar contributed to the reduction of crack propagation and

crack bridging [22, 57]. Zhou et al. [21] indicated that the toughness of mortar could be further improved by enhancing the l/w ratio and fibre length uniformity of rGF.

The drop weight impact test was conducted to evaluate the impact resistance of concrete [48, 49]. The first and ultimate impact resistance of specimens as well as the number of post-initial crack blows (INPB) increased as the rGF content and length increased, and the rate of growth increased when the fibre volume fraction exceeded 1.5%. With higher dosage of rGF, more rGF will participate in the bridging action, resulting in formation of smaller but multiple cracks near the surface of concrete [49].

2.2.4.3 Durability perspective

In this section, the durability of concrete with rGFRP will be discussed through investigating the impact of rGFRP on the porosity, alkali-silica reaction, drying shrinkage and water absorption of hardened concrete.

Hardened density and Porosity

The relationship between hardened density and the content of rGFRP is shown in Figure 2-4 (a). When the replacement percentage of fine aggregates with rGFRP powder increases, the density of the concrete decreases due to the lower density of GFRP waste compared with the density of fine aggregates and an increase in the porosity [53, 54, 57, 60]. Nonetheless, greater GFRP powder content (e.g. 20 wt% fine aggregate replacement) can lead to higher hardened density due to filler effect [15]. Asokan et al. [60] also reported that the density can increase by 15% compared to controlled concrete when 5wt% additional rGF with 20mm length was incorporated. This might be attributed to the higher density of glass fibre, which increases the density of the concrete. Furthermore, it is shown that utilising SP has a positive influence on hardened density. The 2% SP could enhance the compactness of mixture, thus increasing the density of concrete containing rGFRP powder [62].

Porosity has a direct impact on the mechanical and durability properties of concrete. The results of the porosimetry test indicate that replacing 0 to 10wt% of fine aggregates with rGFRP powder increases the total porosity of the concrete from 16 to 21%, respectively, lowering compressive strength [61]. With incorporation of rGFRP powder, the average pore size decreases but the pore size distribution increases, due to the air entrapment (larger voids) and filler effect (small voids). Oliveira et al. [53] also reported the same trend that when GFRP waste increases from 7.5% to 37.5 wt%, the voids increase linearly from 27% to 47 %, respectively. Farinha et al. [15] observed that the open porosity decreases with up to 15 vol%

rGFRP incorporation, then increases with higher rGFRP content, which was explained by the filler effect and the inter-particle voids generated by rGFRP powder. Moreover, Zhou et al. [21] found that the incorporation of rGF reduces total pore volume. Incorporating small-sized rGF increases the number of large pores (> 0.5 mm) in the concrete, leading to reduction of compressive strength.

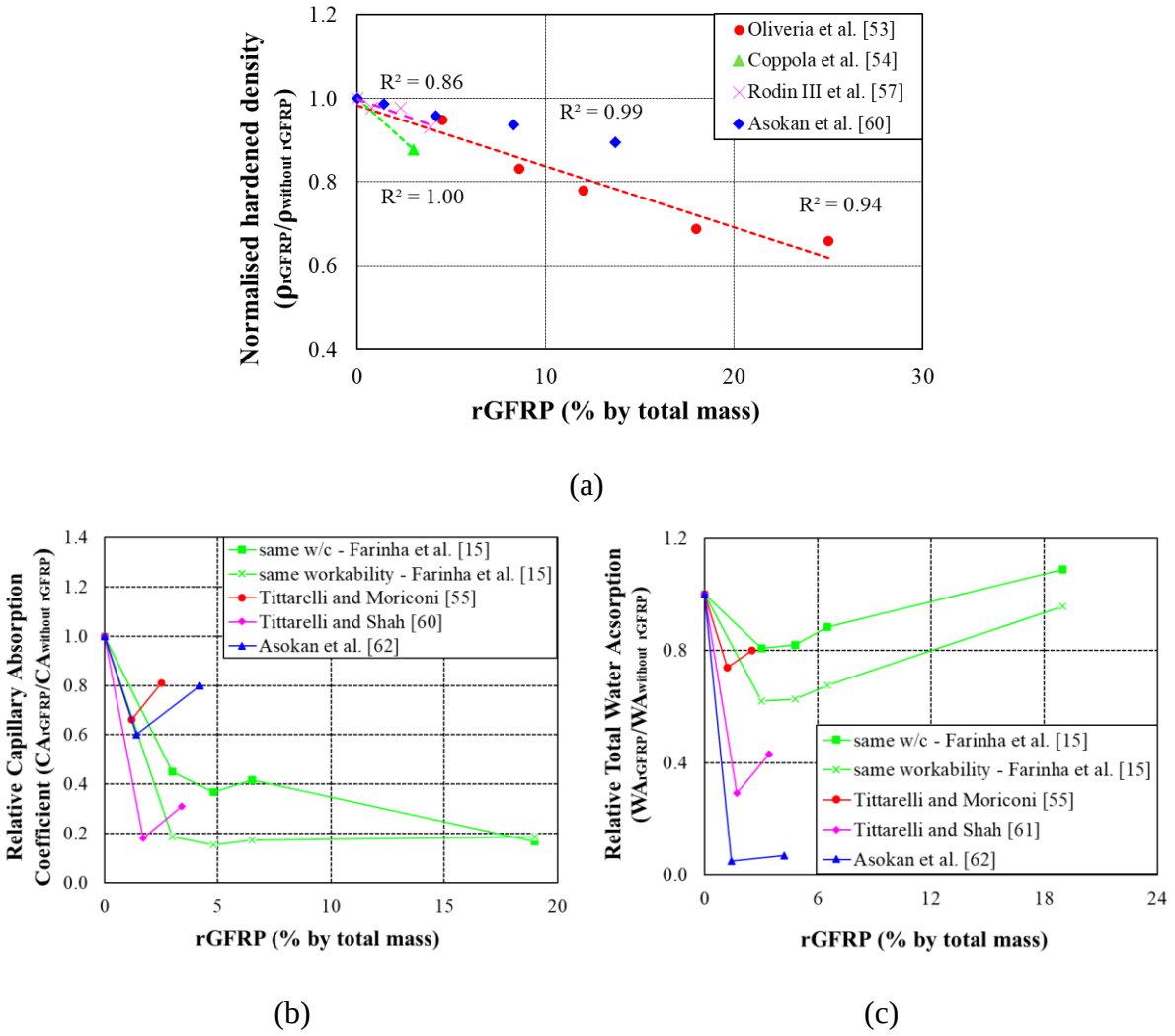

Figure 2-4. The effect of rGFRP content on: (a) hardened density, (b) capillary absorption coefficient, and (c) total water absorption of concrete.

Alkali-silica reaction

Alkali-silica reaction (ASR) is known as the chemical reaction between highly alkaline cement paste and amorphous silica in aggregates. It has been reported that ASR can be promoted by using waste glass in concrete [59, 68, 69]. Research has demonstrated that the ASR expansion for the concrete with rGFRP is below the recommended limit in the standards [47, 57, 70]. This is attributed to the good durability of resin coating, which encloses the glass fibres and protects the fibres from ASR effect [57]. In general, it can be said that incorporating

small amount of rGFRP powder and rGF (up to about 4% of total mass) do not have notable influence on the ASR expansion in concrete. However, there is still lack of data in this area and further research is required to comprehensively investigate the impact of rGFRP incorporation on ASR in concrete by considering different types and sizes of GFRP waste and testing durations.

Drying Shrinkage

Drying shrinkage occurs when concrete loses capillary water, which can be measured by drying shrinkage test. The addition of GFRP recyclates in concrete showed a positive effect on preventing drying shrinkage. Drying shrinkage reduces remarkably (up to 50%) when rGFRP powder is added to the mix [55, 66, 67]. Similarly, García et al. [47] reported that incorporating rGF can result in less shrinkage while no cracks were observed in the specimens after 28 days. Asokan et al. [62] argued that rGFRP incorporation has no or little influence on drying shrinkage while Dehghan et al. [70] showed that the shrinkage value of concrete specimens with rGF slightly exceeds that of controlled samples. This may be attributed to higher porosity and lower stiffness of rGF, resulting in less resistance to shrinkage.

Water absorption

The results from the water absorption test show that the water absorption of the concrete/mortar can be reduced by the incorporation of GFRP recyclates, as shown in Figure 2-4 (b and c). In this figure, the capillary absorption coefficient refers to the rate of initial water absorption (up to the first 30 minutes) and total water absorption is defined as the amount of water absorbed over the immersion duration [55]. During the initial water absorption, the larger capillary pores are more likely to be filled first. The application of around 20wt% rGFRP powder effectively reduces the capillary absorption coefficient by up to 80% compared to plain concrete, see Figure 2-4 (b) [15, 55, 61, 62]. This is attributed to the reduction of the large voids and the non-sorption property of GFRP that slows down the propagation of the imbibition front [55, 61]. It is worthwhile to mention that the relative capillary absorption coefficient can slightly increase with a higher content of rGFRP due to the higher total porosity of mortars with GFRP waste [61].

Partial replacement of 5wt% fine aggregate with rGFRP significantly reduces total water absorption up to 90%, see Figure 2-4 (c) [55, 61, 62]. Nevertheless, the total water absorption can increase at higher dosage of rGFRP. Concrete with replacement of 20wt% fine aggregate with rGFRP powder shows a similar water absorption as a plain concrete, which is attributed

to the total pore volume. Although rGFRP particles can fill large voids between aggregates, the particles probably form smaller voids among themselves at larger dosages, resulting in an increased total water absorption.

2.2.5 Cost benefit and life cycle analyses

Currently, most of GFRP waste composites are disposed of in landfill or incinerated. With growing concerns about environmental impact of conventional landfilling/incineration, various recycling methods have been developed to reuse GFRP composites. Landfill is listed at the bottom of the waste hierarchy based on the UN Sustainable Development Goals [71]. Moreover, traditional waste treatment methods are being increasingly restricted and banned by the governments around the world. For example, Germany, the Netherlands, Austria and Finland have already prohibited the disposal of composite waste in landfills [13, 40].

One of typical repurposing approaches, incorporation of GFRP waste in concrete not only uses waste materials for production of new structures but also saves energy and decreases the environmental impact of concrete by substituting concrete ingredients. Typically, mechanical treatment is required before integrating GFRP waste in concrete to reduce the size of the waste. Compared to incineration, mechanical recycling reduces primary energy consumption and greenhouse gas emissions substantially, however it requires extensive regulatory support to be practicable [72]. As a low-cost recycling process, mechanical recycling also uses much less energy than other recycling methods, such as chemical recycling and pyrolysis [13]. Using GFRP waste in concrete reduces environmental impact of the concrete manufacturing process. For instance, fine aggregates are extracted from riverbeds, which is a non-sustainable approach [53, 58]. Therefore, incorporating GFRP recyclates into concrete has the potential to improve sustainability. To investigate the potential of waste treatments of GFRP composites, a detailed cost-benefit analysis (CBA) on four major GFRP recycling methods was performed in this study.

CBA investigates the economic activities and feasibility of the project and provides a basis for comparing the total expected cost of each recycling option with its total expected benefits during the lifetime of a project. The aim of this analysis is to compare the investment risk, as well as short- and long-term profits for business decision making. In this investigation, the capacity of recycling plants corresponding to each fibre reclamation technique was designed based on the optimum expected recycling function with an annual capacity of 6,000, 4,000, 4,000, 2,000, 1,500 tonne per year for landfill, mechanical recovery, incorporation in concrete

(repurposing), pyrolysis and fluidised bed, respectively. It was assumed that two recycling factories, one located in east coast in New South Wales (NSW) and one in west coast in Western Australia (WA), can provide sufficient recycling plants across Australia. A classical period of 10 years was selected here for evaluating economic feasibility.

Cost analysis was carried out based on capital investment and ongoing expenditure (also known as operational cost). Capital costs are fixed and one-time investment for setting up the recycling plant and material required for starting the operation. These costs include equipment purchase (C1), industrial land rental/purchase (C2) and building preparation and raw material collection (C3). The project with lower capital cost is preferable by small and/or medium companies as it minimises the initial risk for investing in recycling project. Operational cost is related to daily cash flow for supporting continuous waste treatment process. This value is sum of operating and non-operating labour cost (C4), equipment maintenance charges (C5), waste pre-processing cost (C6), waste post-processing cost (C7), supplies (C8) and other cost related to material transportation (C9). In this study, the operational cost of landfill is considered as AU$ 101.5 per tonne based on values stated in the [42] and the assumption of 50% landfilling in urban area and 50% in rural area. The effect of recycling capacity was also considered for the operational cost analysis. It was assumed that if the amount of intake FRP waste is over defined annual capacity, the extra waste will be landfilled and subsequently considered as part of post waste treatment cost. It was assumed that operating personnel required for operation of mechanical, incorporation in concrete, catalytic pyrolysis and fluidised bed are 2, 2, 4 and 3 respectively.

Figure 2-5 (a) shows results of cost divisions for landfill, mechanical recycling, incorporation in concrete, catalytic pyrolysis and fluidised bed. Operating and non-operating labour, waste pre-processing and post-processing cost are the main expenditures required for remanufacturing of recycled products over 10 years. It demonstrates that capital investment (the sum of C1, C2 and C3) forms a significant proportion of the total expenditure required for crushing and milling process of both mechanical recycling and incorporation in concrete methods. In comparison, fluidised bed and catalytic pyrolysis require less initial one-time expenditure but higher investment for supporting daily operations. Figure 2-5 (b) shows the total costs over 10 years of investment period. Mechanical recycling, incorporation in concrete and fluidised bed methods have roughly similar cost for treating GFRP waste while catalytic pyrolysis is relatively more expensive due to its high electrical energy consumption.

Benefit relates to the economic value of recycled fibres/FRP powder, profits from recovered energy and secondary products and expenditure reduction by reducing the amount of landfill. Since the landfill is fully operated by the government, no capital investment and benefit were considered for this treatment method. Mechanical recycling, fluidised bed and catalytic pyrolysis can partially or wholly remove matrix covering the fibres and produce reusable loose recycled fibres, while incorporation in concrete approach mechanically reduces the size of GFRP waste by milling and crushing, producing different shapes of rGFRP for the use in concrete. Therefore, economic benefit value of recycled products is determined based on their potential future use. Based on Dong et al. [73]'s research, the estimated economic value of recycled GF for fibre manufacturing and reprocessed GFRP used in concrete were assumed as AU$390/tonne and AU$ 476.25/tonne, respectively. For the benefit analysis of incorporation in concrete, it was assumed that the weight loss due to matrix removal from GFRP is negligible since both matrix and fibre could be used in concrete. The additional benefit associated with financial savings via reducing the amount of GFRP landfill is also considered in this analysis. Figure 2-5 (c) shows that thermal recycling methods (i.e. catalytic pyrolysis and fluidised bed) have higher benefits since they can produce secondary chemical products and also allow recovery of energy during the heating process. The total benefit values of mechanical method and incorporation in concrete are nearly the same. Incorporation in concrete, on the other side, is more profitable due to its high productivity and additional value of remaining matrix.

Net profit is sum of total benefits minus costs and taxes. A social benefit of 7% and profit tax of 30% for recycling path was considered in the calculations. Figure 2-5 (d) shows the summary of CBA results for different GFRP waste treatment methods. It reveals that landfill and mechanical recovery cannot provide positive cash flow since their net profits are negative over study period. The difference between net profit of mechanical method (using waste composites for manufacturing of new products with lower mechanical properties) and incorporation in concrete approach (using waste composites as aggregate and filler replacement in the concrete) demonstrates the importance of recycling pathway, application and characteristics of the final recycled product on waste management performance. In general, reclaiming loose fibre from waste can lead to higher benefit due to a greater market value. By comparing two thermal recycling techniques, pyrolysis shows better return on investment than fluidised bed since energy and secondary gas products can be recovered with pyrolysis method.

The Benefit Cost Ratio (BCR) is a numeral value that indicates relationship between the matching costs and expected benefits for a defined waste treatment method. An investment with

a BCR greater than 1.0 means that the project could result in a positive net present value, i.e. the corresponding waste treatment is profitable. If BCR is less or equal to 1.0, the project will result in unprofitable actions and the expectation of investment cannot be met. Higher BCR shows a greater economic efficiency ratio of investment, i.e. more profit earned for per dollar expenditure. Figure 2-5 (e) demonstrates that incorporation in concrete, pyrolysis and fluidised bed have a BCR greater than 1.0 and the project could result in a positive net present value at the end of 10 years, while mechanical recovery and landfill are not profitable over this defined life cycle. This highlights the significant impact of economic value of recycled products on capital investment of recycling methods and designed life cycle duration.

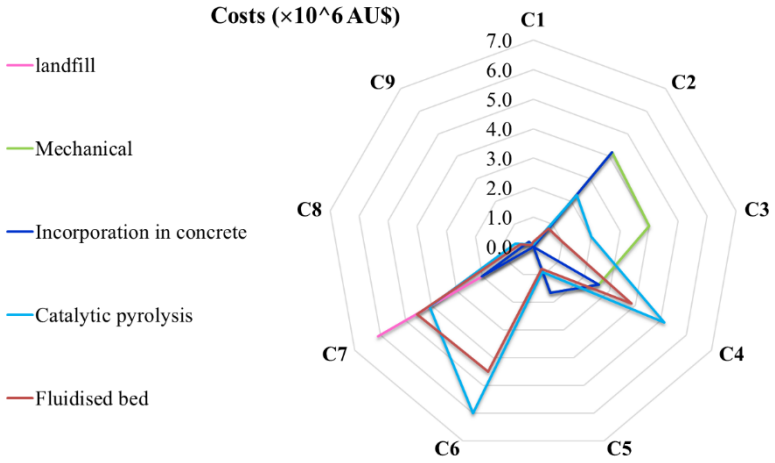

(a)

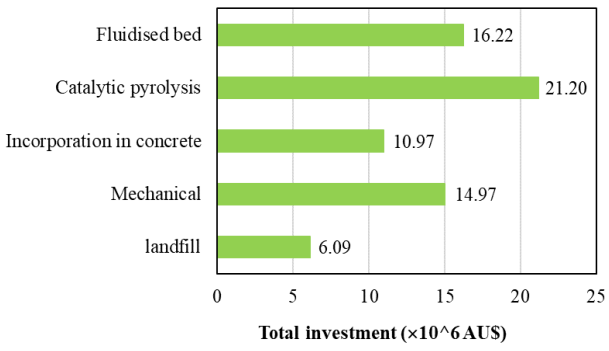

(b)

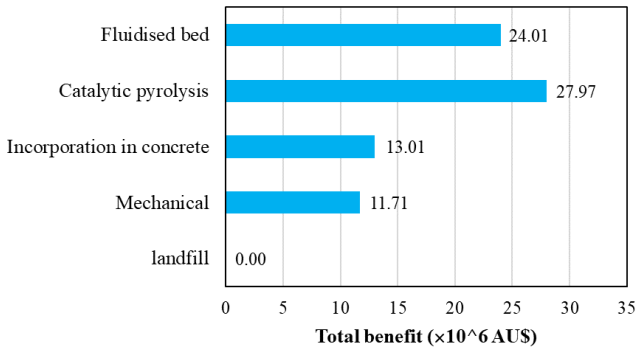

(c)

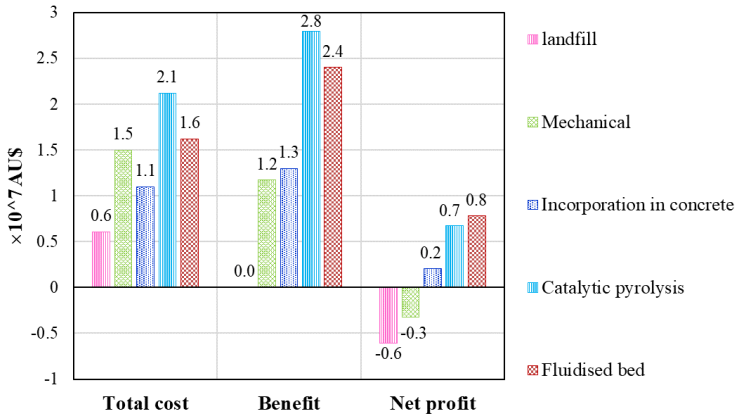

(d)

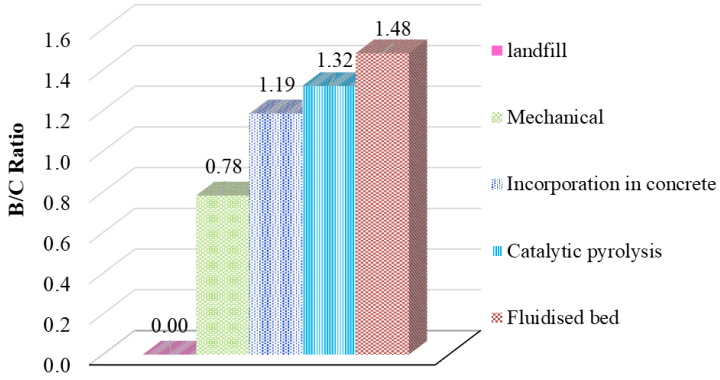

(e)

Figure 2-5. Cost-benefit analysis for different GFRP waste treatments: (a) cost divisions, (b) total investment over 10 years, (c) benefit analysis, (d) total cost, benefit and net profit expected per year, and (e) BCR for different GFRP waste treatment methods.

Cost-benefit analysis provides the indication of financial behaviour of each recycling method, while life cycle analysis aims to evaluate the environmental and social impacts of different FRP waste treatment pathways. In this paper, CML 2001 methodology [74] was adopted to determine possible influencers of energy consumption over FRP life cycle. According to the data provided in the literature [18, 30, 75-79], two main indicators were considered for energy consumption assessment, which were cumulative energy demand (CED) and non-renewable energy use (NREU). Cumulative energy demand was calculated based on the total energy involved from the beginning of fibre manufacturing to the end of rFRP application. These energies can be sourced from either/both renewable and non-renewable resources. Renewable energies have negligible impacts on environment, while high non-renewable energy consumption, such as oil, coal and gas, could result in air pollution and energy exploitation. Hence, the NREU analysis has become a significant indicator in environmental analysis. The values of renewable energy sources, electricity or heat power supply for methods that are yet to be commercialised (e.g. pyrolysis and fluidised bed) were defined based on current lab scale operating temperature and period per kilogram of sample waste. The energy consumption analysis for each method is presented in Figure 2-6. Results show that landfill requires less total energy input but more non-renewable energy than pyrolysis and fluidised bed. This also reveals that thermal recycling methods are highly dependent on renewable energy supply. Mechanical recycling requires higher energy (approximately 25.57 MJ/kg) than catalytic pyrolysis and fluidised bed.

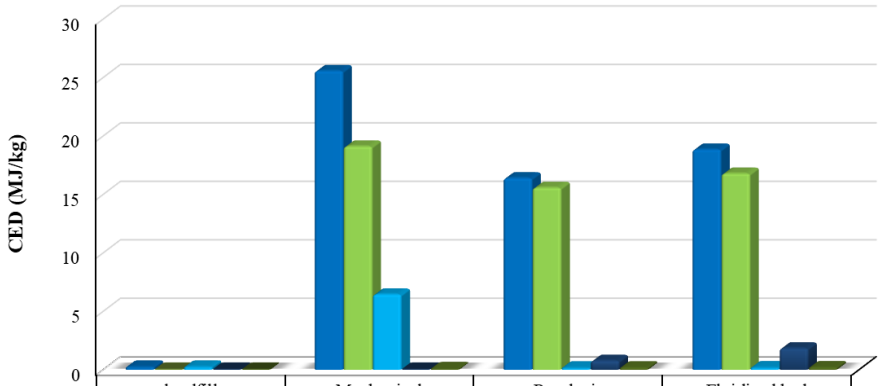

	landfill	Mechanical	Pyrolysis	Fluidised bed
Process CED (MJ/kg)	0.26	25.57	16.40	18.85
Electrical	0.00	19.11	15.58	16.79
Non-renewable energy use (NREU)	0.26	6.46	0.17	0.19
Chemical reaction	0.00	0.00	0.79	1.85
Remaining process	0.00	0.09	0.17	0.19

Figure 2-6. Cumulative energy demand for different FRP waste treatment methods.

2.2.6 Summary of key findings from Section 2.2

Recycling of GFRP composite as a construction material is a potential approach to reduce the volume of composite waste disposed of in landfill or incinerated. Repurposing rGFRP in concrete is an effective and environmentally friendly approach to reduce the use of natural resources and process-related costs. In this research, the use of GFRP wastes in concrete was investigated and the effects of different dosage of GFRP recyclates with various replacement forms and sizes were analysed and discussed. Based on the presented analysis, the following conclusions and recommendations can be drawn:

- The effect of rGFRP on the fresh properties of concrete is associated with its morphology, size and the dosage of GFRP recyclates in concrete. The round shape of rGFRP particles with low roughness improves workability, while the high specific surface area of rGFRP particles increases water consumption. Higher GFRP fibrous recyclate content and longer fibre could reduce workability due to higher possibility of the fibre conglomeration.
- The effect of rGFRP on concrete mechanical strength is associated with the waste component (fibre or resin rich) and physical properties (shape, density, and hydrophilicity) of GFRP recyclates, as well as the incorporated volume in concrete. The filler effect combined with the pozzolanic reaction can improve interfacial and subsequently mechanical strength of concrete. Addition of rGFRP Needles to the concrete can potentially enhance the mechanical strength, depending on the shape of rGFRP and orientation of fibres in the composite. The maximum compressive strength is observed when 20wt% of fine aggregate was replaced with rGFRP powdered waste.
- The resin coating and angular shape of rGF provide extra slip resistance and improves the bonding. The reinforcing effect of rGF also limits crack propagation and significantly improves flexural strength. Around 50% improvement in flexural strength can be observed by addition of 2% (by the total weight) rGF. It is recommended that dimensions of rGF be limited to 6 to 20mm in length and a l/w ratio greater than 6. The incorporation of GFRP recyclates in concrete/mortar leads to higher toughness.
- Porosity decreases with lower rGFRP powder content, then increases with higher rGFRP content. This is due to filler effect and inter-particle voids generated by rGFRP particles. Although incorporating rGF reduces total pore volume, small-sized rGF increases the quantity of large pores, thus reducing compressive strength. The water

absorption of the concrete/mortar can be reduced by the incorporation of GFRP recyclates.

- The addition of GFRP recyclates in concrete does not significantly impact drying shrinkage. Small amount of rGFRP recyclates (up to about 4% of total mass) also does not influence ASR expansion. However, further investigation is recommended study the impact of different types and sizes of rGFRP waste on the ASR expansion. While mechanical strength such as compression, flexural and tensile strengths are understood, limited research has been conducted on modulus of elasticity, impact resistance and abrasion resistance. Further research is also required to comprehensively analyse the effect of rGFRP on durability of concrete/mortar. While some durability aspects (shrinkage, water absorption and ASR expansion) have been previously investigated, the performance of concrete containing rGFRP exposed to aggressive environments such as acid attack, carbonation and marine environment (chloride ingress) has not been examined.
- In practice, FRP composite parts are mostly made of combination of different FRP materials which makes it difficult to separate them. Hence, it is necessary to investigate the effect of repurposing hybrid composites on the performance of the concrete. In addition, further studies are required to focus on the combined usage of rGFRP powder and recycled glass fibre (rGF).
- Due to the market need, high value of recovered short fibre, and energy recovery, catalytic pyrolysis and fluidised bed result in higher overall net benefit, whereas landfill and mechanical recycling have no economic efficiency of investment at the end of 10 years. Based on the results of CBA and BCR analyses, repurposing can reduce the total required investment and generate a positive cashflow.
- Life cycle analysis indicated that the mechanical recycling of FRP requires more energy input (both renewable and non-renewable) than pyrolysis and fluidised bed, while landfill should be avoided as it only consumes the non-renewable energy.

With the increasing need for sustainable waste treatment methods, the information presented in this chapter can serve as a useful guide for industries and organisations seeking to recycle FRP composites in cementitious materials. Moreover, the study emphasises the significance of durability aspects of rGFRP-reinforced concrete, which requires further investigation in future research. Additionally, it should be noted that FRP composite parts are

often fabricated in hybrid formats, which may include different types of fibres (e.g., glass, carbon, etc.). The incorporation of these waste composites in concrete also warrants further investigation.

2.2.7 Appendix 2-A

Table A1 Summary of repurposing GFRP waste in the literature.

Reference (by year)	Source of GFRP composite	Composition of GFRP composite	Types of glass fibre and resin	Mechanical recycling process	Sieving/ sorting process	Size of recyclates	Shape of recyclates	rGFRP replacement				additional rGFRP
								Cement	filler	fine aggregate	coarse aggregate	
Asokan et al. [60]		GRP waste powder with a little quantity of glass fibre (95wt% powder; about 5wt% fibre)	thermoset polyester resin; the glass transition temperature (Tg) of GRP waste powder was about 135.4°C		using a 2mm sieve size and segregated into fibre and powder	GRP powder had a wide particle size ranging from 0.02 to 600 µm	different in size and irregular in shape			5 to 50wt%		
		GRP waste fibre with a length of about 20 mm										5wt% of cement
Asokan et al. [62]		a mixture of GRP ground powder, long fibre and long polyethylene (95wt% powder and about 5wt% fibre)	thermoset polyester resin		processed and polythene and long fibre were separated from powder using 2 mm sieve	ground GRP powder: ranging from 0.02 to 600 µm (almost 90% of the powder particles were below 63 µm)	varying in size and irregular in shape			5 and 15wt%		

Tittarelli and Moriconi [55]	from a shipyard as an industrial by-product was used	20% by volume of glass fibres and 80% by volume of organic material		GF varied from 0.02 to 20mm	irregular in shape and size formed by polymeric granules surrounding fibres of a low alkali glass	10 to 20vol%	25 to 50vol %
Tittarelli et al. [66]	from a shipyard as an industrial by-product was used	about 20% by volume of glass fibres and 80% by volume of polyester resin		average size of GFRP powder slightly coarser than 100 µm (GF varied from 0.02 to 20mm)	irregularity in shape and size of GFRP particles formed by polymeric granules surrounding fibres of a low alkali glass	5 to 10vol%	
Coppola et al. [54]	from a shipyard as an industrial by product			powder		10vol%	
Correia et al. [52]	generated by the cutting of pultruded profiles		cutting devices incorporate a vacuum system that captures and stores the GFRP waste in bags	about 96% of the particles measure less than 63 µm	irregular in shape and size and are non-uniform	5 to 20vol%	
Corinaldesi [67]		about 20% by volume of glass fibres and 80% by volume of organic material				100 vol%	

					between 0.25 and 0.5 inches	fibreglass cubes		50 to 100vol%
Hofmeister [63]			cutting		length of each strip was 1 to 1.25 inches; the width of each strip was around 0.125 inches	GFRP strips (were cut parallel to unidirectional fibres)		1vol% of mix
Tittarelli [51]	from a shipyard as an industrial by-product was added	about 20% by volume of glass fibres and 80% by volume of polyester resin			average size of GFRP powder slightly coarser than 100µm (GF varied from 0.02 to 20mm)	irregularity in shape and size of GFRP particles formed by polymeric granules surrounding the fibres of a low alkali glass	2.5 to 5vol%	
Tittarelli and Shah [61]							5 to 10vol%	
García et al. [47]	source: train fairing	organic matter 50.63%; Inorganic filler (aluminium hydroxide) 18.96%; Glass fibre 30.41%; GF arrangement: chopped strand mat	an optimum route for mechanical processing including shredding, milling and sieving	sieving of the milled material through a mesh size of 5.6 mm	rGF larger than 5.6mm	abundant remains of resin around the glass fibres	1 to 2wt%	

Ribeiro et al. [44]	from the shredding of the leftovers resultant from the cutting and assembly processes of GFRP pultrusion profiles during building sites	an average inorganic material content of 71% (w/w) corresponding to glass fibres (55%, w/w) and calcium carbonate (16%, w/w), and an average resin content of 29% (w/w)	comprised essentially of an unsaturated polyester resin (Aropol® FS3992) loaded with calcium carbonate and reinforced with E-glass roving (4800 Tex), continuous filament mat (25Tex) and surfacing veils	further processed by milling using a Cutting Mill laboratory unit (Retsch SM2000)	two size grades of milled GFRP waste were obtained using bottom sieves inside the grinding chamber with differently sized meshes	CW: coarse pultrusion waste - an average diameter of 950 µm, and a fineness modulus of 2.69; a wide range of fibre lengths varying between 25 mm and a few µm	coarse fibrous mixture	4-12 wt% of total mass
						FW: fine pultrusion waste - an average diameter of 390 µm, and a fineness modulus of 1.64; the maximum fibre length is around 5mm	fine powdered mixture	

Mastali et al. [48]	from GFRP sheet			using a shred machine		rGF (average length 20mm)			0.25 to 1.25vol% of mix
Yazdanbakhsh et al. [64]	from the production of helically wrapped and sand coated glass fibre reinforced polymer rebars			cut by using a diamond saw into short cylindrical pieces	sieving: size gradation according to the ASTM C33 grading size of 56	19 mm and 25 mm (aspect ratio of one)	recycled aggregate: round shape and smooth surface		40 to 100vol%
Dehghan et al. [70]	structural sheet moulding composite; light resin transfer mould	20 to 40vol% glass content	Bisphenol-A/ Novolac-based/ Flame retardant epoxy vinyl ester; Unsaturated polyester	using a model GM2411-50 ECO GrinderTM single stage hammer mill grinding system	enclosed auger feed to a series of 9.5 and 4.75 mm perforated opening trommel screens	average fibre cluster length: 17.2 to 19.5mm	fluff		5wt%
Yazdanbakhsh et al. [64]	from the production of helically wrapped and sand-coated glass fibre–reinforced polymer rebars			cut with a diamond saw into cylindrical pieces		6mm diameter; 100mm length (aspect ratio of 17)	FRP Needles		5 to 10vol%
					a large laboratory sieve shaker, the size gradation according	short cylinder pieces; 6 to 19mm particle sizes	FRP recycled aggregates		

				to the ASTM C33 grading size of 56	(aspect ratio of 1)				
Mastali et al. [49]	recovered from leftover unusable GFRP sheets of thickness 0.11mm		using a shredding machine, the GFRP sheets were cut into small fibres		average lengths of 10, 20 and 30 mm	small fibres			0.5 to 2vol% of mix
Rodin III et al. [57]	rectangular panels from end-of-life wind turbine blades	57% fibreglass and 43% polyester resin	the panels first cut into small rectangular pieces before being fed into a shredder and hammer mill	placed in a sieve shake table to process the different GFRP size groups	0.1mm to 0.42mm	powder: glass powder	3vol%		
					0.42mm to 1.41mm	small fibres			
					1.41mm to 2mm	medium			
					2mm to 2.38mm	large: fibre like strands	1 to 5vol%		
Yazdanbakhsh et al. [22]	produced from the shell of a wind turbine blade;		using a table saw with a diamond blade		square cross-sections (6 by 6 mm) and length of 100 mm	plain needles		5 to 10vol%	

	square pieces of a GFRP wind blade shell with a thickness of approximately one inch				square cross-sections (6 by 6 mm) and length of 100 mm; Grooves with the depth of 2 mm were cut into the surface of half of the flat pieces	Grooved needles	
Farinha et al. [15]	a by-product from the polymer industry; The particles used came from the cutting process of floor grids	the polyester resin (organic matter) was about 29.84% and the glass fibres the remaining (70.16%)			smaller than 63µm, with an irregular shape but no rough particles		10 to 50vol%
Patel et al. [50]	from acrylic waste	proportion of GFRPA waste (by volume): glass fibres 6–9%, resin 65–70%, and PMMA∼25%; an unsaturated polyester resin	the 3-stage ecofriendly mechanical recycling process carried out on a "Crushing and Milling System"	a 600 µm sieve was used to separate the fine dust from the glass fibres obtained	diameter: 13.6 µm; length: less than 15mm	rGF	0.1 to 0.3vol%

Oliveira et al. [53]	collected from a wind blade manufacturer	23.8 ± 0.02% organic material, with 76.2 ± 0.02% being inorganic	the thermoset polymer	the turning process was tested using passes with diameter reduction from 0.5 to 3 mm: convert it to a powder	diameter reduction to 0.5 to 3 mm	powdered waste: the granulometry was similar to that of the sand		7.5 to 37.5wt%	
Baturkin et al. [58]	disassembled wind turbines at the end of their lifecycle	36% non-reactive organic content, namely, 29% resin and 7% wood. The remaining portion (64%) represents glass fibres		ball mill was used to grind fibres into fine powder (*wood removal)	average particle size 3 µm for the GFRP powder		10 to 30wt%		
				panels received from the industrial partner were manually cut into 20 mm cubes using a water jet saw (*wood removal)	20mm cube			33 to 100vol%	
				woodchipper at the site of the industrial partner was used to prepare the fibres (*wood removal)					1 to 1.75vol%

Thamizh Selvan et al. [56]	radomes	53wt% fibreglass and 47wt% resin		broken down using a saw machine first, then a scrap grinder and further using a pulveriser			GFRP powder	40wt%	30 to 60wt%	
Zhou et al. [21]	from different sources (box, lid, offcut)			the GFRP wastes were primarily ground using the shredding equipment	mechanically screened using square-mesh sieves	0.3mm to 9.5mm	GFRP Cluster			2 to 6wt%
					the rGFRP fibre cluster was further separated via hydraulic aerodynamic combined selection process	average diameter: 1.1 to 3.2mm; average length: 3.1 to 9.5mm	rGF			5wt%

2.3 REPURPOSING CFRP COMPOSITE WASTES INTO CC

CFRP composites, composed of CFs as the reinforcing element bonded with a matrix, are among the most advanced composite materials used in modern industry, particularly in high-grade applications. They offer excellent performance characteristics, combining high strength with lightweight properties. Notably, CFRP composites can achieve mechanical properties comparable to those of aluminium while reducing mass by approximately 40 percent [80]. Their outstanding performance has led to widespread use across various industries. In particular, the aerospace and automotive sectors account for 36% and 24% of global CFRP demand respectively, representing the highest shares of global CFRP consumption [81]. Additionally, they are increasingly utilised in the renewable energy and sports leisure industries. However, the overwhelming demand for CFRP composites has resulted in a substantial volume of waste. A major contributor to this waste is the CFRP expected to be generated from the EoL commercial aircraft, the projections estimating that 6000 to 8000 aircraft will retire by 2030 [81, 82]. Although the current usage of CFRP in wind turbine blades is lower than that of GFRP, the increasing adoption of CFRP in the wind industry raises concerns about EoL waste disposal challenges in this sector [83].

In response to these challenges posed by the accumulation of CFRP composite waste from various industries, researchers have proposed several recycling strategies aimed at achieving a closed-loop life cycle for CFRP materials. Section 2.3.1 reviews various recycling methods for CFRP composites. The higher price of CFs economically justifies the costly recycling methods for CFRP composites [83]. Moreover, ongoing research focuses on developing cost-effective and environmentally sustainable recycling technologies for CF recovery, aiming to enable large-scale commercial implementation. With the advancement of modern civil engineering, the incorporation of discrete CFs in CCs has garnered interest in enhancing both mechanical and electrical properties. The use of short fibres in cementitious materials originated in the early 1900s, paving the way for the development of fibre-reinforced concrete [84]. In recent years, there has been a growing emphasis on sustainable practices, with increasing attention on the use of recycled materials in place of virgin materials within the construction sector. Utilising rCFs to replace vCFs in CCs can reduce costs by up to 40 percent [81]. To provide a better understanding of the performance of CCs with recycled CFRP, Section 2.3.2 discusses the effects of different forms of rCF/rCFRP on the properties of these composites. Meanwhile, integrating highly conductive materials into a cementitious matrix has shown promising potential to enhance the conductivity of CC. This enhancement is achieved through the

formation of a conductive network within the composite structure [85-89]. This unique characteristic facilitates self-sensing capabilities, presenting an attractive strategy for monitoring the real-time health state of structures. In this context, Section 2.3.3 introduces cement-based sensors for Structural Health Monitoring (SHM) and reviews their performance incorporating CFs.

2.3.1 Recycling strategies for CFRP composite

Section 2.2.3 has provided an overview of recycling methods for FRP composites. This section focuses specifically on recycling strategies for CFRP composites in more detail, including the most employed industrial methods and recent advancements in these techniques.

Although the majority of CFRP waste has been processed through landfills and incineration over the past few decades due to their low cost and large capacity, these methods are not recognised as beneficial disposal operations. These methods neither recover waste materials for new product manufacturing nor contribute to sustainability objectives. Nowadays, the European Commission and some European countries have pioneered legislation to ban or add taxes on landfilling to minimise its negative environmental impact [20, 90]. These measures encourage industries to seek sustainable and more efficient methods for disposing of CFRP waste, making them commercially viable.

Among the main recycling approaches - mechanical, thermal and chemical recycling, pyrolysis is identified as the predominately viable method for CF recovery. Although pyrolysis requires high temperature and a substantial amount of input energy to decompose the thermoset composites, its environmental impact and energy consumption are lower compared to the energy-intensive vCF production [16, 91]. CBA conducted across Australian and European markets indicated that pyrolysis-based recycling methods for CFRP composites provide high economic returns, particularly in the European market [16]. Moreover, pyrolysis, when conducted under controlled conditions, can produce clean, high-quality CFs that retain approximately 50 to 85 % of the mechanical strength of vCFs [20, 90, 92]. rCF can even achieve better mechanical properties, retaining over 90% of their original vCF mechanical strength with optimised processing or post-oxidation treatments [91, 92]. The optimisation process conducted by Hadigheh et al. [93] revealed that the pyrolysis at temperatures up to 425°C followed by oxidation up to 550°C, results in rCFs with minimum surface damage. This two-step process not only produced clean recyclates but also enhanced efficiency and cost-effectiveness. The same research group subsequently optimised parameters for the pyrolysis and oxidation

processes, including gaseous atmosphere, heating rate and duration of isothermal holding to enhance the quality of rCF while reducing the energy consumption [94]. Furthermore, Wei and Hadigheh [95] developed an innovative hybrid method that incorporated a chemical pre-treatment prior to the pyrolysis thermal degradation of CFRP composites. The optimal recycling procedure they proposed involved pre-solvolysis with acetic acid at 100°C, followed by pyrolysis and oxidation. The mechanical strength of rCFs subjected to this pre-treatment was maintained up to 90.53% of their virgin state, significantly improving their properties compared to those treated solely by thermal degradation. Additionally, they successfully applied this developed approach to recycle a commercial bicycle fork. Other advancements in this field enhance the efficiency and performance of the pyrolysis process through methods such as pyrolysis with superheated steam [96] and microwave pyrolysis [97]. Pyrolysis of CFRP composite waste has been developed into industrial-scale operations in recent years, with recycling companies located across Europe, America and Japan [20, 83]. The fibres recycled from pyrolysis are remanufactured with a thermoplastic matrix to create new composite products for automotive and marine sector applications [83]. According to a review study conducted by Zhang et al. [20], pyrolysis is the predominant technique used by recycling companies, with processing capacities of up to 2,000 tonnes per year.

In contrast to thermal degradation at elevated temperatures, chemical recycling employs various reactive solvents to decompose the polymer matrix at lower operating temperatures. Among recycling methods, solvolysis using supercritical or subcritical solvent produces rCFs with the highest mechanical properties (with no loss in strength), though these approaches require higher energy input and operational costs [20, 90, 92]. Low-temperature solvolysis (less than 200°C) further minimises damage to the rCF surfaces during recovery but it requires a longer processing time [20]. It is well known that the primary advantage of solvolysis techniques for recycling CFRP composites is their capability to reclaim cleaner and longer rCFs, while maintaining the integrity of the fibre structure, including woven fabric configurations [83]. Nevertheless, the solvents utilised in solvolysis may lead to environmental pollution through the generation of waste liquids [95]. In response, ongoing research is aiming at developing efficient and environmentally friendly alternatives to enhance sustainability, which include greener chemical solutions and operation processes that require minimum thermal and energy inputs [98, 99]. Knappich et al. [100] investigated solvent-based recycling of CFRPs with various matrices under subcritical conditions. Their process achieved both high CF strength retention and high solvent recovery rates of up to 99% at small scales. Thus, this

demonstrated the viability of a closed-loop system where solvents maintained their dissolving properties across multiple cycles and recycled successfully, eliminating the environmental discharge of waste solvents. On another hand, the cost of this process is a major concern, as it requires specialised facilities capable of operating under specific temperatures and pressures, often in corrosive environments [91]. However, this technique remains viable for CFRP composite due to the high value and demand for CFs in high-ended applications, which justifies the investment. Conversely, it limits the feasibility of applying this method to GFRP composites on a large scale [83].

Mechanical recycling is a simple, cost-effective and environmentally friendly way to produce recyclates. Similar to pyrolysis, mechanical processing also shows significant potential for use in industrial-scale applications. Although past studies have demonstrated economic and environmental viability, the process produces low-grade fibres, restricting their reusability in manufacturing new FRP composites. As mentioned, mechanical recycling is more suitable for GFRP composites but less ideal for CFRP materials, particularly when considering composite remanufacturing. This is primarily due to the high cost of CF reinforcements, making it crucial to preserve their properties for economic reasons. The limited potential applications of mechanically recycled CFs also pose a significant challenge to justifying this recycling method [91]. Therefore, new applications specifically designed for mechanically recycled CFRP composites must be developed to enhance the feasibility of this approach. The initial attempt to utilise CFRP recyclates obtained through mechanical recycling demonstrated their effective incorporation into the design of new sheet moulding compounds (SMCs) as fibrous reinforcement [101]. Subsequent studies have also explored incorporating powdered CFRP waste into different composite systems and demonstrated their improved performance [20, 102, 103]. Researchers have also increasingly focused on incorporating mechanically recycled CFRP waste into CCs. This alternative repurposing method offers a practical solution for handling large quantities of CFRP waste that would otherwise end up in landfills [83]. In addition, it also promotes sustainable construction practices, contributing to the advancement of green building technology [84]. Integrating rCFs into cementitious materials can reduce costs by up to 40% while facilitating the development of multifunctional cement-based materials [104]. Additionally, rCFs also have the potential to enhance the mechanical performance of CCs due to their rough surface, which improves bonding with the surrounding cement matrix [105]. Conversely, it is argued that conventional mechanical recycling cannot fully remove the polymer matrix from the rCFs, which negatively affects mechanical and electrical properties of

FRCCs. This leads to several critical challenges when incorporating rCFs into CCs, including: (i) inadequate fibre dispersion in cement paste due to poor surface wettability; (ii) fibre agglomeration within the matrix, leading to reduced workability; and (iii) insufficient interfacial adhesion between the rCFs and the cementitious matrix. Therefore, additional processing for surface modification is necessary to improve the properties of such CCs [104, 106]. To expand knowledge on CCs with various CFRP recyclates and to provide an understanding of their multifunctionality, the following sections explore the incorporation of different types of rCFRP wastes into concrete/ mortar, their impact on properties, and the development of cement-based sensors using these recyclates.

2.3.2 Effect of rCF/rCFRP on properties of CC

Over the past decade, efforts have been made to incorporate different CFRP wastes into cementitious matrices, primarily sourced from the aerospace and wind energy sectors or recycling facilities, to investigate their potential for enhancing the performance of CCs. The majority of these studies have utilised CFRP waste that underwent only mechanical processing for incorporation into concrete/ cement mortar. The process and recyclates can be classified into: (i) shredded or milled CFRP EoL wastes, composed of CFs and polymer matrix [107-109], (ii) CF wastes cut from pre-impregnated CF sheets, composed of CFs and adhesive resin [84, 109], and (iii) CFs extracted from CF yarns or sheets [43, 109]. Examples of mechanically processed CFRP recyclates are presented in Figure 2-7. These recyclates were added as additional reinforcement or aggregate replacement at relatively low dosages (up to 2% by volume or 3% of cement weight) and they demonstrated improvements in various concrete/ mortar properties including compressive and flexural strength, fracture toughness, splitting tensile strength, shrinkage resistance, and durability. These enhancements are primarily attributed to the load-transfer mechanisms facilitated by the bond between the recyclates and matrix, which will be discussed in detail in Section 2.4.1.

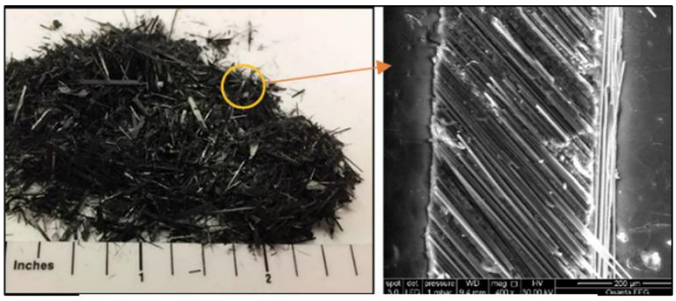

Milled CFRP scraps from the aerospace industry

Pre-impregnated carbon cloth offcuts

rCFs extracted from carbon yarns

Figure 2-7. Photographs of mechanically recycled CFRP wastes [84, 108, 109].

Mechanical recycling can further process recyclates from other recycling methods before their incorporation into CCs. Akbar and Liew [105] incorporated milled rCFs claimed through the pyrolysis technique into cement-based materials. The milled short rCFs had an average length of 95.4 μm with sizing removed and minimal polymer resin residue, allowing easy dispersion in the mix (Figure 2-8). At 1% rCF volume content, the CCs showed significant improvements: a 57% increase in elastic modulus and a 188% enhancement in splitting tensile strength. The roughness on the rCF surface provided a stronger interlocking function to the matrix, resulting in a 325% increase in fracture toughness compared to plain cement paste. Microstructural analysis conducted by the same research group [81] also revealed that pyrolysis-derived rCFs promoted hydration product growth by providing inert nucleation sites. At 1.5% rCF volume content, the degree of hydration and chemically bound water in CCs increased by 6.64% and 1.59%, respectively.

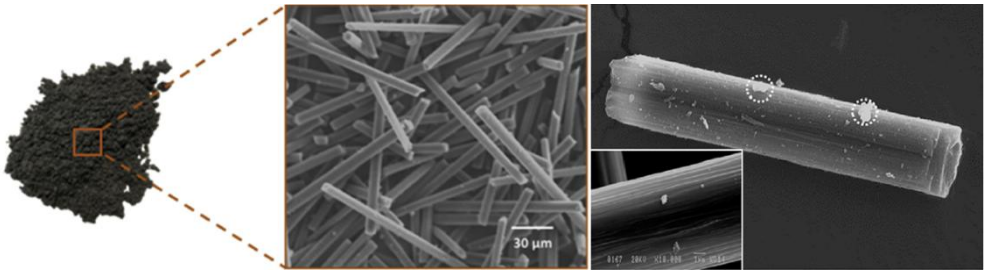

Figure 2-8. Milled pyrolysis rCFs [105].

Chemical treatments combined with mechanical processing have been explored to enhance the performance of CCs incorporating rCFs. Wang et al. [106] treated rCFs with saturated pore solutions or montmorillonite nanoclay emulsion, improving both mechanical properties and chemical adhesion to cementitious mortar. Li et al. [110] conducted a two-step chemical recycling process utilising hydrogen peroxide, resulting in tightly bonded hydrated products on the rCFs after debonding. These highly depolymerised rCFs demonstrated enhanced cement matrix interaction and improved reinforcing effects. In recent work, Wang et al. [104] investigated different chemical treatments to enhance rCF surface roughness and oxygen-containing functional groups, with alkali neutralisation showing the most promising results. These chemically treated rCFs not only improved workability and flexural strength but also increased the electrical conductivity of CCs by approximately 40%. An example of a graphic representation of the incorporation of chemically treated CFRP waste in CCs is shown in the figure below.

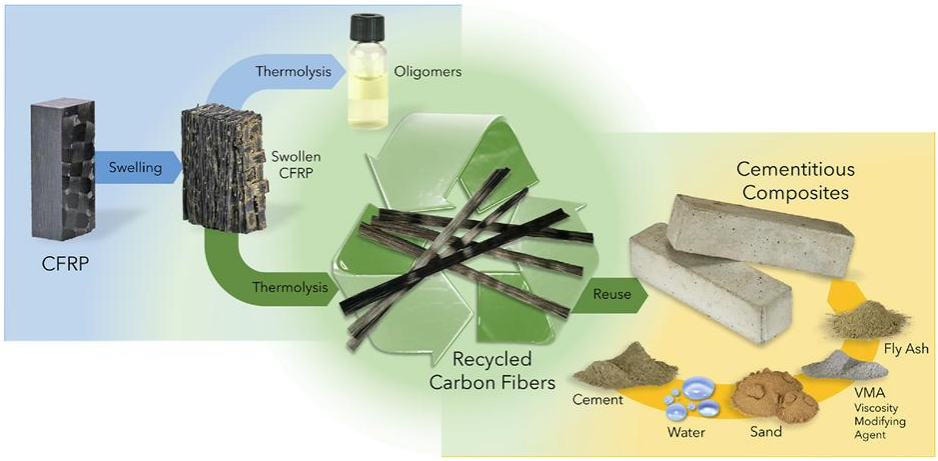

Figure 2-9. Graphic representation of incorporation of chemically treated CFRP waste in CCs [110].

In addition to these recent experimental investigations, recent review studies by Danish et al. [82] and Wang et al. [111] have systematically examined the application of various forms of CFRP waste in cement-based materials. These studies discuss the influences of rCFRP/rCF on the engineering properties of concrete/mortar including workability, compressive, tensile and flexural strength, providing a comprehensive summary and analysis. Wang et al. [111] studied three critical factors that govern the mechanical performance of CCs containing recycled CFRP materials, which are the shape, content and surface treatment of CFRP recyclates. CFRP waste is mostly recycled into CCs as strips or fibrous forms to provide a bridging effect. However, large sizes of CFRP recyclates can adversely affect the fluidity of fresh concrete/mortar. In contrast, waste carbon powder promotes even distribution and

enhances flexural strength, though it may reduce compressive strength. The most commonly studied incorporation content ranges from 0.5% to 2% by volume. The excessive incorporation of recyclates has been shown to impede the enhancement of the mechanical properties of CCs. Based on Danish et al. [82]'s review, several conclusions can be summarised as follows: (i) Higher dosages of rCFRP pieces or rCF adversely affect the workability of concrete/mortar, attributable to the agglomeration of recyclates and fibre balling effect. Through the literature review, the recommended dosage considering workability is 0.25%. (ii) The effects of rCFRP on the compressive properties of concrete/mortar are varied. Compressive strength can be enhanced by incorporating rCFRP or rCF, which reduces the possibility of crack propagation. Nevertheless, epoxy resin residue on the waste can negatively impact strength. (iii) In general, rCFRP-incorporated concrete/mortar exhibits increased tensile and flexural performance, which is attributable to improved interfacial bond strength and fracture delay ability. Usually, the addition of 0.25 to 1% of recyclates positively influences the mechanical properties. (iv) The use of rCFRP in concrete can substantially improve impact resistance. These summaries provide insights from past studies, offering valuable conclusions and recommendations for future research. They have given ongoing researchers a deeper understanding based on previous cases. However, the effects of incorporating different types of CFRP waste may vary slightly depending on the specific case and should be studied individually.

2.3.3 Cement-based sensors with CF and CFRP recyclates

SHM plays a critical role in ensuring the safety, reliability, and longevity of civil infrastructure. It addresses the challenges posed by progressive degradation due to harsh environments, repetitive stress, and unexpected loads such as seismic activity and heavy winds. Through real-time monitoring capabilities, SHM enables early anomaly detection, thereby reducing risks and enhancing structural performance. Over time, SHM techniques have evolved from traditional strain gauges to advanced technologies such as fibre optic sensors and electromechanical impedance [112, 113]. Conventional non-destructive testing (NDT) systems rely on sensors integrated into structural components during construction. While effective, these systems face limitations such as high costs, complex installation processes, and localised data collection, which restrict their ability to monitor the entire structure comprehensively. While traditional inspection methods remain common practice, they are less effective than implementing comprehensive monitoring systems. Despite the clear benefits, no regular monitoring techniques for concrete structures have been widely adopted, even in developed nations where infrastructure management is a priority [114].

The development of self-sensing concrete structures has gained significant attention among researchers for SHM applications. This innovative approach has the potential to overcome traditional monitoring limitations. Cement-based sensors represent a type of self-sensing material that incorporates conductive fillers, forming conductive networks within CCs. These materials function as inherent sensors, enabling structural monitoring without the need for additional sensing devices. Such conductive CCs for this purpose are also known as intrinsic self-sensing concrete, smart concrete, or piezoresistive concrete [115, 116].

2.3.3.1 Materials and fabrication

Cement-based self-sensing composites consist of three main components: conductive fillers, matrix materials, and dispersion materials. While conventional cementitious materials such as concrete, mortar, and cement paste serve as the matrix material forming the bulk of the composite, they inherently possess high electrical resistivity and thus lack functional self-sensing capability. The incorporation of conductive fillers therefore becomes crucial in the development of cement-based sensors. Various carbon-based materials have been employed as conductive fillers to enhance electrical properties, including CF [85, 86, 89], graphite powder (GP) [117, 118], carbon nanotube (CNT) [119, 120], carbon nanofiber (CNF) [121, 122] and carbon black (CB) [123-126]. The electrical conductivity of concrete, defined as its ability to carry electric current, is influenced by multiple factors such as material composition and moisture content. This conductivity operates through two distinct mechanisms: electrolytic conduction, which occurs through mobile ionic species present when the binder is mixed with water, and electronic conduction, which involves free electron mobility across conductive phases [85, 86, 114]. As conductive fillers are progressively incorporated, the concrete's conduction mechanism gradually transitions from electrolytic to electronic [114]. Among all conductive materials, fibrous elements demonstrate improved sensing properties compared to particulate fillers, as their ability to establish conductive networks within the matrix [112]. Additionally, the combined use of two or more conductive materials can potentially enhance mechanical and electrical properties. Incorporating carbon nano-additives densifies the matrix microstructure by filling the pores between hydration products, while fibrous carbon additives improve reinforcement within the matrix. Among these conductive functional fillers, CF has emerged as the most widely utilised fibrous material in previous research, owing to its distinctive properties including outstanding strength-to-density ratio, high aspect ratio, chemical stability, and preferred electrical conductivity [116]. As another component, dispersion materials facilitate better distribution of conductive fillers. When incorporating

fibrous conductive fillers, these materials help minimise agglomeration within the cementitious matrix. Mineral additives such as fly ash and silica fume aid dispersion through their finer particle sizes [116]. Chemical admixtures, such as tributyl phosphate and methylcellulose, improve dispersion by modifying surface properties between conductive fillers and the matrix, thereby enhancing the workability of the fresh mixture [112].

Mixing conductive fillers into fresh paste is an important step in the fabrication of CCs, as the uniformity of this mixture directly affects both mechanical properties and sensing behaviour of the cement-based sensors. The established three ways of mixing are presented in Figure 2-10. The selection of an appropriate mixing sequence should be tailored to the specific type of conductive filler used. A summary of recommended mixing processes for various filler materials can be found in the review studies [116, 127]. Furthermore, when using multiple conductive fillers, a combined mixing process is recommended to enhance overall effectiveness. With respect to mixing methods, previous studies have identified two primary types of dispersion techniques [116, 127]. The first category, known as physical or mechanical methods, includes techniques such as mechanical stirring, high-speed mixing, and ultrasonication, to effectively separate additive fillers. The second category, chemical dispersion, utilises chemicals to alter the surface properties of fillers through covalent or non-covalent interactions. The subsequent step in fabrication involves moulding and curing [116, 127]. Among various fabrication techniques, casting combined with external vibration to minimise air bubbles is the most commonly employed method. Properly designed curing conditions are crucial, as they affect the microstructure of CCs, including hydration products, the interface between conductive fillers and the matrix, and the water content. These factors will collectively influence the overall performance of the CCs.

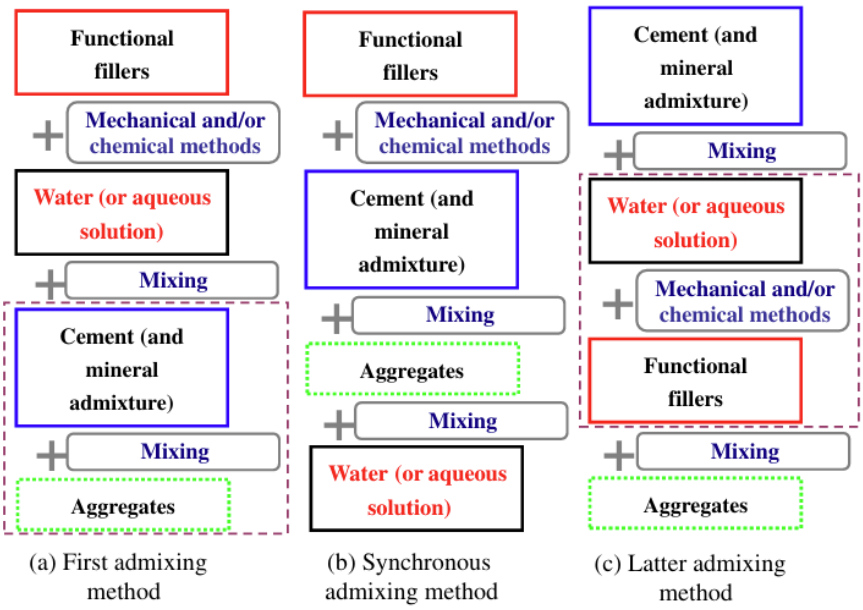

Figure 2-10. The mixing process for CCs fabrication [116].

2.3.3.2 Measurement and testing method

Several methodologies and guidelines have been established for measuring concrete electrical resistivity. Han et al. [116] conducted a comprehensive review of six electrical resistance measurement methods from existing literature, which differ in their electrode materials, fixation methods, and layout configurations. The electrodes require high electrical conductivity and stability in conductive properties, typically utilising metallic materials such as steel and copper, configured in forms of plates, mesh, or rods. These electrodes can be either surface-mounted (Figure 2-11 (a) and (b)) or embedded within the concrete during casting (Figure 2-11 (c) to (f)). Practical implementation has revealed limitations of surface-mounted electrodes, despite being the simplest method. These include susceptibility to debonding from concrete structures, lower durability, and higher contact resistance [127]. The measurement layouts primarily fall into two categories, which are two-probe (Figure 2-11 (a) and (c)) and four-probe (Figure 2-11 (b), (d) to (f)) configurations. While the two-probe method offers simplicity and straightforward implementation, the four-probe approach ensures higher accuracy by eliminating contact resistance, which is the resistance at the electrode-concrete interface [116].

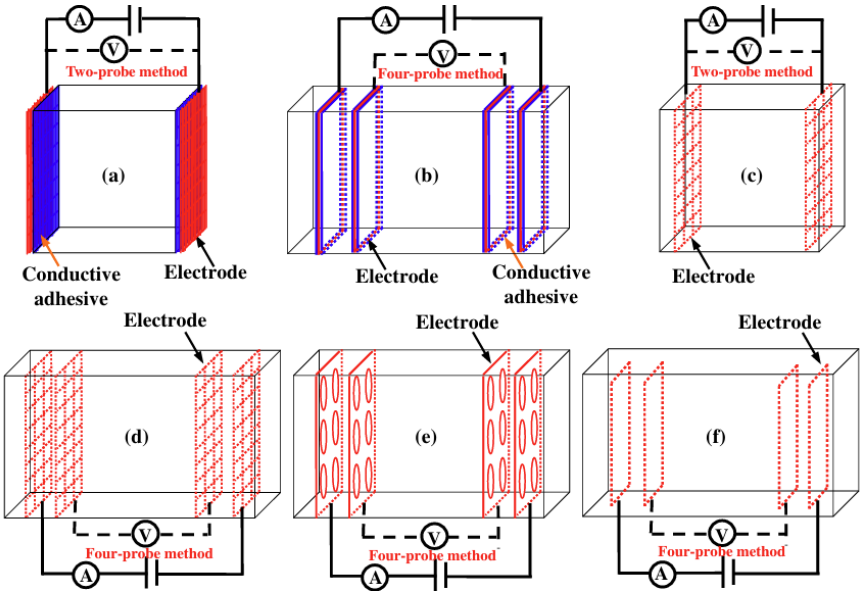

Figure 2-11. Electrical resistance measurement methods [116].

Among these configurations, two methods are commonly used for laboratory-based NDT of electrical resistivity: the bulk electrical resistivity measurement utilising two-point probe configuration, and the surface resistivity measurement employing the Wenner array technique with four-point probe arrangement [114, 128]. Commercial devices, such as Resipod [129], are available for conducting resistivity measurements. The bulk resistivity measurement, also known as the uniaxial method, involves positioning a cylindrical specimen between two electrodes, with conductive foam inserts serving as electrical contacts at the electrode-concrete interfaces. This technique determines the electrical conductivity by measuring the current flow across all phases within the concrete specimen. The setup of bulk resistivity measurement is presented in Figure 2-12. The resistivity (ρ) is determined using the measured voltage and current, following Equation 2-1, derived from Ohm's law:

$$\rho = \frac{VA}{IL} \qquad 2\text{-}1$$

where V is the measured voltage across the specimen, A is the cross-sectional area of the specimen, I is the current passing through the specimen, and L is the length of the specimen.

The electrical resistance of the concrete specimen is determined by subtracting the resistance of both foam inserts from the total measured resistance of the cylinder as Equation 2-2. The specimen resistance calculated is in the unit of kΩ·cm. To convert the measured resistance to bulk electrical resistivity, the geometric characteristics of the measurement configuration must be taken into account. The bulk resistivity of the specimen is calculated using Equation 2-3.

$$R_{specimen} = R_{measured} - R_{upper\ insert} - R_{lower\ insert} \qquad 2\text{-}2$$

where R is the true resistance, $R_{measured}$ is the measured total resistance, and $R_{upper\ insert}$ and $R_{lower\ insert}$ are the measured resistances of the top and bottom inserts.

$$\rho_{specimen} = \frac{A}{L} \times \frac{R_{specimen}}{2\pi a} \quad 2\text{-}3$$

where a is the equal spacing between adjacent electrodes.

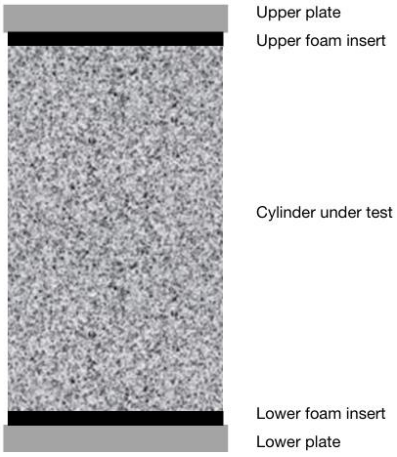

Figure 2-12. Bulk resistivity measurement setup [129].

The four-point probe arrangement, also known as the Wenner array method, is commonly used for field measurements. In this setup, four electrodes are placed in a linear array with equal spacing between them. The outer two electrodes are used to impress current into the material, while the inner two electrodes measure the resulting potential difference. When the electrodes make contact with the surface, the resistivity (ρ) can be calculated using the Equation 2-4:

$$\rho = \frac{2\pi aV}{I} \quad 2\text{-}4$$

where V is the potential difference measured between the inner electrodes, I is the current flowing between the outer electrodes.

The standard AASHTO-T-358 [130] establishes a standardised methodology for evaluating the surface electrical resistivity of water-saturated concrete specimens. The test method requires a four-point Wenner array probe configuration to measure the resistivity of cylindrical specimens with dimensions of either 200 mm × 100 mm or 300 mm × 150 mm (length × diameter). The surface resistivity, measured in kΩ·cm, serves as an indirect indicator of the concrete's resistance to chloride ion penetration.

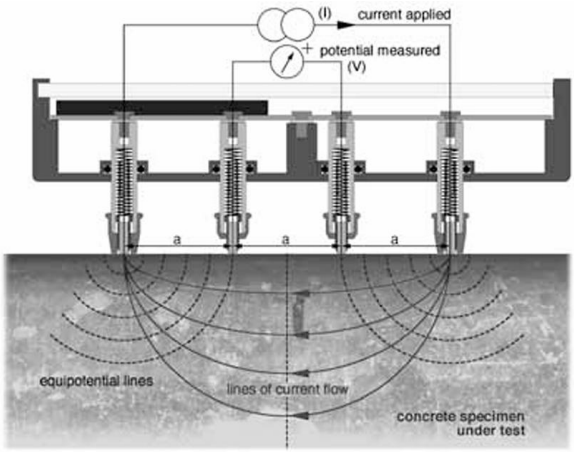

Figure 2-13. Surface resistivity measurement setup [129].

The geometric correction factor (k), which is unitless for surface measurement, is derived from recent research that considers various cylinder geometries. This adaptation standardises surface resistivity measurements across different sample dimensions while maintaining consistency with the established AASHTO methodology. For more detailed procedural specifications regarding measurements on various specimen geometries, researchers and practitioners should refer to AASHTO T 358-15 standard and the methodologies established in recent literature [114, 129, 130].

$$k = \frac{2\pi}{1.09 - \frac{0.527}{\frac{d}{a}} + \frac{7.34}{(\frac{d}{a})^2}} \quad 2\text{-}5$$

where d is the cylinder specimen diameter, and a is the probe spacing.

2.3.3.3 Electrical resistivity and piezoresistivity of CCs with CF/CFRP recyclates

Recent studies have demonstrated that incorporating discrete short CFs into cement-based materials enhances both their mechanical properties and electrical conductivity by establishing a conductive network [85-89, 111]. Han et al. [88] investigated the impact of incorporating 3mm and 6mm CFs at varying concentrations (0 to 2 wt% of cement) on the electrical resistivity of mortar. They found that the minimum electrical resistivity occurred at a CF content of 2 wt% (equivalent to 0.6 vol% of the mixture), due to the tunnel effect, which established a stable conductive network. Additionally, the study indicated that 6mm CFs were more effective in enhancing the electrical properties. However, the authors did not highlight that the reduction in electrical resistivity became less pronounced (flattened slope) when CF content exceeded roughly 1.1 wt% (around 0.33 vol% of the mixture). Subsequent researchers investigated the electrical percolation threshold to establish the optimal CF content for CCs. The electrical percolation threshold in CCs is the critical CF content at which the material transitions from an

insulator to a conductor. For example, Deng et al. [89] reported that with a CF content of 0.2% by volume, a continuous conductive network was fully established, reaching the percolation threshold. Beyond this concentration, while the resistivity continued to decrease, the change was minimal. Previous studies recommend incorporating CFs at volumes between approximately 0.1 to 1 vol% of the mixture to enhance electrical conductivity, and the electrical conductivity is influenced by both the length and concentration of the CFs in the mixture [85-87, 89].

The relationship between electrical conductivity and stress/strain, commonly referred to as piezoresistive behaviour, has been a focal point of research to evaluate the self-sensing abilities of concrete and mortar incorporating various conductive fillers. Donnini et al. [85] investigated the effects of varying concentrations of CF in cementitious materials. They found that electrical resistivity decreases during the loading-unloading cycle due to fibre push-in, while it increases as a result of fibre pull-out. Additionally, the observed high sensitivity to changes in stress was attributed to the elevated fibre concentration near the percolation threshold. According to the research conducted by Wang and Aslani [87], the optimal piezoresistivity of mortar was achieved with 0.7 wt% of 3 mm CFs, resulting in a fractional change in resistivity of 70%. This was followed by a 30% fractional change observed with 0.5 wt% of 6 mm CFs. Furthermore, additional studies showed that combining conductive fibre with fillers results in a more efficient conductive system. Chen et al. [118] found that the simultaneous incorporation of 0.7 wt% CFs and 2.5 wt% graphite (both based on the weight of cement) into CCs enhances its smart properties under flexural loads. CFs created an integrated conductive network through overlapping and entangling, but fibre aggregation reduced electrical conductivity. A small percentage of graphite could effectively fill the gaps between the CFs, thereby improving the electrical characteristics of the CCs. Belli et al. [131] found that while the combination of 0.2% CF by mortar volume and 4% graphene nanoplatelets by weight of cement exhibited high electrical conductivity and reduced noise in the fractional change ratio, its sensitivity is lower than that of 0.2% CF alone. Furthermore, it is important to note that enhanced electrical properties do not necessarily correlate with improved piezoresistive behaviour. In recent years, the hybrid combination of CFs with various functional conductive fillers, such as CNFs and (nano) CB, has been the subject of extensive study [121, 132].

Despite the limited research available, the existing studies on the influence of rCF and rCFRP on the electrical resistivity of CCs suggest that these recyclates can effectively enhance the electrical properties of cementitious structures [82]. Faneca et al. [133] conducted the first

study on the feasibility of incorporating 12mm PAN-based rCFs to create conductive CCs. Using the wet mix method, they maintained the workability of fresh concrete within an acceptable range, while the dry mix method resulted in reduced mechanical performance. For rCF contents ranging from 0.2 to 0.8 vol%, the electrical resistivity of wet mix samples ranged between 3 and 0.6 Ω·m, comparable to values reported for vCFs. These findings highlight the potential of using rCFs to develop multifunctional cementitious materials. Belli et al. [134] compared the effects of incorporating 6mm length commercial and recycled CFs into mortars. While mechanical strength remained similar for both types of fibres when combined with industrial by-product conductive fillers, the carbon micro-fragments on the rCF surface contributed to providing nucleation sites for hydration products and enhancing fibre-matrix adhesion. This in turn led to reduced porosity and increased compressive strength of the mortars. The most significant resistivity changes under strain were observed in specimens containing 2 vol.% used foundry sand and 0.2 vol.% rCFs. Li et al. [135] investigated the incorporation of rCFs with smooth surfaces, minimal resin residue, and lower graphitisation compared to vCFs. They observed that the electrical resistivity of CCs decreased with increasing rCF content, with a conductivity threshold of 0.5 wt.% of cement for 10 mm rCFs. When the fibre length was increased to 20 mm, the higher likelihood of fibre overlap reduced the conductivity threshold to 0.4 wt.%. The same research group also recently explored the impact of chemically modified rCFs on the electrical conductivity of CCs [104]. They found that increased surface roughness and better wettability of rCFs enhanced the electrical conductivity of the composite, while a lower degree of graphitisation negatively affected the conductivity. The resistivity decreased by approximately 91% at 0.2 wt.% rCF content, with a percolation threshold at 0.3 wt.%. Alkali-neutralised modified rCFs further improved conductivity, reducing resistivity by an additional 14.3% compared to unmodified CFs [104].

To summarise, the electrical conductivity of both vCF and recycled CFRP composites are advantageous for developing multifunctional CCs. Whether in their pristine state or after chemically modified-state, rCFs in both fibrous and powder forms can establish conductive networks within the cementitious matrix. The effectiveness of these recyclates largely depends on various parameters, including fibre length, concentration, and both intrinsic and modified fibre properties. Therefore, a more detailed investigation is required to analyse a wide range of parameters that influence the performance of rCF-reinforced CCs. Beyond the rCFs, critical factors to consider include CC formulations, fibre dispersion techniques and their efficiency, diverse curing conditions and their effects, as well as the influence of different additives [82].

2.4 CF SURFACE MODIFICATION TECHNIQUES FOR ENHANCED FRCC

As previously discussed, recovered CFRP waste has the potential to enhance the overall performance of CCs when incorporated with proper design. Most studies have focused on incorporating CF and its recyclates in fibrous form, as fibres in the cementitious matrix enhance load-bearing capacity and distribute stresses effectively, mitigating crack propagation through their bridging effect. It is now widely acknowledged that the bonding properties of the fibre-matrix interface significantly influence the mechanical properties of FRCCs [136]. Stronger fibre-matrix interactions notably enhance tensile properties while also contributing to the high toughness of FRCCs [136]. vCF without surface coating has stable properties, including chemical inertness, non-polarity, and hydrophobicity, which result in poor affinity to water-based mineral matrices [137, 138]. One of the key challenges in enhancing FRCC performance is the insufficient interfacial bond between CF and the cementitious matrix. Although some types of commercial CF are coated with sizing agents, these are designed for compatibility with specific resin systems. These treatments may still limit their effectiveness in cementitious materials and hinder the full utilisation of CFs in FRCCs [87, 139].

Understanding the interface and bonding mechanisms between CF and the cementitious matrix is fundamental to advancing the development of CCs. While some research has focused on modifying CFs surface to improve bonding with the matrix, techniques specifically targeting the cementitious matrix remain an ongoing subject of investigation. This section aims to bridge this gap by providing a review of the interfacial bonding between CF and cementitious matrices (Section 2.4.1), examining surface modification strategies to enhance the performance of FRCCs (Section 2.4.2), and highlighting multi-scale techniques used to evaluate the effectiveness of these enhancements (Section 2.4.3).

2.4.1 CF-matrix interface and bonding mechanisms

In FRCC, the interfacial transition zone (ITZ) between the fibre and the cementitious matrix represents a critical boundary region that significantly influences bonding behaviour at both the nanoscale and microscale [136]. The porous ITZ in FRCC was initially identified in CCs reinforced with macrofibres, which measure a few millimetres in diameter [140, 141]. Recent research has also highlighted the presence of the ITZ in composites with microfibers, typically having diameters in the micron range [142]. Due to their higher aspect ratio and larger surface area, microfibers underscore the critical importance of the ITZ in the performance of

FRCC. The schematic and microstructural illustration of the ITZ between the fibre and cementitious matrix is presented in Figure 2-14.

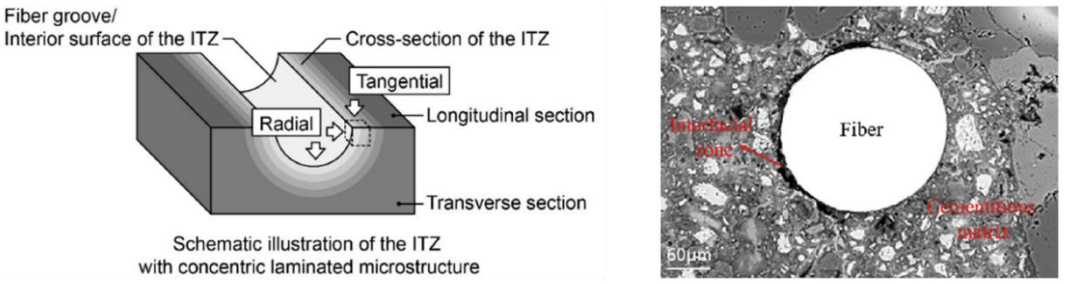

(a) Schematical representation of the longitudinal sectional view of the ITZ

(b) BSEM image of the ITZ between untreated steel fibre and cement matrix

Figure 2-14. Illustration of the ITZ: Schematic and microstructural view [141, 142].

The interaction between CF and the matrix depends on multiple factors, including the type of bond formation (chemical or mechanical) and fibre surface properties (such as surface roughness and wettability). A recent literature review by Lin et al. [136] identifies three major bonding mechanisms between fibres and cementitious matrices: (1) electrostatic attraction, (2) chemical bonding, and (3) mechanical bonding. In most cases, a combination of these bonding mechanisms is preferred for developing enhanced interfacial shear strength [138].

(1) Electrostatic attraction bonding occurs when positive ions (e.g. Ca^{2+}) in the cementitious matrix are attracted to the negatively charged fibre surface. This interaction creates an interface characterised by two charged layers, commonly referred to as the electric double layer (EDL) [143]. As an example, surface imperfections and functional groups present on CNT surfaces could generate negative charges and induce dipole moments, facilitating the deposition and growth of hydration products at the ITZ. At lower CNT concentrations, ion-dipole interactions between the cement paste and CNTs lead to strong intermolecular forces that can extend over longer distances. The optimal mechanical performance, with an improvement of up to 24%, was achieved at a CNT concentration of 0.2% [144]. The electrostatic interaction becomes particularly dominant for small-scale fibres [136].

(2) Chemical bonding, the most recognised and established bonding theory, is fundamentally based on atomic and ionic interactions at the fibre-matrix interface. It has a much larger contribution to bonding with microfibres compared to macrofibres [145]. For instance, Huang et al. [145] reported that the reactive functional groups (e.g. -COOH and -OH) presented on the CF surface enhanced interactions with hydration products (e.g. C-S-H) in the cementitious matrix. Additionally, the surface treated CFs containing these oxygen-containing

functional groups could also form hydrogen bonds and Van der Waals forces at the interface, contributing to enhanced interfacial adhesion. Such functional groups significantly enhance the strength of the ITZ while simultaneously bridging it, thereby improving the mechanical performance of the composite [136].

(3) Mechanical bonding primarily occurs through physical interlocking mechanisms between the CF surface and the cementitious matrix, which are largely dependent on the fibre surface roughness and morphology. The physical interaction between surface irregularities and hydration products creates mechanical anchorage points that contribute to interfacial bond strength. It can be enhanced through two primary approaches: increasing the CF surface roughness and attaching secondary materials to the CF surface. For example, plasma treatment utilising argon, nitrogen and oxygen effectively enhanced CF surface roughness by removing sizing agents and selectively etching disordered carbon structures located between spherical domains, according to the experimental study conducted by Kim et al. [146]. These surface modifications contributed to enhanced interfacial bonding in the transition zone between the CF and cementitious matrix. As another example, Lu et al. [147] modified CF by depositing a thin layer of silicon dioxide on their surface, enabled chemical bonding between the silica layer and calcium hydroxide in the cement matrix while significantly increasing surface roughness. The roughness created additional active sites for bonding and led to the densification of the ITZ, ultimately enhancing fibre-matrix adhesion.

Thus, building on the understanding of fibre-matrix bonding types and mechanisms, researchers have been actively developing and optimising various surface modification strategies, which will be discussed in the next section. These advancements aim to enhance the performance of CCs that incorporate CFs.

2.4.2 Surface modification techniques

The surface modification of CF can generally be categorised into two main approaches: chemical modifications (e.g. the introduction of functional groups to create new active sites that facilitate chemical bonding) and physical modifications (e.g. enhancing the surface roughness of the fibres to promote mechanical interlocking with the matrix) [138]. Additionally, hybrid approaches that combine both chemical and physical methods are also prevalent [137, 148]. For instance, the use of coupling agents and the grafting of CF with nanoparticles can serve as a bridge to improve adhesion between the fibres and the matrix. Successful surface modification is also associated with improved wettability, which plays a crucial role in enhancing adhesion

at the fibre-matrix interface [148]. Over the past few decades, extensive research has focused on developing surface modification techniques to enhance CF in FRCC. The modification methods can be primary categorised into four main groups: Plasma treatment, Oxidation treatment, electrophoresis and grafting treatment [137].

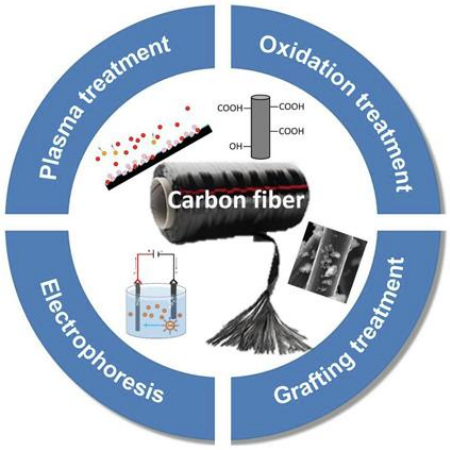

Figure 2-15. CF surface modification methods [137].

2.4.2.1 Plasma treatment

Plasma treatment is one of the predominant techniques for modifying CF surface to enhance its wettability and its interfacial bonding with the cementitious matrix. The process generates free radicals, ions, electrons and other metastable species that interact with the fibre surface [137, 148]. The effects of plasma treatment vary depending on the type of gas used, such as oxygen, nitrogen, or inert gases, as well as the treatment conditions and duration. They can induce various degrees of surface modification, leading to effects such as oxidation, cross-linking and etching of the CFs [138, 148]. Plasma treatment offers several benefits, including the generation of functional groups that facilitate chemical bonding with matrices, enhancement of surface roughness to improve mechanical interlocking, increased surface energy to promote wettability, and the removal of fibre sizing agents or contaminants to ensure better surface contact and adhesion. Zhao et al. [149] demonstrated the improved fibre-matrix bond in FRCC by employing low-pressure, pulsed plasma treatment using oxygen and argon gases over a relatively long treatment. This approach generated a thick layer of silicon oxide films on the CF surface. The induced hydrophilic functional groups and increased surface roughness significantly enhanced the interaction between CF and the cementitious matrix. More localised formation of C-S-H was observed at the CF surface, further improving the fibre-matrix bond. Li et al. [150] studied various process parameters and identified the optimal oxygen plasma

treatment conditions to enhance the bond between CF and cementitious matrix by introducing polar functional groups onto the fibre surface. After treatment, the CF tensile strength was not compromised. It even slightly increased due to the smoothing effect. Moreover, Kim et al. [146] compared the effects of plasma treatment using three different gases to introduce hydrophilic functional groups onto the CF surface, enhance surface roughness, and accelerate the hydration process. Although nitrogen and oxygen plasma treatments proved effective, they induced excessive surface etching, which negatively impacted fibre strength. In comparison, argon plasma treatment demonstrated better efficacy, achieving the highest interfacial shear strength while preserving fibre's integrity. To briefly summarise, plasma treatment requires controlled conditions to achieve the desired effects. Excessive treatment, such as prolonged duration, can degrade fibre strength and wettability. Additionally, the reliance on low-pressure conditions poses challenges for scaling up to continuous large-scale production [137]. While plasma treatment is known for its time efficiency, its application is often constrained by high operational costs due to the specialised equipment and energy-intensive reaction conditions required for the process [137].

2.4.2.2 Oxidation treatment

The oxidation process can be further categorised into gaseous oxidation (e.g. in air or ozone at evaluated temperature), liquid phase oxidation (e.g. using nitric acid or hydrogen peroxide) and anodic oxidation (e.g. electrochemical treatment) based on the oxidizing medium [137]. A comparative investigation was conducted on oxidation treatments on CF powder and 3mm length CFs, using both gaseous and liquid oxidants in different conditions [151]. Among these methods, thermal oxidation in air at 410°C emerged as the most effective approach for enhancing mechanical properties. The best performance is attributed to the dual benefits of improved fibre-matrix anchorage through both chemical surface modifications and physical alterations in surface roughness. The oxidation treatment successfully modified the CF surface by introducing oxygen-containing functional groups, which significantly enhanced the interactions between the fibres and the silicate and aluminate phases of the cementitious matrix. These surface modifications resulted in increased surface polarity, leading to improved wettability and reactivity of the CFs. Consequently, these changes promoted better fibre dispersion within the cementitious matrix and strengthened the fibre-matrix interfacial bond. The enhanced interfacial properties ultimately contributed to improved strength and ductility of the CCs. Lavagna et al. [152] has also demonstrated that oxidative treatment with piranha

solution (a 3:1 mixture of sulfuric and hydrogen peroxide) at 30°C for 30 minutes significantly enhanced both the electrical and mechanical properties of FRCC.

Electrochemical (anodic) oxidation stands out as an industrially attractive method for continuous and large-scale CF modification as it enables systematic control of oxidation parameters through adjustable potential, current, and electrolyte composition [137, 148]. At present, this approach remains limited in its application to CFs specifically tailored for cementitious matrices [137]. A recent study revealed that anodic oxidation in pore solutions can effectively introduce oxygen-containing functional groups on CF surfaces. These groups facilitated calcium ion interactions from the pore solution, promoting the growth of calcite and the formation of a denser interfacial microstructure around the CFs. Their findings demonstrated that mild oxidation conditions (1V for 30 minutes) increased the CF tensile properties by 19.1%, while moderate treatment parameters (3V for 15 minutes) enhanced the fibre-matrix interfacial bond strength by 37.9% [153]. Based on their initial research, Li et al. [154] developed an anodic oxidation process for pyrolysis recovered rCF using a sodium hydroxide solution, specifically for integration into alkali-activated CCs. This process introduced acidic functional groups on the fibre surface, facilitating the formation of sodium-alumina-silicate-hydrate (N-A-S-H) and densifying the ITZ at the fibre-matrix interface. As a result, the electrochemically modified composites with treated rCFs demonstrated a 10% improvement in flexural strength compared to those with untreated fibres. However, a slight reduction in compressive strength was observed, which was attributed to the enhanced surface wettability that increased water demand and subsequently led to higher matrix porosity. In addition, Huang et al. [145] examined the interfacial bonding between CF with anodization and epoxy coating and the high strength paste used in ultra-high performance concrete (UHPC). Their study revealed that anodized CFs exhibited significantly improved properties compared to untreated CFs, including a 117% increase in chemical debonding energy, a 67.8% increase in interfacial friction bond strength, and an 88.6% increase in CF-matrix bond strength. The introduction of oxygen-containing functional groups on the surface of CFs significantly enhanced Van der Waals interactions and promoted stronger hydrogen bonding with the C-S-H gel. This modification resulted in improved chemical adhesion between the treated CFs and the cement paste matrix, contributing to a stronger interfacial bond. Traditional oxidative treatments have faced several limitations, including being time-consuming, costly, and associated with environmental pollution concerns. In contrast, anodic oxidation has been

gaining increasing attention from researchers as a simpler, more cost-effective method with minimal environmental impact [137, 154].

2.4.2.3 Electrophoresis

Electrophoresis, also known as electrophoretic deposition (EPD), is a promising surface modification technique for CFs, offering precision and uniformity in the coating process. This technique involves the migration of charged particles toward oppositely charged electrodes in a solution when an electric field is applied, resulting in the deposition on the CF surface [137]. Several nano materials have been successfully deposited onto the CF surface for enhancing interfacial bond strength and FRCC's overall mechanical properties. Graphene oxide (GO) can be efficiently deposited on CF surfaces through EPD, resulting in enhanced surface properties including wettability, chemical reactivity, and roughness [155]. Thus, this surface modification significantly improved the interfacial interaction between CFs and the cementitious matrix. Additionally, GO served as a nucleation site for cement hydration products around the fibre surface. The incorporation of GO-modified fibres led to at least 14.58% improvement in the flexural strength of the composite, with further enhancements possible through pre-dispersion in GO solution. GO solutions functioned as dispersing media, facilitating improved CF distribution within the matrix. More studies have explored the EPD of nano-silica (NS) onto CF surfaces to enable tailored interfacial bonding with cementitious matrices. EPD at 1V for 5 minutes successfully enabled nano-silica deposition onto CF surfaces, resulting in an 182% enhancement in fibre pullout work [156]. This significant improvement was due to the formation of a pozzolanic reaction with surface-deposited NS. The resulting surface structure promoted mechanical interlocking with the cementitious matrix, while the formation of C-S-H gel and calcite further strengthened the interfacial bond. Furthermore, the authors also investigated the influence of electrolyte pH on both the quality of the NS coating and the resulting CF properties [157]. Acidic conditions in the EPD system facilitated a more uniform and homogeneous distribution of NS onto CF surfaces, whereas alkaline environments resulted in reduced NS deposition. Consequently, the acidic environment yielded a higher degree of interfacial bonding characteristics compared to neutral and alkaline conditions. Moreover, Wang et al. [158] employed a novel combination of NS and soluble calcium salts as electrolytes in EPD for CF modification. This approach effectively reduced defective carbon atoms and enhanced the physical anchoring between CF and the cement matrix. The modification increased oxygen-containing functional groups and CF surface hydrophilicity, promoting uniform hydration product formation and ITZ densification through the reaction of silicon

dioxide with calcium hydroxide. Electrophoresis is a useful technique for CF surface modification, ideal for incorporation into cementitious matrices due to its several benefits, including energy efficiency, operational simplicity, lower cost, and non-hazardous nature [136, 156-158]. While this methodology shows considerable promise, it remains in the developmental research phase.

2.4.2.4 Grafting treatment

Chemical grafting, characterised by covalent bonding, is another surface modification technique that enhances the interfacial bonding strength between CFs and cementitious matrices. Since physical grafting (e.g. Van der Waals interactions) is limited to relatively weak bonding, chemical grafting is now the dominant treatment, enabling robust attachment of nanoparticles to the CF surface [159]. Past studies have successfully demonstrated the grafting of various nanoparticles, including CNT, NS, and GO, for this purpose. Cui et al. [159] proposed a novel chemical grafting approach utilising (3-Aminopropyl) triethoxysilane (KH550 – a silane coupling agent) to bridge oxidised CFs and CNT through chemical bonding. This modification resulted in a 21.5% enhancement in flexural strength when CNT-grafted CFs were incorporated into CCs, compared to composites with ungrafted CFs, while the modification showed minimal impact on the compressive strength of the CC. Similarly, NS can be effectively grafted onto the CF surface using the sol-gel method, which enables the production of consistent, high-purity nanostructures at comparatively low temperatures. As reported by the previous studies [147, 160], pre-treatment with nitric acid and KH550 was employed prior to this process to enhance the surface roughness and reactivity of the fibres. After the sol-gel method, the NS formed on the CF surface interacted with calcium hydroxide, leading to the accumulation of C-S-H gel at the ITZ between the fibre and matrix. This interaction not only improved the interfacial friction strength but also significantly enhanced the mechanical properties of the FRCC. Specifically, compared to untreated samples, the tensile and flexural strengths of the resulting FRCC increased by 22.04% and 29.57%, respectively. Moreover, Zhou et al. [161] proposed the in-situ growth of hybrid NS and CNT to modify CF, aiming to enhance their interaction by introducing fine particles to provide more nucleation sites, enhancing pozzolanic activity, and improving physical friction properties. The synergistic effects of this hybrid grafting method significantly improve the shrinkage resistance and impermeability of FRCC. Additionally, KH550 has been utilised to bridge oxidised CF and GO, facilitating the successful grafting of GO onto the fibre surface [158]. The tensile strength of CF grafted with GO demonstrated a 22% enhancement compared to untreated CF.

Consequently, the strength and toughness of the CCs were also improved following the incorporation of the grafted CF. This enhancement is evidenced by an increased concentration of C-S-H at the fibre-matrix interface. While grafting treatments are relatively mild, minimising damage to the CF surface, they may involve complex procedures and produce harmful waste products [137, 148].

2.4.3 Techniques for examining the effects of surface modification

The effectiveness of CF surface modification can be systematically evaluated through various microstructural and mechanical tests. These techniques characterise both the morphological and physicochemical properties of CFs, as well as their interfacial performance in the cementitious matrix.

Scanning electron microscope (SEM) coupled with energy dispersive spectroscopy (EDS) can be used to examine both fibre surface alterations (e.g., morphology and elemental analysis) and the internal composition within the cementitious matrix (ITZ within the cement-based matrix). In addition, EDS analysis enables the quantitative determination of elemental composition and distribution across the examined region [81]. On another note, although atomic force microscopy (AFM) is not suitable for investigating modified CFs in cementitious matrices, it can provide high-resolution imaging on a nanoscale for surface topography measurement when operating in tapping mode [137]. The surface roughness and any deposition on the CF surface can be visually and quantitatively tested before and after modification [147]. Fibre surface characterisation also includes the identification of surface chemistry and crystalline structure analysis [137]. Techniques used for this purpose include, but not limited to, X-ray photoelectron spectroscopy (XPS), Fourier-transform-infrared (FTIR) spectroscopy, Raman spectroscopy and X-ray diffraction (XRD). The XPS survey spectrum provides an overview of the elemental composition and content of the surface, while changes in the chemical bonds of CFs resulting from modification can be analysed through XPS high-resolution spectra [162]. FTIR spectrums can be used for identifying mineralogical changes in both modified CFs and the resulting CCs following treatment. For example, Xu et al. [163] employed FTIR and XPS to examine the CFs synthesized with boron nitride (BN) nanosheets. Their analyses revealed the formation of robust N-C bonds between BN nanosheets and CF, facilitating strong interfacial adhesion between the two materials. In addition, Raman spectroscopy and XRD are typically used to characterise the crystalline structural changes in CF [137]. The degree of structural disorder in CFs can be evaluated through the analysis of the D-band (disorder-induced) and G-band (graphitic) intensities in Raman spectra. Then the ratio

of these two bands can quantitatively identify the degree of graphitization or disorder. In contrast, XRD analysis can be employed not only to investigate the crystalline structure of CFs but also to characterise phase changes during the cement hydration [81]. Other surface characterisation techniques involve contact angle measurement, which evaluates the surface energy and wettability behaviours of CFs [164]. On the other hand, Zeta potential measurements characterise the electrokinetic properties of CFs, including surface charge distribution and the stability of CF suspension [165, 166].

The mechanical performance of CF, such as tensile strength, is governed by its morphological features and intrinsic physicochemical properties, including graphitic crystallite size, orientation, and internal defects [137]. To assess the mechanical properties of CF, single fibre tensile testing is conducted until fibre failure occurs. The resulting stress-strain curves provide systematic information about key mechanical properties, including elastic modulus, ultimate tensile strength, and maximum elongation [167]. Pullout tests are employed to characterise the interfacial bonding between fibre and matrix, which can be categorised into one-sided and two-sided tests. The one-sided single fibre pullout test is most commonly utilised due to its simplicity and efficiency [136]. Katz et al. [168] introduced a detailed procedure for the test, which offers precise control over fibre placement (Figure 2-16). The test is conducted at a constant loading rate, during which the specimen undergoes distinct stages: initial linear elastic deformation, elastic stretching, maximum load achievement, and finally, the debonding process (crack propagation) until complete fibre separation from the surrounding matrix [137]. Through analysis of the load-displacement curve and sample configuration, crucial results can be determined, including debonding strength, interfacial friction bond strength, and chemical debonding energy [145, 163]. CF pullout tests can also be conducted on bundles or yarns [146]. However, the testing results are influenced by several critical factors, including CF alignment and the distribution of CF filaments across the cross-section. Such variations may result in different bonding strength measurements compared to single fibre pullout tests. The evaluation of bonding performance between CF yarns and the matrix can be also conducted using double-sided pullout tests, where specimens are fabricated in symmetrical configurations, such as tetragonal prisms or dog-bone configurations [136, 137]. Beyond interfacial bonding characterisation, the practical performance of FRCC incorporating modified CFs is typically evaluated through compressive and flexural mechanical testing. These macroscale tests provide valuable insights into how enhanced fibre-matrix interactions improve the overall properties of the CC system.

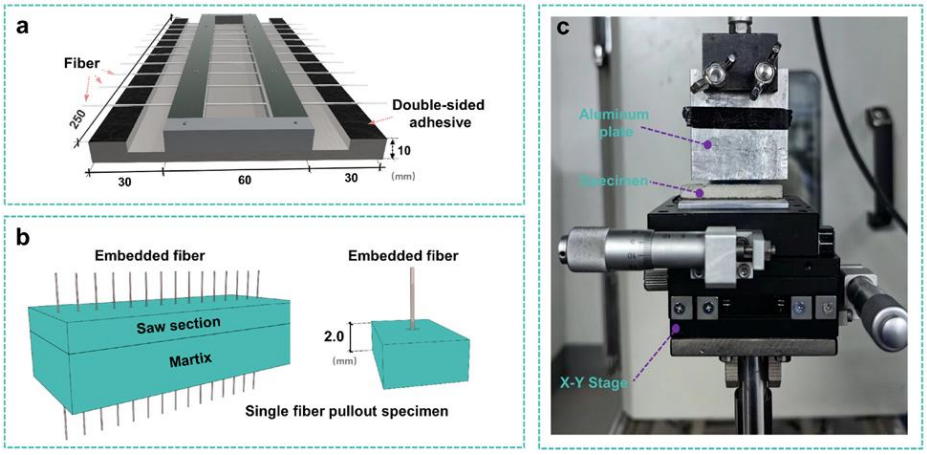

Figure 2-16: Sample preparation and testing setup for single fibre pullout test [163].

2.5 CONCLUSIONS

The incorporation of FRP composite wastes into cementitious materials offers a sustainable solution for managing industrial composite waste, providing both environmental and economic benefits. This repurposing strategy also has the potential to advance the multifaceted performance of the resulting CCs. Reviewing the literature not only provides current knowledge and highlights development trends but also identifies research gaps and limitations that need further investigation.

A systematic review demonstrated the viable potential for incorporating GFRP and CFRP composite wastes into CCs, supporting their widespread application. Although fresh, physical and mechanical properties of the resulting CCs have been investigated, research on their durability and internal structural characteristics remains limited. Therefore, this research conducts a comprehensive investigation into the multifaceted performance of these CCs, focusing on acid diffusion, drying shrinkage, and water absorption, alongside advanced void geometry and feature detection analysis using micro-CT (Chapter 3). In addition, most existing research has primarily utilised laboratory-prepared composites rather than addressing the practical challenges of reusing industrial FRP waste. Thus, this research develops practical solutions for effectively repurposing real industrial waste FRP in cementitious materials (Chapter 5).

Previous research has primarily focused on incorporating vCFs into cementitious materials for developing cement-based sensors for SHM, with limited exploration of the self-sensing capacities of sensors incorporating various CFRP/CF recyclates. The impact of incorporating these recyclates on electrical properties largely depends on different factors such

as fibre properties and concentrations. In this context, Chapter 6 of this research investigates the effectiveness of utilising different forms of recyclates to develop and enhance the self-sensing capacities of cement-based sensors under varying environmental conditions.

Despite the existing surface modification techniques for enhancing the fibre-matrix interface, these conventional methods still present limitations related to cost, complexity, environmental impact, and compatibility with cementitious matrices. This research highlights the need for more efficient, cost-effective and environmentally friendly modification approaches. To address these challenges, two novel CF surface modifications are proposed in Chapter 4 to alter both the physical and chemical properties of CFs, promote fibre dispersion, and strengthen the interfacial interaction between CFs and the matrix, thereby improving the physical and mechanical performance of FRCCs.

2.6 REFERENCES

[1] J.-C. Liu, M.U. Hossain, S.T. Ng, H. Ye, High-performance green concrete with high-volume natural pozzolan: Mechanical, carbon emission and cost analysis, J. Build. Eng. 68 (2023) 106087.

[2] L. Zhang, M. Bian, Z. Xiao, X. Wang, B. Han, A comprehensive review of cementitious composites modified with nano silica: Fabrication, microstructures, properties and applications, Constr. Build. Mater. 409 (2023) 133922.

[3] H. Siad, M. Lachemi, M. Sahmaran, M. Zareechian, W.L. Baloch, 9 - Sustainable cementitious composites with recycled aggregates and fibers, in: A. Ashour, X. Wang, B. Han (Eds.), Sustainable Concrete Materials and Structures, Woodhead Publishing2024, pp. 239-283.

[4] A. Lefeuvre, S. Garnier, L. Jacquemin, B. Pillain, G. Sonnemann, Anticipating in-use stocks of carbon fiber reinforced polymers and related waste flows generated by the commercial aeronautical sector until 2050, Resour. Conserv. Recycl. 125 (2017) 264-272.

[5] D. Glosser, E. Santykul, E. Fagan, P. Suraneni, A thermodynamic perspective on wind turbine glass fiber waste as a supplementary cementitious material, CEMENT 9 (2022) 100039.

[6] M.C.S. Ribeiro, M.C.S. Ribeiro, A. Fiúza, A.J.M. Ferreira, Recycling and Reuse of Fiber Reinforced Polymer Wastes in Concrete Composite Materials, (2017) 155-173.

[7] S.A. Hadigheh, F. Ke, S. Kashi, 3D acid diffusion model for FRP-strengthened reinforced concrete structures: Long-term durability prediction, Constr. Build. Mater. 261 (2020) 120548.

[8] S.K. Gopalraj, T. Kärki, A review on the recycling of waste carbon fibre/glass fibre-reinforced composites: fibre recovery, properties and life-cycle analysis, SN Appl. Sci. 2(3) (2020) 1-21.

[9] S.A. Hadigheh, S.S. Mahini, S. Setunge, S.A. Mahin, A preliminary case study of resilience and performance of rehabilitated buildings subjected to earthquakes, Earthq. Struct. 11(6) (2016) 967-982.

[10] A. Yazdanbakhsh, L.C. Bank, Y. Tian, Mechanical Processing of GFRP Waste into Large-Sized Pieces for Use in Concrete, Recycling 3(1) (2018) 8.

[11] UnitedNations, Sustainable cities and human settlements. https://sustainabledevelopment.un.org/topics/sustainablecities.

[12] Y. Wei, S.A. Hadigheh, Development of an innovative hybrid thermo-chemical recycling method for CFRP waste recovery (In Press), Composite part B: ENGINEERING (2023).

[13] A.E. Krauklis, C.W. Karl, A.I. Gagani, J.K. Jørgensen, Composite Material Recycling Technology—State-of-the-Art and Sustainable Development for the 2020s, J. Compos. Sci. 5(1) (2021) 28.

[14] S. Hadigheh, Y. Wei, S. Kashi, Optimisation of CFRP composite recycling process based on energy consumption, kinetic behaviour and thermal degradation mechanism of recycled carbon fibre, J. Clean. Prod. 292 (2021) 125994.

[15] C.B. Farinha, J. de Brito, R. Veiga, Assessment of glass fibre reinforced polymer waste reuse as filler in mortars, J. Clean. Prod. 210 (2019) 1579-1594.

[16] Y. Wei, S.A. Hadigheh, Cost benefit and life cycle analysis of CFRP and GFRP waste treatment methods, Constr. Build. Mater. 348 (2022) 128654.

[17] H. Haowei, S.A. Hadigheh, Keyvan, Influences of fibre shape on the transverse modulus of unidirectional fibre reinforced composites using finite element and machine learning methods, Composite Structures 312 (2023) 116872.

[18] S.R. Naqvi, H.M. Prabhakara, E.A. Bramer, W. Dierkes, R. Akkerman, G. Brem, A critical review on recycling of end-of-life carbon fibre/glass fibre reinforced composites waste using pyrolysis towards a circular economy, Resour. Conserv. Recycl. 136 (2018) 118-129.

[19] S.A. Hadigheh, K. Feihu, F. Hamid, Durability design criteria for the hybrid carbon fibre reinforced polymer (CFRP)-reinforced geopolymer concrete bridges, Structures 35 (2022) 325-339.

[20] J. Zhang, V.S. Chevali, H. Wang, C.-H. Wang, Current status of carbon fibre and carbon fibre composites recycling, Compos. B. Eng. 193 (2020) 108053.

[21] B. Zhou, M. Zhang, L. Wang, G. Ma, Experimental study on mechanical property and microstructure of cement mortar reinforced with elaborately recycled GFRP fiber, Cem. Concr. Compos. 117 (2021) 103908.

[22] A. Yazdanbakhsh, L.C. Bank, K.-A. Rieder, Y. Tian, C. Chen, Concrete with discrete slender elements from mechanically recycled wind turbine blades, Resour. Conserv. Recycl. 128 (2018) 11-21.

[23] M.C.S. Ribeiro, A. Fiúza, A. Ferreira, M.D.L. Dinis, A.C. Meira Castro, J.P. Meixedo, M.R. Alvim, Recycling approach towards sustainability advance of composite materials' industry, Recycling 1(1) (2016) 178-193.

[24] S. Job, Recycling composites commercially, Reinf. Plast. 58(5) (2014) 32-38.

[25] M. Schmid, N.G. Ramon, A. Dierckx, T. Wegman, Accelerating Wind Turbine Blade Circularity, in: D. Fraile;, C. Walsh (Eds.) WindEurope; Cefic; EuCIA, Brussels, Belgium, 2020.

[26] V. Darli Rodrigues, V. Raimundo Kennedy, C. Milena Chang, Strategy and management for the recycling of carbon fiber-reinforced polymers (CFRPs) in the aircraft industry: a critical review, Int. J. Sustain. Dev. World Ecol. 24(3) (2017) 214-223.

[27] S.J. Pickering, Recycling technologies for thermoset composite materials—current status, Compos. Part A Appl. Sci. Manuf. 37(8) (2006) 1206-1215.

[28] P. Soraia, T.P. Silvestre, Recycling carbon fibre reinforced polymers for structural applications: Technology review and market outlook, Waste Manage. 31(2) (2011) 378-392.

[29] K. Pender, L. Yang, Investigation of catalyzed thermal recycling for glass fiber-reinforced epoxy using fluidized bed process, Polym. Compos. 40(9) (2019) 3510-3519.

[30] H. Lucile, S. Anna, D. Janosch, M.M. Wolfgang, A. Cyril, H. Siegfried, Semi-continuous flow recycling method for carbon fibre reinforced thermoset polymers by near- and supercritical solvolysis, Polym. Degrad. Stab. 133 (2016) 264-274.

[31] G. Jiang, S.J. Pickering, G. Walker, K. Wong, C. Rudd, Surface characterisation of carbon fibre recycled using fluidised bed, Appl. Surf. Sci. 254 (2008) 2588-2593.

[32] E.B. Paulsen, P. Enevoldsen, A Multidisciplinary Review of Recycling Methods for End-of-Life Wind Turbine Blades, Energies 14(14) (2021) 4247.

[33] S. Gharde, B. Kandasubramanian, Mechanothermal and chemical recycling methodologies for the Fibre Reinforced Plastic (FRP), Environ. Technol. Innov. 14 (2019) 100311.

[34] V. Amaral de Oliveira, F. Goettmann, High quality carbon fibers from end-of-life fiber reinforced plastics - a new recycling technology, ECCM18 - 18th European Conference on Composite Materials, Athens,Greece 2018.

[35] G. Oliveux, B. J-L, E. Le Gal La Salle, N. Lefèvre, G. Biotteau, Recycling of glass fibre reinforced composites made of unsaturated polyester by subcritical hydrolysis: Reaction mechanisms and kinetics, Influence of the chemical structure of the resin, Polym. Degrad. Stab. 98 (2013) 785-800.

[36] C. Mattsson, A. André, M. Juntikka, T. Tränkle, R. Sott, Chemical recycling of End-of-Life wind turbine blades by solvolysis/HTL, IOP Conference Series: Materials Science and Engineering 942 (2020) 012013.

[37] G. Oliveux, E. Le Gal La Salle, J.L. Bailleul, Recycling by solvolysis thermosetting composite materials of sustainable surface transport, AIP conference proceedings, American Institute of Physics, 2011, pp. 209-214.

[38] A.J. Nagle, E.L. Delaney, L.C. Bank, P.G. Leahy, A Comparative Life Cycle Assessment between landfilling and Co-Processing of waste from decommissioned Irish wind turbine blades, J. Clean. Prod. 277 (2020).

[39] N. Vijay, V. Rajkumara, P. Bhattacharjee, Assessment of composite waste disposal in aerospace industries, Procedia Environ. Sci. 35 (2016) 563-570.

[40] D. Peter, J.N. Angela, G. Fergal, L. Heloisa, L.D. Emma, M.M. Jennifer, G. Conor, G.L. Paul, P.D. Niall, M. Gerard, End-of-Life alternatives for wind turbine blades: Sustainability Indices based on the UN sustainable development goals, Resour. Conserv. Recycl. 171 (2021) 105642.

[41] N. Ramesh, T. Abbasi, S.M. Tauseef, S.A. Abbasi, Utilization of fiber-reinforced plastic (FRP) waste generated by a wind-turbine manufacturing company, Int. I. Sci. Eng. Res. 6 (2018) 103-129.

[42] A. Yazdanbakhsh, L. Bank, A critical review of research on reuse of mechanically recycled FRP production and end-of-life waste for construction, Polymers 6(6) (2014) 1810-1826.

[43] M. Mastali, A. Dalvand, A. Sattarifard, The impact resistance and mechanical properties of the reinforced self-compacting concrete incorporating recycled CFRP fiber with different lengths and dosages, Compos. B. Eng. 112 (2017) 74-92.

[44] M.C.S. Ribeiro, A.C. Meira-Castro, F.G. Silva, J. Santos, J.P. Meixedo, A. Fiúza, M.L. Dinis, M.R. Alvim, Re-use assessment of thermoset composite wastes as aggregate and filler replacement for concrete-polymer composite materials: A case study regarding GFRP pultrusion wastes, Resour. Conserv. Recycl. 104 (2015) 417-426.

[45] C. Xiong, Q. Li, T. Lan, H. Li, W. Long, F. Xing, Sustainable use of recycled carbon fiber reinforced polymer and crumb rubber in concrete: Mechanical properties and ecological evaluation, J. Clean. Prod. 279 (2021) 123624.

[46] M. Chen, H. Zhong, L. Chen, Y. Zhang, M. Zhang, Engineering properties and sustainability assessment of recycled fibre reinforced rubberised cementitious composite, J. Clean. Prod. 278 (2021) 123996.

[47] D. García, I. Vegas, I. Cacho, Mechanical recycling of GFRP waste as short-fiber reinforcements in microconcrete, Constr. Build. Mater. 64 (2014) 293-300.

[48] M. Mastali, A. Dalvand, A.R. Sattarifard, The impact resistance and mechanical properties of reinforced self-compacting concrete with recycled glass fibre reinforced polymers, Compos. B. Eng. 124 (2016) 312-324.

[49] M. Mastali, A. Dalvand, A.R. Sattarifard, Z. Abdollahnejad, Effect of different lengths and dosages of recycled glass fibres on the fresh and hardened properties of SCC, Mag. Concr. Res 70(22) (2018) 1175-1188.

[50] K. Patel, R. Gupta, M. Garg, B. Wang, U. Dave, Development of FRC materials with recycled glass fibers recovered from industrial GFRP-acrylic waste, Adv. Mater. Sci. Eng. 2019 (2019) 1-15.

[51] F. Tittarelli, Effect of low dosages of waste GRP dust on fresh and hardened properties of mortars: Part 2, Constr. Build. Mater. 47 (2013) 1539-1543.

[52] J.R. Correia, N.M. Almeida, J.R. Figueira, Recycling of FRP composites: reusing fine GFRP waste in concrete mixtures, J. Clean. Prod. 19(15) (2011) 1745-1753.

[53] P.S. Oliveira, M.L.P. Antunes, N.C. da Cruz, E.C. Rangel, A.R.G. de Azevedo, S.F. Durrant, Use of waste collected from wind turbine blade production as an eco-friendly ingredient in mortars for civil construction, J. Clean. Prod. 274 (2020) 122948.

[54] L. Coppola, E. Cadoni, D. Forni, A. Buoso, Mechanical characterization of cement composites reinforced with fiberglass, carbon nanotubes or glass reinforced plastic (GRP) at high strain rates, Appl. Mech. Mater. 82 (2011) 190-195.

[55] F. Tittarelli, G. Moriconi, Use of GRP industrial by-products in cement based composites, Cem. Concr. Compos. 32(3) (2010) 219-225.

[56] R. Thamizh Selvan, P. Vishakh Raja, P. Mangal, N. Mohan, S. Bhowmik, Recycling technology of epoxy glass fiber and epoxy carbon fiber composites used in aerospace vehicles, J. Compos. Mater. 55(23) (2021) 3281-3292.

[57] H. Rodin III, S. Nassiri, K. Englund, O. Fakron, H. Li, Recycled glass fiber reinforced polymer composites incorporated in mortar for improved mechanical performance, Constr. Build. Mater. 187 (2018) 738-751.

[58] D. Baturkin, O.A. Hisseine, R. Masmoudi, A. Tagnit-Hamou, L. Massicotte, Valorization of recycled FRP materials from wind turbine blades in concrete, Resour. Conserv. Recycl. 174 (2021) 105807.

[59] P. Guo, W. Meng, H. Nassif, H. Gou, Y. Bao, New perspectives on recycling waste glass in manufacturing concrete for sustainable civil infrastructure, Constr. Build. Mater. 257 (2020) 119579.

[60] P. Asokan, M. Osmani, A.D.F. Price, Assessing the recycling potential of glass fibre reinforced plastic waste in concrete and cement composites, J. Clean. Prod. 17(9) (2009) 821-829.

[61] F. Tittarelli, S.P. Shah, Effect of low dosages of waste GRP dust on fresh and hardened properties of mortars: Part 1, Constr. Build. Mater. 47 (2013) 1532-1538.

[62] P. Asokan, M. Osmani, A.D.F. Price, Improvement of the mechanical properties of glass fibre reinforced plastic waste powder filled concrete, Constr. Build. Mater. 24(4) (2010) 448-460.

[63] M. Hofmeister, Recycling Turbine Blade Composites: Concrete Aggregate and Reinforcement, Wind Energy Science Engineering and Policy, 2012.

[64] A. Yazdanbakhsh, L. C. Bank, C. Chen, Use of recycled FRP reinforcing bar in concrete as coarse aggregate and its impact on the mechanical properties of concrete, Constr. Build. Mater. 121 (2016) 278-284.

[65] A. Yazdanbakhsh, L.C. Bank, C. Chen, Y. Tian, FRP-needles as discrete reinforcement in concrete, J. Mater. Civ. Eng. 29(10) (2017) 04017175.

[66] F. Tittarelli, S. Kawashima, N. Tregger, G. Moriconi, S.P. Shah, Effect of GRP by-product addition on plastic and hardened properties of cement mortars, Proc. 2nd Int. Conference on Sustainable Construction Materials and Technologies, 2010, pp. 28-30.

[67] V. Corinaldesi, Influence of lightweight aggregates and GRP by-product powders on the properties of self-compacting concretes, Adv. Mater. Res. 548 (2012) 215-220.

[68] S.C. Paul, B. Šavija, A.J. Babafemi, A comprehensive review on mechanical and durability properties of cement-based materials containing waste recycled glass, J. Clean. Prod. 198 (2018) 891-906.

[69] E. Harrison, A. Berenjian, M. Seifan, Recycling of waste glass as aggregate in cement-based materials, Environ. Sci. Technol. 4 (2020) 100064.

[70] A. Dehghan, K. Peterson, A. Shvarzman, Recycled glass fiber reinforced polymer additions to Portland cement concrete, Constr. Build. Mater. 146 (2017) 238-250.

[71] UnitedNations, The 17 Goals Sustainable Development, 2015. https://sdgs.un.org/goals. (Accessed 01 Dec 2021).

[72] H. Herman, M. Fanran, M. Jon, Wind turbine blade wastes and the environmental impacts in Canada, Waste Manage. 133 (2021) 59-70.

[73] P.A.V. Dong, C. Azzaro-Pantel, A.-L. Cadene, Economic and environmental assessment of recovery and disposal pathways for CFRP waste management, Resour. Conserv. Recycl. 133 (2018) 63-75.

[74] J.B. Guinée, E. Lindeijer, Handbook on life cycle assessment: operational guide to the ISO standards, Springer Science & Business Media2002.

[75] L.O. Meyer, K. Schulte, E. Grove-Nielsen, CFRP-recycling following a pyrolysis route: process optimization and potentials, J. Compos. Mater. 43(9) (2009) 1121-1132.

[76] X. Pinglai, L. Juan, D. Jiangping, Chemical recycling of carbon fibre/epoxy composites in a mixed solution of peroxide hydrogen and N,N-dimethylformamide, Compos. Sci. Technol. 82 (2013) 54-59.

[77] M.B.M. Zaini, K.H. Badri, Glycolysis of carbon fiber-epoxy unidirectional mat catalysed by sodium hydroxide, AIP Conference Proceedings, American Institute of Physics, 2014, pp. 446-451.

[78] J.T. Rhys, L.L. Marco, N. Andrew, D.P. Kevin, H. Ian, An evaluation of life cycle assessment and its application to the closed-loop recycling of carbon fibre reinforced polymers, Compos. B. Eng. 184 (2020) 107665.

[79] H. Sun, G. Guo, S.A. Memon, W. Xu, Q. Zhang, J.-H. Zhu, F. Xing, Recycling of carbon fibers from carbon fiber reinforced polymer using electrochemical method, Compos. Part A Appl. Sci. Manuf. 78 (2015) 10-17.

[80] D. Ozkan, M.S. Gok, A.C. Karaoglanli, Carbon Fiber Reinforced Polymer (CFRP) Composite Materials, Their Characteristic Properties, Industrial Application Areas and Their Machinability, in: A. Öchsner, H. Altenbach (Eds.), Engineering Design Applications III: Structures, Materials and Processes, Springer International Publishing, Cham, 2020, pp. 235-253.

[81] A. Akbar, V.K.R. Kodur, K.M. Liew, Microstructural changes and mechanical performance of cement composites reinforced with recycled carbon fibers, Cem. Concr. Compos. 121 (2021) 104069.

[82] A. Danish, M.A. Mosaberpanah, M.U. Salim, M. Amran, R. Fediuk, T. Ozbakkaloglu, M.F. Rashid, Utilization of recycled carbon fiber reinforced polymer in cementitious composites: A critical review, J. Build. Eng. 53 (2022) 104583.

[83] F. Spini, P. Bettini, End-of-Life wind turbine blades: Review on recycling strategies, Compos. B. Eng. 275 (2024) 111290.

[84] Z. Zhou, B. Zhao, U.A. Lone, Y. Fan, Experimental study on mechanical properties of shredded prepreg carbon cloth waste fiber reinforced concrete, J. Clean. Prod. 436 (2024) 140456.

[85] J. Donnini, T. Bellezze, V. Corinaldesi, Mechanical, electrical and self-sensing properties of cementitious mortars containing short carbon fibers, Journal of Building Engineering 20 (2018) 8-14.

[86] A. Belli, A. Mobili, T. Bellezze, F. Tittarelli, Commercial and recycled carbon/steel fibers for fiber-reinforced cement mortars with high electrical conductivity, Cem. Concr. Compos. 109 (2020) 103569.

[87] L. Wang, F. Aslani, Mechanical properties, electrical resistivity and piezoresistivity of carbon fibre-based self-sensing cementitious composites, Ceramics International 47(6) (2021) 7864-7879.

[88] B. Han, L. Zhang, C. Zhang, Y. Wang, X. Yu, J. Ou, Reinforcement effect and mechanism of carbon fibers to mechanical and electrically conductive properties of cement-based materials, Constr. Build. Mater. 125 (2016) 479-489.

[89] L. Deng, Y. Ma, J. Hu, S. Yin, X. Ouyang, J. Fu, A. Liu, Z. Zhang, Preparation and piezoresistive properties of carbon fiber-reinforced alkali-activated fly ash/slag mortar, Constr. Build. Mater. 222 (2019) 738-749.

[90] J. Qureshi, A Review of Recycling Methods for Fibre Reinforced Polymer Composites, Sustainability 14(24) (2022) 16855.

[91] E. Pakdel, S. Kashi, R. Varley, X. Wang, Recent progress in recycling carbon fibre reinforced composites and dry carbon fibre wastes, Resour. Conserv. Recycl. 166 (2021) 105340.

[92] J.A. Butenegro, M. Bahrami, J. Abenojar, M.Á. Martínez, Recent Progress in Carbon Fiber Reinforced Polymers Recycling: A Review of Recycling Methods and Reuse of Carbon Fibers, Materials 14(21) (2021) 6401.

[93] S.A. Hadigheh, Y. Wei, S. Kashi, Optimisation of CFRP composite recycling process based on energy consumption, kinetic behaviour and thermal degradation mechanism of recycled carbon fibre, J. Clean. Prod. 292 (2021) 125994.

[94] Y. Wei, S.A. Hadigheh, Enhancing carbon fibre recovery through optimised thermal recycling: Kinetic analysis and operational parameter investigation, Materials Today Sustainability 25 (2024) 100661.

[95] Y. Wei, S.A. Hadigheh, Development of an innovative hybrid thermo-chemical recycling method for CFRP waste recovery, Compos. B. Eng. 260 (2023) 110786.

[96] K.-W. Kim, H.-M. Lee, J.-H. An, D.-C. Chung, K.-H. An, B.-J. Kim, Recycling and characterization of carbon fibers from carbon fiber reinforced epoxy matrix composites by a novel super-heated-steam method, J. Environ. Manage. 203 (2017) 872-879.

[97] Q. Jiang, L. Xu, Y. Ren, Y. Sun, S. Xiao, Z. Shen, Carbon fiber recovery from carbon fiber reinforced polymer matrix composite by microwave pyrolysis, Materials Today Communications 40 (2024) 109462.

[98] W. Ballout, N. Sallem-Idrissi, M. Sclavons, C. Doneux, C. Bailly, T. Pardoen, P. Van Velthem, High performance recycled CFRP composites based on reused carbon fabrics through sustainable mild solvolysis route, Scientific Reports 12(1) (2022) 5928.

[99] C. Morin, A. Loppinet-Serani, F. Cansell, C. Aymonier, Near- and supercritical solvolysis of carbon fibre reinforced polymers (CFRPs) for recycling carbon fibers as a valuable resource: State of the art, The Journal of Supercritical Fluids 66 (2012) 232-240.

[100] F. Knappich, M. Klotz, M. Schlummer, J. Wölling, A. Mäurer, Recycling process for carbon fiber reinforced plastics with polyamide 6, polyurethane and epoxy matrix by gentle solvent treatment, Waste Manage. 85 (2019) 73-81.

[101] J. Palmer, L. Savage, O.R. Ghita, K.E. Evans, Sheet moulding compound (SMC) from carbon fibre recyclate, Compos. Part A Appl. Sci. Manuf. 41(9) (2010) 1232-1237.

[102] C. Thomas, P.H.R. Borges, T.H. Panzera, A. Cimentada, I. Lombillo, Epoxy composites containing CFRP powder wastes, Compos. B. Eng. 59 (2014) 260-268.

[103] W. Song, A. Magid, D. Li, K.-Y. Lee, Application of recycled carbon-fibre-reinforced polymers as reinforcement for epoxy foams, J. Environ. Manage. 269 (2020) 110766.

[104] Y. Wang, L. Sun, A. Li, W. Li, B. Guo, Effect of modified recycled carbon fibers on the conductivity of cement-based materials, Constr. Build. Mater. 415 (2024) 135033.

[105] A. Akbar, K.M. Liew, Assessing recycling potential of carbon fiber reinforced plastic waste in production of eco-efficient cement-based materials, J. Clean. Prod. 274 (2020) 123001.

[106] Y. Wang, S. Zhang, D. Luo, X. Shi, Effect of chemically modified recycled carbon fiber composite on the mechanical properties of cementitious mortar, Compos. B. Eng. 173 (2019) 106853.

[107] A. Singh, A. Charak, K.P. Biligiri, V. Pandurangan, Glass and carbon fiber reinforced polymer composite wastes in pervious concrete: Material characterization and lifecycle assessment, Resour. Conserv. Recycl. 182 (2022) 106304.

[108] S. Nassiri, O. AlShareedah, H. Rodin, K. Englund, Mechanical and durability characteristics of pervious concrete reinforced with mechanically recycled carbon fiber composite materials, Materials and Structures 54(3) (2021) 107.

[109] H. Nguyen, V. Carvelli, T. Fujii, K. Okubo, Cement mortar reinforced with reclaimed carbon fibres, CFRP waste or prepreg carbon waste, Constr. Build. Mater. 126 (2016) 321-331.

[110] H. Li, E. Schamel, M. Liebscher, Y. Zhang, Q. Fan, H. Schlachter, T. Köberle, V. Mechtcherine, G. Wehnert, D. Söthje, Recycled carbon fibers in cement-based composites: Influence of epoxide matrix depolymerization degree on interfacial interactions, J. Clean. Prod. 411 (2023) 137235.

[111] Y. Wang, A. Li, S. Zhang, B. Guo, D. Niu, A review on new methods of recycling waste carbon fiber and its application in construction and industry, Constr. Build. Mater. 367 (2023) 130301.

[112] A. Dinesh, S. Indhumathi, M. Pichumani, Self-sensing cement composites for structural health monitoring: From know-how to do-how, Automation in Construction 160 (2024) 105304.

[113] P.O. Junior, S. Conte, D.M. D'Addona, P. Aguiar, F. Bapstista, An improved impedance-based damage classification using Self-Organizing Maps, Procedia CIRP 88 (2020) 330-334.

[114] G. Cosoli, A. Mobili, F. Tittarelli, G.M. Revel, P. Chiariotti, Electrical resistivity and electrical impedance measurement in mortar and concrete elements: A systematic review, Applied Sciences 10(24) (2020) 9152.

[115] E. Team, Smart Concrete, (2007).

[116] B. Han, S. Ding, X. Yu, Intrinsic self-sensing concrete and structures: A review, Measurement 59 (2015) 110-128.

[117] S. Liu, M. Wu, M. Rao, L. Li, H. Xiao, Preparation, properties, and microstructure of graphite powder-containing conductive concrete, Strength of Materials 51(1) (2019) 76-84.

[118] M. Chen, P. Gao, F. Geng, L. Zhang, H. Liu, Mechanical and smart properties of carbon fiber and graphite conductive concrete for internal damage monitoring of structure, Constr. Build. Mater. 142 (2017) 320-327.

[119] A.L. Materazzi, F. Ubertini, A. D'Alessandro, Carbon nanotube cement-based transducers for dynamic sensing of strain, Cem. Concr. Compos. 37 (2013) 2-11.

[120] L. Coppola, A. Buoso, F. Corazza, Electrical properties of carbon nanotubes cement composites for monitoring stress conditions in concrete structures, Appl. Mech. Mater., Trans Tech Publ, 2011, pp. 118-123.

[121] J. Han, D. Wang, P. Zhang, Effect of nano and micro conductive materials on conductive properties of carbon fiber reinforced concrete, Nanotechnology Reviews 9(1) (2020) 445-454.

[122] O. Galao, F.J. Baeza, E. Zornoza, P. Garcés, Strain and damage sensing properties on multifunctional cement composites with CNF admixture, Cem. Concr. Compos. 46 (2014) 90-98.

[123] W. Dong, W. Li, Z. Luo, G. Long, K. Vessalas, D. Sheng, Structural response monitoring of concrete beam under flexural loading using smart carbon black/cement-based sensors, Smart Materials and Structures 29(6) (2020) 065001.

[124] A.O. Monteiro, P.B. Cachim, P.M. Costa, Self-sensing piezoresistive cement composite loaded with carbon black particles, Cem. Concr. Compos. 81 (2017) 59-65.

[125] A. Monteiro, P. Cachim, P. Costa, Electrical properties of cement-based composites containing carbon black particles, Mater. Today: Proc. 2(1) (2015) 193-199.

[126] H. Li, H.-g. Xiao, J.-p. Ou, Effect of compressive strain on electrical resistivity of carbon black-filled cement-based composites, Cem. Concr. Compos. 28(9) (2006) 824-828.

[127] L. Wang, F. Aslani, A review on material design, performance, and practical application of electrically conductive cementitious composites, Constr. Build. Mater. 229 (2019) 116892.

[128] M. Cheytani, Concrete Resistivity Impact on the Design of Impressed Current Cathodic Protection Systems, UNSW Sydney, 2021.

[129] Resipod Operating Instructions Concrete Durability Testing, Screening Eagle Technologies AG, Proceq SA, Schwerzenbach, 2013.

[130] AASHTO Designation: T 358 - Standard Method of Test for Surface Resistivity Indication of Concrete's Ability to Resist Chloride Ion Penetration, American Association of State Highway and Transportation Officials, Washington, D.C, 2015.

[131] A. Belli, A. Mobili, T. Bellezze, F. Tittarelli, P. Cachim, Piezoresistive behavior of mortars loaded with graphene and carbon fibers for the development of self-sensing composites, (2019) 37-42.

[132] S. Wen, D. Chung, Partial replacement of carbon fiber by carbon black in multifunctional cement–matrix composites, Carbon 45(3) (2007) 505-513.

[133] G. Faneca, I. Segura, J.M. Torrents, A. Aguado, Development of conductive cementitious materials using recycled carbon fibres, Cem. Concr. Compos. 92 (2018) 135-144.

[134] A. Belli, A. Mobili, T. Bellezze, P.B. Cachim, F. Tittarelli, Commercial and recycled carbon-based fillers and fibers for self-sensing cement-based composites: Comparison

of mechanical strength, durability, and piezoresistive behavior, J. Build. Eng. 73 (2023) 106836.

[135] A. Li, Y. Wang, S. Zhang, D. Niu, B. Guo, Study on the mechanical and electrical conductivity properties of waste short carbon fibers concrete and the establishment of conductivity models, J. Build. Eng. 95 (2024) 110296.

[136] C. Lin, T. Kanstad, S. Jacobsen, G. Ji, Bonding property between fiber and cementitious matrix: A critical review, Constr. Build. Mater. 378 (2023) 131169.

[137] H. Li, M. Liebscher, D. Zhao, B. Yin, Y. Du, J. Yang, M. Kaliske, V. Mechtcherine, A review of carbon fiber surface modification methods for tailor-made bond behavior with cementitious matrices, Progress in Materials Science 132 (2023) 101040.

[138] M.S. Ansari, S. Zafar, H. Pathak, A comprehensive review of surface modification techniques for carbon fibers for enhanced performance of resulting composites, Results in Surfaces and Interfaces 12 (2023) 100141.

[139] Z. Kang, F. Aslani, B. Han, Prediction of mechanical and electrical properties of carbon fibre-reinforced self-sensing cementitious composites, Case Stud. Constr. Mater. 20 (2024) e02716.

[140] S. Igarashi, A. Bentur, S. Mindess, The effect of processing on the bond and interfaces in steel fiber reinforced cement composites, Cem. Concr. Compos. 18(5) (1996) 313-322.

[141] Z. Pi, H. Xiao, J. Du, M. Liu, H. Li, Interfacial microstructure and bond strength of nano-SiO2-coated steel fibers in cement matrix, Cem. Concr. Compos. 103 (2019) 1-10.

[142] S. He, E.-H. Yang, Strategic strengthening of the interfacial transition zone (ITZ) between microfiber and cement paste matrix with carbon nanofibers (CNFs), Cem. Concr. Compos. 119 (2021) 104019.

[143] J. Zhang, A. Heath, H.M.T. Abdalgadir, R.J. Ball, K. Paine, Electrical impedance behaviour of carbon fibre reinforced cement-based sensors at different moisture contents, Constr. Build. Mater. 353 (2022) 129049.

[144] M. Azeem, M. Azhar Saleem, Role of electrostatic potential energy in carbon nanotube augmented cement paste matrix, Constr. Build. Mater. 239 (2020) 117875.

[145] H. Huang, J. Luo, C. Peng, T. Sun, T. Deng, J. Hu, K. Guzal Anvarovna, N. Azizbek Davlatali Ugli, D. Hou, J. Wei, Q. Yu, Interfacial bond between modified micro carbon fiber and high-strength cement paste in UHPC: Bond-slip tests and molecular dynamic simulation, Cem. Concr. Compos. 142 (2023) 105168.

[146] J.H. Kim, J.H. Han, S. Hong, D.-W. Kim, S.H. Park, J.-H. Wee, K.S. Yang, Y.A. Kim, Effect of plasma surface modification on pullout characteristics of carbon fiber-reinforced cement composites, Carbon Trends 3 (2021) 100030.

[147] M. Lu, H. Xiao, M. Liu, J. Feng, Carbon fiber surface nano-modification and enhanced mechanical properties of fiber reinforced cementitious composites, Constr. Build. Mater. 370 (2023) 130701.

[148] N. Raphael, K. Namratha, B.N. Chandrashekar, K.K. Sadasivuni, D. Ponnamma, A.S. Smitha, S. Krishnaveni, C. Cheng, K. Byrappa, Surface modification and grafting of carbon fibers: A route to better interface, Progress in Crystal Growth and Characterization of Materials 64(3) (2018) 75-101.

[149] J. Zhao, M. Liebscher, A. Michel, K. Schneider, R. Foest, M. Fröhlich, A. Quade, V. Mechtcherine, Plasma-generated silicon oxide coatings of carbon fibres for improved bonding to mineral-based impregnation materials and concrete matrices, Cem. Concr. Compos. 114 (2020) 103667.

[150] H. Li, M. Liebscher, A. Michel, A. Quade, R. Foest, V. Mechtcherine, Oxygen plasma modification of carbon fiber rovings for enhanced interaction toward mineral-based impregnation materials and concrete matrices, Constr. Build. Mater. 273 (2021) 121950.

[151] G. Catalá, E.V. Ramos-Fernández, E. Zornoza, L.G. Andión, P. Garcés, Influence of the Oxidation Process of Carbon Material on the Mechanical Properties of Cement Mortars, 23(3) (2011) 321-329.

[152] L. Lavagna, S. Musso, G. Ferro, M. Pavese, Cement-based composites containing functionalized carbon fibers, Cem. Concr. Compos. 88 (2018) 165-171.

[153] H. Li, M. Liebscher, M. Ranjbarian, S. Hempel, L. Tzounis, C. Schröfl, V. Mechtcherine, Electrochemical modification of carbon fiber yarns in cementitious pore solution for an enhanced interaction towards concrete matrices, Appl. Surf. Sci. 487 (2019) 52-58.

[154] H. Li, M. Liebscher, J. Yang, M. Davoodabadi, L. Li, Y. Du, B. Yang, S. Hempel, V. Mechtcherine, Electrochemical oxidation of recycled carbon fibers for an improved interaction toward alkali-activated composites, J. Clean. Prod. 368 (2022) 133093.

[155] Z. Lu, A. Hanif, G. Sun, R. Liang, P. Parthasarathy, Z. Li, Highly dispersed graphene oxide electrodeposited carbon fiber reinforced cement-based materials with enhanced mechanical properties, Cem. Concr. Compos. 87 (2018) 220-228.

[156] H. Li, M. Liebscher, I. Curosu, S. Choudhury, S. Hempel, M. Davoodabadi, T.T. Dinh, J. Yang, V. Mechtcherine, Electrophoretic deposition of nano-silica onto carbon fiber surfaces for an improved bond strength with cementitious matrices, Cem. Concr. Compos. 114 (2020) 103777.

[157] H. Li, M. Liebscher, M. Micusik, J. Yang, B. Sun, B. Yin, M. Yu, V. Mechtcherine, Role of pH value on electrophoretic deposition of nano-silica onto carbon fibers for a tailored bond behavior with cementitious matrices, Appl. Surf. Sci. 600 (2022) 154000.

[158] Z. Wang, E. Bai, C. Liu, B. Ren, J. Zhang, Strength, toughness and interface modification of graphene oxide grafted carbon fiber modified concrete, Constr. Build. Mater. 428 (2024) 136336.

[159] H. Cui, Z. Jin, D. Zheng, W. Tang, Y. Li, Y. Yun, T.Y. Lo, F. Xing, Effect of carbon fibers grafted with carbon nanotubes on mechanical properties of cement-based composites, Constr. Build. Mater. 181 (2018) 713-720.

[160] M. Lu, H. Xiao, M. Liu, X. Li, H. Li, L. Sun, Improved interfacial strength of SiO2 coated carbon fiber in cement matrix, Cem. Concr. Compos. 91 (2018) 21-28.

[161] F. Zhou, G. Pan, L. Zhang, Enhancing the shrinkage resistance and impermeability of cement-based materials using carbon fiber modified by in situ-grown nano-SiO2 and carbon nanotubes, J. Build. Eng. 63 (2023) 105542.

[162] F. Huang, J. Zhang, X. Zheng, Y. Wu, T. Fu, S. Easa, W. Liu, R. Qiu, Preparation and performance of autoclaved aerated concrete reinforced by dopamine-modified polyethylene terephthalate waste fibers, Constr. Build. Mater. 348 (2022) 128649.

[163] Z. Xu, H. Yu, M. Jia, Y. Liu, Y. Yang, Enhancing mechanical properties of cementitious composites by boron nitride nanosheets modified carbon fiber, Cem. Concr. Compos. 153 (2024) 105685.

[164] S. Qiu, C.A. Fuentes, D. Zhang, A.W. Van Vuure, D. Seveno, Wettability of a Single Carbon Fiber, Langmuir 32(38) (2016) 9697-9705.

[165] X. Zhang, M. Liu, X. Zhang, F. Deng, C. Zhou, J. Hui, W. Liu, Y. Wei, Interaction of tannic acid with carbon nanotubes: enhancement of dispersibility and biocompatibility, J Toxicology Research 4(1) (2015) 160-168.

[166] D. Lin, B. Xing, Tannic Acid Adsorption and Its Role for Stabilizing Carbon Nanotube Suspensions, Environmental Science & Technology 42(16) (2008) 5917-5923.

[167] M. Mohammadi, A. Bashiri Rezaie, M. Liebscher, T. Köberle, A. Drechsler, R. Frenzel, F. Simon, A. Synytska, V. Mechtcherine, Interfacial properties of high-strength, limestone-calcined clay cement (LC3) matrix and PE fibers, surface-modified using dopamine and tannic acid, Constr. Build. Mater. 408 (2023) 133537.

[168] A. Katz, V.C. Li, A. Kazmer, Bond Properties of Carbon Fibers in Cementitious Matrix, J. Mater. Civ. Eng. 7(2) (1995) 125-128.

Chapter 3: Multifaceted Evaluation of Cement-based Mortar Incorporating CF and GF Offcuts

3.1 INTRODUCTION

FRCCs have gained significant attention in the construction field, particularly those incorporating short CF and GF as discrete reinforcements. The addition of fibres demonstrates a bridging effect and transfers stress throughout the matrices, thereby enhancing flexural strength, limiting crack propagation and improving overall FRCC performance. In addition to this, durability is a paramount criterion in concrete structure design, especially in aggressive corrosive environments. However, research on the durability of mortars incorporating CF and GF remains limited. On the other hand, understanding the internal structure of FRCCs is crucial for ensuring their safe design and practical application. Yet there is a notable lack of quantitative analysis regarding void geometry and distribution when additional fibres are incorporated into cementitious materials. While Micro-CT serves as a powerful tool for visualising and quantifying the spatial distribution and orientation of internal elements, detailed characterisation of CF within the cementitious matrix remains challenging. This is primarily due to low-contrast images where phases overlap in grey values, reducing the effectiveness of conventional segmentation methods, and highlighting the need for advanced approaches.

These challenges are especially relevant when considering the use of fibre offcuts, an abundant yet underutilised form of waste generated throughout the FRP composite lifecycle, such as scraps from manufacturing lines, as reinforcement in CCs. Gaining a deeper understanding of how these offcuts affect the internal structure and durability of CCs is also essential for validating their potential in sustainable construction applications.

This chapter addresses these research gaps and challenges through three interconnected studies. The first study in Section 3.2 examines void characteristics in FRCC through micro-CT analysis using Gaussian blur filtration, investigating how different fibre types and contents influence void geometry and distribution. Additionally, the study explores the effects of acid diffusion through both experiments and simulations. The relationships between microstructures and various properties, including mechanical, durability, and electrical properties, are then assessed and discussed. While isotropic Gaussian filtering is suitable for void characterisation

in the first study, the second study in Section 3.3 develops a new Anisotropic Gaussian filter to more precisely detect CFs within the cementitious matrix. The segmentation accuracy of this method, compared to other conventional methods, is then evaluated and verified. Furthermore, to address the limitation of micro-CT related to its high cost and unsuitability for field testing, the third study in Section 3.4 investigates the potential of using ultrasound testing (UT) techniques in identifying CF features within a high-attenuation cementitious matrix, a capability that is yet to be fully recognised. The performance of these two NDT methods in characterising CF and voids across various scales is then compared and analysed.

3.2 VOID GEOMETRY ANALYSIS AND MULTIFACETED CHARACTERISATION OF CEMENTITIOUS MORTAR REINFORCED WITH SHORT CARBON AND GLASS FIBRES – A COMPARATIVE STUDY

Y. Tao[1], S.A. Hadigheh[1,*], Z. Wang[1]

[1]School of Civil Engineering, Faculty of Engineering, The University of Sydney, Sydney, New South Wales 2006, Australia

[*]Corresponding Author: Dr Ali Hadigheh

Journal of Building Engineering, https://doi.org/10.1016/j.jobe.2024.109283, Published in April 2024.

3.2.1 Abstract

This paper presents comprehensive experimental and numerical studies on void analysis, durability performance, electrical properties, and microstructural behaviour of fibre-reinforced cementitious composites (FRCC) with varying short carbon and glass fibre volume fractions. Durability and electrical properties are evaluated based on the hydrochloric acid effect, water absorption, drying shrinkage and electrical resistivity changes over time. The incorporation of CF and GF remarkably limits drying shrinkage, primarily attributed to the bridging and bonding effects of fibres within the matrix. The addition of 1.0% carbon fibre significantly decreases the electrical resistivity and improves acid resistance performance. Furthermore, for the first time, the influence of fibre type and quantity on the formation of elongated and eccentric voids is investigated by using X-ray computed tomography (micro-CT). The results demonstrate that higher porosity leads to lower strength and durability performance, while a greater occurrence of elongated voids contributes to increased length change in shrinkage.

Keywords: Durability; Void analysis; Fibre reinforced cementitious composite; Electrical resistivity; Diffusion

3.2.2 Introduction

Since the first invention of Portland cement in 1824, modern infrastructure has evolved, and cementitious concrete is now the most commonly used material in the building sector [1, 2]. Although concrete is a highly versatile material for construction with excellent compressive properties, it exhibits lower tensile strength and insufficient ductility. A range of measures has been employed to address the shortcomings of concrete materials, including integrating reinforcing steel in concrete, effective utilisation of supplemental cementitious materials (SCMs), application of suitable dosage of admixtures, and various curing procedures [2, 3].

Among the key pathways for improving the performance of cementitious materials in a wider range of applications, the addition of fibres to concrete is now of considerable attention to increase flexural strength and limit cracking. FRCC has recently been successfully commercialised [4, 5] and is used in a variety of structural applications such as structure anchoring zones, bridge deck overlays, and slabs [6-8]. Nevertheless, ongoing advancements in FRCC are aiming to optimise its performance and further broaden its application in sustainable structural engineering practices.

The performance of FRCC depends greatly on the fibre type, fibre length and amount of reinforcement. Many researchers have been experimenting with different fibres to reinforce cementitious materials and improve various properties. Steel fibre [4, 9, 10], basalt fibre [10, 11], polypropylene (PP) fibre [9, 10], glass fibre (GF) [12, 13], jute fibre [10] and carbon fibre (CF) [14-16] are the most utilised fibre types, as they are considered to have a bridging effect to limit crack formation and shrinkage and improve mechanical properties. Among them, CF and GF stand out as superior micro-reinforced materials used to enhance the performance of cementitious materials, owing to their high strength-to-weight ratio, effectiveness in resisting corrosion and non-combustible nature [17, 18]. Previous studies have demonstrated the benefits of carbon and glass fibre-reinforced concrete in enhancing its mechanical performance [13, 19, 20]. For instance, Safiuddin et al. [21] observed that CFs improved the splitting strength, flexural strength and toughness by up to 17%, 3.6% and 41.4% of self-consolidating concrete. Hilles and Ziara [22] pointed out that compressive, splitting tensile and flexural strength of high-strength concrete could be increased by 13.14%, 63.22% and 52.36% with 1.2% GF. Besides, several studies have recently demonstrated that incorporating CFs into cement-based materials can improve both their mechanical performance and conductivity by forming a conductive network [14, 23-26]. Fibrous conductive materials can effectively overlap each other to form a conductive network within cementitious composites, even with low dosages. A stable conductive network could be established through the tunnel effect as the fibre content increases, up to 2wt%, particularly with CF lengths of 3mm and 6mm [25]. The electrical resistivity would reach its minimum value when the CF dosage reaches the percolation threshold. This electrical conductivity of FRCC is of current interest due to its potential for the development of an effective non-destructive technique for structural health monitoring of structures [27].

In addition to mechanical and electrical properties, durability is often considered the paramount criterion in the design of concrete structures. Concrete made of Portland cement is

highly alkaline with pH values normally higher than 12 [28, 29]. Based on this chemical nature, concrete structures are susceptible to acid attack when they come into contact with low-pH environments. The hydration products from hardened concrete react with acid to form dissolved ions, which result in expansive compounds that may cause loss of strength, loss of weight, and propagation of cracks [29-31]. Aggressive corrosive media covers a wide range of acid environments [29, 30, 32]. Some progress has been made in investigating the behaviour of FRCC incorporated with CF and GF to enhance sulfuric acid resistance performance, highlighting the significant role played by fibres in improving the durability and structural integrity of concrete in acidic environments. Employing GF in concrete prevents weight loss by binding the concrete together, despite the fact that GF may cause the acid solution to enter the internal structure through the formation of microchannels [33, 34]. In addition, chloride is recognised as one of the primary chemicals that can adversely affect the long-term durability of concrete. It is prevalent in both industrial environments and nature settings, including the textile industry, deicing salt and seawater [35-37]. Chloride-induced corrosion of reinforcing steel bar occurs when the concentration of chloride ions at the steel surface reaches a threshold level sufficient to breakdown the passive oxide film layer on the reinforcing bar [38]. It then initiates an electrochemical corrosion process where the anodic regions experience oxidation of iron atoms into ferrous ions, while at the cathode, the released electrons react with oxygen and water to produce hydroxyl ions that subsequently react with the ferrous ions to form the rust. This process can lead to the degradation of reinforcing bar and cause expansion-induced cracks in the surrounding concrete, resulting in spalling or delamination [37, 39]. Chloride ions can also dissolve in water to form hydrochloride acid (HCl), which penetrates the porous structure and diffuses into the cementitious matrix, ultimately causing deterioration. Fatemi et al. [37] conducted an extended experimental program to investigate the acid resistance capacity of mortar specimens when formulating a novel cementitious matrix for marine environments. They emphasised the importance of the cementitious matrix's permeability to chloride ingress during acidification. Examining FRCC's resistance to HCl acid is essential for safeguarding the durability and longevity of the structure. Nevertheless, very few studies have investigated the mitigation effect of CF and GF on the HCl acid resistance of cementitious materials.

Currently, research on the durability of mortar incorporated with short carbon and glass fibre is very limited [40]. There is also a need to investigate the microstructural and porosity changes that occur after incorporating short fibres in cementitious materials, which can be used to explain the mechanical and durability behaviour. Although the commonly used water

absorption test for cementitious materials provides a measure of total permeable void space in concrete, it has limitations in providing detailed information about the specific characteristics of the pore system. Micro-CT can examine concrete microstructures non-destructively through a three-dimensional (3D) reconstruction, enabling the visualisation of entrained and entrapped air voids. However, there is still a lack of quantitative analysis regarding void size and shape distribution influenced by the incorporation of additional fibres in cementitious materials. Thus, the present study aims to gain insight into how the incorporation of additional fibres affects the void geometry distribution within FRCC, and how the influences reflect on its performance. The paper also assesses the durability behaviour of FRCC in an aggressive HCl acid environment. The conducted experiments include the HCl acid effect, water absorption, drying shrinkage, electrical resistivity changes over time, as well as morphological and chemical characterisation.

In this study, two types of short fibre (CF and GF) were incorporated into the mortar as additional reinforcements with different volume fractions. The effects of different fibre types and contents on the performance of cementitious mortar were investigated and compared through a comprehensive test matrix. The influences of different combinations on the microstructure and porosity of mortar were also characterised by utilising different microscopy techniques and micro-CT. Furthermore, this study presents a pioneering examination of how the type and quantity of fibres influence the geometry of voids, along with their eccentricity.

3.2.3 Materials and experimental methodologies

3.2.3.1 Specimen preparation and mix design

Carbon and glass fabrics were used in this study. Fibres were manually cut for use as additional reinforcing materials in mortar. In the experiments, 6mm short fibres were prepared to ensure appropriate dispersion within the mortar mix while maintaining the desired properties [23, 41]. CF has a diameter of 8μm, featuring surface grooves attributed to sizing, whereas GF has an 18μm diameter and a smooth surface. The density of carbon and glass fibre is 1.8 g/cm^3 and 2.5 g/cm^3, respectively. The average tensile strength of CF used in this experiment is 3,000MPa [42, 43], which is notably higher than that of GF (540MPa).

Mortar specimens were prepared using general-purpose cement complying with AS3972 type GP [44] and Macka's sand that complies with AS2758.1 [45]. Table 3-1 shows the proportions of each mortar mixture. The volume fractions of short fibres added to the mortar were 0.1%, 0.5%, and 1.0%, respectively. The water-to-cement ratio was kept constant at 0.55.

During batching, cement was first poured into the bowl, then short fibres were progressively added and stirred for 3 minutes to get a homogeneous dry mix. Then, sand and water were gradually added to the mix and stirred for 5 minutes to get the appropriate consistency stated in BS EN 1015-3 [46]. The flow table method was utilised to assess the consistency of fresh mortar, (see Table 3-1 for the characteristics of the freshly mixed mortar). The flow value was larger than 140mm, indicating the plastic and soft mortar according to BS EN 1015-6 [47]. Both measured flow value and fresh density decreased with the addition of fibres, which was related to fibre conglomeration and density differences between fibre and mortar constituents.

Following mixing, a vibration table was used to aid in mortar compaction and reduce air entrapment. The fresh mortar was then poured into various-sized metallic moulds in preparation for testing. All mortar specimens were cured in the moulds for 24-48 hours before being cured at the standard laboratory temperature of 23°C. Mortar specimens were moist wrapped in a wet cloth and sealed with an impermeable plastic sheet [48].

Table 3-1. Mix design of mortar and fresh properties.

Mixing proportions of mortar ((kg/m^3)						Flow value (mm)	Fresh density (g/cm^3)
Mixture	Cement	Sand	Water	CF	GF		
Plain Mortar	726	1088	400			240.05	2.21
CF0.1	726	1088	400	1.8		170.58	2.16
CF0.5	726	1088	400	9.0		156.41	2.09
CF1.0	726	1088	400	18.0		155.58	2.08
GF0.1	726	1088	400		2.5	223.24	2.20
GF0.5	726	1088	400		12.7	187.78	2.06
GF1.0	726	1088	400		25.4	174.39	2.05

3.2.3.2 Experimental program

As shown in Figure 3-1, the analysis of void dimension analysis and eccentricity distribution were characterised by micro-CT. The multifaceted characterisation of mortar reinforced with short carbon and glass fibre with different volumes was assessed, by HCl acid attack, water absorption, drying shrinkage measurement and electrical resistivity. In addition, analytical and numerical analyses were also carried out to simulate the acid diffusion activity within fibre-reinforced mortar. Following the experimental tests, microstructures and phases/composition of cured and deteriorated mortar specimens were examined using both SEM equipped with EDS and XRD techniques. FTIR was utilised to further identify compounds for determining components in the mortar mixture.

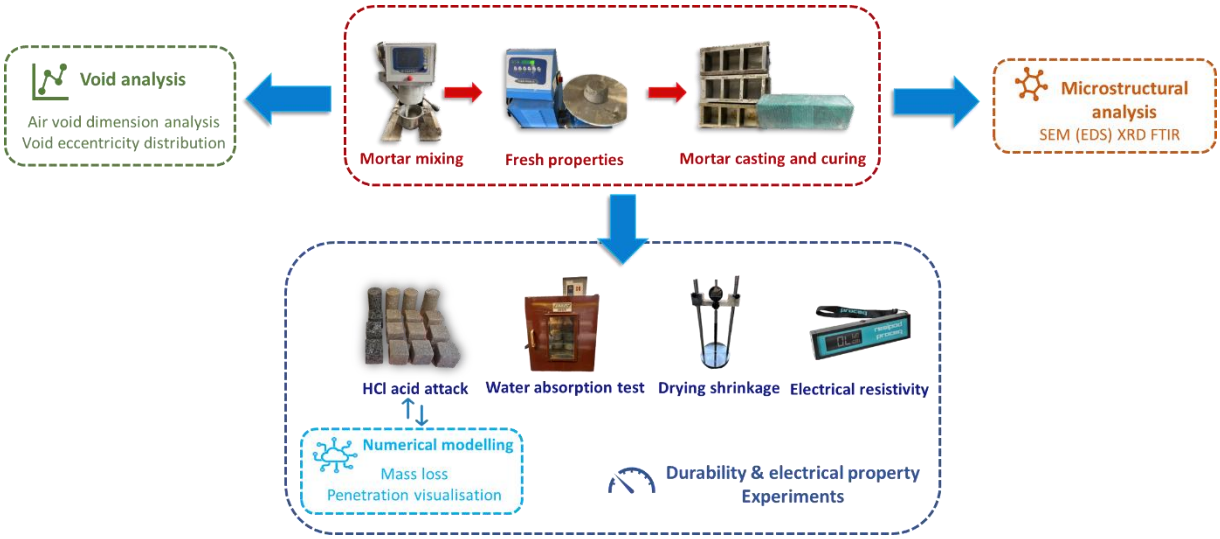

Figure 3-1. Illustration of the experimental program.

Micro-CT and void analysis

Micro-CT was used to explore and compare the void distribution within the mortar samples (50×50×50mm^3) before and after the addition of fibres, conducted at a curing age of 90 days. The scans were conducted by using Bruker Skyscan 2214 micro-CT scanner. To ensure comparability of micro-CT images and void analyses across different samples, consistent parameters and settings for the micro-CT scanner and reconstruction were maintained for all samples. 40µm pixel resolution was adjusted to obtain the entire volumetric view of each specimen through one scan. The scans were taken at 120 kV with a beam current of 100µA with a 1mm copper filter. Each sample was scanned 360° with a 0.2° rotation angle per step. Therefore, a total of 1800 projections were acquired after each scan, and imported into Bruker NRecon software for 3D reconstruction to create a stack of greyscale images representing cross-sections along the vertical axis of the sample. Figure 3-2 (a) shows a typical cross-sectional image where darker and black regions with lower pixel intensity represent voids, and lighter and greyish regions with higher pixel intensity represent the mortar matrix.

The framework for micro-CT image processing and void segmentation was programmed using MATLAB. For each specimen, a volume of interest of 40×44×32mm^3 (1,000× 1,100× 800 voxels) was selected and cropped after stacking all the micro-CT cross-sectional images, as shown in Figure 3-2 (b). A Gaussian blur filter was applied to smooth the mortar matrix and remove the noise, as shown in Figure 3-2 (c). To improve the contrast and sharpness between the mortar matrix and the voids, the mean intensity of the cross-sectional image was used as the threshold to further smooth out the mortar matrix regions. The pixel intensity and contrast of the void may vary depending on many factors, such as the size of the voids and the intensity of

the surrounding mortar matrix. Thus, a local adaptive threshold algorithm using first-order statistics within the MATLAB image toolbox [49] was used to binarize the image and segment voids from the background. As shown in Figure 3-2 (e), the smaller voids were well segmented, but it can be seen that the larger voids were not fully closed within the centre. To solve this issue, large voids were separately identified by applying a low global threshold as shown in Figure 3-2 (f), and then added to the binarization image by the local adaptive threshold to provide a more accurate void segmentation as shown in Figure 3-2 (g) and Figure 3-2 (h). Comparing the zoomed region (4×4mm^2) from Figure 3-2 (b) to (h), after smoothing the mortar matrix pixel intensities, the combination of local adaptive and global thresholds provided a reasonable segmentation for both large and small voids.

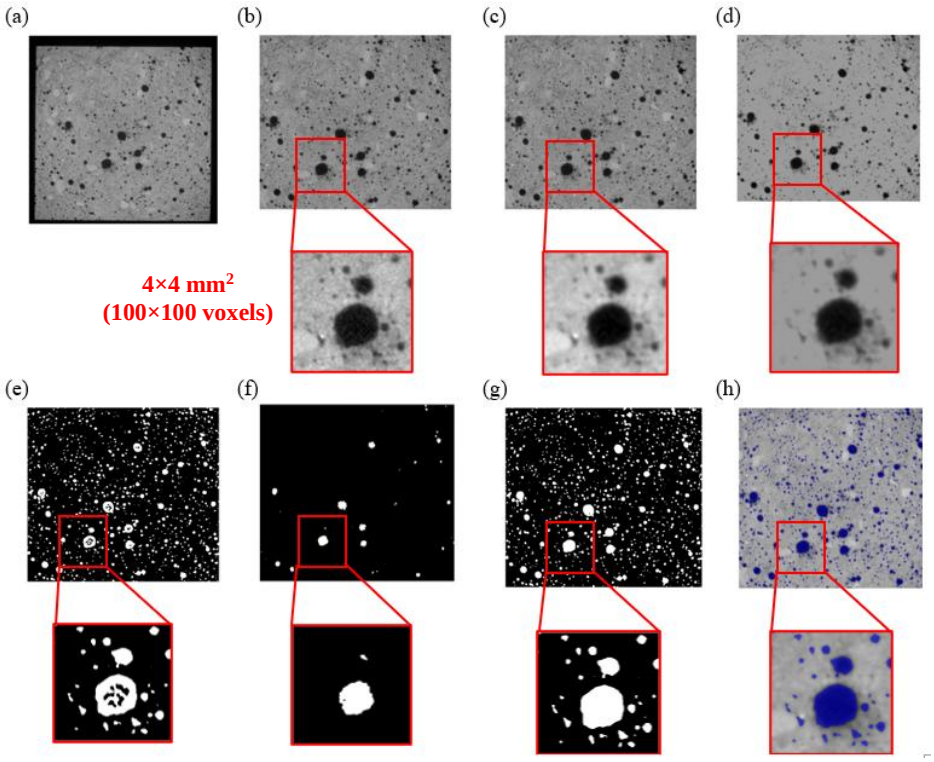

Figure 3-2. Framework for image processing and void segmentation with zoomed visualisation (a) original image (b) region of interest (40×44 mm^2) (c) Gaussian blur and smoothing (d) mortar matrix smoothing (e) local adaptive threshold (f) global threshold for larger voids (g) combined binarization results (h) segmented voids within the region of interest.

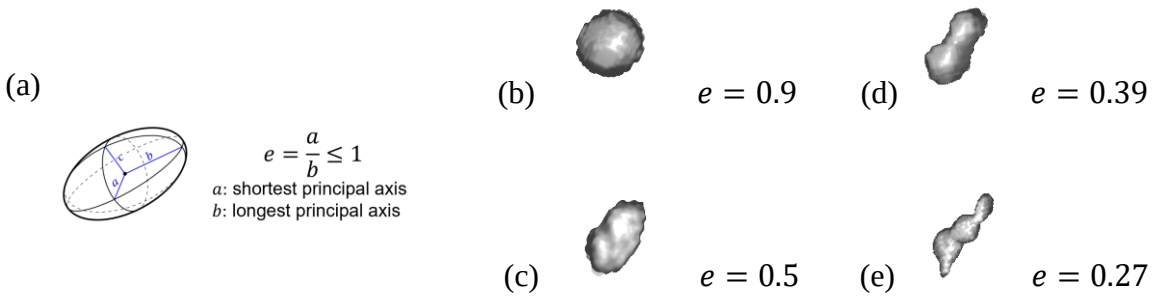

Figure 3-3. Demonstration of eccentricity and examples of voids with different eccentricities.

After segmentation, the properties of voids were quantitatively analysed through MATLAB programming. Voids were identified individually based on the three-dimensional connectivity of the voxels. For each void, the volume was calculated based on the number of voxels within each identified void. The three primary axes of the voids were estimated by the major axes lengths of the ellipsoid that have the same normalized second central moments as the void (see Figure 3-3 (a)). Then, the void eccentricity was estimated by the ratio of the shortest to the longest axis length, which ranges between 0.0 to 1.0. As shown in Figure 3-3 (b) to (e), the void appears more sphere when the eccentricity was close to 1.0, and more elongated when the eccentricity was smaller. As the maximum stress at the crack tip depends on the geometry of the void, particularly the radius of curvature of a crack tip and the crack length, these elongated voids may have a significant effect on the mortar's strength. Sharp corners within these elongated voids can act as stress concentrators, leading to the initiation and propagation of cracks [50]. To further reduce the influence of noise, only the voids larger than 200μm were considered. Then, the void volume fraction was calculated by summing up the number of voxels belonging to all the voids and dividing by the total number of voxels within the volume of interest. In this study, following the criteria from previous literature [51], the voids smaller than 1mm3 were considered small voids, and those larger than $1mm^3$ were considered large voids. The volume fraction of small voids and large voids are calculated respectively. As both the micro-CT scanning process and the image processing framework were controlled for all the samples, the void distributions from different samples could be compared quantitatively.

Durability tests and electrical resistivity measurements

The impact of HCl acid on the fibre-reinforced mortar was investigated through gravimetric change, mechanical properties, and penetration depth. For each combination, three 50mm cubic specimens and one small cylindrical specimen with 50mm diameter and 100mm length were produced. Following the procedure in ASTM C267-20 [52], the samples were removed from the curing condition and then were wiped to surface dry condition after 28 curing days. To determine the initial weight, each mortar specimen was weighed and then fully immersed in the acid solution for 8 weeks until testing. HCl solutions with a concentration of 5wt% were used as the environmental aging condition in this study. To maintain the pH level within an acceptable range, concentrated acid was frequently refreshed. The samples were taken out of the acid bath at regular intervals during the immersion test, washed with three rapid rinses

under running cold water, and then immediately dried by blotting with paper towels. Then, the specimen was allowed to air dry for 0.5 hours before its weight was measured to calculate the weight change. After 8 weeks, the impact of acid on the compressive strength of mortar was determined. At the end of the immersion period, cylindrical samples were cut in half to measure the extent of acid penetration using the Bromothymol blue pH indicator.

The water absorption test was also performed on 50mm cubes cured for 7, 28 and 90 days according to ASTM C948–81 [53]. The dry bulk density of hardened mortar was calculated as the ratio of the recorded oven-dry mass to volume according to BS EN 1015-10 [54].

The drying shrinkage was undertaken on 25×25×285mm^3 prism samples by measuring the length change starting from 7 days after casting in accordance with ASTM C490/C490M–2 [55]. During the experiment, the initial lengths of specimens were measured after demolding using a length comparator. Subsequently, length changes of specimens were recorded on certain days (until 120 days) after the initial measurement. Drying shrinkage for each mix combination was calculated by averaging two specimens.

The electrical properties of mortar were reported through surface resistivity and bulk resistivity measurement on cylindrical samples (100mm dia.×200mm) after 7, 28 and 90 days of curing. Proceq ResiPod fully integrated 4-point Wenner probe was used for measuring surface resistivity based on AASHTO T 358-15 [56]. The bulk resistivity was measured based on:

$$\text{bulk resistivity } \rho = K \times R_{cylinder}, \text{ where } K = A/L \quad (3\text{-}1)$$

A = cylinder top surface area (mm^2)

L = length of the cylinder (mm)

$$R_{cylinder} \text{ (cylinder resistance)} = R_{measured} - R_{upper} - R_{lower} \quad (3\text{-}2)$$

$R_{measured}$ = the sum of the resistance of the cylinder plus the two inserts

R_{upper} = resistance of the upper foam insert

R_{lower} = resistance of the lower foam insert.

Microstructural analysis

The microstructure of cured and acid-deteriorated mortar specimens was examined using SEM with EDS, XRD and FTIR. Zeiss Ultra Plus machine, which uses a Schottky field-emission source for high resolution and beam current was used for imaging of surface

topography. SEM samples (5-10mm) were collected from mortar specimens after the mechanical testing and coated with 10nm gold before the analysis to reduce the charging on the material surface. Chemically elemental analysis was conducted by using an Oxford Instrument AZtec integrated EDS system with an X-Max 20mm^2 silicon drift EDS detector. XRD was carried out for phase identification. XRD samples were back-loaded into a flat-plate sample holder and X-ray powder diffraction data were collected in Bragg-Brentano geometry on a PANalytical X'Pert Pro powder diffractometer, with Cu Kα X-ray radiation and a PIXcel1D detector in continuous scanning mode over the 2θ angle range 5-90°. FTIR analysis was performed to identify the functional group in the cement powder. ATR-FTIR spectra were collected using a Bruker ALPHA portable spectrometer (Bruker Optiks GmbH, Ettlingen, Germany) equipped with a single reflection diamond ATR module and DTGS detector. The diamond crystal has a refractive index of 2.4. Spectra were collected over the region of 4,000 cm^{-1} with the co-addition of 64 scans at a spectral resolution of 400 cm^{-1}.

3.2.4 Results and discussion

3.2.4.1 Void analysis using micro-CT

The air void volume fraction and the average air void size are summarised in Table 3-2. A total of five samples were selected for micro-CT scans, including a plain mortar sample, a 0.5% CF, a 1.0.% CF, a 0.5% GF, and a 1.0% GF-reinforced mortar specimen. For each sample, three cross-sectional images (40mm×44mm) at various depths (0mm, 16mm and 32mm) of the volume of interest (VOI) were evaluated which can be seen in Figure 3-4.

The control sample showed the lowest void fraction, measuring merely 0.48% by volume, and more than 95% of the void volume was small with less than 1mm3 dimensions. This can also be seen from the cross-sectional images where the voids are sparsely distributed. In comparison, the mortar samples with fibres had significantly higher void fractions, ranging from 6.26% to 8.94%. Within the cross-sectional images of fibre-reinforced mortar, there was a much greater number of both small voids and large voids. Referring to the results of the flow table tests, the fibre-reinforced mortar samples had much smaller flow values and poorer workability compared to the plain mortar sample. Thus, the plain mortar sample was nearly fully compacted with a few air voids, while the fibre-reinforced mortar samples seemed to be incompletely compacted with the same fabrication process, which resulted in the formation of larger voids. As shown in red circles, some small voids joined with each other via a channel and formed more elongated larger voids. The brighter grey colour regions represent the regions

where hydration products concentrate as shown in the green circles in Figure 3-4. Small voids (darker and black dots) had been developed around the hydration zones. As the chemical composition of fibres, especially carbon fibre, has lower atomic numbers and density compared to the products of cementitious material, the regions where fibres concentrate appear in a darker grey colour as marked within the yellow circles. Voids can usually be visualised within and around the fibre-rich regions, which indicates the existence of fibres and hydration regions increased the number of ITZ, and therefore, increased the number of voids.

Table 3-2. Summary of air void dimension analysis by Micro-CT.

	Control	CF0.5	CF1.0	GF0.5	GF1.0
Air void volume fraction %	0.48	8.94	7.91	6.26	7.61
Small air void (<1mm^3) volume fraction %	0.46	6.06	6.36	3.69	5.64
Small air void (<1mm^3) %	95.51	67.83	80.47	58.90	74.21
average air void volume mm^3	0.048	0.126	0.099	0.141	0.134
average air void diameter mm	0.491	0.788	0.713	0.784	0.792

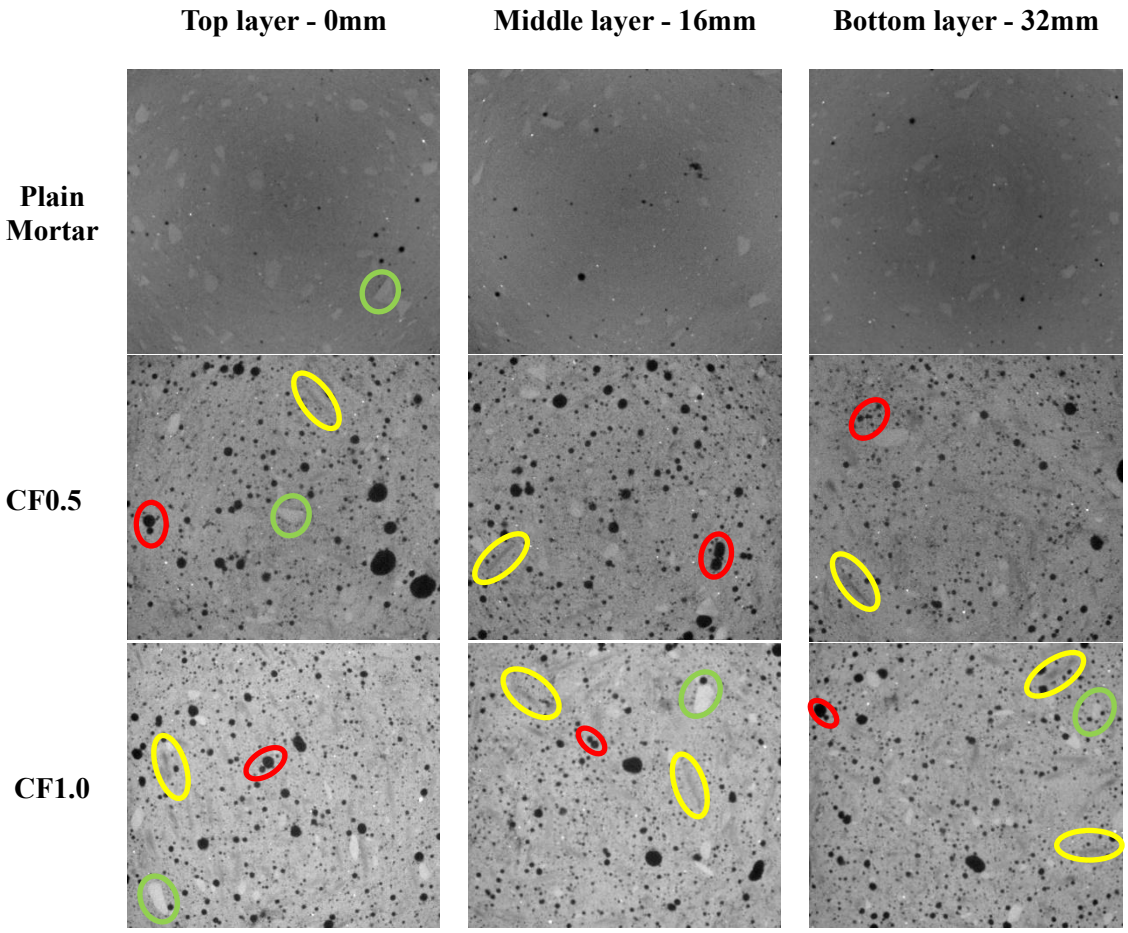

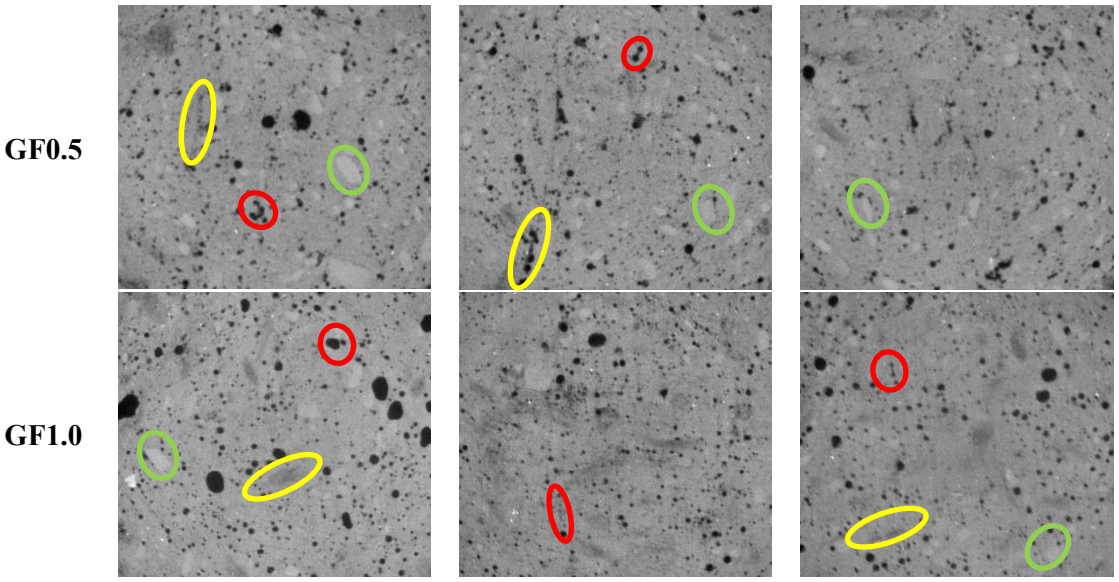

Figure 3-4. Cross-sectional images of the volume of interest (red circle: void; green circle: hydration product; yellow circle: fibre).

The influence of additional fibre on void shapes, especially the formation of elongated and eccentric voids, was investigated by studying void eccentricity. When comparing voids with the same volume, it was observed that voids with greater eccentricity tend to exhibit a larger opening in the primary direction and a smaller radius at the tip, compared to less eccentric voids. Therefore, this leads to easier crack initiation and higher local stress concentration for voids with higher eccentricity, as shown in Figure 3-3. The void eccentricity distribution for the control sample followed the skewed left distribution with an average of about 0.8, which means the voids were relatively round as shown in the zoomed VOI in Table 3-3. However, the void eccentricity distributions for the mortar after adding fibres demonstrate bimodal distributions with one peak around 0.3 to 0.5 and the other peak around 0.7 to 0.9, which indicates a mixture of round and elongated voids. The carbon fibre samples demonstrate a more obvious peak at 0.3 to 0.5 and have more elongated voids compared to the glass fibre samples, confirming the hypothesis that CF is more likely to generate more sub-millimetre voids due to its shape. The zoomed VOI images for fibre-reinforced mortar samples show some voids were stretched in one direction, but more elongated voids were formed due to the connection of multiple smaller voids. The ITZ between fibres and the cement matrix introduces gaps, facilitating the formation of small voids along the fibre direction during the curing process. When a fibre spans between two closely situated voids, it becomes more susceptible to forming a channel along the fibre direction, thereby connecting the two voids. Hence, the addition of fibres introduces a higher number of voids and makes the voids more elongated.

Table 3-3. Void distribution within original and zoomed VOI and eccentricity distribution for each sample.

	Void distribution 40×44×32mm (1,000×1,100×800 voxels)	Zoomed VOI 4×4×4mm (100×100×100 voxels)	Eccentricity distribution
Plain Mortar	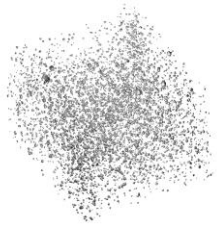	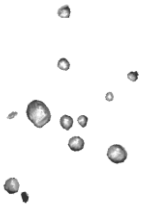	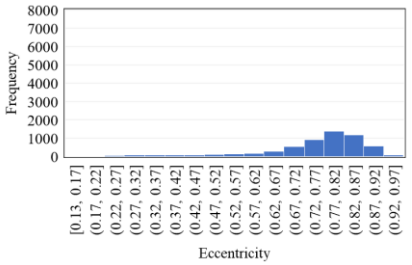
CF0.5	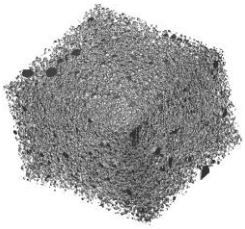	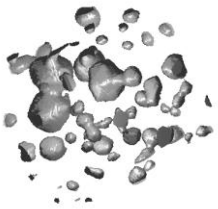	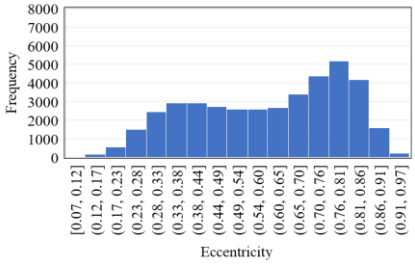
CF1.0	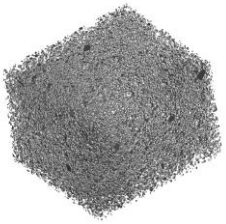	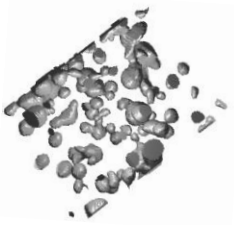	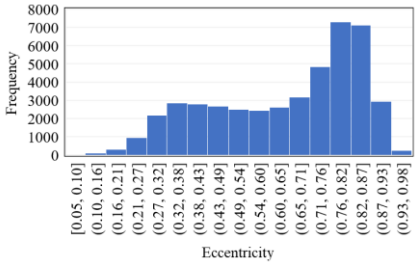
GF0.5	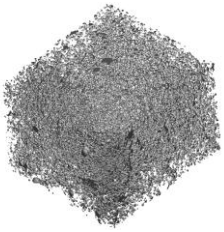	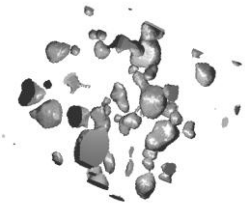	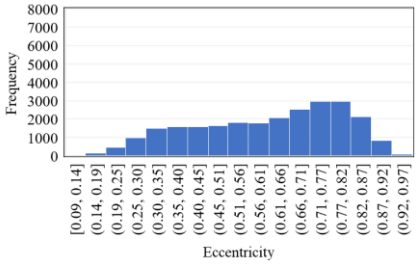
GF1.0	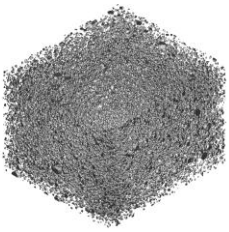	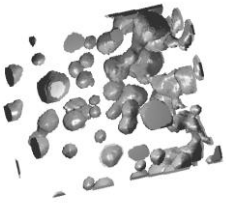	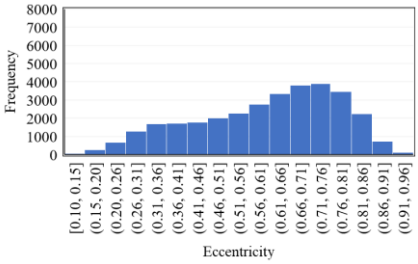

3.2.4.2 Hydrochloric acid effect

Visual inspection, mass loss and compressive strength loss

In this section, the resistance of fibre-reinforced mortars to hydrochloric (HCl) acid solution was evaluated. The visual inspection of samples at different time intervals and the

corresponding weight loss after exposure to HCl attack are presented in Figure 3-5 (a). The progressive deterioration is easily visible over time. The outer layer of specimens was soft and fragile, with bundles of both carbon and glass fibre visible on the surface. As a result of the reaction between the chloride ion and the hydration products, pores and white precipitates could be found on the surface. The formation of calcium chloride decomposed the mortar matrix, leading to a significant weight loss. Although short fibres reduced compactness and created voids in the mortar matrix (as discussed earlier), their bridging action compensated for the increased porosity and slowed down the matrix degradation. As demonstrated in Figure 3-5 (b), the higher fibre volume in carbon fibre-reinforced mortar resulted in lower mass losses. Conversely, porosity dominated the rapid deterioration of mortar mixtures containing 0.5% and 1.0% GF.

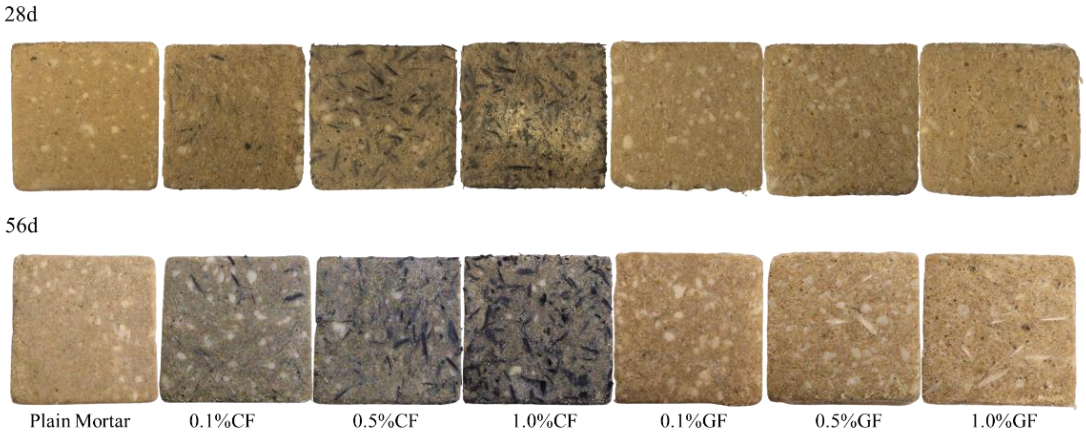

(a)

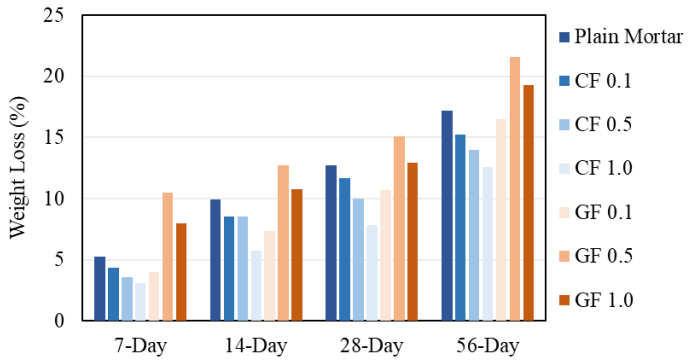

(b)

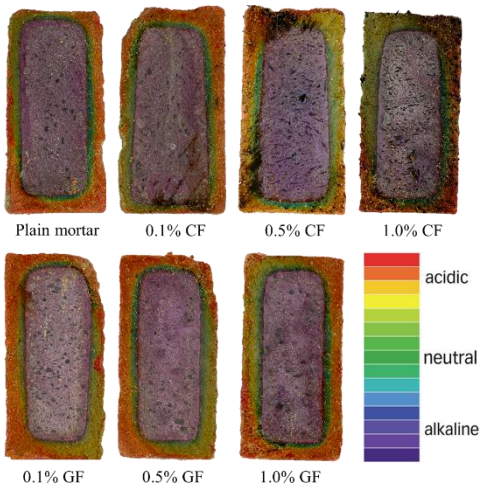

(c)

Mix	Penetration Depth (mm)	Calculated D ($\times 10^{-6}$ mm^2/s)
Plain mortar	8.7	0.978
0.1% CF	8.4	0.911
0.5% CF	8.4	0.911
1.0% CF	8.4	0.911
0.1% GF	8.7	0.978
0.5% GF	8.9	1.023
1.0% GF	9.4	1.141

(d)

Figure 3-5. (a) Visual inspection after 28 and 56-day immersion; (b) Weight loss of mortar specimens; (c)Penetration depth in 5% HCl: Cross-section using Bromothymol blue; and (d) Experimental diffusion coefficients.

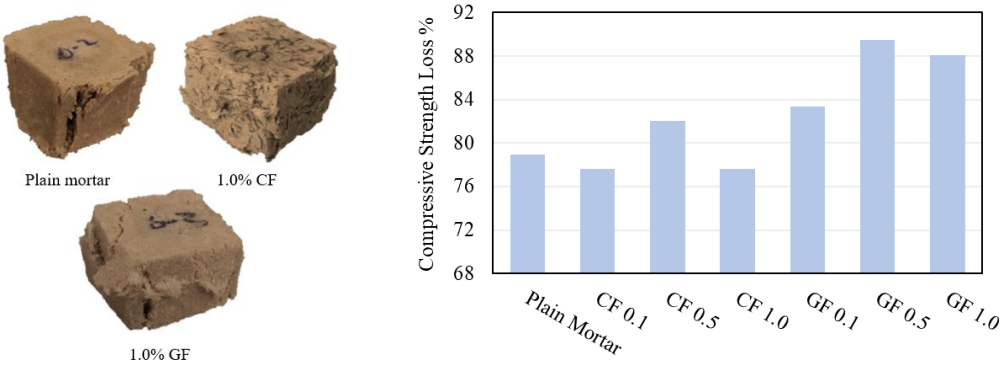

(a) (b)

Figure 3-6. (a) Mortar samples after compressive test; (b) Compressive strength loss of acid-immersed mortar samples.

After the treatment period, mortar samples were cut in half to investigate the degree of acid penetration from the external layers. Bromothymol blue (pH indicator) was applied to the cross-section to indicate the depth of penetration and the pH value. Figure 3-5 (c) displays photos of the cut samples with acid penetration. Figure 3-5 (d) shows the values of acid penetration depth and diffusion coefficients computed using Equation 3-11. Based on the results, reductions in penetration depth and diffusion coefficient were observed in all CF-reinforced mortar samples.

The results of compressive strength tests after acid attack are presented in Figure 3-6 (b), with the samples after testing illustrated in Figure 3-6 (a). After 56 days of exposure to 5% HCl acid solution, the compressive strength of 0.1% and 1.0% CF reinforced mortar declined by

77.6%, slightly less than that of plain mortar (78.9% strength reduction). In comparison, the strength reduction of mortar reinforced with GF varied between 83.4% and 89.5%.

Proposed diffusion model

The acid diffusion phenomenon in this study can be characterised by Fick's First Law [57, 58], which is represented as

$$\frac{\partial C}{\partial t} = \nabla(D \times \nabla C) \quad 3\text{-}3$$

where D is the diffusivity coefficient, C is the acid concentration percentage and t represent the time. As the diffusivity in mortar is uniform ($\nabla D = 0$), Equation 3-3 can be simplified as

$$\frac{\partial C}{\partial t} = D\nabla^2 C \quad 3\text{-}4$$

Analogously, conduction heat transfer can be described by Fourier's law as

$$\rho C_P \frac{\partial T}{\partial t} = \nabla(k \times \nabla T) \quad 3\text{-}5$$

where ρ and C_P are density and specific heat respectively. ∇ is the gradient operator and k is the thermal conductivity for isotropic conductivity (W m^{-1} K^{-1}).

The governing equation can be represented as Equation 3-6 assuming thermal conductivity is uniform ($\nabla k = 0$).

$$\frac{\partial T}{\partial t} = \alpha\nabla^2 T \quad 3\text{-}6$$

where α is the thermal diffusivity (m^2 s^{-1}), which equals to $k/\rho C_P$.

The heat transfer and mass diffusion models share a similar analogy, with both having identical forms of governing equations. This direct analogy can be expressed through the equations below.

$$\text{Temperature (T)} = \text{Concentration (C)} \quad 3\text{-}7$$

$$\text{Diffusion coefficient } (\alpha) = \text{Moisture diffusion (D)} \quad 3\text{-}8$$

Since the acid diffusion process into mortar specimens is assumed to be primarily one-dimensional through the thickness direction, the analytical solution giving the moisture concentration C at time t is expressed by Equation 3-9, which has been confirmed by many previous studies [58-61].

$$\frac{C}{C_\infty} = 1 - \frac{4}{\pi}\sum_{n=0}^{\infty}\frac{(-1)^n}{(2n+1)}\exp[-\frac{Dt}{h^2}\pi^2(2n+1)] \quad 3\text{-}9$$

where C_∞ is the maximum equilibrium moisture concentration (constant surface concentration), and D is the diffusion coefficient (m^2/s). h is the thickness of the mortar, which can be simplified as:

$$C(x,t) = C_\infty(1 - erf\,[\frac{x}{2\sqrt{Dt}}]) \quad 3\text{-}10$$

where $C(x,t)$ represents the chloride concentration at penetration depth x and time t.

In terms of diffusion within porous concrete materials, Equation 3-10 can be simplified as:

$$x = 4\sqrt{Dt} \quad 3\text{-}11$$

Mortar specimens absorb acid through the external surface when immersed in acid solutions. Then the expression is integrated, given the moisture absorption content M_t as a function of time, in the following equation:

$$M_t = M_\infty\,[1 - \frac{8}{\pi^2}\sum_{n=0}^{\infty}\frac{1}{(2n+1)^2}\exp[-\frac{Dt}{h^2}\pi^2(2n+1)^2]] \quad 3\text{-}12$$

where M_∞ is the maximum equilibrium amount of absorption.

The theoretical diffusion process is depicted as the acid absorption content plotted against the square root of time (t_1 and t_2) to establish the initial linear slope, as illustrated in Figure 3-7. The diffusion process is then approximated by simplifying the equation as 3-13.

$$M_t = M_\infty\,[1 - \exp\,[-7.3\,(\frac{Dt}{h^2})^{0.75}]\,] \quad 3\text{-}13$$

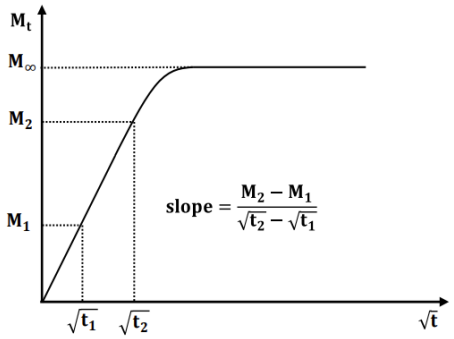

Figure 3-7. Gravimetric curve of Fickian diffusion process.

For the initial linear part of Fick's diffusion curve ($\frac{\sqrt{Dt}}{h} \leq 0.28$),

$$D = \pi \left(\frac{h}{4M_\infty}\right)^2 \left(\frac{M_1 - M_2}{\sqrt{t_1} - \sqrt{t_2}}\right)^2 \quad 3\text{-}14$$

For short time period (M_t/M_∞ is < 0.5), the equation can be simplified as

$$M_t = \frac{4M_\infty}{h}\sqrt{\frac{Dt}{\pi}} \quad 3\text{-}15$$

Numerical modelling

In the present study, Abaqus software [62] was employed to perform the numerical finite element (FE) analysis to simulate the acid diffusion in mortar. As mentioned above, both mass diffusion and heat transfer can be utilised to simulate the diffusion process due to the analogous expression of the governing equations. To verify the proposed FE model, a replication of previous studies from the literature [31] was conducted. Subsequently, this model was employed to simulate acid diffusion in the current study. The comparison in Figure 3-8 is in agreement with previously published work, demonstrating a high degree of consistency (R^2 above 0.99). This confirms the validity of the modelling approach.

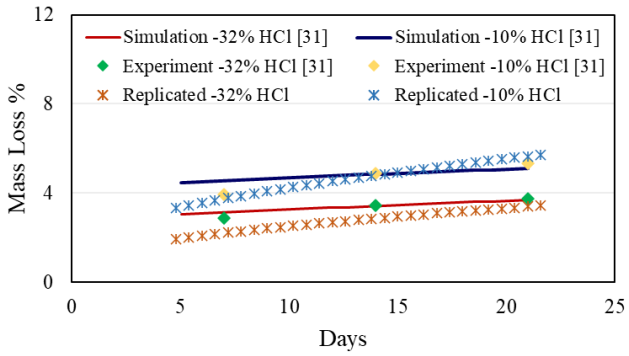

Figure 3-8. Replication of published FE models and experimental results.

The FE 3D models were built with the same dimensions as those of the experimental cylinder specimens, depicted in Figure 3-9 (a). The experimentally determined acid diffusion coefficients (Figure 3-5 (d)) and the maximum saturated acid content at equilibrium state Equation 3-14 were used as input parameters in the FE models for material properties and boundary conditions. Transient field analysis was chosen as the most appropriate form for FE-based diffusion modelling as the acid/moisture diffusion process is a transient phenomenon in nature. The output of mass diffusion analysis was the concentration at integration points (CONC). A specific post-processing step was performed by Python script to compute the mass loss curves as a function of time. The penetration simulation that was close to the experimental penetration depth is shown in Figure 3-9 (b). The experimental results and the simulated values show a strong agreement (Figure 3-9 (c)), with most of the R^2 values exceeding 0.95. Using

this FE modelling approach, the long-term service life of a structure made of fibre-reinforced mortar could be predicted. The FE simulations yielded higher mass losses over the tested period and greater variations in the initial diffusion stage. This could be attributed to experimental uncertainties and higher diffusivities that are solely measured at the final stages of the experiments.

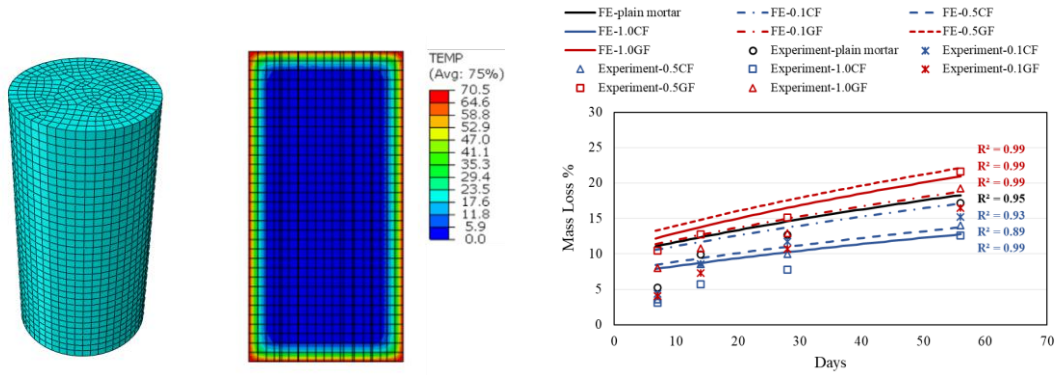

(a) (b) (c)

Figure 3-9. (a) Mesh configuration of FE models; FE analysis of (b) penetration depth and (c) mass loss of acid-immersed mortar

3.2.4.3 Water absorption and dry bulk density

The total pore volume of the fibre-reinforced mortar is examined by the water absorption test (Figure 3-10 (a)). The density of the mortar increased as reaction products developed over time (Figure 3-10 (b) and (c)), leading to a reduction in water absorption values at 28 days before reaching a stabilisation point at 90 days. Fibre-reinforced mortar exhibits a lower density than plain mortar, which could be explained by the relatively light weight of fibres and the presence of additional air voids. It is also interesting to note that the mortar containing 1.0% CF shows better compactness in terms of higher density than the mortar with 0.5% CF. Based on the observations, the addition of fibres increased water absorption for all the mix combinations at the ages of 28 and 90 days. Liaqat Ali et al. [63] suggested that the inclusion of fibres could potentially increase porosity by introducing an additional Interfacial Transition Zone (ITZ) within the matrix, but it might also restrain microcrack formation due to the additional fibre reinforcement. In this experiment, the effect of ITZ introduction seems to outweigh the effect on microcrack restraining. The addition of CF slightly increased water absorption by less than 10%, with the smallest increase observed at 90 days when incorporating 1.0% CF. In contrast, 1.0% GF had a more adverse effect on the water absorption of mortar, seemingly contributing to the development of larger porosity volumes.

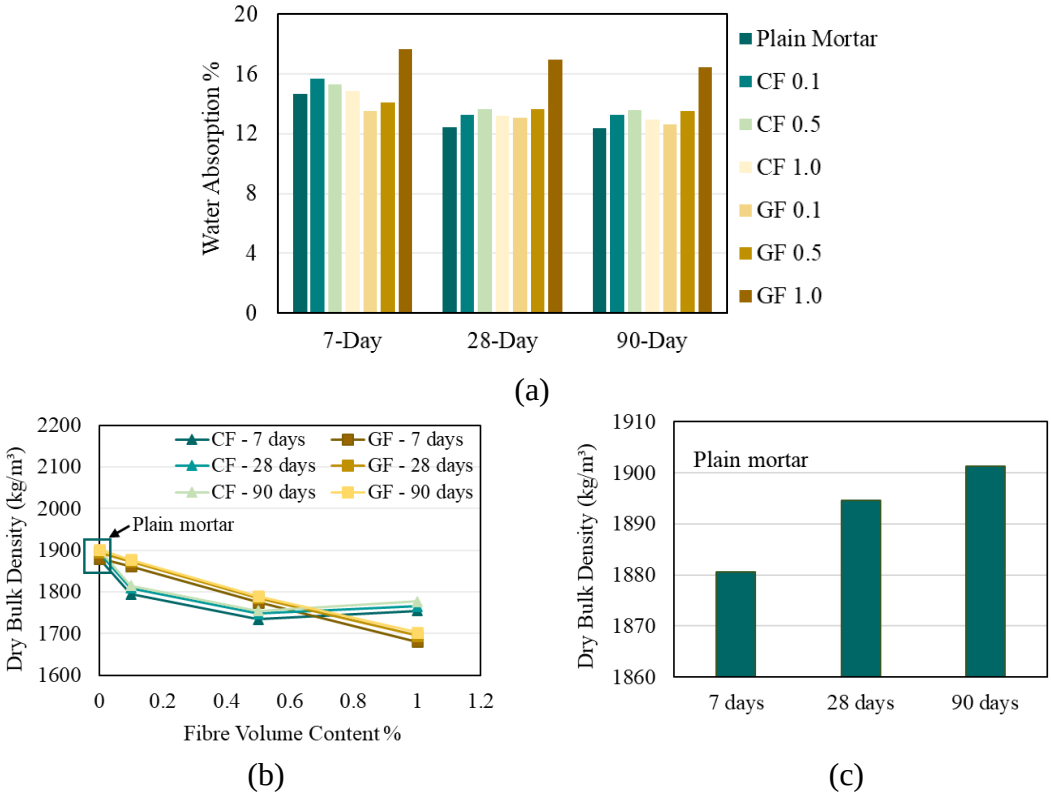

Figure 3-10. (a) Water absorption; (b) and (c) Dry bulk density.

3.2.4.4 Drying shrinkage

The results of the drying shrinkage test for the fibre-reinforced mortar are shown in Figure 3-11. The shrinkage of mortar incorporated with 0.1% and 0.5% CF exhibited a slight increase, whereas reinforcement with 1.0% CF resulted in reduced shrinkage. This suggests that a higher volume of CF effectively limits shrinkage. Upon the addition of GF into the mortar, the drying shrinkage of all mortar specimens was significantly reduced. Moreover, the strain induced in the mortar due to shrinkage decreased with an increase in GF concentration. It is widely known that drying shrinkage occurs when mortar loses capillary water, and that water loss created the tensile stress. Fibres oriented parallel to the measured length can interconnect the mortar components, thereby minimising shrinkage strain through the interface shear force. A possible explanation for the contrasting behaviours of the fibres could be attributed to the smaller diameter of CF compared to GF and the grooves on the CF surface. This difference has the potential to promote the formation of sub-millimetre pores. Previous research has demonstrated that the presence of small pores exerts a significant influence on shrinkage deformation [14, 64].

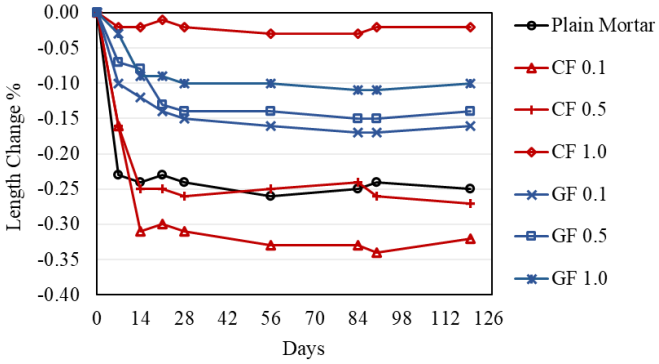

Figure 3-11. Drying shrinkage of fibre-reinforced mortar.

3.2.4.5 Surface and bulk resistivity

The electrical conductivity of mortar is considered as its ability to carry the electric current, which depends on various factors, including mixed materials and moisture content. This can be attributed to two distinct mechanisms: electrolytic, which involves the mobility of ionic species generated when the binder is mixed with water, and electronic, which entails the free mobility of electrons across conductive phases [14, 23, 27]. Based on the experimental results, the electrical resistivity of mortar increased with increasing curing age. It has been shown that the water content in the mortar decreases over time, leading to increased compaction through hydration. This process results in a reduction in conductivity by lowering the mobility of the ions within the pore solution [65]. The results clearly show that the addition of CF improved the conductivity by forming a conductive network, while GF did not have a significant impact on resistivity. With 0.5% and 1.0% CF reinforcement, surface resistivity dropped from 3.68 kΩ.cm of plain mortar to less than 1 kΩ.cm at 90 days. Similarly, the bulk resistivity of mortar decreased remarkably with a higher concentration of CF. At 90 days, the bulk resistivity of mortars reduced from 1.96 kΩ.cm (plain mortar) to 1.84 kΩ.cm with 0.1% CF, 0.61 kΩ.cm with 0.5% CF and only 0.15 kΩ.cm with 1.0% CF (Figure 3-12 (a)). Figure 3-12 (b) depicts the relationship between bulk resistivity and surface resistivity of GF-reinforced mortars at various cured ages. Due to measurement limitations, only three points for each curing age could be plotted, whereas the coefficient of determination (R^2) for the linear trend line was higher than 0.82, indicating a high degree of correlation between surface and bulk resistivity of mortar with GF. R^2 measured at 90 and 120 days was close to 1.0. The correction ratio of bulk to surface resistivity (slope) is computed to increase from about 0.55 at 7 and 28 days to 0.62 at 90 and 120 days. Prior research has similarly suggested a strong linear correlation between bulk and surface resistivity [66, 67].

The correlation between resistivity and mechanical strength offers the potential for estimating onsite strength without using destructive testing. Figure 3-12 (c) to (f) shows the compressive and flexural strength of CF- and GF-reinforced mortar at different ages. Figure 3-12 (g) and (i) show the correlation between both compressive and flexural strength and bulk resistivity over time (7, 28 and 90 days) for GF- and CF-reinforced mortar. The high R^2 values indicate a strong linear correlation between mechanical strength and electrical bulk resistivity. Nevertheless, the correlation between mechanical strength and surface resistivity in GF-reinforced mortar was lower (Figure 3-12 (h)), pointing to variability in the data. Quang and Pratanu [68] have established a relationship between resistivity and compressive strength in different kinds of concrete mixtures based on a logarithmic equation. Given the limitations of the data recorded in this study, it is recommended that more experimental results be collected to formulate accurate equations for determining the relationships between resistivity and different properties of FRCC.

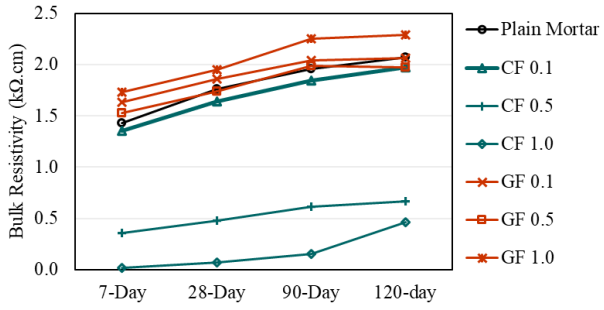

(a)

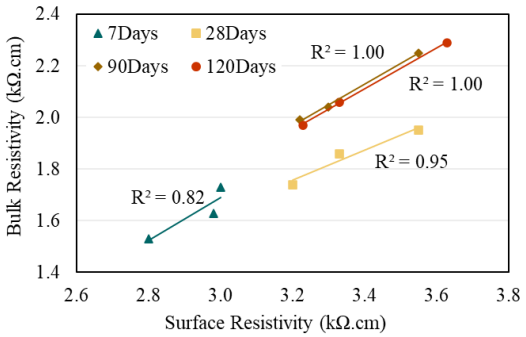

(b)

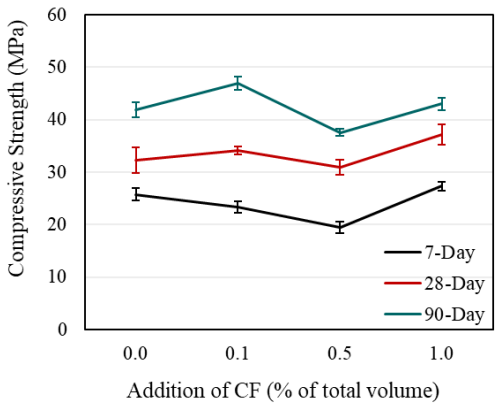

(c)

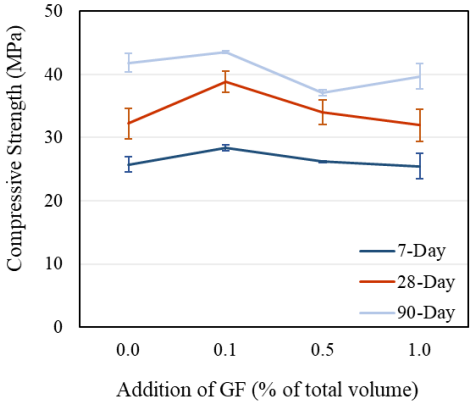

(d)

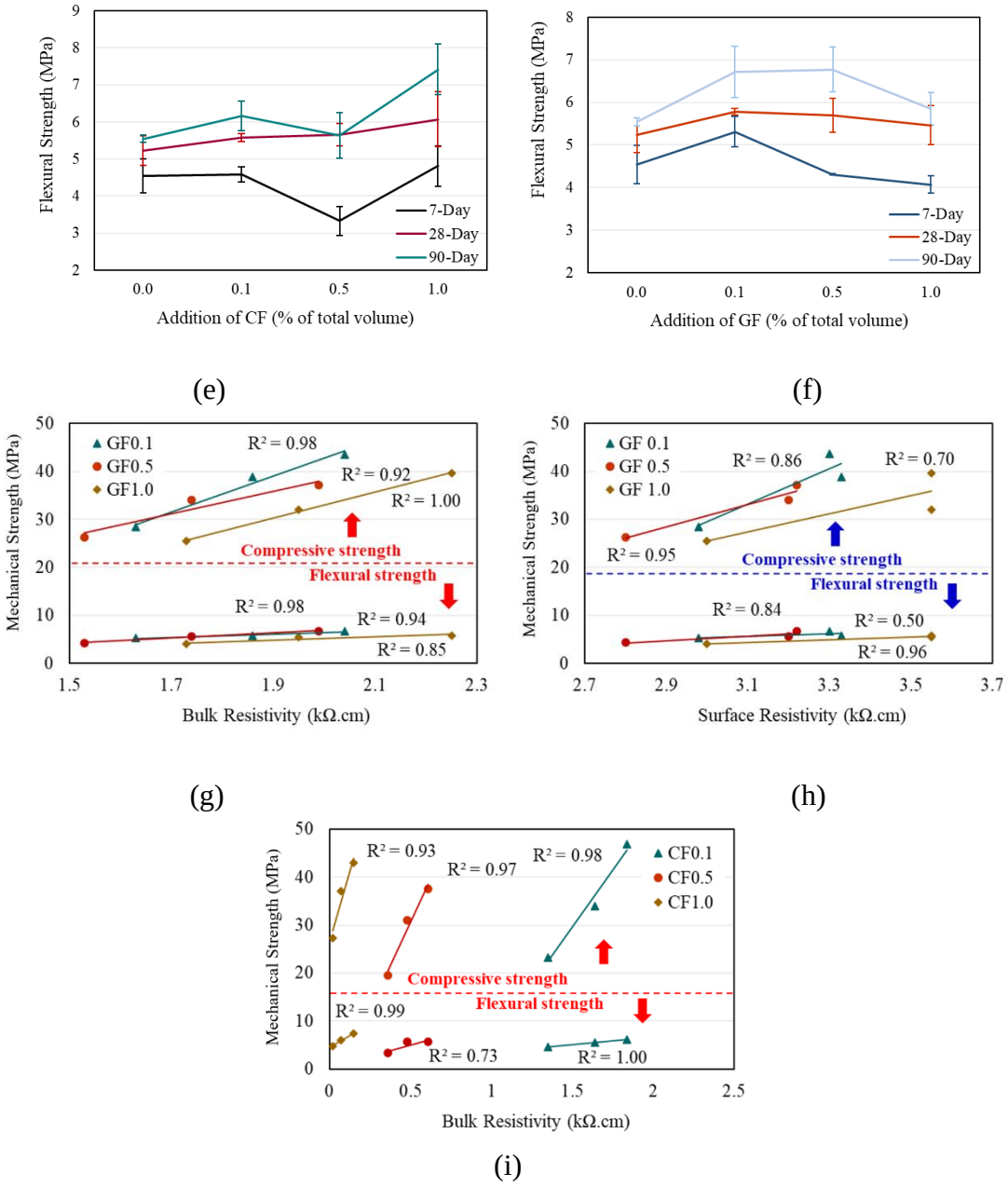

Figure 3-12. (a) Bulk Resistivity; (b) Correlation between surface and bulk resistivity; and (c) to (f) Compressive and flexural strengths of fibre-reinforced mortars; (g) Correlation between mechanical strength and bulk resistivity of GF-reinforced mortar; Correlation between (h) mechanical strength and surface resistivity and (i) mechanical strength and bulk resistivity of CF-reinforced mortar.

3.2.4.6 Microstructural analysis

Microstructural observation after mechanical testing

Figure 3-13 (a) shows the unrestrained growth of continuous microcracks in plain mortar resulting from mechanical testing. In contrast, the incorporation of fibres effectively limits the microcrack propagation by forming strong bonds with the matrix. Figure 3-13 (d) to (f) shows

the microstructural morphology of the interfacial transition zone (ITZ) between fibres and microcracks formed around fibres, demonstrating the fibres' ability to transfer stress. Small gaps were observed around the fibres, wherein hydration products adhered to the fibre surface, thereby improving bonding performance. As shown in Figure 3-13 (g) to (i), two failure mechanisms observed on the fractured surface were fibre pullout and fibre breakage. Initially, bridging fibres carried the stress transferred from the matrix through the interface, preventing further microcrack propagation in the matrix. As loading continued, fibres experienced either debonding, owing to the fibres' high tensile strength and shear frictional forces (referred to as pullout), or fibre breakage, which occurred when the bond strength between fibres and the matrix was higher.

Table 3-4 shows the elemental composition of selected spectrums on the surface of plain mortar and fibre-reinforced mortar (Figure 3-13 (a) to (c)). Predominant chemical elements present in the matrix included calcium (Ca), oxygen (O), carbon (C) and silicate (Si), with notably higher atomic percentages. Meanwhile, small contents of chemical elements were also detected, including aluminium (Al) and iron (Fe). Elemental analysis confirmed that the addition of fibres would not alter the primary chemical elements in the mortar, although the elemental content could display some variation. It reveals that Ca, O and Si were the principal elements in the calcium silicate hydrate (CSH) gel products. The presence of the calcium hydroxide (CH) phase was attributed to a calcium-to-silicate ratio exceeding 2 [69]. This finding is in line with the XRD results (Figure 3-14 (a)), where the predominant mineral phases identified were CSH, CH and SiO_2. In comparison to spectrum No.1, spectrum No.2 and No.3 have a lower calcium-to-silicate ratio, indicating that more CSH hydration products were formed near the fibres in fibre-reinforced mortars. Fibres potentially served as nucleation sites, facilitating the development of hydration products along the fibres' surface and filling the gaps (see Figure 3-13 (b) and (c)).

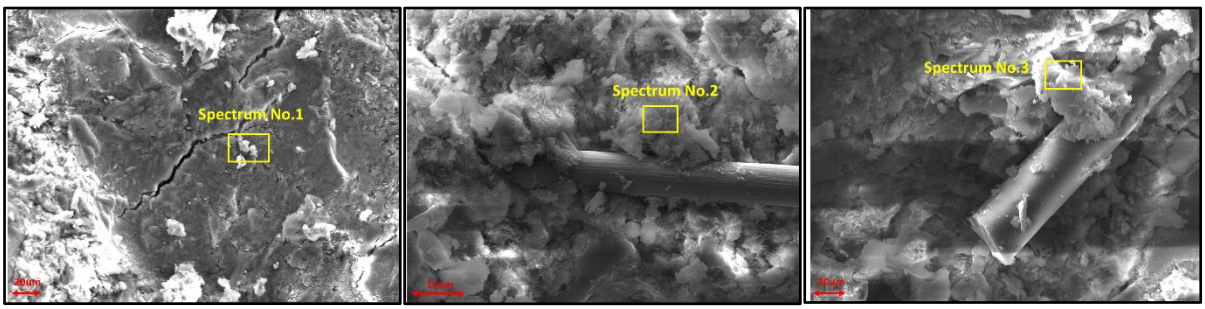

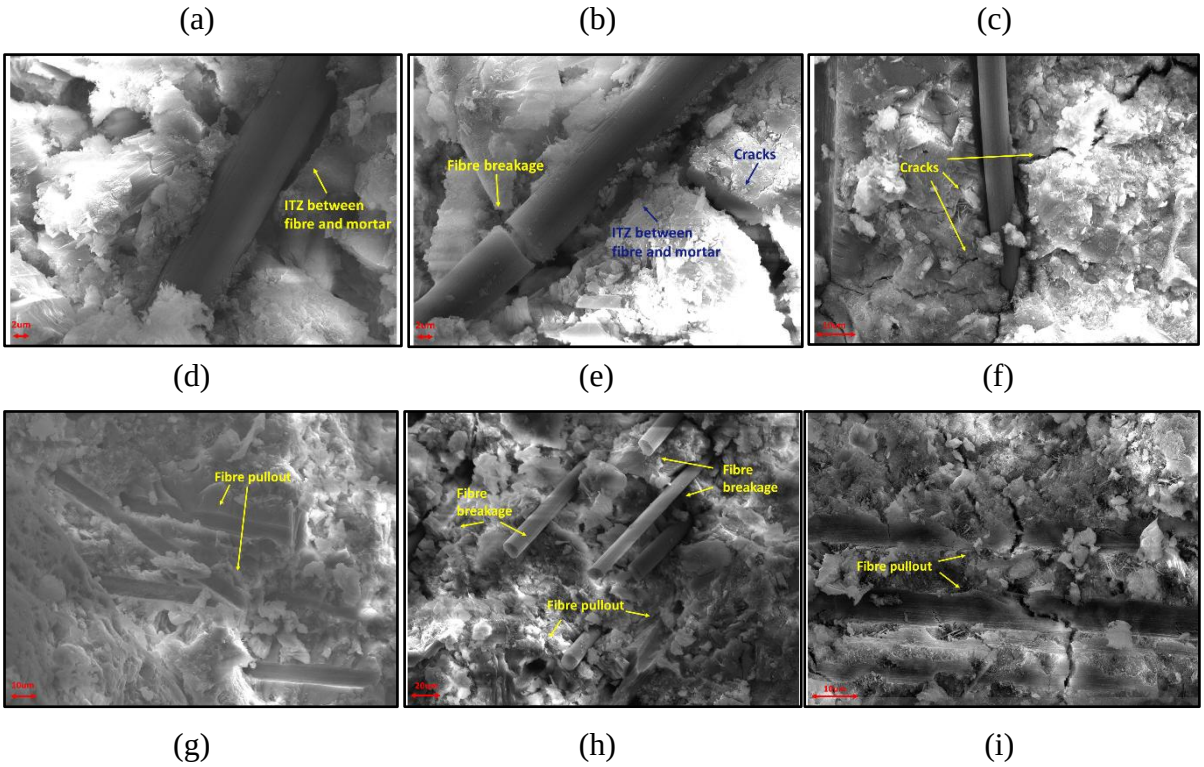

Figure 3-13. SEM image with spectrums for EDS analysis. (a) Plain mortar, (b) CF reinforced mortar, (c) GF reinforced mortar, (d) to (f) ITZ between CF and mortar and CF across microcracks, (g) to (i) CF and GF failure mode in mortar: fibre pullout and fibre breakage.

Table 3-4. Elemental analysis of plain mortar, CF-reinforced mortar and GF-reinforced mortar samples at 90 days.

Spectrum	Percentage of chemical element by atomic weight (At %)										
	O	C	Ca	Si	Fe	Al	Mg	S	K	Na	Total
No.1	37.2	8.5	45	6.5		1.7		1.0			100
No.2	43.2	19.7	24.4	9.2	0.6	1.3		1.2	0.4		100
No.3	43.9	16.7	21.7	7.4	2.0	1.8	2.6		2.3	1.6	100

The FTIR spectra of mortar mixes with fibres are shown in Figure 3-14 (b). The wavenumber of 3634 cm^{-1} represents the O-H stretching vibration of portlandite, while the wavenumbers of 3515 and 1651 cm^{-1} are identified as the vibration of water molecules [70, 71]. The small peaks at around 873, 1418 and 2334 cm^{-1} represent the stretching vibration of CO_3^{2-}, which is assigned to $CaCO_3$ due to the absorption of atmospheric CO_2 [72-74]. The SO_4^{2-} asymmetric stretching vibration of gypsum is observed at the peak at a wavenumber of 1,111 cm^{-1}. The peaks around 453, 527, 642 and 955 cm^{-1} are attributed to the Si-O vibration, indicating the presence of main constituents of cement and the formation of hydraulic products (CSH) [70, 74, 75]. The band at 780 cm^{-1} wavenumber corresponds to the asymmetric stretching vibration of SiO_2, indicating the presence of quartz [76].

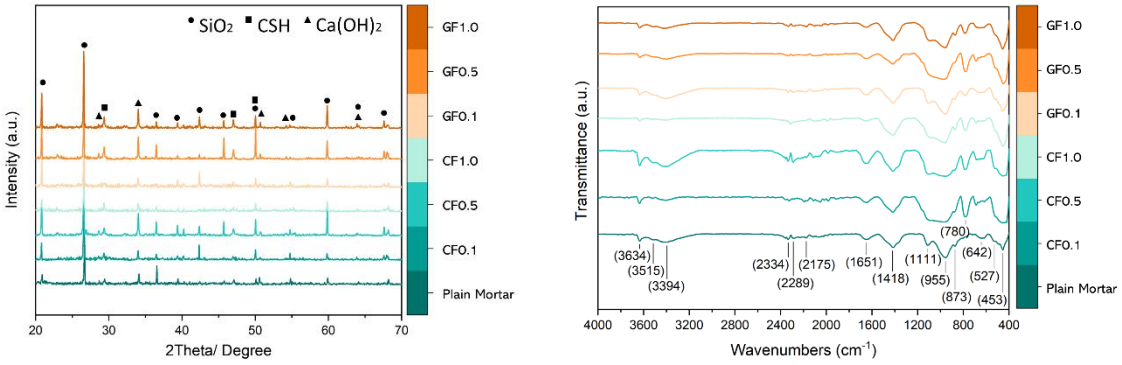

Figure 3-14. (a) XRD pattern and (b) FTIR spectra of fibre-reinforced mortar.

Microstructural observation after acid attack

SEM images in this sub-section show the significant morphological changes in the mortar samples caused by the acid attack (Figure 3-15). Compared to Figure 3-13, the homogeneity of the matrix is significantly diminished, and notable microcracks and voids are visibly formed, indicating the deterioration process of the mortar matrix. Meanwhile, the interfacial bond between the fibres and the matrix appears to be weakening. Despite this, the fibres have not dissolved and continue to uphold the structural integrity of the matrix. The porosity and microcracks created channels, enabling the acid solution to permeate deeper into the interior layers. This ultimately resulted in a significant reduction in mortar strength. The chemical reactions caused by the HCl attack were determined by XRD and FTIR tests (Figure 3-16). The C-O-C vibration from CO_3^{2-} was untraceable after immersion in the HCl acid solution due to the dissolution of carbonates. Meanwhile, the absorption band that appeared at 1,634 cm^{-1} was assigned to physisorbed water on the surface of silica due to the acid attack [77]. Calcium carbonate and portlandite chemically interacted with HCl acid to form calcium chloride, which then reacted with silicon dioxide. As a result, a peak of calcium silicates formed.

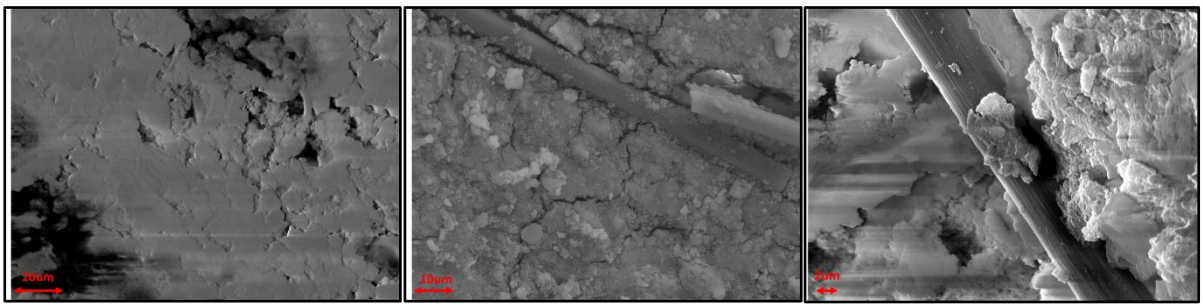

(a) Plain mortar; (b) and (c) CF-reinforced mortar

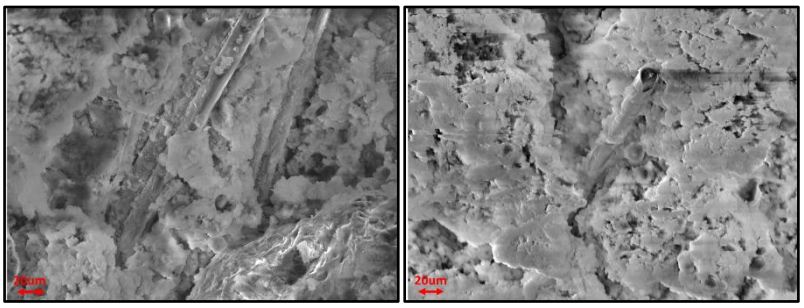

(d) and (e) GF-reinforced mortar

Figure 3-15. SEM images of mortar samples exposed to 5% HCl acid.

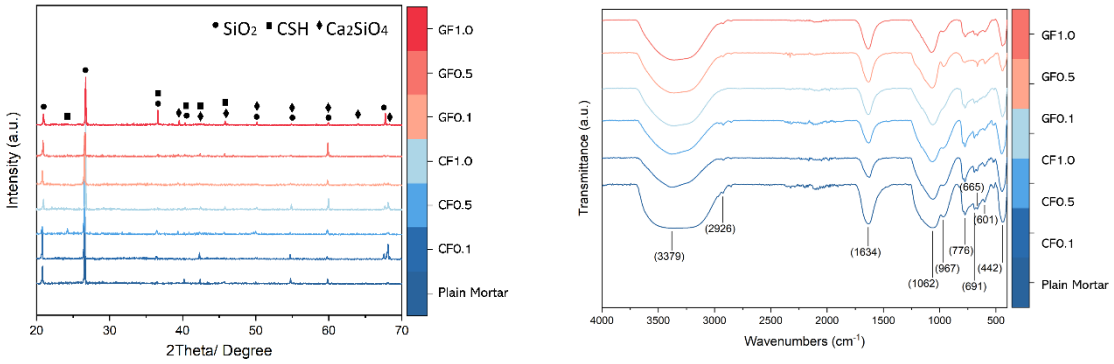

Figure 3-16. (a) XRD pattern and (b) FTIR spectra of acid-immersed mortar samples.

Overall, porosity is a critical factor in FRCC as it has a great influence on mechanical and durability properties. In this study, porosity analysis encompassed different pore characteristics, including the volume fraction of air voids larger than 200μm, void eccentricity and average air void size, as detailed in Section 3.2.4.1 and Figure 3-17 (a). The relatively elevated air void volume fraction in fibre-reinforced mortar (ranging from 6.26% to 8.94%) compared to the air void content of plain mortar (0.48%) can be primarily attributed to the inclusion of fibres. The addition of short fibres reduces the flow value of fresh mortar and leads to an increased air void volume fraction. Similarly, the small air void volume fraction exhibited the same trend. These results align with the water absorption findings (Figure 3-17 (b)), which measure the total porosity of mortar samples, including both air voids and capillary voids.

While fibres can enhance mechanical strength and reduce shrinkage mainly due to their bonding behaviour in the matrix, their addition can impact the porosity characteristics including volume fraction, pore shape, and pore size, which affect the mortar's performance. The mortar with 1.0% CF had higher ultimate compressive and flexural strengths than 0.5% CF-reinforced mortar (Figure 3-17 (c)). For GF-reinforced mortar, 0.5% GF-reinforced mortar outperformed 1.0% GF-reinforced mortar in terms of overall mechanical performance. The opposite relationship between air void volume fraction and mechanical strength can be explained by the

fact that voids can act as potential crack initiation sites, which reduce the mortar strength. After HCl immersion, 0.5% CF still showed lower compressive strength than 0.1% CF, while GF-reinforced mortar exhibited much lower compressive strength. The average size of air voids also plays a role in this process. Generally, an increase in average air void volume reduces the mechanical and durability characteristics by inducing more significant stress concentration sites and fosters the formation of interconnected voids, facilitating the penetration of acidic solutions. Consequently, this accelerates deterioration following exposure to HCl acid. Additionally, this study demonstrated that the drying shrinkage is also influenced by the elongated voids generated by fibres, as shown in Figure 3-17 (d). The void eccentricity valued at 0.3 to 0.5 indicated more elongated voids. For both CF and GF-reinforced mortar, the decreasing percentage of elongated voids led to a reduced length change percentage in terms of shrinkage. In addition, the SEM images of ITZ in Figure 3-13 explain the findings micro-CT results concerning void eccentricity, given the observed small gaps between fibres and cement matrix (as discussed in Section 3.2.4.1).

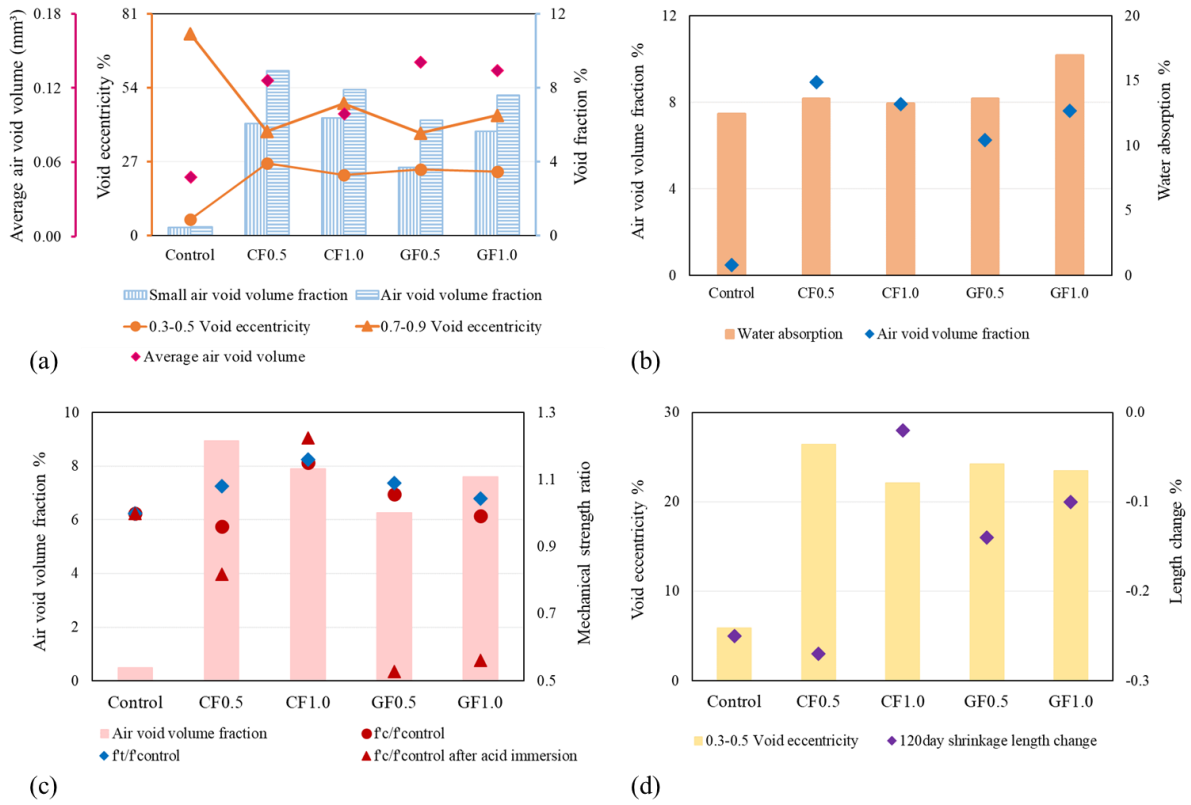

Figure 3-17. Evaluation of porosity and impacts on the mortar performance.

3.2.5 Summary of key findings from Section 3.2

In this study, void dimension and eccentricity distribution analysis in cementitious composites reinforced with short carbon and glass fibre were investigated using micro-CT. The

properties of voids were analysed quantitatively in a three-dimensional manner to understand their influences on mortar performance. Furthermore, this research explored the effects of acid diffusion on mortar through experiments and finite element simulations. The relationship between microstructures and various properties, including mechanical, durability, and electrical properties, was also discussed throughout the paper. The following outcomes can be drawn from this research:

- The inclusion of fibres led to the introduction of more air voids in the mortar. Compared to 0.48% air voids in plain mortar, fibre-containing mortars exhibited void contents ranging from 6.26% to 8.94%. Higher air void volume fraction and larger air voids result in lower mechanical strength and reduced durability performance. Raising the fibre concentration to 1.0% reduced drying shrinkage due to increased shear strength between fibre and matrix. A higher fibre volume fraction could effectively limit drying shrinkage. As fibres were added, elongated voids formed around the fibres due to stretching or the merging of small voids. Voids with lower eccentricity were identified as contributing factors to an increased length change in shrinkage. The results also demonstrate a greater occurrence of elongated voids in specimens containing CF, attributed to its shape, when compared to those with GF. Future research is needed to investigate the interface transition zone between fibre and cementitious matrix, along with the impact of capillary pores on shrinkage behaviour.
- The acid resistance of fibre-reinforced mortar in acidic conditions was examined via experimental and numerical approaches. Mortar containing 1.0% carbon fibre exhibited the lowest weight loss, compressive strength reduction, and diffusion coefficient, as validated by FE modelling. Carbon fibre's bridging action compensated for porosity and decelerated matrix degradation. Conversely, for mortar mixtures containing 0.5% and 1.0% GF, porosity was the key factor driving rapid deterioration, allowing the acid solution to penetrate deeper into the interior layers.
- The addition of CF contributed to an improvement in the mortar's electrical conductivity. With an increase in CF content to 1.0%, the electrical resistivity decreased to below 1 kΩ.cm. Notably, a strong correlation was observed between bulk and surface electrical resistivity in fibre-reinforced mortar.
- Future studies could use micro-CT at a higher resolution to further visualise the FRCC voids of sub-micron size, which provides a more detailed and accurate analysis in

addition to the pore size distribution. In-situ micro-CT is expected to observe the development of elongated voids during the FRCC curing process and investigate the acid attack process. Further research is recommended to investigate the local stress distribution surrounding the elongated voids and their impacts on mechanical performance.

3.3 ENHANCING X-RAY MICRO-CT ANALYSIS FOR DETECTING VOIDS AND CARBON FIBRE FEATURES IN FIBRE-REINFORCED CEMENTITIOUS COMPOSITES USING ADVANCED 3D GAUSSIAN FILTERING

Y. Tao[1,†,*], Z. Wang[1,†], S.A. Hadigheh[1,*]

[1]School of Civil Engineering, Faculty of Engineering, The University of Sydney, Sydney, New South Wales 2006, Australia

[*]Corresponding Authors: Dr Ali Hadigheh

Yunyun Tao

[†]These authors contributed equally (first authors) to this work

Measurement, https://doi.org/10.1016/j.measurement.2025.117018, Published in February 2025.

3.3.1 Abstract

With the growing applications of carbon fibre-reinforced cementitious composites (carbon-FRCC), X-ray micro-computed tomography (micro-CT) has become essential for evaluating their internal microstructures. However, analysing carbon fibres in the cementitious matrix using X-ray imaging is challenging due to poor phase contrast and image noise. This study contributes to the development and application of a 3D second-order Gaussian kernel in X-ray micro-CT analysis, specifically tailored for detecting voids and carbon fibres in cementitious materials. A novel Anisotropic Gaussian filtering was developed to achieve precise and sharp boundaries between fibres and the matrix. Higher accuracy was verified, which outperformed conventional methods across performance metrics, confirming the effectiveness of the proposed segmentation framework. The study also demonstrated the successful application of the proposed Gaussian filtering for void analysis and detecting the spatial location of carbon fibre bundles. These advancements led to more reliable feature analysis, expanding the applicability of X-ray micro-CT for examining internal features in carbon-FRCC.

Keywords: X-ray micro-CT; Non-destructive testing; Fibre-reinforced cementitious composite (FRCC); isotropic and anisotropic Gaussian filter; fibre orientation; void analysis

3.3.2 Introduction

X-ray micro-computed tomography (micro-CT) is a non-destructive radiographic imaging technique that enables detailed visualisation and analysis of the internal three-dimensional (3D) geometry of materials. The use of CT-scan technology in civil engineering emerged as a pioneering tool during the 1980s through rock mechanics and mineralogy research, and it has since expanded to study various construction materials and composites for material microstructural analysis in the field [78]. Cement-based materials, such as concrete and mortar, are ubiquitous in the construction industry due to their advantages of cost-effectiveness, high compressive strength, and long-term durability [79, 80]. Concrete is made up of various raw ingredients that, upon curing, form distinct phases within its structure, such as aggregates, the cementitious matrix, hydration products, voids, and other additives. The inherent complexity of this multi-phase system requires examining its microstructural characteristics to understand the material's properties and behaviour. Various microstructural analysis techniques are employed for this purpose, but each has limitations in its application. For example, scanning electron microscopy (SEM) with Energy Dispersive X-ray spectroscopy (EDS) has been used for particle surface characterisation, interfacial transition zone (ITZ) analysis, and elemental ratio analysis [81, 82]. However, SEM only provides two-dimensional surface images and is limited by sample size. X-ray diffraction (XRD) is used to identify crystalline phases and quantify hydration products [83-85]. Fourier transform infrared spectroscopy (FTIR) evaluates hydration or carbonation products through bond characterisation [86]. While both techniques provide valuable chemical information, they require sample extraction and preparation and do not offer insights into the internal structure of the material. To characterise pore size distribution, mercury intrusion porosimetry (MIP) and backscatter SEM are commonly used techniques [87-89]. They provide statistical measurements for both nano-scale capillary pores and large air voids. SEM also allows visualisation and investigation of the relationship between pores and other microstructural features [88]. However, these techniques are categorised as destructive methods and have limitations in revealing the morphological and volumetric features of individual pores, such as shape and spatial position [90]. To address the gap in understanding the 3D internal structure and spatial relationships within cement-based materials, X-ray micro-CT distinguishes various components of cementitious materials based on their differential X-ray attenuation coefficients.

Among the critical microstructural characteristics of cementitious materials, porosity significantly influences mechanical properties, freeze-thaw durability, and transport properties

such as electrical conductivity, chloride diffusivity, and permeability [40, 89, 91-93]. Previous studies have demonstrated that pore size distributions, particularly capillary pores, affect shrinkage and swelling behaviour due to the strong pore water pressure [51, 94]. X-ray micro-CT imaging allows for the segmentation of cementitious materials into solid and pore phases [95]. The excellent contrast differentiation between air voids and the cementitious matrix facilitates void segmentation, enabling visualisation and quantitative analysis of individual void shape, size, and spatial position. This quantitative void data allows for exploring the correlation between void distributions and the mechanical behaviour of cementitious material, as well as the evolution of void formation, damage, and cracking within the materials [95-97]. Within the solid phase, further distinctions can be made between aggregates, cement hydration products, and other additives such as carbon fibres and steel fibres [90, 95, 98, 99]. Currently, the investigation of fibre-reinforced cementitious composites (FRCC) remains an active area of research [100, 101]. X-ray micro-CT serves as a powerful tool for visualising and quantifying the spatial distribution and orientation of fibres within the matrix. Segmentation is a crucial step for accurate phase detection from reconstructed X-ray micro-CT tomograms. However, it remains a challenging research area, particularly when dealing with low-contrast images where phases overlap in grey values. Such overlap reduces the effectiveness of conventional segmentation methods, highlighting the need for advanced techniques to improve phase detection.

In recent years, machine learning (ML) approaches have rapidly developed and are increasingly being used for the segmentation of composite fibres. Xu et al. [102] employed in-situ automated microtomography segmentation to quantify pore and polyvinyl alcohol fibre characteristics in cementitious composites. Among six representative supervised ML models, the random forest model showed highest segmentation accuracy and computational efficiency in processing 3D tomographic data. Deep learning methods, such as convolutional neural networks (CNNs), have been applied for image segmentation in this application. Hong et al. [103] proposed a novel deep learning model based on the DeepLabV3+ network for automatic segmentation of short glass fibres from FRCC, which outperformed traditional segmentation methods by achieving a segmentation accuracy of 99.3% and aiding in fibre distribution identification. In addition, Badran et al. [104] applied a CNN architecture (FCDenseNet, Dragonfly toolbox) to achieve a 98% accuracy in phase segmentation of fibre-reinforced ceramic composites based on shape and edge features instead of depending on image intensities. ML offers significant advantages in the automated and accurate recognition of complex features

within the matrix, leading to more precise segmentation. Its adaptability to diverse datasets makes it particularly effective for handling complex tasks, over traditional methods. The computational time required for ML process depends on various factors, including task complexity, the size and number of data, and the availability of hardware resources. Despite the benefits of the above-mentioned ML approaches, one of the key challenges in 3D image segmentation using supervised learning methods is the need for high-quality data labelling [104, 105]. To overcome this challenge, a semi-automatic labelling approach was developed, developed that combines k-means clustering for initial segmentation of 2D concrete tomograms with subsequent manual refinement [106]. Future work also includes the development of semi-supervised or unsupervised learning approaches [107].

While machine learning approaches typically require large training datasets to avoid overfitting, rule-based algorithms offer a simpler and more precise solution for segmenting cylindrical fibres from the cementitious matrix. Effective segmentation methods can also serve as preprocessing methods for ML. Miletić et al. [108] proposed a novel image processing technique for analysing ultra-high-performance fibre-reinforced concrete (UHPC). Their approach leverages the local intensity gradient of fibres to determine their spatial distribution and orientation within the cementitious matrix. The developed two-step segmentation technique incorporates edge-preserving filters to reduce image noise while maintaining fibre boundary definition, resulting in highly accurate volumetric estimation of fibre content. Gao et al. [109] utilised X-ray micro-CT to construct 3D models for determining the volume fraction of carbon fibre bundles. They also captured consecutive layer images, which allowed for the identification of various morphologies, such as carbon bundles and sub-millimetre pores, based on greyscale analysis. Additionally, fibre planar and spatial distribution were identified to further describe the carbon fibre distribution [98]. While X-ray micro-CT imaging and analysis offer insights into the fibre distribution and void features in carbon-FRCC, the limitations and uncertainties should be acknowledged: (i) due to the smaller diameter and lower density of carbon fibres compared to the other fibres (such as steel), distinguishing them from cementitious materials could be more challenging in the presence of high noise level and low contrast, (ii) as demonstrated in Gao et al. [109]'s study, the accuracy of their identification was highly dependent on the selected greyscale thresholds, and achieving precise greyscale determination required supplementary techniques, such as SEM, to capture images at specific locations, and (iii) further optimisation of the processing method should be developed to enhance the identification accuracy of carbon fibre bundles. Commercial image processing software was

used to optimise and analyse X-ray micro-CT images. However, the efficiency and accuracy of the applied filters for detecting carbon fibres still need to be validated.

Current X-ray micro-CT based approaches for measuring 3D Fibre Orientation Distribution (FOD) fall into two main categories: single fibre segmentation and local orientation analysis [110-113]. The first type of algorithm focuses on segmenting individual fibres. Once segmented, the centreline of each fibre can be tracked, allowing for the calculation of the complete FOD. However, this method requires manual validation and deals with many false detections, making it impractical for large volumes. It also needs very high-resolution and high-contrast images to ensure the accuracy of the results. Commercial image processing programs, such as Dragonfly, Avizo, VGSTUDIO MAX and ImageJ, are increasingly available for advanced segmentation applications [114-117]. For example, ImageJ with its macro has been used for root segmentation in soil matrix based on the shape and greyscale detection, while offering plugins for application-specific needs [114, 118, 119]. Dragonfly has also been successfully applied for fibre distribution and pore connectivity analysis in fibre-reinforced composites [104, 116, 120]. OpenFiberSeg is another open-source tool that demonstrates its advantages in fibre tracking and segmentation, which achieved an average segmentation precision of 93.1% on per-voxel basis [116]. However, it has limitations when it comes to fibres with significant curvatures. Several limitations of these commercial software and programs include: (i) limited accessibility for researchers due to high costs or academic-only licensing restrictions; (ii) limited flexibility for customisation and specialised workflows; and (iii) the processing algorithms applied in the program often present challenges for result validation and case-specific algorithm tuning to achieve accuracy and reliability. Therefore, developing an accessible implementation directly for carbon-FRCC with reduced computational time is one of the objectives of this paper. Instead of detecting and tracking individual fibres, the second method derives the FOD through global measurements. It is especially beneficial when spatial resolution is not very high. Popular algorithms for this type include the Anisotropic Gaussian filter, Hessian matrix, and structure tensor calculation [111, 121, 122]. In the case of 2D images, Keilmann et al. [121] improved efficiency and accuracy of Anisotropic Gaussian filters by combining low memory usage with minimised interpolation errors through axis-aligned filtering and in-place processing, which outperformed the established structure tensor and Hessian matrix on synthetic fibre images including the bent fibres. While the Anisotropic Gaussian filter demonstrated a merit performance in 2D applications due to simpler unit circle sampling and less time-intensive, it exhibited lower accuracy compared to Hessian matrix and

structure tensor-based methods when evaluated on 3D synthetic datasets [122]. Pinter et al. [111] further examined these methods by comparing their error estimation and testing procedures. They concluded that the structure tensor method yielded the best results, exhibiting minimal deviations of only 0.6% for glass fibre reinforced polymers (GFRP) and also performing well with low-contrast images of carbon fibre reinforced polymers (CFRP). The Hessian matrix method provided better results for curved fibres. The Anisotropic Gaussian filter method showed its advantages in computational efficiency and requiring the least working memory, while its accuracy was related to the number of angles analysed. The lower computational cost of using Anisotropic Gaussian filter in the examination of FRP composites, along with the opportunity for enhanced precision, makes it particularly interesting for investigating low-contrast 3D images of other materials, such as carbon-FRCC.

This work primarily contributes to the development and application of a 3D second-order Gaussian kernel in X-ray micro-CT analysis, specifically tailored for detecting voids and carbon fibre in cementitious materials ranging from micron to macro levels. The proposed approach enhances the robustness of segmentation against noise and improves contrast between voids, fibres and the surrounding cementitious matrix based on volumetric X-ray micro-CT images. The application of Isotropic Gaussian filtering for void analysis in carbon-FRCC is illustrated in Section 3.3.4.1. Furthermore, by leveraging characteristics and optimising parameters of the Anisotropic Gaussian filter, the proposed Anisotropic Gaussian method achieves more precise and sharp boundaries between carbon fibres and the cementitious matrix, facilitating accurate fibre segmentation. This enhancement further advances the microstructural analysis of carbon-FRCC, enabling more reliable quantification of carbon fibre orientation and spatial positions. The new Anisotropic Gaussian method, with its noise reduction capability, is mathematically derived and proven in Section 3.3.3.2. The section details the theoretical foundations and operational principles of the algorithm. To evaluate the efficacy of this proposed method, its segmentation accuracy is quantitatively assessed against conventional methods using various performance metrics, with ground truth data as a benchmark (Section 3.3.4.2). Results consistently showed the superior performance of the proposed method across two different scales. Following validation, Section 3.3.4.3 illustrates the practical application of our refined Anisotropic Gaussian approach. In this paper, Isotropic Gaussian filtering is employed for void characterisation and distribution, while the proposed Anisotropic Gaussian filtering is utilised to detect the orientation, length and spatial location of carbon fibre bundles within a

cementitious matrix. The feasibility and effectiveness of these proposed methods are thoroughly validated.

3.3.3 Materials and methodology

3.3.3.1 Sample preparation

This section describes the experimental samples used for microstructural characterisation, which were subjected to X-ray micro-CT scanning. A 50×50×50 mm^3 carbon-FRCC block with 1 vol.% short discrete carbon fibres (6mm in length) was prepared for void analysis (Figure 3-18 (a)). Carbon fibres were manually chopped for use as reinforcing materials in the cementitious composite. These fibres were sourced from a 300gsm T300 grade carbon fabric reinforcement sheet, which possesses a tensile strength of 3,000 MPa and a tensile modulus of 210 GPa. Each individual carbon fibre has a diameter of approximately 8 μm and a density of 1.8 g/cm^3. The FRCC specimen was prepared using general-purpose cement (type GP) as specified in AS3972 [44] and Macka's sand (less than 0.6mm) that complies with AS2758.1 [45], with a cement-to-sand-to-water weight ratio of 1:1.5:0.55.

Two smaller samples (50×20×15mm^3) embedded with carbon fibres were prepared for fibre characterisation, using a cement-to-water ratio of 0.55. The carbon fibre bundles and strips were extracted from the same fabric reinforcement sheet. As displayed in Figure 3-18 (b) and (c), the sample labelled 'C-Bundle' contained three carbon fibre bundles embedded at intervals within the cementitious matrix. Each carbon fibre bundle has a diameter of 1 mm. Another sample labelled 'C-Strip' contains three carbon fibre strips, each 5 mm wide. These two samples feature two different sizes of carbon fibre elements for X-ray micro-CT examination. The blue and red markers indicate the placement of the carbon fibre components within the cementitious matrix.

(a)

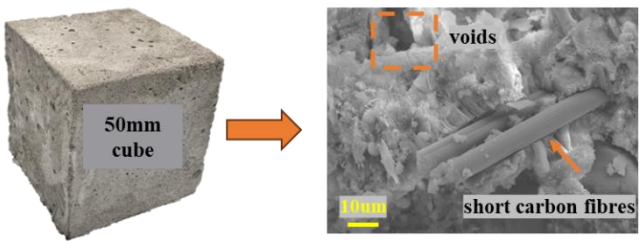

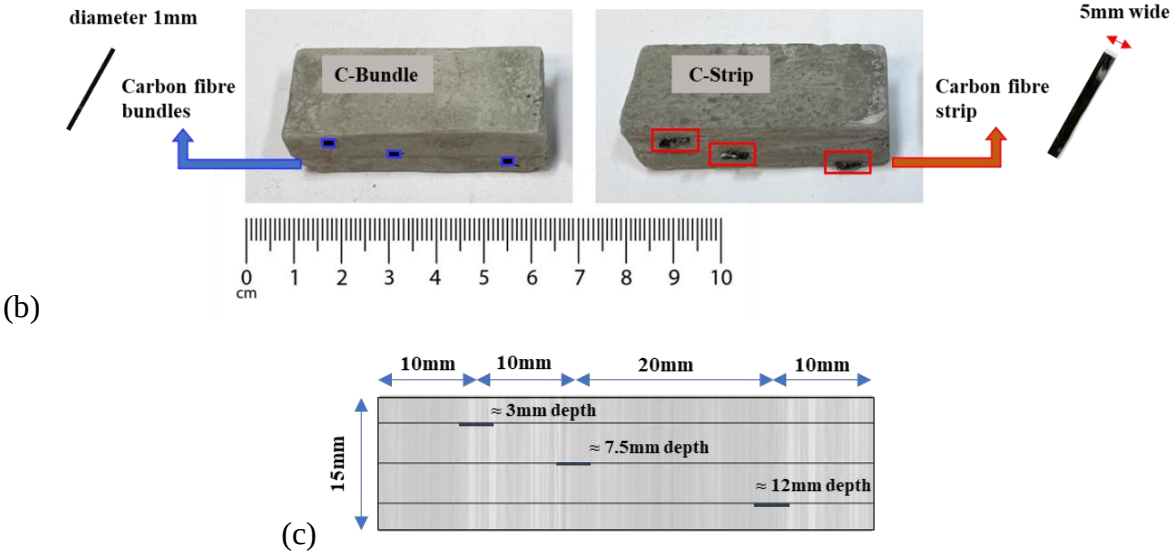

Figure 3-18. Samples for X-ray micro-CT analysis: (a) Cementitious composite reinforced with 1 vol.% short carbon fibres, (b) Carbon fibre bundles and strips embedded in the cementitious matrix, and (c) Schematic side view illustrating carbon fibres positioning.

3.3.3.2 Methodology

X-ray micro-CT scans were conducted using a Bruker Skyscan 2214 system at the Sydney Microscopy and Microanalysis Centre. The scanner, equipped with a 180 kV/15 W X-ray tube and a 12-bit Hamamatsu flat panel detector, provided high-resolution imaging capabilities. This section outlines the technical parameters of the X-ray micro-CT system, along with the detailed procedures for image acquisition, processing and our proposed Gaussian filtering.

Image acquisition

Samples were mounted on a custom holder, with particular emphasis on precise centring and alignment with the rotation axis. This exacting setup process was critical for achieving optimal spatial resolution, maximising magnification, and ensuring the highest possible accuracy in the reconstructed images. For the carbon-FRCC sample (Figure 3-18 (a)), scans were performed at 120 kV with a beam current of 100 µA, using a 1 mm copper filter. Each sample was scanned through a full 360° rotation with a 0.2° rotation angle per step. A 40 µm pixel resolution was adjusted to obtain the entire volumetric view. For smaller cementitious samples embedded with carbon fibres (Figure 3-18 (b)), scans were conducted at 120 kV with a beam current of 70 µA, utilising a 1 mm aluminium filter and a 0.075 mm copper filter. The scans progressed at 0.8° rotation per step until completing a full 360° rotation. A 27 µm pixel resolution was found to be the best fit for fibre feature detection, allowing the features to be visualised from the CT images. Bruker NRecon software was employed for 3D reconstruction,

generating a stack of greyscale images representing cross-sections along the vertical axis of the sample.

The following image processing and feature segmentation were programmed using MATLAB [123]. Two Gaussian filters were applied separately for different cases: an Isotropic Gaussian filter for void analysis on a 50×50×50 mm^3 carbon-FRCC sample and a proposed Anisotropic Gaussian filter tailored for carbon fibre characterisation on smaller mortar samples embedded with carbon fibre features. The detailed framework is elaborated in the following sections.

Isotropic Gaussian filter and void analysis

The images were loaded, and a 3D image stack was created by reading a series of images, which was then cropped to focus on the region of interest (ROI) with 1000×1100×800 voxels. The typical 3D Isotropic Gaussian filter was applied to smooth the image and improve the ratio of signal to noise, where it is defined as:

$$g(\mathbf{x};\sigma) = \frac{1}{(2\pi)^{\frac{3}{2}}\sigma^3}\exp\left(-\frac{1}{2\sigma^2}\boldsymbol{x}^{\boldsymbol{T}}\boldsymbol{x}\right) \quad 3\text{-}16$$

where x is the position vector (a spatial coordinate) in 3D space, and the Isotropic Gaussian filter is defined only by a single scale parameter, σ. The mean intensity of the cross-sectional image was used as a threshold to further smooth out the cementitious matrix regions, creating a binary image. Due to variations in pixel intensity and contrast, a local adaptive threshold algorithm using first-order statistics was applied to binarise the image and segment voids from the background. To address the issue of larger voids not being fully closed, a low global threshold was applied to separately identify large voids, which were then added to the binarised image from the local adaptive thresholding. This combination of local adaptive and global thresholds provided an effective segmentation for both large and small voids.

Proposed Anisotropic Gaussian filter and fibre characterisation

The image processing involved separating the sample from the background and distinguishing features within the sample. Otsu's threshold method segmented darker regions from lighter ones based on pixel intensity [124]. Misidentified pixels were corrected using morphological operations. Morphological operations, specifically closing (imclose) and erosion (imerode), were sequentially applied to the binary images: the closing operation filled small gaps and connected fragmented features, while the subsequent erosion removed small noise and refined feature boundaries while preserving the main feature. The images were then rotated to

align the vertical boundary in the y-direction. This background removal and alignment enabled more accurate measurement of carbon fibre positions and orientations.

A typical 3D Anisotropic Gaussian filter can be defined in Equation 3-17 by both scale parameters, σ, and elongation factor ϕ. The direction of the Anisotropic Gaussian filter is controlled by rotation matrix R [111]. The angles θ_x and θ_y were defined as the rotation applied around the x- and y-axis. When the origin filter direction is defined with θ_x and θ_y both to 0.0, the major axis extends along the z-axis with a factor of ϕ, while the x- and y-axes act as the symmetric minor axes of the filter. To better suit the carbon fibre detection scenario, this study proposes a novel 3D filter by summing the second derivatives of this typical Anisotropic Gaussian filter as defined in Equation 3-18. The new coordinate system with u, v, w represents the three major axes for the proposed anisotropic filter after rotation. This study defined σ as the number of pixels of estimated fibre radius r. The typical volumetric view of the primary segmentation can be visualised in Figure 3-19. The iso-surfaces are represented as ellipsoids elongated along the z-axis, with symmetric minor axes along the x- and y-axes. The image intensity plot reveals an annular region with negative values surrounding a central peak, which aids in contrast enhancement by emphasising the differences between regions of varying intensity. To eliminate minor noise distributed throughout the sample, the volume of each identified object was measured. Only the largest objects were retained as desired features, while the smaller ones were discarded. A comparison between different filtering methods is discussed in Section 3.3.4.2.

$$g(\mathbf{x};\sigma,\phi,\theta_x,\theta_y) = \frac{1}{(2\pi)^{\frac{3}{2}}\phi\sigma^3}\exp\left(-\frac{1}{2\sigma^2}\boldsymbol{x^T R^T}\begin{bmatrix}1 & 0 & 0\\ 0 & 1 & 0\\ 0 & 0 & \phi^{-2}\end{bmatrix}\boldsymbol{Rx}\right) \quad 3\text{-}17$$

where

$$\boldsymbol{R} = R_x(\theta_x)R_y(\theta_y), R_x(\theta_x) = \begin{bmatrix}1 & 0 & 0\\ 0 & cos\theta_x & -sin\theta_x\\ 0 & sin\theta_x & cos\theta_x\end{bmatrix}, R_y(\theta_y) = \begin{bmatrix}cos\theta_y & 0 & -sin\theta_y\\ 0 & 1 & 0\\ sin\theta_y & 0 & cos\theta_y\end{bmatrix}, \phi \geq 1$$

$$\hat{g}''(\mathbf{x};\sigma,\theta_x,\theta_y) = 2\sigma^2 \cdot \left(\frac{u_n^2+v_n^2}{\sigma^4} - \frac{2}{\sigma^2}\right)\cdot g(\mathbf{x};\sigma,\phi,\theta_x,\theta_y) \quad 3\text{-}18$$

where

$$\begin{bmatrix} u_n \\ v_n \\ w_n \end{bmatrix} = \boldsymbol{R}\mathbf{x}, \boldsymbol{R} = \begin{bmatrix} \cos\theta_y & 0 & sin\theta_y \\ sin\theta_x sin\theta_y & cos\theta_x & -sin\theta_x cos\theta_y \\ -cos\theta_x sin\theta_y & sin\theta_x & cos\theta_x cos\theta_y \end{bmatrix}$$

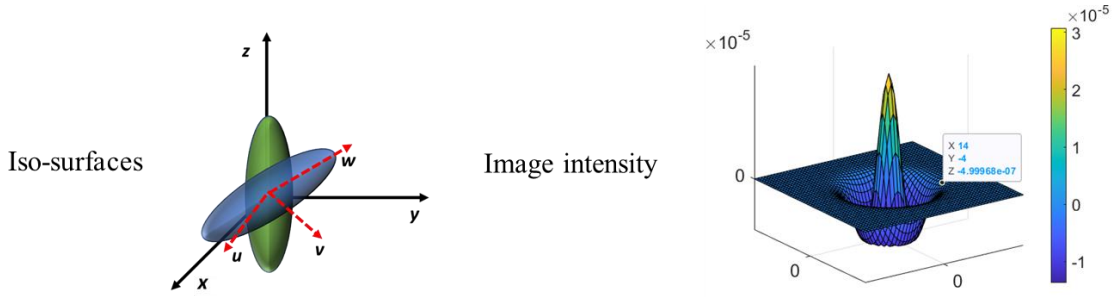

Figure 3-19. Iso-surfaces and the image intensity at the x-y plane for the proposed anisotropic kernel in this study (σ=4, ϕ=2).

3.3.4 Results and discussion

This section presents the results of applying the proposed Gaussian filter and image processing framework and the discussion and analysis of the outcomes. In Section 3.3.4.1, void analysis is performed after applying the Isotropic Gaussian Filter to the X-ray micro-CT image processing of the carbon-FRCC specimen. This is followed by the identification of the void system, including the analysis of volume percentage, size distribution, and eccentricity distribution. In Section 3.3.4.2, the accuracy of fibre segmentation using the proposed Anisotropic Gaussian Filter is evaluated through a confusion matrix and performance evaluation metrics and compared against other filtering methods. Subsequently, the validated method is employed for detecting and characterising multiple carbon fibre features within the two cementitious matrix specimens in Section 3.3.4.3.

3.3.4.1 Isotropic Gaussian filtering for void analysis in carbon-FRCC

Pore structures in cementitious materials can be classified into gel pores, capillary pores, and air voids [88-90, 95, 97]. Gel pores are tiny pores within the structure of calcium silicate hydrate (C-S-H) gel, typically measuring less than 10nm in size. Capillary pores are formed when there are residuals of water-filled spaces in the fresh cementitious paste after hardening and curing [88]. They are nano-scale and micro-scale pores with sizes up to 100μm [90]. Air voids are introduced due to incomplete compaction and are relatively large in size with more than 10μm [89]. Entrained air voids are smaller than 1,000μm, while entrapped air voids are

larger than 1,000μm [51]. As the resolution of X-ray micro-CT is limited by the size of the samples and the equipment, the features of capillary pores are commonly incorporated into the solid phase and cannot be distinguished [97, 125]. In this study, X-ray micro-CT primarily captured the small entrained and large entrapped air voids, allowing for the visualisation and quantitative analysis of the void system.

As shown in Figure 3-20, a 3D Gaussian filter is applied to smooth the image and reduce noise. To enhance the contrast and sharpness between the mortar matrix and the voids, the mean intensity of the cross-sectional image was applied as a threshold. This process further refined and smoothed the mortar matrix regions. The intensity and contrast of voids can fluctuate due to factors such as void size and the intensity of the surrounding mortar matrix. To account for these variations, a local adaptive thresholding algorithm utilising first-order statistics was applied. This algorithm adjusted the threshold based on local image characteristics, effectively separating the voids from the cement matrix. While the smaller voids were segmented accurately, the larger voids remained partially open at the centre. To resolve this, a lower global threshold was applied to isolate the larger voids. These voids were then integrated into the binarized image produced by local adaptive thresholding, achieving a more precise segmentation

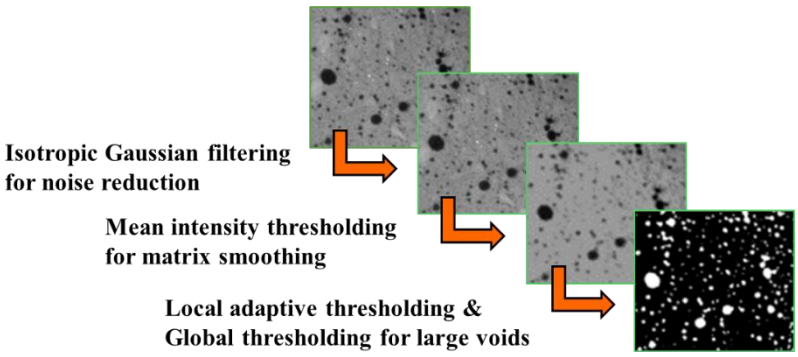

Figure 3-20. Workflow of the image processing steps used for void detection.

Table 3-5 presents the outcomes of the void analysis, with the visualisation of the void system shown in Figure 3-21 (a). A total of 45,040 voids were identified, with individual voids determined based on the three-dimensional connectivity of the voxels. A binary image stack was created to represent these filtered voids, with each voxel within a void set to 1. This binary image stack enabled the calculation of the void volume fraction by summing the binary values and dividing by the total number of voxels, thus providing a quantitative measure of the void content in the cementitious composite. In this carbon-FRCC specimen, 7.91% of the volume

consisted of voids, with 2.52% smaller voids less than 0.125 mm^3. Each void volume was identified, as shown in Figure 3-21 (b), which presents both the percentage of voids for each specific volume and the accumulated percentage. The rapid rise and plateau of both curves indicate the significant contribution of smaller voids, with around 50% of the voids being smaller than 0.417 mm^3. The average avoid volume was calculated as 0.099 mm^3. In addition, the void diameter distribution is captured in the bar chart in Figure 3-21 (c). Most voids have diameters between 0.3 to 0.6 mm, with a peak in the 0.4 to 0.5 mm bin. As the void diameter increases, the number of voids sharply decreases, indicating fewer large voids.

The shape of each void was estimated using its two principal axes, which describe its 3D geometry. The eccentricity of each void was calculated by taking the ratio of the length of the minor axis to the length of the major axis of the ellipsoid that best approximates the void, providing a measure of how elongated or circular the void is. A lower eccentricity (value close to 0.0) indicates a more spherical shape, while a higher eccentricity (value close to 1.0) suggests a more elongated shape. A bimodal distribution was observed in Figure 3-21 (d), indicating two peaks in the voids' eccentricity distribution. More round voids were found at the peak around 0.81 to 0.87, while elongated voids were found around 0.34 to 0.40, suggesting the impact of fibre inclusion on the void shape. It was observed that when a fibre bridged two nearby voids, it created a channel along its length, effectively linking the voids. As a result, the presence of fibres not only increases the number of voids but also elongates their shape. The porosity distribution and the presence of elongated voids both affect the performance of FRCC performance, as discussed by the authors in their previous study [101].

Table 3-5. Summary of void analysis.

Void percentage	Percentage of voids (< 0.125mm^3)	Average volume of voids
7.91 vol.%	2.52 vol.%	0.099 mm^3

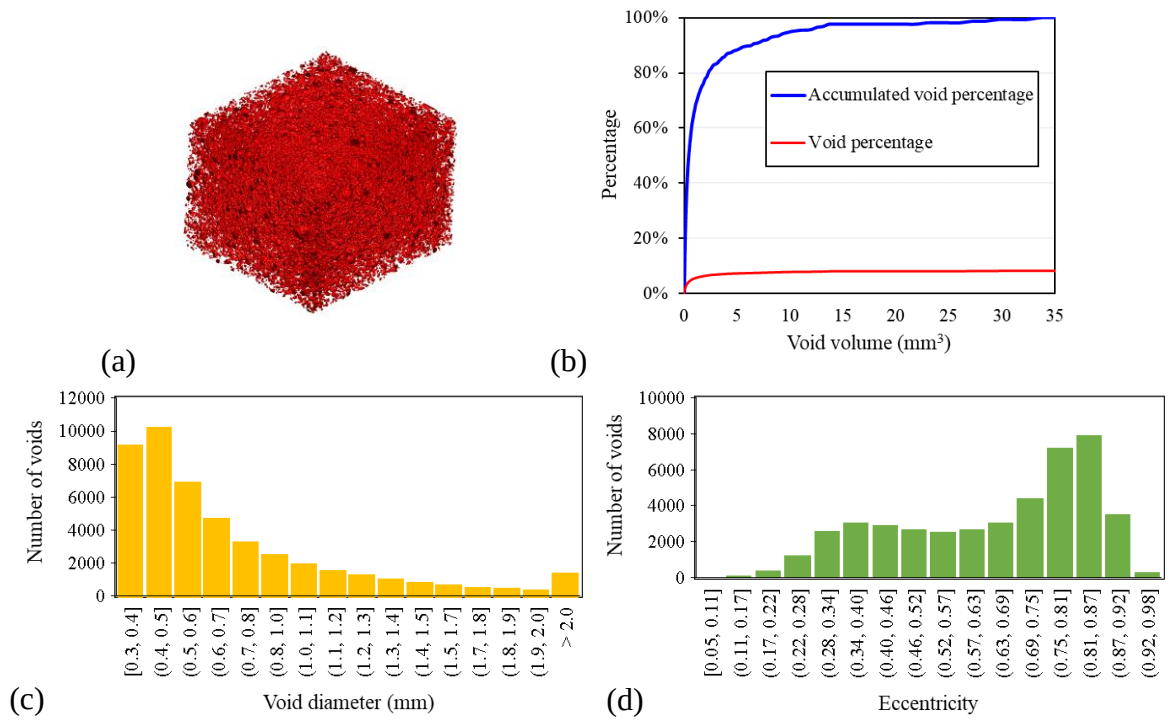

Figure 3-21. (a) 3D visualisation of the void system; (b) Void volume percentage; (c) and (d) Void diameter and eccentricity distribution.

3.3.4.2 Comparative analysis of carbon fibre segmentation using different filtering methods

As mentioned in Section 3.3.3.2, the proposed anisotropic Gaussian filtering was developed to enhance the detection and segmentation of carbon fibres within the cementitious matrix, based on its directional characteristics and improved detection accuracy. This section compares three different filtering methods: Direct Binarisation, Isotropic Gaussian and our proposed Anisotropic Gaussian tailored for detecting carbon fibre in the cementitious matrix. As shown in Figure 3-22 (a), X-ray micro-CT images were 8-bit images with pixel intensity values ranging from 0-255. In the Direct Binarisation method, an arbitrary greyscale threshold of 92 was found to be a reasonable criterion to binarise the images and perform the primary segmentation. In the Isotropic Gaussian method, a 3D Gaussian filter with single scale parameter σ, as defined in Equation 3-19 and shown in Figure 3-22 (b), was applied to smooth the image and mitigate the impact of noise on fibre segmentation. The scale parameter σ dictates the size of the filter, and in this context, σ is defined as the number of pixels of r but not exceeding 5. For example, the diameter of small fibre bundles was estimated in the scale of less than 100μm, and therefore the number of pixels for diameter is approximately 4 pixels (≈100/27) and σ was assigned as 2 for radius. In contrast, for large fibre bundles whose diameter was about 1000μm, σ was assigned as 5. In comparison to the Isotropic Gaussian filter, the

typical Anisotropic Gaussian filter in Figure 3-22 (c) incorporates an elongation factor ϕ, which enables the filter to elongate along a single major axis, thereby more closely matching the shape of carbon fibre. The parameters used in the proposed Anisotropic Gaussian filter are identical to those in the typical Anisotropic Gaussian filter, while the new filter generates an annulus of negative values in the x-y plane (refer to Figure 3-19), in contrast to the typical filter. This characteristic of the modified Anisotropic Gaussian filter results in a much sharper boundary between features and the matrix (Table 3-6). Following the individual application of these filters, a similar threshold binarisation procedure was employed to clean the noise from the images. The sharper boundary produced by the proposed Isotropic Gaussian filter facilitated easier separation through binarisation and enhanced the effectiveness of the noise-cleaning process.

$$g(\mathbf{x};\sigma) = \frac{1}{(2\pi)^{\frac{3}{2}}\sigma^3}\exp\left(-\frac{1}{2\sigma^2}\boldsymbol{x}^{\boldsymbol{T}}\boldsymbol{x}\right), with\ \sigma = \begin{cases} r & ,if\ \mathrm{r} \le 5 \\ 5 & ,otherwise \end{cases} \qquad 3\text{-}19$$

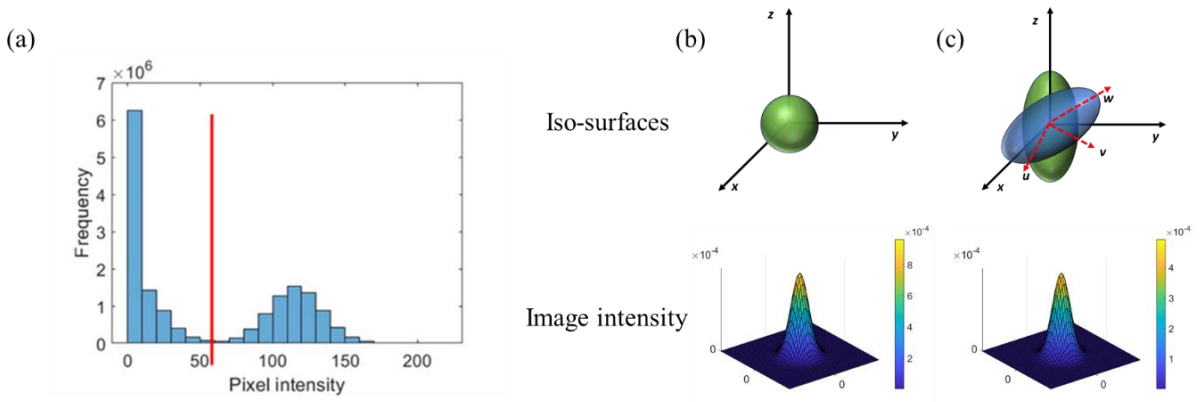

Figure 3-22. (a) Pixel intensity histogram in the Direct Binarisation; Iso-surfaces and the image intensity at x-y plane for: (b) Isotropic Gaussian kernel and (c) Anisotropic Gaussian kernel.

The segmentation accuracy of predictions using Direct Binarisation, Isotropic Gaussian, and the proposed Anisotropic Gaussian methods was analysed against the ground truth. The performance of these filtering methods was evaluated and compared using a confusion matrix and various evaluation metrics: sensitivity (precision and recall), accuracy index, dice coefficient (F1 score) and Jaccard index (UoI – union of intersection). The calculation of these elevation metrics is defined by the equations in Figure 3-23 (a). To illustrate their applicability to both carbon fibre bundles and strips, the segmentation accuracy was tested as given in Figure 3-23 (b) and (c). All three filtering methods exhibited relatively high accuracy in correctly detecting fibre voxels, ranging from 97.29% to 98.86%. Remarkably, the proposed Anisotropic

Gaussian method consistently outperformed both Direct Binarisation and Isotropic Gaussian methods. Specifically, our developed method demonstrated superior precision (87.70% for carbon fibre bundle and 92.90% for carbon fibre strip), dice coefficient (87.36% for carbon fibre bundle and 91.81% for carbon fibre strip), and Jaccard index (77.56% for carbon fibre bundle and 84.86% for carbon fibre strip). These results indicated more accurate detection of carbon fibres from noise and background, and a greater overlap between predictions and the ground truth.

The images of ground truth and processing results after applying different filters are presented in Table 3-6 and Table 3-7. The cropped volumes of interest (VOIs) for carbon fibre bundles and strips embedded in the cementitious matrix sample, measuring 548×176×86 pixels and 691×261×207 pixels respectively, were selected for representative analysis. These volumetric and cross-sectional images provide direct visualisation of the carbon fibre bundle and strip detection, supporting the findings of accuracy. Compared to Direct Binarisation, the Isotropic Gaussian method effectively reduced noise and smoothed feature edges. However, some inaccuracies in 3D segmentation and 2D cross-sectional views remained. The red circles in the column of the proposed Anisotropic Gaussian method (in both Table 3-6 and Table 3-7) show that this novel method was able to capture the entire structures of carbon fibres, including tipping ends and uneven edges, and could accurately predict the original shape. In addition, to illustrate the improvement in segmentation performance with the proposed method, comparative greyscale histograms for the large fibre bundle sample were plotted and analysed (Figure 3-23 (d)). The Otsu thresholding method was applied to cross-sectional images both before and after filter processing to determine the optimal threshold for distinguishing the feature from the background. As shown in Figure 3-23 (d), the unfiltered image exhibits background noise and poor feature distinction, evidenced by the overlapping pixel intensity distributions shown in red. Both isotropic and anisotropic methods can produce bimodal distributions; however, our proposed anisotropic method exhibits more pronounced peak separation. This is evident from the green distribution peaks, which display a greater distinction between the feature and background intensity ranges. The lack of clear intensity peak separation hinders effective segmentation, whereas the better results achieved in Table 3-6 in the row "Cross-section view after binary," demonstrate that the anisotropic filter is more reliable for determining an optimal threshold and enabling effective feature segmentation. Consequently, the proposed method better fits the fibre shapes within the cementitious matrix, improves the resistance to noise interference and increases accuracy compared to other filtering techniques.

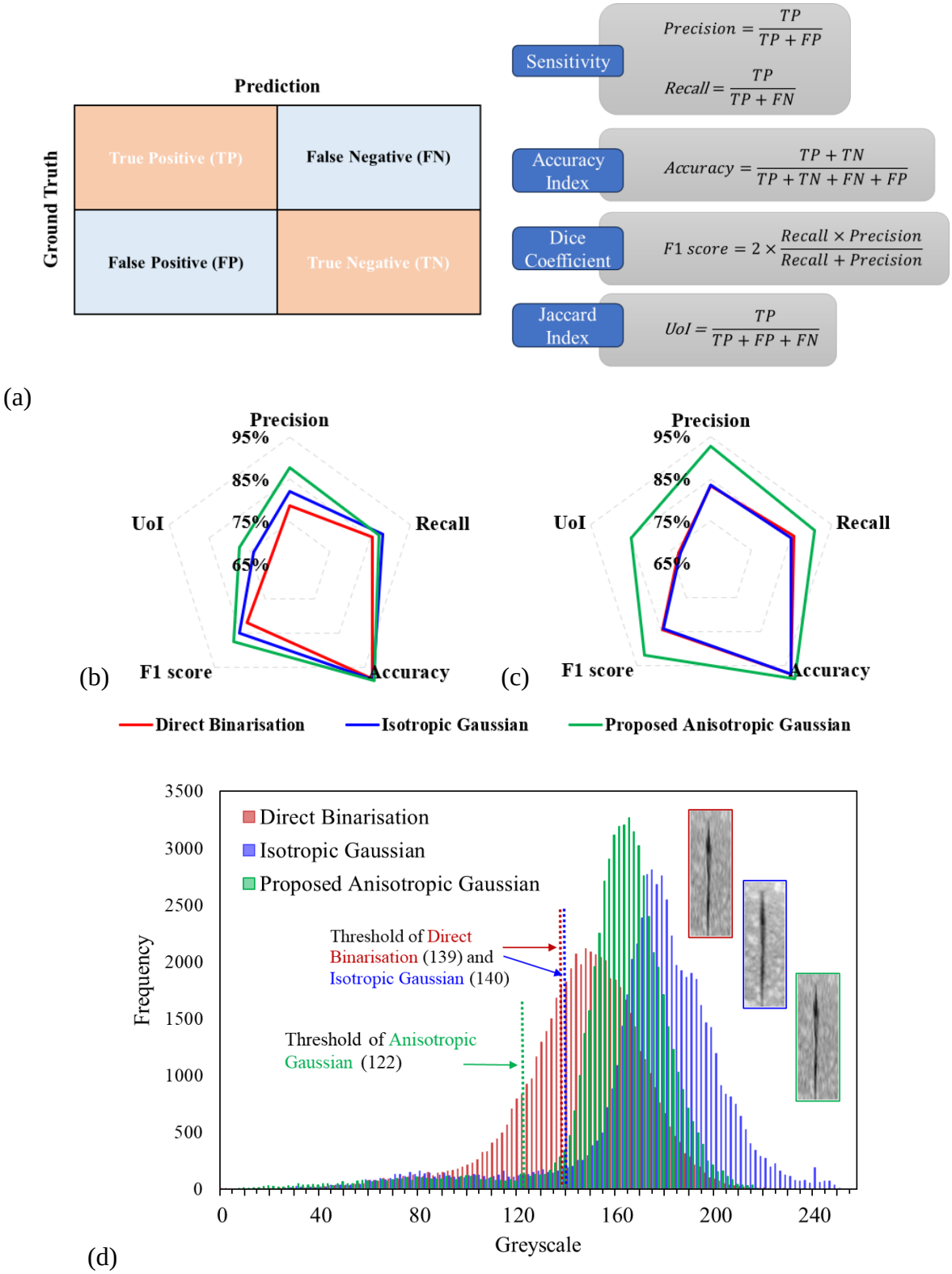

Figure 3-23. (a) Confusion matrix and performance evaluation metrics; Radar chart for comparison of different filter techniques on a cementitious matrix sample embedded with (b) carbon fibre bundle and (c) carbon fibre strip; and (d) greyscale frequency histogram of VOIs images.

Table 3-6. Volumetric and cross-sectional views of processing images after applying different filters (Carbon fibre bundles embedded in the cementitious matrix).

	Ground Truth	Direct Binarisation	Isotropic Gaussian	Proposed Anisotropic Gaussian
Cropped VOI: 548×176×86 pixels			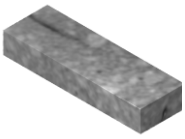	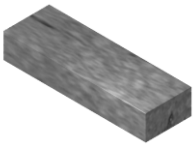
Segmentation	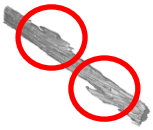	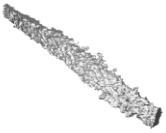		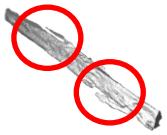
Cross-section view after filter processing				
Cross-section view after binary	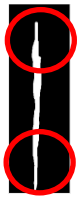			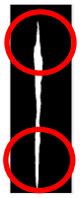

Table 3-7. Volumetric and cross-sectional views of processing images after applying different filters (Carbon fibre strips embedded in the cementitious matrix).

	Ground Truth	Direct Binarisation	Isotropic Gaussian	Proposed Anisotropic Gaussian
Cropped VOI: 691×261×207 pixels			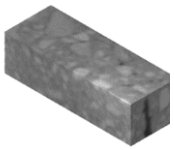	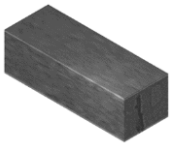
Segmentation	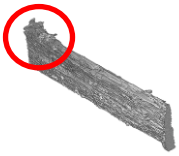	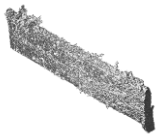		

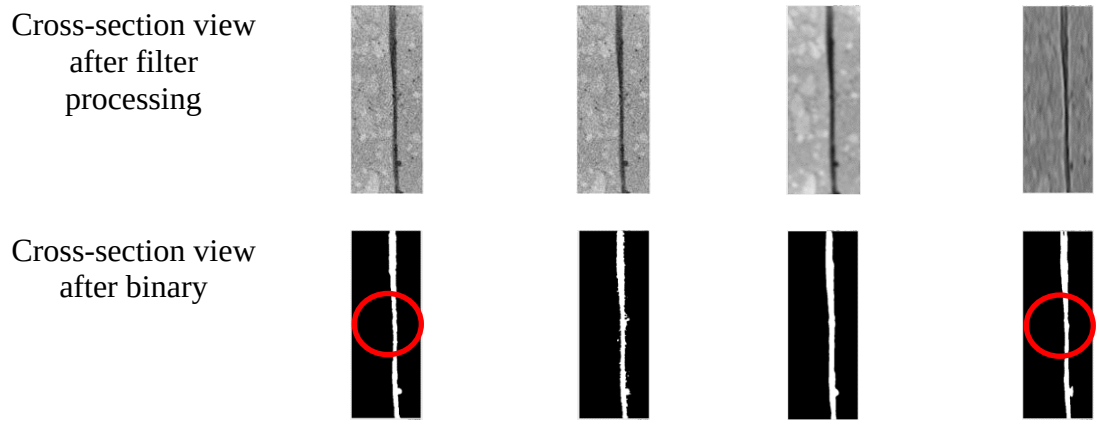

3.3.4.3 Application of the proposed Anisotropic Gaussian filtering for carbon fibre detection

After analysing the accuracy of the proposed processing filtering for X-ray micro-CT scanned images in Section 3.3.4.2, this section focuses on the practical application of the validated Isotropic Gaussian filtering method for detecting and characterising multiple carbon fibre features within the cementitious matrix. As shown in Figure 3-18 (b), both samples for X-ray micro-CT scans have three carbon fibre features, each with different depths to the top surface, arranged from left to right. The goal of image processing and analysis is to efficiently identify the orientation and spatial positions of these carbon fibre features within the cementitious matrix.

As noted in the image acquisition process, there is a trade-off between resolution and field of view when using X-ray micro-CT. In this study, a 27μm pixel resolution was identified as the most suitable for the smaller samples, allowing all relevant features to be clearly visible in the X-ray micro-CT images. However, due to the limited depth of view of approximately 15mm, each sample required two scans to capture all features. Figure 3-24 displays a section of one scan for both samples. Based on the carbon fibre feature segmentation using our proposed Anisotropic Gaussian filtering method, the characterisation was analysed from both 3D individual perspectives and cross-sectional views. XZ-plane cross-sectional views were utilised to visualise each feature, with the area counted by the white pixel count and the centroid position calculated as the centre of mass. This centroid provided information on the depth to the surface z and the position in the x-direction. In the y-direction, a series of centroids from XZ-plane cross-sections were calculated, representing the carbon fibre feature centrelines. Based on the centrelines, the interval space between these features could be determined. The carbon fibre bundles and strips might exhibit some degree of waviness due to the manual casting

and cement pouring process. Therefore, the total length of each feature was determined by summing the distances between adjacent centroids. Linear regression was applied to the series of centroid coordinates. The coefficients of the linear regression represented the orientation vector of each feature. Based on the orientation vector, the angle to z-direction θ_z and the angle of XY-plane projection to x-direction ϕ could be derived. As the carbon fibre direction was designed to be aligned in y-direction, both θ_z and ϕ should be around 90° (as shown in the sample design in Figure 3-18 (b)). The positioning and orientation of both carbon fibre bundles and strips within the cementitious matrix were individually examined and are summarised in Table 3-8. Both θ_z and ϕ fall within the range of 88° to 96°, within lengths around 20mm. The average depth to surface exhibited three designed positions. The X-ray micro-CT scans, combined with the proposed filtering method, offer a detailed visualisation of the internal features in cementitious material samples. The level of detail and accuracy is essential for reliable defect characterisation and analysis, enabling effective detection of the alignment and placement of these carbon fibre features.

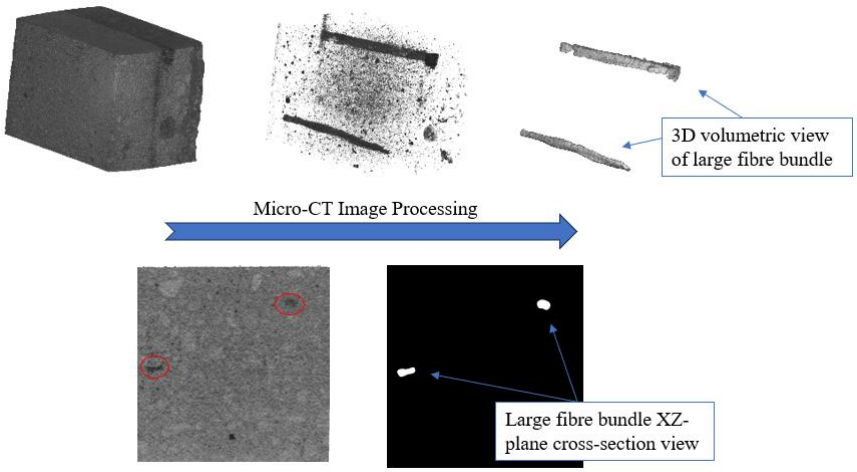

(a)

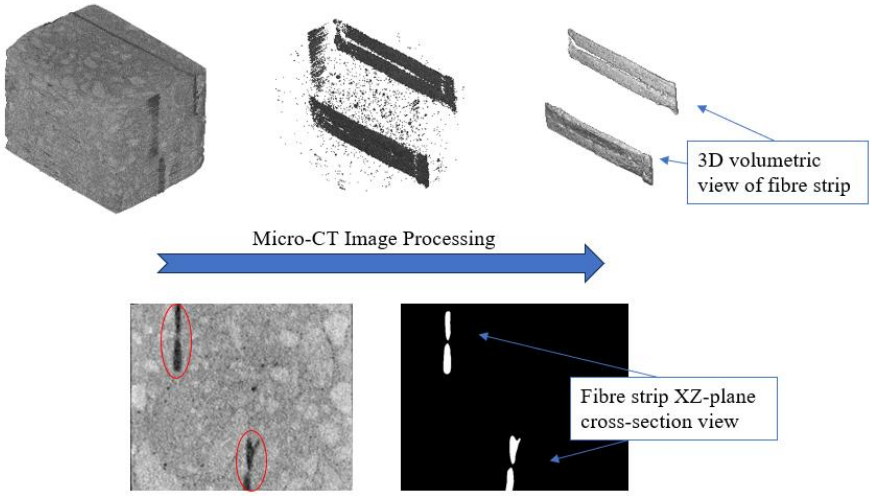

(b)

Figure 3-24. X-ray micro-CT scan volume reconstruction and carbon fibre bundles and strip detection.

Table 3-8. Artificial features spatial positioning and dimensions.

Carbon fibre features	Position	Angle to z-direction θz (°)	Angle of XY-plane projection to x-direction ϕ (°)	Length (mm)	Avg. depth to surface (mm)
Carbon fibre bundle	Left	92.143	91.622	19.57	2.755
	Middle	90.272	95.792	20.496	8.084
	Right	89.143	88.299	19.272	12.579
	Left	93.157	91.366	22.864	2.882

Carbon fibre strip	Middle	91.387	91.002	22.424	8.187
	Right	90.891	92.736	22.920	12.762

3.3.5 Summary of key findings from Section 3.3

This study proposed a novel 3D second-order anisotropic Gaussian filter designed to enhance the detection of carbon fibres in cementitious materials in low-contrast and noisy X-ray micro-CT images. This was achieved by summing the second derivatives of the standard anisotropic Gaussian filter to better capture changes in intensity, tailored for more precise and sharp boundaries between carbon fibres in the cementitious matrix. A comparative analysis was conducted to evaluate the impact of different filtering methods on carbon fibre segmentation in image processing. The results showed that the developed anisotropic Gaussian filtering method significantly improved the accuracy of carbon fibre detection by effectively minimising noise and background interference. There was also a greater alignment between the processed results and the ground truth, indicating enhanced precision in segmenting the carbon fibres.

To evaluate the efficiency in real-world scenarios, samples of various scales were prepared, and two different 3D second-order Gaussian kernels were applied in the X-ray micro-CT analysis, including the proposed method. Based on the nature of the features to be detected, isotropic Gaussian filtering was used for the characterisation of void geometry and analysis of void distribution in a carbon-FRCC specimen. Meanwhile, the developed anisotropic Gaussian filtering was used to detect the orientation, length, and spatial location of carbon fibre bundles and strips within the cementitious matrix specimens. The advancements in image processing not only expanded the applicability and feasibility of using X-ray micro-CT with the proposed filters to derive features in carbon FRCC, but also significantly improved the accurate segmentation of both voids and carbon fibres within the cementitious composites.

The findings confirm that the X-ray micro-CT technique is an invaluable tool for examining the internal microstructure of FRCC. Critical parameters such as fibre reinforcement and voids play a significant role in determining the integrity, performance, and durability of FRCC, underscoring the necessity for precise internal analysis. Future research will further investigate the detection of discrete carbon fibre features, particularly within larger structural elements, to further enhance the application of these techniques in such materials.

3.4 MULTI-SCALE DETECTION OF CARBON FIBRE AND VOID IN CEMENTITIOUS MATERIALS USING GAUSSIAN-ENHANCED MICRO-CT ANALYSIS AND ULTRASONIC IMAGING WITH A TOTAL FOCUSING METHOD

Y. Tao[1,*,†], Z. Wang[1,†], S.A. Hadigheh[1,*] Z. Zhou[2], J. Rao[2]

[1] School of Civil Engineering, Faculty of Engineering, The University of Sydney, Sydney, New South Wales 2006, Australia

[2] School of Instrumentation and Opto-Electronic Engineering, Beihang University, Beijing 100191, China

*Corresponding Author: Dr Ali Hadigheh

Yunyun Tao

†These authors contributed equally (first authors) to this work

3.4.1 Abstract

The integration of carbon fibres (CFs) into cementitious materials has found wide applications in the construction field. The quality of fibre-reinforced cementitious composites (FRCCs) and their internal structure are essential for durability and safety. Non-destructive testing (NDT) like X-ray microtomography (micro-CT) is used to assess concrete defects and microstructures but faces challenges in accurately evaluating the spatial position of CFs in the cement-based matrix due to noise and segmentation limitations. Ultrasonic phased array testing shows promise for defect detection, yet its application for CFs in cementitious materials remains underexplored. In response to these challenges, this study developed and applied Gaussian filters to process micro-CT images, and in parallel, employs the ultrasonic total focusing method (TFM) as an efficient technique for detecting CF and void in a cementitious matrix. Multi-scale features, including CFs and voids ranging from micrometres to millimetres, were examined. Micro-CT analysis provided high-resolution spatial visualisation and captured comprehensive details of the features within the specimens, while 1D ultrasonic phased array testing with the TFM method was able to detect the feature depth. The deviation of the post-processed TFM image compared to micro-CT analysis demonstrated its high accuracy for CF features located deeper within the matrix. The best performance was observed with a 3.26% error for the CF bundle and a 0% error for the CF strip. The void features located at mid-depth achieved more reliable detection. This study advances the understanding and expands the

practical application of NDT for FRCC characterisation, demonstrating enhanced feasibility for future industrial implementation.

Keywords: Fibre-reinforced cementitious composite; Non-destructive testing; X-ray microtomography; Spatial positioning; Ultrasonic phased array; Total focusing method

3.4.2 Introduction

Fibre-reinforced cementitious composites (FRCC) are increasingly used in construction applications, which have advantages over conventional materials in terms of their enhanced flexural properties, higher fracture toughness, improved shrinkage control as well as favourable electrical properties [23, 40, 126, 127]. The performance of these composites is recognised to be primarily dependent on the interfacial bonding properties between the fibrous reinforcement and cementitious matrix, as it establishes an effective load-transfer system and limits crack propagation through the fibre-bridging effects [82, 128-130]. In recent years, FRCC has been extensively found in various structures, such as bridges [131], pavements [132, 133], hydraulic structures [134], tunnels [135, 136] and railway sleepers [137]. In addition, as a functional filler in cementitious materials, CF is adopted for structural health monitoring (SHM), demonstrating its versatility in integrating smart technologies into building and infrastructure projects [24, 138]. FRCC applications have grown rapidly in recent years and are projected to reach a market value of $4 billion by 2030, with an increasing growth rate of 6.8% [139]. As the demand for fibre-reinforced mortar and concrete with enhanced material and structural performance continues to rise, it is essential to consider key parameters influencing their quality, including fibre length, fibre spatial distribution, and porosity. The characterisation of fibre reinforcement and voids is important as the strength and durability of FRCC is highly related to the distribution and alignment of fibres, as well as the presence of voids within the cement matrix [127, 140].

To evaluate the integrity and condition of FRCC without causing additional damage, non-destructive testing (NDT) methods such as X-ray radiography [109, 140, 141], computed tomography (CT) [109, 141, 142], ultrasound testing (UT) [141, 143, 144], and electrical resistivity measurements [145, 146] have been employed. These techniques provide detailed insights into the material quality, especially the porosity system, as well as the dispersion and orientation of fibres or additives. X-ray CT and Micro-computed tomography (micro-CT), combined with image analysis, enable detailed 3D assessments of voids and fibres within cementitious materials, providing precise measurements of their spatial distribution,

orientation, dimensions and shapes [127, 147]. Gao et al. [109] highlighted the importance of optimised grayscale thresholds and X-ray CT image processing for accurately distinguishing between CFs and pores. By setting thresholds based on grayscale peaks and supplementary scanning electron microscope (SEM) validation, they improved the ability to differentiate CF bundles, uniformly dispersed areas, and sub-millimetre voids in the cement-based matrix, which often overlap in density. Gao et al. [98] also demonstrated CT imaging and 3D reconstruction as effective tools for quantifying CF distribution and volume fractions, correlating these parameters with the mechanical and electrical properties of FRCC. Lauff et al. [148] successfully examined CF alignment in a 3D printed specimen with a cross-sectional area of 3.1×2.2 mm using X-ray CT analysis and various filters. Their findings indicated that 68% of the CFs were oriented in the desired direction, significantly improving both the composite's tensile and flexural strength. Moreover, Patchen et al. [149] used high-resolution micro-CT analysis on a larger sample (18 mm in diameter and 25 mm in length) to obtain information on spatial pore size distribution and potential CF clumping. However, while large CF bundles were detectable, individual CFs remained indistinguishable due to similar grayscale values between the CFs and cementitious matrix as well as insufficient resolution. Additionally, reducing computational cost while improving precision remains a critical requirement.

While micro-CT provides high-resolution imaging and detailed analysis of internal features within composites, UT testing proves to be a feasible and reliable technique for the characterisation and quality assessment of cementitious materials, with applications in both in-situ evaluations and laboratory research [144, 150]. The ultrasonic pulse velocity (UPV) method has been the most commonly used non-destructive onsite testing method since the early 1940s, primarily due to its affordability, simplicity, and efficacy [151]. This method capitalises on the characteristics of ultrasonic wave propagation to assess the concrete's overall conditions and detect major defects based on the velocity of the ultrasonic waves. Due to the heterogeneous nature of concrete, low-frequency transducers with frequency ranges of 25 to 250 kHz are often used to detect cracks and aggregate sizes and to inspect the integrity of concrete structures [152, 153]. However, this method poses challenges due to the excessive attenuation observed in concrete and the UPV results should be complemented with other tests for a comprehensive evaluation of structures [154]. While this method can be used to examine the concrete strength, its accuracy is limited within a range of 20% [155].

Ultrasonic phased array testing is one of the most widely used NDT methods, which is used in aerospace, petrochemical, and civil industries [156-161]. It offers a dependable solution

for accurately sizing defects in different materials [162-165]. The methodology involves a series of steps [166]. Initially, full matrix capture (FMC) is executed, wherein each transducer in the array sequentially transmits a signal, with the response measured by all transducers. This process results in a comprehensive set of signals corresponding to every possible transmit-receive combination, effectively capturing the entire scattering problem's data. This dataset enables the execution of various imaging algorithms in the post-processing stage to detect the inspection area. Among these, the total focusing method (TFM) is notably prevalent [167]. TFM operates by directing a focused sound beam to each point within the region of interest and analysing the reflections from these points. This method has been applied widely to fibre-reinforced polymer (FRP) materials, where the complex composite structure requires precise imaging for defect detection and characterisation [168, 169]. For example, Yu et al. [170] proposed an adaptive ultrasonic imaging method for arbitrarily anisotropic carbon fibre reinforced polymer (CFRP) laminates through FMC and TFM, which derived elastic constants and corrected for anisotropic effects to accurately reconstruct internal defects in CFRP laminates with arbitrary stacking sequences. Tian et al. [171] developed a high-quality ultrasonic TFM imaging method for detecting defects in cross-ply CFRP used in aerospace structures. The optimised parameters for TFM imaging were identified by the properties of propagating and non-propagating waves calculated using the Floquet wave homogenisation theory. However, the application of employing TFM to detect CFs in cementitious materials is not yet widespread.

Despite the abovementioned advancements made in the previous studies utilising X-ray CT and UT methods for assessing cementitious materials and polymer composites, several research gaps remain unaddressed. In the case of CT methods, a notable challenge arises from the high noise levels and low-contrast images of CF within the cementitious matrix, where overlapping phases result in similar grey values. Further optimisation of CT image processing techniques is essential to enhance the accuracy and efficiency of characterising CFs in the cementitious matrix. For UT methods, the heterogeneous nature of cement-based materials causes excessive attenuation of ultrasonic waves, limiting detection reliability. Although TFM is an advanced technique proven effective for FRP composites, its capability for carbon-FRCC remains underexplored. This leaves room for further investigation on the detection capacity and precision of processed UA imaging in FRCC applications. Addressing these limitations through targeted research is essential for enhancing the precision and applicability of NDT methods in evaluating the internal structures of carbon-FRCC.

3.4.3 Research significance

With the expanding implementation of FRCCs in modern construction, there is a need to investigate their internal structure, including key characteristics such as fibre distribution, orientation and porosity, which govern the quality and performance of these materials. NDT methods have been adopted as non-invasive and effective techniques for internal assessment of cementitious materials while maintaining structural integrity. However, such micro-CT and UA imaging techniques encounter difficulties in accurately differentiating CFs and defects from cement-based matrices.

To address the issues, firstly, this study utilised a newly developed Gaussian filtering method for fibre segmentation in micro-CT analysis. This novel anisotropic Gaussian filtering method has been proposed, and high accuracy was achieved in the previous study [172]. This method enables the precise characterisation of CF bundle features at the microscopic scale, overcoming conventional difficulties caused by overlapping densities. Building on the previous work, this study further investigates the application and feasibility of the proposed method by testing features spanning multiple scales. The experimental preparation included customised cement-based specimens with artificial features embedded for the NDT testing. The investigated features included small CF bundles (diameter < 100 μm), large CF bundles (diameter ≈ 1 mm), CF strips (≈ 5 mm wide), and void channels (diameters ≈ 1 mm and 1.8 mm). Recognising the field application limitations and high costs associated with micro-CT, this study also explores the potential of the ultrasonic TFM technique. TFM is a fast 2D detection method that can be used to verify the location and shape of some defects. However, its application in identifying CF features within high-attenuation cementitious matrices is yet to be fully recognised. The post-processed TFM imaging results were then validated against advanced micro-CT analysis, and cross-comparison between these complementary techniques demonstrated the reliability of FRCC characterisation.

3.4.4 Materials and methodologies

3.4.4.1 Materials and specimen preparation

Cement-based specimens with artificial features (CFs or voids) were prepared for the NDT inspection. The specimens were prepared using general-purpose cement (type GP) as specified in Australian Standard AS3972 [44] with a cement-to-water ratio of 0.55 (refer to Table 3-10 for cement properties). T300 CFs (with a single fibre diameter of 8μm) with different configurations including small and large fibre bundles and 5mm fibre strips were

incorporated in the cement-based matrix. Additionally, two distinct void channels of varying sizes were created as the second type of artificial feature for evaluation. A 3D-printed assembled mould was designed for positioning these artificial features and subsequent cement pouring. The dimension of each cement-based specimen was 20mm×50mm×15mm. The features were placed at three varying depths from the top surface of the specimens, with intervals of 10mm or 20mm. Specifically, the depths were set at around 3mm (upper position), 7.5mm (middle position) and 12mm (bottom position). This deliberate placement allowed for the subsequent assessments of features at different locations within the specimens and avoided any potential interference between individual features during the inspection process.

The artificial features are summarised in Table 3-10. These features varied in type and size and were used to evaluate the capabilities and limitations of the detection methods developed in this project. An illustrative specimen (Sample C) is provided in Figure 3-25.

Table 3-9. Properties of GP cement.

Chemical entity		Physical and chemical properties	
Portland Clinker	<97%	Appearance	A fine powder ranging in colour from grey to off-white
Gypsum ($CaSO_4.2H_2O$)	2-5%	Boiling/Melting Point	Melting point >1200°C
Limestone ($CaCO_3$)	0-7.5%	Specific Gravity	3.0 – 3.2
Calcium Oxide	0-1%	Solubility in Water	Slight, reacts on mixing with water forming an alkaline (caustic) solution (pH >11)

Table 3-10. Artificial feature design.

Sample ID	Feature type	Configuration
A	CF	small fibre bundle (diameter < 100 μm)
B	CF	large fibre bundle (diameter ≈ 1 mm)
C	CF	fabric strip (≈ 5mm wide)
D	void	small void channel (diameters ≈ 1 mm)
E	void	large void channel (diameters ≈ 1.8 mm)

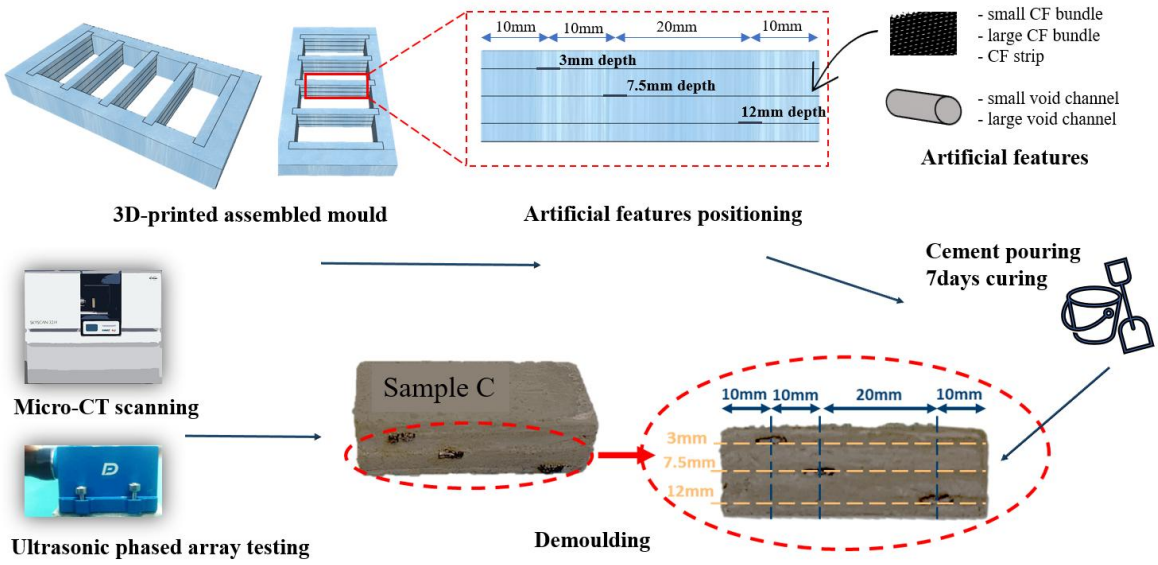

Figure 3-25. Schematic illustration of the experimental preparation process and the placement of artificial features.

3.4.4.2 Micro-CT testing

Image acquisition

A 3D schematic drawing with three features at varying depths was constructed, as shown in Figure 3-26 (a). The "upper", "middle" and "bottom" features were identified in order from top to bottom, and the coordinate system was defined where the y-axis represented the fibre direction, the x-axis represented the length of the sample and the z-axis measures the depth of each feature to the surface (Figure 3-26 (b)). Micro-CT was used to visualise and characterise the CF and void features within cementitious material from a 3D perspective. To extract useful information from micro-CT images, an image processing framework was developed to segment the CF and voids from the cement matrix and derive the characterisations, such as location, distribution and cross-sectional morphology.

Micro-CT scans were acquired by the Bruker Skyscan 2214 micro-CT scanner at the Sydney Microscopy and Microanalysis (SMM) Centre, the University of Sydney. The samples were vertically placed on the micro-CT scanner stage, as shown in Figure 3-26 (d). There is a trade-off between resolution and field of view when using micro-CT. In this study, 27µm pixel resolution was found to be the best fit for most of the samples (Sample A-D). Under this resolution, all the features could be visualised from micro-CT images. However, as shown in the schematic drawing below (Figure 3-26 (c)), each sample requires two scans to include all the features because the depth of view was only about 15mm. For sample E, 40µm pixel

resolution was adjusted to obtain the entire volumetric view of the sample, which allows the analysis of the relative location between the three voids. To facilitate the segmentation and make the analyses more comparable within this study, the other parameters and settings for the micro-CT scanner and reconstruction were the same for Samples A-D. The scans were taken at 120 kV with a beam current of 70µA with 1mm aluminium filter and 0.075mm copper filter and progressed at 0.8° rotation per step until the full 360° rotation with an average of 3 frames per position. Bruker NRecon software [173] for 3D reconstruction was used to reconstruct and create a stack of greyscale images from the yz-cross-sectional view. The micro-CT image processing framework, which was designed for detecting various features, is separated into multiple steps, as illustrated in the workflow (Figure 3-27).

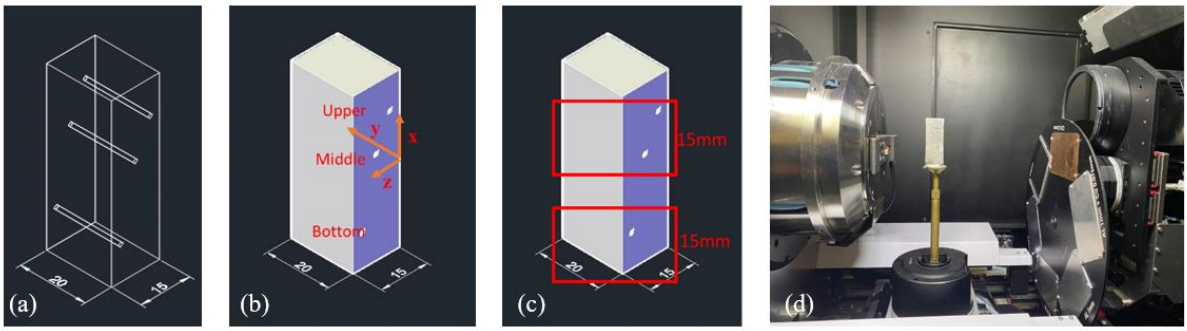

Figure 3-26. (a) Schematic drawing for the sample in the vertical position; (b) feature labels and coordinate system definition; (c) schematic drawing for micro-CT scanning under 27µm resolution; (d) images taken for the sample in Bruker Skyscan 2214 scanner.

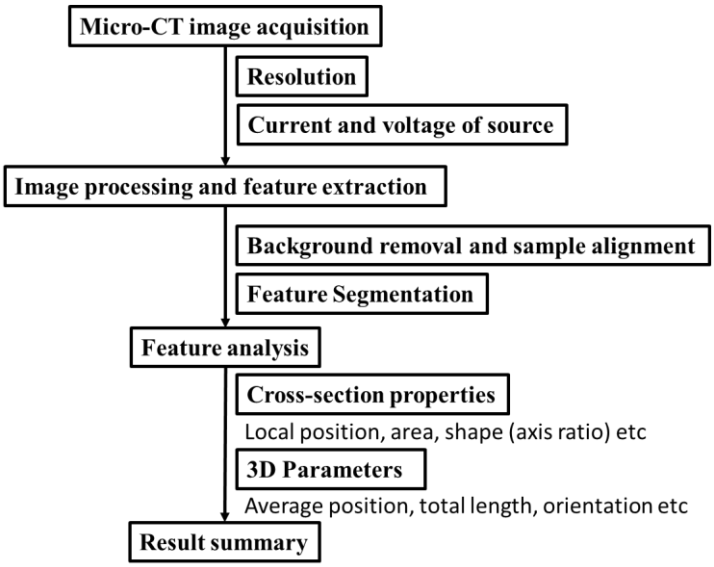

Figure 3-27. Workflow for micro-CT image analysis designed for detecting features.

Image processing and feature extraction

Figure 3-28 (a) and (b) show typical cross-sectional views of CF and voids, respectively. As both CF and air have lower X-ray attenuation than the cement matrix, they appear darker, and their pixel intensity is smaller than that of the cement matrix [92, 109, 174]. In this study, the CF and artificial voids exist throughout the entire sample in the y-direction. Thus, from the YZ-plane cross-section, the features appear as tabular shapes passing through the entire sample. The processing framework was developed in MATLAB [123] and contained two main steps: segmentation and characterisation analyses. In this section, the large fibre bundle sample (Sample B) was taken as an example to demonstrate the workflow of the developed framework.

The image processing includes the segmentation of the sample from the background and the segmentation of features from the sample. Otsu's threshold selection method was used to initially segment the darker regions from the lighter regions based on the pixel intensity distribution of the entire image stack, as shown in Figure 3-28 (c) [124]. The pixels with intensity smaller than the threshold were set to 0.0 as black and those above the threshold were set to 1.0 as white as shown in Figure 3-28 (d). However, some pixels of the features within the sample were misidentified, necessitating morphological operations (Figure 3-28 (e)). The sample was then rotated to align the vertical boundary in the cross-sectional images with the y-direction, ensuring the entire sample was vertically aligned, as shown in Figure 3-28 (f). The background removal and the sample alignment to the defined coordinate system allow for a more accurate measurement of the position and orientation of various features.

After background removal, the volumetric view of the sample can be clearly visualised, as shown in Figure 3-29 (a). A traditional isotropic filter was used for void features, while a new 3D anisotropic filter has been proposed to smooth images and reduce noise impact on fibrous feature segmentation. This method is specifically designed for detecting elongated fibre structures in a cementitious matrix. The filter is based on summing the second derivatives of the typical anisotropic Gaussian filter, as shown in Equation 3-20.

$$\hat{g}''(\mathbf{x};\sigma,\theta_x,\theta_y) = 2\sigma^2 \cdot \left(\frac{u_n^2+v_n^2}{\sigma^4} - \frac{2}{\sigma^2}\right) \cdot g(\mathbf{x};\sigma,\phi,\theta_x,\theta_y) \qquad 3\text{-}20$$

where

$$\begin{bmatrix} u_n \\ v_n \\ w_n \end{bmatrix} = \boldsymbol{R}\mathbf{x}, \boldsymbol{R} = \begin{bmatrix} \cos\theta_y & 0 & sin\theta_y \\ sin\theta_x sin\theta_y & cos\theta_x & -sin\theta_x cos\theta_y \\ -cos\theta_x sin\theta_y & sin\theta_x & cos\theta_x cos\theta_y \end{bmatrix}$$

where $\hat{g}''$ represents a second derivative of the function. σ is the scale parameter and ϕ is the elongation factor. The direction of the filter is controlled by the rotation matrix R. θ_x and θ_y denote the rotation to the x- and y-axis, respectively. The new coordinate system with u, v, and w represents the three major axes for the proposed anisotropic filter after rotation.

An arbitrary greyscale threshold of 92 was found to be a reasonable criterion to binarise the images and perform the primary segmentation. The volumetric view of the primary segmentation can be visualised in Figure 3-29 (b). Even though the two major features could be visualised, there was still a lot of small noise spreading across the entire sample. To remove the noise, the volume of each identified object was counted. As shown in Figure 3-29 (c), only the largest ones were reserved as desired features while the other small ones were removed. This approach could enhance CF detection in the cementitious matrix, enabling precise 3D localisation and definition of features. A more detailed demonstration of the development and verification of the new anisotropic Gaussian filter was reported in the study before [172].

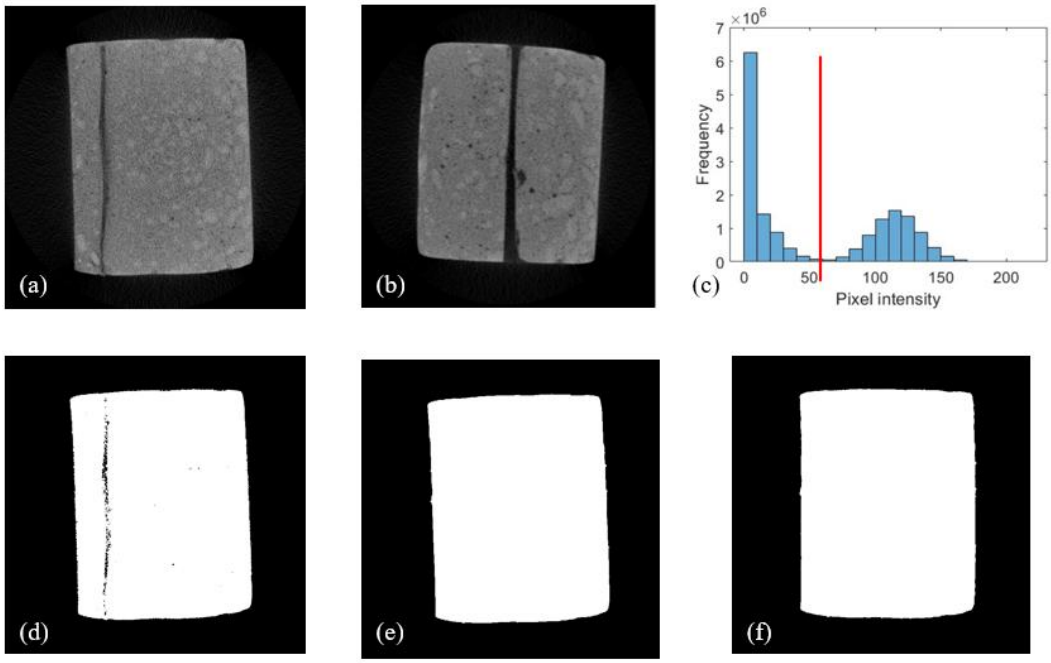

Figure 3-28. a YZ-plane cross-sectional image of (a) large fibre bundle sample (Sample B) and (b) small void sample (Sample D); (c) pixel intensity histogram for the entire large fibre bundle sample; binarised image (d) based on Otsu's method, (e) after morphological operation, and (f) after sample orientation alignment.

Feature analysis

Following the image process and segmentation, feature analysis could be performed from both 2D cross-sectional and 3D volumetric perspectives. The XZ-plane cross-sectional views could visualise the cross-sections of each feature, as shown in Figure 3-29 (e). For each XZ-

plane cross-section of each feature, the area was counted by the number of white pixels, and the position of the centroid was calculated as the centre of mass (Figure 3-29 (d)). As labelled in Figure 3-29 (f), the centroid provides information on the depth to the surface z and x-direction position. The difference between the x-direction positions of two features measures the spacing between them. An ellipse that has the same normalised second central moments as the feature cross-section was fitted around the cross-section as shown in Figure 3-29 (g). The minor and major axes of this ellipse represent the dimensions of feature cross-sections. The ratio of the lengths of these two axes indicates the shape of the cross-section (Equation 3-20). An axis ratio close to 1.0 means a rounder shape, while an axis ratio close to 0.0 means a flatter shape. Along the y-direction, a series of centroids of XZ-plane cross-sections were calculated and could consist of the feature centrelines, as shown in Figure 3-29 (d). The features might represent some degree of waviness. Thus, the total length of each feature was calculated as the sum of the distances of adjacent centroids. As most of the features are designed to be straight in this study, linear regression was fitted to the series of centroid coordinates. The coefficients of the linear regression consist of the orientation vector of each feature. Based on the orientation vector, the angle to z-direction (θ_z) and the angle of XY-plane projection to x-direction (ϕ) could be derived as shown in Figure 3-29 (h). The feature direction was designed to be aligned in the y-direction, both θ_z and ϕ should be around 90°.

$$Axis\ ratio = \frac{length\ of\ minor\ axis}{length\ of\ major\ axis} \qquad 3\text{-}20$$

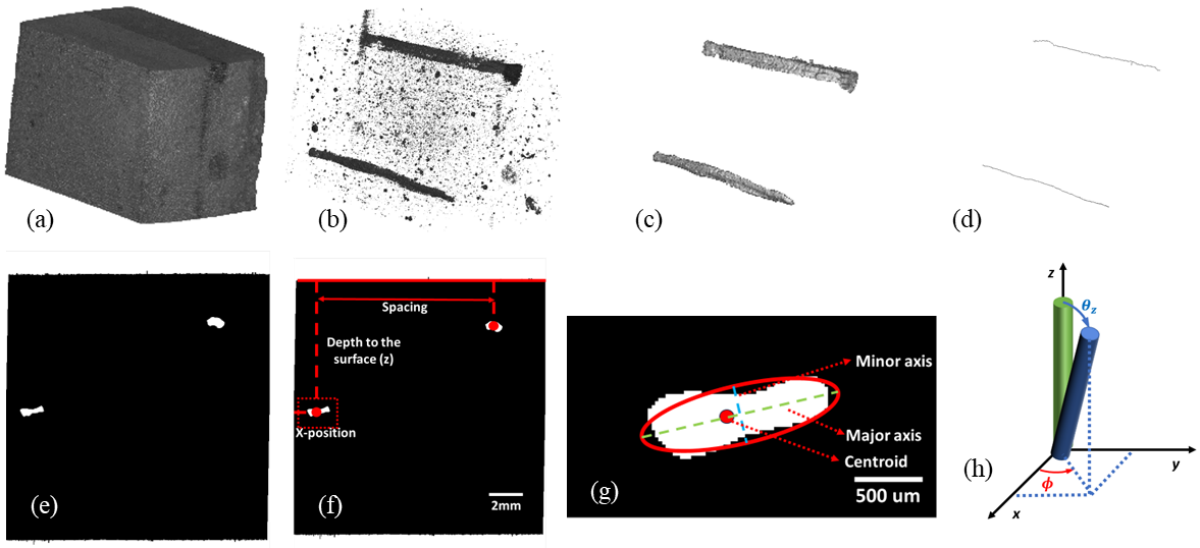

Figure 3-29. (a) 3D volume view and a typical YZ-plane cross-sectional view after background removal; (b) 3D volumetric view after binarisation and YZ-plane cross-sectional views after Gaussian blurring and threshold binarisation; (c) 3D volumetric view of the two

desired features and its typical YZ-plane cross-sectional view; (d) the centreline extracted for each feature; (e) a typical XZ-plane cross-section view; (f)-(h) labels for various measurement.

3.4.4.3 Ultrasonic testing

Post-processing method

TFM is one of the most frequently used post-processing methods in detecting defects. This method begins by dividing a spatial area in front of the array into a grid. The size of this grid is determined by the longest duration in the individual A-scans. Following this, the beam is concentrated at each point within this grid, enabling the creation of a completely focused image [175]. When x is the directional axis along the phased array and z is the vertical direction into the specimen, the intensity of the image at any given coordinate (x, z) can be expressed as I (x, z) and is determined as follows [175]:

$$I(x, z) = \left|\sum_{t=1}^{N}\sum_{r=1}^{N} h\left(t, r, \frac{d_1+d_2}{c_l}\right)\right| \quad 3\text{-}21$$

where N is the total number of elements and c_l is the velocity of the longitudinal wave in the test object. t and r represent the transmitting and receiving elements, respectively. $d_1$is the distance from the transmitting element to the focus point, and d_2 is the distance from the receiving element to the focus point, as depicted in Figure 3-30. h (t, r, $\frac{d_1+d_2}{c_l}$) represents the Hilbert-transformed time-trace signal, which is generated by element t and received by element r, containing extensive information about each grid point.

In this work, TFM is applied to process full matrix capture (FMC) data obtained from various cementitious specimens, enabling the detection of fully focused images that illustrate the different features.

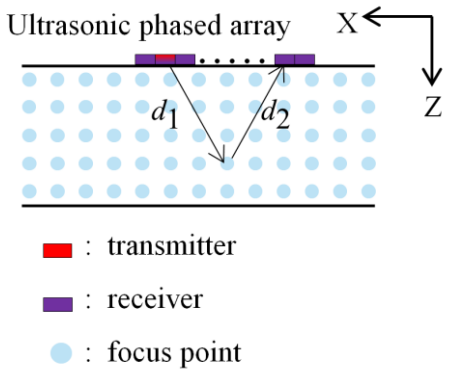

Figure 3-30. Total focusing method.

Experimental setup

The experimental setup of the ultrasonic phased array is shown in Figure 3-31. The ultrasonic probe is a 64-element phased array with an element pitch of 0.6 mm and a central frequency of 5 MHz. The full details are shown in Table 3-11. The probe, manufactured by Guangzhou Doppler Electronic Technologies Co., Ltd., was used to excite and receive signals. The ultrasound signals were successively generated by each element and received by all elements. The one-dimensional (1D) probe is positioned in the middle on the upper surface of the sample. The sampling frequency was 50 MHz and the total sampling points were 1251 in this work.

Figure 3-31. Experimental setup for ultrasonic phased array testing.

Table 3-11. Linear ultrasonic phased array parameters.

Array parameters	Probe
Element number	64
Element pitch (mm)	0.6
Element width (mm)	10
Central frequency (MHz)	5

It should be noted that while the preparation process for the five FRCC specimens is generally similar, it is not entirely consistent. The experimentally measured ultrasonic longitudinal wave velocities for samples A through E are presented in Table 3-12.

Table 3-12. Ultrasonic longitudinal wave velocity of different specimens.

Sample ID	Longitudinal wave velocity(m/s)
A	2950
B	3150
C	2900

D	3000
E	2900

3.4.5 Results

3.4.5.1 Micro-CT analysis and processing results

This section shows micro-CT scans for detailed cross-sectional analysis and micro-CT volume reconstruction with feature extraction for each sample. The depth variation, cross-sectional shape, cross-sectional area and spacing between features vary throughout the entire length of the feature (as depicted in Figure 3-32 (a)-(d) for fibre features and (e)-(h) for void features). Figure 3-33 (a) and (b) show two examples of clear representations, both in 3D volumetric and XZ-plane cross-section views, for positioned artificial features in samples A and E. While the assembled mould assists in positioning the fibres, the practical placement of these features is not precise due to the manual placement and pouring of cement. These variations explain the occurrence of loose fibres in the bundle and curvature in the fibre placement, thereby confirming the high resolution and effective detectability of size and shape by micro-CT.

Three CF features are analysed, with measurements taken at the upper, middle and bottom of samples B and C, and at the bottom of sample A. As shown in Figure 3-32 (a), the bottom small CF bundle feature in sample A shows more variation in depth ranging from 10.6 to 12.03mm, compared to the other CF features showing variations within 1mm. The principal axis ratio represents the ratio between the length of the minor axis and that of the major axis (Figure 3-32 (b)), offering insight into the circularity of the cross-sectional shape of the feature. The ratio of the principal axis ranges between 0.24 to 0.97 for samples A and B, representing small and larger fibre bundles. In contrast, sample C comprising the CF strips, exhibits a significantly lower ratio of the principal axis, with most values lower than 0.2, which is consistent with the flattened cross-sectional shape. The cross-sectional areas are also examined in Figure 3-32 (c). Notably, sample C exhibits the largest cross-sectional area, followed by sample B and sample A. In addition, the spacing between the upper and middle features is assessed in Figure 3-32 (d). Along the y-direction, the spacing measures approximately 10-10.5mm for sample C, while in sample B, the spacing increases to over 11mm along the y-direction.

The depth, interval and cross-sectional shape of small and large void channels were revealed in Figure 3-32 (e) to (h). Similarly, the depth of voids to the surface is measured along the y-direction at 3.2 to 4.5mm, 7.5 to 8.2mm and 11.95 to 13.26mm for upper, middle and bottom, respectively. The principal axis ratios for most of the cross sections range between 0.8 and 1.0, indicating the circular shape. The cross-sectional areas are determined to be approximately 1.0 mm^2 and 2.7 mm^2 for smaller and larger voids, respectively, which are slightly larger than those of the designed void features with diameters of 0.8mm and 1.8mm. Furthermore, the spacing between the upper and middle void channels along the axis shows notable variation in both the distances between voids and their orientations.

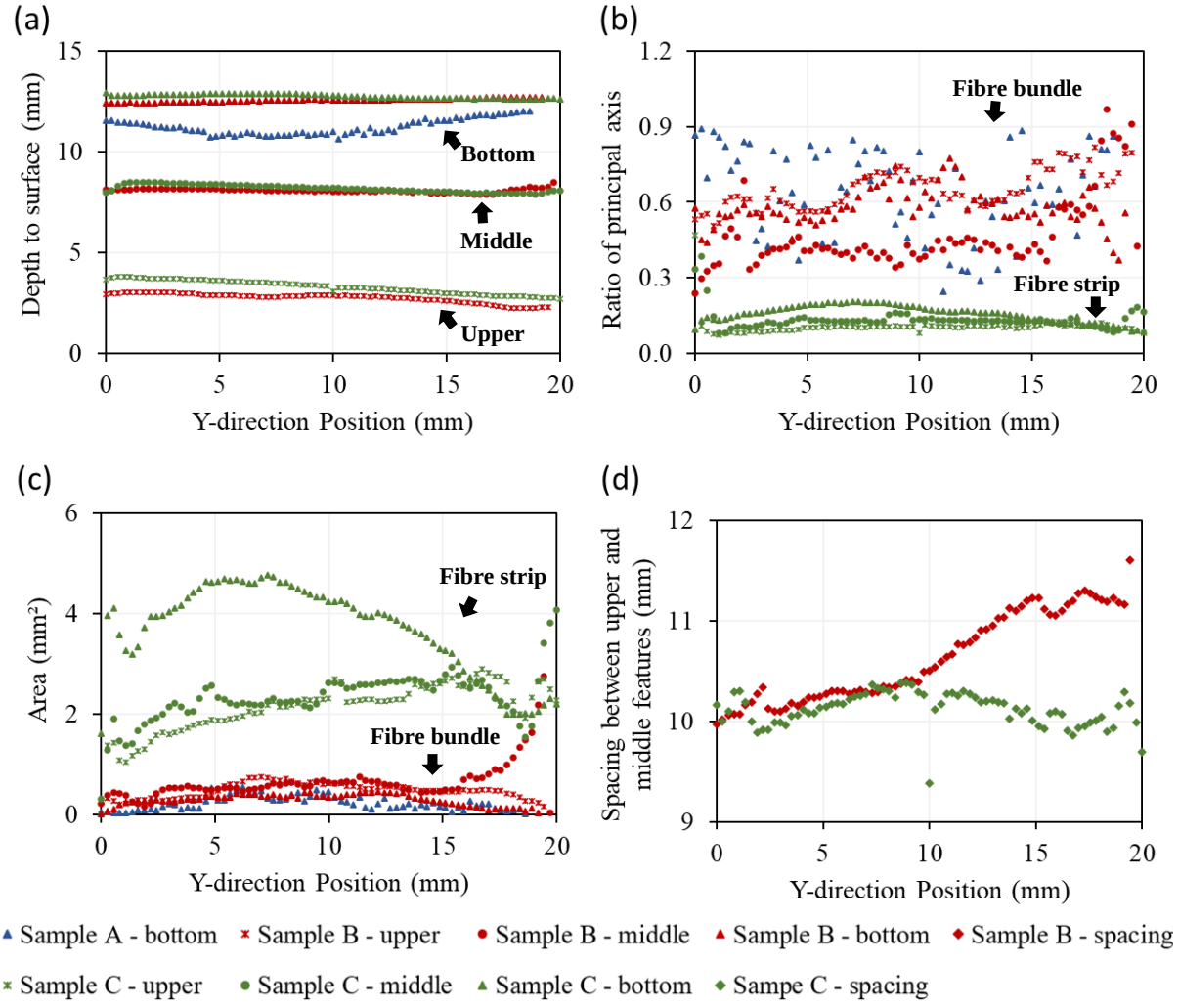

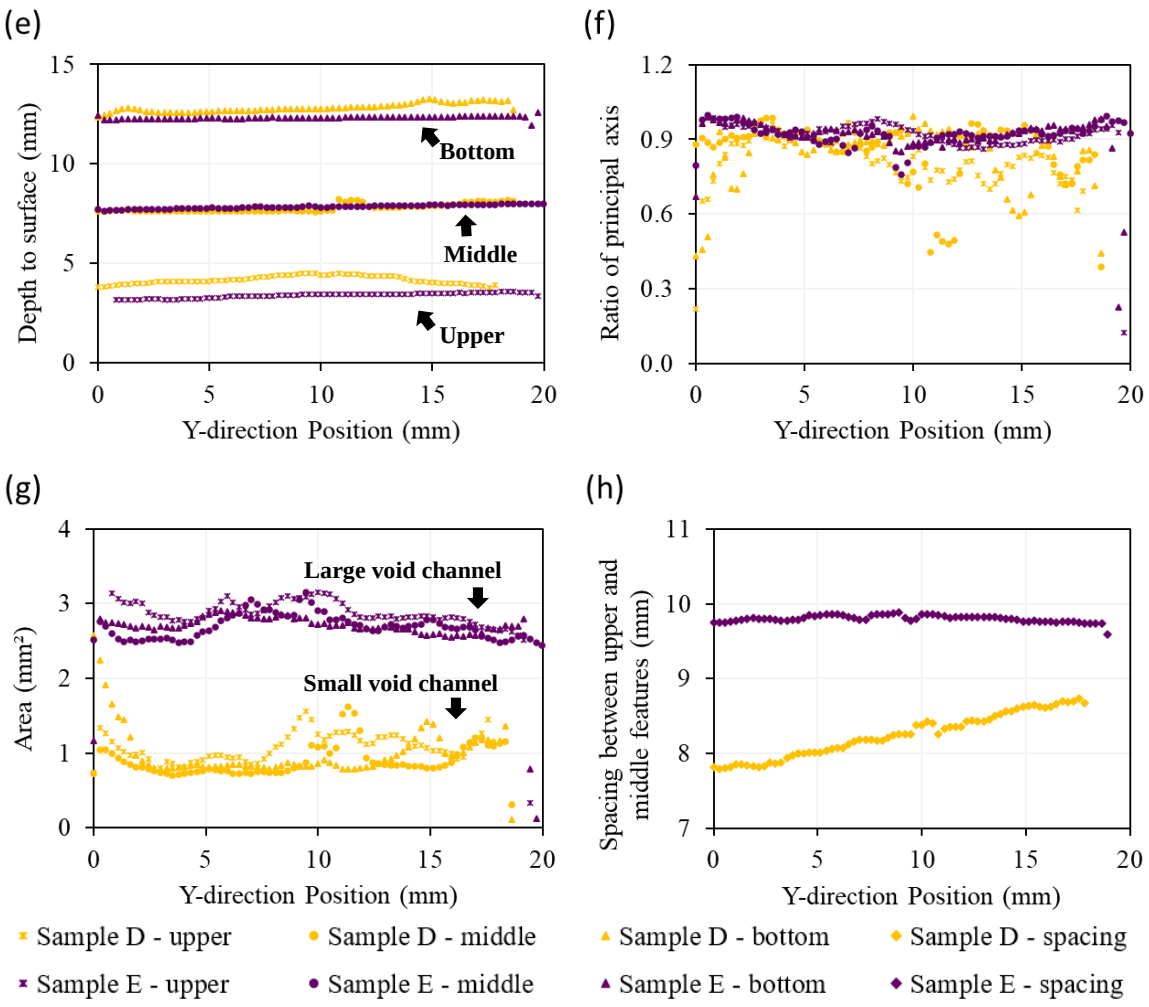

Figure 3-32. Cross-sectional analysis for (a)-(d) sample A-C and (e)-(h) sample D-E: depth to surface, ratio of principal axis, the cross-sectional area in y direction, and spacing between features along fibre y-direction.

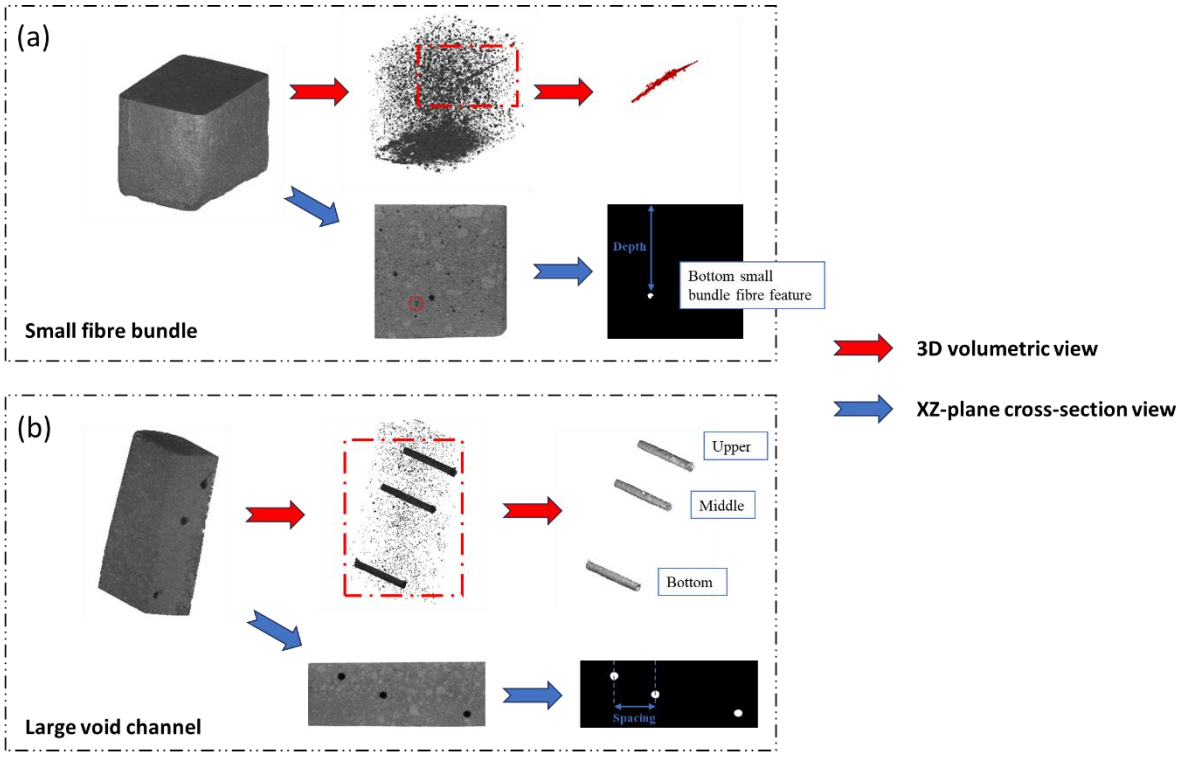

Figure 3-33. Micro-CT scan volume reconstruction and feature detection: (a) small fibre bundle and (b) large void channel.

3.4.5.2 Ultrasonic TFM imaging

Figure 3-34 shows both the standard and post-processed TFM images produced using the original experimental FMC data for sample A to sample E. In sample A (Figure 3-34 (a)), only direct waves and backwall echoes are observable, with no detectable defects. It is important to note that the artificial features in sample A consist of small fibre bundles, with diameters less than 100 µm. However, the wavelength in sample A is 0.59 mm. This implies that the defects are substantially smaller than half the wavelength, and such small defects cannot be detected by TFM. This limitation arises because TFM relies solely on travel time information [176]. When comparing the post-processed image (Figure 3-34 (b)) with the standard image, it represents the result of TFM imaging after the removal of the direct wave [13]. It is clear that only the bottom reflections are visible in this comparison. Sample B contains the same defect type (CF bundle) as sample A but with larger dimensions. Contrasting with sample A, the diameters of defects in Sample B are nearly 1mm, surpassing half the wavelength of 0.63 mm. Consequently, defects within sample B are detectable, as indicated at depths of 4.2 mm, 9.3 mm, and 13 mm in the z direction in Figure 3-34 (c). It is observed that the defect located at z = 4.2 mm is influenced by direct waves. Despite the identifiability of the defect at z = 13 mm, its size appears considerably smaller than its true value. This discrepancy is primarily due to the viscoelastic attenuation properties of the cementitious materials. This attribute causes a

significant decrease in signal levels, an effect that becomes more pronounced with increasing propagation depth, consequently leading to a lower signal-to-noise ratio. Figure 3-34 (d) shows the TFM imaging using the FMC data after removing direct waves and using a bandpass FIR filter [176]. In comparison to the standard TFM image, the location and size of defects depicted in Figure 3-34 (d) more closely align with the true values, although some artifacts are still present. The defects in sample C consist of three strips of fibre fabric, each with a width of 5 mm. Figure 3-34 (e) displays the imaging obtained using the conventional TFM algorithm. The defects at depths of z = 8.4 mm and z = 12.8 mm are detected effectively, whereas the first defect at z = 3 mm is obscured by near-field clutter. Figure 3-34 (f) presents the TFM imaging following the removal of the direct waves. As seen in this figure, the first defect at z = 4.1 mm is identifiable, but its size and shape are not discerned accurately. Compared to the standard TFM image, the defects at z = 8.4 mm and z = 12.8 mm are rendered with greater clarity after post processing.

Sample D features three identical voids, each with a diameter of 1.0 mm. Figure 3-34 (g) shows the imaging results from conventional TFM. The features near 8 mm in the z direction are clearly visible, while those at 3 mm and 12 mm are nearly indiscernible. For comparison, Figure 3-34 (h) depicts TFM imaging after the removal of the direct waves. In this figure, defects at z = 4.8 mm and z = 7.9 mm are observable, but the defect at z = 12 mm remains elusive. This is primarily because the defect's small diameter of 1.0 mm results in relatively weak useful signals, and the FRCC sample has high attenuation. An effective approach to enhance detection in such cases involves improving the signal-to-noise ratio, thereby eliminating noise and efficiently extracting the valid signal from the small defect [177]. The defects in sample E are three identical holes of the same type as in sample D but with larger sizes. In contrast to sample D, the diameters of the defects in sample E are 1.8mm, almost twice those of sample D. Figure 3-34 (i) shows the TFM image using the original experimental FMC data. The defects at z=7.8 mm and z=11.3 mm are observable, while the defect at z=3 mm is not discernible. Figure 3-34 (j) presents the post-processed TFM image after removing direct waves. Compared with the standard TFM image, in Figure 3-34 (j), the defects located at z=7.8mm and z=11.3mm are still visible, while the defect at z=3mm is not easily identifiable. Therefore, the method for removing direct waves can be further improved, particularly in terms of effectively separating the information of defects very close to the upper surface from the direct waves.

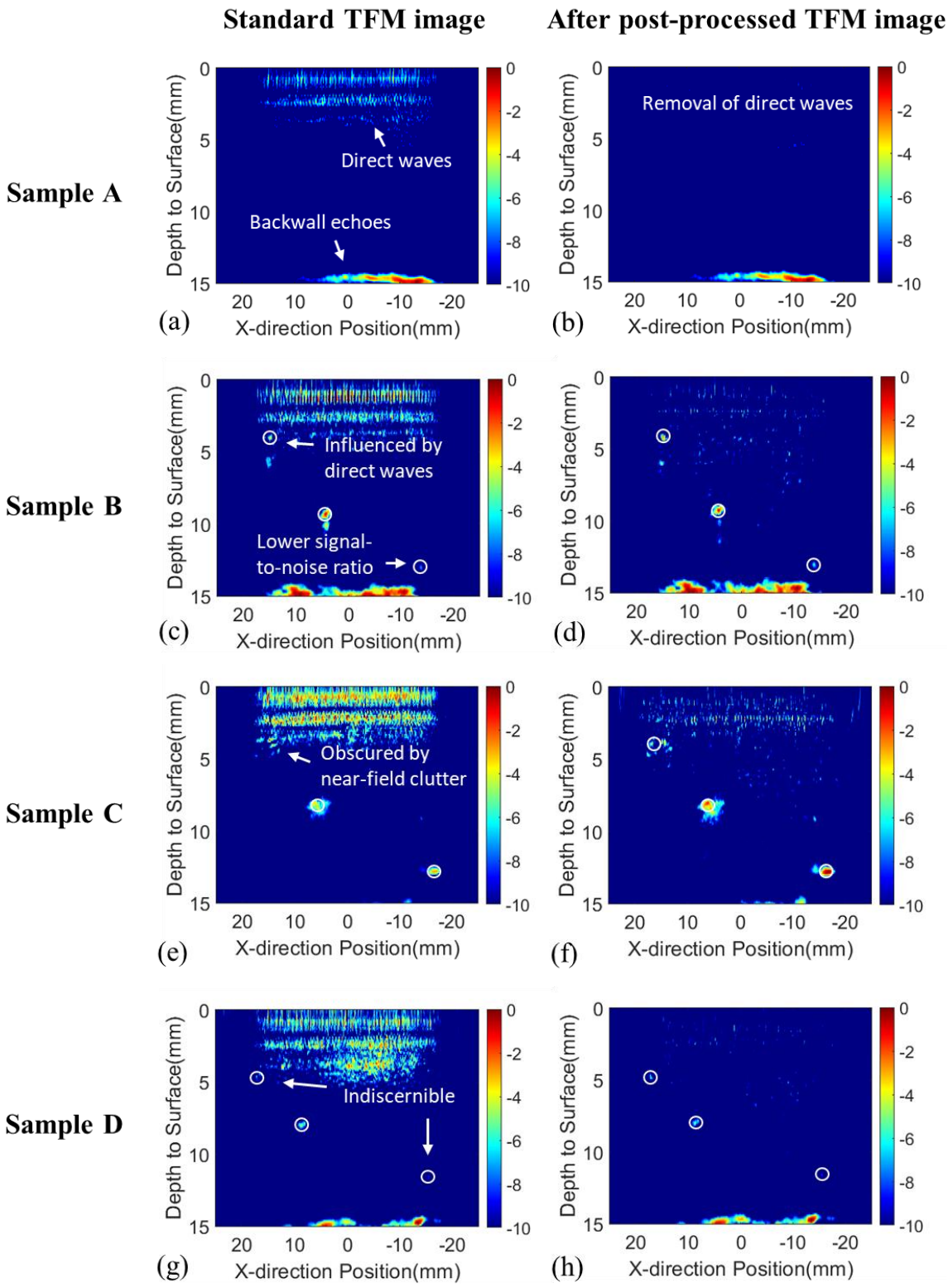
Standard TFM image
After post-processed TFM image
Sample A
Sample B
Sample C
Sample D
Direct waves
Backwall echoes
Removal of direct waves
Influenced by direct waves
Lower signal-to-noise ratio
Obscured by near-field clutter
Indiscernible
Depth to Surface(mm)
X-direction Position(mm)
(a)
(b)
(c)
(d)
(e)
(f)
(g)
(h)

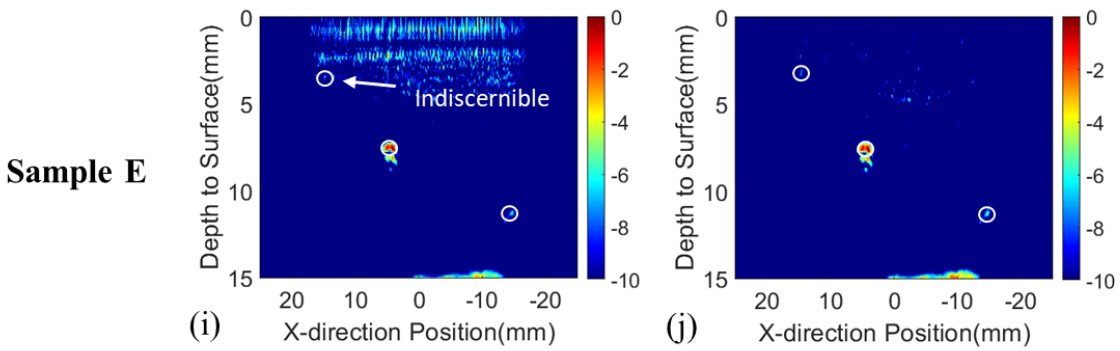

Figure 3-34. TFM images before and after post processing (with feature positions indicated by circles).

3.4.6 Discussion

The experimental results obtained from micro-CT and ultrasonic testing demonstrate their capabilities in feature detection and characterisation. This section investigates the performance of these two commonly used NDT methods in capturing CF and voids at various scales, specifically for FRCC.

Micro-CT operates on the principle of X-ray imaging, where a series of X-ray projections are acquired as the sample rotates incrementally through a range of angles. These projections are then reconstructed using sophisticated computer algorithms to generate a 3D representation of the internal structure of the sample with high spatial resolution. One of the key advantages of micro-CT is its capability to provide a detailed visualisation of the internal features in cementitious composite samples. The previous research has proven that the developed anisotropic Gaussian method can enhance the accuracy of CF detection by reducing noise and background interference. The result showed a better alignment with the ground truth measurements [172]. In this study, the micro-CT testing with the developed anisotropic filter showed its capacity to provide a comprehensive characterisation of multiple artificial features embedded in the cementitious matrices. This enabled quantitative analysis of feature depth, cross-sectional area, shape and spacing between different features throughout the specimens. As shown in Section 3.1, it not only provided high-resolution imaging in different planes (e.g. XZ plane) and volumetric views but also allowed for the extraction of quantitative data on the placement and morphology of features. In comparison, as a real-time imaging and portable option for non-destructive evaluation, TFM imaging has been employed in detecting internal void defects in concrete for years [57, 58]. However, there is a lack of studies examining its ability to detect CF features in a cementitious matrix. In this experiment, the ultrasonic phased

array probe is 1D and treats the y-axis as infinite. Ultrasonic shear waves are ignored for imaging due to the fact that they only propagate negligible distances in such high attenuation materials [154]. Only longitudinal waves are considered, and the minimum resolvable size, according to diffraction limitations, is determined by the half-wavelength of the longitudinal waves [178]. Therefore, ultrasonic TFM was only used to investigate the depth of different CF and void features.

Table 3-13 presents a comparison of feature depth measurements obtained from micro-CT and TFM imaging. By comparing the obtained results, the relative variations were quantified. Micro-CT testing can precisely measure the feature depth at all positions for these specimens with varying scaled features. In contrast, TFM is not able to detect small-scale defects that are smaller than half the wavelength of the ultrasound waves employed. In this case, CF bundles with a diameter of less than 100μm in Sample A were too small to be accurately identified by TFM due to the limited resolution of ultrasound. The relative variations for samples B to E are presented in the right column of Table 3-13. It is observed that the upper feature consistently exhibited a larger relative variation, reaching up to 45.33%, while the middle and bottom detectable features showed smaller variations, with the best performance being zero percent error. This observation suggests the presence of interference from direct waves, which travel directly from the transducer to the surface and then back again, potentially affecting signals from defects near the surface. Notably, the upper void feature was indiscernible in sample E, potentially due to this interference effect from direct waves masking the signal response from the near-surface defect even after post-processing to remove direct waves. While this post-processing step helped reduce the impact of near-field artifacts, it did not completely resolve the defect detection issue for the near-surface void in sample E. In addition, when detecting deeper features along the sample thickness, the signal-to-noise ratio is low for smaller diameter voids in high attenuation materials, such as the bottom feature in sample D.

Through the comparison, it revealed the capabilities and limitations of ultrasonic TFM testing in the ultrasonic phased array for detecting features of different sizes and depths in cementitious materials. Several key factors should be considered influential when employing TFM imaging. Firstly, the characteristics of the ultrasonic transducer, such as frequency, element size, and bandwidth, impact the resolution and depth of field, affecting the accuracy of TFM images. Secondly, material properties, including Young's modulus, density, and attenuation, can lead to inaccuracies in wave speed calculations. Cement-based materials with

high attenuation characteristics pose challenges in maintaining adequate signal-to-noise ratios, especially for smaller defects located at greater depths. The absorption and scattering effects in such materials can severely degrade the energy and strength of the ultrasonic signals, hampering defect detection capabilities. The choice of different wave modes, whether longitudinal or shear waves, affects the penetration depth and resolution. While longitudinal waves were primarily employed in this study, ignoring shear waves can impact the detection capabilities in certain materials. Furthermore, the signal processing algorithms employed for reconstructing TFM images from the raw data can significantly influence the image quality and accuracy.

Table 3-13. Comparison of feature depth measurements obtained from TFM imaging and micro-CT.

Sample ID	Feature types & Configuration	Features	Depth to surface (mm)		Relative variation %
			Micro-CT scanning	Ultrasonic TFM imaging	
B	large CF bundle	Upper	2.89	4.2	45.33
		Middle	8.02	9.3	15.96
		Bottom	12.59	13	3.26
C	CF fabric strip	Upper	3.09	4.1	32.69
		Middle	8.21	8.4	2.31
		Bottom	12.8	12.8	0.00
D	small void channel	Upper	4.43	4.8	8.35
		Middle	7.64	7.9	3.40
		Bottom	12.78	-	-
E	large void channel	Upper	3.46	-	-
		Middle	7.84	7.8	-0.51
		Bottom	12.33	11.3	-8.35

The findings of this research contribute to the advancement and application of NDT methods for the characterisation of FRCC. Micro-CT scanning offers high-resolution 3D visualisation and captures comprehensive details of the features within the specimens, but is hampered by its limited sample capacity, high operational costs, and lengthy image reconstruction times. The anisotropic Gaussian filter applied to micro-CT images is suitable for processing elongated structures such as fibres [121]. This facilitates precise segmentation and detection of features in cementitious specimens, especially to overcome the similar X-ray attenuation coefficients between CFs and cementitious materials. Future research could explore the potential of micro-CT to analyse CF dispersion in FRCC, including the spatial distribution and clustering of discrete CFs within the cementitious matrix. Furthermore, efforts could be made to optimise computational costs while preserving accuracy and effective performance in

image analysis. As mentioned above, the application of TFM in cementitious materials faces challenges due to their inherent heterogeneity and complexity, which complicates the propagation and interpretation of ultrasonic waves. Moreover, the high attenuation and scattering properties of these materials tend to limit the penetration depth of ultrasound waves, potentially affecting the clarity and accuracy of the resulting images. Despite this limitation, TFM provides a practical and efficient solution for in-situ inspections, making it particularly suitable for initial assessments and routine maintenance. In future work, the use of a 3D TFM method using a 2D ultrasonic array probe to capture spatial wavefield information could significantly enhance the TFM algorithm's capability to detect internal defects in cementitious materials. Additionally, in signal processing, noise suppression techniques such as block-wise singular value decomposition can effectively reduce random noise, thereby improving TFM imaging quality [164, 179]. The integration of deep learning algorithms with TFM could further enhance imaging quality. Other potential research avenues include investigating the high attenuation characteristics of ultrasonic signals in cement materials and employing advanced ultrasonic focusing or signal compensation technologies to improve the detection of deep defects.

3.4.7 Summary of key findings from Section 3.4

In this study, the performance of two NDT methods in characterising CF and void features across various scales within cementitious matrices was investigated. Micro-CT testing and image processing, by employing the newly developed Gaussian filter, provides a comprehensive examination of the spatial positioning and dimensions of CF and void channels, including their location, orientation, size, and shape in 3D representation. Understanding these internal features is critical, as it could benefit the mix design of FRCC and improve its performance in both structure and durability. The application of the TFM ultrasonic technique provides an efficient alternative for detecting feature locations using the 1D ultrasonic phased array. Accurate depth detection was achieved for CF bundles and strips, as well as mid-depth void channels. However, challenges such as limited resolution for small-scale defects, interference from direct waves, and a low signal-to-noise ratio for deeper features still remain. Building on the understanding of the capacities and limitations of micro-CT and ultrasonic testing, the findings of this work revealed the feasibility of NDT methods for FRCC characterisation. Optimising computational efficiency, advancing processing methods, and expanding potential applications of these NDT methodologies could be the goals for future research.

3.5 CONCLUSION

This chapter thoroughly investigated the characteristics and performance of FRCC incorporated with CFs and GFs through experimental and numerical studies. Micro-CT analysis provided quantitative insights into void geometry and distribution in carbon and glass- FRCCs. This chapter also highlighted their influence of fibre type and content on FRCC properties, including mechanical, physical and electrical properties. The study of acid diffusion effects through experiments and FE simulations further contributed to understanding FRCC durability in aggressive environments. Additionally, the development of an anisotropic Gaussian filter significantly improved CF detection in low-contrast micro-CT images, overcoming segmentation challenges. The comparative analysis of micro-CT and ultrasonic testing techniques demonstrated their accuracy, advantages, and limitations in characterising CFs and voids in the cementitious matrix. Detailed key findings have been summarised in sections 3.2.5, 3.3.5, and 3.4.7. These findings enhance the understanding of the internal microstructure of FRCCs and the relationship to their performance. This study also supports the advancement of NDT methods and provide valuable guidance for optimising material design, durability, and practical application in construction.

3.6 REFERENCES

[1] G.C. Bye, Portland Cement: Composition, Production and Properties, Thomas Telford1999.

[2] J.J. Biernacki, J.W. Bullard, G. Sant, N. Banthia, K. Brown, F.P. Glasser, S. Jones, T. Ley, R. Livingston, L. Nicoleau, J. Olek, F. Sanchez, R. Shahsavari, P.E. Stutzman, K. Sobolev, T. Prater, Cements in the 21(st) Century: Challenges, Perspectives, and Opportunities, J Am. Ceram. Soc. 100(7) (2017) 2746-2773.

[3] J. Zhang, T. Liu, B. Dong, S. Zhou, R. Guo, Experimental Investigation of Mechanical Characterizations of a POM Fiber-Reinforced Mortar Material, Frontiers in Physics 10 (2022).

[4] FIBER-REINFORCED CONCRETE. https://www.sika.com/en/construction/concrete-admixtures/fibers.html. (Accessed 30 April 2023).

[5] Fibre reinforced concrete. https://www.holcim.com.au/products-and-services/concrete-readymix/high-performance/fibre-reinforced-concrete. (Accessed 30 April 2023).

[6] G. Debusschere, New applications for steel fiber reinforced concrete and combined reinforcement, Bekaert, Germany, 2018.

[7] A.A. Ghadban, Fiber-Reinforced Concrete for Structure Components, (2017).

[8] M. Vavrus, J. Kralovanec, Study of Application of Fiber Reinforced Concrete in Anchorage Zone, Buildings 13(2) (2023) 524.

[9] S. Messaoud, S. Danah, G. Michael, Behaviour of different types of fibre reinforced concrete without admixture, Eng. Struct. 113 (2016) 328-334.

[10] W. Heyang, L. Xiaoshan, Z. Annan, A review of mechanical properties of fibre reinforced concrete at elevated temperatures, Cem. Concr. Res. 135 (2020) 106117.

[11] K. Subramanian Kala, S.K. Singh, Experimental Investigations on Basalt Fibre-Reinforced Concrete, Journal of The Institution of Engineers (India): Series A 99 (2018).

[12] Hermawan, F.M. Puti, A. Muhamad, R. Driejana, Identification of Source Factors of Carbon Dioxide (CO2) Emissions in Concreting of Reinforced Concrete, Procedia Engineering 125 (2015) 692-698.

[13] M. Mastali, A. Dalvand, A. Sattarifard, The impact resistance and mechanical properties of the reinforced self-compacting concrete incorporating recycled CFRP fiber with different lengths and dosages, Compos. B. Eng. 112 (2017) 74-92.

[14] A. Belli, A. Mobili, T. Bellezze, F. Tittarelli, Commercial and recycled carbon/steel fibers for fiber-reinforced cement mortars with high electrical conductivity, Cem. Concr. Compos. 109 (2020) 103569.

[15] M. Safiuddin, G. Abdel-Sayed, N. Hearn, Absorption and Strength Properties of Short Carbon Fiber Reinforced Mortar Composite, Buildings 11(7) (2021) 300.

[16] Y.A. Orban, D.L. Manea, C. Aciu, Study on the influence of chopped carbon fibre reinforcements on the behaviour of cementitious composites, Bulletin of the Transilvania University of Braşov 10(59) (2017).

[17] S.A. Hadigheh, S. Kashi, Effectiveness of vacuum consolidation in bonding fibre reinforced polymer (FRP) composites onto concrete surfaces, Constr. Build. Mater. 187 (2018) 854-864.

[18] Y. Wei, S.A. Hadigheh, Cost benefit and life cycle analysis of CFRP and GFRP waste treatment methods, Constr. Build. Mater. 348 (2022) 128654.

[19] S.T. Tassew, A.S. Lubell, Mechanical properties of glass fiber reinforced ceramic concrete, Constr. Build. Mater. 51 (2014) 215-224.

[20] A. Kizilkanat, Experimental Evaluation of Mechanical Properties and Fracture Behavior of Carbon Fiber Reinforced High Strength Concrete, Periodica Polytechnica Civil Engineering 60 (2016).

[21] M. Safiuddin, M. Yakhlaf, K.A. Soudki, Key mechanical properties and microstructure of carbon fibre reinforced self-consolidating concrete, Constr. Build. Mater. 164 (2018) 477-488.

[22] M.M. Hilles, M.M. Ziara, Mechanical behavior of high strength concrete reinforced with glass fiber, Engineering Science and Technology, an International Journal 22(3) (2019) 920-928.

[23] J. Donnini, T. Bellezze, V. Corinaldesi, Mechanical, electrical and self-sensing properties of cementitious mortars containing short carbon fibers, Journal of Building Engineering 20 (2018) 8-14.

[24] L. Wang, F. Aslani, Mechanical properties, electrical resistivity and piezoresistivity of carbon fibre-based self-sensing cementitious composites, Ceramics International 47(6) (2021) 7864-7879.

[25] B. Han, L. Zhang, C. Zhang, Y. Wang, X. Yu, J. Ou, Reinforcement effect and mechanism of carbon fibers to mechanical and electrically conductive properties of cement-based materials, Constr. Build. Mater. 125 (2016) 479-489.

[26] L. Deng, Y. Ma, J. Hu, S. Yin, X. Ouyang, J. Fu, A. Liu, Z. Zhang, Preparation and piezoresistive properties of carbon fiber-reinforced alkali-activated fly ash/slag mortar, Constr. Build. Mater. 222 (2019) 738-749.

[27] G. Cosoli, A. Mobili, F. Tittarelli, G.M. Revel, P. Chiariotti, Electrical resistivity and electrical impedance measurement in mortar and concrete elements: A systematic review, Applied Sciences 10(24) (2020) 9152.

[28] S. Yousuf, P. Shafigh, Z. Ibrahim, The pH of Cement-based Materials: A Review, Journal of Wuhan University of Technology-Mater. Sci. Ed. 35 (2020) 908-924.

[29] S.A. Hadigheh, R. Gravina, S. Smith, Effect of acid attack on FRP-to-concrete bonded interfaces, Constr. Build. Mater. 152 (2017) 285-303.

[30] A.M. Al-Swaidani, M.K. Baddoura, S.D. Aliyan, W. Choeb, Acid resistance, water permeability and chloride penetrability of concrete containing crushed basalt as aggregates, J. Mater. Eng. 5(7-8) (2015) 285-304.

[31] S.A. Hadigheh, K. Feihu, F. Hamid, Durability design criteria for the hybrid carbon fibre reinforced polymer (CFRP)-reinforced geopolymer concrete bridges, Structures 35 (2022) 325-339.

[32] E. Arunakanthi, H. Rao, Effects of Sulphuric Acid in Mixing And Curing Water on Strength of High-Performance Metakaolin Concrete, Int. J. Sci. Res. 2 (2012) 147-150.

[33] A. Babar, Q. Liaqat Ali, S. Syed Haroon Ali, R. Safi Ur, H. Iqrar, I. Maria, A step towards durable, ductile and sustainable concrete: Simultaneous incorporation of recycled aggregates, glass fiber and fly ash, Constr. Build. Mater. 251 (2020) 118980.

[34] M. Yıldırım, H. Özhan, Residual Durability Performance of Glass Fiber Reinforced Concrete Damaged by Compressive Stress Loads, Periodica Polytechnica Civil Engineering (2023).

[35] M.K. Baddoura, S.D. Aliyan, W. Choeb, Acid Resistance, Water Permeability and Chloride Penetrability of Concrete Containing Crushed Basalt as Aggregates, 2015.

[36] Y. Farnam, S. Dick, A. Wiese, J. Davis, D. Bentz, J. Weiss, The influence of calcium chloride deicing salt on phase changes and damage development in cementitious materials, Cem. Concr. Compos. 64 (2015) 1-15.

[37] H. Fatemi, S.A. Hadigheh, Y. Tao, G. Adam, Development of a novel and specialised cementitious matrix overlay for anode embedment in impressed current cathodic protection (ICCP) systems for reinforced concrete bridges Case Stud. Constr. Mater. 20 (2024) e02908.

[38] C.G. Berrocal, K. Lundgren, I. Löfgren, Corrosion of steel bars embedded in fibre reinforced concrete under chloride attack: State of the art, Cem. Concr. Res. 80 (2016) 69-85.

[39] D. Chen, S. Mahadevan, Chloride-induced reinforcement corrosion and concrete cracking simulation, Cem. Concr. Compos. 30(3) (2008) 227-238.

[40] Y. Tao, S.A. Hadigheh, Y. Wei, Recycling of glass fibre reinforced polymer (GFRP) composite wastes in concrete: A critical review and cost benefit analysis, Structures 53 (2023) 1540-1556.

[41] A. Mobili, G. Cosoli, N. Giulietti, P. Chiariotti, G. Pandarese, T. Bellezze, G.M. Revel, F. Tittarelli, Effect of Gasification Char and Recycled Carbon Fibres on the Electrical Impedance of Concrete Exposed to Accelerated Degradation, Sustainability, 2022.

[42] Y. Wei, S.A. Hadigheh, Enhancing carbon fibre recovery through optimised thermal recycling: Kinetic analysis and operational parameter investigation, Materials Today Sustainability 25 (2024) 100661.

[43] Y. Wei, S.A. Hadigheh, Development of an innovative hybrid thermo-chemical recycling method for CFRP waste recovery, Compos. B. Eng. 260 (2023) 110786.

[44] AS 3972 General purpose and blended cements, Standards Australia, Australia, 2021.

[45] AS 2758.1 Aggregates and rock for engineering purposes Concrete aggregates, Standards Australia, Australia, 2014.

[46] BS EN 1015-3 Methods of test for mortar masonry - Part 3: Determination of consistence of fresh mortar (by flow table), British Standards Institution, UK, 1999.

[47] BS EN 1015-6 Methods of test for mortar for masonry - Part 6: Determination of bulk density of fresh mortar, British Standards Institution, UK, 1999.

[48] N. Kamal, S.A. Hadigheh, Sodium hydroxide-free geopolymer binder for prestressed concrete applications, Constr. Build. Mater. 293 (2021) 123397.

[49] D. Bradley, G. Roth, Adaptive Thresholding using the Integral Image, J. Graphics Tools 12 (2007) 13-21.

[50] W.D. Callister Jr, D.G. Rethwisch, Callister's materials science and engineering, John Wiley & Sons2020.

[51] P. Choi, J.H. Yeon, K.-K. Yun, Air-void structure, strength, and permeability of wet-mix shotcrete before and after shotcreting operation: The influences of silica fume and air-entraining agent, Cement and Concrete Composites 70 (2016) 69-77.

[52] C 267 Standard Test Methods for Chemical Resistance of Mortars, Grouts, and Monolithic Surfacings and Polymer Concretes, ASTM International, West Conshohocke, United States, 2020.

[53] C948-81, Standard Test Method for Dry and Wet Bulk Density, Water Absorption, and Apparent Porosity of Thin Sections of Glass-Fiber Reinforced Concrete, ASTM International, West Conshohocken, United States, 2016.

[54] BS EN 1015-10 Methods of test for mortar for masonry — Part 10: Determination of dry bulk density of hardened mortar, British Standards Institution, UK, 1999.

[55] C490/C490M, Standard Practice for Use of Apparatus for the Determination of Length Change of Hardened Cement Paste, Mortar, and Concrete, ASTM International, West Conshohocken, United States, 2021.

[56] AASHTO Designation: T 358 - Standard Method of Test for Surface Resistivity Indication of Concrete's Ability to Resist Chloride Ion Penetration, American Association of State Highway and Transportation Officials, Washington, D.C, 2015.

[57] Y. Pan, H. li, Modeling of moisture diffusion in CFRP strengthened concrete based on thermal-moisture analogy, (2015) 536-542.

[58] S.A. Hadigheh, F. Ke, S. Kashi, 3D acid diffusion model for FRP-strengthened reinforced concrete structures: Long-term durability prediction, Constr. Build. Mater. 261 (2020) 120548.

[59] J. Xu, K. Henk, S.K.B. Frans, Moisture diffusion in glass–fiber-reinforced polymer composite bridge under hot/wet environment, Compos. B. Eng. 45(1) (2013) 407-416.

[60] F. Pierron, Y. Poirette, A. Vautrin, A novel procedure for identification of 3D moisture diffusion parameters on thick composites: theory, validation and experimental results, J. Compos. Mater. 36(19) (2002) 2219-2243.

[61] O. Ayinde, Numerical analysis of concrete degradation due to chloride-induced steel corrosion, Adv. Concr. Constr. 7 (2019) 203-210.

[62] Abaqus Analysis User's Manual, Rhode Island, USA Providence: Dassault Systemes Simulia Corp., 2014.

[63] Q. Liaqat Ali, A. Babar, A. Asad, Combined effects of supplementary cementitious materials (silica fume, GGBS, fly ash and rice husk ash) and steel fiber on the hardened properties of recycled aggregate concrete, Constr. Build. Mater. 263 (2020) 120636.

[64] B. Zhou, M. Zhang, L. Wang, G. Ma, Experimental study on mechanical property and microstructure of cement mortar reinforced with elaborately recycled GFRP fiber, Cem. Concr. Compos. 117 (2021) 103908.

[65] X. Jing, W. Xiaomin, W. Zhongrui, X. Shuquan, L. Hongbo, Investigations on influencing factors of resistivity measurement for graphite tailings concrete, Cem. Concr. Compos. 123 (2021) 104206.

[66] M. Horňáková, P. Lehner, Relationship of Surface and Bulk Resistivity in the Case of Mechanically Damaged Fibre Reinforced Red Ceramic Waste Aggregate Concrete, Materials 13 (2020) 5501.

[67] P. Ghosh, Q. Tran, Correlation Between Bulk and Surface Resistivity of Concrete, Int. J. Concr. Struct. Mater. 9 (2014) 119-132.

[68] T. Quang, G. Pratanu, Influence of pumice on mechanical properties and durability of high performance concrete, Constr. Build. Mater. 249 (2020) 118741.

[69] M.N. Amin, A. Ahmad, K. Shahzada, K. Khan, F.E. Jalal, M.G. Qadir, Mechanical and microstructural performance of concrete containing high-volume of bagasse ash and silica fume, Scientific Reports 12(1) (2022) 5719.

[70] M. Trezza, Hydration study of ordinary Portland cement in the presence of zinc ions, Materials Research-ibero-american Journal of Materials - MATER RES-IBERO-AM J MATER 10 (2007).

[71] H. Yi, L. Runsheng, W. Xiao-Yong, Performance and sustainability of quaternary composite paste comprising limestone, calcined Hwangtoh clay, and granulated blast furnace slag, J. Build. Eng. 43 (2021) 102655.

[72] D.-I.M. Izadifar, Interaction in Calcium Silicate Hydrates and new Composite Materials.

[73] R. Ylmén, U. Jäglid, Carbonation of Portland Cement Studied by Diffuse Reflection Fourier Transform Infrared Spectroscopy, Int. J. Concr. Struct. Mater. 7(2) (2013) 119-125.

[74] K. Vikram Singh, A. Utkarsh, A. Karanpreet, S. Gaurav, FTIR Analysis of Nanomodified Cement Concrete Incorporating Nano Silica and Waste Marble Dust, IOP Conference Series: Earth and Environmental Science 796(1) (2021) 012022.

[75] T. Shi, Y. Gao, D. Corr, S. Shah, FTIR study on early-age hydration of carbon nanotubes-modified cement-based materials, Adv. Cem. Res. 31 (2019) 353-361.

[76] Z. Yasong, G. Jianming, X. Zhenhai, L. Shujun, L. Xu, C. Gaofeng, Combined effect of slag and clay brick powder on the hydration of blended cement, Constr. Build. Mater. 299 (2021) 123996.

[77] N.A. Edama, The Effect of Hydrochloric Acid on the Surface Area, Morphology and Physico-chemical Properties of Sayong Kaolinite Clay, Key Eng. Mater. 594-595 (2014) 49-56.

[78] A.V. Miguel, C.G. Dorys, M. Jesús, Recent advances in the use of computed tomography in concrete technology and other engineering fields, Micron 118 (2019) 22-34.

[79] H. Fatemi, S.A. Hadigheh, Y. Tao, G. Adam, Development of a novel and specialised cementitious matrix overlay for anode embedment in impressed current cathodic protection (ICCP) systems for reinforced concrete bridges, Case Stud. Constr. Mater. 20 (2024) e02908.

[80] S.A. Hadigheh, M. Maheri, S. Mahini, Performance of weak-beam, strong-column RC frames strengthened at the joints by FRP, Iranian Journal of Science and Technology - Transactions of Civil Engineering 37 (2013) 33-51.

[81] B. Smita, Arun, Microstructural analysis of Self-Compacting Concrete– A review, Mater. Today: Proc. 65 (2022) 1250-1259.

[82] Y. Tao, S.A. Hadigheh, Enhancing the strength, microstructural integrity, and shrinkage performance of cement-based mortar using pulverised carbon and glass FRP composite waste, J. Build. Eng. 94 (2024) 110053.

[83] A.M. Rashad, H.E.-D.H. Seleem, A.F. Shaheen, Effect of Silica Fume and Slag on Compressive Strength and Abrasion Resistance of HVFA Concrete, Int. J. Concr. Struct. Mater. 8(1) (2014) 69-81.

[84] S. Anjali, P.K. Mehta, K. Rakesh, Performance of binary admixtures (Fly Ash and Silica Fume) on Self Compacting concrete, Mater. Today: Proc. 58 (2022) 970-977.

[85] S.A. Hadigheh, F. Ke, H. Fatemi, Durability design criteria for the hybrid carbon fibre reinforced polymer (CFRP)-reinforced geopolymer concrete bridges, Structures 35 (2022) 325-339.

[86] V.H.J.M.d. Santos, D. Pontin, G.G.D. Ponzi, A.S.d.G.e. Stepanha, R.B. Martel, M.K. Schütz, S.M.O. Einloft, F. Dalla Vecchia, Application of Fourier Transform infrared spectroscopy (FTIR) coupled with multivariate regression for calcium carbonate (CaCO3) quantification in cement, Constr. Build. Mater. 313 (2021) 125413.

[87] H. Ma, Mercury intrusion porosimetry in concrete technology: tips in measurement, pore structure parameter acquisition and application, Journal of Porous Materials 21(2) (2014) 207-215.

[88] S. Diamond, Aspects of concrete porosity revisited, Cement and Concrete Research 29(8) (1999) 1181-1188.

[89] H.S. Wong, A.M. Pappas, R.W. Zimmerman, N.R. Buenfeld, Effect of entrained air voids on the microstructure and mass transport properties of concrete, Cem. Concr. Res. 41(10) (2011) 1067-1077.

[90] Y.-S. Wang, J.-G. Dai, X-ray computed tomography for pore-related characterization and simulation of cement mortar matrix, NDT & E International 86 (2017) 28-35.

[91] H. Ma, D. Hou, Z. Li, Two-scale modeling of transport properties of cement paste: Formation factor, electrical conductivity and chloride diffusivity, Computational Materials Science 110 (2015) 270-280.

[92] J.-S. Kim, J.H. Kim, T.-S. Han, Microstructure characterization of cement paste from micro-CT and correlations with mechanical properties evaluated from virtual and real experiments, Materials Characterization 155 (2019) 109807.

[93] A.M. Neville, Properties of concrete, 4 ed., Longman Australia Pty Limited, Melbourne, Australia1995.

[94] J.H. Yeon, S. Choi, M.C. Won, Effect of Relative Humidity on Coefficient of Thermal Expansion of Hardened Cement Paste and Concrete, Transportation Research Record 2113(1) (2009) 83-91.

[95] A. du Plessis, W.P. Boshoff, A review of X-ray computed tomography of concrete and asphalt construction materials, Constr. Build. Mater. 199 (2019) 637-651.

[96] A. ArRejaie, S.A. Alsuliman, M.O. Aljohani, H.A. Altamimi, E. Alshwaimi, A.M. Al-Thobity, Micro-computed tomography analysis of gap and void formation in different prefabricated fiber post cementation materials and techniques, The Saudi Dental Journal 31(2) (2019) 236-241.

[97] J.-S. Kim, S.-Y. Chung, T.-S. Han, D. Stephan, M.A. Elrahman, Correlation between microstructural characteristics from micro-CT of foamed concrete and mechanical behaviors evaluated by experiments and simulations, Cem. Concr. Compos. 112 (2020) 103657.

[98] J. Gao, A. Sha, Z. Wang, L. Hu, D. Yun, Z. Liu, Y. Huang, Characterization of carbon fiber distribution in cement-based composites by Computed Tomography, Constr. Build. Mater. 177 (2018) 134-147.

[99] S.-Y. Chung, P. Sikora, D.J. Kim, M.E. El Madawy, M. Abd Elrahman, Effect of different expanded aggregates on durability-related characteristics of lightweight aggregate concrete, Materials Characterization 173 (2021) 110907.

[100] Anton, P.B. William, A review of X-ray computed tomography of concrete and asphalt construction materials, Constr. Build. Mater. 199 (2019) 637-651.

[101] Y. Tao, S.A. Hadigheh, Z. Wang, Void geometry analysis and multifaceted characterisation of cementitious mortar reinforced with short carbon and glass fibres – A comparative study, J. Build. Eng. 89 (2024) 109283.

[102] K. Xu, Q. Jin, J. Li, D.M. Ushizima, V.C. Li, K.E. Kurtis, P.J.M. Monteiro, In-situ microtomography image segmentation for characterizing strain-hardening cementitious composites under tension using machine learning, Cem. Concr. Res. 169 (2023) 107164.

[103] L. Hong, P. Zhang, D. Liu, P. Gao, B. Zhan, Q. Yu, L. Sun, Effective segmentation of short fibers in glass fiber reinforced concrete's X-ray images using deep learning technology, Mater. Des. 210 (2021) 110024.

[104] A. Badran, D. Marshall, Z. Legault, R. Makovetsky, B. Provencher, N. Piché, M. Marsh, Automated segmentation of computed tomography images of fiber-reinforced composites by deep learning, Journal of Materials Science 55(34) (2020) 16273-16289.

[105] E. Qoku, K. Xu, J. Li, P.J.M. Monteiro, K.E. Kurtis, Advances in imaging, scattering, spectroscopy, and machine learning-aided approaches for multiscale characterization of cementitious systems, Cem. Concr. Res. 174 (2023) 107335.

[106] J. Ying, J. Tian, J. Xiao, Z. Tan, Identification and reconstruction of concrete mesostructure based on deep learning in artificial intelligence, Constr. Build. Mater. 352 (2022) 129018.

[107] Z. Hao, C. Lu, B. Dong, V.C. Li, 3D crack recognition in Engineered Cementitious Composites (ECC) based on super-resolution reconstruction and semantic segmentation of X-ray Computed Microtomography, Compos. B. Eng. 285 (2024) 111730.

[108] M. Miletić, L.M. Kumar, J.-Y. Arns, A. Agarwal, S.J. Foster, C. Arns, D. Perić, Gradient-based fibre detection method on 3D micro-CT tomographic image for defining fibre orientation bias in ultra-high-performance concrete, Cem. Concr. Res. 129 (2020) 105962.

[109] J. Gao, Z. Wang, T. Zhang, L. Zhou, Dispersion of carbon fibers in cement-based composites with different mixing methods, Constr. Build. Mater. 134 (2017) 220-227.

[110] A. Bernasconi, M. Carboni, R. Ribani, On the combined use of Digital Image Correlation and Micro Computed Tomography to measure fibre orientation in short fibre reinforced polymers, Compos. Sci. Technol. 195 (2020) 108182.

[111] P. Pinter, S. Dietrich, B. Bertram, L. Kehrer, P. Elsner, K.A. Weidenmann, Comparison and error estimation of 3D fibre orientation analysis of computed tomography image data for fibre reinforced composites, NDT & E International 95 (2018) 26-35.

[112] M.J. Emerson, K.M. Jespersen, A.B. Dahl, K. Conradsen, L.P. Mikkelsen, Individual fibre segmentation from 3D X-ray computed tomography for characterising the fibre orientation in unidirectional composite materials, Compos. Part A Appl. Sci. Manuf. 97 (2017) 83-92.

[113] T. Riedel, Evaluation of 3D fiber orientation analysis based on x-ray computed tomography data. 4th Conference on Industrial Computed Tomography (iCT), 19-21 September 2012, Wels, Austria, e-Journal of Nondestructive Testing 17(2) (2012).

[114] L. Hou, W. Gao, F. der Bom, Z. Weng, C.L. Doolette, A. Maksimenko, D. Hausermann, Y. Zheng, C. Tang, E. Lombi, P.M. Kopittke, Use of X-ray tomography for examining root architecture in soils, Geoderma 405 (2022) 115405.

[115] P.J. Creveling, W.W. Whitacre, M.W. Czabaj, A fiber-segmentation algorithm for composites imaged using X-ray microtomography: Development and validation, Compos. Part A Appl. Sci. Manuf. 126 (2019) 105606.

[116] F. Sosa-Rey, Y. Abderrafai, A. Diouf Lewis, D. Therriault, N. Piccirelli, M. Lévesque, OpenFiberSeg: Open-source segmentation of individual fibers and porosity in tomographic scans of additively manufactured short fiber reinforced composites, Compos. Sci. Technol. 226 (2022) 109497.

[117] J. Maurer, D. Salaberger, M. Jerabek, B. Fröhler, J. Kastner, Z. Major, Fibre and failure characterization in long glass fibre reinforced polypropylene by X-ray computed tomography, Polymer Testing 130 (2024) 108313.

[118] Y. Sato, S. Nakajima, N. Shiraga, H. Atsumi, S. Yoshida, T. Koller, G. Gerig, R. Kikinis, Three-dimensional multi-scale line filter for segmentation and visualization of curvilinear structures in medical images, Medical Image Analysis 2(2) (1998) 143-168.

[119] M. Phalempin, M. Landl, G.-M. Wu, A. Schnepf, D. Vetterlein, S. Schlüter, Maize root-induced biopores do not influence root growth of subsequently grown maize plants in well aerated, fertilized and repacked soil columns, Soil and Tillage Research 221 (2022) 105398.

[120] Y. Chen, Y. Zhang, B. Pang, D. Wang, Z. Liu, G. Liu, Steel fiber orientational distribution and effects on 3D printed concrete with coarse aggregate, Materials and Structures 55(3) (2022) 100.

[121] A. Keilmann, M. Godehardt, A. Moghiseh, C. Redenbach, K. Schladitz, Improved anisotropic Gaussian filters, Image Analysis and Stereology 43 (2024) 9-22.

[122] O. Wirjadi, K. Schladitz, P. Easwaran, J. Ohser, Estimating fibre direction distributions of reinforced composites from tomographic images, Image Analysis and Stereology 35(3) (2016) 167-179.

[123] MATLAB R2023b, The MathWorks Inc. (2023), Natick, Massachusetts, United States.

[124] N. Otsu, A Threshold Selection Method from Gray-Level Histograms, IEEE Transactions on Systems, Man, and Cybernetics 9(1) (1979) 62-66.

[125] S.-Y. Chung, J.-S. Kim, D. Stephan, T.-S. Han, Overview of the use of micro-computed tomography (micro-CT) to investigate the relation between the material characteristics and properties of cement-based materials, Constr. Build. Mater. 229 (2019) 116843.

[126] H. Nguyen, V. Carvelli, T. Fujii, K. Okubo, Cement mortar reinforced with reclaimed carbon fibres, CFRP waste or prepreg carbon waste, Constr. Build. Mater. 126 (2016) 321-331.

[127] Y. Tao, S.A. Hadigheh, Z. Wang, Void Geometry Analysis and Multifaceted Characterisation of Cementitious Mortar Reinforced with Short Carbon and Glass Fibres – A Comparative Study, J. Build. Eng. (2024) 109283.

[128] E.R.K. Chandrathilaka, S.K. Baduge, P. Mendis, P.S.M. Thilakarathna, Structural applications of synthetic fibre reinforced cementitious composites: A review on material properties, fire behaviour, durability and structural performance, Structures 34 (2021) 550-574.

[129] N.P. Tran, C. Gunasekara, D.W. Law, S. Houshyar, S. Setunge, Microstructural characterisation of cementitious composite incorporating polymeric fibre: A comprehensive review, Constr. Build. Mater. 335 (2022) 127497.

[130] S.A. Hadigheh, R.J. Gravina, Generalization of the interface law for different FRP processing techniques in FRP-to-concrete bonded interfaces, Compos. B. Eng. 91 (2016) 399-407.

[131] M. Domingo, G. Ramos, Á.C. Aparicio, Use of fiber reinforced concrete in bridges – Metrorrey Line 2 case study, Eng. Struct. 276 (2023) 115373.

[132] H. Shakir, A. Al-Tameemi, A. Al-Azzawi, A review on hybrid fiber reinforced concrete pavements technology, Journal of Physics: Conference Series 1895 (2021) 012053.

[133] P.J. Robins, S.A. Austin, M.R. Richards, The resistance of steel fibre concrete to VTOL engine jet blast, Cem. Concr. Compos. 16(1) (1994) 57-64.

[134] G.C. Hoff, Use of Fiber-reinforced Concrete in Hydraulic Structures and Marine Environments, US Army Engineer Waterways Experiment Station1975.

[135] X. Wang, F. Fan, J. Lai, Y. Xie, Steel fiber reinforced concrete: A review of its material properties and usage in tunnel lining, Structures 34 (2021) 1080-1098.

[136] X. Liu, Q. Sun, Y. Yuan, L. Taerwe, Comparison of the structural behavior of reinforced concrete tunnel segments with steel fiber and synthetic fiber addition, Tunnelling and Underground Space Technology 103 (2020) 103506.

[137] A. Shakeri, A.M. Remennikov, M. Neaz Sheikh, Development of fibre-reinforced concrete mix for manufacturing non-prestressed concrete sleepers, Structures 37 (2022) 588-599.

[138] A. Belli, A. Mobili, T. Bellezze, F. Tittarelli, P. Cachim, Piezoresistive behavior of mortars loaded with graphene and carbon fibers for the development of self-sensing composites, (2019) 37-42.

[139] Fiber-reinforced Cementitious Composites Market Research Report - Segmented by Fiber (Glass Fiber, Steel Fiber, Natural Fiber, Synthetic Fiber (Micro-synthetic Fiber, Macro-synthetic Fiber), and others); Application (Building & Construction, Industrial Flooring, Infrastructure, Mining & Tunnel, Others); and Region - Size, Share, Growth Analysis | Forecast (2023 – 2030), Virtue Market Research, 2023.

[140] B. Marks, M. Miletić, B.C.H. Lee, M.H. Zia, J.A.O. Barros, D. Dias-da-Costa, Monitoring steel fibre orientation in self-compacting cementitious composite slabs during pouring with dynamic X-ray radiography, Cem. Concr. Res. 143 (2021) 106390.

[141] A.A. Hassen, H. Taheri, U.K. Vaidya, Non-destructive investigation of thermoplastic reinforced composites, Compos. B. Eng. 97 (2016) 244-254.

[142] A.C. Bordelon, J.R. Roesler, Spatial distribution of synthetic fibers in concrete with X-ray computed tomography, Cem. Concr. Compos. 53 (2014) 35-43.

[143] A.A. Hassen, A. Poudel, T. Chu, M. Yester, U. Vaidya, Tracing Defects in Glass Fiber/Polypropylene Composites Using Ultrasonic C-Scan and X-Ray Computed Tomography Methods, 2014.

[144] S. Guo, Q. Dai, X. Sun, Y. Sun, Ultrasonic scattering measurement of air void size distribution in hardened concrete samples, Constr. Build. Mater. 113 (2016) 415-422.

[145] J. de la Cruz, I. Segura, P. Pujadas, J.M. Torrents, A. de la Fuente, Non-destructive test approach for assessing the amount of fibre in polymeric fibre reinforced concrete, Constr. Build. Mater. 317 (2022) 125964.

[146] K. Karhunen, A. Seppänen, A. Lehikoinen, P.J.M. Monteiro, J.P. Kaipio, Electrical Resistance Tomography imaging of concrete, Cem. Concr. Res. 40(1) (2010) 137-145.

[147] Ł. Skarżyński, J. Suchorzewski, Mechanical and fracture properties of concrete reinforced with recycled and industrial steel fibers using Digital Image Correlation technique and X-ray micro computed tomography, Constr. Build. Mater. 183 (2018) 283-299.

[148] P. Lauff, P. Pugacheva, M. Rutzen, U. Weiß, O. Fischer, D. Volkmer, M.A. Peter, C.U. Grosse, Evaluation of the Behavior of Carbon Short Fiber Reinforced Concrete (CSFRC) Based on a Multi-Sensory Experimental Investigation and a Numerical Multiscale Approach, Materials, 2021.

[149] A. Patchen, S. Young, D. Penumadu, An Investigation of Mechanical Properties of Recycled Carbon Fiber Reinforced Ultra-High-Performance Concrete, Mater. Des. 16(1) (2022) 314.

[150] G. Trtnik, M. Gams, Recent advances of ultrasonic testing of cement based materials at early ages, Ultrasonics 54(1) (2014) 66-75.

[151] H. Jain, V. Patankar, M. Kulkarni, ULTRASONIC TESTING OF CONCRETE STRUCTURES: A REVIEW, 2021.

[152] S.A. Abo-Qudais, Effect of concrete mixing parameters on propagation of ultrasonic waves, Constr. Build. Mater. 19(4) (2005) 257-263.

[153] H. Jain, V.H. Patankar, Embedded system for ultrasonic imaging of under-water concrete structures, Journal of Instrumentation 16(07) (2021) P07049.

[154] C.-W. Tseng, Y.-F. Chang, C.-Y. Wang, Total Focusing Method or Phased Array Technique: Which Detection Technique Is Better for the Ultrasonic Nondestructive Testing of Concrete?, J. Mater. Civ. Eng. 30(1) (2018) 04017256.

[155] A. Ndagi, A. Umar, F. Hejazi, M. Jaafar, Non-destructive assessment of concrete deterioration by ultrasonic pulse velocity: A review, IOP Conference Series: Earth and Environmental Science, IOP Publishing, 2019, p. 012015.

[156] E. D'Accardi, F. Palano, R. Tamborrino, D. Palumbo, A. Tatì, R. Terzi, U. Galietti, Pulsed Phase Thermography Approach for the Characterization of Delaminations in CFRP and Comparison to Phased Array Ultrasonic Testing, Journal of Nondestructive Evaluation 38 (2019).

[157] Z. Luo, J. Kang, H. Cao, L. Lin, Enhanced ultrasonic total focusing imaging of CFRP corner with ray theory-based homogenization technique, Chinese Journal of Aeronautics 36(1) (2023) 434-443.

[158] E. Spyrou, T. Tsenis, V. Kappatos, Acousto-ultrasonic analysis of defects in composite specimens used in transportation domain, Journal of Measurements in Engineering 9 (2021) 117-127.

[159] D. Wei, Study on Ultrasonic Phased Array Detection of Hot Meltbutt Joint of Polyethylene Pipe, 2022 International Conference on Image Processing, Computer Vision and Machine Learning (ICICML), 2022, pp. 65-68.

[160] A. Chabot, N. Laroche, E. Carcreff, M. Rauch, J.Y. Hascoët, Towards defect monitoring for metallic additive manufacturing components using phased array ultrasonic testing, Journal of Intelligent Manufacturing 31(5) (2020) 1191-1201.

[161] X. Xu, B. Ran, N. Jiang, L. Xu, P. Huan, X. Zhang, Z. Li, A systematic review of ultrasonic techniques for defects detection in construction and building materials, Measurement 226 (2024) 114181.

[162] J. Rao, A. Saini, J. Yang, M. Ratassepp, Z. Fan, Ultrasonic imaging of irregularly shaped notches based on elastic reverse time migration, NDT & E International 107 (2019) 102135.

[163] B. Shan, J. Ou, An ultrasonic phased array system for NDT of steel structures, Fundamental Problems of Optoelectronics and Microelectronics II, SPIE, 2005, pp. 273-277.

[164] J. Rao, H. Qiu, G. Teng, R. Al Mukaddim, J. Xue, J. He, Ultrasonic array imaging of highly attenuative materials with spatio-temporal singular value decomposition, Ultrasonics 124 (2022) 106764.

[165] E.B. Ndiaye, P. Maréchal, H. Duflo, Adhesion characterization and defect sizing of sandwich honeycomb composites, Ultrasonics 62 (2015) 103-11.

[166] C. Zhang, P. Huthwaite, M. Lowe, The Application of the Factorization Method to the Subsurface Imaging of Surface-Breaking Cracks, IEEE Trans Ultrason Ferroelectr Freq Control 65(3) (2018) 497-512.

[167] X. Zhifei, R. Jing, E. Sascha, Y. Ka-Veng, S.A. Hadigheh, Generative adversarial network-based ultrasonic full waveform inversion for high-density polyethylene structures, Mechanical Systems and Signal Processing 224 (2025) 112160.

[168] J. Tian, Z. Chen, S. Lu, X. Qi, S. Pu, M. Liu, Phase coherence weighted ultrasound total focusing method towards the improved imaging of CFRP defects, Composites Communications 43 (2023) 101736.

[169] Z. Luo, S. Zhang, S. Jin, Z. Liu, L. Lin, Heterogeneous ultrasonic time-of-flight distribution in multidirectional CFRP corner and its implementation into total focusing method imaging, Composite Structures 294 (2022) 115789.

[170] Z. Yu, J. Chen, S. Wu, Y. Xie, H. Wu, H. Wang, H.-X. Peng, Adaptive ultrasonic full-matrix imaging of internal defects in CFRP laminates with arbitrary stacking sequences, Compos. B. Eng. 275 (2024) 111309.

[171] J. Tian, M. Liu, H. Xiao, Z. Zhang, W. Yang, Z. Long, C. Ming Leung, Optimized ultrasonic total focusing imaging of diverse and multiple defects in crossply CFRP: Floquet wave theory, numerical simulation, and experimental validation, Mechanical Systems and Signal Processing 199 (2023) 110486.

[172] Y. Tao, Z. Wang, S.A. Hadigheh, Enhancing X-ray micro-CT analysis for detecting voids and carbon fibre features in fibre-reinforced cementitious composites using advanced 3D Gaussian filtering, Measurement (2025) 117018.

[173] NRecon Version 2.0, Bruker Belgium, Kontich, Belgium, 2020.

[174] E.N. Landis, D.J. Corr, Three dimensional analysis of air void systems in concrete, Measuring, Monitoring and Modeling Concrete Properties: An International Symposium dedicated to Professor Surendra P. Shah, Northwestern University, USA, Springer, 2006, pp. 517-524.

[175] C. Clark, B. Drinkwater, P. Wilcox, The post-processing of ultrasonic array data using the total focusing method, Insight - Non-Destructive Testing and Condition Monitoring 46 (2004) 677-680.

[176] W. Zhu, Y. Xiang, H. Zhang, M. Zhang, G. Fan, H. Zhang, Super-resolution ultrasonic Lamb wave imaging based on sign coherence factor and total focusing method, Mechanical Systems and Signal Processing 190 (2023) 110121.

[177] A. Loshelder, J. He, M. Aktharuzzaman, M. Harb, J. Rao, Apex-shifted Radon transform for baseline-subtraction-free (BSF) damage scattered wave extraction, Structural Health Monitoring 22 (2023) 147592172311563.

[178] C. Fan, M. Caleap, M. Pan, B.W. Drinkwater, A comparison between ultrasonic array beamforming and super resolution imaging algorithms for non-destructive evaluation, Ultrasonics 54(7) (2014) 1842-1850.

[179] J. Rao, L. Zeng, M. Liu, H. Fu, Ultrasonic defect detection of high-density polyethylene pipe materials using FIR filtering and block-wise singular value decomposition, Ultrasonics 134 (2023) 107088.

Chapter 4: Improving Carbon-FRCC Performance through Fibre Surface Modification - Bio-based Treatments and Electrochemical Grafting

4.1 INTRODUCTION

As established in Chapter 3, the incorporation of short fibres was beneficial to enhance the mechanical and durability performance of CCs. However, this improvement was accompanied by the formation of elongated voids and increased porosity, primarily attributed to inefficient fibre dispersion and weak interfacial bonding. Advanced microstructural characterisation techniques, using X-ray micro-CT with a developed second-order anisotropic Gaussian filtering method, revealed that these elongated voids predominantly concentrated around the fibres. This microstructural deficiency poses a critical limitation, potentially undermining the long-term durability and shrinkage resistance of CCs by facilitating moisture ingress and microcracking.

CFs are widely utilised as discrete reinforcement in construction applications due to their excellent strength-to-weight ratio and durability. Repurposing short CF offcuts not only offers environmental and economic benefits but also presents an opportunity to enhance the sustainability and performance of CCs. Beyond enhancing mechanical and physical properties, CFs enable the development of smart concrete materials through their exceptional electrical conductivity. Despite their promising attributes and extensive research into carbon-FRCC, the inherent hydrophobic nature of the untreated CF surface leads to fibre agglomeration due to poor wettability and weak interfacial bonding with the cementitious matrix, which may ultimately compromise FRCC performance.

While commercial CFs typically include sizing designed for specific resin systems, this customisation complicates their direct incorporation into cementitious matrices. These challenges limit the effective utilisation of vCFs and rCF offcuts in mineral-based matrices, preventing the full realisation of performance potential. To address these challenges, researchers have developed various surface modification methods to alter the physical and chemical properties of CFs. These modifications aim to enhance fibre dispersion, reduce agglomeration, and improve interfacial load transfer between the fibres and cementitious

matrix. However, conventional treatment methods often face limitations in terms of cost-effectiveness, process complexity, environmental sustainability, and compatibility with cementitious systems.

In this chapter, two innovative CF surface modification approaches are proposed to solve the above-mentioned problems. Section 4.2 presents bio-based surface modifications using tannic acid (TA) and citric acid (CA), offering environmentally sustainable alternatives to conventional aggressive chemical treatments and providing efficient CF surface modifications at reduced costs. Section 4.3 introduces an in-situ electrochemical grafting approach for hydroxyl and amine groups on CFs, demonstrating its efficacy and suitability for continuous large-scale processing. The effectiveness of both modification approaches is systematically evaluated. Surface alterations of CFs are characterised through multiple analytical techniques, while the influence on interfacial properties and FRCC performance is assessed through mechanical testing. Microscopy analysis reveals the underlying interaction mechanisms between the treated CFs and the cementitious matrix.

4.2 BIO-BASED CROSS-LINKING AND ESTERIFICATION PROCESS FOR SURFACE FUNCTIONALISATION OF CARBON FIBRES IN FIBRE-REINFORCED CEMENTITIOUS COMPOSITES

Y. Tao[1,*], S.A. Hadigheh[1,*]

[1]School of Civil Engineering, Faculty of Engineering, The University of Sydney, Sydney, New South Wales 2006, Australia

[*]Corresponding Author: Dr Ali Hadigheh

Yunyun Tao

Composites Part A: Applied Science and Manufacturing,
https://doi.org/10.1016/j.compositesa.2025.109037, Published in May 2025.

4.2.1 Abstract

There has been growing research interest in surface modifications of carbon fibres (CFs) to enhance their bond performance with cementitious materials. While some methods are effective, they are often limited by environmental impact, high costs, and procedural complexity. Herein, this paper proposes novel bio-based surface modifications using tannic acid (TA) and citric acid (CA) to functionalise CF. These surface modifications are developed to promote fibre-matrix interactions and thus enhance the fibre-reinforced cementitious composites (FRCC) performance. The alterations in CF's physical and chemical properties are characterised by multiple tests. Enhanced mechanical strength is evaluated through compressive and flexural testing. The interaction mechanisms of surface-treated CFs within the cementitious matrix are analysed using SEM coupled with EDS. Co-deposition of TA with ethanolamine on the CF surface results in a polymeric layer that contributes to additional functional groups and significantly increases surface roughness. CA-treated CF also demonstrates irregular texture on the surface with the presence of ester groups through esterification reactions. The modifications facilitate hydration product precipitation, creating a denser microstructure between CF and matrix and increasing surface roughness which boosts mechanical adhesion. The proposed bio-based treatments also significantly enhance CF hydrophilicity and dispersibility, further facilitating better interactions with the cementitious matrix. Consequently, FRCC specimens containing 0.1 vol.% 12mm CF-TA and CF-CA exhibit notably enhanced compressive strength, with increases of 30.11% and 19.82% compared to the controlled mortar. These findings offer a new strategy for sustainable CF

surface modification techniques and their application in the construction industry, promising advancements in enhancing FRCC performance.

Keywords: Carbon fibre (CF), Fibre-reinforced cementitious composite (FRCC), Surface modification, Bio-based chemicals

4.2.2 Introduction

Fibre-reinforced cementitious composites (FRCCs) have become indispensable as an innovative and promising alternative to traditional steel-reinforced concrete in the construction industry. This type of material offers combined enhanced tensile and flexural properties, superior fire and corrosion resistance, as well as multifunctional capacities by incorporating various fibres, categorised as synthetic fibres (SyF) [1-3], steel fibres (SF) [4, 5], glass fibres (GF) [2, 3, 6], and natural fibres [7-9]. In addition to the benefits in structural performance and functionality, FRCCs also offer significant advantages in terms of environmental and economic sustainability. The use of fibre reinforcement in cementitious materials instead of traditional steel rebars contributes to a more cost-effective and environmentally sustainable infrastructure design [10, 11]. The building sector has a substantial influence on the global environment, responsible for over 40 percent of the total energy consumption worldwide [12], whereas the replacement of traditional steel bars with steel fibre in a tunnelling project can lead to significant material savings of over 50 percent and reduce the embodied carbon dioxide of the segmental lining by around 10kt for every 10km of tunnels on average [13]. Another case study, such as the CR44 Bridge in Hinckley, United States, has demonstrated that the use of synthetic fibres can significantly reduce maintenance requirements over a 50-year design life and extend service life, resulting in long-term cost savings and an approximate 10% reduction in carbon footprint compared to a standard concrete mix [14]. Moreover, comparative analyses of slab systems have shown that the adoption of fibre-reinforced concrete (FRC) can potentially reduce CO_2-equivalent emissions by over 66% compared to conventional reinforced concrete, demonstrating its value as a sustainable alternative in structural design [15]. Among the aforementioned benefits of FRCCs, carbon fibres (CFs) are widely used as reinforcement in construction applications owing to their high tensile strength-to-weight ratio and superior durability. Increasingly, carbon-FRCCs are being extensively studied and employed as smart concrete materials for applications such as self-heating [16], self-healing [17] and structural health monitoring [18]. However, commercial CFs are manufactured with sizing and are designed to be compatible with different resin systems on a case-by-case basis. This hampers

the direct and effective incorporation of virgin CFs (vCFs) and CF offcuts in cementitious or mineral-based matrices, hindering the full realisation of their potential for higher performance.

Recently, there has been a growing research interest in surface modifications of CFs to enhance the bond performance between CFs and cementitious materials. Those modifications target the alteration of CF physical and chemical properties and are categorised as plasma treatment, oxidation treatment, electrophoresis and grafting treatment [19, 20]. Surface oxidation treatment stands out as one of the most commonly used methods for fibre surface modification [21]. Oxidation induced by gases or liquids under various temperatures, durations, and concentration conditions can form oxygen-containing functional groups. These activated CF surfaces can chemisorb ions from the cementitious matrix, forming chemical bonds and promoting the precipitation of hydration products on the fibre surface. It was reported that both the electrical and mechanical properties of FRCC were greatly improved with acidic oxidation treatment (a piranha solution for 30 min at 30°C), which was attributed to the enhanced interaction and adhesion between the CFs and cement matrix [22]. However, the application of oxidative treatments has faced limitations due to its time-consuming nature and related environmental pollution implications. Plasma treatment using argon, nitrogen or oxygen is used as a more time-efficient approach to enhance surface roughness and introduce polar functional groups onto the CF surface, while it is associated with high operational costs from the required equipment and energy-intensive reaction conditions. This process increases the polarity and wettability of the CF surface and facilitates the fibre-matrix interphase region by forming more chemical bonds and accelerating the deposition of hydration products onto the CF surface. Jin Hee et al. [23] observed the improved interfacial bonding strength between a CF bundle and cement matrix for the argon plasma sample, which resulted from an interlocking mechanism. Recent developments in plasma functionalisation [24] have shown that SiOx films significantly enhance fibre-cement matrix bonding. This improvement is achieved by promoting the formation of localised calcium silicate hydrate (C-S-H) directly on the fibre surface, thereby enhancing both interfacial adhesion and mechanical anchorage. Another efficient method is coating CF with nanomaterials such as graphene oxide (GO) and nano-silica (NS) through an electrophoretic deposition (EPD) process, which enhances the interaction between CFs and cementitious matrices, effectively improving the pullout resistance and mechanical properties of the resulting cementitious composites [21, 25]. Grafting surface treatments such as silane coupling agent (SCA) treatment and GO grafting have also been reported as effective and efficient alternatives. By using the chemical graft approach, the tensile strength of CF grafted

with GO exhibited 22 percent enhancement compared to the untreated CF. Both chemical and physical properties of the CF surface and matrices were improved through mechanical interlocking and the development of hydration products [26]. These grafting techniques are less aggressive in damaging the CF surface while improving the bonding strength, leading to an increase in pullout load. Nevertheless, they may require complicated procedures and generate harmful waste products [19, 27].

Given the challenges of existing treatment methods, this study aims to develop environmentally friendly CF surface modification tailored to cementitious matrices. In contrast to conventional aggressive chemical treatment conditions, bio-based surface modification techniques offer a greener and more sustainable alternative while achieving efficiency in enhancing CF surface properties at a lower cost. Recent advances have demonstrated that strategies such as the use of bio-derived sizing agents and self-assembled hybrid interphases can significantly improve interfacial shear strength and fibre-epoxy matrix compatibility, while reducing environmental impact [28, 29]. The ideas and advancements are also expected to benefit cementitious systems by improving the adhesion between CF and the cementitious matrix through increased roughness for physical interlocking and the introduction of functional groups for hydrophilicity and chemical bonding mechanisms. Tannic acid (TA) and citric acid (CA) were selected primarily for their widespread availability and biodegradability. TA is a natural plant polyphenol with abundant reserves, widely obtained from various herbs, fruits and trees. Due to its non-toxic nature, it is widely used in the food and medical industries [30]. Polyphenol-based functionalisation has shown promising potential for fibre surface modification in cementitious systems [31, 32]. In particular, polydopamine (PDA), inspired by marine mussels, has demonstrated the ability to form adhesive coatings under mild conditions. PDA-functionalised waste carbon fibres (WCFs) have exhibited improved wettability, increased Ca^{2+} adsorption, and enhanced cement hydration at the fibre-matrix interface, resulting in denser microstructures and an 18% increase in compressive strength [33]. It has been reported in the literature that TA, which possesses a structure like dopamine, was utilised as a cost-effective and sustainable alternative, enhancing the hydrophilicity and chemical reactivity of fibre surfaces [34, 35]. While TA cannot self-polymerise through oxidative reactions like dopamine, it can undergo polymerisation with amino-terminated substances to create a thin layer coating containing amino and hydroxyl functional groups on the fibre surface, thereby improving the fibre-matrix interfacial bonding [30, 34, 36]. In contrast to the amino-functionalised system, where grafting with amino-containing compounds such as amino silanes

typically require fibre surface pretreatment in most cases [37-39], TA combined with amino-terminated substances enables more diverse functionalisation through multiple bonding mechanisms, without strictly requiring pretreatment. In addition to its functional benefits, TA offers key advantages such as lower cost, plant-based origin, and ease of processing [34, 36]. These attributes make it a promising candidate for green and scalable surface modification strategies in fibre-reinforced cementitious systems. Another weak organic acid from natural sources, CA, has been increasingly recognised in past studies for its ability to modify surfaces, including materials like activated carbon [40, 41], carbon nanotubes [42], and natural fibres [43]. The modification process introduces carboxyl functional groups, enhancing material properties for specific applications. In detail, the modification of activated carbon with CA has been reported to improve copper ion adsorption from aqueous solutions. In another case, the flexural and compressive strength of cementitious composites with flax fibres treated with a 5 wt.% CA solution improved by 18% compared to the control mortar and by 6% compared to those with untreated flax fibres. Previous research has demonstrated the application and promising effectiveness of TA and CA in surface modification. However, to the best of the authors' knowledge, there is a notable lack of research on the development of bio-based surface modification approaches using these acids for improving FRCC performance incorporating discrete CFs.

With this in mind, novel bio-based surface modifications using TA and CA to treat CF are developed in this research to promote fibre-matrix interactions, thus enhancing FRCC performance. Compared to conventional amino- and polyphenol-based functionalisation methods, the proposed TA-based approach offers a simpler, milder, and more sustainable alternative, while offering functionality and preserving fibre integrity. Previous studies have not yet explored the application of CA on CFs in cementitious matrices, which represents a critical research gap. Our proposed method advances beyond existing bio-based methods by providing an integrated and scalable approach, especially tailored and optimised for discrete CF reinforcement in cementitious matrix. In addition to its simplicity, low expense, and environmental safety, it is vital to ensure that these treatment procedures are designed to maximise their functionality while minimising any potential disadvantages related to damage to the CF surface that could compromise its inherent mechanical strength. To compare the effectiveness of TA and CA surface modifications without the interference of the sizing agent, an effective desizing process is proposed prior to the surface modification. The bio-based solution ratio is controlled to optimise its effectiveness, while the reaction occurs under mild

conditions, ensuring the process is both efficient and practical for applications. Subsequently, the chemical properties - introduction of functional groups (such as OH, NH_2, COOH and C=O) and physical properties - fibre tensile strength and surface roughness are examined. These characterisations of CF before and after treatment are used to elucidate the underlying mechanisms and alterations induced by these surface modifications. Furthermore, the improvements in dispersion, flowability, and mechanical performance of FRCCs with surface-modified CFs are investigated through multiple testing methods.

4.2.3 Materials and methods

4.2.3.1 Materials

The vCF (T700SC-12000-50C) were received on a spool and supplied by Toray Industries, Inc. (France). The technical sheet indicates that the fibre properties include a diameter of 7µm, a density of 1.8 g/cm³ and a tensile strength of 4,900 MPa. All the chemicals in this study were used as received. TA ($C_{76}H_{52}O_{46}$) and ethanolamine (EA) (C_2H_7NO) were purchased from Sigma-Aldrich Pty Ltd. CA monohydrate ($C_6H_8O_7 \cdot H_2O$) AJAX Finechem was purchased from Thermo Fisher Scientific Inc. Acetone and ethanol used in the experiments were analytical grade. The pH buffer solution complied with BS EN ISO 3696 [44], and deionised water was used for the fibre modification process.

A general-purpose cement (type GP as specified in Australian Standard AS3972 [45]), with 90% of particles finer than 42.4µm, was used for casting FRCC. Macka's sand, with 90% of aggregates finer than 576µm and compliant with AS2758.1 [46], was used as the fine aggregate. Tap water was used for fresh mortar mixing.

Table 4-1. Properties of GP cement (SDS No. CASDS01).

Chemical entity		Physical and chemical properties	
Portland Clinker	<97%	Appearance	A fine powder ranging in colour from grey to off-white
Gypsum ($CaSO_4.2H_2O$)	2-5%	Boiling/Melting Point	Melting point >1200°C
Limestone ($CaCO_3$)	0-7.5%	Specific Gravity	3.0 – 3.2
Calcium Oxide	0-1%	Solubility in Water	Slight, reacts on mixing with water forming an alkaline (caustic) solution (pH >11)

4.2.3.2 CF surficial treatment with bio-based chemicals

The entire process for the CF surficial treatment is schematically illustrated in Figure 4-1. The vCFs underwent desizing by using acetone as a solvent within a reflux system at 60 degrees for a duration of 12 hours. In contrast to thermal desizing, this desizing process required lower energy requirements and minimised the risk of damaging the CF surface, thereby offering an alternative to high-temperature operations. The degree of desizing achieved through this acetone treatment was previously validated and reported in the authors' previous work [47]. The decrease in the oxygen-to-carbon ratio and functional groups in the XPS spectra, along with the smoother fibre surfaces observed via SEM, collectively confirmed the successful removal of the sizing layer.

After this initial treatment, the desized CFs were treated by TA/EA and CA individually to produce two bio-based chemical-treated-CFs. For the first portion of desized CFs, the solution was prepared by mixing TA and EA in an alkaline aqueous solution with a pH of 8.5 (1L for each batch) following the recommended mass ratio of 2:5 by Bashiri Rezaie et al. [34]. CFs were immersed in the respective solution allowing the reactions to proceed at ambient temperature for the next 12 hours. The second portion of desized CFs was treated by a two-step process. A mild air oxidation procedure at a relatively low temperature of 250°C for 30 minutes was conducted. Subsequent to this pretreatment, the oxidised CFs were introduced into a 5% CA solution and the mixture was heated in a reflux system maintained at a temperature of 90 degrees for an hour. For both treatments, a magnetic stirrer and a sonicator were employed to facilitate mixing and ensure sufficient interaction between the fibre surface and the respective chemicals. After the functionalisation, treated CFs were thoroughly rinsed with ethanol and deionised water to remove the remaining unreacted chemicals on the surface, followed by the drying process. For simplification, vCF was denoted as CF-V in this paper, while CFs treated with TA and CA were designated as CF-TA and CF-CA, respectively.

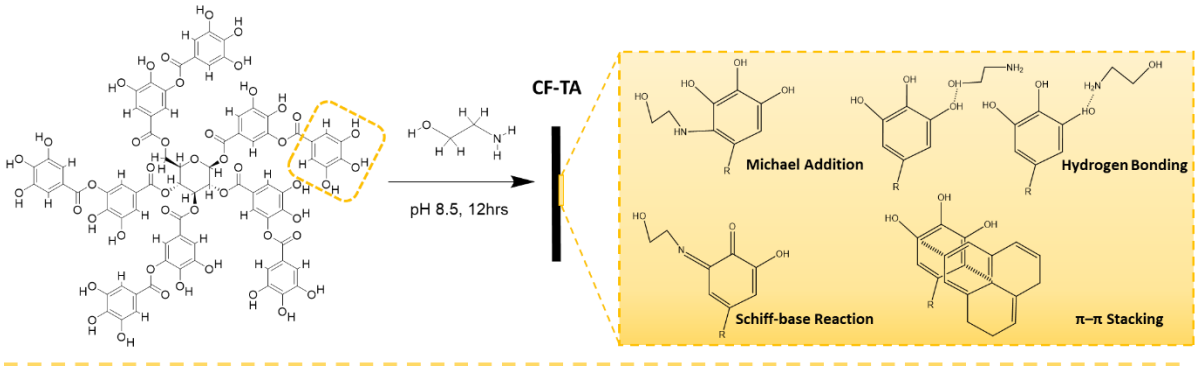

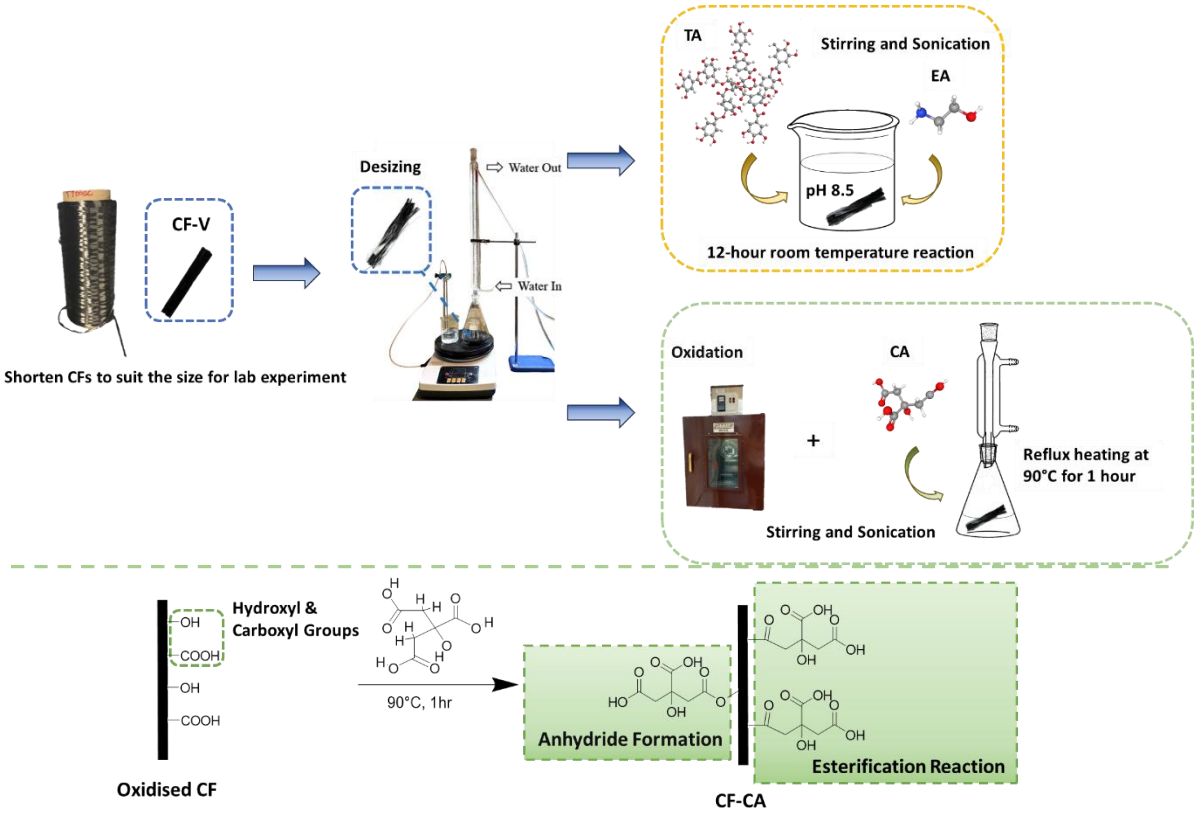

Figure 4-1. Schematic illustration of bio-based chemical CF surface modification.

4.2.3.3 Preparation of CF-reinforced cementitious composites

Two doses (0.1%, 0.5% volume of mixture) and two lengths (6mm, 12mm) of CFs were examined, resulting in four combinations for each type of CF, as shown in Table 4-2. A controlled mortar specimen without any CF was used as a reference, and a group of FRCC specimens with vCFs were also prepared for comparison with the specimens containing bio-based surface-modified CFs.

Dry CFs were mixed with cement initially and stirred for three minutes to ensure the fibres were uniformly dispersed in the dry cement mix. Sand and water were then gradually added to the mix and stirred until the flow value showed consistency as stated in BS EN 1015–3 [48]. A vibration table was used to assist in compacting the mortar mixture and reducing pores. The fresh mortar paste was poured into 50×50×50 mm³ moulds for compressive testing, electrical resistivity measurement, and water absorption tests, and 40×40×160 mm³ moulds for flexural testing. Subsequently, the specimens were demoulded and stored in a standard curing environment (temperature of 23°C and 95% humidity) until testing. The mass ratios of cement, water, and sand were specified as 1:0.55:1.5.

Table 4-2. Designations of FRCC specimens with varying dose, length, and surface modification combinations.

Surface modification	Samples ID (Dose-Length)	Dose (%)	Length (mm)
Controlled Mortar	CM	-	-
CF-V/ CF-TA/ CF-VA	0.1-6	0.1	6
	0.5-6	0.5	6
	0.1-12	0.1	12
	0.5-12	0.5	12

4.2.3.4 Characterisation and testing methods

CF Surface Characterisation

The surface morphology of CF was examined using a Zeiss Ultra Plus scanning electron microscope (SEM) at an acceleration voltage of 10 kV with the SE2 detector. CF specimens were directly mounted onto the specimen stub using carbon tape without coating.

Raman spectroscopies were recorded using a Renishaw Raman InVia Qontor Microscope for CF specimen excitation, achieved with a Renishaw RL532C CW diode laser emitting at 532 nm. Spectra were recorded using the 50× objective, with the accumulation of 3 scans, 10-second exposure, and a laser power of 3.95%.

CF surface chemical analysis was conducted by using X-ray spectroscopy (XPS) to determine the success of surface modifications. X-ray photoelectron spectra were collected using a Thermo Scientific K-alpha+ XPS spectrometer, equipped with a monochromatic Al K-alpha X-ray source and a 180° double focusing, hemispherical analyser with a 128-channel detector. A spot size of 400 µm was used. A spot size of 400 µm was used with 10 scans for each specimen to ensure accurate surface analysis while reducing the signal-to-noise ratio. The instrument was operated in Constant Analyzer Energy (CAE) mode, with a pass energy of 50.0 eV for high-resolution elemental scans and 200.0 eV for wide survey scans, optimising energy resolution. A step size of 0.10 eV was employed, allowing for the precise determination of the binding energies of surface elements. Analysis of photoelectron spectra was carried out using the Avantage (v6.6.0 Alpha) software [49].

A Bruker Innova atomic force microscope (AFM) was employed to acquire 3D topographical images at the nanometre scale for quantitative analysis of surface roughness. Prior to testing, a very thin layer of CFs (approximately 5 × 5 mm area) was adhered to carbon

double-sided tape to ensure no movement of each individual CF, with silver paint used to fix both ends. The AFM tip scanned the CFs in tapping mode, focusing on surface features with a scan rate of 0.5 Hz and scan ranges of 2 μm. Nasoscope Analysis software (3.0) [50] was then used for cropping, processing, and calculating the roughness of the images.

In order to determine the dispersibility of CF before and after surface treatments, the Zeta potentials of CF suspensions were measured with the Malvern Zetasizer Nano-ZS. During the process, CF suspensions were prepared at three different concentration levels: 0.1%, 0.2%, and 0.3%. The separation or uniform dispersion of CF with different treatments was also visually assessed at three different time intervals.

Single fibre tensile test

Single fibre tensile test (SFTT) was performed according to ASTM C1557-20 [51] using a Dynamic Mechanical Analyser (DMA) 850 with an 18N load cell. Single CFs were randomly sampled from virgin and surface-modified CF bundles for testing. For the preparation of the test specimens, typical paper coupons (24mm×7mm) were used with a 12mm gauge length. A 5mm diameter hole was created in the middle of the tab, and superglue was used to secure the fibre's position. Before loading, a test specimen was positioned and secured by tensile clamps into the DMA machine. The axis of a single CF was oriented perpendicular to the crosshead of the machine. The paper coupon was then cut along the middle line. The experimental setup is illustrated in Figure 4-6. An initial load of 0.01N was introduced before the commencement of the loading phase to ensure the fibre was properly engaged and resisting the load. The crosshead was then set to operate at a speed of 0.2 mm/min. A small portion of each CF sample was collected for measuring the fibre diameter using SEM.

A two-parameter Weibull statistical analysis was performed to assess the variability of the tensile strength across 30 single fibre specimens for each type of CF. The data were fitted to a linearised Weibull distribution, yielding a correlation coefficient $R^2 > 0.9$, indicating a strong linear relationship and minimal variability in fibre tensile strength [52]. The Weibull probability (P), was calculated using the following equation:

$$P = 1 - exp\left[-\left(\frac{\sigma}{\sigma_0}\right)^m\right] \quad 4\text{-}1$$

where P represents the cumulative probability of failure of a CF at applied tensile stress σ, m is the Weibull modulus (or shape parameter) characterising the variability in fibre strength, and σ_0 is the Weibull scale parameter, also known as the characteristic stress. The probability P for each data point is determined using the median rank method:

$$P = \frac{i-0.3}{n+0.4} \quad 4\text{-}2$$

where n is the total number of sample points, and i represents the rank of each data point. By rearranging the Weibull probability expression into a linearised form, the Weibull modulus m and scale parameter σ_0 can be determined through linear regression.

Flowability and mechanical properties

The effect of CF surface modification on FRCC flowability was investigated by conducting a flow table test based on BS EN 1015-3 [53]. Compressive strengths of 50×50×50 mm^3 cubic specimens at 28 days were determined using an MTS Sintech 65/G machine with a 300kN load cell at a loading rate of 0.5mm/min, in accordance with ASTM C109/C109M [54]. The combination of 0.1% dosage and 12 mm CF length was selected from each group for an additional round of flexural testing, based on the optimum compressive strength results (Section 4.2.4.4). The 28d flexural strengths were evaluated using a three-point bending test on 40×40×160 mm^3 prism specimens at a loading rate of 0.1mm/min according to ASTM C348–21 [55]. Three duplicated specimens were used for mechanical testing. A digital image correlation (DIC) system was implemented to monitor surface cracks with high resolution during the bending tests. A Canon EOS 6D Mark II camera equipped with an EF 24-105mm lens, was used to capture surface patterns (white speckles on a black background) at regular intervals of 3 seconds throughout the testing.

Bulk resistivity measurement and water absorption

Bulk resistivity and water absorption measurements were also conducted using 50×50×50 mm^3 cubic specimens. The testing allowed for the evaluation of the impact of various factors, including CF surface treatment, lengths and concentrations on FRCCs' electrical properties and durability. Water absorption served as a key indicator of the total porosity in cementitious materials by measuring the total amount of water absorbed. The measuring procedure followed AASHTO T 358-15 [56] for bulk resistivity and ASTM C948–81 [57] for water absorption.

Microstructural analysis

The Zeiss Ultra Plus SEM was also used to investigate the internal microstructure of 28-day specimens, focusing on the interfacial transition zone (ITZ) between CFs and the cementitious matrix. Smaller mortar samples (5–10 mm) were collected after mechanical testing and coated with a 10 nm layer of gold spray to reduce surface charging for imaging

quality. During the test, the acceleration voltage and working distance were set to 10 kV and around 8 mm, respectively.

4.2.4 Results and discussion

4.2.4.1 Surface characterisation of modified CFs

The SEM images of the CFs before and after bio-based treatments revealed minimal physical differences, as anticipated, indicating no observable damage during the process. CF-V showed a completely smooth surface (Figure 4-2 (a)). In contrast, a coating layer was observed on the CF surface after the co-deposition of TA and EA, resulting in a less distinct and flat surface profile, as shown in Figure 4-2 (b). Additionally, protrusions and deposits were clearly visible on the surface (Figure 4-2 (c)). The CF surface treated with CA also exhibited an irregular texture with some agglomerates covering the surface (Figure 4-2 (d) to (e)). These features suggest successful chemical deposition and alteration of the surface morphology, potentially increasing its physical roughness.

To evaluate the changes in the carbon structure on the CF surface subjected to bio-based treatments, the I_D to I_G ratio from Raman spectra (calculated as the ratio between the integral areas under the D and G bands) was determined. The D and G bands are two prominent peaks at around 1350 cm^{-1} and 1600 cm^{-1}. The D band presents the disordered structures within graphite, while the G band corresponds to the planar configuration of carbon atoms. Thus, I_D/I_G ratio in this study was used for measuring any structural disorder resulting from the treatments. Figure 4-2 (f) plot displays the comparison of intensity ratios of I_D/I_G before and after bio-based treatments. The CF-V had a ratio of 1.66. In comparison, the CF-TA and CF-CA showed slight increases of 1.5% and 3.2% individually. Hence, the results indicate that more disordered sites were introduced onto CF surfaces due to the surface modification without causing significant damage, which is expected to enhance the interactions between CF surfaces and the cementitious matrix.

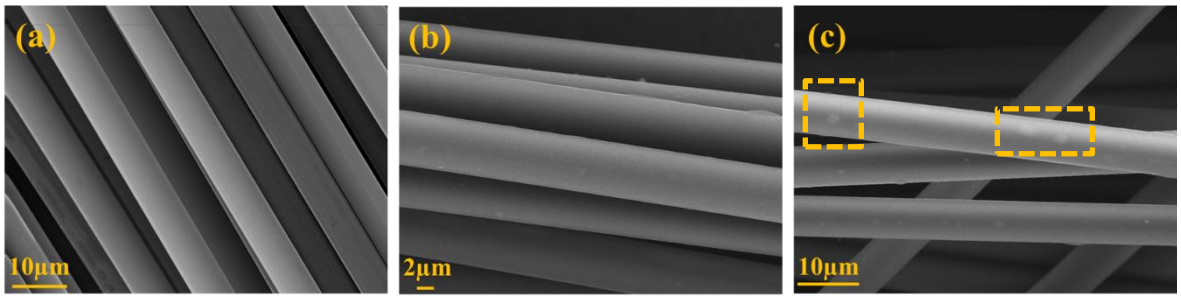

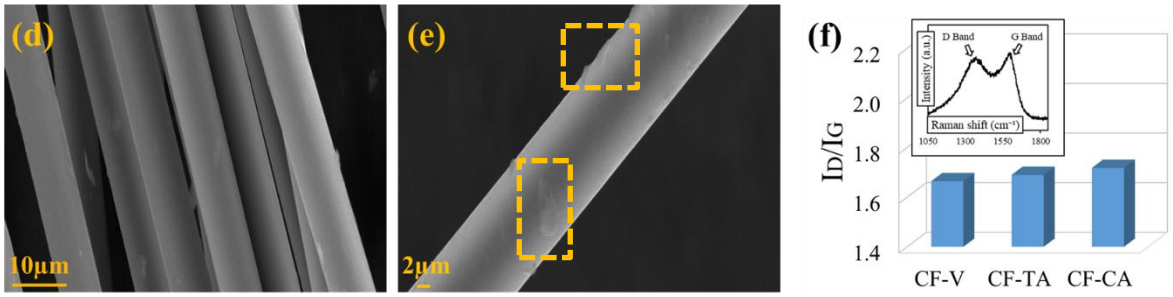

Figure 4-2. SEM images on the surface morphology of (a) CF-V, (b) to (c) CF-TA, (d) to (e) CF-CA; and (f) Raman Spectroscopy I_D/I_G.

The chemical composition of the CF surface was investigated by XPS to evaluate the effectiveness of the bio-based modification. Figure 4-3 (a) shows the wide-scan XPS spectra of all three CF bundles. As expected, all specimens show dominant peaks at around 533 eV and 285 eV, corresponding to oxygen (O1s) and carbon (C1s), respectively. Minor peaks of nitrogen (N1s) and silica (Si2s and Si2p) are also observed. The oxygen-to-carbon ratio of CF-V was detected as 0.219, consistent with the findings of previous research conducted by other authors [30], while only minimal traces of nitrogen were found, with a nitrogen-to-carbon ratio of 0.009.

The spectra of TA- and CA- modified CFs showed increased proportions of both oxygen (O/C) and nitrogen (N/C) after treatment, as listed in Figure 4-3 (d). The high resolution of C1s, N1s and O1s spectra are displayed in Figure 4-3 (b), (c) and (e). For CF-V, the main peaks were attributed to C-C, C-O, C=O, and O-C=O/COOH, with C-C and C-O accounting for 62.8% and 27.2%, respectively. The high proportion of C-O peaks observed in both the C1s and O1s spectra is attributed to the presence of a commercial sizing layer typically applied to as-received T700 CFs. In the case of CF-TA, the wide peak at 289.6 eV (accounts for 2.4%) indicated the π-π interactions between the electron clouds of the aromatic rings in TA and those on the CF, enhancing the adhesion of TA to the CF surface [35]. The additional C-N peaks (accounting for 20.1%) were observed at 285.5 eV, alongside the existing peaks. The N1s spectrum also exhibited more distinct nitrogen peaks at 400.2 eV (-NH-), 401.3 eV (-NH_2-), and 397.8 eV (=N-). In mild alkaline conditions, EA reacts with the phenolic hydroxyl groups of TA to form a polymeric layer on the CF surface [34]. Based on the XPS qualitative and quantitative analysis, the participation of EA and TA on the CF surface is evidenced through reactions, including Michael addition, Schiff-base reactions, or hydrogen bonding. This is further supported by the significant increase in carbonyl groups (C=O /O–C=O) in the O1s spectrum, which rose from 2.92% in CF-V to 22.37% in CF-TA (Figure 4-3 (f)), indicating the successful introduction of additional oxygen-containing polar functionalities.

In the bio-based treatment using CA, in addition to the increased O/C and N/C ratios from the XPS survey, the high-resolution C1s spectra of CF after CA treatment revealed certain C-O groups (18.5%) and higher proportions of C=O (12.6%) and O-C=O/COOH (5.2%) compared to CF-V. This indicates that CA underwent dehydration of carboxyl groups and esterification reactions with the carboxyl groups, resulting in the presence of ester groups and anhydride bonds. Both the O1s spectrum and quantitative O1s deconvolution (Figure 4-3 (e) and (f)) revealed a marked increase in C=O / O–C=O, reaching 21.04%. CF-CA also exhibited a moderate level of -COOH, suggesting the presence of residual carboxyl groups following the treatment process. The introduction of additional functional groups on the CF surface is also expected to contribute to increased reactive interaction between CF and the cementitious matrix.

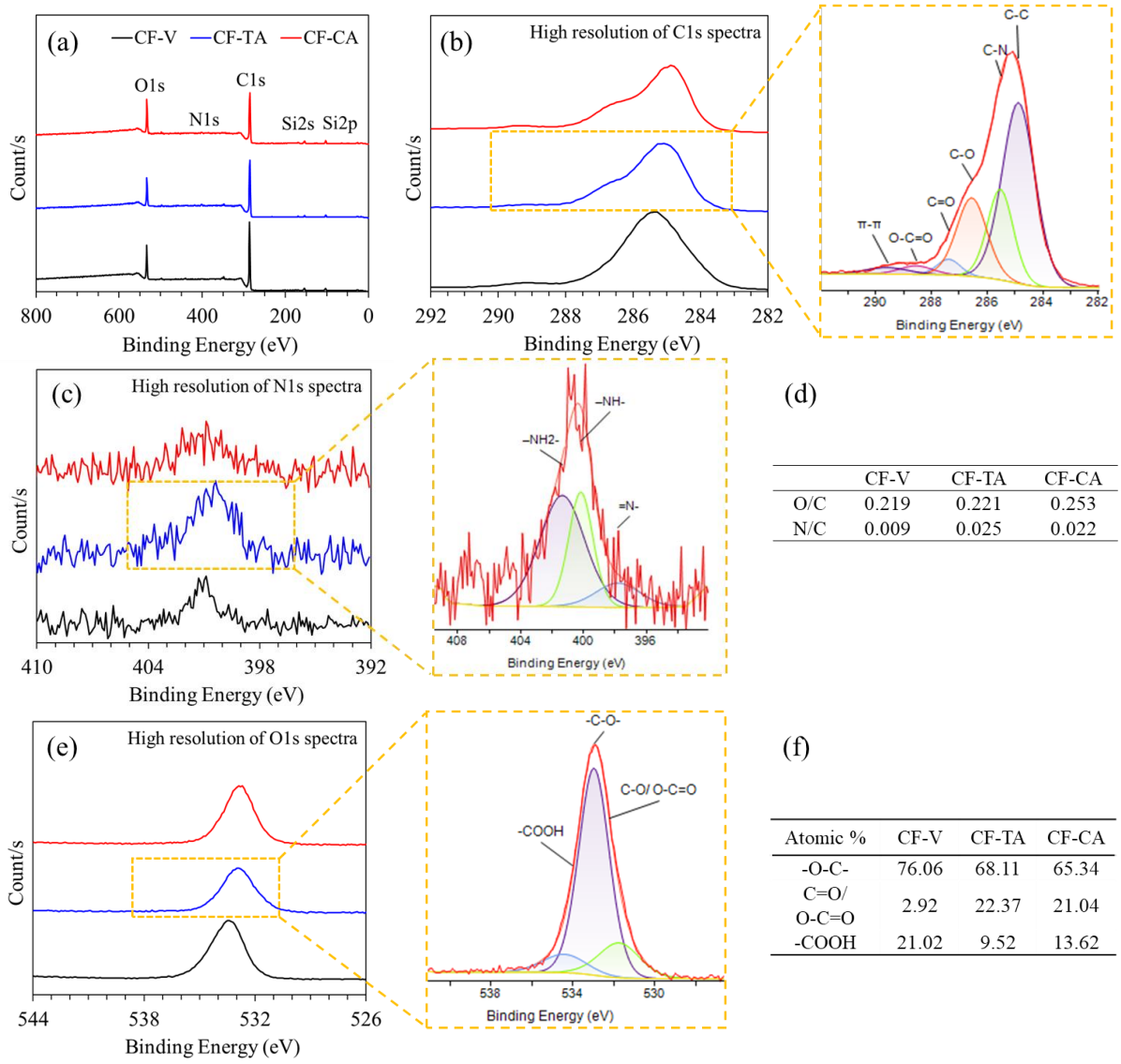

	CF-V	CF-TA	CF-CA
O/C	0.219	0.221	0.253
N/C	0.009	0.025	0.022

Atomic %	CF-V	CF-TA	CF-CA
-O-C-	76.06	68.11	65.34
C=O/ O-C=O	2.92	22.37	21.04
-COOH	21.02	9.52	13.62

Figure 4-3. (a) XPS Survey, (b) & (c) High-resolution C1s & N1s spectra, (d) Surface element atomic ratios, and (e) & (f) High-resolution of O1s spectra of CF surface from XPS analysis.

In addition to morphology, graphite structure, and chemical information on the CF surface, visualising the topography also helps in understanding the effects of bio-based treatment on the CF surface and its impact when incorporating these CFs into a cementitious matrix. In this case, AFM was used to scan the CF surface and provide quantitative roughness analysis at the nanoscale. The topography and surface height profiles are presented in Figure 4-4 (a). The scans focused on the area of 2 × 2μm. The cross-sectional height profiles were extracted along the midline of each scan area, as indicated by the green arrows. It is observed that CF-V exhibited a relatively smooth surface, consistent with the SEM images, while CF-TA and CF-CA displayed varying degrees of roughness. From these images, the deposits on the curvature of the CF surface are more clearly visible. A layer of protrusions of varying heights was clearly observed on the CF-TA surface, and noticeable deposits were also evident on the CF-CA surface. (as highlighted by the green circles in Figure 4-4 (a)). The images were then processed with 2nd order flattening for roughness calculations, which means only the height variations on the surface were considered, excluding curvature influences. As seen in Figure 4-4 (b), the brightness shown on the processed 2D images represents the height variations. Average roughness (Ra) and root mean square roughness (Rq) were compared to provide a more comprehensive assessment of surface texture. Ra provides a general measure of surface roughness by averaging deviations from the mean line, whereas Rq accounts for the variation in roughness by giving more weight to larger deviations. Although Ra offers a simplified representation of surface texture, it lacks the sensitivity to accurately reflect the morphological characteristics of surface irregularities. Due to the coating layer on the CF-TA surface, the roughness of CF-TA doubled, with a significant increase of 103.8% in Ra and 88.4% in Rq, compared to CF-V. This reflects the uniform and substantial roughening effect. The yellow highlights regions of interest where distinct surface features are observed. In contrast, there was a reduction in Ra (-24.5%) after treatment with CA, but Rq is larger than that of CF-V (+12.5%), compared to CF-V. The as-received CF-V contains a sizing layer, which contributes to its initial surface roughness. The decrease in Ra following CA treatment likely reflects the removal of this sizing layer through desizing process. Meanwhile, the increase in Rq indicates greater surface height variation. This divergence suggests that the CA treatment created a less uniformly rough surface with localised surface features of greater height variation. These variations are evident in the brighter spots highlighted in yellow in the 2D AFM images of CF-CA in Figure 4-4 (b).

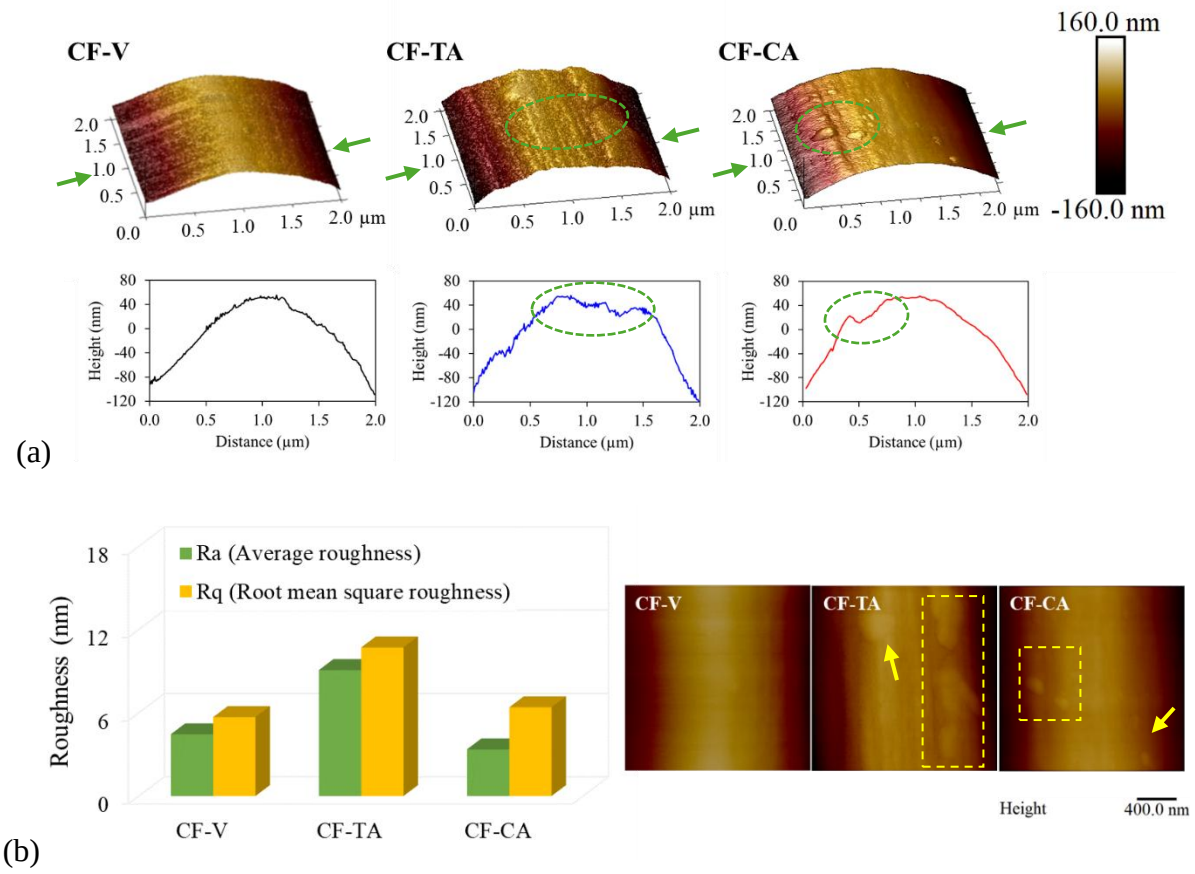

Figure 4-4. (a) Representative AFM images and surface height profiles, and (b) surface roughness of CFs.

4.2.4.2 Dispersion level and tensile strength

The dispersity of CFs in cementitious materials before and after bio-based treatment was characterised by zeta potential testing. The zeta potential value was measured to assess the stability of CF suspensions, with larger absolute values indicating greater stability. Short CFs were milled and sieved into powder passing through 600 μm sieves, with a dosage of up to 0.3% considered suitable for measuring the CF suspension in the cuvette. The mixed suspension was sonicated before being injected into the cuvette for testing. The dispersion of CF in water was monitored for up to 120 minutes. Figure 4-5 (b) provides a visual comparison between the two treatments, demonstrating that TA treatment resulted in a better dispersion. Visual observations were recorded at three time points: 30, 60, and 120 minutes. CF-V suspension was observed either floating on the surface of the suspension or depositing at the bottom, with separation becoming more pronounced over time. In contrast, CF-TA exhibited enhanced uniformity of dispersion in water and resistance to agglomeration. The influence of bio-based treatments and different CF concentrations in solution on the zeta potential values was

investigated. As shown in Figure 4-5 (a), for CFs both before and after treatment, zeta potential values decreased from 0.1% to 0.2%, indicating the best stability at 0.2%, and increased slightly at 0.3%. Compared to the CF-V measured at -25 mV at 0.2%, CF-CA and CF-TA had larger negative values of -29.77 mV and -25.97 mV, respectively. This results in greater electrostatic repulsion between CFs, especially for the TA-treated ones, due to modifications in fibre surface chemistry. Both bio-based treatments introduce multiple functional groups onto the CF surface (as seen in Figure 4-1), thereby enhancing the hydrophilicity and negative charge. These surface modifications expand the electrical double layer surrounding fibres, intensifying electrostatic repulsion [58, 59]. This repulsive force counteracts van der Waals attractions and mitigates hydrophobic interactions that typically lead to fibre agglomeration [58]. In cementitious suspensions, the enhanced electrostatic interactions are critical for maintaining fibre separation, thereby improving dispersion stability.

Overall, the results demonstrate the beneficial impact of functional groups on the CF surface introduced through bio-based chemical surface modification. This kind of surface modification enhances CF dispersion and stability in the mixture, preventing fibre agglomeration. Consequently, it potentially facilitates better interactions between CF and the cementitious matrix and reduces void formation.

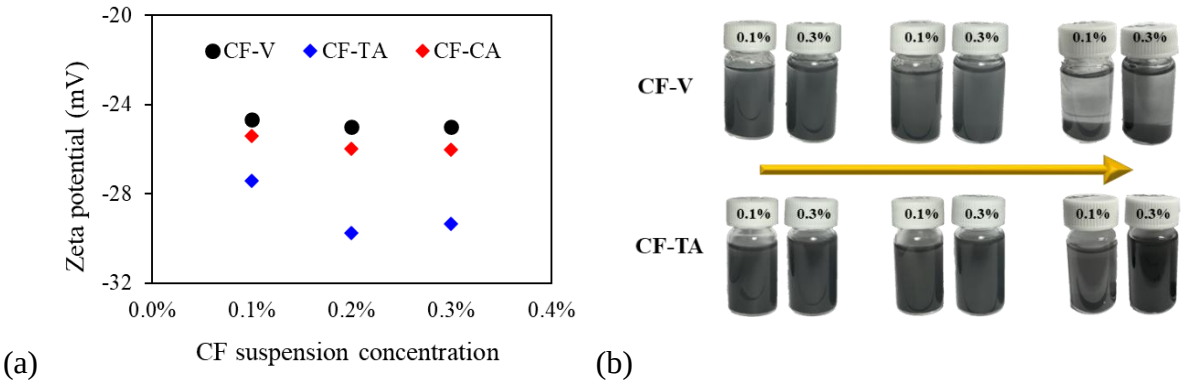

Figure 4-5. (a) Zeta potential of different CF suspension concentrations, and (b) Visual observation of CF dispersion in water.

The effect of bio-based surface modification on fibre tensile strength was investigated using SFTT performed with a DMA machine. The results of average and median tensile strength are shown in Figure 4-6 (a). While fibre strength is typically affected by surface defects [52], the bio-based treatment employed in this study did not significantly alter the axial tensile strength of individual CFs. The treated fibres maintained even slightly higher strength capacity, and no substantial damage occurred during the treatment process, as the SEM images confirmed (Section 4.2.4.1). This preservation of strength was observed despite a slight increase in the

I_D/I_G ratio (up to 3.2%), as indicated by Raman analysis. This can be attributed to the surface morphology resulting from the treatment with these bio-based chemicals. The deposition of TA and EA formed a nano-layer coverage on the CF surface, which effectively covered minor defects [60]. Similarly, gentle surface modification with CA also produced a smoothing effect on the CF surface.

As shown in Figure 4-6 (b) and Table 4-3, a two-parameter Weibull statistical analysis was conducted to evaluate the adequacy of the collected data points (comprising 30 measurements in this study) in determining the variability of SFTT. The Weibull modulus increased from 6.86 for CF-V to 7.25 and 8.31 for CF-TA and CF-CA, respectively, indicating relatively homogeneous bio-based treatment and less variability in the strength of CF. Concurrently, the scale parameter for bio-based treated CFs showed a slight increase compared to CF-V, suggesting an improvement in overall strength. All the correlation coefficients (R^2) derived from the tensile testing were ensured to be greater than 0.9, indicating that these measurements followed a statistical distribution and were acceptable for evaluating the tensile performance with negligible variability [52, 61].

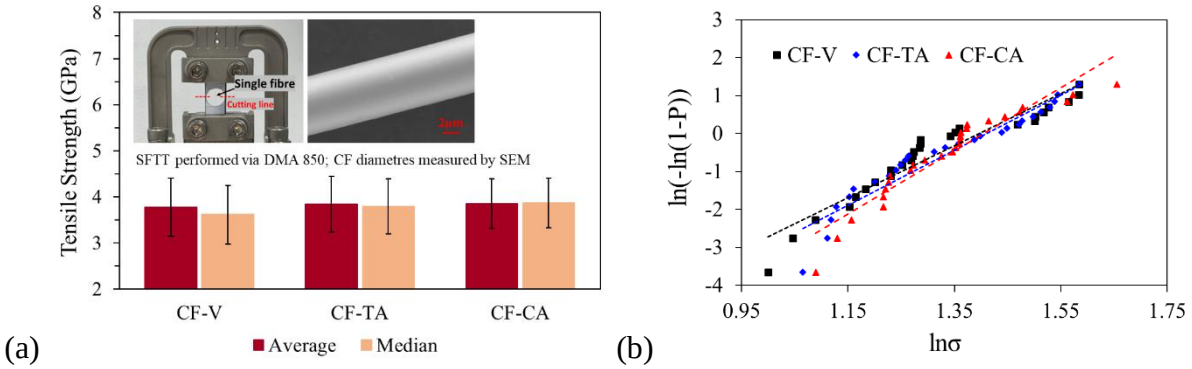

Figure 4-6. (a) Tensile strength, and (b) Weibull distributions for SFTT.

Table 4-3. Weibull parameters for SFTT.

	Linear Trendline Equation	R-squared Value	Weibull Modulus (m)	Scale Parameter (σ_0)
CF-V	y = 6.859x - 9.575	0.92	6.86	4.03
CF-TA	y = 7.2471x - 10.217	0.92	7.25	4.10
CF-CA	y = 8.305x - 11.666	0.90	8.31	4.07

4.2.4.3 Flowability, porosity and bulk resistivity of FRCC

The incorporation of CFs notably impacted the flowability of the fresh cement paste as CF dosage and length increased. As shown in Figure 4-7 (a), visual observation during the casting process revealed that the CM fresh paste appeared smooth without fibre addition. In contrast, the pastes with incorporated CFs exhibited a rougher surface with visible entangled fibres, primarily due to fibre agglomeration and air entrapment. Figure 4-7 (b) also indicates that, compared to CM, the incorporation of CFs reduced the flow value in all combinations, with up to a 26.52% reduction observed in the mix CF-V/0.5-12 compared to CM in the flow table test. Bio-based surface modification was employed to mitigate the potential side effects caused by the incorporation of CFs. The flowability of the mixes with surface-modified CFs (CF-TA and CF-CA) showed different levels of improvement compared to CF-V. The mix containing CF-TA, incorporating 0.1% of 6mm modified CFs resulted in a 3.81% increase in flow value. The influence of CF-CA on flowability was more pronounced, with an enhancement in flow value of up to 11.73% of the mix with the addition of 0.5 vol.% 12mm CFs. The overall improvement in the flowability of the cementitious mortar with bio-based modified CFs was attributed to the hydrophilic CF surface. As discussed in Sections 4.2.4.1 and 4.2.4.2, the chemical elements and functional groups attached to the CF surface after bio-based surface modification included polar functional groups such as hydroxyl, carboxyl, and amine groups. These groups enhance the hydrophilicity of CF surfaces, making them more compatible with the cement matrix and improving dispersion. While hydrophilic CFs may absorb water, their improved dispersion in the cementitious matrix can enhance the overall flowability. Compared to CF-CA, CF-TA showed reduced flowability, likely due to greater water absorption. Additionally, the relatively lower roughness of CA-treated CF compared to TA-treated CF resulted in reduced internal friction within the cement matrix, leading to a more pronounced enhancement in flowability.

Through water absorption measurements, it was revealed that the total porosity of all CF-V mixes increased by up to 12.60% compared to the CM (Figure 4-7 (c)). This increase was attributed to the additional ITZ between the vCF and the cement matrix, leading to the presence of gaps and potentially due to the fibre clusters creating more voids. However, after bio-based surface modification, this negative behaviour was mitigated for all combinations. Notably, the voids were even reduced in the combinations of 0.1-6, 0.5-6, and 0.1-12 for both TA and CA-treated groups, with reductions of up to 4.27% compared to the CM. This indicates that the treated CFs potentially had a more uniform distribution, which reduced the fibre agglomerates

and showed good interaction with the cement matrix, thus reducing ITZ gaps and creating a denser microstructure.

As shown in Figure 4-7 (d), the scatter with black lines represents the changes in surface resistivity of the mortar specimens before and after the addition of CFs. A variation in electrical resistivity was observed with different dosages and lengths of incorporated CFs with various treatments. A significant drop in resistance was found in CF-V compared to the CM, primarily due to the conductive CFs forming a network within the cement matrix. The increased voids might also contribute to the reduced resistivity, but they were less likely to cause such a substantial reduction. Compared to CM, CF-V led to a maximum reduction in electrical resistivity of 71.64%. It is also clear that the electrical resistivity could be further reduced by longer CF lengths and higher CF dosages. Compared to the CF-V group, the mortar containing surface-modified CFs exhibited higher electrical resistance than untreated CFs. The bio-based surface treatment on the CF surface, which increased roughness and the I_D/I_G intensity ratio while reducing porosity in the mix, resulted in slightly higher bulk resistivity in the FRCC specimens.

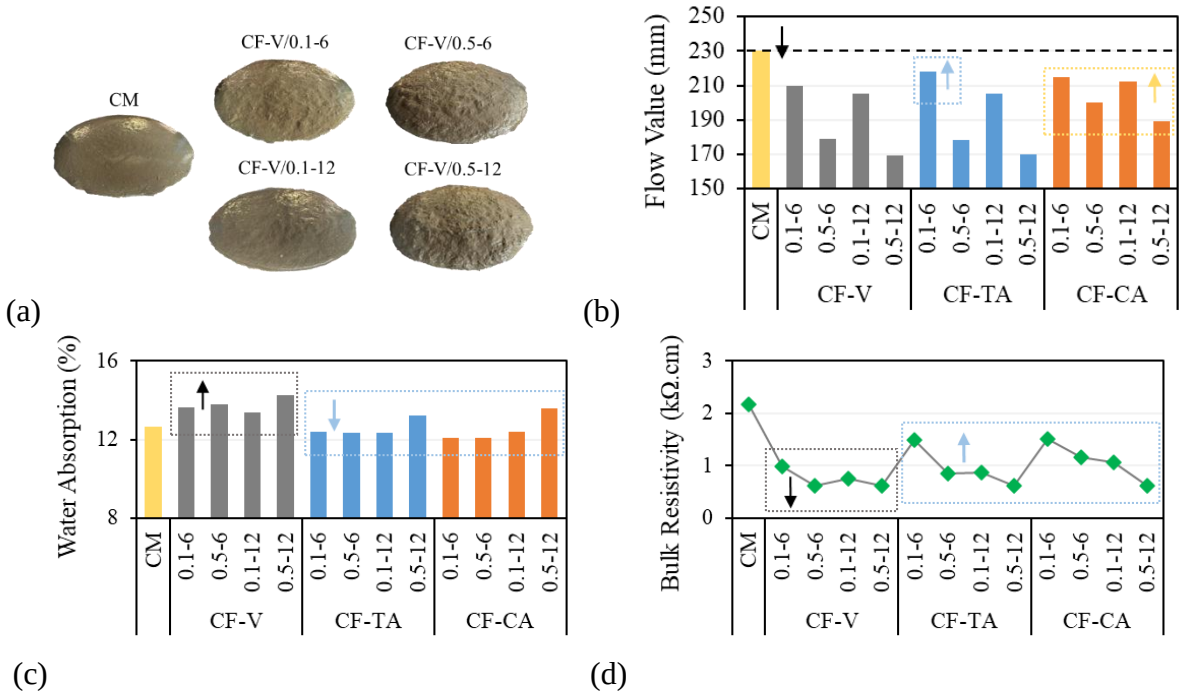

Figure 4-7. (a) Visual comparison of fresh mortar samples, (b) Flow table test results, (c) Water absorption and (d) bulk resistivity measurements.

4.2.4.4 Mechanical strength of FRCC

Mechanical testing, including both compression and flexural strength, was conducted to investigate the effects of bio-based surface modifications on the mechanical properties of the CF at a curing age of 28 days. The test results were categorised into four groups, based on the combinations of CF dosage and length, as shown in Figure 4-8 (a). The compressive strength was compared across these groups and was also compared to the compressive strength of the CM, indicated by the black dashed line. The specimens containing 0.1 vol.% 12mm CFs exhibited higher compressive strength among the four groups tested. Specifically, the CF-TA group achieved the highest compressive strength of 41.73 MPa, followed by the CF-CA group, which reached 38.43 MPa. These values represent increases of 30.11% and 19.82%, respectively, compared to CM. The outcomes indicate that the bio-based treated CFs were superior in enhancing the compressive strength of FRCC, outperforming both the CM and CF-V groups. Conversely, the CF-V specimens, which included 0.5 vol.% of 6mm and 12mm CFs, demonstrated a decrease in compressive strength, with reductions of 10.96% and 3.14% relative to the CM individually.

Three-point bending tests were conducted on the FRCC specimens with a 0.1 vol.% dosage of 12mm CF to investigate the impact of different treatments on flexural strength. The results indicate that the flexural strength follows a similar trend to the compressive strength (Figure 4-8 (b)), with CF-TA demonstrating the highest flexural strength of 5.39 MPa, which is 32.11% higher than that of the CM at 4.08 MPa, and 11.13% higher than CF-V at 4.85 MPa. The CF-CA also shows a relatively high flexural strength of 4.90 MPa.

Figure 4-8 (c) displays a typical load-displacement curve of FRCC during bending tests. The progression of a crack in the middle region of the prism was captured through DIC images. The first microcrack was initiated from the bottom of the prism when the specimen exceeded its elastic limit. As the load increased, the curve exhibited non-linear behaviour, and the crack propagated extensively upwards, indicating plastic deformation. After reaching the ultimate flexural load, the load gradually decreased, with the assistance of CFs, demonstrating ductile behaviour as the crack fully developed. The CFs in the FRCC exhibited a bridging effect, effectively transferring forces to the surrounding cement matrix and facilitating a more uniform stress distribution across the matrix. This mechanism enabled the FRCC to sustain higher loads and improve its ductility, rather than experiencing brittle, sudden failure. In addition to the dominant crack, a few fine microcracks were also observed. This suggests that the improved interface between the CFs and the cement matrix is crucial, as it enhances the bridging effect

provided by the CFs, leading to greater overall performance [62, 63]. After the bending test failure, optical microscopy images revealed CFs being pulled out from one side, illustrating their role as crack-bridging fibres. Small cementitious particles were still visibly adhered to the surface of the CFs. These CFs slowed crack propagation by interacting with the cement matrix, effectively providing resistance against further crack growth.

In addition to the fibre-bridging effect, the CF surface treatment facilitated the hydration process in the surrounding cement matrix and enhanced the interfacial bonding characteristics through both chemical and physical interactions. According to the authors' preliminary study [47], fibre pullout tests demonstrated that surface-modified CFs exhibited notably enhanced interfacial bond performance due to improved mechanical interlocking and chemical adhesion. Specifically, CA-modified CF showed higher frictional resistance, whereas TA-modified CF primarily benefited from stronger chemical bonding. Collectively, the bio-based surface modifications resulted in up to an 18.3% increase in maximum bond strength compared to vCF. Key values obtained from the fibre bundle pull-out tests are summarised in Table 4-4. A more thorough analysis of the microstructural mechanisms is provided in the subsequent section.

(a)

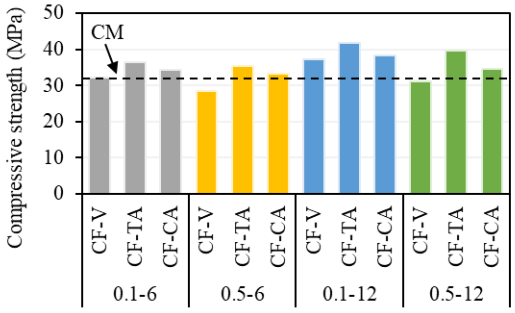

(b)

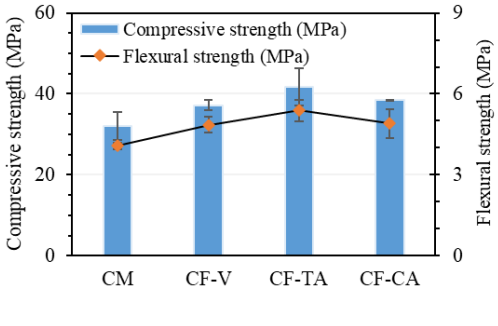

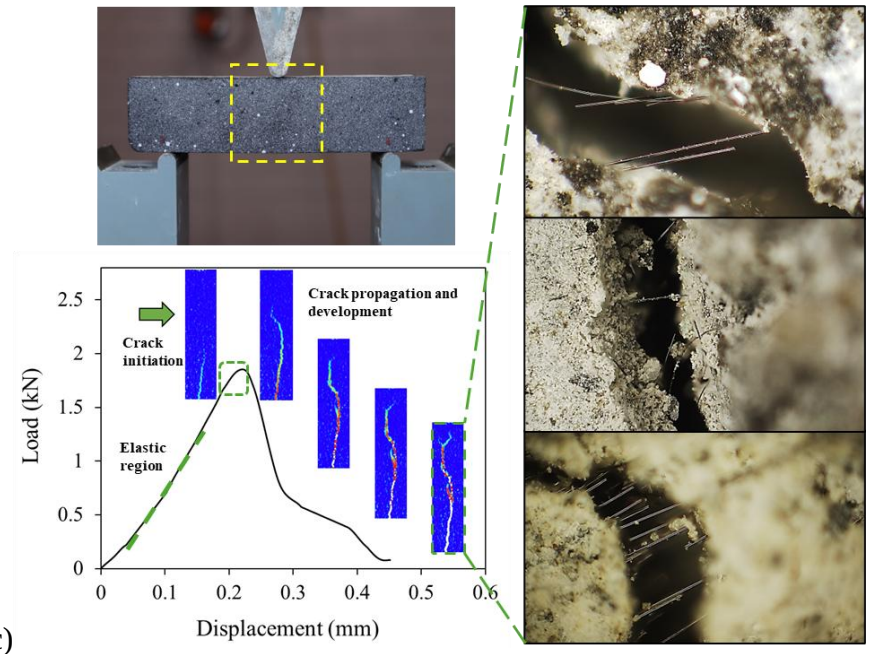

(c)

Figure 4-8. (a) Compressive strength for CM and FRCC specimens with CFs, (b) Compressive and flexural strength for the specimens with 0.1 vol.% dosage and 12mm CF, and (c) Crack pattern observation from DIC during bending test and microscopy images.

Table 4-4. Fibre bundles pull-out test results for virgin and modified CF embedded in cementitious matrix (7-day cured).

	Virgin CF	TA-modified CF	CA-modified CF
Maximum bond strength τ (MPa)	3.10	3.50	3.67
Interface friction bond strength τf (MPa)	2.38	2.49	2.67
Chemical bonding energy Gd (J/m²)	2.60	3.58	3.35

4.2.4.5 Microstructural analysis of the interface between CFs and the matrix

To validate the hypothesis and investigate the mechanism behind the improved interfacial properties between CFs and the cement matrix developed through bio-based chemical treatment, the internal microstructure of the FRCC specimens was observed using SEM. This observation allowed for detailed visualisation of the fibre-matrix interface for CF-V, CF-TA and CF-CA specimens. For CF-V specimens without CF surface treatment, it is evident that the ITZ between the CF and cement matrix was not compacted, with a noticeable gap in between, as shown in Figure 4-9 (a). During the initial loading phase, the fibres bridged the microcracks (Figure 4-9 (b)), facilitating stress transfer across the cement matrix through the fibre-matrix interface. As the applied load increased, the fibres ultimately underwent either pull-out or rupture mechanisms, as evidenced in Figure 4-9 (c) and (d). However, the weak interfacial

bonding between the CF and cement matrix led to insufficient load transfer, hindering the composite's mechanical performance and potential for higher load capacity.

For the bio-based surface-modified CF, enhanced interfacial bonding was attributed to both chemical and physical mechanisms (as illustrated in Figure 4-9 (e) and (g)). The active polar groups attached to the CF surface not only improved hydrophilicity, leading to stable fibre dispersibility and better physical adhesion between CF and cement matrix, but also significantly enhanced chemical bonding [32]. The synergistic co-deposition of TA and EA introduced both hydroxyl (OH) and amino (NH_2) functional groups onto the CF surface. These groups enhanced fibre-matrix interactions by reacting with calcium ions (Ca^{2+}) from the cement matrix, thereby promoting chemical ionic bonding between the CF and the cement matrix [33]. The modifications resulted in a densified ITZ and enhanced interfacial bonding strength between the cementitious matrix and the CF (Figure 4-9 (e)). In addition, the EDS results in Figure 4-10 indicate that the primary components of the hydration products were oxygen (16%), calcium (7.9%), silica (4.4%), and minor aluminium (0.2%). The Ca/Si ratio of 1.8 suggests the presence of calcium silicate hydrates (C-S-H) along with additional calcium hydroxide ($Ca(OH)_2$) in the hydration products surrounding the CF surfaces [64]. The CF channel morphology after pull-out, observed in Figure 4-9 (d), exhibited a rough surface compared to the smooth surface observed with the vCF. Residuals from the CF surface were observed in the channel, indicating the interaction between the polymeric layer of CF-TA and the matrix. This interaction further underscores the enhanced adhesion and mechanical performance of the FRCC. On the other hand, the presence of major carboxyl (COOH) and other functional groups, such as hydroxyl (OH) and carbonyl (C=O), on CF-CA surfaces facilitated the chemisorption of calcium and aluminium ions (Ca^{2+} and Al^{3+}) from the cementitious matrix [19, 33, 40, 42]. Subsequently, these chemical interactions enhanced the precipitation of calcium silicate hydrates (C-S-H) and calcium hydroxide ($Ca(OH)_2$), and other hydration products onto the CFs, leading to improved fibre-matrix interfacial bonding [19, 31]. Figure 4-9 (f) depicts the robust adhesion between the cement matrix and CFs, indicating that the fibres were effectively embedded within the matrix. Figure 4-9 (g) shows the presence of residual hydration products remaining on the CF surface after separation. Furthermore, it is expected that all these functional groups could form hydrogen bonds and covalent bonds with cement hydrates, further strengthening the fibre-matrix interface [19, 36].

The increased surface roughness of CF-TA and CF-CA enhanced the mechanical adhesion to the matrix through improved frictional bonding, often referred to as mechanical

interlocking [19, 34]. Higher roughness with a larger contact area provided more sites for the nucleation and deposition of hydration products onto the CF surface [32]. Overall, the bio-based surface modification of CFs effectively enhanced the fibre-matrix interfacial properties through both chemical and physical mechanisms. The treatments improved the interfacial bonding characteristics and compactness between the CFs and cement matrix, leading to enhanced stress transfer efficiency and superior FRCC performance.

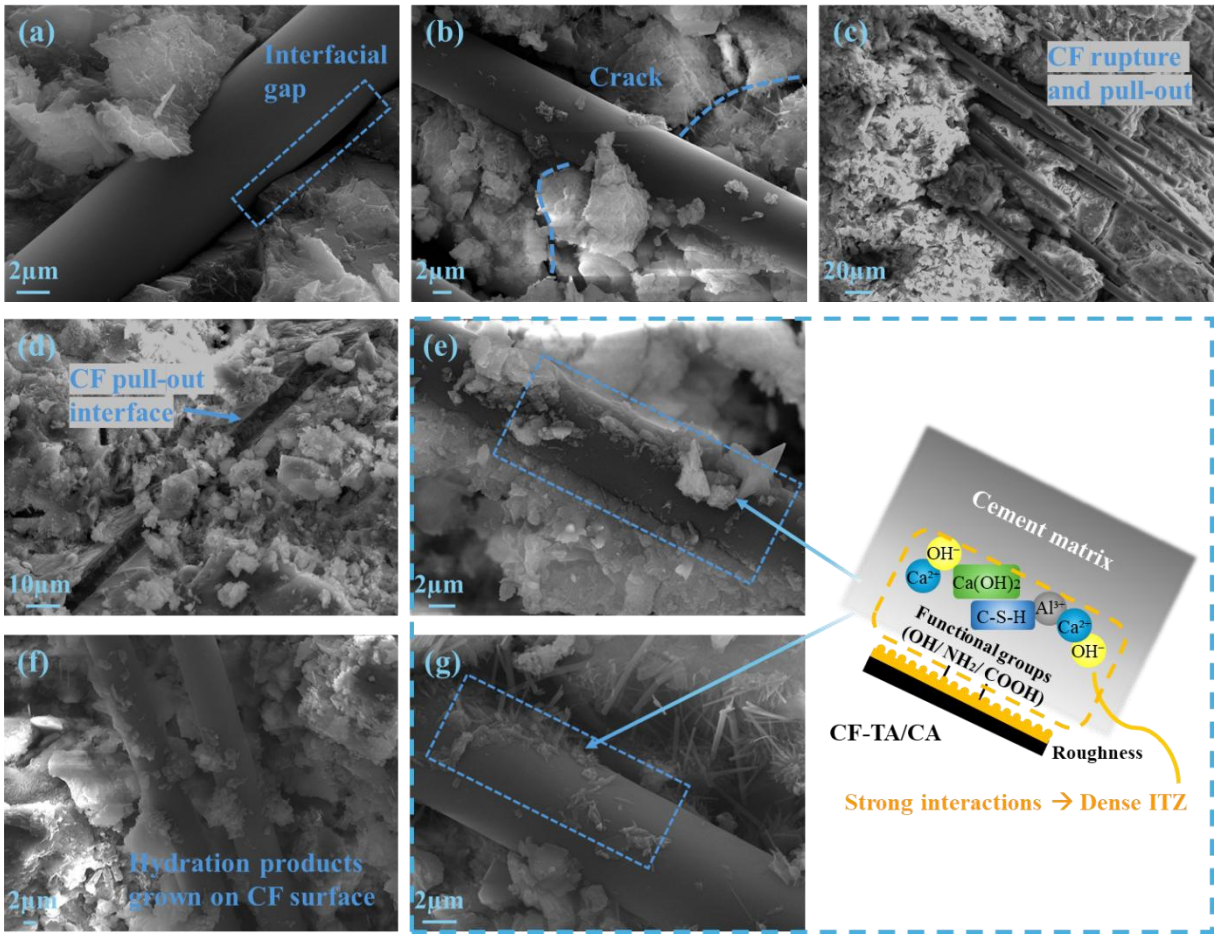

Figure 4-9. Micrographs of the interface between CFs and cementitious matrix: (a) to (c) CF-V, (d) to (e) CF-TA, and (f) to (g) CF-CA.

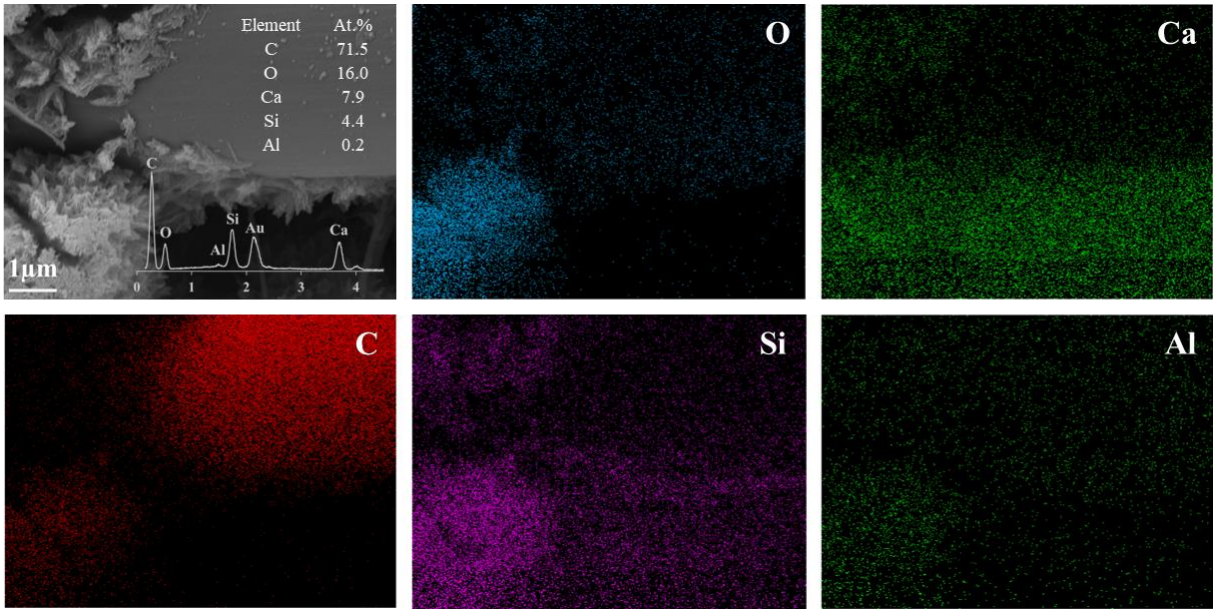

Figure 4-10. Micrograph and EDS analysis of CF-TA.

4.2.5 Summary of key findings from Section 4.2

This study developed environmentally friendly and effective surface modification methods for CF using bio-based chemicals, TA and CA. Surface characterisation confirmed that the co-deposition of TA and EA formed a polymeric layer through both covalent and non-covalent interactions, significantly enhancing surface roughness with a 103.8% increase. Additionally, bio-based treatments with TA significantly improved CF's dispersion and stability in cementitious materials, preventing fibre agglomeration and facilitating better interactions with the cementitious matrix. Similarly, CA treatment introduced ester groups through dehydration and esterification reactions, creating an irregular texture on the surface. Both treatments maintained high CF strength capacity without damage. Mechanical testing of FRCCs revealed that 0.1 vol.% 12mm CF-TA exhibited the highest compressive and flexural strength, with increases of 30.11% and 32.11% compared to the controlled mortar, and 12.33% and 11.13% compared to the FRCC with untreated CFs. The FRCC containing CF-CA also demonstrated enhanced mechanical performance, with compressive strength gains of up to 19.82%. Active polar groups on the CF surface promoted chemical bonding and ion chemisorption, improving hydration product precipitation and microstructure densification. Increased surface roughness enhanced mechanical adhesion, leading to better interfacial bonding and stress transfer, ultimately contributing to higher performance in carbon-FRCCs.

These bio-based surface treatments offer a sustainable and cost-effective method to commercial-scale CF modification for construction applications. The demonstrated mechanism

offers a clear pathway for industrial implementation, providing a foundational approach for scaling up these bio-based surface modification techniques. Future work should focus on optimising treatment parameters for manufacturing-scale production and exploring these techniques for other fibre types to expand the portfolio of high-performance, eco-friendly construction materials.

4.3 ELECTROCHEMICAL GRAFTING OF HYDROXYL AND AMINE GROUPS ON CARBON FIBRES FOR IMPROVED PERFORMANCE IN CEMENTITIOUS COMPOSITES

Y. Tao[1*], S.A. Hadigheh[1*], D.J. Hayne[2], B. Newman[2] and L.C. Henderson[2]

[1] School of Civil Engineering, Faculty of Engineering, The University of Sydney, Sydney, New South Wales 2006, Australia

[2] Institute for Frontier Materials, Deakin University, Waurn Ponds, Victoria 3216, Australia

*Corresponding Authors: Dr Ali Hadigheh

Yunyun Tao

Construction and Building Materials, https://doi.org/10.1016/j.conbuildmat.2025.141843, Published in May 2025.

4.3.1 Abstract

The use of electrochemistry to functionalise carbon fibre (CF) surface has proven effective in enhancing the performance of polymer composites, offering benefits of time efficiency and precise control. However, its current application to CFs within cementitious matrices remains limited and confined to laboratory-scale studies, restricting broader implementation in the construction industry. The bond between CF and the cementitious matrix is relatively poor due to the CF surface's chemical inertness and hydrophobic nature, which hinders the effective utilisation of fibre-reinforced cementitious composites (FRCC). This study addresses this issue by functionalising CFs with diazonium aryl salts through an in situ electrochemical modification process. This process applies a reductive potential of 3V to successfully graft phenolic hydroxyl and amino functional groups onto the CF surface, enhancing the interfacial strength. The debonding force of hydroxyl- and amino-functionalised CF within the matrix increased by 48.33% and 9.70%, respectively, compared to the untreated CF specimens. The active polar groups enriched the CF surface, notably enhancing chemical adhesion at the CF-matrix interface. Additionally, the rougher surface improved the mechanical interlocking mechanism and created sites for nucleation and hydration product deposition. Overall, the FRCC specimens incorporating hydroxyl-functionalised CFs outperformed those with amino-functionalised CFs, achieving the highest compressive and flexural increases of 32.30% and 21.04%, respectively, compared to the plain mortar. Moreover, this approach also reduced the total porosity of FRCC, proving the formation of a denser microstructure. The results indicated

the enhanced interfacial bonding efficacy by large-scale electrochemical treatment and highlighted its promising potential for future applications.

Keywords: Carbon fibre; Fibre-reinforced cementitious composite; Surface modification; Interfacial property; Mechanical property

4.3.2 Introduction

Portland cement is extensively used in the construction industry due to its high durability, ease of application, and abundant availability of inexpensive raw materials [65, 66]. Conventionally, steel reinforcement has been incorporated to overcome the tensile weakness and brittle behaviour of plain Portland cement concrete, thereby enhancing its overall performance. On the other hand, the development of fibre-reinforced cementitious composites (FRCC) has garnered increasing interest over the past 70 years, beginning with early work that utilised steel and glass fibres within the cementitious matrix. Despite not possessing the tensile strength as high as the continuous reinforcement bars, FRCCs are effective for crack control due to the random distribution of short fibres throughout the cementitious matrix [67]. The adoption of polyacrylonitrile (PAN)-based carbon fibres (CFs) into cementitious materials was first reported in 1972, driven by their high specific strength, elastic modulus, and excellent chemical stability [68]. In the 1980s, the use of pitch-based CFs was employed in practical applications within the construction industry in Japan, offering a lower-cost alternative [69]. Moreover, due to the excellent electrical conductivity of CFs, carbon fibre-reinforced cementitious composite (carbon-FRCC) has also been studied as a multifunctional structural material, based on the concept of smart concrete [70, 71]. Since then, subsequent studies have focused not only on the improved mechanical and physical performance of carbon-FRCCs [2, 72], but also on their functional capabilities, such as strain-sensing [73, 74], self-heating [75, 76] and electromagnetic shielding [77, 78]. Several studies have also revealed their specialised applications in concrete walls and floors of buildings [16, 79], pavements [80-82] and strategic structures such as power plants and military establishments [77, 83]. Although the initial cost of virgin CF (vCF) is relatively high, buildings constructed with carbon fibre-reinforced high-strength concrete require lower total lifecycle costs compared to traditional structures requiring remediation and re-strengthening [72]. In addition, utilising vCF offcuts or recycled CFs (rCFs) presents a promising opportunity to improve the performance of cementitious composites while reducing economic costs and promoting sustainability [2, 62].

However, the inherent hydrophobic nature of CF surface without treatment leads to a greater tendency for CF agglomeration due to poor wettability and weak interfacial bonding between CFs and the cementitious matrix [19, 20]. This limitation hinders the effective utilisation of CFs and restricts the optimal mechanical performance of carbon-FRCCs. Therefore, the surface functionalisation of CFs should be specifically tailored to enhance bond behaviour when embedded within a cementitious matrix.

To date, different approaches have been proposed by researchers to modify the CF surface in order to enhance interfacial load transfer between the CFs and the cementitious matrix. Methods such as oxidation, plasma, electrophoresis and grafting treatment have been recognised as effective strategies to alter CF surface [19]. These techniques chemically introduce functional groups and form chemical bonds between CFs and the matrices, and physically increase roughness to achieve better affinity between CFs and the surrounding matrices. For example, Wang et al. [26] reported increases of 13.11% in compressive strength, 9.29% in splitting tensile strength, and 20.13% in flexural strength of concrete containing 0.3% graphene oxide grafted CFs, compared to concrete with untreated CFs. The enhanced roughness, which increased mechanical interlock, and the presence of functional groups that promoted the formation of hydration products, contributed to better interfacial performance. Consequently, this led to greater strength and toughness in fibre-reinforced concrete. Lavagna et al. [22] reported significant improvements in both the electrical and mechanical properties of FRCC following acidic oxidation treatment with a piranha solution for 30 min at 30°C. These enhancements were attributed to the improved interaction and adhesion between the CFs and cement matrix. However, both grafting and liquid oxidative modification have faced limitations due to their time-consuming nature, complicated procedures and associated environmental pollution implications. Li et al. [84] utilised a unique combination of nano silica and calcium salts as electrolytes in electrophoretic deposition (EPD) modification, which ameliorated fibre surface defects and enhanced physical anchoring between CF and cement. This modification also increased oxygen-containing functional groups and improved the hydrophilicity of the CF surface, resulting in the uniform formation of hydration products that densified the interfacial transition zone (ITZ) through the reaction of silicon dioxide and calcium hydroxide. Li et al. [85] improved up to a 25% increase in compressive strength and a 19% increase in flexural strength in alkali-activated composites by adding 1% CFs compared to plain composites. This enhancement was achieved through anodic oxidation during electrochemical modification in a sodium hydroxide electrolyte. Considering their low energy consumption, time efficiency,

simplicity in operation, and environmentally safe nature, EPD and anodic oxidation are identified as promising approaches for CF surface modification before mixing into cementitious matrices [19].

Building on the principles of CF surface modification for cementitious materials as discussed above, electrochemical oxidation presents a promising alternative method. Currently, this technique has been widely adopted for CF surface functionalisation to enhance the interfacial properties of the composites in the polymer industry, owing to their speed and controllable performance [86]. The effectiveness of the functionalisation largely depends on factors such as the duration of treatment, electrolyte solution, its concentration and the applied potential [87, 88]. Following oxidative processes, the surface activity of CFs is significantly enhanced, introducing functional groups that improve interfacial bonding between the CFs and polymer matrix. Nevertheless, the CF strength can be reduced under aggressive oxidative treatment conditions, such as increased voltage and extended treatment times, which could lead to damage to the CF surface [19, 89]. Furthermore, the formulation for the electrochemical approach is determined on a case-by-case basis, meaning that it may not be compatible with various matrix systems. Notably, to the authors' knowledge, the application of electrochemical oxidation for CF in cementitious matrices is still very limited, with only a few studies having developed appropriate electrochemical methods for this purpose. According to Li et al. [88]'s research, anodic oxidation in pore solutions shows significant potential for improving the compatibility between CF and cementitious matrices. Their study demonstrated a 37.9% increase in the shear bond strength of CF with a treatment voltage of 3V and a duration of 15 minutes. Li et al. [85] investigated the anodic oxidation of rCF in sodium hydroxide solution to enhance the mechanical properties of CF-reinforced alkali-activated composites. With the same duration and voltage (15 minutes, 3V), this method improved flexural performance by increasing interfacial adhesion through the introduction of acidic groups on the rCF surfaces, which can form chemical bonds with the matrix. However, this remains an ongoing research topic, with current constraints such as the need to scale up to continuous production. Further investigation into the electrochemical treatment parameters and their long-term environmental impact is essential.

In the field of electrochemical treatment, grafting using diazonium salts has been proven to be a more efficient method for covalently functionalising CF surfaces [90, 91]. This method involves grafting small molecules onto the CF surface to promote stronger interaction between the matrix and the CF surface. The use of a reductive potential under relatively mild conditions

benefits the process by preventing detrimental effects on the CF properties while still activating the CF surface and reducing its inertness [89, 90]. The use of cyclic voltammetry (CV) allows for better control of the potential and duration, ensuring that over-oxidation and damage to the CFs are avoided. Inspired by the benefits of this technique and its successful application in enhancing the performance of carbon-fibre reinforced polymer (CFRP) composites, this paper aims to investigate the effects of electrochemically functionalised CFs on interfacial adhesion within cementitious composites. The objectives include physical and chemical characterisation of hydroxyl- and amino-functionalisation on CF surfaces, as well as examining the influences of these surface modifications on the interfacial properties and performance of the resulting FRCCs.

4.3.3 Materials and methodology

4.3.3.1 Materials

The CF used in this study was T700SC-12000-50C, supplied by Toray Industries, Inc. (France). The chemicals, reagents, and solvents utilised in this research project were supplied by Sigma-Aldrich (Australia) and used as received. The raw materials for the preparation of cementitious composites include cement, fine aggregates and tap water. The cement used for casting was general-purpose cement (type GP) as specified in Australian Standard AS3972 [45], supplied by Cement Australia. Macka's sand, complying with AS2758.1 [46], was used as fine aggregate. The CF and mortar raw materials were summarised in Table 4-5 to Table 4-7.

Table 4-5. Physical properties of CF.

Product No.	Filaments	Modulus of Elongation (GPa)	Elongation (%)	Density (g/cm^3)	Diameter (μm)
T700SC-12000-50C	12k	230	2.1	1.8	7

Table 4-6. Properties of cement.

Chemical entity		**Physical and chemical properties**	
Portland Clinker	<97%	Boiling/Melting Point	Melting point >1200°C
Gypsum ($CaSO_4.2H_2O$)	2-5%	Specific Gravity	3.0 – 3.2
Limestone ($CaCO_3$)	0-7.5%	Solubility in Water	Slight, reacts on mixing with water forming an alkaline (caustic) solution (pH >11)
Calcium Oxide	0-1%		

Table 4-7. Properties of fine aggregate.

Chemical entity		**Physical and chemical properties**	
Crystalline Silica (Quartz)	>95%	Boiling/Melting Point	Melting point >1200°C
Mineral and Organic impurities	<5%	Specific Gravity	2.7
Particle size distributions		Solubility in Water	Slight, reacts on mixing with water forming an alkaline solution (caustic, pH>11)
Sieve (mm)	Passed (%)		
1.18	100	Uncompacted bulk Density	1.48 t/m^3
0.6	100	Compacted bulk Density	1.62 t/m^3
0.425	91	Methylene Blue	
0.3	40	Adsorption Value	2 mg/g
0.15	1	Water Absorption	0.30%
0.075	0	Sodium Sulphate Soundness	0.20%

4.3.3.2 Electrochemical grafting for functionalisation of CF

The surface modification process utilised a scale-up, continuous functionalisation production line. This setup includes a series of stations, such as a furnace, electrochemical bath, wash bath, dryer, and spooling system. Firstly, the CF de-sizing process was subjected to a thermal treatment in a furnace at 450˚C for 6 minutes. This process ensured the removal of the sizing designed for the resin system compatibility, providing a clean substrate for further chemical modifications. The desized CFs obtained were then immersed in an electrochemical bath with diazonium salts, generated in situ to facilitate the functionalisation process. The electrochemical setup was configured to allow for the controlled application of a reductive potential. A reductive potential of 3 V was passed through the CFs to form the corresponding aryl radical, which enabled the covalent attachment of the chosen functional group. The synthesis mechanism of electrochemical grafting of 4-aminophenol (4AMP) and 4-nitroaniline (4NA) onto the CF surface is illustrated in Figure 4-11. At lower concentrations, the active areas on the CF surface participated in the grafting reaction, facilitating the installation of the desired chemical groups. The reaction conditions were carefully monitored to ensure optimal radical formation and functionalisation efficiency. Similar detailed procedures for CF grafting solution preparation and grafting operations were reported in the authors' previous studies [89].

After the completion of the treatment, the CFs underwent two wash baths to remove any unreacted diazonium species and by-products from the electrochemical reaction. The washing process was conducted using suitable solvents to eliminate any physiosorbed content on the CF surface before drying under reduced pressure. After washing, CFs were dried under controlled conditions to eliminate any residual moisture. Once dried, the CFs were spooled for subsequent characterisation and application in cementitious composites.

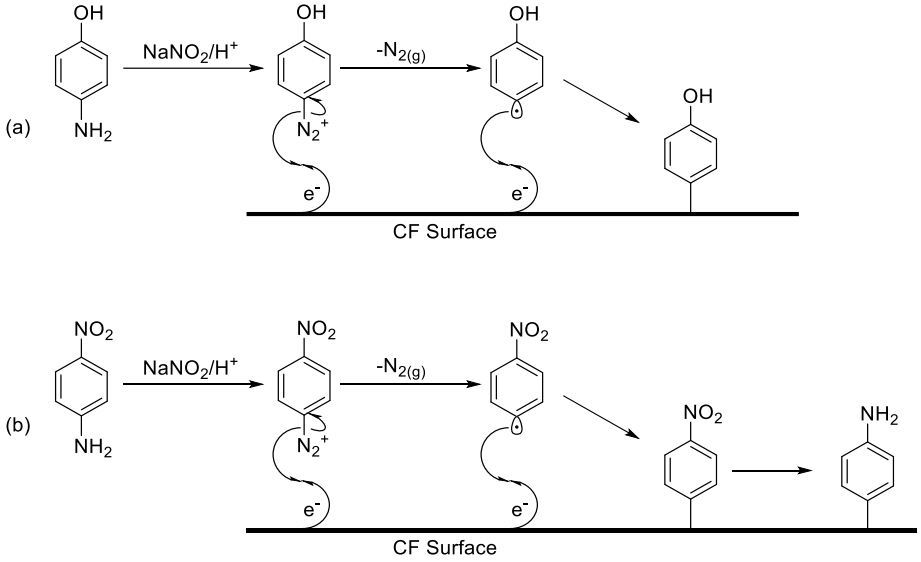

Figure 4-11. Reaction mechanism for surface modification on CF surfaces using (a) 4AMP to form hydroxyl-grafted CFs, and (b) 4NA to form amino-grafted CFs.

4.3.3.3 Preparation of FRCC specimens

Two lengths (6 mm, 12 mm) and two doses (0.1%, 0.5% volume of mixture) of CF were examined, leading to four combinations (FRCC specimens) for each type of CF; see Table 4-8. A controlled mortar specimen without any additives was used as a reference, named CM. Additionally, a group of FRCC specimens with vCFs was prepared for comparison with the FRCC specimens containing functionalised CFs. Untreated vCFs and those functionalised with hydroxyl (OH) and amino (NH_2) and their corresponding cementitious composites are denoted as CF-V, CF-OH, and CF-NH_2.

Dry CFs were mixed with cement and stirred for three minutes to ensure the fibres were uniformly dispersed in the dry cement mix. Sand and water were then gradually added to the mix and stirred until the flow value showed consistency as stated in BS EN 1015–3 [48]. A vibration table was used to assist in compacting the mortar mixture and reducing pores. The fresh pastes were poured into 50×50×50 mm^3 moulds for compressive testing, electrical resistivity measurement, and water absorption testing; 40×40×160 mm^3 moulds for flexural

testing; and 25×25×285 mm³ prism moulds for shrinkage measurements. Subsequently, the specimens were demoulded and stored in a standard curing environment (temperature of 23°C and 95% humidity) until testing. The mass ratios of cement, water, and sand were specified as 1:0.55:1.5.

Table 4-8. Samples IDs indicating corresponding surface modifications and parameters.

Designation of surface modifications		Samples ID	Dosage (%)	Length (mm)
Controlled mortar without CF addition		CM	-	-
Untreated vCF (T700SC-12000-50C)		CF-V	0.1	6
			0.5	12
			0.1	6
			0.5	12
Electrochemical grafting functionalised CFs	Using 4AMP	CF-OH	0.1	6
			0.5	12
			0.1	6
			0.5	12
	Using 4NA	CF-NH2	0.1	6
			0.5	12
			0.1	6
			0.5	12

4.3.3.4 Methods

CF surface characterisation

To examine the microstructural changes of elements and chemical bonds on CF surface, X-ray Photoelectron Spectroscopy (XPS) was performed using a Thermo Scientific K-alpha+ XPS spectrometer, which provided evidence for the successful grafting of CFs. A spot size of 400 µm was employed, and the signal was accumulated for 10 cycles for each sample to ensure accurate data collection.

The morphology of CF surface was observed using a Zeiss Ultra Plus scanning electron microscope (SEM) at an acceleration voltage of 10 kV with the SE2 detector. D surface morphology and roughness analysis before and after functionalisation were also performed using a Bruker Innova atomic force microscope (AFM). A very thin layer of CF filaments was attached to the substrate with double-sided carbon tape, and silver paint was used to fix both ends to ensure no movement. The scanning was performed in tapping mode with a 5 × 5 µm range and a rate of 0.5 Hz. Additionally, the surface defects of CFs were analysed using Raman

spectroscopy. A Renishaw Raman InVia Qontor Microscope was utilised for CF specimen excitation, achieved with a Renishaw RL532C CW diode laser emitting at 532 nm. Spectra were recorded using the 50× objective, with the accumulation of 3 scans, 10-second exposure, and a laser power of 3.95%.

Fibre tensile test and pullout test

Single fibre tensile test and pullout test were performed using Dynamic Mechanical Analyser (DMA) 850 with an 18N load cell. Single CF tensile tests were conducted following ASTM C1557-20 [51]. Single CFs were randomly sampled from vCF and treated CF bundles for testing. For the preparation of the test specimens, typical paper coupons (24mm×7mm) were used with a 12mm gauge length. A 5mm diameter hole was created in the middle of the tab and superglue was used to secure the fibre's position. Before loading, a test specimen was positioned and secured by tensile clamps into the DMA machine. The axis of a single CF was oriented perpendicular to the crosshead of the machine. The paper coupon was then cut along the middle line. The experimental setup is illustrated in Figure 4-12 (a). An initial load of 0.01N was introduced before the commencement of the loading phase to ensure the fibre was properly engaged and resisting the load. The crosshead was then set to operate at a speed of 0.2 mm/min. After each tensile test, a small portion of each CF sample was collected for measuring the fibre diameter using SEM.

A two-parameter Weibull statistical analysis was performed to assess the variability of the tensile strength across 30 single fibre specimens for each type of CF. The data were fitted to a linearised Weibull distribution, yielding a correlation coefficient $R^2 > 0.9$, indicating a strong linear relationship and minimal variability in fibre tensile strength [52]. The Weibull probability (P), was calculated using the following equation:

$$P = 1 - exp\left[-\left(\frac{\sigma}{\sigma_0}\right)^m\right] \quad 4\text{-}3$$

where P represents the cumulative probability of failure of a CF at applied tensile stress σ, m is the Weibull modulus (or shape parameter) characterising the variability in fibre strength, and σ_0 is the Weibull scale parameter, also known as the characteristic stress. The probability P for each data point is determined using the median rank method [92-94]:

$$P = \frac{i-0.3}{n+0.4} \quad 4\text{-}4$$

where n is the total number of sample points, and i represents the rank of each data point. By rearranging the Weibull probability expression into a linearised form, the Weibull modulus m and scale parameter σ_0 can be determined through linear regression.

To study the effect of functionalisation on the interfacial bonding properties between CFs and the cement matrix, a typical setup for casting samples was designed for CF bundle pullout tests. Fresh cement paste with a fixed water-to-cement ratio of 0.55 was poured into a custom-designed steel mould (Figure 4-12 (b)), based on the setup described by Katz and Li [95] for micro-fibres with fine diameters in a cementitious matrix. The specimen was cured in a standard moist environment at a temperature of 23°C until 7-day testing. Testing specimens (10 mm × 10 mm × 5 mm) were precisely cut from the hardened cement blocks, resulting in a 5 mm embedded fibre length. As depicted in Figure 4-12 (b), the top end of the fibre bundle was glued to a masking tape tab, allowing it to be clamped onto the frame. The lower end of the fibre bundle was embedded into a square cementitious cube. This cube was then adhered to a sample holder, ensuring that the fibre bundle was positioned centrally within the frame and could be vertically pulled out. An initial load of 0.01N was introduced before the commencement of the loading phase. The crosshead was then set to operate at a speed of 0.5 mm/min. The interfacial shear strength (IFSS) was obtained using the following equation [96]:

$$\tau = \frac{P_{max}}{\pi d L} \quad 4\text{-}5$$

where Pmax is the maximum pullout load, d is the diameter of the CF bundle (representing the external boundary of the fibre bundle), and L is the embedded length of the bundle. IFSS for each CF type was calculated as the average of three specimens. The chemical debonding energy G_d was calculated using the following equation [97]:

$$G_d = \frac{2(F_a - F_b)^2}{\pi^2 E d^3} \quad 4\text{-}6$$

where E is the elastic modulus of the CF, Fa is the maximum debonding force, and Fb is the maximum frictional force.

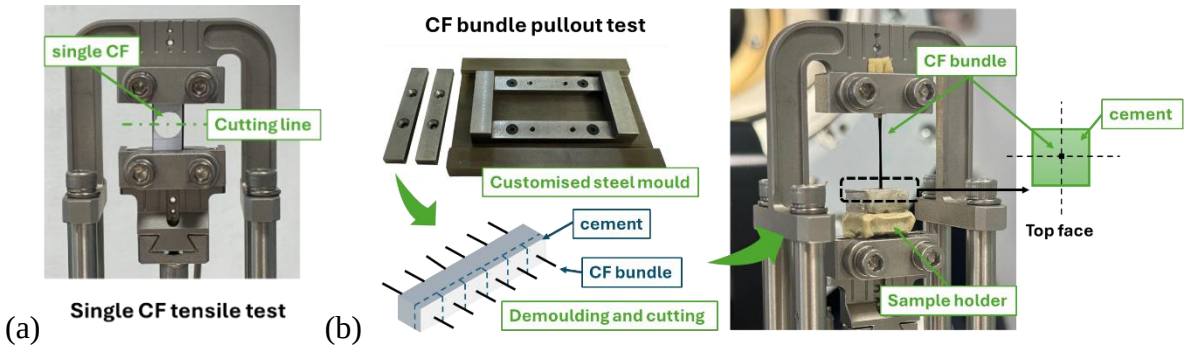

Figure 4-12. Illustration and photos of (a) single CF tensile test and (b) CF bundle pullout test.

FRCC testing method

The effect of CF surface modification on flowability was investigated by conducting a flow table test based on BS EN 1015-3 [53]. Compressive strengths of 50×50×50 mm^3 cubic specimens at 28 days were determined using an MTS Sintech 65/G machine with a 300 kN load cell at a loading rate of 0.5mm/min, in accordance with ASTM C109/C109M [54]. The 28d flexural strengths were evaluated using a three-point bending test on six 40×40×160 mm^3 prism specimens at a loading rate of 0.1mm/min according to ASTM C348–21 [55]. Three duplicated specimens were used for mechanical testing. After mechanical testing, small cementitious samples (5–10 mm) were collected from the failed FRCC specimens and observed under SEM to evaluate the interfacial transition zone (ITZ) between the CFs and the cementitious matrix. Prior to imaging, samples were coated with a 10 nm layer of gold to improve surface conductivity and minimise charging effects.

Bulk resistivity and water absorption measurements were both conducted using 50×50×50 mm^3 cubic specimens. The testing allowed for the evaluation of the impact of CF surface treatment, lengths and concentrations on FRCCs' electrical properties and porosity. Water absorption served as a key indicator of the total porosity in cementitious materials by measuring the total amount of water absorbed. The measuring procedure followed AASHTO T 358-15 [56] for bulk resistivity and ASTM C948–81 [57] for water absorption.

Two replicate specimens of each cementitious composite were cast into 25×25×285 mm^3 prims for the measurement of drying shrinkage by using a length comparator according to ASTM C490/C490M–2 [98]. The initial length reading was measured at the age of 3 days from demoulding. Then the specimens were cured in a humidity chamber in a controlled environment with a temperature of 23°C and a relative humidity of 50%. Subsequent measurements were then taken at various time points to monitor any changes in length.

4.3.4 Results and discussion

4.3.4.1 Functionalised carbon fibres

The wide-scan XPS survey of CF before and after electrochemical functionalisation is shown in Figure 4-13 (a). From this figure, the main chemical elements on the surface of untreated vCF were carbon (C) at 286 eV and oxygen (O) at 533 eV, while the CF after treatment contained additional fluorine (F) at 687 eV and nitrogen (N) at 401 eV. Fluoride was detected on the surface, possibly as a remnant of the spin finish used in the manufacture of PAN or from the tap water used in the washing processes, therefore F1s peaks could be observed in the XPS survey spectra of the functionalised CFs. The slight increase in silica (Si) content after functionalisation suggests formation of Si-F bonds, likely accounting for the fluoride detected by XPS. As the fluoride is bound in this form, its impact on adhesion and interfacial mechanics is minimal.

From Table 4-9, compared with the untreated CF, which had 78.62% C element, the C content on the surface of CF after treatment decreased to around 72 to 74%. Meanwhile, the content of N element on the functionalised CF surface increased from 0.69% on CF-V to 2.33% and 2.95% on the surfaces of CF-OH and CF-NH_2, respectively. The use of 4AMP and sodium nitrite ($NaNO_2$) facilitated the chemical grafting of phenolic hydroxyl groups on the CF-OH surface, resulting in an increased N/C and O/C ratio, confirming the attachment of oxygen-containing functional groups on the CF surface. Note that it is possible for the diazonium salt to graft to the fibre surface via the terminal nitrogen of the diazonium, which may be responsible in part for the increased N concentration in this instance. Notably, a significantly higher presence of amine and nitro functional groups was observed on the CF-NH_2 surface in Figure 4-13 (b) due to the initial grafting of the nitrophenyl group using 4NA, followed by its reduction to the corresponding amine, yielding the desired product [89].

To further investigate the chemical bonds on the CF surface after electrochemical grafting, the original spectrum and fitted curves of C1s peak are presented in Figure 4-13 (c) and (d). The CF surface exhibited characteristic peaks at 284.8 eV for C-C, 286 eV for C-O/C-N, 287 eV for C=O, and around 290 eV for O-C=O and π-π* satellite. In addition to the dominant C-C peak, the augmented C-O/C-N peaks at approximately 287 eV were attributed to the successful grafting of hydroxyl and amino groups onto the CF surfaces.

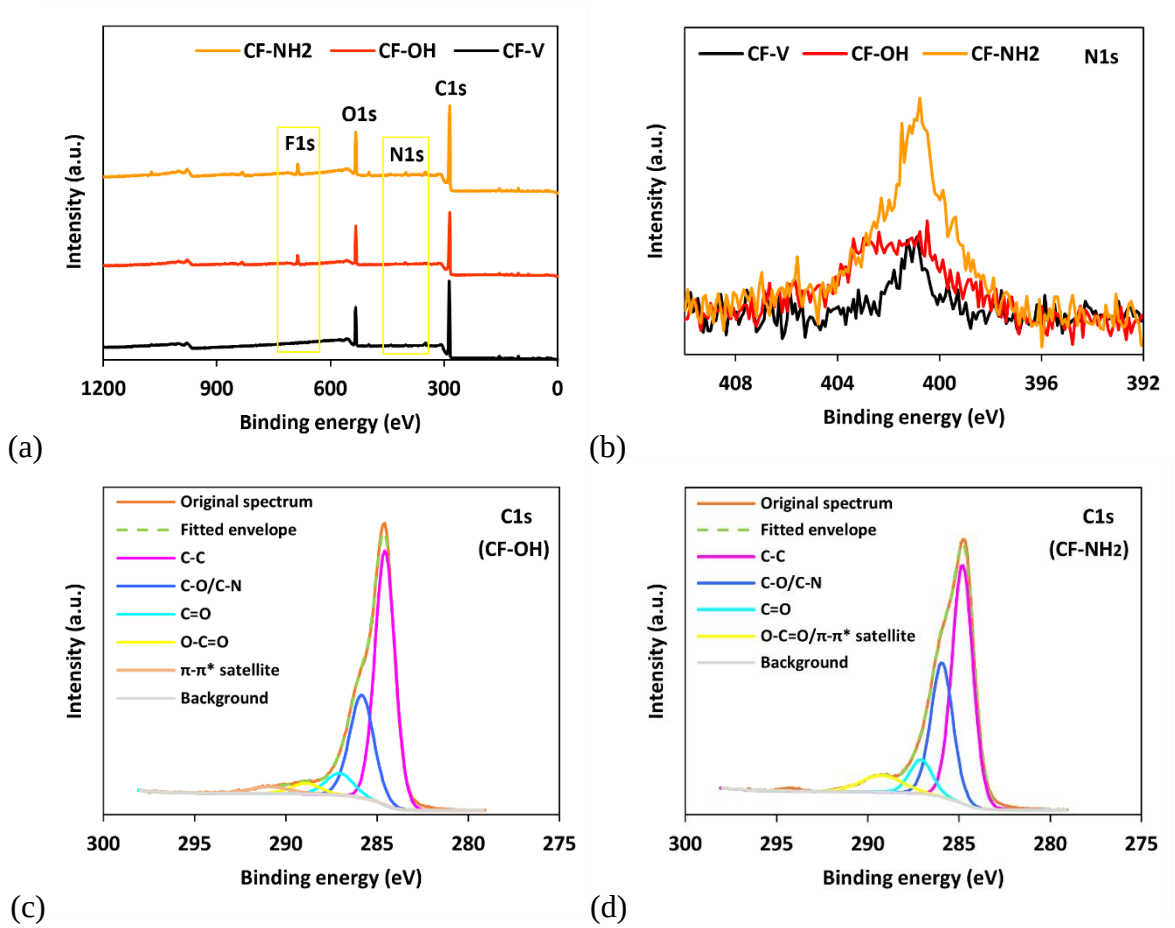

Figure 4-13. XPS spectra of CF specimens: (a) Wide-scan spectra, (b) High-resolution N1s spectra, and deconvolved C1s spectra for CF functionalised with (c) hydroxyl and (d) amine groups.

Table 4-9. Chemical elemental composition of CF specimens.

Specimens	Element compositions (Atomic%)							O/C	N/C
	C	O	Si	Ca	N	F	Total		
CF-V	78.62	17.22	2.52	0.95	0.69	-	100	0.22	0.01
CF-OH	72.01	16.98	2.82	0.67	2.33	5.19	100	0.24	0.03
CF-NH_2	73.87	15.83	2.77	0.91	2.95	3.67	100	0.21	0.04

The untreated vCF displayed a uniformly flat surface morphology, as shown in Figure 4-14 (a) and (d). Mild electrical potentials applied during the electrochemical modification with diazonium salts did not lead to defects on the CF surface (see SEM images of CF-OH in Figure 4-14 (b, e) and CF-NH_2 in Figure 4-14 (c, f). The changes in the I_D/I_G ratios calculated from the Raman spectra were less than 1%, further confirming that no significant structural disorder was induced by the electrochemical treatments [96] (Figure 4-16 (b)).

The increased roughness observed on the modified CF surface is attributed to the presence of attached particulates or deposits. These may potentially be crystals of unreacted or reacted

materials from the modification process. Alternatively, the increased polarity of the CF surface after modification could enhance its ability to participate in electrostatic interactions, making it more prone to attracting such particulates. The surface topography and corresponding roughness profiles after applying a flattening filter, are illustrated in Figure 4-15. As observed in the AFM analysis, even though the vCF surface was not entirely smooth at the nanoscale, the height variations were minimal. In contrast, residual deposits are clearly observed on the functionalised CF surface, appearing as protrusions, as shown in Figure 4-15 (b) and (c). Enhanced colour contrast and brightness in Figure 4-15 (e) and (f), indicate spots of height variation. To quantitatively assess the surface roughness, Figure 4-16 (a) compares the average roughness (Ra), root mean square roughness (Rq), as well as the maximum distance between the highest and lowest points (Rm) of these CF samples. The Ra values of CF-OH and CF-NH_2 were approximately the same, around 20.7 nm, compared to 6.61 nm for CF-V. Similarly, Rq and Rmax also followed the same trend, indicating that the roughness of the functionalised CF surface was much higher than that of the vCF surface, roughly doubling in magnitude. Moreover, the surface roughness of amino-functionalised CF was slightly higher than that of the hydroxyl-attached CF. All these microstructural examinations mentioned above confirm the effectiveness of electrochemical grafting in introducing functional groups onto the CF surface and increasing surface roughness, thereby enhancing the interfacial bonding capability of the functionalised CFs within the cement matrix.

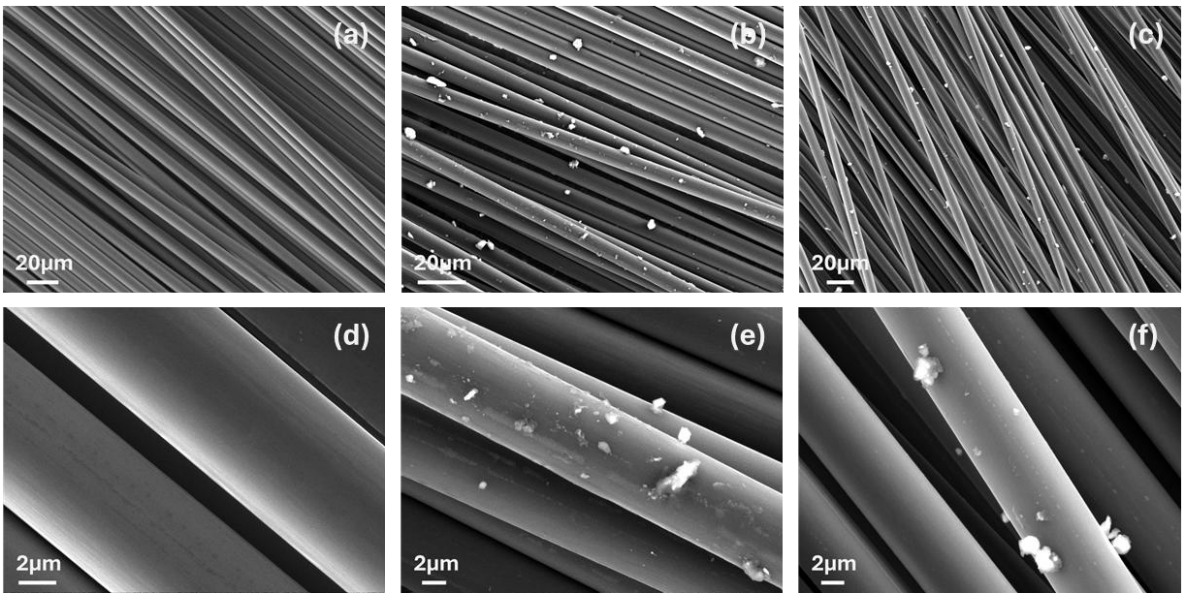

Figure 4-14. SEM images of CF surface: (a, d) as-received CF, (b, e) CF functionalised with hydroxyl groups and (c, f) CF functionalised with amine groups.

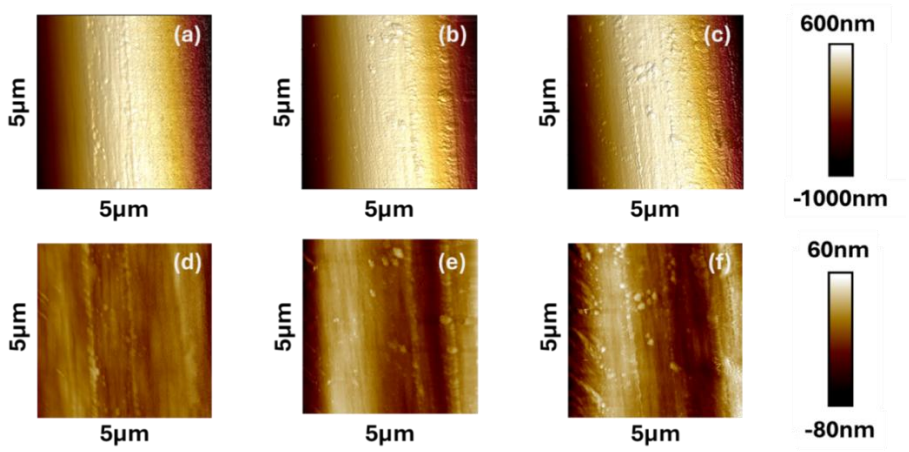

Figure 4-15. CF surface topography (a-c) and corresponding roughness profiles after flattening filter (d-f): (a,d) as-received CF, (b,e) CF functionalised with hydroxyl groups and (c,f) CF functionalised with amine groups.

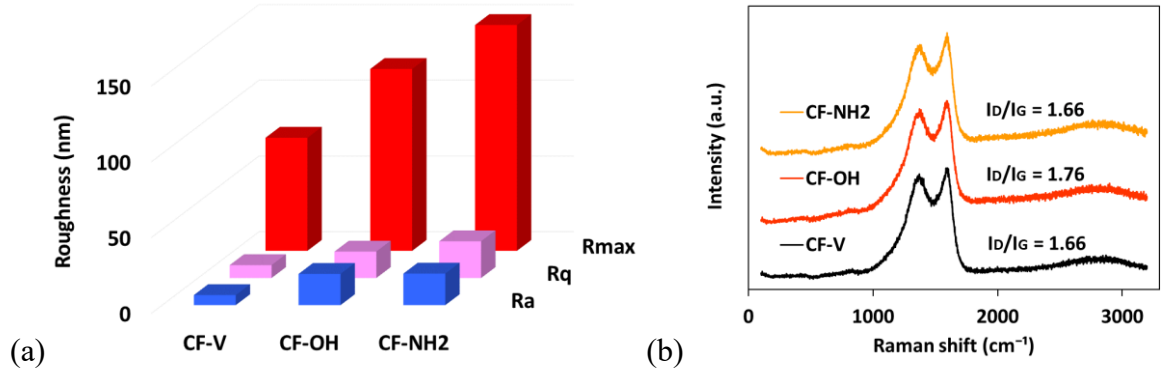

Figure 4-16. (a) Roughness and (b) Raman spectrum of CF before and after functionalisation.

Figure 4-17 (a) compares the tensile strength and Weibull parameters of individual functionalised CFs with those of untreated vCF. Statistically, the hydroxyl- and amino-functionalised CFs show improvements with average tensile strength increase of 3.04% and 1.29%, respectively, and median tensile strength gain of 5.05% and 1.07%, respectively.

The Weibull modulus (m) increased from 6.86 for CF-V to 7.29 for CF-OH, indicating relatively homogeneous grafting of phenolic hydroxyl groups and reduced variability in the strength of CFs. However, it reduced to 4.47 for CF-NH_2, suggesting that this treatment may be slightly less homogeneous. Nonetheless, the minimal difference in the m value indicates that the effect on variability is very limited. Concurrently, the scale parameter (σ) for functionalised CFs showed a slight increase compared to CF-V, suggesting an improvement in overall strength. All the correlation coefficients (R^2) derived from the tensile testing were ensured to be greater than 0.9 (Figure 4-17 (b)), indicating that these measurements followed a statistical distribution and were acceptable for evaluating the tensile performance with negligible variability [52, 61].

The SFTT investigation demonstrated that CFs, despite undergoing mild electrochemical treatment and surface modification, retain their high tensile strength, making them well-suited for application in cementitious materials.

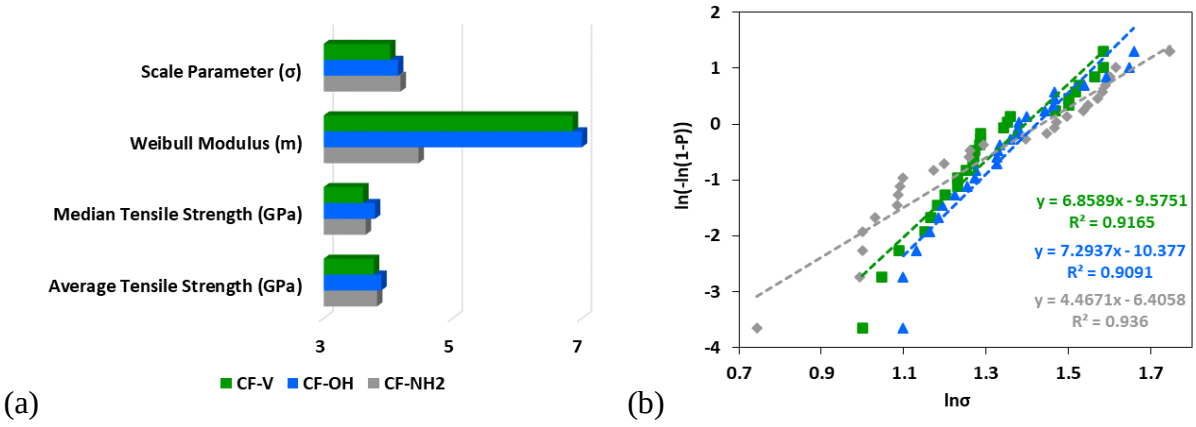

Figure 4-17. (a) Single fibre tensile test and Weibull parameters, (b) Weibull distributions.

4.3.4.2 Enhancing interfacial bonding strength through phenolic and amine group functionalisation

The typical pullout load-displacement curves of CF bundles in Figure 4-18 (a) were obtained by averaging the results from three tests conducted on three replicate specimens for each type of CF. As shown in Figure 4-18 (b), the debonding force (F_a) represents the maximum pullout force that the CF can achieve within the cementitious matrix. The maximum friction force (F_b) reflects the peak frictional resistance encountered after F_a, where the pullout force decreases to a lower value as CF and matrix slip occur [99]. The F_a of CF functionalised with hydroxyl groups was the highest (a 48.33% increase compared to the untreated CF sample), followed by the CF functionalised with amine groups, indicating both surface modifications can effectively improve the bond strength between CF and the cementitious matrix (Figure 4-18 (c)). The Fb of CF-V, CF-OH and CF-NH_2 were 5.2N, 4.8N and 5.5N, respectively, corresponding to interfacial friction contribution ratios of 0.64, 0.40, and 0.62 (Figure 4-18 (d)). The F_b of CF-V, CF-OH and CF-NH_2 were 5.2N, 4.8N and 5.5N, respectively. This means that although CF-OH exhibited higher surface roughness (as observed under SEM and AFM), which improved interfacial friction bond strength, the overall improvement in bonding strength was primarily due to chemical adhesion between the CF surface and the cementitious matrix. Figure 4-18 (d) also illustrates that the chemical interaction between CF-OH and the cementitious matrix was significantly enhanced. CF-NH_2 exhibited slightly greater chemical adhesion compared to CF-V, but the contribution of mechanical interlocking was found to be more

significant than that of the chemical reaction with the cementitious matrix. This observation is consistent with the noted increase in surface roughness (Section 4.3.4.1).

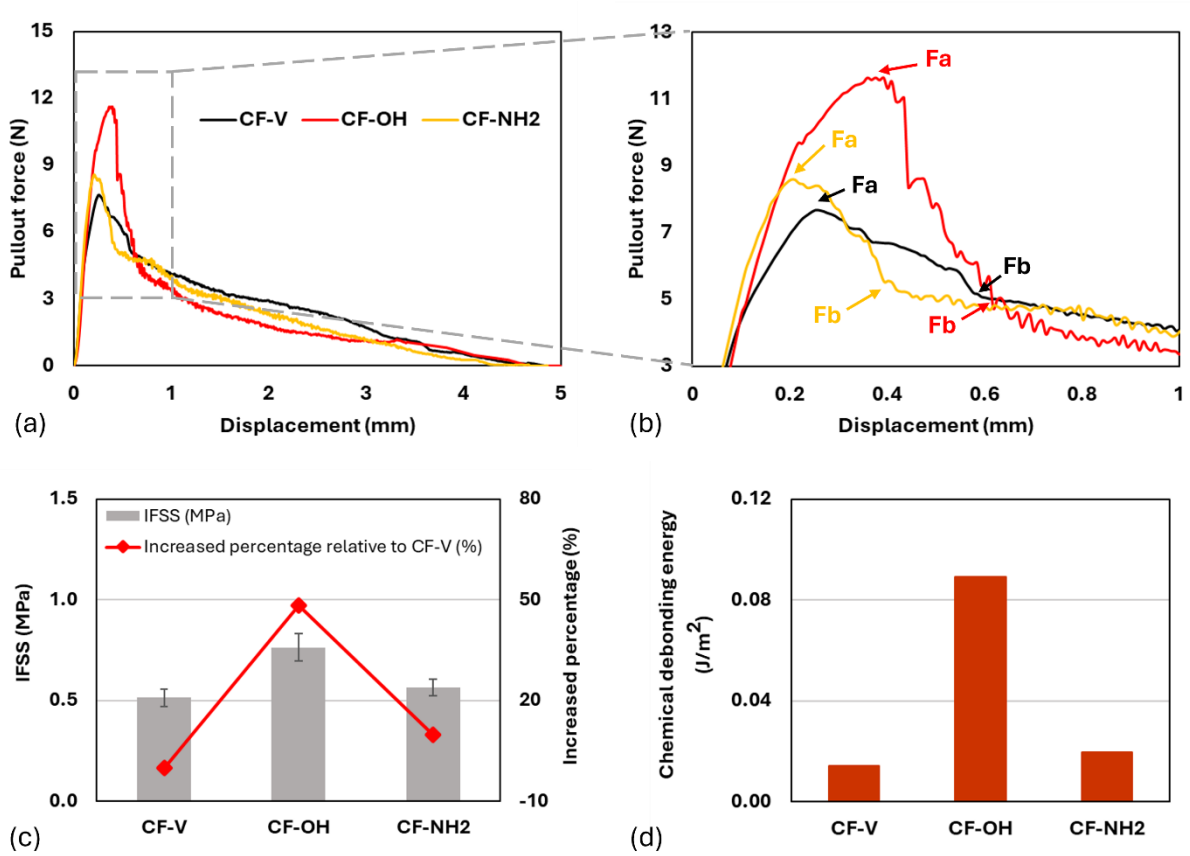

Figure 4-18. (a) Average pullout load-displacement curves, (b) magnified region highlighting debonding force (Fa) and maximum friction force (Fb), (c) interfacial shear strength, and (d) chemical debonding energy, for untreated vCF and functionalised CFs.

Figure 4-19 (a) displays the flowability of fresh cementitious pastes, and Figure 4-19 (b) to (f) show the mechanical strength performance of FRCCs. Regarding the incorporation of CFs in cementitious paste, it is notable that the flow value was reduced in all combinations compared to the controlled mortar, primarily due to fibre agglomeration and air entrapment. It is also evident that flowability was negatively affected by both increased fibre dosage and length. The surface modification strategy altered the CF surface from hydrophobic to hydrophilic through the introduction of polar functional groups, thereby enhancing the dispersion of CFs within the aqueous cementitious matrix. This improved dispersion effectively mitigates fibre clumping. However, the presence of hydrophilic functional groups adversely impacted flowability, as they increased the fibres' affinity for water, resulting in water absorption by the CFs. Consequently, this phenomenon led to a reduction in flowability during testing. As indicated in Figure 4-19 (a), the CF-OH group exhibited a significant reduction in flow values, reaching up to 30.43% in the mixture containing 0.5 vol.% 12mm hydroxyl-functionalised CFs compared to CM. The

CF-NH_2 group has a similar trend to CF-V regarding flowability, but a slightly diminished effect.

All specimens incorporating phenolic hydroxyl-functionalised CFs demonstrated higher compressive strength compared to the other mixtures (Figure 4-19 (b) to (e)). Specifically, the CF-OH specimen containing 0.1 vol.% 12mm hydroxy-functionalised CFs achieved the highest compressive strength of 42.44 MPa in Figure 4-19 (e), representing a 32.30% increase compared to the CM. The CF-NH_2 specimen with amine-functionalised CFs also demonstrated a moderate improvement in compressive strength relative to those FRCCs with vCFs. Based on the optimal compressive testing results presented in Figure 4-19 (e), flexural tests were conducted on the FRCC specimens with 0.1 vol.% of 12mm CFs to investigate the impact of different treatments on flexural strength. The results indicate that flexural strength trends are similar to compressive strength (Figure 4-19 (f)), with CF-OH and CF-NH_2 demonstrating strong flexural strengths of 5.81 MPa and 5.28 MPa, respectively, which are 21.04% and 10.00% higher than the CM value of 4.08 MPa. In contrast, CF-V exhibited a negligible effect on flexural strength, registering only a 1.04% increase.

To validate the hypothesis and investigate the mechanism behind the improved interfacial properties between CFs and the cementitious matrix, the internal microstructures of the FRCC specimens were observed after mechanical testing using SEM. For CF-V specimens without CF surface treatment, a weak interaction between the CF and the cementitious matrix was observed, attributed to the inherent hydrophobic nature of vCF. This resulted in a less compacted ITZ, as shown in Figure 4-20 (a).

In comparison, the functionalised CFs exhibited a rougher surface, thereby enhancing the mechanical interlocking mechanism with the cementitious matrix. The increased surface roughness and contact area also created more sites for the nucleation and deposition of hydration products on the CF surface. Moreover, the active polar groups enriched on the CF surface not only enhance hydrophilicity, promoting better dispersion, but also enable the formation of a closer and more cohesive interface between the CFs and the cementitious matrix. The functionalised CF facilitated the chemisorption of calcium and aluminium ions (Ca^{2+} and Al^{3+}) from the cementitious matrix. Subsequently, the accumulation of hydration products on the CFs led to improved fibre-matrix interfacial bonding. Between the two surface modifications, CFs functionalised with hydroxyl groups exhibited superior interfacial bonding performance compared to those with amine groups. This enhanced performance could be explained by several chemical and microstructural advantages. Hydroxyl groups possess high

polarity and strong electronegativity, facilitating the formation of robust hydrogen bonds with oxygen atoms in Calcium-Silicate-Hydrate (C-S-H) gels, surpassing the strength of van der Waals forces [19, 99]. These strong hydrogen bonds enhance the affinity between the CF surface and the cement hydration products, promoting C-S-H nucleation and continuous growth directly on the fibre surface. Additionally, hydroxyl groups on the fibre surface effectively interact with divalent Ca^{2+} ions from cement hydration products $Ca(OH)_2$ and C-S-H gels through lone-pair electron donation from the oxygen atom, forming coordination bonds that anchor the fibres within the matrix and promote hydration product nucleation at the interface [19, 100]. Both ionic interactions and hydrogen bonding mechanisms contribute to hydration product nucleation and precipitation near CFs, thereby strengthening the interfacial zone between the fibres and the cementitious matrix. As indicated in Figure 4-20 (b), the interaction between the functionalised CFs and the cementitious matrix is evident. Hydration products were clearly observed forming on the surface of the functionalised CFs, indicating that the hydroxyl functional groups provided effective nucleation sites. In contrast, while amine groups are also capable of interacting with Ca^{2+} and hydration products, they typically form weaker hydrogen bonds due to nitrogen's lower electronegativity compared to oxygen. This was confirmed through mechanical testing results compared to the hydroxyl-functionalised specimens. Even though the bonding mechanisms can also be interpreted through SEM images. Figure 4-20 (e) shows residual hydration products attached to the fibre surface after partial pull-out. The adherence of these hydration products even after mechanical testing demonstrates the dense interaction between the functionalised fibre surface and cementitious phases.

Overall, this resulted in a stronger adhesion between functionalised CFs and cementitious matrix, significantly enhancing the densification and effectiveness of the ITZ in transferring stress between the fibre and matrix. This improved bonding plays a critical role in fibre bridging and pullout mechanisms in FRCC, thereby increasing its ability to resist crack propagation and enhancing its load-carrying capacity. This is further supported by the morphology observed in Figure 4-20 (c), where crack-bridging CFs are clearly visible, accompanied by multiple microcracks radiating into the surrounding matrix. These microstructural features demonstrate that the strong bonding between functionalised CFs and the cementitious matrix enabled effective stress transfer, allowing the fibres to absorb and redistribute localised stresses uniformly throughout the surrounding matrix, thereby mitigating crack propagation and enhancing the composite's crack resistance properties. Moreover, the rough fibre channel observed post-pullout in Figure 4-20 (d) shows extensive microcracking and matrix disruption,

rather than a smooth surface. This is indicative of frictional resistance, consistent with strong fibre-matrix adhesion, particularly in hydroxyl-functionalised CFs. Similarly, Figure 4-20 (f) shows residual matrix material adhered to an amine-functionalised CF after pullout. Collectively, these microstructural features observed in SEM provide direct visual evidence of enhanced fibre-matrix bonding, increased pullout resistance, and improved crack-bridging capacity in FRCCs incorporating functionalised CFs.

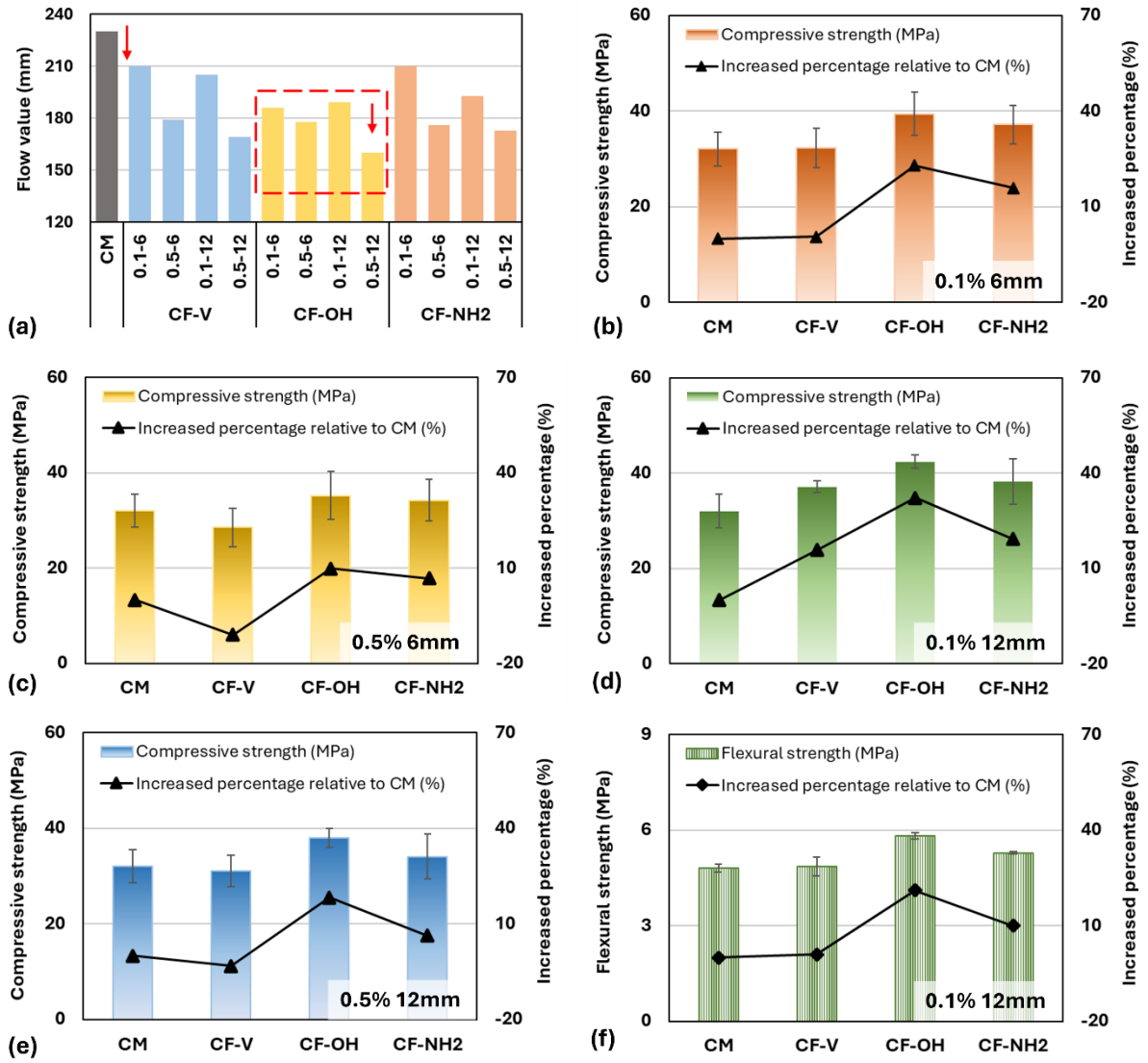

Figure 4-19. (a) Flow table test results; (b) Compressive strength of CM and FRCC with 0.1% dosage, 6mm CFs; (c) 0.5% dosage, 6mm CFs; (d) 0.5% dosage, 12mm CFs; and (e) Compressive Strength and (f) Flexural Strength of FRCC with 0.1% dosage, 12mm CFs.

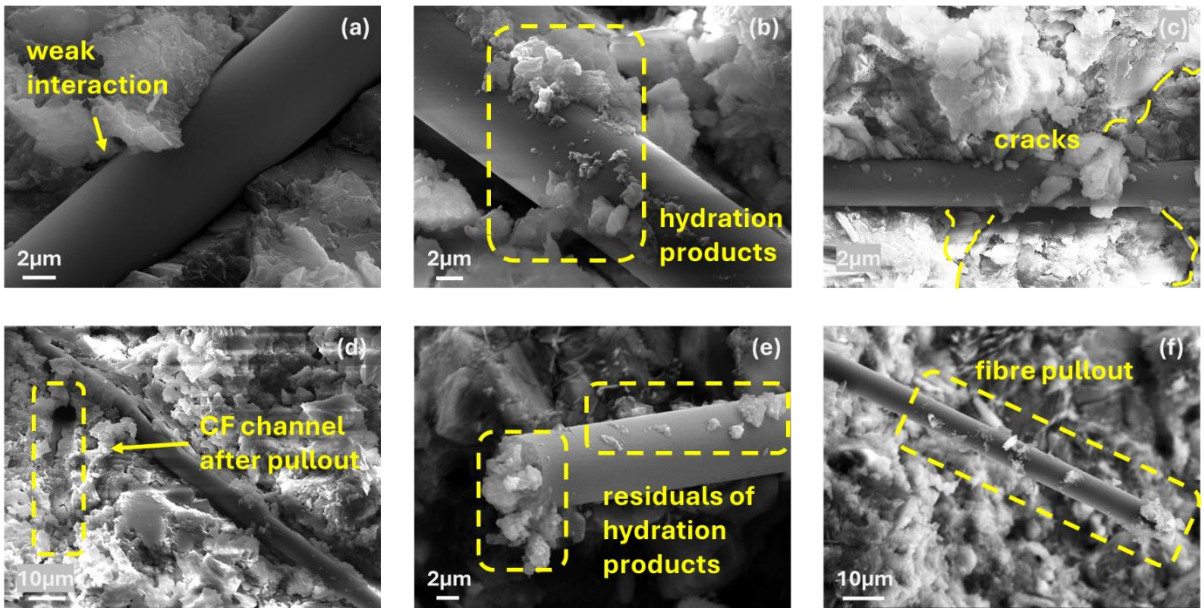

Figure 4-20. SEM micrographs of cementitious composites with (a) untreated vCFs, (b) to (d) hydroxyl-functionalised CFs, and (e) to (f) amino-functionalised CFs.

4.3.4.3 Physical properties of FRCC enhanced by CF surface functionalisation

The water absorption percentage, representing the total porosity of the cementitious composites, revealed that all CF-V mixes exhibited an increase of up to 12.60% compared to the CM (Figure 4-21 (a)). This increase was attributed to the additional ITZ between the vCF and the cement matrix, leading to the presence of gaps and potentially due to the fibre clusters creating more voids. In contrast, FRCC mixtures containing functionalised CFs demonstrated a mitigating effect on the negative impact of fibre inclusion on porosity. Interestingly, the incorporation of 0.1 vol.% 12 mm hydroxyl-functionalised CFs resulted in a porosity reduction of 0.98%, while the addition of 0.1 vol.% 6 mm amino-functionalised CFs led to a porosity reduction of 1.81%, compared to the CM. This indicates a more uniformly distributed fibre mixture, which reduces the likelihood of fibre agglomeration and enhances interaction with the cement matrix. As a result, this leads to a reduction in ITZ gaps and contributes to the formation of a denser microstructure.

The bulk resistivity exhibited an opposite trend compared to water absorption and was influenced by the dosages and lengths of CFs incorporated under different treatments. A notable decrease in resistance was observed in CF-V compared to the CM, mainly attributed to the conductive CF creating a network within the cementitious matrix. It is also clear that the electrical resistivity could be further reduced by longer CF lengths and higher CF dosages. Compared to CM, CF-V led to a maximum reduction in electrical resistivity of 71.64%. Compared to the CF-V group, the FRCC mixtures containing functionalised CFs exhibited

higher electrical resistance overall. The increase in bulk resistivity was particularly pronounced in mixtures with lower porosity. Both water absorption and bulk resistivity are key aspects when considering the durability of FRCC. Lower porosity reduces pathways for chemical penetration, thereby decelerating degradation. Higher bulk resistivity indicates reduced ionic movement, contributing to improved resistance against chemical attacks. Measuring these physical properties can help understand and predict the durability of FRCC and serve as indicators of long-term performance.

Figure 4-21 (b) shows the drying shrinkage of FRCC specimens containing functionalised CFs in comparison to those with untreated CFs. Initially, the changes in shrinkage length increased significantly, followed by a reduction in the rate of change after 28 days. Drying shrinkage in cementitious composites occurs as they lose capillary water, generating tensile stress. The amino-functionalised CFs incorporated into the cementitious composites exhibited limited restraining effects, showing a trend similar to that of specimens with untreated CFs. In contrast, the hydroxyl-functionalised CFs demonstrated reduced shrinkage strain, attributed to their enhanced chemical adhesion and physical friction with the cementitious matrix. These fibres oriented along the specimen length, effectively mitigate drying shrinkage along the specimen. As a result, CF-OH demonstrated better reinforcing capabilities and effectively limited drying shrinkage.

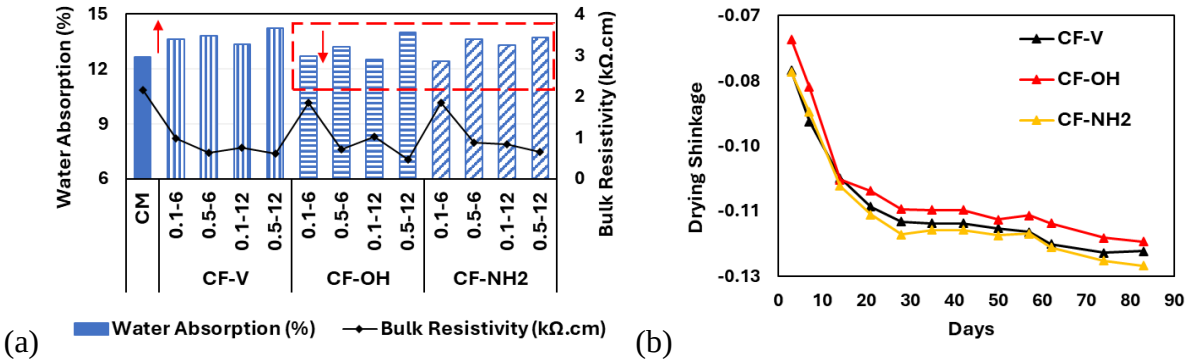

Figure 4-21. (a) Water absorption and bulk resistivity measurements at 28 days, and (b) Drying shrinkage measurements.

4.3.5 Summary of key findings from Section 4.3

In this study, we evaluated modified CF with hydroxyl or amino groups through an in situ electrochemical modification process, aiming to improve the performance of FRCC in construction applications. The interfacial bonding properties and mechanical strength between the functionalised CFs and the cementitious matrix were quantitatively investigated through CF

bundle pullout tests, compressive and flexural testing, and SEM examinations. The conclusions drawn are as follows:

(i) Functional groups were successfully grafted onto the CF surface, as characterised chemically and physically by a series of microstructural examinations. The electrochemical surface modification offers the advantages of efficiency and controlled performance without compromising the tensile strength of CFs.

(ii) The debonding force of hydroxyl- and amino-functionalised CFs within the cementitious matrix increased by 48.33% and 9.70%, respectively, compared to the untreated CF specimens. The chemical adhesion between fibres and the matrix was significantly improved by grafting hydroxyl groups onto the CF surface.

(iii) FRCC specimens with hydroxyl-functionalised CFs outperformed those with amino-functionalised CFs, achieving the highest compressive strength of 42.44 MPa and flexural strength of 5.81 MPa with a combination of 0.1 vol.% and 12mm CFs, representing increases of 32.30% and 21.04%, respectively, compared to plain mortar. Hydroxyl-functionalised CFs also exhibited effectively limited drying shrinkage. Moreover, the surface modification reduced the total porosity of FRCC, proving the formation of a denser microstructure.

(iv) The functional groups attached to the CF surface improved chemical adhesion at the interface with the matrix through the chemisorption of calcium and aluminium ions, as well as strong hydrogen bonds and covalent bonding with the C-S-H gels and cementitious matrix. Additionally, the rougher surface enhanced the mechanical interlocking mechanism and created sites for nucleation and hydration product deposition. SEM observations further demonstrated that functionalisation increased the attachment of hydration products to the CF surface, improved stress transfer between the CF and the matrix, and enhanced resistance to fibre pullout.

This study highlights the efficacy of the proposed electrochemical grafting technique for CF in large-scale continuous processing, while the findings validate the outstanding performance and commercial potential of the resulting FRCCs in the construction field. Future research could focus on durability testing of these FRCCs and performing a life cycle analysis to further emphasise the sustainability benefits of the technique's environmental friendliness and time efficiency.

4.4 CONCLUSION

This chapter proposed two innovative CF surface modification approaches to address the hydrophobic nature of CFs and enhance their dispersion and interfacial bonding in FRCC. Both bio-chemical-based treatment and in-situ electrochemical grafting successfully introduced functional groups, increased surface roughness, and maintained CF tensile properties, leading to improved chemical adhesion and mechanical interlocking with the cementitious matrix. Mechanical testing demonstrated remarkable enhancements in FRCC performance. Detailed key findings have been summarised in sections 4.2.5 and 4.3.5. These findings highlight the effectiveness and industrial applicability of the proposed surface modification strategies for optimising CF reinforcement in cementitious materials. Improved FRCC properties contribute to stronger, more durable, and resilient infrastructure, advancing high-performance CCs in the construction industry.

4.5 REFERENCES

[1] E.R.K. Chandrathilaka, S.K. Baduge, P. Mendis, P.S.M. Thilakarathna, Structural applications of synthetic fibre reinforced cementitious composites: A review on material properties, fire behaviour, durability and structural performance, Structures 34 (2021) 550-574.

[2] Y. Tao, S.A. Hadigheh, Z. Wang, Void geometry analysis and multifaceted characterisation of cementitious mortar reinforced with short carbon and glass fibres – A comparative study, J. Build. Eng. 89 (2024) 109283.

[3] Z. Yuan, Y. Jia, Mechanical properties and microstructure of glass fiber and polypropylene fiber reinforced concrete: An experimental study, Constr. Build. Mater. 266 (2021) 121048.

[4] L. Li, Q. You, W. Liu, Q. Zeng, C. Zhou, J. Wang, Z. Li, K. Li, Enhanced flexural performances of cementitious composite beams with continuously graded steel fiber distribution, Mater. Des. 227 (2023) 111728.

[5] A.M. Mohamed, B.A. Tayeh, Y.I. Abu Aisheh, M.N.A. Salih, Exploring the performance of steel fiber reinforced lightweight concrete: A case study review, Case Stud. Constr. Mater. 18 (2023) e01968.

[6] C. Devi, D.S. Vijayan, R. Nagalingam, S. Arvindan, A review of the implementations of glass fiber in concrete technology, Mater. Today: Proc. 62 (2022) 2010-2015.

[7] O. Onuaguluchi, N. Banthia, Plant-based natural fibre reinforced cement composites: A review, Cem. Concr. Compos. 68 (2016) 96-108.

[8] T. Jirawattanasomkul, S. Likitlersuang, N. Wuttiwannasak, T. Ueda, D. Zhang, M. Shono, Structural behaviour of pre-damaged reinforced concrete beams strengthened with natural fibre reinforced polymer composites, Composite Structures 244 (2020) 112309.

[9] M. Asim, G.M. Uddin, H. Jamshaid, A. Raza, Z.u. Rehman Tahir, U. Hussain, A.N. Satti, N. Hayat, S.M. Arafat, Comparative experimental investigation of natural fibers reinforced light weight concrete as thermally efficient building materials, J. Build. Eng. 31 (2020) 101411.

[10] B. Ali, L.A. Qureshi, R. Kurda, Environmental and economic benefits of steel, glass, and polypropylene fiber reinforced cement composite application in jointed plain concrete pavement, Composites Communications 22 (2020) 100437.

[11] C. Ryan, E. Garcia-Taengua, Fibre-Reinforced Concrete Is Sustainable and Cost-Effective for Water-Retaining Structures, Sustainability 13(20) (2021) 11479.

[12] J.-W. Oh, K.-S. Park, H.S. Kim, I. Kim, S.-J. Pang, K.-S. Ahn, J.-K. Oh, Comparative CO2 emissions of concrete and timber slabs with equivalent structural performance, Energy and Buildings 281 (2023) 112768.

[13] B. Rivaz, Low carbon lining for tunnelling precast segment – How Dramix® fibre reinforced concrete could facilitate this achievement, 2023, pp. 40-47.

[14] Using Concrete Fiber Reinforcement to Reduce Carbon Footprint, 2023. https://www.nudura.com/company/blog/architects/using-concrete-fiber-reinforcement-to-reduce-carbon-footprint/. (Accessed 8 March 2025).

[15] M.G. Alberti, A. Enfedaque, D.M.V. Faria, M. Fernández Ruiz, The Potential of Fiber-Reinforced Concrete to Reduce the Environmental Impact of Concrete Construction, Appl. Sci. 14(15) (2024) 6629.

[16] M. Hambach, H. Möller, T. Neumann, D. Volkmer, Carbon fibre reinforced cement-based composites as smart floor heating materials, Compos. B. Eng. 90 (2016) 465-470.

[17] H. Ran, M. Elchalakani, S. Yehia, M.A. Sadakkathulla, X. Guo, Mechanical, electrical and self-healing properties of carbon fibre-reinforced ultra-lightweight ECC, J. Build. Eng. 84 (2024) 108513.

[18] J. Zhang, A. Heath, H.M.T. Abdalgadir, R.J. Ball, K. Paine, Electrical impedance behaviour of carbon fibre reinforced cement-based sensors at different moisture contents, Constr. Build. Mater. 353 (2022) 129049.

[19] H. Li, M. Liebscher, D. Zhao, B. Yin, Y. Du, J. Yang, M. Kaliske, V. Mechtcherine, A review of carbon fiber surface modification methods for tailor-made bond behavior with cementitious matrices, Progress in Materials Science 132 (2023) 101040.

[20] C. Lin, T. Kanstad, S. Jacobsen, G. Ji, Bonding property between fiber and cementitious matrix: A critical review, Constr. Build. Mater. 378 (2023) 131169.

[21] Z. Lu, A. Hanif, G. Sun, R. Liang, P. Parthasarathy, Z. Li, Highly dispersed graphene oxide electrodeposited carbon fiber reinforced cement-based materials with enhanced mechanical properties, Cem. Concr. Compos. 87 (2018) 220-228.

[22] L. Lavagna, S. Musso, G. Ferro, M. Pavese, Cement-based composites containing functionalized carbon fibers, Cem. Concr. Compos. 88 (2018) 165-171.

[23] K. Jin Hee, H. Jong Hun, H. Seungki, K. Doo-Won, P. Sang Hee, W. Jae-Hyung, Y. Kap Seung, K. Yoong Ahm, Effect of plasma surface modification on pullout characteristics of carbon fiber-reinforced cement composites, Carbon Trends 3 (2021) 100030.

[24] J. Zhao, M. Liebscher, A. Michel, K. Schneider, R. Foest, M. Fröhlich, A. Quade, V. Mechtcherine, Plasma-generated silicon oxide coatings of carbon fibres for improved bonding to mineral-based impregnation materials and concrete matrices, Cem. Concr. Compos. 114 (2020) 103667.

[25] H. Li, M. Liebscher, I. Curosu, S. Choudhury, S. Hempel, M. Davoodabadi, T.T. Dinh, J. Yang, V. Mechtcherine, Electrophoretic deposition of nano-silica onto carbon fiber surfaces for an improved bond strength with cementitious matrices, Cem. Concr. Compos. 114 (2020) 103777.

[26] Z. Wang, E. Bai, C. Liu, B. Ren, J. Zhang, Strength, toughness and interface modification of graphene oxide grafted carbon fiber modified concrete, Constr. Build. Mater. 428 (2024) 136336.

[27] N. Raphael, K. Namratha, B.N. Chandrashekar, K.K. Sadasivuni, D. Ponnamma, A.S. Smitha, S. Krishnaveni, C. Cheng, K. Byrappa, Surface modification and grafting of carbon fibers: A route to better interface, Progress in Crystal Growth and Characterization of Materials 64(3) (2018) 75-101.

[28] S. Dai, F. Yan, S. Zhang, J. Guo, L. Zhang, Y. Liu, L. Liu, Y. Ao, Synthesis of a fully bio-based self-catalyzed hyperbranched waterborne polyurethane as a sizing agent for enhancing the interfacial properties of CF/PA6 composites, Green Chemistry 26(7) (2024) 4127-4134.

[29] F. Yan, Q. Zhou, Y. Xu, G. Wang, G. Li, C. Ma, G. Su, X. Zhan, L. Liu, Learning from nature: Constructing “rigid-soft” structure on carbon fibers surface by self-assembly to improve the performance of epoxy composites, Compos. Part A Appl. Sci. Manuf. 176 (2024) 107888.

[30] Z. Mengjie, C. Chunxia, G. Chunqi, J. Lin, L. Liu, L. Ming, S. Lei, L. Yu, A. Yuhui, Co-depositing bio-inspired tannic acid-aminopropyltriethoxysilane coating onto carbon fiber for excellent interfacial adhesion of epoxy composites, Compos. Sci. Technol. 204 (2021) 108639.

[31] A. Bashiri Rezaie, M. Liebscher, M. Ranjbarian, F. Simon, C. Zimmerer, A. Drechsler, R. Frenzel, A. Synytska, V. Mechtcherine, Enhancing the interfacial bonding between PE fibers and cementitious matrices through polydopamine surface modification, Compos. B. Eng. 217 (2021) 108817.

[32] F. Huang, J. Zhang, X. Zheng, Y. Wu, T. Fu, S. Easa, W. Liu, R. Qiu, Preparation and performance of autoclaved aerated concrete reinforced by dopamine-modified polyethylene terephthalate waste fibers, Constr. Build. Mater. 348 (2022) 128649.

[33] Z. Gu, P. Chen, C. Wang, A. Wang, Y. Wang, P. Qian, X. Li, Bio-inspired polydopamine modification of recycled carbon fibers for improving the performance of recycled carbon fiber reinforced mortars, Constr. Build. Mater. 414 (2024) 134912.

[34] A. Bashiri Rezaie, M. Liebscher, A. Drechsler, A. Synytska, V. Mechtcherine, Tannic acid/ethanolamine modification of PE fiber surfaces for improved interactions with cementitious matrices, Cem. Concr. Compos. 131 (2022) 104573.

[35] C. Chen, H. Yang, X. Yang, Q. Ma, Tannic acid: a crosslinker leading to versatile functional polymeric networks: a review, RSC Advances 12(13) (2022) 7689-7711.

[36] M. Mohammadi, A. Bashiri Rezaie, M. Liebscher, T. Köberle, A. Drechsler, R. Frenzel, F. Simon, A. Synytska, V. Mechtcherine, Interfacial properties of high-strength, limestone-calcined clay cement (LC3) matrix and PE fibers, surface-modified using dopamine and tannic acid, Constr. Build. Mater. 408 (2023) 133537.

[37] N. Zheng, J. He, D. Zhao, Y. Huang, J. Gao, Y.-W. Mai, Improvement of atomic oxygen erosion resistance of carbon fiber and carbon fiber/epoxy composite interface with a silane coupling agent, Mater. Des. 109 (2016) 171-178.

[38] H. Yuan, C. Wang, S. Zhang, X. Lin, Effect of surface modification on carbon fiber and its reinforced phenolic matrix composite, Appl. Surf. Sci. 259 (2012) 288-293.

[39] M. Iorio, F. Marra, M.L. Santarelli, J. González-Benito, Reinforcement-matrix interactions and their consequences on the mechanical behavior of basalt fibers-cement composites, Constr. Build. Mater. 309 (2021) 125103.

[40] J.P. Chen, S. Wu, K.-H. Chong, Surface modification of a granular activated carbon by citric acid for enhancement of copper adsorption, Carbon 41(10) (2003) 1979-1986.

[41] U.S. Rashid, A.N. Bezbaruah, Citric acid modified granular activated carbon for enhanced defluoridation, Chemosphere 252 (2020) 126639.

[42] Y. Banba, T. Umeda, H. Kuroe, T. Toyama, Y. Musha, K. Itatani, Homogeneous Coating of Hydroxyapatite on Multi-Wall Carbon Nanotube Immersed in Calcium Phosphate Solution by Microwave Heating, Phosphorus Research Bulletin 28 (2013) 51-57.

[43] S. Chafei, L.F. Dutra, A. Jamali, Enhancing Mechanical Behavior of Cement Composites through Citric Acid Treatment of Flax Fibers, J. Mater. Civ. Eng. 36(1) (2024) 04023486.

[44] BS EN ISO 3696 Water for analytical laboratory use — Specification and test methods, International Organization for Standardization, Switzerland, 1987.

[45] AS 3972 General purpose and blended cements, Standards Australia, Australia, 2021.

[46] AS 2758.1 Aggregates and rock for engineering purposes Concrete aggregates, Standards Australia, Australia, 2014.

[47] Y. Tao, S.A. Hadigheh, D.J. Hayne, B. Newman, L.C. Henderson, Eco-friendly surface modification of carbon fibres for application in cement-based composites, 21th European Conference on Composite Materials (ECCM 21) Nantes, Paris, 2024.

[48] BS EN 1015-3 Methods of test for mortar masonry - Part 3: Determination of consistence of fresh mortar (by flow table), British Standards Institution, UK, 1999.

[49] Avantage v6.6.0 Alpha Thermo Fisher Scientific, 2022.

[50] NanoScope Analysis 3.00. Bruker Corporation, 2021.

[51] ASTM C1557 Standard Test Method for Tensile Strength and Young's Modulus of Fibers, ASTM International, West Conshohocken, United States, 2020.

[52] D. He, V.K. Soo, F. Stojcevski, W. Lipiński, L.C. Henderson, P. Compston, M. Doolan, The effect of sizing and surface oxidation on the surface properties and tensile behaviour of recycled carbon fibre: An end-of-life perspective, Compos. Part A Appl. Sci. Manuf. 138 (2020) 106072.

[53] B. EN1015-6, Methods of test for mortar for masonry - Part 6: Determination of bulk density of fresh mortar, British Standards Institution, UK, 1999.

[54] C109/C109M Standard Test Method for Compressive Strength of Hydraulic Cement Mortars (Using 2-in. or [50 mm] Cube Specimens), ASTM International, West Conshohocken, United States, 2021.

[55] C348 Standard Test Method for Flexural Strength of Hydraulic-Cement Mortars, ASTM International, West Conshohocken, United States, 2021.

[56] AASHTO Designation: T 358 - Standard Method of Test for Surface Resistivity Indication of Concrete's Ability to Resist Chloride Ion Penetration, American Association of State Highway and Transportation Officials, Washington, D.C, 2015.

[57] C948-81, Standard Test Method for Dry and Wet Bulk Density, Water Absorption, and Apparent Porosity of Thin Sections of Glass-Fiber Reinforced Concrete, ASTM International, West Conshohocken, United States, 2016.

[58] D. Lin, B. Xing, Tannic Acid Adsorption and Its Role for Stabilizing Carbon Nanotube Suspensions, Environmental Science & Technology 42(16) (2008) 5917-5923.

[59] M. Zhang, H. Li, M. Na, B. Zhou, J. Zhang, Improving dispersion of recycled GFRP fiber in cement mortar with sodium hexametaphosphate, Cem. Concr. Compos. 143 (2023) 105232.

[60] D. Wu, X. Liu, Y. Sheng, N. Wu, L. Liu, Q. Dong, M. Wang, R. Zhang, Polyhedral Oligomeric Silsesquioxane Encountering Tannic Acid: A Mild and Efficient Strategy for Interface Modification on Carbon Fiber Composites, Langmuir 38(27) (2022) 8334-8341.

[61] K.M. Beggs, L. Servinis, T.R. Gengenbach, M.G. Huson, B.L. Fox, L.C. Henderson, A systematic study of carbon fibre surface grafting via in situ diazonium generation for improved interfacial shear strength in epoxy matrix composites, Compos. Sci. Technol. 118 (2015) 31-38.

[62] Y. Tao, S.A. Hadigheh, Enhancing the strength, microstructural integrity, and shrinkage performance of cement-based mortar using pulverised carbon and glass FRP composite waste, J. Build. Eng. 94 (2024) 110053.

[63] P. Bian, Q. Yu, B. Zhan, P. Gao, B. Guo, L. Hong, Y. Yang, A. Han, Enhancing electromagnetic wave absorption and flexural properties in carbon fiber-reinforced foamed cement-based composites, Constr. Build. Mater. 415 (2024) 134989.

[64] A.I. Ruiz, E. Reyes, C. Argiz, M.A. de la Rubia, A. Moragues, Nano-scale aluminium interaction in synthetic hydrated calcium silicate gel studied by 29Si MAS-NMR, Boletín de la Sociedad Española de Cerámica y Vidrio 62(5) (2023) 388-401.

[65] J.J. Biernacki, J.W. Bullard, G. Sant, K. Brown, Fredrik P. Glasser, S. Jones, T. Ley, R. Livingston, L. Nicoleau, J. Olek, F. Sanchez, R. Shahsavari, P.E. Stutzman, K. Sobolev, T. Prater, Cements in the 21st century: Challenges, perspectives, and opportunities, 100(7) (2017) 2746-2773.

[66] K.L. Scrivener, R. Snellings, The Rise of Portland Cements, Elements 18(5) (2022) 308-313.

[67] A. Bentur, S. Mindess, Fibre reinforced cementitious composites, Crc Press2006.

[68] M.A. Ali, A.J. Majumdar, D.L. Rayment, Carbon fibre reinforcement of cement, Cem. Concr. Res. 2(2) (1972) 201-212.

[69] Y. Ohama, Carbon-cement composites, Carbon 27(5) (1989) 729-737.

[70] D.D.L. Chung, Cement reinforced with short carbon fibers: a multifunctional material, Compos. B. Eng. 31(6) (2000) 511-526.

[71] E. Team, Smart Concrete, (2007).

[72] T.V. Muthukumarana, M.A.V.H.M. Arachchi, H.M.C.C. Somarathna, S.N. Raman, A review on the variation of mechanical properties of carbon fibre-reinforced concrete, Constr. Build. Mater. 366 (2023) 130173.

[73] W. Zhang, H. Yu, B. Yin, A. Akbar, J.-G. Dai, X. Zhang, K.M. Liew, Effects of recycled carbon fibers on mechanical and piezoresistive properties and environmental impact in alkali-activated cementitious materials, J. Clean. Prod. 450 (2024) 141902.

[74] A. Belli, A. Mobili, T. Bellezze, P.B. Cachim, F. Tittarelli, Commercial and recycled carbon-based fillers and fibers for self-sensing cement-based composites: Comparison of mechanical strength, durability, and piezoresistive behavior, J. Build. Eng. 73 (2023) 106836.

[75] S. Gwon, H. Kim, M. Shin, Self-heating characteristics of electrically conductive cement composites with carbon black and carbon fiber, Cem. Concr. Compos. 137 (2023) 104942.

[76] M.L. Rahman, A. Malakooti, H. Ceylan, S. Kim, P.C. Taylor, Identifying the best mixing procedure practice for ready-mix concrete plant production of carbon fibre reinforced electrically conductive concrete, International Journal of Pavement Engineering 24(1) (2023) 2225119.

[77] G. Park, S. Kim, G.-K. Park, N. Lee, Influence of carbon fiber on the electromagnetic shielding effectiveness of high-performance fiber-reinforced cementitious composites, J. Build. Eng. 35 (2021) 101982.

[78] D. Wanasinghe, F. Aslani, G. Ma, Electromagnetic shielding properties of carbon fibre reinforced cementitious composites, Constr. Build. Mater. 260 (2020) 120439.

[79] M. Safiuddin, G. Abdel-Sayed, N. Hearn, Absorption and Strength Properties of Short Carbon Fiber Reinforced Mortar Composite, 11(7) (2021) 300.

[80] H.B. Birgin, A. D'Alessandro, A. Corradini, S. Laflamme, F. Ubertini, Self-sensing asphalt composite with carbon microfibers for smart weigh-in-motion, Materials and Structures 55(5) (2022) 138.

[81] X. Liu, S. Wu, Study on the graphite and carbon fiber modified asphalt concrete, Constr. Build. Mater. 25(4) (2011) 1807-1811.

[82] M. Monazami, A. Sharma, R. Gupta, Evaluating performance of carbon fiber-reinforced pavement with embedded sensors using destructive and non-destructive testing, Case Stud. Constr. Mater. 17 (2022) e01460.

[83] S. Muthusamy, D. Chung, Carbon-Fiber Cement-Based Materials for Electromagnetic Shielding, J ACI Materials Journal 107(6) (2010).

[84] Z.-q. Li, J.-H. Zhu, C. Pei, Enhanced interfacial bonding in cement composites through electrophoretic deposition of nano silica on carbon fibers, Constr. Build. Mater. 435 (2024) 136835.

[85] H. Li, M. Liebscher, J. Yang, M. Davoodabadi, L. Li, Y. Du, B. Yang, S. Hempel, V. Mechtcherine, Electrochemical oxidation of recycled carbon fibers for an improved interaction toward alkali-activated composites, J. Clean. Prod. 368 (2022) 133093.

[86] Y. Fu, H. Li, W. Cao, Enhancing the interfacial properties of high-modulus carbon fiber reinforced polymer matrix composites via electrochemical surface oxidation and grafting, Compos. Part A Appl. Sci. Manuf. 130 (2020) 105719.

[87] J. Gulyás, E. Földes, A. Lázár, B. Pukánszky, Electrochemical oxidation of carbon fibres: surface chemistry and adhesion, Compos. Part A Appl. Sci. Manuf. 32(3) (2001) 353-360.

[88] H. Li, M. Liebscher, M. Ranjbarian, S. Hempel, L. Tzounis, C. Schröfl, V. Mechtcherine, Electrochemical modification of carbon fiber yarns in cementitious pore solution for an enhanced interaction towards concrete matrices, Appl. Surf. Sci. 487 (2019) 52-58.

[89] S. Dabees, A. Borkar, B. Newman, Ž. Simon, D.J. Hayne, P. Coia, L.C. Henderson, Improving carbon fibre reinforced polyphenylene sulfide using amine and phenolic interphase modifications, Compos. Part A Appl. Sci. Manuf. 179 (2024) 108045.

[90] S. Wang, S. Zhang, Y. Yang, Z. Dong, G. Wang, Direct electrochemical grafting of crystalline PAEK macromolecule on carbon fiber to enhance the interfacial properties of PEEK/CF composites, Compos. Sci. Technol. 220 (2022) 109262.

[91] D.J. Eyckens, C.L. Arnold, Ž. Simon, T.R. Gengenbach, J. Pinson, Y.A. Wickramasingha, L.C. Henderson, Covalent sizing surface modification as a route to improved interfacial adhesion in carbon fibre-epoxy composites, Compos. Part A Appl. Sci. Manuf. 140 (2021) 106147.

[92] S. Joannès, F. Islam, L. Laiarinandrasana, Uncertainty in Fibre Strength Characterisation Due to Uncertainty in Measurement and Sampling Randomness, Applied Composite Materials 27 (2020).

[93] K. Naresh, K. Shankar, R. Velmurugan, Reliability analysis of tensile strengths using Weibull distribution in glass/epoxy and carbon/epoxy composites, Compos. B. Eng. 133 (2018) 129-144.

[94] N. Defoirdt, S. Biswas, L.D. Vriese, L.Q.N. Tran, J.V. Acker, Q. Ahsan, L. Gorbatikh, A.V. Vuure, I. Verpoest, Assessment of the tensile properties of coir, bamboo and jute fibre, Compos. Part A Appl. Sci. Manuf. 41(5) (2010) 588-595.

[95] A. Katz, V.C. Li, A special technique for determining the bond strength of micro-fibres in cement matrix by pullout test, Journal of Materials Science Letters 15(20) (1996) 1821-1823.

[96] H. Li, M. Liebscher, K.H. Ly, P.V. Ly, T. Köberle, J. Yang, Q. Fan, M. Yu, I.M. Weidinger, V. Mechtcherine, Effect of electrophoretic deposition of micro-quartz on the microstructural and mechanical properties of carbon fibers and their bond performance toward cement, Journal of Materials Science 57(48) (2022) 21885-21900.

[97] H. Li, M. Liebscher, J. Yang, Y. Zhang, V. Mechtcherine, Influence of electrophoretic deposition of micro- or nanosized silica particles on the microstructure of carbon fibers and their bond behavior with cementitious matrices, Materials and Structures 57(5) (2024) 107.

[98] C490/C490M, Standard Practice for Use of Apparatus for the Determination of Length Change of Hardened Cement Paste, Mortar, and Concrete, ASTM International, West Conshohocken, United States, 2021.

[99] H. Huang, J. Luo, C. Peng, T. Sun, T. Deng, J. Hu, K. Guzal Anvarovna, N. Azizbek Davlatali Ugli, D. Hou, J. Wei, Q. Yu, Interfacial bond between modified micro carbon fiber and high-strength cement paste in UHPC: Bond-slip tests and molecular dynamic simulation, Cem. Concr. Compos. 142 (2023) 105168.

[100] S.P. Kundu, S. Chakraborty, S. Chakraborty, Effectiveness of the surface modified jute fibre as fibre reinforcement in controlling the physical and mechanical properties of concrete paver blocks, Constr. Build. Mater. 191 (2018) 554-563.

Chapter 5: Repurposing Industrial FRP Composite Waste into Cement-based Mortars

5.1 INTRODUCTION

The growing demand for FRP composites in various industries such as aviation and renewable energy sectors, has led to significant waste generation. Their disposal presents environmental challenges due to their non-biodegradable nature and complex composition, which creates an urgent need for developing effective waste management and sustainable recycling solutions. In this regard, repurposing FRP composite waste in cement-based mortars, rather than for its intended use in the polymer industry, provides a promising alternative for reusing these recyclates in construction. This approach offers benefits in terms of cost savings and reduced energy requirements for processing FRP recyclates and incorporating them into concrete. While multiple studies have explored the recycling of CFRP and GFRP composite waste in concrete and mortars, most have focused on laboratory-prepared composites, overlooking the practical challenges of reusing industrial FRP waste. Additionally, inconsistent findings on the effects of rFRP due to size and composition variations highlight the need for further investigation to clarify their interactions within cementitious matrices.

This chapter presents a practical approach for repurposing industrial FRP waste from the utility and aerospace sectors without resin removal in cementitious materials. This is achieved using a two-step mechanical size reduction process, offering a viable option for recycling irregularly shaped and variably sized FRP waste. This study evaluates the effects of incorporating varying amounts of CFRP and GFRP recyclates on the fresh, mechanical, durability, and electrical properties of the resulting CCs. Microstructural analysis, including morphology with a focus on the interfacial transition zone (ITZ), as well as mineralogical changes and chemical composition, is also performed to further assess the impact of incorporating CFRP and GFRP powders.

5.2 ENHANCING THE STRENGTH, MICROSTRUCTURAL INTEGRITY, AND SHRINKAGE PERFORMANCE OF CEMENT-BASED MORTAR USING PULVERISED CARBON AND GLASS FRP COMPOSITE WASTE

Y. Tao[1,*], S.A. Hadigheh[1,*]

[1]School of Civil Engineering, Faculty of Engineering, The University of Sydney, Sydney, New South Wales 2006, Australia

[*]Corresponding Author: Dr Ali Hadigheh

Journal of Building Engineering, https://doi.org/10.1016/j.jobe.2024.110053, Published in June 2024.

5.2.1 Abstract

Adopting sustainable materials is a pressing concern for the construction industry to achieve net-zero carbon emissions, driving ongoing research to address environmental challenges. With a particular focus on the fibre-reinforced polymer (FRP) byproducts and wastes generated by various industries, this paper investigates the viability of pulverising and repurposing waste materials from electrical cross-arms and aerospace composite parts in cementitious materials as a partial substitute for cement. Micro fibres with crushed resin particles (passing through a 600μm sieve) were incorporated into the mortar, up to 10% relative to the mass of cement. A series of tests was conducted to evaluate the effects of varying FRP recyclates on the mechanical, durability and electrical performance of mortars. The results indicated that at the 28-day curing age, the inclusion of FRP recyclates led to a 19% reduction in water absorption and significant enhancement in the compressive (up to 67 %) and flexural strength (up to 43%). The optimal restraint of drying shrinkage was observed when replacing 5% by weight of cement with FRP recyclates from electrical cross-arms. The inclusion of FRP recyclates from aerospace offcuts resulted in a 25% reduction in electrical resistivity, indicating a potential for reusing aerospace recyclates for electrically conductive cementitious composites (ECCCs). Further analyses were conducted to assess the effects of FRP recyclate addition on the microstructural properties of the cementitious matrix. This research offers a promising pathway to repurpose composite wastes from the utility and aerospace industries as valuable additions to construction materials.

Keywords: Fibre reinforced polymer (FRP) waste powder; Mechanical properties; Repurposing; Water absorption; Electrical properties

5.2.2 Introduction

The production and use of cement in construction significantly contribute to greenhouse gas emissions (GHG) through raw material extraction, chemical reactions during manufacturing, and energy-intensive transportation throughout its lifecycle. Several studies have indicated that the cement industry is responsible for at least 5-9% of anthropogenic greenhouse gas (GHG) emissions [1-4], while the building and construction sector currently accounts for around 36% of energy consumption [5]. Although these emissions are challenging to fully eliminate, efforts to develop sustainable and smart solutions are critical in limiting the negative environmental impact of the construction sector. Global Cement and Concrete Association (GCCA) has announced a global technology roadmap to achieve a target of net zero by the year 2050 and further lower emissions by 25% over the next decade [6]. To achieve this goal and in adherence to the outlined plan, design optimisation, resource efficiency, recycling and reutilisation components derived from pre-existing products have been prioritised in order to foster environmental sustainability and economic resilience within the built environment.

End-of-life (EoL) and manufacturing scraps of fibre-reinforced polymer (FRP) composites pose environmental challenges due to their non-biodegradable nature. This requires sustainable strategies for their EoL product management and disposal [7, 8]. Carbon fibre-reinforced polymer (CFRP) is in considerable demand in the aviation industry for weight reduction to promote the fuel efficiency of aircraft applications. The high demand is projected to result in a substantial accumulated 500 thousand tonnes of CFRP waste by 2030, encompassing wastes from both production and EoL phases [9-12]. Currently, in the renewable energy sector, the volume of EoL wind turbine blades has been continuously increasing as a consequence of their designed 20-year service life. glass fibre-reinforced polymer (GFRP) is one of the primary components used in wind turbine blades. It has been estimated that the amount of GFRP waste generated could potentially reach 100 thousand tonnes by 2030 [7, 8]. The combined annual accumulation of CFRP waste from the aircraft and wind turbine industries alone is anticipated to exceed 840 thousand tonnes [13]. As such, it is necessary to develop effective waste management and recycling practices for FRP disposals.

The increasing awareness of sustainable development has driven research into recycling and reusing FRP wastes in cementitious composites as an end-use application instead of their original intended use [8, 14]. Efforts have been made to utilise different types of CFRP wastes, including pyrolysis recycled carbon fibre (rCF) [15-17], chemically modified rCF [18], prepreg

carbon fibre (CF) waste [19, 20], and crushed CFRP pieces [20, 21] into concrete to explore their potential for enhancing concrete performance. The incorporation of recycled CFRP (rCFRP) with various lengths and concentrations resulted in improved mechanical properties and reduced shrinkage. These improvements were mainly attributed to the fibre reinforcement, as well as the good bonding with hydration products, particularly evident at 1% by volume rCFRP content. However, thermal or chemical treatments on rCFRP involve relatively high energy consumption, environmental impact and operating costs [8, 22]. An alternative recycling approach could be mechanically repurposing CFRP into powder form without removing resins, presenting a viable option for recycling irregularly shaped and differently sized CFRP wastes.

Recently, the reutilisation of GFRP waste from wind turbine blades in concrete has also garnered attention among researchers, especially with the retirement of older wind turbine structures reaching the end of their lifecycle [3, 22-25]. Fu, et al. [23, 24] reported that macro fibres containing both fibres and resin, mechanically cut from wind turbine blades, can significantly enhance compressive and flexural performance normal strength and ultra-high-performance seawater sea-sand concrete. However, achieving precise control over the macro fibre size and producing thinner strips during the mechanical process is challenging without a specifically designed machine. Various studies have examined the effects of incorporating recycled GFRP (rGFRP) derived from wind turbine blades, in the forms of powder, aggregate, and fibre, on concrete performance [3, 22, 25]. The incorporation of rGFRP as fibre reinforcement has been found to enhance flexural strength while potentially diminishing compressive strength in concrete. Incorporating rGFRP in either powder or aggregate form resulted in a notable decrease in both the compressive and flexural capacity of concrete. In addition, a separate treatment of other components of wind turbine blades, such as wood and polyurethane, may be required during the crushing process. The study conducted by Oliveira, et al. [25] revealed that the incorporation of rGFRP powder from a wind turbine (with an average particle size of 3μm and subjected to the removal of organic constituents) as a replacement for cement exhibited a slight increase in concrete compressive performance at the 90-day curing age. Furthermore, Zhou, et al. [26] demonstrated that incorporating rGFRP powder with particle sizes less than 303μm, directly recycled from different sources (cable boxes, oil tank lids and GFRP dust) into cement-based material led to enhanced fresh and mechanical properties, attributed to improved microstructural compactness. The studies mentioned above have revealed the potential benefits of incorporating rGFRP in improving the performance of cementitious composites and hold promise for reuse in the construction sector.

Reusing rGFRP as a powder or microfibres in cementitious material presents unique opportunities for improving the performance of cementitious composites. Furthermore, rGFRP derived from different source materials can have varying effects on composite performance, attributed to their material compositions and characteristics.

Although multiple studies have investigated the recycling and utilisation of CFRP and GFRP waste in concrete, there has been limited practice in recycling FRP composites within the utility and aerospace industries, especially in reutilising recycled composites in cement-based materials. Given the contradictory results in previous studies regarding the influence of rFRP on concrete properties, attributed to size effects and the diverse composition of waste composites from different sources, there remains a need for extensive research to enhance understanding of the interactions between different recycled FRP (rFRP) and cementitious matrices. One of the promising recycling strategies proposed in this project involves a two-step mechanical size reduction process of FRP wastes without the need for resin removal, followed by repurposing the resulting FRP powder into cementitious materials, leading to a cementitious composite. Currently, the influence of rFRP on the performance of mortar and concrete is a major focus, while the optimum size and dosage of rFRP are still being researched owing to the differences in the properties of the various recyclates [8]. This study focuses on investigating the feasibility of repurposing mechanically recycled CFRP and GFRP composite waste, collected from Australian local industry, encompassing both production and EOL wastes, into the mortar. The research aims to evaluate the performance of cementitious composites incorporated with these rFRP and determine their microstructure behaviour. The material characterisation of raw materials and FRP waste was carried out prior to the cementitious composite casting, which involves particle size distribution, chemical and mineralogical composition as well as mechanical performance of composite products before recycling. The pulverised rFRP were sieved out and served as 1%, 5%, and 10% cement replacements by weight in the mortar mixture, representing low, medium, and high concentrations respectively. The effects of varying dosages of rCFRP and rGFRP on the performance of cementitious composites were examined in this study, in order to offer valuable insights towards the reutilisation of greener materials from various industries for construction, thereby contributing to sustainable development efforts.

5.2.3 Material and methodology

5.2.3.1 Raw materials

FRP recyclates

In this study, FRP recyclates were mechanically reclaimed from two sources (Figure 5-1). The GFRP recyclates incorporated in mortar in this study were provided from the end-of-life electrical crossarms. The CFRP recyclates were obtained from the offcuts of the discarded aerospace manufacturing parts.

Initially, the size of both GFRP electrical crossarms and CFRP panels were primarily reduced to 5mm small cubes using the waterjet cutter. To further downsize the cubes for use in the mix, a Tema ring mill with a tungsten carbide bowl was utilised to pulverise composites. The pulverised composite scraps were mechanically screened using sieves and categorised into smaller recyclates (passed 600µm) and larger flakes (remained on 600µm). The portion that remained on the sieve, they were loaded into the Tema ring mill for a second round of pulverisation before sieving for an additional round. Only FRP recyclates passing through 600 µm, which included a mixture of powdered and fibrous components, were selected for this research.

Cement and fine aggregates

General-purpose cement (fully complied with the requirements of Type GP cement in AS3972 [27]) and fine aggregate (fulfilling the requirements of AS3700 [28]) were used to prepare mortar mix in this study. Portable water was used for mortar mixing.

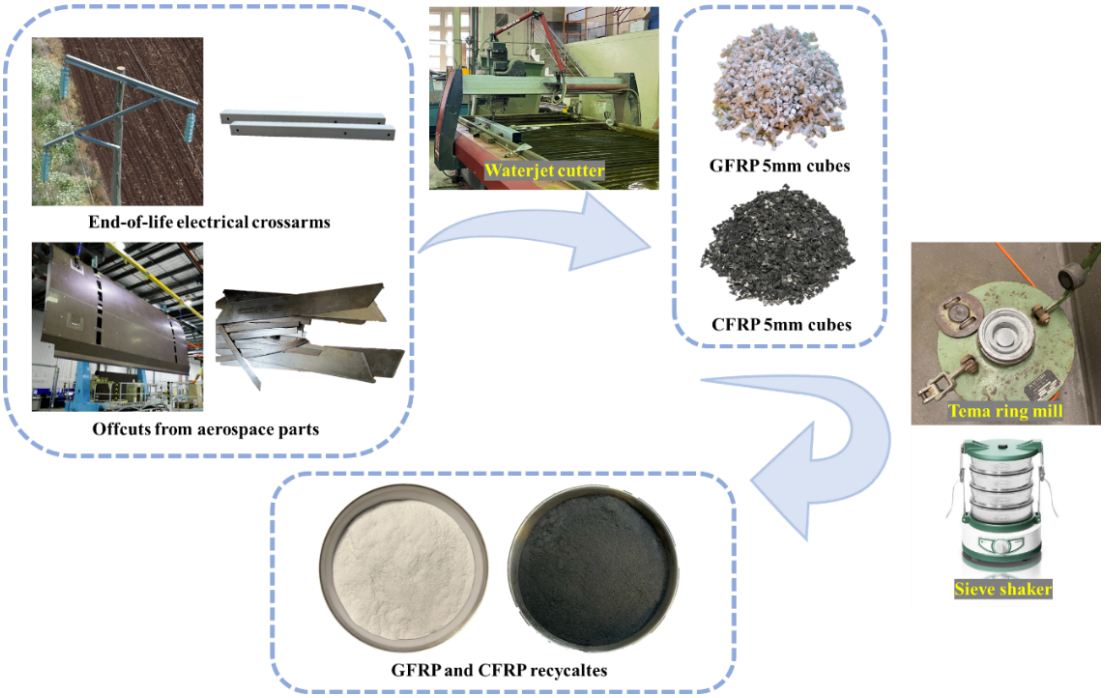

(b)

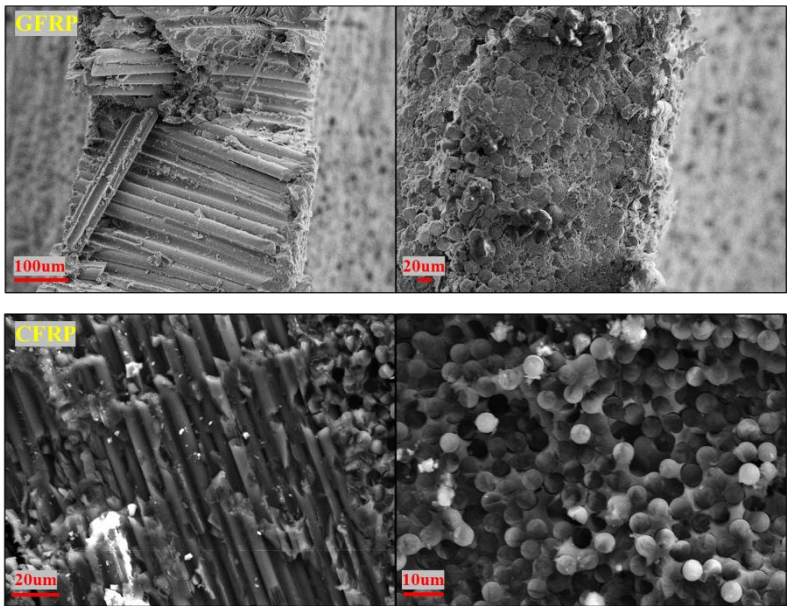

Figure 5-1. (a) Mechanical recycling process of FRP wastes; (b) Cross-sectional view of FRP composite.

5.2.3.2 Experimental program

Mix design and sample preparation

The proportions of cement, sand and FRP recyclates used to prepare the cementitious composites in this study are shown in Figure 5-2, based on the authors' prior research [29]. Both GFRP and CFRP recyclates were incorporated to replace cement at a dosage of 1%, 5% and 10% relative to the mass of cement. This variable was studied to investigate its impact on the properties of the cementitious composites. For each mix batch, the dry ingredients were

initially blended with a mixer for 3 minutes. Then tap water was gradually added, and mixing was continued until uniformity was achieved. The mixed cementitious composites were cast into various metallic moulds to investigate different properties. All mortar specimens were cured in the moulds for 24-48 hours before being cured at the standard laboratory temperature of 23°C. To minimise moisture loss, mortar specimens were wrapped in a wet cloth and sealed with an impermeable plastic sheet until testing [30].

Table 5-1. Mix proportions of mortar with FRP recyclates (kg/m^3).

Mix ID	Control	GFRP1	GFRP5	GFRP10	CFRP1	CFRP5	CFRP10
Water	399.3	395.3	379.3	359.4	395.3	379.3	359.4
Cement	726.0	718.7	689.7	653.4	718.7	689.7	653.4
Sand	1088	1088	1088	1088	1088	1088	1088
rGFRP	-	7.26	36.30	72.60	-	-	-
rCFRP	-	-	-	-	7.26	36.30	72.60

Mechanical and physical tests

The flow value was determined using a flow table test according to BS EN 1015-3 [31] to characterise the influence of milled FRP recyclates on the fluidity of fresh mortars. The bulk density of the fresh mortar was determined according to BS EN 1015-6 [32]. The reported flow diameter and fresh bulk density value represented the mean value of the two measurements with less than 10% deviation.

The analysis of water absorption in terms of porosity was conducted by determining the difference between immersed mass and saturated surface dry mass of the specimens (50×50×50 mm^3), following ASTM C948–81 [33]. The bulk density of hardened mortar at different ages was determined as the ratio of the oven-dry mass to volume in accordance with BS EN 1015-10 [34]. Three specimens per mix were analysed.

Mortar specimens were cast into two 25×25×285 mm^3 prisms per mix for the measurement of drying shrinkage by using a length comparator according to ASTM C490/C490M–2 [35]. The specimens were cured in a humidity chamber in a controlled environment with a temperature of 23°C and a relative humidity of 50%. The initial length reading was measured at the age of 7 days from demoulding. Subsequent measurements were then taken at various time points to monitor length changes.

The mechanical properties of mortars were evaluated through compressive and flexural strength tests at ages of 7, 28 and 90 days. An MTS Sintech 65/G machine was used to perform the compressive and flexural tests with 300kN and 50kN load cells at the loading rate of 0.5 mm/min and 0.1 mm/min, respectively, until failure. The compressive strength was tested on 50×50×50 mm^3 cubic specimens according to ASTM C109/C109M [36]. The flexural strength and ductility tests were conducted on 40×40×160 mm^3 prism specimens using a three-point bending test according to ASTM C348–21 [37]. For each mix, three specimens were tested. The crack propagation behaviour of flexural specimens was analysed by the digital image correlation (DIC) technique.

Electrical surface and bulk resistivity measurements were conducted using a 100 dia.×200mm cylindrical specimen following the guidelines of AASHTO T358-15 [38]. A Proceq ResiPod equipped with a 4-point Wenner probe was used on samples that had been cured for 7, 28, 56 and 90 days. Surface resistivity was recorded by taking four measurements per sample and calculating the average. Bulk resistivity was obtained by using a module including two metal and sponge contacts, which were attached to the top and bottom surfaces of the sample. Two readings were taken for each sample, and the average was calculated.

Microstructural Analysis

The microstructure and fracture surface were examined by using Zeiss Ultra Plus scanning electron microscope (SEM). SEM samples (5-10mm) were collected from mortar specimens after the mechanical testing and coated with 10nm gold prior to the analysis to decrease the charging on the material surface. Energy dispersive spectroscopy (EDS) mapping was conducted by using an Oxford Instrument AZtec integrated EDS system with X-Max 20 mm^2 silicon drift EDS detector. The mineralogical change was characterised by X-ray diffraction (XRD) analysis, which was performed on the 28-day cured samples, with Cu Kα X-ray radiation and a PIXcel1D detector in continuous scanning mode over the 2θ angle range 5-90°. ATR- Fourier transform infrared (FTIR) spectra were collected using a Bruker ALPHA portable spectrometer equipped with a single reflection diamond ATR module and DTGS detector. The diamond crystal had a refractive index of 2.4. Spectra were collected over the region of 4000 cm^{-1} with the co-addition of 64 scans at a spectral resolution of 400 cm^{-1}.

5.2.4 Results and Discussions

5.2.4.1 Material characterisation

Comprehensive characterisations of mortar materials and rFRP composites were performed and are stated in this section.

Granulometry and particle size distribution

The surface morphology was captured by using Zeiss Ultra Plus SEM. The surface morphology of different ingredients used in the mix was assessed through SEM micrographs, as shown in Figure 5-2. Compared to fine aggregate and cement, rFRP showed varying sizes and irregular shapes, including small powdery particles, short cylindrical shape particles, longer fibres, as well as fibre bundles. Figure 5-2 (c) and (d) indicate that some irregular resin remained on the fibre surface after milling. Particle size distribution of these ingredients (Figure 5-3), obtained by Mastersizer equipment, revealed the wider rFRP size distribution, ranging from 0.3µm to 2mm. The specific surface area of rGFRP and rCFRP was determined to be 160.1 m^2/kg and 328.5 m^2/kg respectively. The intention of using a mix of powdered and fibrous form FRP recyclates was to maximise the beneficial physical effects such as filling and nucleation effects of incorporating smaller particles and reinforcing effects of fibrous particles.

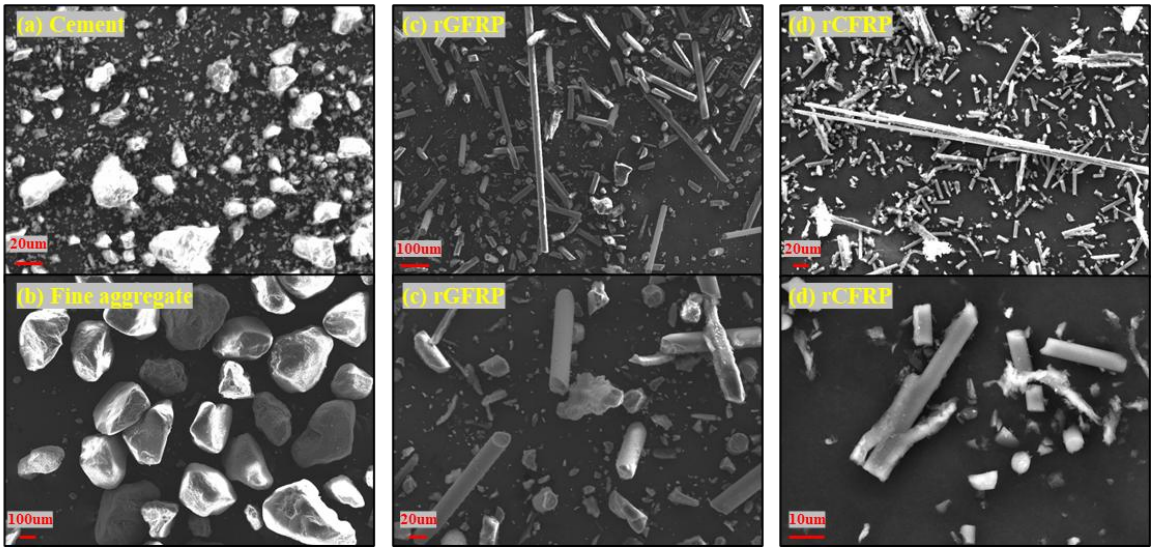

Figure 5-2. SEM images of different ingredients used in the mix: (a) cement, (b) fine aggregate, (c) rGFRP (with zoom-in view on smaller particles), (d) rCFRP (with zoom-in view on smaller particles).

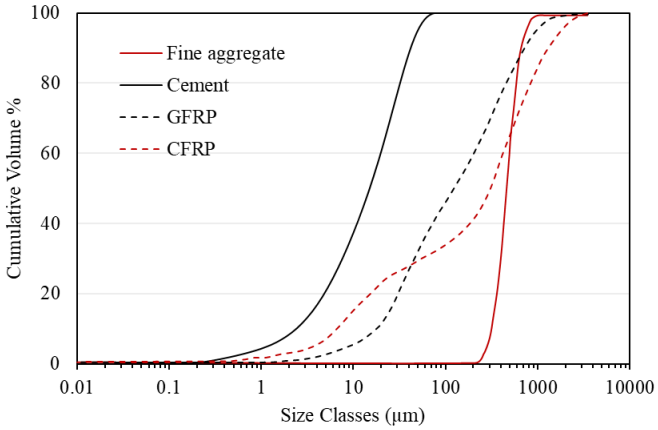

Figure 5-3. Particle size distributions of fine aggregate, cement and FRP recyclates.

Chemical and mineralogical composition

XRD was used for phase identification, which provides important information on the mineralogical composition and chemical reactivity. The test was performed using PANalytical X'Pert Powder XRD. Figure 5-4 (a) validates the Portland cement phase composition with the main components of Alite and Belite. The fine aggregate spectrum in Figure 5-4 (b) shows a crystalline quartz structure and few amorphous elements. Figure 5-4 (c) shows the observed two broad peaks ($2\theta = 25^{\circ}$ and 44°) identified as hexagonal graphic structures (002) and (100) in rCFRP [39], and the broad hump without distinct peaks corresponding to the amorphous glass phase in rGFRP [40].

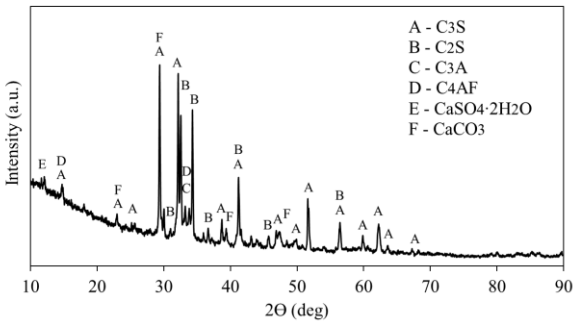

(a) cement

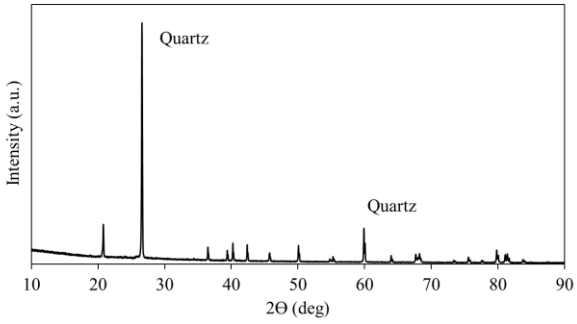

(b) fine aggregate

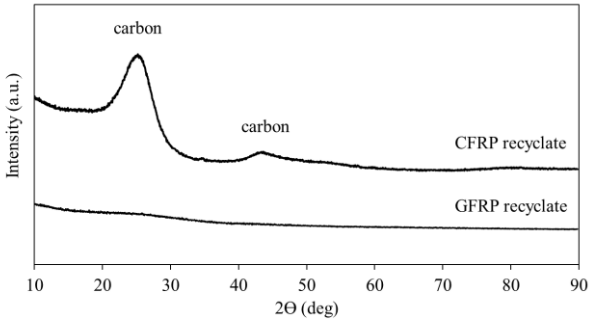

(c) FRP recyclates

Figure 5-4. XRD spectrum for cement, aggregate and FRP recyclates.

FTIR was employed to understand the molecular components and chemical structure of materials. The presence of organic compounds in the FRP composite was detected using Bruker ALPHA FTIR spectrometer. The FTIR spectra of GFRP and CFRP recyclates are shown in Figure 5-5 (a). The typical bands of thermoset epoxy vinyl ester were found at 2,930 cm^{-1} for the C-H aliphatic, 1,728 cm^{-1} for the C=O bond stretching, 1,507 cm^{-1} for the C-H aromatic benzene ring and 699 cm^{-1} for the C-H monosubstituted aromatic benzene ring [41, 42]. Besides, the epoxide ring vibrations (C-O-C bonds) were observed at 969 cm^{-1} and 873 cm^{-1} [43, 44]. The carbonyl compounds (C=O) were detected at 1,701 cm^{-1} and 1,770 cm^{-1}, indicating the possible presence of a variety of products such as ketones, esters, and aldehydes [45, 46]. The presence of glass fibre (GF) in rGFRP was identified by bands corresponding to Si-O at 556 cm^{-1} [47].

GFRP recyclates were comprised of an epoxy vinyl ester resin and E-glass fibre (77.4 wt.%), as reported by the manufacturer's Technical Information Guide. The content of GF was determined by ISO 1172 [48]. The thermogravimetric analysis (TGA) of CFRP composite material (using TA Instruments Discovery Thermogravimetric Analyser) indicated that CFRP recyclates consisted of approximately 50 wt.% CF in the composite, as shown in Figure 5-5 (b). The TGA was performed with a ramp rate of 20.00 °C/min up to 700.00 °C under a nitrogen atmosphere, using sample masses ranging from 15-40 mg over a total duration of 33 minutes. The initial weight loss was small, which was followed by a significant weight loss between around 400˚C to 500˚C, indicating the possibility of epoxy resin decomposition at this temperature range [49].

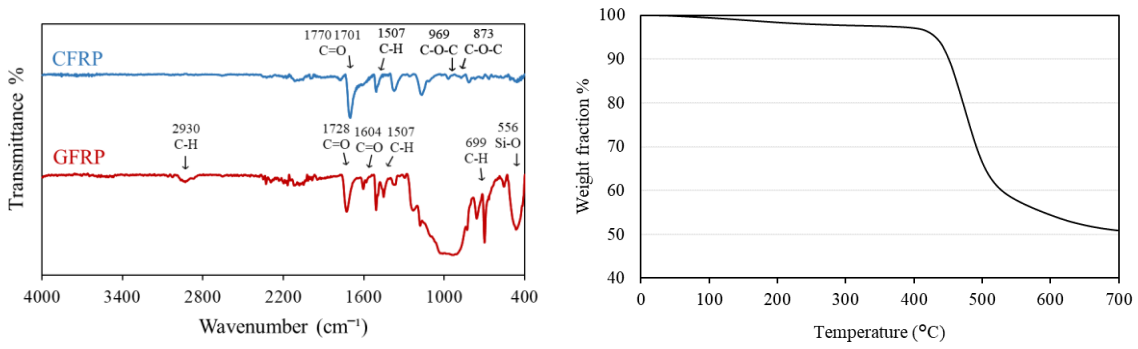

Figure 5-5. (a) FTIR spectrum of FRP recyclates; (b) Weight loss during pyrolysis process for CFRP.

Tensile strength of FRP composites

The mechanical properties of the GFRP and CFRP were evaluated through tensile testing. FRP composite coupons were prepared from original electrical crossarms and aerospace panels using water jet cutting with the dimensions of 250mm length and 25mm width based on ASTM 3039/D3039M [50]. Testing was conducted by using a 300kN Sintech 65/G machine at a 3mm/min loading rate until failure occurred. Strain measurements were performed using an extensometer with a 25mm gauge length.

The resulting stress-strain curves of FRP composites are shown in Figure 5-6. The curves show an approximately linear-elastic behaviour up to failure for both materials. The tensile characteristics are influenced by material properties (fibre and resin types), fibre weight/volume fraction as well as the layup configurations (fibre orientations). For GFRP composites, the average ultimate tensile strength and Young's modulus were 531.2MPa and 416.5MPa, respectively. The slope of the curves reflects the relative stiffness of the composites, with GFRP being stiffer. In specific layer sequences of 0°/90°, as observed in SEM images, GFRP composites exhibited a brittle longitudinal splitting failure mode. This failure mode involved fibre breakage within the 0° layers and transverse separation between the matrix and fibres within the 90° layers. CFRP composites showed a quasi-isotropic behaviour with fibre layers oriented at 0°, ±45° and 90°. The resulting failure mode was sudden and multi-directional, leading to the ultimate tensile strength of 496.4 MPa and Young's modulus of 351.2 MPa.

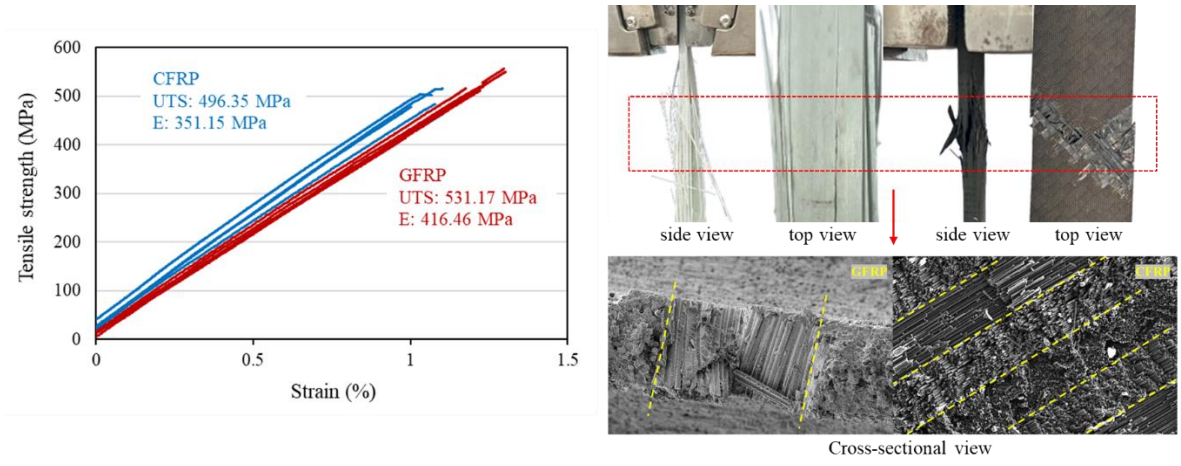

Figure 5-6. FRP composite tensile characteristics and failure modes.

5.2.4.2 Effect of rFRP on mortar water absorption, bulk density and shrinkage

Figure 5-7 (b) and (c) show the water absorption and bulk density of the control mortar and the mortar with various FRP recyclates at different curing ages. The results demonstrated that the water absorption of mortars incorporating FRP recyclates was consistently lower than that of the control mortar across different ages, and a progressive increase in mortar

compactness was observed over the curing period. Fine rFRP particles effectively filled the voids between larger particles, resulting in a reduction in the volume of pores in the matrix. The interaction between particles with varying sizes and densities enabled enhanced compaction through more efficient packing arrangements. In addition, the combined effect of denser structure and void reduction led to the obstruction of interconnected porous networks within the cementitious matrix [51, 52]. Thereby, the inclusion of rFRP resulted in lower water absorption. As shown in Figure 5-7 (a), the water absorption of the mortar with 10% GFRP and CFRP decreased by 12.7% and 19.1%, respectively.

The hardened bulk density exhibited a similar trend to the fresh bulk density, exhibiting a decline with the increasing content of FRP recyclates in mortar. This observation can be attributed to the lower specific gravity of FRP composite, comprising fibres and polymer matrix, partially replacing the cement in the mix design. The hardened bulk density of CFRP mortar specimens was higher than that of the GFRP mortar specimens. These differences in water absorption and density behaviour can be ascribed to the nature of fibres and variations in particle size between CFRP and GFRP recyclates. In these recycled composites, carbon fibres had smaller diameters averaging 7 microns, compared to the diameters of glass fibres, which were around 20 microns, as shown in Figure 5-2 (c) and (d). Also as illustrated in Figure 5-3, CFRP recyclates contained a higher proportion of fine particles smaller than 40μm, which was a comparable or even smaller size than cement grains. The filling effect of smaller FRP particles between cement grains led to a wider dispersion of cement grains and improved packing of the solid particles by filling up the interstitial voids. The principle that a decrease in porosity corresponds to an increase in material density could also explain why the CFRP-specimens group generally exhibited lower water absorption but higher bulk density compared to the GFRP-specimens group, due to finer particles and better packing [51]. However, it adversely affected the hydration process when a larger quantity of cement was substituted [53, 54]. This explanation might also be applicable in understanding the compressive characteristics.

Drying shrinkage refers to the contraction or change in length experienced by the hardened concrete due to the loss of capillary moisture. This loss of moisture can lead to the development of capillary tension within the pore structure, potentially resulting in the formation of cracks [55]. This study investigated the effect of drying shrinkage up to 120 days on the durability of FRP recyclates-incorporated mortars, as shown in Figure 5-8. The percentage change in length of all mortar specimens decreased in the first 7-21 days, and then stabilised. Compared to the control specimen, all mortar specimens containing FRP recyclates exhibited

significantly lower shrinkage. The microfibres effectively constrained the length change from the initial state until after 28 days. The zoomed image in Figure 5-8 revealed that the GFRP group exhibited lower shrinkage compared to the CFRP group, with GFRP 5 showing the most reduction, which was due to the higher weight percentage (77.4 wt.%) of GFs in the original electrical crossarms. The higher amount of glass fibres with a greater surface area provided more interfacial bonding with the matrix, assisting in restraining the length change. In contrast, the relatively limited effect of CFRP recyclates on resisting the length change was because fewer carbon fibres (50 wt.% CF) were involved to provide the internal reinforcement.

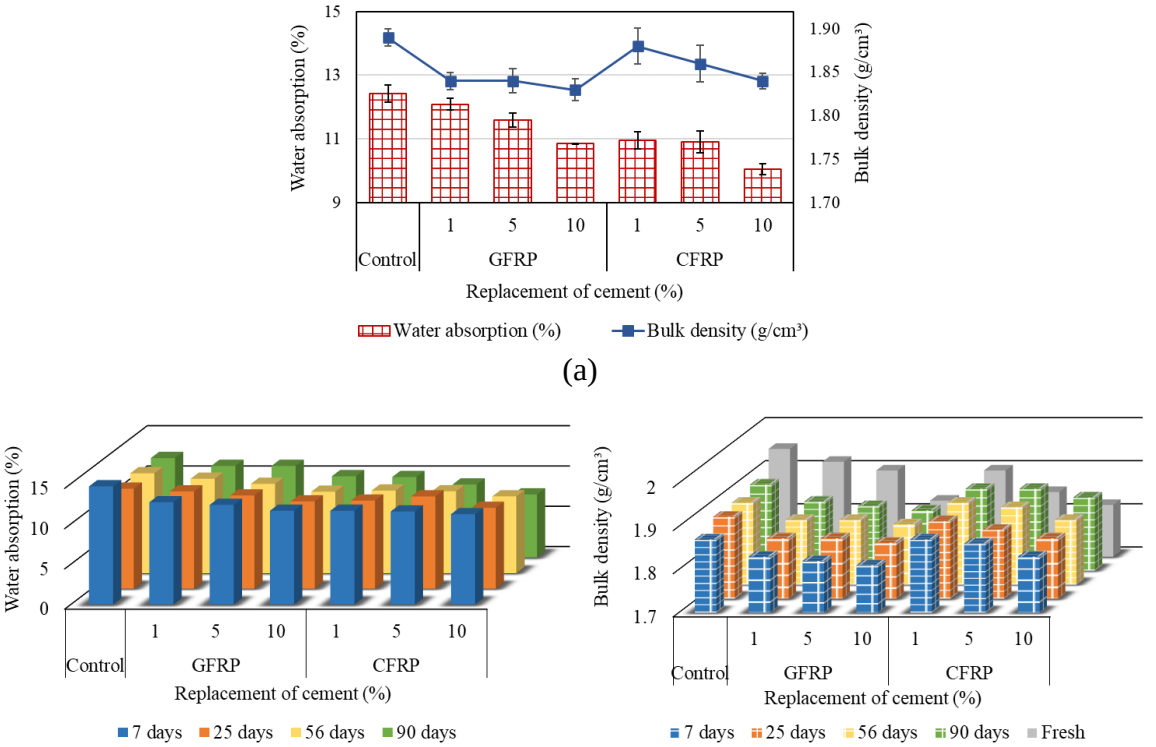

Figure 5-7. (a) Water absorption and hardened bulk density of mortars with FRP recyclates at 28 days, (b) Water absorption and (c) bulk density of mortars with different concentrations of FRP recyclates at different curing ages.

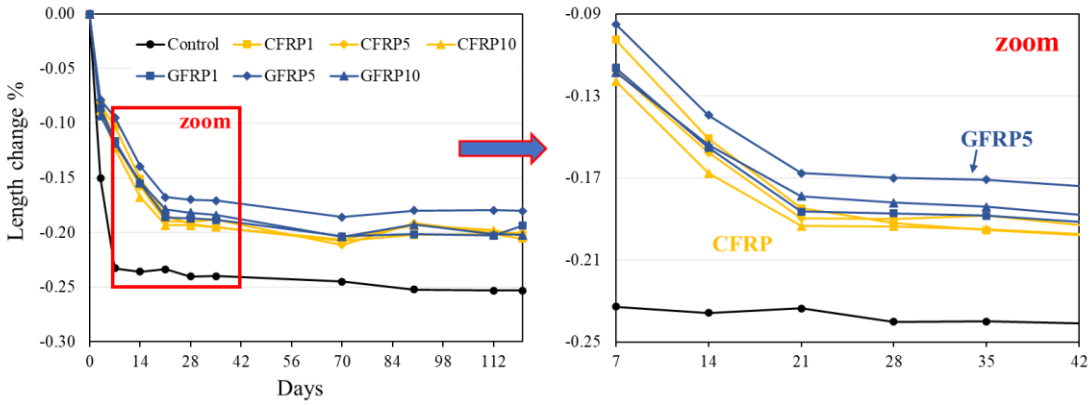

Figure 5-8. Drying shrinkage of mortars with FRP recyclates.

5.2.4.3 Effect of rFRP on mortar fresh and mechanical properties

The incorporation of FRP recyclates with higher dosages improved workability (Figure 5-9 (a)). In mortars containing 10% GFRP and CFRP recycaltes, the flow value increased by about 2.0% and 0.8%, respectively. This improvement in flowability could be attributed to the filling effects, wherein small FRP particles filled the voids between the larger sand particles. The fresh densities decreased from 2.01 g/cm³ in the control mortar to 1.83 g/cm³ and 1.80 g/cm³ in mortars with GFRP and CFRP recyclates (Figure 5-9 (a)), primarily due to the lighter weight of the FRP composite. Similar findings were also reported in the earlier studies [26, 56]. The variations in fresh properties between GFRP and CFRP mortars could be due to the particle shape and size of FRP powder. The improvement of flowability in mortars with GFRP recyclates was attributed to the lower specific surface area, whereas CFRP recyclates exhibited a more angular shape (higher specific surface area).

The mechanical testing results are shown in Table 5-2. Compared to the control mortar, the compressive and flexural strength of the rFRP-incorporated mortar generally increased at 7, 28 and 90 days, and it showed a progressive increase with curing age. The overall enhancement could be attributed to the reinforcing effect of micro fibres in the mortar matrix (as shown in Figure 5-2 (c) & (d)), the filling effect of fine FRP particles that increased the compactness, and the creation of nucleation regions created by smaller particles for hydration products [57, 58].

The compressive strength of GFRP1 and CFRP1 specimens at 28 days exhibited the highest value with an increase of 44% and 67%, respectively, compared to the control mortar (Figure 5-9 (b)). However, the ultimate compressive strength reduced with the higher replacement percentage, indicating a negative impact on strength development as more cement

was replaced. Flexural strength and ductility noticeably increased with higher rFRP replacement percentages (Figure 5-9 (c) to (e)), with the CFRP group demonstrating a more significant effect owing to the higher tensile characteristics of CF. Specifically, the CFRP10 specimen exhibited higher ductility at around 0.26mm while the control mortar without recyclates showed brittle behaviour (around 0.07mm extension at failure). The DIC diagram of CFRP10 further supports the role of micro fibres in restraining crack propagation, in contrast to the straighter line without much curvature observed in the DIC diagram of GFRP10, as indicated in Figure 5-9 (d) and (e).

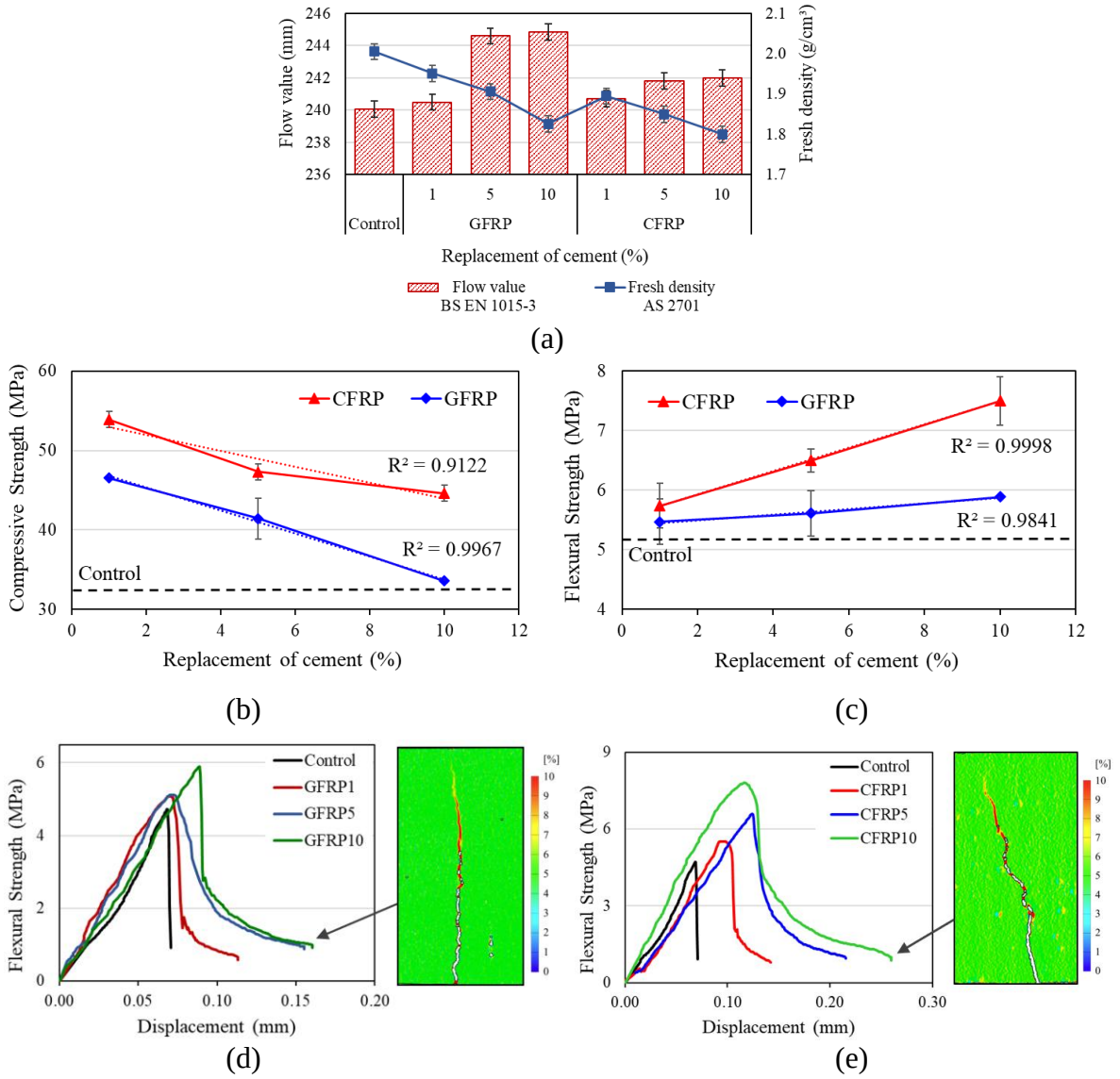

Figure 5-9. (a) Fresh properties, (b) 28-day compressive strength, (c) 28-day flexural strength, and (d) and (e) 28-day stress-displacement diagrams of mortars with FRP recyclates.

Table 5-2. Mechanical testing results of rFRP-incorporated mortar.

Mix ID		Control	GFRP1	GFRP5	GFRP10	CFRP1	CFRP5	CFRP10
Compressive strength (MPa)	7d	25.74	36.83 (43.08%)	32.99 (28.17%)	25.73 (-0.04%)	38.24 (48.56%)	35.62 (38.38%)	30.17 (17.21%)
	28d	32.23	46.55 (44.43%)	41.43 (28.54%)	33.57 (4.16%)	53.88 (67.17%)	47.32 (46.82%)	44.63 (38.47%)
	90d	41.83	59.55 (42.36%)	53.53 (27.97%)	43.61 (4.26%)	62.21 (48.72%)	57.97 (38.58%)	48.59 (16.16%)
Flexural strength (MPa)	7d	4.54	4.6 (1.32%)	5.17 (13.88%)	5.76 (26.87%)	5.58 (22.91%)	5.64 (24.23%)	6.49 (42.95%)
	28d	5.23	5.47 (4.59%)	5.61 (7.27%)	5.89 (12.62%)	5.74 (9.75%)	6.5 (24.28%)	7.5 (43.40%)
	90d	5.54	5.47 (-1.26%)	5.73 (3.43%)	6.85 (23.65%)	6.51 (17.51%)	7.4 (33.57%)	8.02 (44.77%)

Numbers in parentheses indicate variation compared to the control sample.

5.2.4.4 Effect of rFRP on mortar electrical properties

In recent years, there has been growing interest in utilising electrically conductive cementitious composites (ECCCs) across various applications, including serving as sensors for structural health monitoring (SHM) [59] and used for electromagnetic interference (EMI) shielding in buildings [60]. Previous studies have confirmed the success of incorporating either virgin CF (vCF) or rCF to enhance the electrical properties of cementitious composites [61-63]. However, there is limited research on investigating the effectiveness of incorporating FRP recyclates (a mix of microfibres and resin) in improving electrical resistivity.

The electrical properties of mortar with FRP recyclates, which are linked to the microstructure and porosity of the mortar mix, were measured through both surface and bulk resistivity. It was observed that resistivity was increased with curing time from 7 days to 28 days due to the enhanced hydration degree and refinement of pore structures (Figure 5-10 (a)). The resistivity either remained similar or slightly increased from 56 to 120 days. Incorporating rCFRP could improve conductivity by forming a carbon fibre (microfibre) network, especially with higher dosages of CFRP recyclates. However, the electrical resistivity increased with increasing dosages of GFRP recyclates. Interestingly, in the initial stage, the GFRP mortar group exhibited lower resistivity compared to the control mortar, attributed to the chemical composition change in pores and the substitution of cement by GFRP recyclates. Conversely, after 56 days, the resistivity of GFRP mortar group greatly improved due to reduced porosity, production of hydration and pozzolanic products, and the electrical resistivity of GFRP10

showed much higher than the control mortar. As shown in Figure 5-10 (b), carbon fibre materials showed various effects on the electrical properties of cementitious materials, exhibiting different responses in terms of the changes in electrical resistivity. The incorporation of CF in cementitious materials resulted in a higher electrical conductivity as electronic conductivity between fibres predominates over ionic conduction within the pores [29, 61, 62]. Remarkably, even the addition of 0.2 vol% CF was very effective, yielding over 80% reduction in electrical resistivity at 28 days. In contrast, the incorporation of CFRP waste into mortar led to comparatively less significant changes in electrical resistivity (up to 26% reduction) when compared to fibre-reinforced cementitious materials. rCFRP powder was mainly composed of microfibres with lower aspect ratios and polymer matrix, which might not contribute to the electrical conductivity. Consequently, there was less chance of forming a strong conductive network within the cementitious matrix. Despite these challenges, rCFRP contributed to reducing electrical resistivity to some degree, presenting a unique opportunity to utilise CFRP recyclates in construction materials.

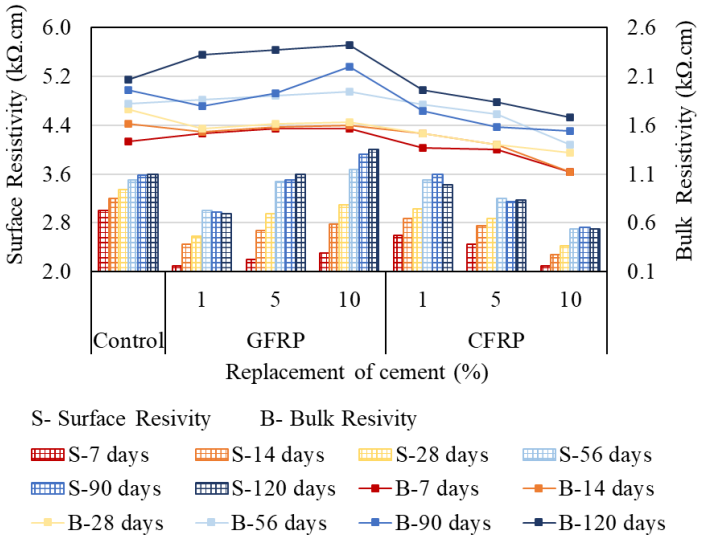

(a)

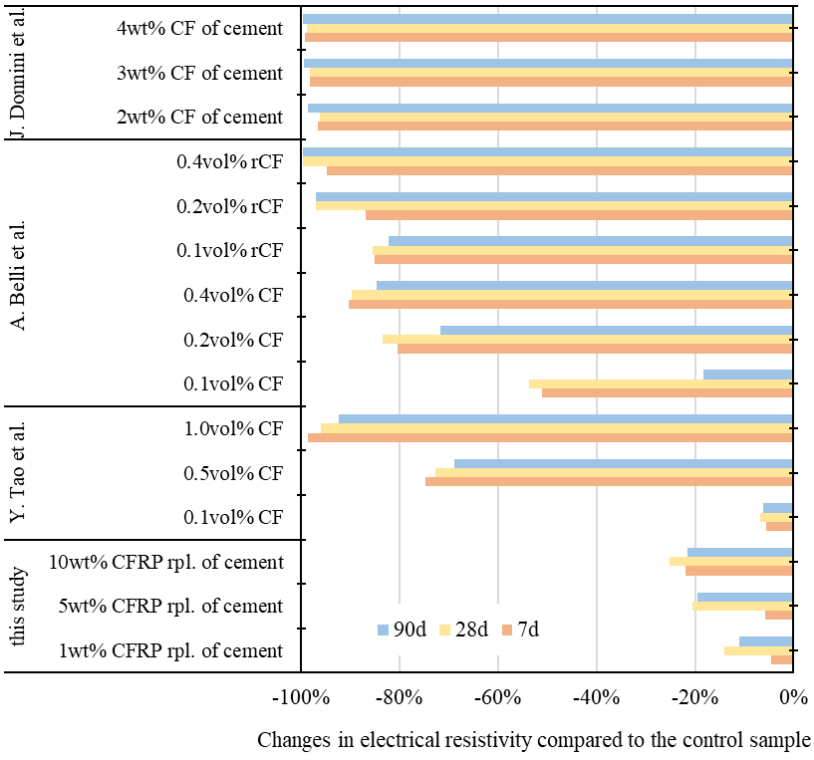

(b)

Figure 5-10. (a) Resistivity measurement of mortars with FRP recyclates at different curing ages, and (b) comparison of electrical resistivity changes in different studies [29, 61, 62].

5.2.4.5 Microstructural analysis

The SEM images provided valuable insights into the fracture surface of the composite materials, revealing two distinct failure mechanisms, which were fibre pullout and fibre breakage (Figure 5-11 (c), (e), (f)). Additionally, the microstructural morphology in Figure 5-11 (d) highlighted the interfacial transition zone (ITZ) between microfibres and microcracks formed around fibres, demonstrating the fibres' ability to take over the stress. Moreover, Figure 5-11 (a) and (b) displayed the presence of hydrated products near the fibre surface, including calcium silicate hydrate (CSH), calcium hydroxide (CH) and ettringite. Hydration products were found adhering to the fibre surface in Figure 5-11 (d) and (f), indicating an improvement in bonding performance. The SEM images in Figure 5-12 also indicate the surface of recycled glass fibre (rGF) was covered by hydration products, with the formation of CSH gel in the matrix. These observations suggested the development of a denser structure facilitated by the formation of CSH gel at various locations.

Two small pieces of cementitious composite materials were randomly collected from the samples following the mechanical tests. Samples were prepared for EDS mapping to study the interface between micro-fibre and matrix, as marked by the white dotted line in Figure 5-13. The gel product was found around the CF surface and the interface between CF and the surrounding cement matrix (Figure 5-13 (a)). Although some voids could be observed within the matrix, there was no distinct gap at the interface. Instead, the interfacial transition zone between CF and the cement matrix was characterised by spherical gel particles. In Figure 5-13 (b), the formation of CSH (network structure), the presence of CH (hexagonal crystalline products) and ettringite (needle-like shape) were evident within the cement matrix. Notably, a combination of gel products and calcite was observed at the interface between GF and cement matrix, which could be explained by the secondary reaction occurring between silicates and CH during hydration, along with the additional reaction between carbon dioxide and CH to form calcite.

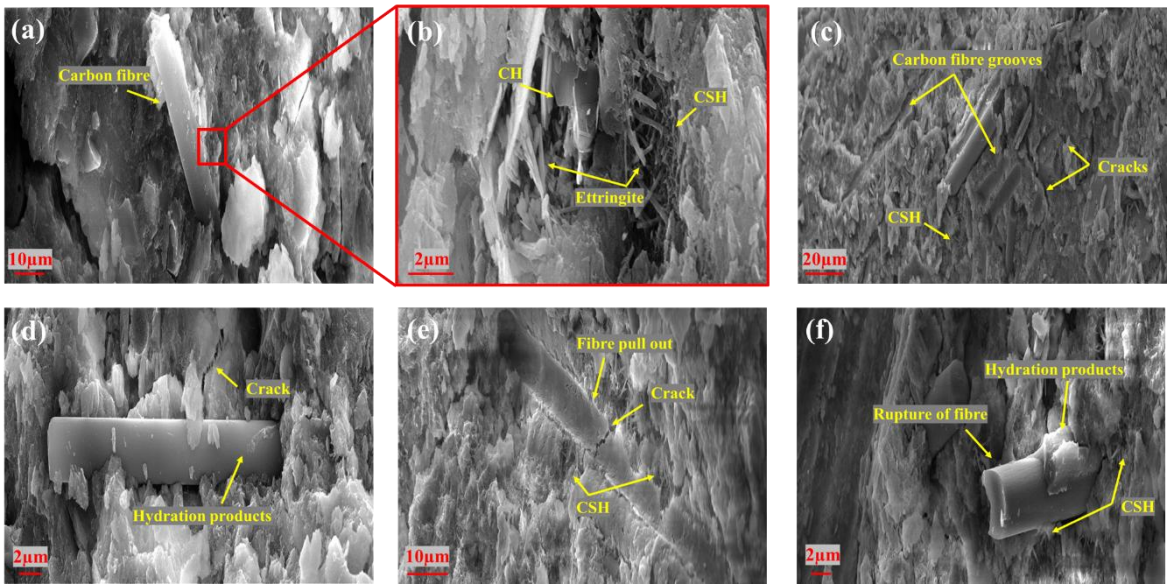

Figure 5-11. The microstructure of mortar incorporated with CFRP recyclates.

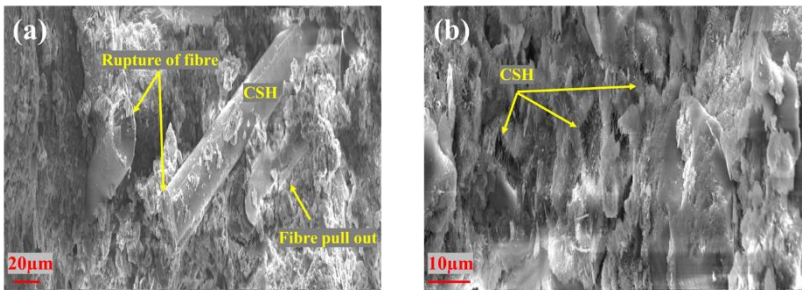

Figure 5-12. The microstructure of mortar incorporated with GFRP recyclates.

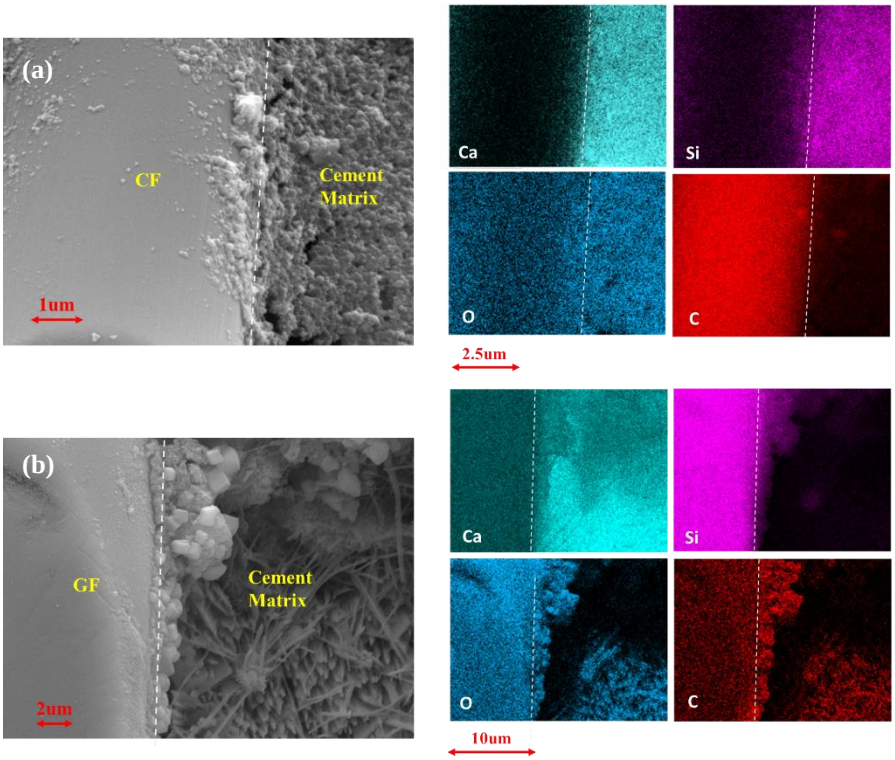

Figure 5-13. SEM-EDS images of mortar incorporated with (a) CFRP and (b) GFRP recyclates.

XRD patterns present the major chemical phases in mortar, as shown in Figure 5-14. The primary crystalline phases observed in all cementitious composite samples were CH, CSH, ettringite, quartz, and calcite (Figure 5-14 (a)). The intensities of the main diffraction peaks of CH were located in the 2θ region of 18.1°, 28.6° and 34°, corresponding to the (001), (100) and (101) crystal planes, respectively. For rFRP-incorporated mortar at 28 days of curing, the portlandite intensity was observed to be notably higher compared to the control sample without rFRPs. This increase in portlandite was due to the acceleration of the early-stage cement hydration and rapid precipitation of portlandite in the presence of rFRPs [64].

To further investigate the influence of varying rFRP addition, complementary analyses were conducted using both XRD and FTIR on the mature 90-day samples, enabling cross-validation of the results. Figure 5-14 (b) indicates that the intensity of CH peaks generally decreased as higher amounts of GFRP recyclates were incorporated to replace cement in the mortar. The reduction in Portlandite content could be attributed to both the pozzolanic reaction (where CH reacts with silica to form CSH) and the dilution effect (resulting from reduced available unreacted cement). As a vibrational spectroscopic technique, FTIR is particularly useful in evaluating the hydration of cementitious materials by identifying various bond arrangements, which can determine both the crystalline and amorphous forms of hydration products. Figure 5-15 shows the FTIR spectra of all the mixed pastes in the range of 400-4,000

cm^{-1}. The vibration absorption peak of the O-H stretching band of CH was observed at about 3,640 cm^{-1}, whose intensity was lower with the addition of FRP, consistent with the XRD findings. The absorption peak at 3,400 cm^{-1} and 1,650 cm^{-1} were attributed to the O-H stretching and H-O-H bending vibrations of molecular water individually. The intensity of both bands decreased with the addition of FRP, at the minimal peaks including 1% rCFRP and rGFRP. This phenomenon indicated the decrease in free water due to the formation of CSH gel. The bands located around 1,415 cm^{-1} and 870 cm^{-1} wavelengths in spectra corresponded to the vibrations associated with CO_3^{2-}, indicating the formation of calcite. For the CFRP groups as shown in Figure 5-15 (b), the mortar including 1% CFRP exhibited remarkably higher calcite formation than the control sample, despite having a lower porosity. This behaviour could be explained as the microstructural changes that created the pathways for carbonation diffusion to form calcite. However, the integration of 5% and 10% CFRP then gradually reduced the carbonation, which was due to the denser structure narrowing the pathways for carbonation diffusion and the reduced availability of portlandite due to the dilution effect. As demonstrated in Figure 5-15 (a), the calcite bands continuously became smaller with increasing dosage of GFRP. This contrasting behaviour could be attributed to the presence of silica in GFRP promoting pozzolanic reaction to form additional CSH and contributing to a denser structure. Concurrently, the reduced amount of available portlandite effectively limited carbonation. Furthermore, different absorption peaks were related to the hydration products. The broad absorption band at 960-1,100 cm^{-1} was identified as the Si-O stretching vibration of CSH gel. The peak at 452 cm^{-1} Si-O bending vibration also reflected the polymerisation of SiO_4 within the CSH structure. In addition, wavelengths of 675-800 cm^{-1} corresponded to the symmetric stretching vibrations of silicon-oxygen and aluminum-oxygen bonds, characterising cement hydration products such as CSH and ettringite. A notable observation was that these peak areas were larger in the CFRP and GFRP samples in comparison to the control mortar. Particularly, mortars containing 1% CFRP and GFRP exhibited more intense peaks within the region, indicating the extensive development and formation of CSH hydration products, which aligns with the results of compressive strength tests.

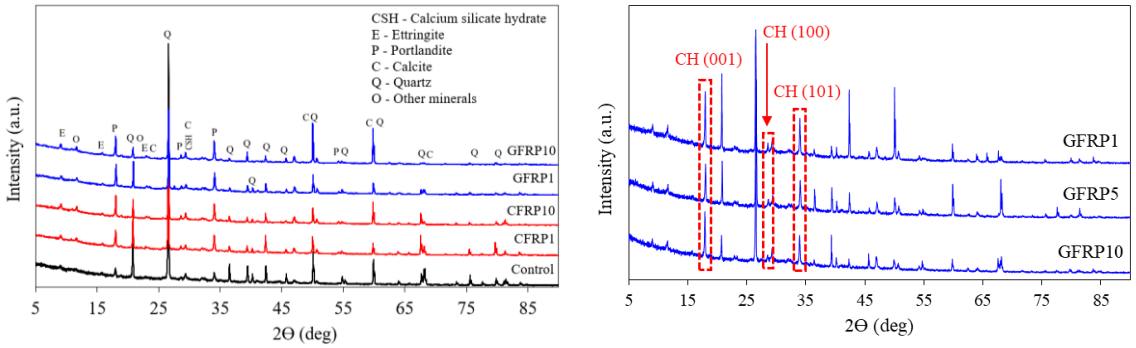

(a) (b)

Figure 5-14. XRD pattern of (a) control mortar and rFRP mortar at 28 days and (b) mortar with rGFRP at 90 days.

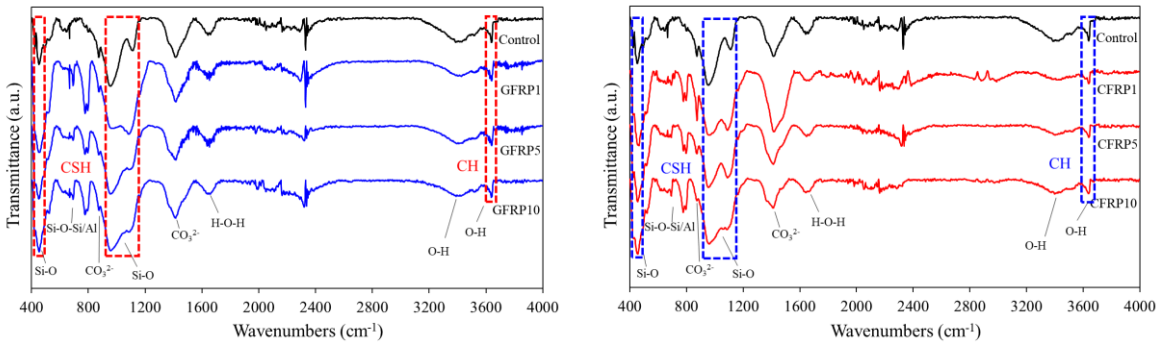

(a) (b)

Figure 5-15. FRIT spectra of rFRP mortar at 90 days.

5.3 CONCLUSION

This study addressed the pressing need for the development of sustainable practices for waste management in the utility and aerospace sectors. This paper investigated the influence of repurposing end-of-life electrical GFRP crossarms and CFRP aerospace manufacturing scraps on the performance of cementitious mortar. The physical properties (i.e., flowability and bulk density), mechanical properties (i.e., compressive and flexural characteristics), durability (i.e., water absorption and drying shrinkage) and electrical properties (i.e., surface and bulk resistivities) were evaluated. Microstructural analysis was performed to further assess the physical and chemical changes caused by the incorporation of FRP powder into the matrix. The following conclusions and future research directions were drawn:

(i) The incorporation of FRP recyclates into mortar demonstrated a lower water absorption and bulk density. This improvement can be attributed to the filling effect of the small FRP particles, reducing the porosity within the matrix. Moreover, the inclusion of microfibres from FRP waste significantly mitigated

the drying shrinkage. Particularly, incorporating 5% FRP recyclates showed the most substantial reduction in length change, while a higher percentage of FRP recyclates (10%) had limited effectiveness in restraining the shrinkage.

(ii) The observed variation in fresh properties of mortar was directly influenced by the type, shape and size of the FRP recyclates. The fresh densities decreased in mortars containing FRP recyclates due to the lightweight nature of the composite materials. The GFRP recyclates with lower specific surface area exhibited an increase in flow value by about 2.0%.

(iii) At 28 days, the compressive strength of mortar specimens containing 1% GFRP and 1% CFRP displayed the highest values, showing respective increases of 44% and 67%, compared to the control mortar. The compressive strength exhibited an inverse relationship with the percentage of FRP, indicating a negative impact on strength development as more cement was replaced. In contrast, flexural strength and ductility noticeably increased with higher FRP replacement up to approximately 43% and 0.26mm, respectively.

(iv) While incorporating higher amounts of rCFRP into mortar resulted in relatively minor reductions in electrical resistivity compared to the use of longer carbon fibres in other studies, the utilisation of these CFRP recyclates in construction materials still presents the potential opportunities for applications such as for structural health monitoring and de-icing on concrete pavement.

(v) The microstructural analysis confirmed that FRP recyclates could enhance the performance of cementitious materials through a fibre-reinforcing effect and the development of a denser structure by forming CSH gels. Moreover, good interfacial bonding was observed between microfibres and matrix.

(vi) Based on the findings of this study, future research could focus on conducting comprehensive durability studies, such as chloride penetration and sulphate attack resistance, to understand the long-term behaviour of cementitious composites incorporating recycled FRP composites. Optimisation of the rFRP inclusion content and mix combination could also be considered for different application purposes to maximise repurposing efficiency and performance. Additionally, given that rCFRP in the cementitious composite can provide electronic conductive pathways for composite conductivity, it is worth investigating the piezoresistivity

of cementitious composites with varying sizes and amounts of rCFRP. Exploring self-sensing properties leads to the potential development of smart materials with advanced functions for SHM and EMI.

In conclusion, this study presented a viable approach to repurposing GFRP and CFRP composite waste from the utility and aerospace sectors. Through the two-step pulverisation process for size reduction of FRP wastes and subsequently repurposing them into cementitious composites by replacing cement at various percentages, a promising recycling strategy was developed. This strategy offers a practical method of transforming composite wastes into valuable resources for construction applications and conserving natural resources.

5.4 REFERENCES

[1] A. Talaei, D. Pier, A.V. Iyer, M. Ahiduzzaman, A. Kumar, Assessment of long-term energy efficiency improvement and greenhouse gas emissions mitigation options for the cement industry, Energy 170 (2019) 1051-1066.

[2] S.A. Miller, G. Habert, R.J. Myers, J.T. Harvey, Achieving net zero greenhouse gas emissions in the cement industry via value chain mitigation strategies, One Earth 4(10) (2021) 1398-1411.

[3] D. Baturkin, O.A. Hisseine, R. Masmoudi, A. Tagnit-Hamou, L. Massicotte, Valorization of recycled FRP materials from wind turbine blades in concrete, Resour. Conserv. Recycl. 174 (2021) 105807.

[4] S.A. Hadigheh, F. Ke, H. Fatemi, Durability design criteria for the hybrid carbon fibre reinforced polymer (CFRP)-reinforced geopolymer concrete bridges, Structures 35 (2022) 325-339.

[5] Global Status Report for Buildings and Construction 2019, IEA, Paris, 2019.

[6] GLOBAL CEMENT AND CONCRETE INDUSTRY ANNOUNCES ROADMAP TO ACHIEVE GROUNDBREAKING 'NET ZERO' CO2 EMISSIONS BY 2050, 2021. https://gccassociation.org/news/global-cement-and-concrete-industry-announces-roadmap-to-achieve-groundbreaking-net-zero-co2-emissions-by-2050/.

[7] Y. Wei, S.A. Hadigheh, Cost benefit and life cycle analysis of CFRP and GFRP waste treatment methods, Constr. Build. Mater. 348 (2022) 128654.

[8] Y. Tao, S.A. Hadigheh, Y. Wei, Recycling of glass fibre reinforced polymer (GFRP) composite wastes in concrete: A critical review and cost benefit analysis, Structures 53 (2023) 1540-1556.

[9] F. Meng, Y. Cui, S. Pickering, J. McKechnie, From aviation to aviation: Environmental and financial viability of closed-loop recycling of carbon fibre composite, Compos. B. Eng. 200 (2020) 108362.

[10] D.N. Markatos, C.V. Katsiropoulos, K.I. Tserpes, S.G. Pantelakis, A holistic End-of-Life (EoL) Index for the quantitative impact assessment of CFRP waste recycling techniques, Manufacturing Review 8 (2021) 18.

[11] Y. Wei, S.A. Hadigheh, Enhancing carbon fibre recovery through optimised thermal recycling: Kinetic analysis and operational parameter investigation, Materials Today Sustainability 25 (2024) 100661.

[12] Y. Wei, S.A. Hadigheh, Development of an innovative hybrid thermo-chemical recycling method for CFRP waste recovery, Compos. B. Eng. 260 (2023) 110786.

[13] The looming 840,000 tonne waste problem that isn't single-use plastics, 2023. https://www.sydney.edu.au/news-opinion/news/2023/07/03/-the-looming-840-000-tonne-waste-problem-that-isn-t-single-use-p.html#:~:text=The%20annual%20accumulation%20of%20CFRP,to%20landfill%20or%20is%20incinerated.

[14] A. Danish, M.A. Mosaberpanah, M.U. Salim, M. Amran, R. Fediuk, T. Ozbakkaloglu, M.F. Rashid, Utilization of recycled carbon fiber reinforced polymer in cementitious composites: A critical review, J. Build. Eng. 53 (2022) 104583.

[15] Y.-F. Li, J.-Y. Li, G.K. Ramanathan, S.-M. Chang, M.-Y. Shen, Y.-K. Tsai, C.-H. Huang, An Experimental Study on Mechanical Behaviors of Carbon Fiber and Microwave-Assisted Pyrolysis Recycled Carbon Fiber-Reinforced Concrete, Sustainability 2021 13(12) (2021) 6829.

[16] A. Akbar, V.K.R. Kodur, K.M. Liew, Microstructural changes and mechanical performance of cement composites reinforced with recycled carbon fibers, Cem. Concr. Compos. 121 (2021) 104069.

[17] A. Akbar, K.M. Liew, Assessing recycling potential of carbon fiber reinforced plastic waste in production of eco-efficient cement-based materials, J. Clean. Prod. 274 (2020) 123001.

[18] Y. Wang, S. Zhang, D. Luo, X. Shi, Effect of chemically modified recycled carbon fiber composite on the mechanical properties of cementitious mortar, Compos. B. Eng. 173 (2019) 106853.

[19] Z. Zhou, B. Zhao, U.A. Lone, Y. Fan, Experimental study on mechanical properties of shredded prepreg carbon cloth waste fiber reinforced concrete, J. Clean. Prod. 436 (2024) 140456.

[20] H. Nguyen, V. Carvelli, T. Fujii, K. Okubo, Cement mortar reinforced with reclaimed carbon fibres, CFRP waste or prepreg carbon waste, Constr. Build. Mater. 126 (2016) 321-331.

[21] K. Ogi, T. Shinoda, M. Mizui, Strength in concrete reinforced with recycled CFRP pieces, Compos. Part A Appl. Sci. Manuf. 36(7) (2005) 893-902.

[22] V. Revilla-Cuesta, J. Manso-Morato, N. Hurtado-Alonso, M. Skaf, V. Ortega-López, Mechanical and environmental advantages of the revaluation of raw-crushed wind-turbine blades as a concrete component, J. Build. Eng. 82 (2023) 108383.

[23] B. Fu, L.B. Lin, X. Zhou, X.M. You, D.Y. Deng, Effect of incorporating recycled macro fibres on the properties of ultra-high-performance seawater sea-sand concrete, J. Build. Eng. 83 (2024) 108460.

[24] B. Fu, K.C. Liu, J.F. Chen, J.G. Teng, Concrete reinforced with macro fibres recycled from waste GFRP, Constr. Build. Mater. 310 (2021) 125063.

[25] P.S. Oliveira, M.L.P. Antunes, N.C. da Cruz, E.C. Rangel, A.R.G. de Azevedo, S.F. Durrant, Use of waste collected from wind turbine blade production as an eco-friendly ingredient in mortars for civil construction, J. Clean. Prod. 274 (2020) 122948.

[26] B. Zhou, M. Zhang, G. Ma, Multi-scale experimental study on the effect of crushed GFRP powder and dust on physical-mechanical properties of cement mortar, J. Build. Eng. 57 (2022) 104853.

[27] AS 3972 General purpose and blended cements, Standards Australia, Australia, 2021.

[28] AS 3700 Masonry Structures, Standards Australia, Australia, 2018.

[29] Y. Tao, S.A. Hadigheh, Z. Wang, Void geometry analysis and multifaceted characterisation of cementitious mortar reinforced with short carbon and glass fibres – A comparative study, J. Build. Eng. 89 (2024) 109283.

[30] N. Kamal, S.A. Hadigheh, Sodium hydroxide-free geopolymer binder for prestressed concrete applications, Constr. Build. Mater. 293 (2021) 123397.

[31] BS EN 1015-3 Methods of test for mortar masonry - Part 3: Determination of consistence of fresh mortar (by flow table), British Standards Institution, UK, 1999.

[32] BS EN 1015-6 Methods of test for mortar for masonry - Part 6: Determination of bulk density of fresh mortar, British Standards Institution, UK, 1999.

[33] C948-81, Standard Test Method for Dry and Wet Bulk Density, Water Absorption, and Apparent Porosity of Thin Sections of Glass-Fiber Reinforced Concrete, ASTM International, West Conshohocken, United States, 2016.

[34] BS EN 1015-10 Methods of test for mortar for masonry — Part 10: Determination of dry bulk density of hardened mortar, British Standards Institution, UK, 1999.

[35] C490/C490M, Standard Practice for Use of Apparatus for the Determination of Length Change of Hardened Cement Paste, Mortar, and Concrete, ASTM International, West Conshohocken, United States, 2021.

[36] C109/C109M Standard Test Method for Compressive Strength of Hydraulic Cement Mortars (Using 2-in. or [50 mm] Cube Specimens), ASTM International, West Conshohocken, United States, 2021.

[37] C348 Standard Test Method for Flexural Strength of Hydraulic-Cement Mortars, ASTM International, West Conshohocken, United States, 2021.

[38] AASHTO Designation: T 358 - Standard Method of Test for Surface Resistivity Indication of Concrete's Ability to Resist Chloride Ion Penetration, American Association of State Highway and Transportation Officials, Washington, D.C, 2015.

[39] A. Osikoya, W. Donbebe, R. Vala, C. Dikio, A. Afolabi, A. Nimibofa, E. Dikio, Synthesis, characterization and sorption studies of nitrogen-doped carbon nanotubes, Digest J. Nanomater. Biostruct. 10 (2015) 125-134.

[40] C. Li, Z. Duan, Q. Chen, Z. Chen, F.E. Boafo, W. Wu, J. Zhou, The effect of drying condition of glassfibre core material on the thermal conductivity of vacuum insulation panel, Mater. Des. 50 (2013) 1030-1037.

[41] S. Vemuganti, R. Chennareddy, A. Riad, M.M.R. Taha, Pultruded GFRP Reinforcing Bars Using Nanomodified Vinyl Ester, Materials 13(24) (2020) 5710.

[42] M.M. Haider, S. Nassiri, K. Englund, H. Li, Z. Chen, Exploratory Study of Flexural Performance of Mechanically Recycled Glass Fiber Reinforced Polymer Shreds as Reinforcement in Cement Mortar, Transp. Res. Rec. 2675(10) (2021) 1254-1267.

[43] P. Maity, S. Kasisomayajula, V. Parameswaran, S. Basu, N. Gupta, Improvement in Surface Degradation Properties of Polymer Composites due to Pre-processed Nanometric Alumina Fillers, Dielectrics and Electrical Insulation, IEEE Transactions on 15 (2008) 63 - 72.

[44] Q. Lin, Y. Lu, W. Ren, Y. Zhang, The grafting reaction of epoxidized natural rubber with carboxyl ionic liquids and the ionic conductivity of solid electrolyte composites, RSC Advances 5(109) (2015) 90031-90040.

[45] S. Piqueras, S. Füchtner, R. Rocha de Oliveira, A. Gómez-Sánchez, S. Jelavić, T. Keplinger, A. de Juan, L.G. Thygesen, Understanding the Formation of Heartwood in Larch Using Synchrotron Infrared Imaging Combined With Multivariate Analysis and Atomic Force Microscope Infrared Spectroscopy, Front. Plant Sci. 10 (2020).

[46] J. Coates, Interpretation of Infrared Spectra, A Practical Approach, Encyclopedia of Analytical Chemistry 2006.

[47] O. Paulo Silas, A. Maria Lúcia Pereira, C. Nilson, R. Elidiane Cipriano, G. Afonso Rangel, D. Steven Frederick, Use of waste collected from wind turbine blade production as an eco-friendly ingredient in mortars for civil construction, J. Clean. Prod. 274 (2020) 122948.

[48] ISO Textile-glass-reinforced plastics - Prepregs, moulding compounds and laminates - Determination of the textile-glass and mineral-filler content - Calcination methods, International Standard, Switzerland, 2023.

[49] M. Rashid, K. Chetehouna, L. Lemée, C. Roudaut, N. Gascoin, Study of flame retardancy effect on the thermal degradation of a new green biocomposite and estimation of lower flammability limits of the gaseous emissions, Journal of Thermal Analysis and Calorimetry 147(17) (2022) 9367-9382.

[50] ASTM 3039/D3039M Standard Test Method for Tensile Properties of Polymer Matrix Composite Materials, ASTM International, West Conshohocken, 2017.

[51] A. Nana, E. Kamseu, A.-T. Akono, J. Ngouné, J.N. Yankwa Djobo, H.K. Tchakouté, M.C. Bignozzi, C. Leonelli, Particles size and distribution on the improvement of the mechanical performance of high strength solid solution based inorganic polymer composites: A microstructural approach, Materials Chemistry and Physics 267 (2021) 124602.

[52] H. Campos, N. Klein, J. Filho, Comparison of the Silica Fume Content for High-Strength Concrete Production: Chemical Analysis of the Pozzolanic Reaction and Physical Behavior by Particle Packing, Materials Research 23 (2020).

[53] Z. Zhang, Y. Gao, F. Qin, F. Sun, Y. Huang, Mechanical properties of sustainable high strength ECC with substitution of cement by limestone powder, Case Stud. Constr. Mater. 19 (2023) e02434.

[54] E. Harrison, A. Berenjian, M. Seifan, Recycling of waste glass as aggregate in cement-based materials, Environ. Sci. Technol. 4 (2020) 100064.

[55] P.O. Awoyera, O.E. Babalola, O.G. Aluko, The use of slags in recycled aggregate concrete, in: P.O. Awoyera, C. Thomas, M.S. Kirgiz (Eds.), The Structural Integrity of Recycled Aggregate Concrete Produced with Fillers and Pozzolans, Woodhead Publishing 2022, pp. 145-170.

[56] C.B. Farinha, J. de Brito, R. Veiga, Assessment of glass fibre reinforced polymer waste reuse as filler in mortars, J. Clean. Prod. 210 (2019) 1579-1594.

[57] M.C.S. Ribeiro, A.C. Meira-Castro, F.G. Silva, J. Santos, J.P. Meixedo, A. Fiúza, M.L. Dinis, M.R. Alvim, Re-use assessment of thermoset composite wastes as aggregate and filler replacement for concrete-polymer composite materials: A case study regarding GFRP pultrusion wastes, Resour. Conserv. Recycl. 104 (2015) 417-426.

[58] M.R. Irshidat, N. Al-Nuaimi, Industrial Waste Utilization of Carbon Dust in Sustainable Cementitious Composites Production, Materials, 2020.

[59] L. Wang, F. Aslani, Mechanical properties, electrical resistivity and piezoresistivity of carbon fibre-based self-sensing cementitious composites, Ceramics International 47(6) (2021) 7864-7879.

[60] D. Wanasinghe, F. Aslani, G. Ma, Electromagnetic shielding properties of carbon fibre reinforced cementitious composites, Constr. Build. Mater. 260 (2020) 120439.

[61] A. Belli, A. Mobili, T. Bellezze, F. Tittarelli, Commercial and recycled carbon/steel fibers for fiber-reinforced cement mortars with high electrical conductivity, Cem. Concr. Compos. 109 (2020) 103569.

[62] J. Donnini, T. Bellezze, V. Corinaldesi, Mechanical, electrical and self-sensing properties of cementitious mortars containing short carbon fibers, J. Build. Eng. 20 (2018) 8-14.

[63] G. Faneca, I. Segura, J.M. Torrents, A. Aguado, Development of conductive cementitious materials using recycled carbon fibres, Cem. Concr. Compos. 92 (2018) 135-144.

[64] H. Fatemi, S.A. Hadigheh, Y. Tao, G. Adam, Development of a novel and specialised cementitious matrix overlay for anode embedment in impressed current cathodic protection (ICCP) systems for reinforced concrete bridges, Case Stud. Constr. Mater. 20 (2024) e02908.

Chapter 6: Electrochemical and Piezoresistive Properties of Cementitious Composites Incorporating Pulverised CFRP Waste and Reclaimed CF

6.1 INTRODUCTION

Following the successful investigation of fibre offcuts incorporation in Chapters 3 and 4, and the reuse of real-world FRP waste in Chapter 5, this research has demonstrated the viability of using both short CFs and rCFRPs in CCs to achieve enhanced mechanical performance and improved microstructural integrity. Beyond their structural role, CFs also impart valuable electrical properties, enabling self-sensing capabilities that pave the way for smart cement-based materials. This advancement sets the stage for the next phase of the study: investigating how these multifunctional composites can support structural health monitoring (SHM) to improve infrastructure safety and resilience.

SHM is important throughout the entire service life of infrastructure. It provides continuous performance assessment, enabling the early detection of anomalies and defects, while offering the benefits of a cost-effective, real-time, and automated monitoring system for civil infrastructure. Recent research has focused on developing CCs with intrinsic self-sensing capacities by incorporating CF serving as conductive fillers to enhance their piezoresistive behaviours. This strategy, also known as smart concrete, allows the CC itself to monitor structural integrity without the need for external sensors. In real-world conditions, structures are exposed to varying climates, which can significantly influence their electrical properties. While studies have examined the effects of temperature and humidity on the electrical resistance and piezoresistivity of CCs, few studies have addressed their performance under chemical deterioration. Therefore, further investigation into piezoresistive behaviour under various environmental and chemical exposures is essential for advancing effective cement-based sensors for SHM. In terms of repurposing CFPR composite wastes in CCs, there has been very limited research on the influences of utilising these recyclates as conductive fillers on the self-sensing capabilities of cement-based sensors.

This chapter mainly investigates the effectiveness of utilising CFRP and CF recyclates to develop and enhance the self-sensing capacities of cement-based sensors under varying

environmental conditions, including chloride-induced corrosion. Section 6.2 first provides an understanding of the corrosion behaviour and electrochemical properties of these CCs with embedded steel mesh reinforcement when exposed to a simulated marine environment. Section 6.3 experimentally investigates the influence of CFRP and CF recyclates on the electrical properties and piezoresistivity of CCs by examining factors such as filler dosage, curing age, temperature, humidity, and exposure to a chloride-induced corrosion environment.

6.2 ELECTROCHEMICAL PERFORMANCE AND CORROSION MITIGATION OF STEEL-EMBEDDED CEMENTITIOUS COMPOSITES WITH RECYCLED CF AND CFRP COMPOSITES IN ACCELERATED MARINE CONDITIONS

Y. Tao[1,*], S.A. Hadigheh[1,*]

[1]School of Civil Engineering, Faculty of Engineering, The University of Sydney, Sydney, New South Wales 2006, Australia

[*]Corresponding Author: Dr Ali Hadigheh

Yunyun Tao

6.2.1 Abstract

This study investigates the corrosion mechanisms and electrochemical performance of steel reinforcement in cementitious composites that incorporate recycled carbon fibre (CF) and carbon fibre reinforced polymer (CFRP) composite waste in a marine environment. Three types of recyclates are utilised, including chopped CF from fabric offcuts, chemically recycled CF, and mechanically recycled CFRP from aeroplane components. The surface characteristics of these recycled materials are examined after different treatments to assess the chemical and physical properties and their effects on the internal structure of the cementitious composites. A 3.5% sodium chloride marine environment with an impressed current is employed to accelerate the degradation of stainless-steel mesh in cementitious composites. Corrosion progression and electrochemical performance of specimens with different recyclates are monitored using a potentiostat and analysed through linear polarisation resistance (LPR) and electrochemical impedance spectroscopy (EIS) measurement. The most effective mix design for corrosion resistance contained 10 wt.% CFRP recyclates, showing a 43% reduction in corrosion rate and a 32% increase in polarisation resistance compared to control specimens without additives after 15 simulated years. In contrast, the inclusion of short CFs enhanced conductivity but accelerated the corrosion rate. The specimens containing acid-treated recycled CF exhibited slightly higher corrosion resistance than those with untreated CF. This research provides a detailed analysis of the corrosion processes in steel-reinforced cementitious structures and supports the effective repurposing of CFRP composite waste into cementitious materials. This sustainable approach aims to mitigate steel corrosion and enhance the durability of reinforced structures in marine environments.

Keywords: Fibre-reinforced cementitious composite (FRCC); Fibre-reinforced polymer (FRP); Carbon fibre (CF); Recycling; Steel corrosion; Electrochemical measurement

6.2.2 Introduction

Steel-reinforced concrete (SRC) is extensively utilised in construction due to its excellent mechanical properties, durability, and flexibility for specialised design applications [1]. The steel reinforcement in concrete provides a superior tensile capacity that complements the inherent compressive strength of the cementitious matrix. The cementitious matrix typically maintains a pH level of around 13, and this high alkalinity contributes to the formation of a protective passivating film on the surface of embedded steel reinforcement [2, 3]. Additionally, the impermeability and density of the concrete cover serve as a physical barrier, effectively blocking the corrosion reaction to some extent [2]. Together, these properties help preserve the structural integrity and performance of the composite system throughout its designed service life. However, adverse environmental conditions, such as urban, industrial and marine settings, can result in (i) a decrease in the alkalinity of the cementitious matrix due to the carbonation and (ii) the ingress of chloride ions, both of which compromise the stability of the passivation film on the steel reinforcement [1, 2, 4]. As the steel reinforcement corrodes, it produces expansive iron oxides and hydroxides, commonly known as rust. This reduces the steel's strength and exerts expansive forces on the surrounding concrete, forming and propagating cracks. Consequently, this degradation process negatively impacts both the serviceability and load-bearing capacity of the SRC structure in a time-dependent manner.

To mitigate these challenges, researchers have explored various strategies, including the development of both chemical and natural corrosion inhibitors [5, 6], the application of cathodic protection [1, 7], the addition of supplementary cementitious materials (SCMs) [8] as well as the incorporation of fibres [9, 10]. Among various types of fibres, carbon fibre-reinforced cementitious composites (FRCCs) have garnered significant attention due to their potential to enhance both the mechanical properties and durability of the SRC in terms of reduced water penetration and enhanced acid resistance [11, 12]. Furthermore, due to the electrically conductive nature of CF, carbon-FRCCs have been utilised in the development of smart concrete [13]. This enables non-destructive testing (NDT) capabilities for real-time monitoring of structural deformation. The effect of adding short carbon fibres (sCFs) on the corrosion resistance of steel rebars in concrete was first studied by Hou and Chung [14]. Subsequent

investigations have examined the effects of various CF sizes, dosages, and combinations with other additives on the mechanical performance and corrosion of steel reinforced cement-based mortars and concrete [10, 11, 15-19]. Several conclusions can be drawn from the literature as follows: (i) The contact between conductors (steel and CF) can form a galvanic couple. Due to their electrochemical potential difference, this galvanic couple can accelerate the corrosion of steel reinforcement, especially with high chloride ion concentration. Surface treatments of CFs, such as epoxy coating, can be applied to eliminate this adverse effect [10, 17, 18]. On the other hand, when steel comes into contact with CFs in an alkaline environment, a shift in potential occurs towards more positive values. An increase in the content of CFs within cementitious materials leads to a reduction in steel corrosion and promotes the formation of a more compact passivating layer on the steel surface [10]. This helps to mitigate potential galvanic effects, enabling the materials to enhance the overall polarisation resistance without significantly accelerating corrosion [10]. (ii) The optimal CF ratio in cementitious material should be carefully determined to minimise corrosion activity, as an appropriate amount of CFs can act as a barrier to chloride penetration by reducing the permeability and pathways for chloride ingress [17]. Conversely, increased total porosity in concrete and voids at the interface between solid particles and cement facilitates the penetration of chloride, which can reach the steel reinforcement more easily and decrease the electric resistance [10, 16]. (iii) The densification of concrete microstructure through the combined use of CFs and other additives, such as silica fume, can enhance the overall corrosion resistance of the reinforced concrete [14, 16]. Hence, based on previous studies, when applied in appropriate dosages and with proper treatments, CF has the potential to reduce the corrosion rate of steel reinforcement within the cementitious composites.

The benefits of FRCC with CFs have motivated researchers to explore the potential of integrating recycled carbon fibres (rCFs) in construction materials. This strategy aligns with the increasing demand for sustainable practices in the composite industry and also provides an opportunity for repurposing recyclates derived from carbon fibre-reinforced polymer (CFRP) waste [19]. FRP materials are widely used in various industries, including construction, aerospace, transport, defence, and sports, due to their superior mechanical properties and lightweight characteristics. However, a significant amount of waste is generated during the manufacturing of FRP composites, which accounts for 40% of the total waste, as well as at the end of their service life, posing substantial environmental challenges. The global CFRP waste is projected to increase to twenty kilotons annually in 2025. The aerospace and renewable

energy sectors are facing a significant challenge due to the impending retirement of aircraft and wind turbines. If effective recycling methods are not implemented, the annual accumulation of CFRP waste from these two sources is projected to surge to 840,300 tonnes by 2050 [20]. Moreover, estimates suggest that waste CFs could reach 263,000 tonnes by 2030 [21]. Currently, the two predominant traditional methods for composite waste disposal are incineration and landfilling. However, both approaches pose high risks to the environment and public health due to the release of harmful emissions and the non-biodegradable nature of CFRP composites. The development of a closed-loop lifecycle for CFRP composites, including effective recycling approaches, is urgently needed. Incorporating these recyclates into concrete presents a viable solution for composite waste management and sustainable development in the construction industry [19]. However, research on the utilisation of CF and CFRP recyclates obtained through different recycling methods in concrete remains limited, highlighting the need for further detailed investigation to evaluate their performance.

This research explores an alternative sustainable pathway for repurposing CFRP waste by incorporating it into cementitious materials, diverging from the conventional approach of reclaiming CFs for their original use. The study contributes to investigating the feasibility of incorporating various CFRP recyclates into the cementitious mortar and examines their effects on the corrosion resistance and electrochemical properties of stainless-steel mesh embedded cementitious composites. Firstly, the surface morphology, roughness and composition of three recyclates (namely virgin CF (vCF) offcuts, chemically recycled CF (rCF), and mechanically recycled CFRP (rCFRP)) were characterised after collection to understand their chemical and physical properties. These recyclates were used to formulate three corresponding cementitious composites, serving either as additional reinforcement or as a partial replacement for cement. Water absorption testing was subsequently conducted to evaluate porosity, a key factor influencing moisture and chloride ingress, which accelerates steel corrosion. A simulated marine environment with an impressed current was designed to accelerate the corrosion process and examine the corrosion of stainless-steel mesh embedded in cementitious composites. The electrochemical behaviours of each specimen containing different CF recyclates were monitored by connecting to a potentiostat and analysed through Tafel, Nyquist and Bode plots. The equivalent electrical circuits were proposed to understand the effects of various CF recyclates on the electrical network within cementitious composites. This analysis would reveal the role of different CF recyclates in the conduction mechanism and their contributions to the overall electrochemical response during the corrosion process. This study presents a

comprehensive analysis of chloride-induced corrosion resistance and electrochemical characteristics of cementitious composites with embedded steel reinforcement. The findings of this study also demonstrate the feasibility of repurposing recycled CF and CFRP composite wastes for use in infrastructures, particularly under aggressive environmental conditions.

6.2.3 Materials and experimental methodologies

6.2.3.1 CFRP recycling process

Short CFs were produced by manually chopping virgin fibre mats into lengths of approximately 6mm. Two types of composite wastes were considered as sources for the recycled CF and CFRP. As shown in Figure 6-1, the first type of composite waste consisted of 2-ply CFRP composites, which were composite offcuts from the process of manufacturing CFRP in the lab. This type of CFRP composite plate, with a unidirectional configuration, was produced using vacuum vacuum-assisted wet lay-up technique. Kinetix Resin R240 and Hardener H160 were used as the epoxy binder, while vCF fabric reinforcement served as reinforcement in the manufacturing process. The main characteristics of the vCF and epoxy binder used for this composite are presented in Table 6-1. After curing at room temperature for one week, the resultant fibre fraction was 76.7 wt.% with a thickness of 0.5 mm. Acid solvolysis is a CF recycling method that employs solvents to disrupt the matrix bond through a chemical reaction between the solution and the matrix [21, 22]. Previous reports have demonstrated that strong acids, such as sulfuric acid, can effectively recycle fibres, reacting with ether and benzene groups in epoxy-based composites at room temperature [23, 24]. In this experiment, 98% sulfuric acid was employed to reclaim CFs from 2-ply thin CFRP composites. The degradation of the epoxy matrix occurred relatively quickly, requiring only an hour of immersion in the acid at room temperature. Further information about the recycling process can be found in the previous study [21]. After this process, the rCFs were removed from the solution, rinsed thoroughly with water to eliminate excess chemicals on the surface, and then dried at ambient temperature. Due to the curvature of the fibres and their tendency to become intertangled after chemical recycling, the size of the rCFs could not be as precisely controlled as the original 6mm vCFs. However, they were manually cut to lengths ranging from 6 to 10mm.

Table 6-1. Properties of virgin carbon fibre and epoxy adhesive.

vCF		Uncured properties	Resin R240	Hardener H160
Areal weight (gsm)	300	Viscosity mPas @ 25°C	1600	30

Tensile modulus (GPa)	210	Specific Gravity g/ml @ 25°C	1.15	0.95
Tensile strength (MPa)	3,000			
Nominal thickness (mm/ply)	0.12			
Density (g/cm^3)	1.79			
Epoxy adhesive (Resin R118 and Hardener H160)				
Tensile modulus (GPa)	3.1			
Tensile strength (MPa)	69.6			
Density (g/cm^3)	1.09			

The second type of CFRP composite waste was collected from a manufacturer in the aerospace industry and consisted of discarded aerospace manufacturing parts (Figure 6-1). These composite panels exhibited quasi-isotropic behaviour with an ultimate tensile strength of 496 MPa and a Young's modulus of 351 MPa, as previously tested by the authors [19]. CFRP parts, with a thickness of approximately 5 mm, were processed with a two-step mechanical recycling approach using a Tema ring mill. After sieving, a mixture of short carbon fibres and irregular resin powder (particles passing through 600µm sieves) was selected as rCFRP for mixing into the cementitious matrix.

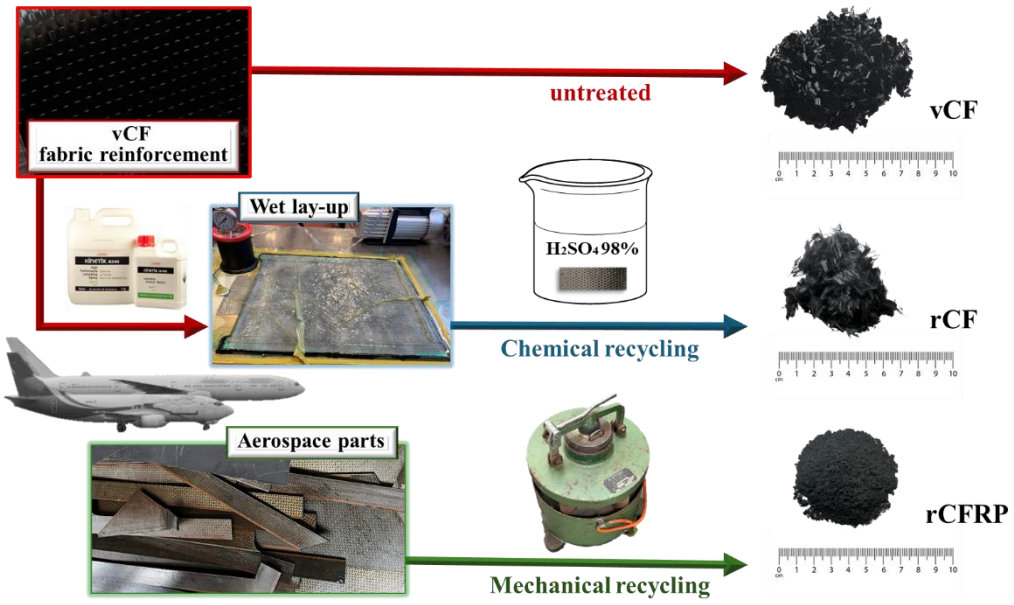

Figure 6-1. Three types of CF and CFRP recyclates used in this study.

6.2.3.2 Mix design and specimen preparation

Three different cementitious composite mixes with recyclates were prepared. vCFs and rCFs were added at 1.0% and 0.5% by volume, respectively, based on the authors' preliminary

testing and considering different CF lengths [11, 19, 25]. Meanwhile, rCFRPs replaced 10% of the cement by mass. The design ensured an optimal balance between the compressive strength of the cementitious composites and the conductive network formed by CFs within the matrix. This resulted in more stable piezoresistive behaviour, providing sufficient electrical conductivity and mechanical performance. In this study, these specimens were named VCF, RCF, and RCFRP, with a plain mortar used as a reference, labelled REF. The mix was formulated with a binder-to-fine aggregate-to-water ratio of 1:1.5:0.55, consistent with the author's previous work [19].

The cementitious composite preparation process involved dry-mixing cement and recycled materials at low speed for three minutes to achieve a homogeneous blend. Fine aggregates and water were gradually added in two stages, followed by five minutes of mixing, transitioning from low to high speed until a uniform consistency was achieved. The mixture was stirred for an additional two minutes at low speed. The pastes were then cast into moulds for water absorption (50×50×50 mm^3) and electrochemical tests (40×40×160 mm^3). The fresh mixes were poured into moulds in two layers and vibrated for 30 seconds to compact the mortar and remove air. After 24 hours, the specimens were demolded and cured at 23 °C, wrapped in damp cloths, and sealed in plastic until testing.

6.2.3.3 Experimental methods

Characterisation of CF and CFRP recyclates

The surface morphology of recyclates, namely vCFs, rCFs and rCFRPs samples was observed using a scanning electron microscopy (SEM) (Zeiss ULTRA Plus) at an acceleration voltage of 10 kV with the SE2 detector employed. The surface roughness analysis of CFs was performed by a Bruker Innova Atomic Force Microscope (AFM). Prior to testing, a very thin layer of CFs (approximately 5mm × 5mm area) was adhered to carbon double-sided tape to ensure no movement of each individual CF, with silver paint used to fix both ends. The AFM tip scanned the CFs in tapping mode, focusing on surface features with a scan rate of 0.5 Hz and scan ranges of 2 μm. Nasoscope Analysis software (3.0) [26] was then used for cropping, processing, and calculating the roughness of the images.

The structure of CF and CFRP recyclates was further characterised by a Renishaw Raman InVia Qontor Microscope with a 532nm laser excitation wavelength, and spectra were recorded using the 50× objective with the accumulation of 3 scans, 10s exposure and a laser power of 3.95%. In addition, TA Instruments Discovery Thermogravimetric Analyser and Bruker

ALPHA Fourier transform infrared (FTIR) were used to assist in determining the fibre weight fraction and the presence of organic compounds in the industrial CFRP composites. FTIR spectra were collected over the region of 4000 cm^{-1} with the co-addition of 64 scans at a spectral resolution of 400 cm^{-1}.

Water absorption testing

The water absorption in terms of total porosity of the cementitious composite was evaluated in accordance with ASTM C948-81 [27] by measuring the difference between the immersed mass and the saturated surface-dry mass of the 50×50×50 mm^3 specimens at 7 and 28 days. The dry bulk density of the hardened cementitious composites was calculated as the ratio of the recorded oven-dry mass to the specimen's volume, in accordance with BS EN 1015-10 [28]. Three repeated specimens were tested for each group.

Simulated marine environment and electrochemical measurement

To investigate the impact of incorporating various CF and CFRP recyclates on the corrosion behaviour of reinforcing stainless-steel mesh embedded in cementitious composites exposed to a simulated marine environment, each specimen was connected to a Metrohm Autolab PGSTAT302N potentiostat. Given that the corrosion of stainless steel is typically a slow electrochemical process under natural conditions, a constant impressed current density of 3.125 A/m^2 was applied to accelerate the corrosion process of stainless-steel mesh, particularly to simulate the extremely aggressive conditions. This current density was determined to ensure that the total amount of electrical charge passed over time in the accelerated test corresponded to that in natural conditions. In practice, the current density of metastable pits in stainless steel ranges from 0.5 to 2.5 A/cm^2 [29, 30]. Under laboratory conditions, based on the total charge passed over time calculated, each specimen was subjected to accelerated corrosion for 2 hours and 6 hours, simulating the equivalent of 5 years and 15 years of natural corrosion, respectively. In this setup (as shown in Figure 6-2), the stainless-steel mesh served as the working electrode, the titanium rod as the counter electrode, and an Ag/AgCl electrode as the reference. A 3.5% NaCl solution was used as the electrolyte to simulate the marine environment, ensuring complete immersion up to the surface level of the cementitious composites.

During the process of immersion, linear polarisation resistance (LPR) and electrochemical impedance spectroscopy (EIS) measurement techniques were employed to study the stainless-steel corrosion mechanism. Firstly, measurements were performed at open circuit potentials (OCP), with the process beginning only after the potential deviation, dE/dt,

stabilised to 1E-06 V/s, ensuring sufficient potential stability. LPR measurements were then conducted using a linear sweep voltammetry (LSV) staircase method with a scan rate of 0.01 V/s, before and after each accelerated corrosion operation. This approach was used to evaluate the corrosion rate and polarisation resistance, with key parameters including corrosion potential (Ecorr) and corrosion current density (icorr) determined by Tafel analysis. To further investigate the impedance characteristics of internal components within the cementitious composites, a Frequency Response Analysis (FRA), commonly known as EIS, was conducted over a frequency range of 0.01 to 100,000 Hz, with 20 frequency points per decade. A sine wave was used as the applied signal, and the input configuration was set to internal. The Nyquist and Bode plots were then used to present the resulting data, highlighting the resistance of different components across both low and high-frequency regions. In addition, equivalent circuits were evaluated for each cementitious composite to represent the complex electrochemical system as a series of manageable electrical components, such as solution resistance and the resistance at the steel-matrix interface. These equivalent circuits were subsequently fitted to the experimental data, with the parameters (values of the electrical components) optimised to achieve the best alignment with the observed results.

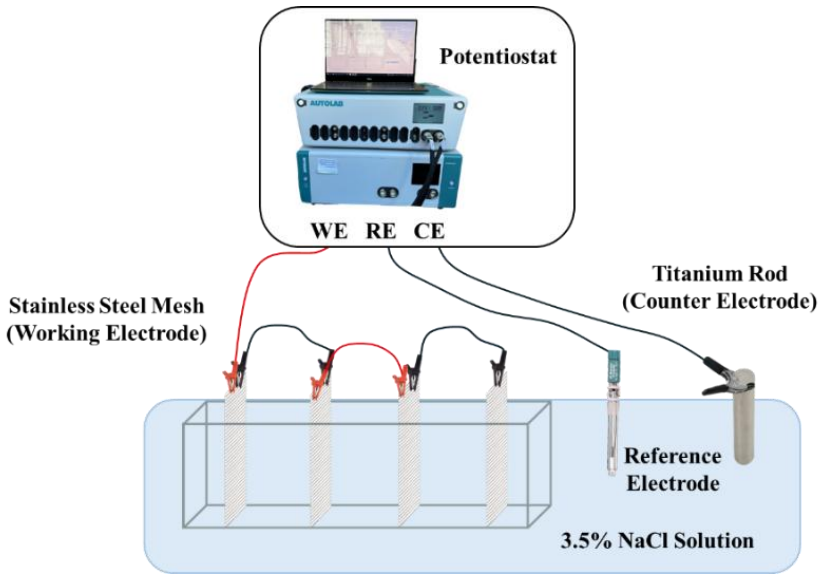

Figure 6-2. Experimental setup of accelerated corrosion using impressed current and electrochemical measurement in 3.5% NaCl solution.

6.2.4 Results and Discussion

6.2.4.1 Surface morphology and roughness of recyclates

To evaluate the recyclate surface morphology, SEM micrographs of vCF, rCF, and CFRP recyclates were compared. As shown in Figure 6-3 (a), the surface of vCF exhibited distinct

grooves along the fibre direction caused by the wet-spinning process during manufacturing. These surface grooves can enhance mechanical interlocking between the fibre and the surrounding matrix, leading to improved interfacial bonding. Figure 6-3 (b) shows individual CFs reclaimed by sulfuric acid recycling, indicating the matrices were degraded and lost their binding functions, in contrast to Figure 6-3 (d) where CFs were embedded in the epoxy matrix and completely covered. In some regions on the rCF surface, sulfuric acid etching also resulted in the formation of deeper grooves. The acid etched the surface, degrading the matrix and potentially deepening existing grooves. In other areas, a thin layer of matrix and resin debris was still observable on the CF surface after chemical recycling. Figure 6-3 (c) shows the CFRP recyclates, including both CF and fragmented resin debris, which were mechanically recycled from industrial CFRP panels. The cylindrical shapes of short CFs and resin particles were clearly distinguishable, with some portion of resin particles attached to the CFs. Figure 6-3 (e) displays the cutting surface of these composites, where the vCFs were closely packed in the matrix in different orientations.

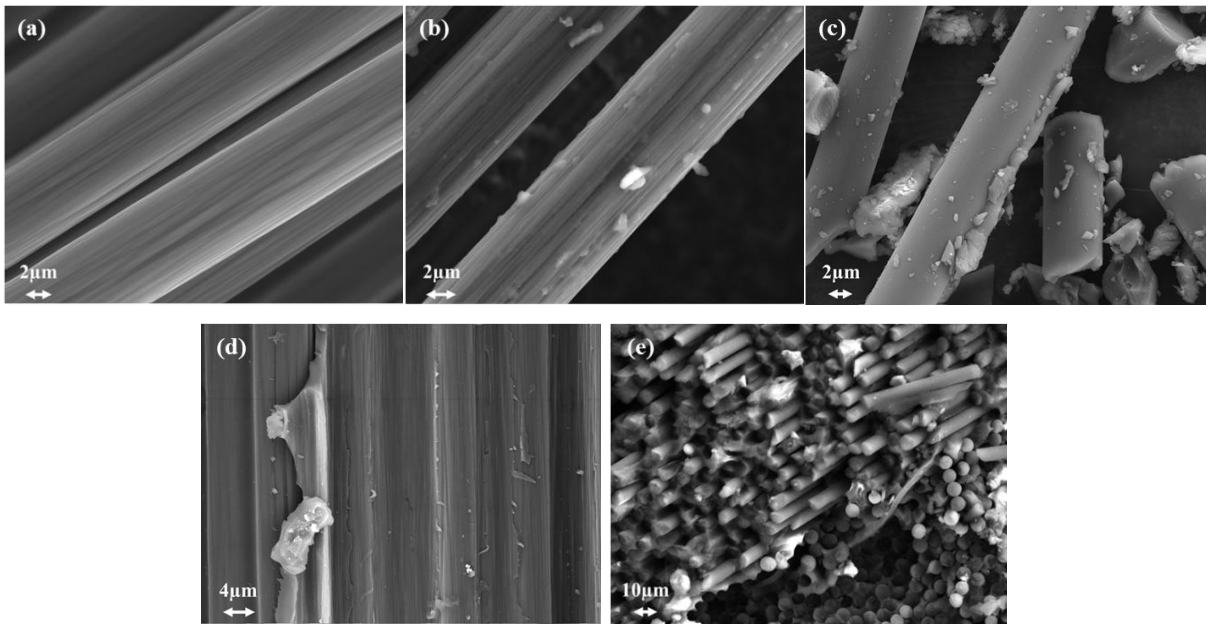

Figure 6-3. SEM micrographs of (a) vCF; (b) rCF from sulfuric acid treatment; (c) rCFRP from mechanical recycling method; (d) lab-manufactured CFRP surface; and (e) cross-sectional view of aerospace-grade CFRP.

The AFM morphology, surface height profiles and roughness are presented in Figure 6-4 and Table 6-2. It can be observed that vCF exhibited prominent parallel longitudinal grooves, which is consistent with the SEM morphology image. The horizontal line across the image indicates the height of the cross-section, labelled as Line 1 in Figure 6-4 (a). Regular undulations were clearly visible, representing ravines on the surface of the vCF, with the

maximum groove depth measuring approximately 150 nm. Lines 2 and 3 were measured along the direction of the fibres. Both lines indicate a relatively smooth surface in this direction, with minor fluctuations in height. The rCF surface still showed some grooves, although they were not as pronounced as those on the vCF. Obvious bumps were present on the surface, obscuring the grooves. However, in certain regions, deep pits or grooves were still visible. As seen in Figure 6-4 (b), line 1 represents the cross-sectional height perpendicular to the fibre direction. Between 0 and 1 μm, the height variation exceeded 300 nm, possibly due to etching. In contrast, the right side, from 1 to 2 μm, exhibited a smoother surface, suggesting the presence of residual resin covering the grooves, resulting in a flatter texture. In Figure 6-4 (c), most regions on the rCFRP surface exhibited a smooth appearance without any visible grooves, likely attributed to the different types of CFs used in manufacturing the original CFRP composites. The surface roughness observed was primarily caused by residual resins, as indicated by Lines 1 and 3. An obvious hump between distances of 1 to 1.5 μm was observed in the height profile along Line 3. However, this examination only covers the surface of a random micro-CF in the recyclates. There is a large amount of polymer matrix debris with irregular particles, exhibiting wide size variations, as shown in the SEM image Figure 6-3 (c).

Table 6-2 presents a quantitative comparison of two parameters. The average roughness (Ra) of the entire image was calculated after second-order flattening using Nasoscope Analysis [26]. The results indicate that vCF had the highest roughness at 39.8 nm, due to its distinct grooves. This is followed by rCF with a roughness of 27.5 nm, and rCFRP with a roughness of 18 nm, which is consistent with the previous qualitative analysis. The ratio between the surface topography area and the projected area (Ar) was also calculated, indicating the additional surface contact area. Again, vCF exhibited the highest surface area with a 26.8% excess compared to an ideal smooth surface. For the parameter Ar, the rCFRP surface showed the second largest Ar value of 1.264 due to its large protrusions, while the rCF surface exhibited the least excess contact area of 0.24%.

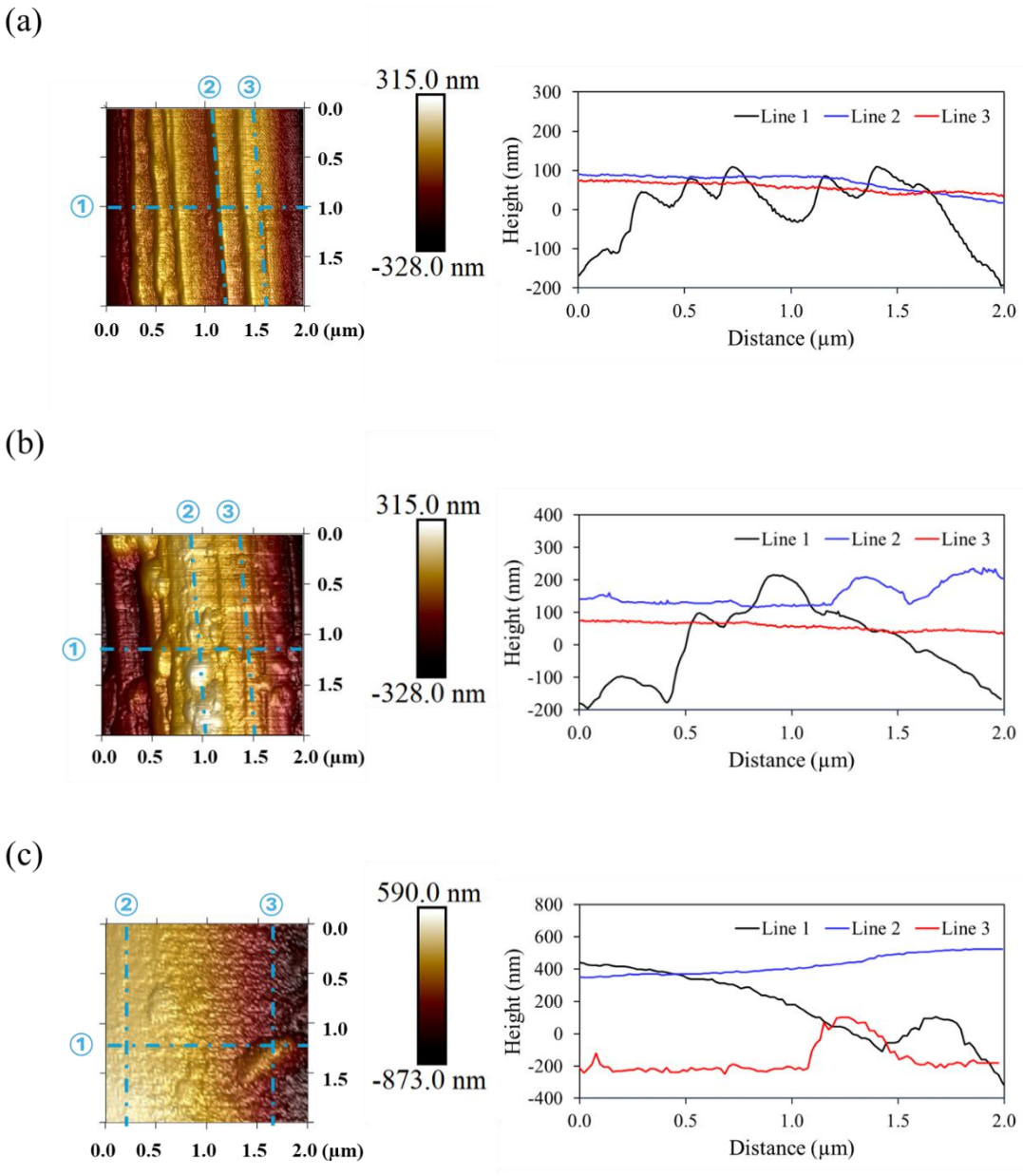

Figure 6-4. AFM images and surface height profiles (blue dashed lines indicate measurement location) of recyclates: (a) vCF; (b) rCF; (c) rCFRP (Line 1: Cross-sectional height profile perpendicular to the fibre direction; Lines 2 & 3: Longitudinal height profile along the fibre direction.).

Table 6-2. Average roughness and ratio between the surface topography area and the projected area of recyclates.

	vCF	rCF	rCFRP
Ra (nm)	39.8	27.5	18
Ar	1.268	1.240	1.264

6.2.4.2 Structural and compositional analysis of recyclates

The Raman spectra of the CF surface were used to characterise the degree of graphitic structural disorder in the carbon-based materials. Two distinct peaks, namely graphite and disorder bands, are evident in Figure 6-5 (a). The D peak (around 1350-1360 cm^{-1}) is associated with the presence of disorder defects, while the G peak (around 1592-1599 cm^{-1}) presents the ordered graphite structure. The intensity ratio (I_D/I_G) of vCF surface was calculated to be 1.41. A higher I_D/I_G ratio in the recycled CF surface indicates more severe surface defects and imperfections. The CF reclaimed from the mechanical recycling approach showed the lowest degree of graphitic structure, followed by the chemical recycling method.

The composition of the industrial-use CFRP composite was evaluated in Figure 6-5 (b). The derivative weight percentage per degrees Celsius (in terms of the rate of weight loss with respect to temperature), as shown in the Derivative Thermogravimetric (DTG) curve, indicated that the CFRP composite experienced significant weight loss between around 400-500 degrees Celsius. TGA was conducted at 20 °C/min to 700 °C under nitrogen, using 15-40 mg samples over 33 minutes. This suggests that the decomposition of the resin matrix occurred within this temperature range. The Thermogravimetric Analysis (TGA) curve indicated that CFRP recyclates consisted of approximately 50wt.% CF. From FTIR analysis (Figure 6-5 (c)), functional groups of organic compounds on CFRP composite can be determined. The C–H aromatic benzene ring vibration was observed at 1507cm^{-1}. The epoxide ring vibrations (C–O–C bonds) were observed at 969cm^{-1} and 873cm^{-1}. The carbonyl compounds (C=O) were detected at 1701cm^{-1} and 1770cm^{-1}, indicating the possible presence of various products such as ketones, esters, and aldehydes [31, 32].

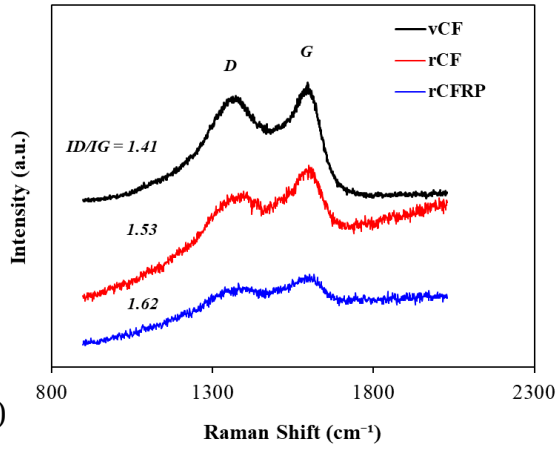

(a)

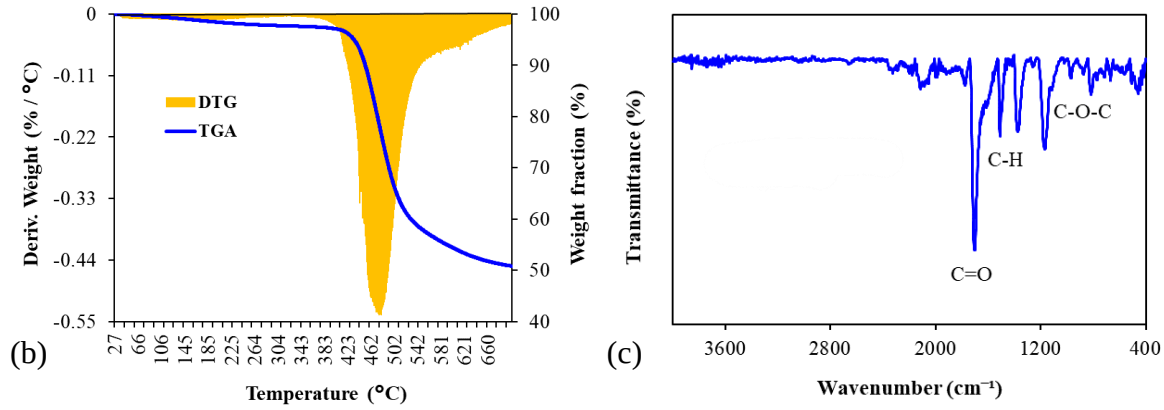

Figure 6-5. (a) Raman spectra of CF surfaces; (b) Thermal stability, and (c) FTIR spectrum of CFRP recyclates.

6.2.4.3 Total porosity by water absorption measurements

The total porosity of the resulting cementitious composite containing CF and CFRP recyclates was measured by the water absorption experiment. As the density of all specimens' microstructure increased due to the development of hydration reactions over time, the water absorption percentage decreased from 7 days to 28 days. As shown in Figure 6-6, VCF and RCF exhibited higher porosity and lower dry bulk density than the REF. This was attributed to the presence of additional air entrapment, potential clustering of fibres, and the lightweight nature of CFs. RCF with 0.5 vol.% rCF had similar water absorption and dry density values to VCF with 1.0 vol.% vCF. This similarity could be attributed to the rCF being longer than the vCF and being cut and collected after acid treatment. At 28 days, the specimen containing rCF had 4.86% higher water absorption and 6.05% lower bulk density compared to the REF. In comparison, the specimen with vCF showed a much higher water absorption of 6.44% and a bulk density that was 6.81% lower than that of the REF. A denser structure with rCF was observed, probably due to enhanced interfacial bonding from oxygen-containing functional groups introduced by the acid treatment.

The inclusion of CFRP recyclates significantly decreased the porosity by 19.15% within the cementitious composites, as the fine particles filled voids and spaces between larger particles, enhancing compaction through more efficient packing arrangements. When a larger amount (10%) of CFRP recyclates with lower specific gravity was added to the cementitious matrix to replace cement, the bulk density was still higher than that of VCF and RCF, again demonstrating its compactness.

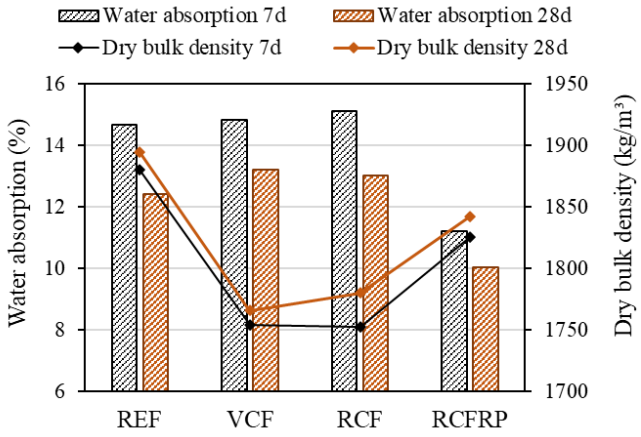

Figure 6-6. Water absorption and dry bulk density of specimens containing different CF and CFRP recyclates.

6.2.4.4 Electrochemical measurements

Visual observation

Visual inspection was carried out throughout the corrosion experiment. During the corrosion process, greenish to yellowish-brown products gradually formed on the mesh near the cementitious composite surface. These corrosion products are primarily due to the presence of ferrous hydroxide, ferric hydroxide, and ferrous chloride, resulting from the oxidation reactions occurring on the steel surface, as illustrated in Equations 6-1 to 6-5. Over time, this led to the formation of reddish-brown ferric oxide (Equation 6-6) and a minor mixture of the other corrosion products including chromium, as stainless-steel mesh was used in the experiment. This indicates that the chloride ions penetrated the steel's passive layer and led to pitting corrosion and rust formation. The titanium rod remained unaffected but showed bubbles around its surface, which means the presence of hydrogen gas caused by the reduction reaction. Figure 6-7 shows the top, bottom and side views of specimens after equivalent to 15 years of corrosion. The rust initiated from the embedded stainless-steel mesh and spread to the surrounding surfaces. Minimal rust was observed in the specimen containing CFRP recyclates (Figure 6-7 (d)), while the specimen with vCF showed more extensive corrosion (Figure 6-7 (b)). This observation suggests that rCFRP is probably effective in mortar for mitigating corrosion under harsh conditions, as further supported by electrochemical measurements.

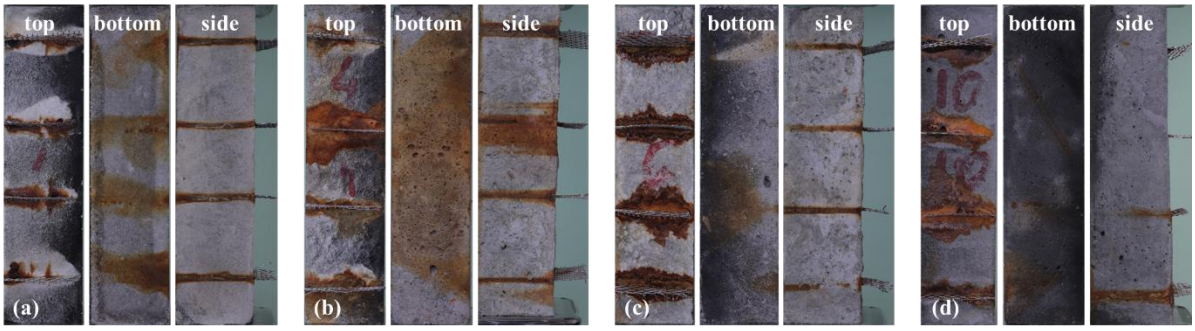

Figure 6-7. Photographs of specimen surfaces after corrosion equivalent to 15 years: (a) REF; (b) VCF; (c) RCF; (d) RCFRP.

$$Fe = Fe^{2+} + 2e^{-} \quad (6\text{-}1)$$

$$Fe^{2+} + 2OH^{-} = Fe(OH)_2 \quad (6\text{-}2)$$

$$Fe(OH)_2 + O_2 + 2H_2O = 4Fe(OH)_3 \quad (6\text{-}3)$$

$$Fe^{2+} + 2Cl^{-} = FeCl_2 \quad (6\text{-}4)$$

$$FeCl_2 + 2H_2O = Fe(OH)_2 + 2HCl \quad (6\text{-}5)$$

$$2Fe(OH)_3 = Fe_2O_3.H_2O\ (rust) + 2H_2O \quad (6\text{-}6)$$

LPR measurement and Tafel polarisation plot

LPR measurements were conducted on each specimen before and after corrosion acceleration in the absence of external potential. Tafel polarisation plots and analyses were carried out to calculate the corrosion rates and polarisation resistance. The Butler-Volmer equation describes the relationship between the current density (I) and the difference between the applied potential (E) and the corrosion potential (Ecorr), as shown in Equation 6-7. In this equation, icorr represents the corrosion current density. b_a and b_c are the Tafel slopes of the anodic and cathodic reactions, respectively.

$$I = i_{corr}[e^{\frac{2.303(E-E_{corr})}{b_a}} - e^{\frac{-2.303(E-E_{corr})}{b_c}}] \quad (6\text{-}7)$$

Figure 6-8 shows the Tafel plots for cementitious composites before and after equivalent corrosion times of 5 and 15 years. The icorr on the x-axis represents the rate at which the stainless-steel mesh corrodes, while Ecorr indicates the tendency for the steel to corrode. A more negative value of Ecorr suggests a higher likelihood of corrosion. The slope of the potential-current curve near corrosion potential Ecorr is used to calculate the polarisation resistance. Table 6-3 provides more detailed quantitative corrosion parameters. Before corrosion began, REF and RCFRP exhibited similar corrosion rates, and the specimens containing CFs (VCF and RCF) demonstrated similarly higher corrosion rates. Likewise, REF

showed the highest polarisation resistance, followed by the RCFRP, due to the limited influence of CFRP recyclates on reducing electrical resistance [19]. In contrast, the specimens containing CFs exhibited lower polarisation resistance values, as anticipated. This reduction was attributed to the significant enhancement of electrical conductivity due to the presence of CFs [11]. In terms of Ecorr , CF demonstrated its ability to stabilise the electrochemical environment by creating a more uniform distribution of potential across the steel surface, which reduced the likelihood of localised corrosion.

The Tafel plots then shifted in the direction indicated by the yellow arrows as exposure time increased. The curve of REF shifted in the negative direction on the y-axis and positive direction on the x-axis, indicating that the steel in plain mortar experienced steadily increasing corrosion over time. VCF and RCF exhibited higher corrosion rates over time due to the inclusion of 6 mm to 10 mm CFs. Additionally, the higher porosity observed in VCF and RCF (Figure 6-6) demonstrated more internal void channels, which provided pathways for aggressive ions and moisture to reach the stainless-steel mesh, further exacerbating corrosion [17]. RCF exhibited lower polarisation resistance at the equivalent corrosion time of 5 years, followed by an increase, possibly due to the improved rCF-matrix bonding over time. Although rCF exhibited a generally smoother surface than vCF, as shown in the AFM scan (Figure 6-4), this improvement could be attributed to the functional groups on the rCF surface induced by sulfuric acid treatment, which reacted with calcium ions and hydration products. To some extent, these reactions densified the microstructure and limited the ingress of aggressive ions that can cause corrosion. The Ecorr of RCF also became less negative over time, suggesting a less prone to corrosion trend. RCFRP demonstrated overall lower corrosion rates and greater polarisation resistance at the end of the 15-year equivalent corrosion period compared to the other specimens. Additionally, the corrosion potential in RCFRP was less negative compared to REF, indicating improved long-term durability.

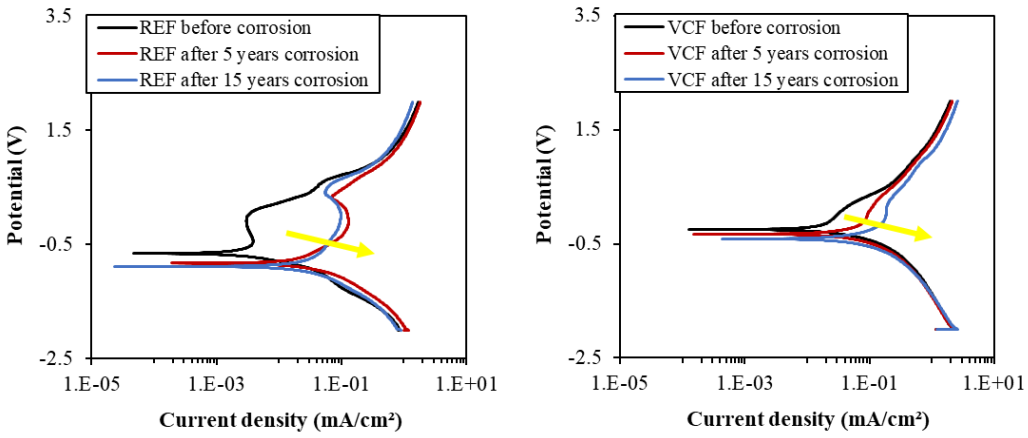

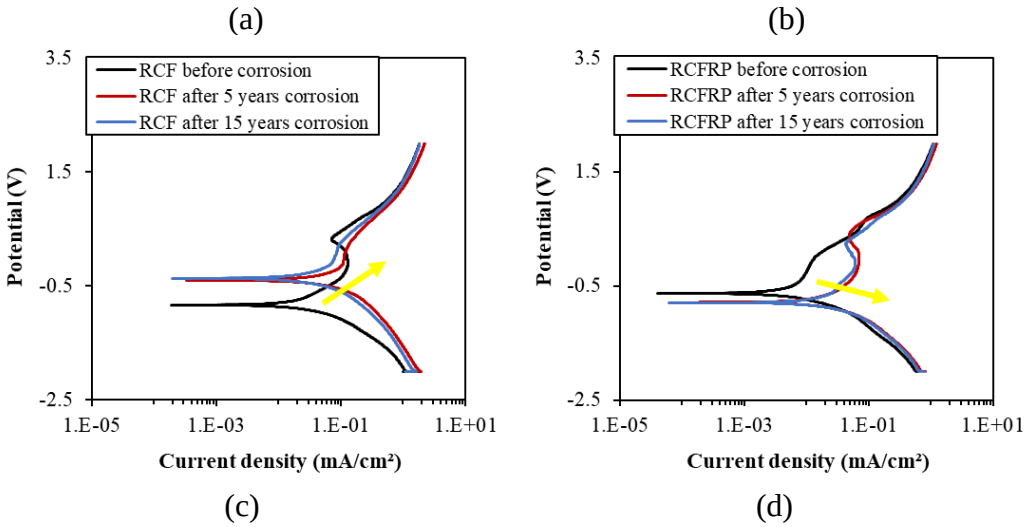

Figure 6-8. Tafel polarisation curves for plain mortar and cementitious composites containing vCF, rCF and rCFRP.

Table 6-3. Tafel analysis before and after exposure to the accelerated marine environment.

	Condition	i_{corr} (A)	Corrosion rate (mm/year)	E_{corr} (V)	Polarisation resistance (Ω)
REF	Before	0.0018	0.33	-0.65	350.88
	5 years Corrosion	0.0118	2.12	-0.83	56.74
	15 years Corrosion	0.0146	2.63	-0.89	58.54
VCF	Before	0.0079	1.42	-0.25	53.26
	5 years Corrosion	0.0271	4.87	-0.33	28.79
	15 years Corrosion	0.0360	6.49	-0.42	22.62
RCF	Before	0.0079	1.43	-0.83	56.60
	5 years Corrosion	0.0314	5.66	-0.40	28.40
	15 years Corrosion	0.0223	4.01	-0.34	45.10
RCFRP	Before	0.0018	0.32	-0.65	235.63
	5 years Corrosion	0.0049	0.87	-0.79	76.07
	15 years Corrosion	0.0083	1.50	-0.81	77.27

EIS analysis using Bode and Nyquist plots

Both Nyquist and Bode plots were analysed to further show the EIS properties of specimens. A Nyquist plot is generated by plotting the real part of the impedance against the imaginary part. The shape of the curves in the Nyquist plot provides a qualitative interpretation

of the data. As reported by Zhang et al. [33] and Li et al. [34], it is expected that cement-based sensors containing conductive fillers will exhibit an additional arc in the Nyquist plot at intermediate frequencies, attributed to the fibre effect. As clearly seen in Figure 6-9 (b) and (d), which show the zoomed-in areas of interest, both VCF and RCF specimens exhibited this type of arc pattern because of the formation of electrical double layers (EDLs) on the carbon fibre surface. The arc corresponding to the RCFRP specimen was not prominent at intermediate frequencies, instead, a plateau region was observed. In the Nyquist plot, the larger diameter of the semicircle generally indicates a higher impedance. The REF specimen demonstrated the highest corrosion resistance at the equivalent of 5 years. However, the diameter notably decreased over time, indicating a reduction in corrosion resistance. Upon the inclusion of CFs, both the bulk and electrode arc diameters decreased, corresponding to the increased conductivity. The RCFRP specimen showed a relatively large semicircle, suggesting good long-term corrosion resistance in a more stable manner.

The Bode plots in Figure 6-9 (e) and (f) were used to compare the total electrical impedance including the solution resistance at high frequencies and charge transfer resistance at lower frequencies. In these plots, the absolute value of impedance is plotted as a function of frequency. A negative slope over the entire tested frequency range was observed for all specimens, indicating the solution resistance is much smaller than the charge transfer resistance such as Rct and Rf (Resistors Rct and Rf represent the interface resistance between the steel-matrix interface and the fibre-matrix interface, respectively). At a lower-frequency range, a lower steep slope indicates better corrosion resistance performance. Among these specimens, REF demonstrated the highest impedance, but it decreased the most over time, representing the progressive long-term corrosion of the plain mortar. The RCFRP specimen also demonstrated higher impedance with a lower corrosion rate, while the specimens including CFs indicated lower solution resistance within the material.

Figure 6-9 (g) and (h) represent the conventional simplified equivalent circuit models for plain mortar [35] and carbon fibre reinforced mortar respectively, corresponding to the given mix combination and the observed experimental behaviour. The equivalent circuit models are used to interpret impedance data. Resistor Rs represents the resistance of pore solution in the cementitious matrix. CPE denotes the constant phase element associated with capacitance, which models the non-ideal capacitive behaviours. The impedance of CPE is expressed as the following equation:

$$Z_{CPE} = \frac{1}{Y_0(j\omega)^N} \quad 6\text{-}8$$

where Y_0 is the admittance of the CPE, which is the inverse of impedance. j is the imaginary unit (equal to $\sqrt{-1}$). ω is the angular frequency, and N is an empirical constant ranging from 0 to 1. When N approaches 0, the CPE behaves more like a pure resistor, while when N is closer to 1, the CPE behaves more like a capacitor.

Table 6-4 presents the fitting parameters of cementitious composites with or without recyclates based on the equivalent circuit models. The smaller Rs value represents the effective chloride ions' accelerated transfer. RCFRP with a higher Rs value showed enhanced resistance, likely due to the refined pore structures, as evidenced by the lower porosity in Figure 6-6, while Rs reduced sharply with the inclusion of CFs into the mortar. VCF and RCF showed lower Rct values, indicating that more chloride ions reached the stainless-steel mesh surface, thereby accelerating the corrosion reaction and promoting the dissolution of metal. The formation of a CF conductive network reduced the electron transfer resistance. The fitting parameters are consistent with previous discussions.

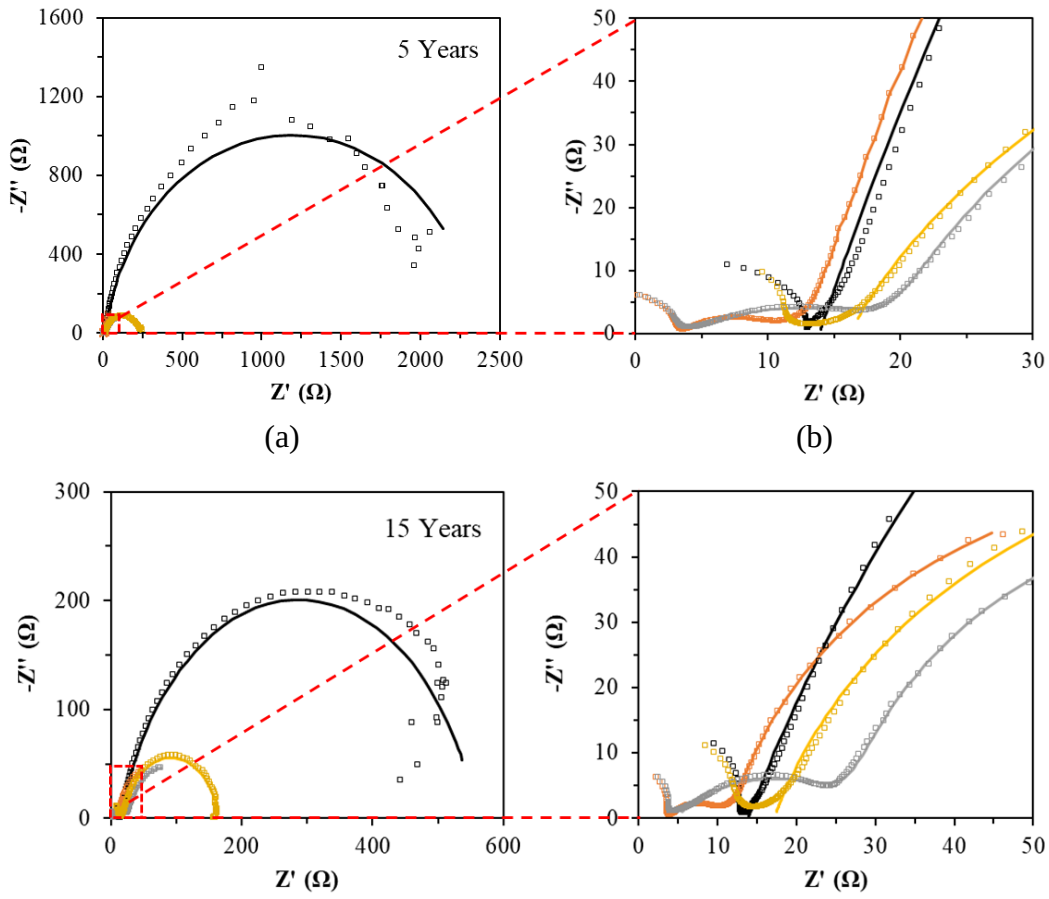

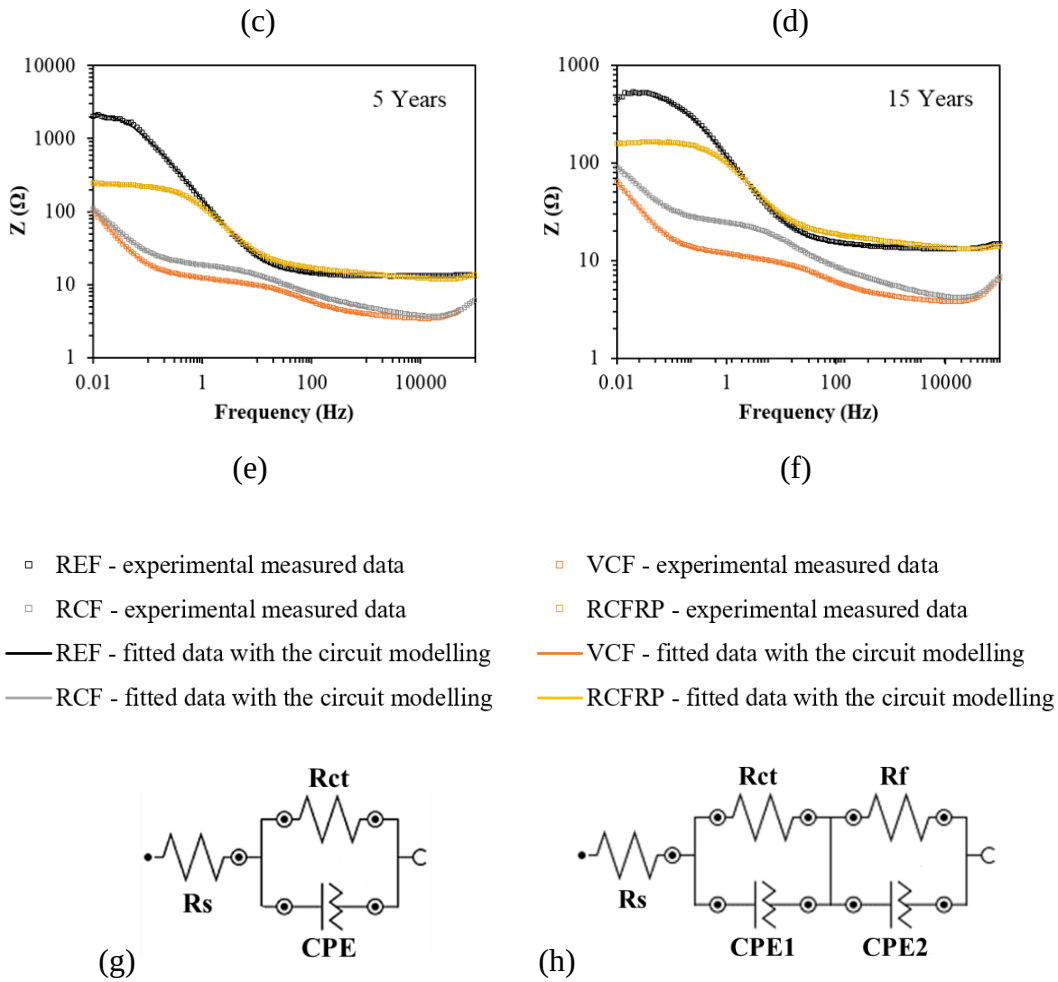

Figure 6-9. The impedance behaviour characterised by Nyquist plots: (a) to (d), and Bode plots: (e) and (f), corresponding to corrosion periods equivalent to 5 and 15 years; (g) and (h) illustrate the equivalent circuit models. The EIS diagrams were plotted using both experimental results (represented by hollow scatters) and fitting results based on the equivalent electrical circuits (represented by solid lines).

Table 6-4. Fitting parameters based on the equivalent circuit models.

	Equivalent Corrosion Years	Rs (Ω)	R_{ct} (Ω)	CPE1		Rf (Ω)	CPE2	
				Y0 (mMho·s^N)	N		Y0 (mMho·s^N)	N
REF	5	13.88	2351.90	0.00135	0.900			
	15	13.86	546.38	0.00191	0.807			
VCF	5	3.21	9.44	0.00506	0.606	2123.20	0.122	0.896
	15	3.65	8.50	0.00653	0.583	124.92	0.167	0.872
RCF	5	3.85	16.48	0.00523	0.561	194.73	0.098	0.883
	15	4.69	23.28	0.00440	0.583	108.05	0.121	0.901
RCFRP	5	16.12	224.04	0.00164	0.839			
	15	17.16	149.79	0.00177	0.815			

6.2.5 Discussion

The integration of multiple evaluation methods provides a comprehensive understanding of the material phase, and the physical and electrochemical properties related to the corrosion behaviour of steel-embedded cementitious composites. These methods collectively examine the influence of incorporating different CF and CFRP recyclates on the internal structure of cementitious composites and their effectiveness in mitigating or accelerating stainless-steel mesh corrosion. The CFRP recyclates, consisting of micro-CFs and fine polymer matrix particles, have proven effective in mitigating steel corrosion in an aggressive marine environment by reducing the corrosion rate and enhancing resistance. This was achieved by limiting chloride ingress to the stainless-steel mesh, due to the denser structure and lower porosity compared to plain mortar (Figure 6-6).

However, the inclusion of discrete short CFs led to an increased corrosion rate and reduced corrosion resistance, primarily due to the higher porosity observed, as shown in Figure 6-6. The greater pore volume created additional pathways for aggressive ions to penetrate, accelerating their access to the stainless-steel mesh. The presence of CFs also decreased electron transfer resistance by forming a strong conductive network. Furthermore, the lack of additional surface treatment on the CFs may have exacerbated corrosion through galvanic coupling between the CFs and the steel. The specimen containing rCF with acid treatment exhibited slightly more resistance to corrosion than the vCF specimen, as evidenced by both visual inspection and parameter analysis. The rCF exhibited lower surface roughness due to residual matrix material and an increased ID/IG ratio, indicating more significant surface imperfections (as shown in Figure 6-4 and Figure 6-5). These characteristics reduced their conductivity for free electron transmission, thereby contributing to an overall decrease in the resistivity of the cementitious composites [36]. In addition, oxygen functional groups were introduced during the acid recycling process, resulting in improved interfacial bonding between rCF and the cementitious matrix. As a result, the water absorption percentage of the specimen containing rCFs at 28 days showed a slight decrease compared to the specimen with vCF. As suggested by Wei et al. [17], CF waste can undergo additional surface treatment with epoxy before being incorporated into concrete, which has been shown to reduce the corrosion rate of reinforced concrete (RC) structures.

6.2.6 Summary of key findings from Section 6.2

In conclusion, this study examines the material characterisation of chopped vCF offcuts, chemically recycled CF, and mechanically pulverised CFRP, as well as the total porosity and the corrosion behaviours of their corresponding stainless-steel mesh-embedded cementitious composites. The specimens were exposed to a 3.5% NaCl solution with impressed current to simulate an accelerated harsh marine environment. The corrosion behaviour of stainless-steel mesh was monitored using a potentiostat, and the electrochemical performance was measured and analysed through LPR and EIS techniques. The key findings derived from the results are as follows:

- The recyclates exhibited distinct surface characteristics. vCF exhibited prominent grooves, while rCF from acid solvolysis treatment displayed surface bumps, residual matrices and etched areas. The mechanically recycled CFRP had the lowest surface roughness but the highest disorder defects, along with pulverised resin matrix particles.
- The inclusion of additional CFs in cementitious composites increased the total porosity and lowered the dry bulk density compared to plain mortar, primarily due to air entrapment and fibre clustering. Conversely, CFRP recyclates notably reduced pore volume, achieving a 19.15% reduction in water absorption compared to the plain specimen, by filling voids between larger particles, improving particle packing and providing nucleation sites for hydration products in the matrix.
- The incorporation of CFRP recyclates in cementitious composites has been shown to effectively mitigate steel corrosion under harsh environmental conditions. After simulating 15 years of aggressive corrosion, the specimen with CFRP recyclates demonstrated a 43% reduction in corrosion rate and a 32% increase in polarisation resistance compared to the plain specimen. EIS investigations also confirmed its ability to provide greater stability in long-term corrosion resistance. Visual inspection revealed minimal rust on the CFRP recyclate specimen, further confirming its protective effect.
- The inclusion of discrete short CFs increased corrosion rates and reduced corrosion resistance due to higher porosity, which created pathways for aggressive ions and formed a conductive network that decreased electron transfer resistance. The specimen with rCF from acid recycling showed slightly better corrosion resistance than the vCF specimen.

This study primarily examined the impact of various CF and CFRP recyclates on the corrosion behaviour of stainless-steel mesh-reinforced cementitious composites. The findings confirmed that CFRP recyclates are effective as sustainable materials for use in cementitious materials, particularly in aggressive marine environments. Future research is recommended to explore different treatments for rCF and the optimal dosage of recyclates to further enhance corrosion resistance performance. Additionally, future studies could examine the effect of chloride ingress on cementitious composites with varying compositions.

6.3 PULVERISED CFRP WASTE AND RECLAIMED CF FOR CEMENT-BASED SENSORS: INVESTIGATING ELECTRICAL RESISTIVITY AND PIEZORESISTIVITY UNDER VARYING ENVIRONMENTAL CONDITIONS

Y. Tao[1,*], S.A. Hadigheh[1,*], S. Saha[1] and Y. Wei[1]

[1]School of Civil Engineering, Faculty of Engineering, The University of Sydney, Sydney, New South Wales 2006, Australia

[*]Corresponding Author: Dr Ali Hadigheh

Yunyun Tao

Construction and Building Materials, https://doi.org/10.1016/j.conbuildmat.2025.140516, Published in February 2025.

6.3.1 Abstract

Cementitious composites with carbon fibres (CFs) have been developed as functional cement-based sensors for real-time structural health monitoring (SHM). However, few studies have investigated the piezoresistive performance of these cementitious composites under different external environmental conditions. This research studies the influence of carbon fibre-reinforced polymer (CFRP) recyclates on the electrical resistivity and piezoresistivity of cementitious composites under varying temperature, humidity and chloride-induced corrosion. The experiments involved the use of recycled carbon fibre (rCF) reclaimed through acid solvolysis and recycled CFRP (rCFRP) derived from mechanical recycling. Their performance in cementitious composites was evaluated against benchmarks containing virgin carbon fibre (vCF) offcuts and plain mortar without additives. The results show that while incorporating rCFRP increased the electrical resistivity of cementitious composites compared to those with CFs, the rCFRP specimens demonstrated more consistent and repeatable piezoresistive behaviour under cyclic loading in both low and high-humidity environments. Under 30% humidity conditions, the rCFRP specimen achieved an average stress sensitivity (SS) of 0.42%/MPa and a gauge factor (GF) of 17.50. The piezoresistivity decreased after exposure to chloride-induced corrosion. However, the behaviour remained stable through a well-distributed conductive network, which proved more effective than ionic conduction pathways. These findings demonstrate the potential of rCFRP-based cementitious sensors for SHM applications, offering both technical effectiveness and environmental sustainability.

Keywords: Self-sensing materials; Piezoresistivity; Electrical resistivity; Fibre-reinforced polymer (FRP); Recycling

6.3.2 Introduction

Structural health monitoring (SHM) offers an economical, real-time, and automated solution for monitoring civil infrastructure. This strategy enables the early detection of anomalies or defects, enhancing the reliability and safety of structures. Factors such as harsh environmental conditions, natural disasters, and manufacturing deficiencies can lead to the degradation of structures both in the short term and over time [37]. Therefore, the application of SHM at every stage of the infrastructure's service life is important. Over the last decades, multiple techniques have been employed in SHM to assess the performance of concrete structures, including electro-mechanical impedance (EMI) [38, 39] and Fibre Bragg gratings (FBGs) sensors [40, 41]. Conventional SHM systems utilise sensors embedded in or attached to structural components during construction. They rely on wired or wireless networks to transfer data, enabling non-destructive and long-term management of the infrastructure. Despite their benefits, these applications are constrained by the limitations of sensor technologies, including high costs, installation challenges, and restricted data collection capabilities that typically focus on specific points rather than the entire structure [42-44]. As an alternative, self-sensing cementitious composites with functional fillers, also known as smart concrete, have gathered great interest in engineering practice. These cementitious composites incorporate functional additives within the cementitious matrix to form a conductive network, where changes in this network can indicate deformation and defects [45]. Therefore, without the need for additional sensors, the cementitious composite itself functions as a sensory material, providing comprehensive monitoring of the entire structure [46].

Among various conductive fillers, carbon-based materials such as carbon fibres (CFs) [11, 44, 47], graphite powder (GP) [46], carbon nanotubes (CNTs) [44, 47], carbon nanofibers (CNFs) [34], and carbon black (CB) [34] are most studied for developing intrinsic self-sensing cementitious composites due to their effectiveness in enhancing piezoelectric behaviour. The integration of carbon nano additives fills the pores between hydration products, densifying the microstructure of the matrix. On the other hand, fibrous carbon additives enhance the reinforcing effect within the surrounding matrix. Both types of additives contribute to improved electrical conductivity by creating a denser microstructure that facilitates electron transport and establishing continuous conductive pathways. In addition, well-distributed CFs are particularly effective in reducing the electrical resistivity of composites due to their higher aspect ratio, which facilitates the development of conductive networks. Researchers have been investigating different combinations to achieve the optimal piezoresistive performance for their mixes. For

example, Li et al. [34] determined that the optimal dosage of CB for both compressive strength and piezoresistivity was 0.5 wt.% of binder in the development of self-sensing ultra-high-performance concrete (UHPC). Deng et al. [48] proposed a type of conductive mortar combined with alkali-activated fly ash and slag (AAFS). They found that, when investigating CF additions ranging from 0 to 0.5 vol.%, the mortar with 0.1 vol.% CF exhibited the best piezoresistive behaviour with the most distinct response to cyclic loads, and with 0.2 vol.% CF, it reached the percolation threshold.

In real-world cases, structures are exposed to different climate conditions, which impact their electrical properties. Studies have emphasised the influences of temperature variations and different levels of humidity on the electrical resistance and piezoresistivity of cementitious composites. According to Wang et al. [49]'s study, the relationship between temperature and electrical resistance could be linear or follow a Gaussian function, depending on CNFs content and moisture state. The self-sensing performance was temperature-dependent, with optimal performance at 20°C. Performance deteriorated at both lower and higher temperatures due to two primary mechanisms: (i) reduced carrier transport current, thermal voltage, and ionic conduction at lower temperatures; and (ii) decreased tunnelling effect caused by increased distance between CNF particles. On the other hand, the fluctuation in humidity alters the ion concentration in the pore solution, thereby affecting its conductive behaviour. Water content reduced electrical resistivity due to induced ionic conduction when incorporating a lower amount of conductive fillers, while electronic conduction dominates with more conductive fillers [50]. The increased water content could also increase the contact resistance between fillers, thus reducing the electronic conduction [51]. In such cases, the higher water content would deteriorate the piezoresistive sensitivity. Contradictory observations have been reported, as piezoresistive sensitivity initially decreased due to the electric polarisation effect but subsequently increased with rising water content, attributed to a larger number of free ions [49]. In addition, since most structures are susceptible to chemical attacks, it is crucial to ensure that their piezoresistivity remains stable for effective self-sensing, even after degradation. However, only a few studies have investigated the ability of self-sensing cementitious composites under chemical deterioration mechanisms, including chloride-induced and sulphate attacks [52, 53]. These two studies revealed the mechanisms behind altered piezoresistivity from a microstructural perspective, including the formation of erosion products and changes in the ion concentration of pore solutions. Further investigation into the piezoresistivity under varying humidity and chemical attack conditions is still essential for the development of

cement-based sensors for SHM. This research is essential to understand how self-sensing cementitious materials perform in real-life service conditions.

On another aspect, in the last five years, there has been growing interest in utilising recycled CFs (rCFs) in cementitious materials to enhance conductivity and piezoresistive behaviour purpose. The first study, initiated by Faneca et al. [54] in 2018 confirmed the feasibility of using rCFs to create conductive cementitious materials without compromising electrical properties. Belli et al. [12] compared the effects of incorporating 6mm length commercial and recycled CFs in mortars. While there were no noticeable differences in mechanical strength when combined with industrial by-product conductive fillers, the micro-fragments present on the surface of rCFs contributed to lower porosity in the mortars. The largest resistivity changes under strain were obtained in specimens containing 2 vol.% used foundry sand and 0.2 vol.% rCFs. Indeed, the shift from using vCFs in cementitious composites to incorporating rCFs recycled from the composite industry is driven by the pursuit of sustainable development, addressing both economic and environmental aspects. Annual CFRP waste from the aircraft and wind turbine industries is projected to exceed 840 thousand tonnes, posing a substantial environmental burden due to the non-biodegradable nature of these composites [19, 22]. Currently, researchers are dedicated to developing a closed-loop cycle for CFRP composites, with various fibre recovery methods emerging as promising solutions [21, 55]. Although reclaimed CFs cannot fully maintain their original properties and dimensions like vCFs, they can retain up to 90% of their original mechanical properties when recycled using the proper method [21, 54]. The cost savings of 30% to 40% when using rCFs compared to vCFs are also valuable [36], illustrating that rCFs present great opportunities for reuse or repurposing in other applications beyond their original use.

While previous studies have shown the potential of using rCFs in cementitious composites, research gaps remain. Specifically, further investigation is needed into the self-sensing capabilities of cement-based sensors incorporating CFRP waste. Additionally, research on the effects of temperature, humidity and corrosion on the electrical properties and piezoresistivity of these composites is still limited [56]. In this regard, this study mainly investigates the electrical and self-sensing performance of cement-based mortars with different types of CF and CFRP waste. The effects of varying dosages of fillers, curing age, humidity and temperature variation on the electrical resistivity of cementitious composites were investigated. A micro-scale investigation was also conducted based on a scanning electron microscope (SEM). The self-sensing abilities (piezoresistivity) of cementitious composites

incorporating CFRP recyclates were studied at different humidities. Additionally, to assess the impact of chloride ingress and corrosion, the specimens were retested under cyclic loading after exposure to an accelerated corrosion environment in sodium chloride solutions.

6.3.3 Materials and experimental methodologies

6.3.3.1 Raw materials

General purpose (GP) cement and dried sand, which conformed to AS3972 [57] and AS3700 [58], respectively, served as binder material and fine aggregate in the experiments. The main physical and chemical properties are shown in Table 6-5.

Table 6-5. Properties of mortar raw materials.

	Chemical Entity	Proportion (%)	Specific Gravity	Particle Size (μm)
Dried Sand	Crystalline silica (Quartz)	> 95	2.7	90% finer than 576
GP Cement	Portland clinker	< 97	3.0 - 3.2	90% finer than 42.4
	Gypsum ($CaSO_4.2H_2O$)	2 - 5		
	Limestone ($CaCO_3$)	0 - 7.5		
	Calcium oxide	0 - 1		

Three types of CF and CFRP were used as carbon-based fillers in the cementitious matrix. Virgin CF offcuts with a diameter of 8μm and a length of 6mm (VCF) were chopped from the fabric reinforcement in the laboratory (Figure 6-10 (a)). Two types of CFRP recyclates (RCF and CFRP) were chemically and mechanically recycled from the CFRP composite individually. RCF was reclaimed from 2-ply thin CFRP composites using 98% sulfuric acid recycling and reused as 6 and 10 mm-long fibres (Figure 6-10 (b)). CFRP was recycled through a two-step mechanical recycling method from the CFRP composite waste, sourced from aeroplane components (Figure 6-10 (c)). The electrical resistivity of CF typically ranges from 2 to 20 μΩ.m, while the electrical properties of CFRP composites largely depend on measurement direction, spanning from 0.022 to 310 mΩ.m [59]. Before mixing carbon-based fillers into cement paste, electrical resistance was measured for short CF bundles. The electrical resistance was 4 Ω/mm for RCF and 1.1 Ω/mm for VCF. CFRP composites were milled into a powder form. Instead of measuring the electrical resistance of the composite, they were considered as a mixture of conductive short CFs and non-conductive polymer matrix debris.

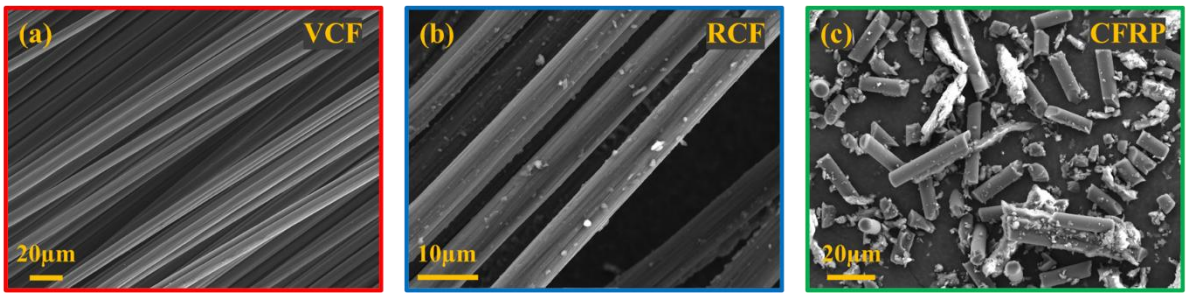

Figure 6-10. SEM images of the carbon-based fillers used in the mix.

6.3.3.2 Mix design and specimen preparation

The composite mix was formulated based on a binder-to-fine aggregate-to-water ratio of 1:1.5:0.55, consistent with the author's previous work [19]. A plain mortar without additives was prepared as a reference (REF). Each carbon-based filler was evaluated at three different dosages, covering a range from low to high concentrations. These dosage ranges were selected based on a review of the literature, where similar studies have reported optimal performance within these parameters. Specifically, VCF and RCF were added at 0.1%, 0.5% and 1.0% by volume of the mortar, while CFRP (rCFRP in Table 6-6) were used to replace cement at 1%, 5% and 10% by mass. In total, ten mortar mixes were prepared, as detailed in Table 6-6.

The mortar specimen preparation process with various fillers is as follows: First, the cement and carbon-based fillers were dry mixed at low speed for three minutes using a laboratory mortar mixer to achieve a homogeneous dry blend. Fine aggregates and water were gradually and separately added to the mix in two stages; then, the materials were mixed for an additional five minutes, starting at a low speed and then increasing to high speed, until visual inspection confirmed a uniform consistency. The mixer was then stopped for one minute, during which the mixer head was lifted, and the sides of the bowl and paddle were scraped down. The mixing cycle was recommenced for 2 minutes at low speed, after which the mixer was stopped for the final time. Immediately afterwards, a flow table test was performed to determine the consistency and flowability of the fresh mortar. The mixture was then cast into moulds for different tests: 50×50×50 mm^3 for compressive strength and 40×40×160 mm^3 for electrical resistivity and cyclic piezoresistivity measurements. The fresh paste was poured into the moulds in two layers, and then the moulds were placed on a vibration table for 30 seconds to facilitate mortar compaction and eliminate air entrapment. After 24 hours, the specimens were demolded and cured under standard laboratory conditions at 23 °C, wrapped in damp cloths, and sealed with impermeable plastic sheeting until testing.

Table 6-6. Mix proportions of cementitious composites (kg/m^3).

Mixture	Cement	Fine Aggregate	Water	Carbon-based Fillers		
				vCF	rCF	rCFRP
REF	726	1088	399.3	-	-	-
VCF-1				1.8	-	-
VCF-2				9	-	-
VCF-3				18	-	-
RCF-1				-	1.8	-
RCF-2				-	9	-
RCF-3				-	18	-
CFRP-1	718.7		395.3	-	-	7.3
CFRP-2	689.7		379.3	-	-	36.3
CFRP-3	653.4		359.4	-	-	72.6

6.3.3.3 Experimental methods

Flow table and Compressive testing

To evaluate the fresh and physical properties of cementitious composites with varying carbon-based fillers, flow table and bulk density tests were performed according to BS EN 1015-6 and 1015-3 [60, 61], respectively. Two measurements were taken for each mix. The compressive strength tests were conducted on 50×50×50 mm³ specimens after 28 days of curing, in accordance with the standard ASTM C109/C109M [62]. Three specimens per mixture were tested, and the average results were calculated. Compressive strength tests were carried out using an MTS Sintech 65/G machine equipped with a 300 kN load cell, applying a loading rate of 0.5 mm/min until failure. In addition, water absorption was determined by measuring the difference between the immersed mass and the saturated surface-dry mass of the 50×50×50 mm³ specimens, in accordance with ASTM C948-81[63].

Microstructure

The surface morphology of cementitious mortars containing carbon-based fillers was examined by an SEM (Zeiss ULTRA Plus) at an acceleration voltage of 10 kV with the SE2 detector employed. For the non-conductive cement-based samples (approximately 5-10 mm in size), a 10 nm gold coating was applied to the surface before scanning to minimise charging effects and enhance imaging quality [1].

Electrical resistivity and Piezoresistivity measurement

As shown in Figure 6-11, a four-electrode configuration was employed to measure the electrical resistivity and piezoresistivity of the 40×40×160 mm³ specimens [64]. Four stainless

steel mesh pieces (40×50 mm², with 2 mm openings) were embedded along the length of each sample, with an interval distance of 40 mm between them, during casting. To investigate the effect of various conditions on the electrical resistivity of cementitious composites, including different carbon-based fillers, the resistivity of the specimens was measured and analysed individually at different curing ages, drying conditions, and temperatures. A direct current (DC) power supply (RS-6005P) was used to apply the current through the samples, providing a maximum voltage of 60 V to accommodate the diverse resistive characteristics of the specimens. Voltage was applied to the outer electrodes, while the corresponding current was simultaneously measured by a datalogging multimeter (Model UT181A). The resistivity (ρ) was then determined by applying the measured voltage and current values to Equation 6-9, derived from Ohm's law.

$$\rho = \frac{VA}{IL} \tag{6-9}$$

where V is the voltage measured across the inner electrodes, A is the cross-sectional area of the specimen, I is the current flowing through the specimen, and L is the distance between the inner electrodes.

The piezoresistivity was assessed under cyclic loading using an MTS 810 testing machine. To examine the effects of two different humidity levels (90% and 30%) on the piezoresistive properties of the cementitious composites, the specimens were conditioned in a humidity chamber at a controlled temperature of 23°C with the required humidity for two weeks prior to testing. The tests started at higher humidity levels and then moved to lower levels. Also, to investigate the impact of corrosion on the self-sensing properties, the piezoresistivity was measured after exposure to an accelerated corrosion process with a constant impressed current (3.125 A/m²) for 6 hours, simulating 15 years of natural corrosion. The methodology simulates 15 years of corrosion by calculating the total electrical charge passed through specimens, which corresponds to the anticipated corrosion effects under aggressive environmental conditions. During the process, specimens were completely immersed in a 3.5% NaCl-simulated marine environment [65]. The maximum load of the dynamic testing was controlled at approximately 30% of the specimens' ultimate compressive strength, with a loading frequency of 0.01 Hz. A total of five cycles of loading and unloading were performed. The specimen configuration and experimental setup are illustrated in Figure 6-11. The fractional change in resistivity (FCR) is calculated using Equation 6-10, which quantifies the deviation from the initial resistivity value as a function of the applied load over time.

$$FCR = \frac{\rho_t - \rho_0}{\rho_0} \quad 6\text{-}10$$

where ρ_0 represents the initial resistivity, serving as a baseline or reference point against which changes are evaluated, and ρ_t represents the measured resistivity at a specific time t under a certain loading. FCR provides the change in resistivity as a percentage of the initial value, with a larger FCR indicating greater sensitivity to changing conditions. A digital image correlation (DIC) system was implemented to measure precise surface deformation and strain changes at a higher resolution. A Canon EOS 6D Mark II camera, equipped with an EF 24-105mm lens, was used to capture surface patterns (white speckles on a black background) at regular intervals of 3 seconds throughout the loading process [66, 67]. Strain sensitivity (gauge factor, GF) and stress sensitivity (SS) were calculated as the ratios of FCR to strain or stress, respectively.

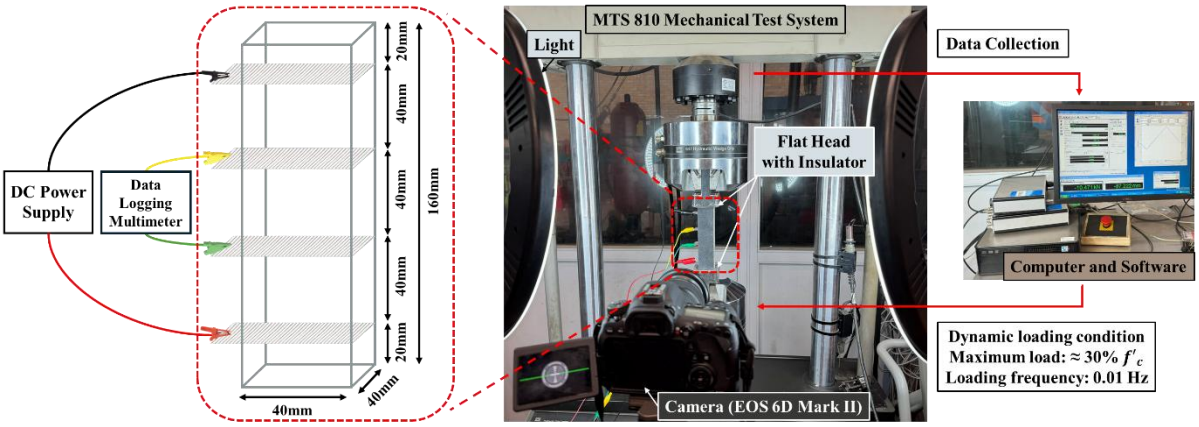

Figure 6-11. Experiment setup: cyclic piezoresistivity testing using an MTS 810 testing machine.

6.3.4 Results and discussion

6.3.4.1 Characterisation of carbon-based fillers

Carbon-based fillers were examined both physically and chemically prior to their incorporation into cementitious materials to understand their properties and differences. As shown in Figure 6-12 (a), grooves were clearly shown on the RCF surface, possibly due to the sulfuric acid etching, while resin debris remained in certain areas after recycling. In addition, a small amount of sulfate could be detected in the Energy Dispersive Spectroscopy (EDS) mapping, which came from the solvent used in the solvolysis recycling process. Figure 6-12 (b) shows the CFRP recyclates consisting of short CF and smaller resin particles. Some residual resin matrix was also observed on the surface of the CF after mechanical recycling. The size distribution of CFRP was tested with a Matersizer, as shown in Figure 6-12 (c). The peak near

8 microns represents the CF diameter, and a second peak was found around 500 microns. It was also noticed that 50% of the particle sizes were smaller than 306µm and the specific surface area was 328.5 m^2/kg.

The surface roughness detected using atomic force microscopy (AFM) indicates a sequence of surface roughness from high to low as VCF, RCF, and CFRP (Figure 6-13). The surface of VCF exhibited distinct grooves along the fibre direction caused by the wet-spinning process during manufacturing. Both RCF and CFRP showed residual epoxy after recycling, with RCF exhibiting more bumps. The recycled CFRP from the aeroplane components contains a different type of CF with a flat surface. Figure 6-13 (c) only scanned a random CF surface from CFRP recyclates. However, there is CFRP epoxy debris with irregular shapes that cannot be fully captured by AFM.

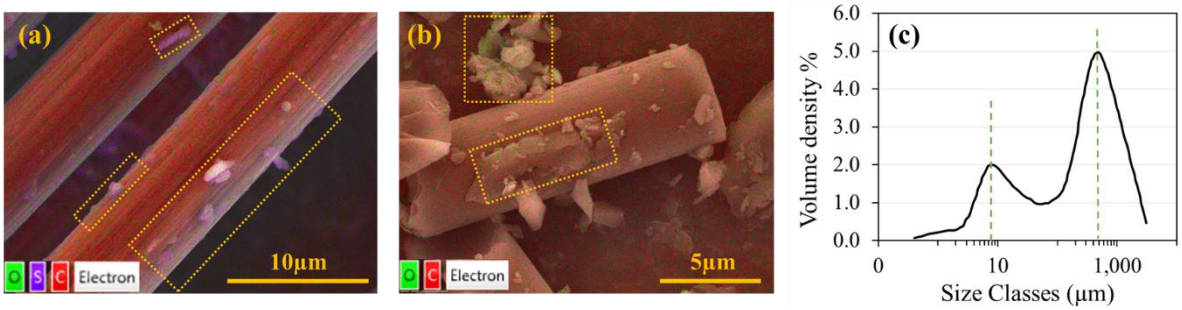

Figure 6-12. SEM-EDS mapping of (a) RCF and (b) CFRP; (c) The particle size distribution curve of CFRP.

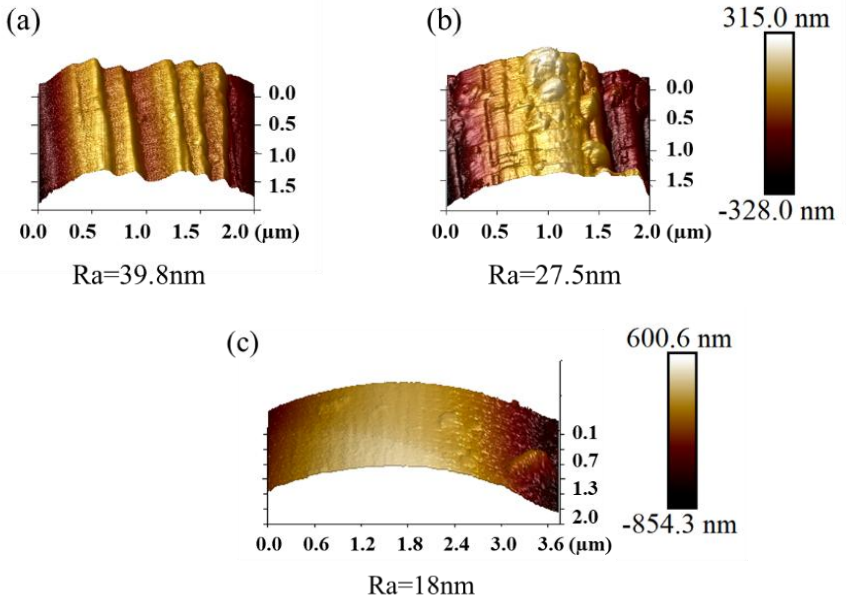

Figure 6-13. AFM surface profile of CFs: (a) VCF; (b) RCF; (c) CFRP.

X-ray Photoelectron Spectroscopy (XPS) analysis was performed on both VCF and RCF with a spot size of 400µm. The primary elements detected on the surface of VCF were carbon

(66%), oxygen (20%), and silica (14%). Carbon was the dominant element on the surface of both virgin and recycled CF. In contrast, RCF showed the addition of sulfate (7%) and nitrogen (3%), as well as an increased oxygen content (30%) on its surface with a higher oxygen-to-carbon ratio. This reflected the impact of the chemical recycling process, which introduced more oxygen-containing functional groups to the surface of CF (Figure 6-14 (d)). The amount of C=O/C-O functional groups rose to 24% in RCFRCF, compared to only 17% on the surface of VCF. The C1s high-resolution XPS spectra also revealed a notable chemical shift in the functional groups between VCF and RCF.

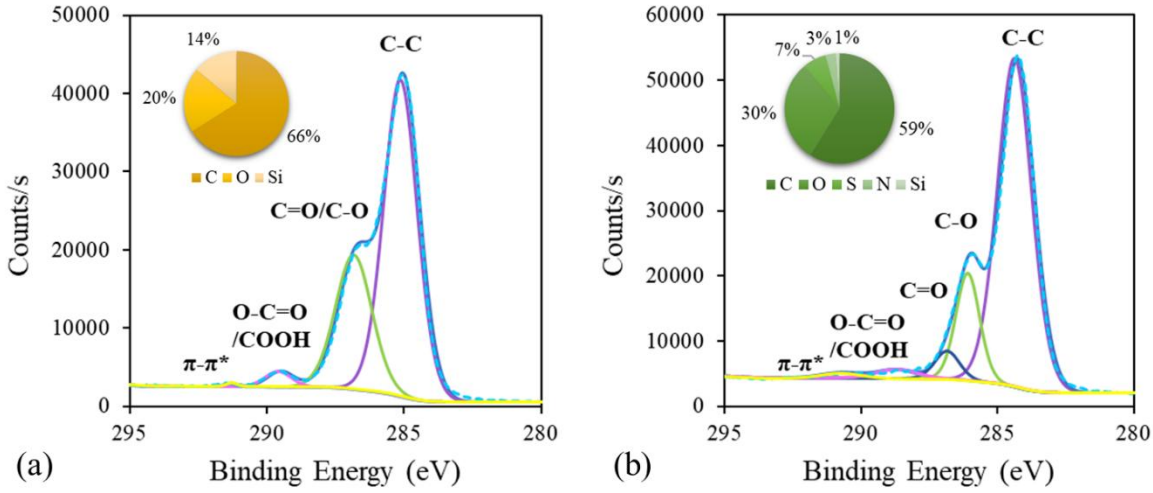

Figure 6-14. CF surface chemistry using XPS Survey and C1s high-resolution XPS spectra of (a) VCF and (b) RCF.

6.3.4.2 Flowability, compressive strength and water absorption

Figure 6- 15 (a) illustrates the change of fresh properties with the inclusion of different carbon-based fillers and their comparison with the REF mortar. The incorporation of CFs notably reduced the flowability and density of the fresh cementitious composites as CF's content increased. The flow values decreased to as low as 156 mm for the VCF group, which was mainly due to the fibre conglomeration and air entrapment. This was also affirmed by the visual observation Figure 6- 15 (b). The surface of REF mortar appeared smooth and flowable, while the VCF-1 and VCF-3 gradually showed a rougher surface with visible entangled fibres. In comparison, the RCF group exhibited slightly improved flowability than the VCF group. This could be due to the smoother surface, as demonstrated by the AFM detection (Figure 6-13). The rCF surface treatment with sulfuric acid not only removed the epoxy resin from CFRP but also enhanced the hydrophilic polarity and wettability of the CF surface. Similar claims have been made by other researchers [36, 68, 69]. The flowability of all CFRP specimens was

comparable to that of the REF mortar, with a slight improvement. Milled CFRP particles filled the voids between larger particles, improving the particle packing density and reducing the inter-particle friction, particularly with the smaller particles with smooth surfaces. Compared to the REF, the partial replacement of cement with CFRP particles reduced the fresh density as the content increased. CFRP recyclates consisted of both CF and polymer matrix, which had a lower specific gravity compared to cement.

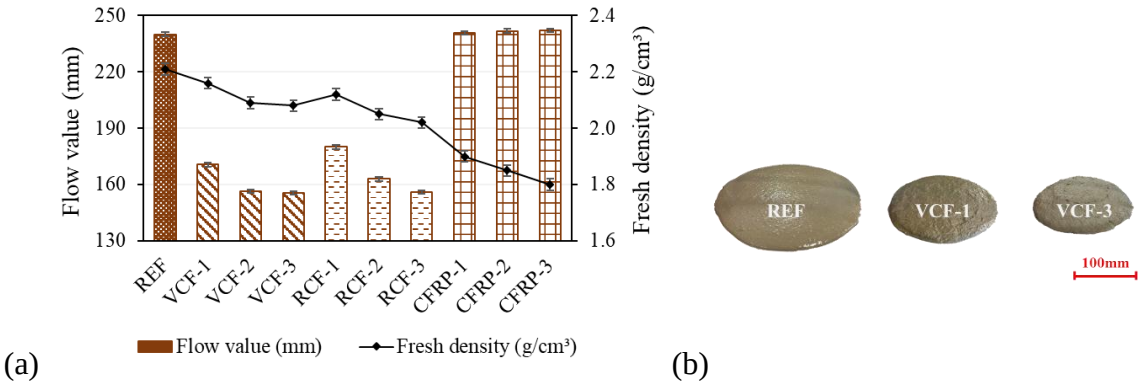

Figure 6- 15. (a) Effect of carbon-based fillers on flowability and fresh density of cementitious composites; (b) Photos of flow table testing of fresh pastes.

Figure 6-16 shows the change in water absorption and compressive strength at 28 days with the inclusion of different carbon-based fillers, compared to the REF. Water absorption, which indicates the composite's capacity to uptake water through its porosity, demonstrated an inverse relationship with compressive strength in both VCF and RCF. Porosity is a critical factor as it greatly influences mechanical properties, with voids acting as potential crack initiation sites that reduce mortar strength [11]. VCF-3 showed higher compressive strength, demonstrating a 15% increase compared to the REF. Similarly, RCF-1 also displayed improved compressive strength with an 11% increase compared to the REF. While the inclusion of CFs increased porosity by creating an extra Interfacial Transition Zone (ITZ) within the matrix, fibre reinforcement helped prevent microcrack formation through chemical reactions or mechanical interlocking between the CF surface and the cementitious matrix. Based on the surface characterisation of CF, vCF exhibited high roughness due to sizing and distinct grooves on its surface, which facilitated better mechanical interlocking within the matrix. In contrast, rCF showed a smoother surface after sulfuric acid treatment, which also introduced more oxygen-containing functional groups, potentially enhancing the interfacial bonding between rCF and the matrix (see Figure 6-13 and Figure 6-14). An increase in water absorption was also observed with higher dosages of rCF (RCF-2 and RCF-3), accompanied by a decrease in compressive strength. This might be due to the longer length of rCF compared to vCF, as the curvature and

fluffy nature of rCF after recycling make size control difficult. Additionally, the strength of rCF might be diminished after chemical treatment, as surface damage can occur.

In the CFRP group, the compressive strength of CFRP-1 specimens at 28 days exhibited the highest value, with a 67% increase compared to the REF. CFRP recyclates primarily contributed to the filling effect, where fine particles filled voids between larger ones, reducing pore volume in the matrix [19, 70]. Smaller CFRP particles enhanced packing and particle distribution, creating nucleation sites for hydration products. Additionally, the reinforcing effect of microfibres in the matrix further contributed to the overall improvement in compressive strength. However, substituting larger quantities of cement with rCFRP negatively affected the hydration process, decreasing compressive strength.

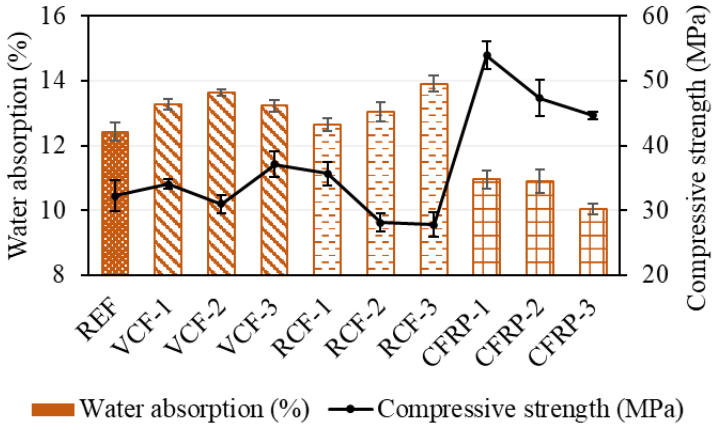

Figure 6-16. Effect of carbon-based fillers on compressive strength and water absorption of cementitious composites.

6.3.4.3 Microstructure

CF can reinforce the cementitious matrix by bridging microcracks, thereby slowing down and arresting crack growth. When microcracks develop, the embedded CFs act as barriers, distributing tensile stress throughout the matrix. This mechanism prevents cracks from widening or propagating further, which could finally lead to failure. Compared to the dominant microcrack in the REF plain mortar (see Figure 6-17 (a)), smaller microcracks were distributed over a larger area within the matrix, interacting with the CFs, as indicated by the yellow dashed lines in Figure 6-17 (b) and (c). This stress transfer was facilitated by the bond between the CFs and the cementitious matrix, allowing the CFs to take over the load that the cracked matrix can no longer bear. As a result, CFs not only delay the initiation of cracks but also enhance the strength and ductility of the cementitious composites by preventing the development of larger, critical cracks. The failure mechanisms observed include fibre pullout and fibre breakage as

shown in Figure 6-17 (c) and (f), in both the cementitious composites containing rCFs and CFRP recyclates. Figure 6-17 (d) shows the hydration products on the rCF surface, indicating a chemical reaction between the rCF surface and the surrounding cementitious matrix. This enhanced the interfacial bonding between CF and matrix, improving the load transfer mechanism at the fibre-matrix interface. Consequently, this strengthened interaction led to the better mechanical performance of the resulting composites. In contrast, the clustering of fibres was also observed in the matrix (Figure 6-17 (e)) due to the non-uniform distribution of CFs. Fibre clustering could cause adverse effects, such as trapping air and preventing proper packing of particles around the CFs, leading to the formation of porosity. This clustering also hindered stress transfer and weakened the bond between the CFs and the matrix, reducing the cementitious composite's ability to arrest cracks and resulting in inconsistent mechanical properties.

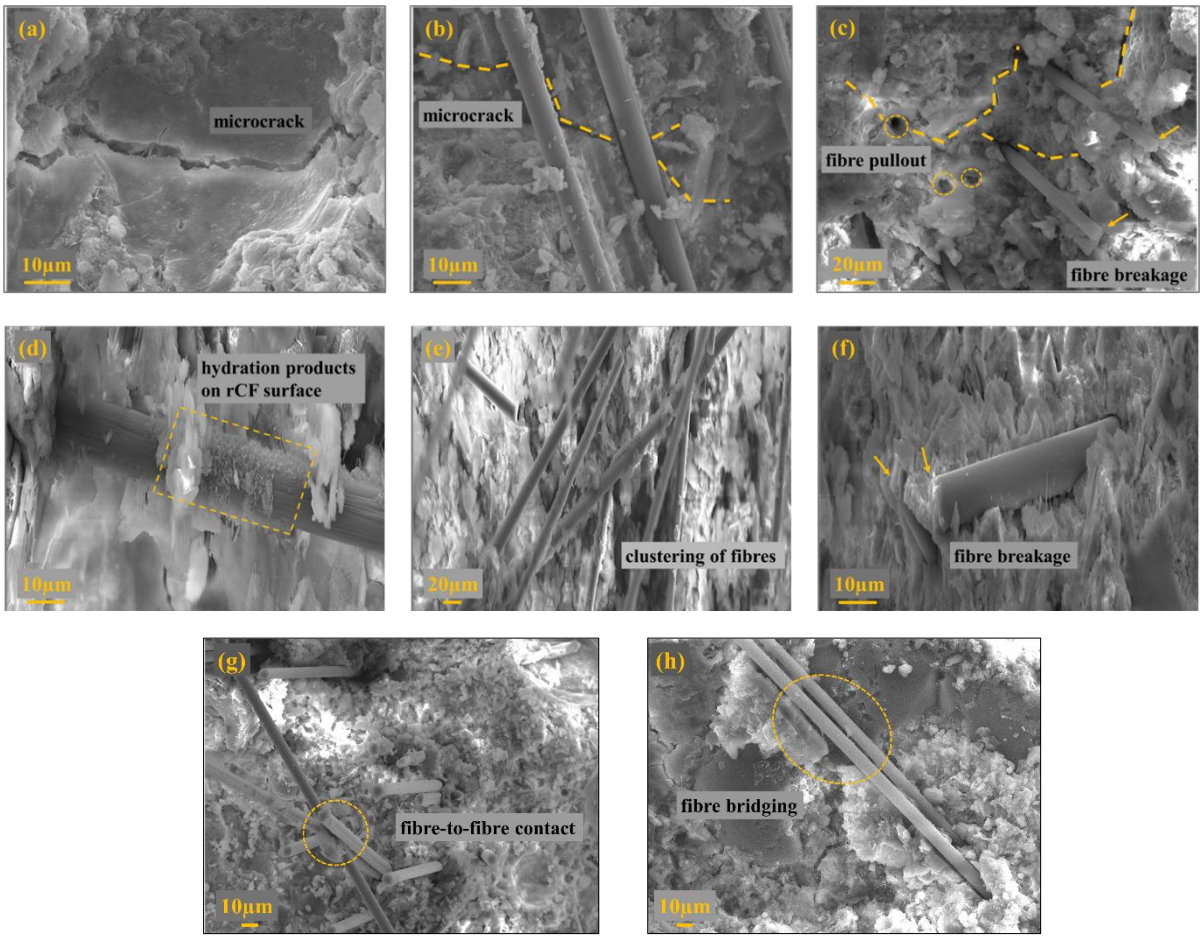

Figure 6-17. SEM microscopic images of the cementitious matrix: (a) REF; (b) and (c) VCF; (d) and (e) RCF; and (f) CFRP; (g) and (h) CF conductive network including fibre-to-fibre contacts and fibre bridging within the matrix.

6.3.4.4 Effect of curing age, drying condition and temperature on electrical resistivity

As shown in Figure 6-18, incorporating both virgin and recycled fibres reduced the resistivity of cementitious composites (VCF and RCF groups). These highly conductive carbon-based fibrous fillers could form conductive networks within the matrix, resulting in a significant decline in resistance. The SEM images showed evidence of CFs contacting each other, thereby forming a conductive pathway (Figure 6-17 (g)). Proper entanglement of fibres at junction points could enhance the conductivity. Additionally, CFs within the cementitious matrix could span across cracks or voids, not only providing reinforcement but also bridging matrix discontinuities (voids and microcracks) to form new conductive pathways (Figure 6-17 (h)). Lower resistivity was observed, particularly at higher CF dosages of 0.5 vol.% and 1.0 vol.%. Doubling the dosage at this stage resulted in only a slight improvement in resistivity (See VCF-2 and VCF-3; RCF-2 and RCF-3), indicating that a sufficient network had already formed. At low CF concentrations of 0.1 vol.%, CFs are widely spaced, preventing electrons from crossing the potential barriers between them. Thus, CFs had limited functions in reducing the resistivity of the cementitious composite by lapping with each other. In contrast, the CFRP group exhibited a slightly higher electrical resistivity than the REF. rCFRP particles contained in this mixture could denser the microstructure and reduce the total porosity, which reduced the impact of free water. Due to mechanical recycling, the micro-CFs had lower aspect ratios and were incorporated with non-conductive polymer particles in the mixture, making it challenging to decrease the overall resistivity.

Figure 6-18 (a) displays the changes in electrical resistivity affected by the curing ages. At the early stage of 7 days, the pore network was saturated with free water, facilitating ionic conduction and resulting in relatively low electrical resistivity. As hydration progresses and water content decreases, the formation of a denser microstructure within the mixture reduces matrix porosity, thereby increasing resistivity. Electrical resistivity gradually increased from 7 to 14 days, and the highest resistivity was observed in all specimens at a curing age of 28 days. The electrical resistivity of REF was about 55,000 Ω.mm. The effect of humidity on the electrical resistivity of cementitious composites was also investigated, as shown in Figure 6-18 (b). During the drying process from 90% to 30% humidity, the electrical resistivity of specimens REF, VCF-1, RCF-1, and the CFRP group increased remarkably, whereas specimens with higher amounts of CFs (VCF-2, VCF-3, RCF-2 and RCF-3) either decreased or stayed nearly unchanged. The former specimens relied more on the impact of ionic conduction, with moisture

and free water acting as carriers for ionic diffusion. Consequently, the loss of moisture led to a significant increase in resistivity. In contrast, electrical conductivity was predominantly governed by CF contact conductivity for the latter specimens. Due to less moisture, the hydro-ion conduction gradually weakened and transitioned to tunnel-effect conduction, facilitated by the CFs bridging the material. Therefore, it was less impacted by the drying conditions.

Surface properties of rCF could also impact the electronic conduction of CFs. The decreased degree of graphitisation of the CF surface worsened the conductivity of the cementitious composite, while increased roughness could improve the conductivity [36]. The rCF exhibited a lower degree of graphitisation than the vCF, indicating increased surface imperfections. Therefore, incorporating rCFs resulted in higher resistivity. Figure 6-18 (a) and (b) clearly show that RCF-3, with a higher dosage of 1.0 vol.% rCF, exhibited greater resistivity compared to the specimen containing VCF-3. The lower surface roughness of rCF compared to vCF (as shown in Figure 6-13) further supports the observation that reduced surface roughness can enhance resistivity.

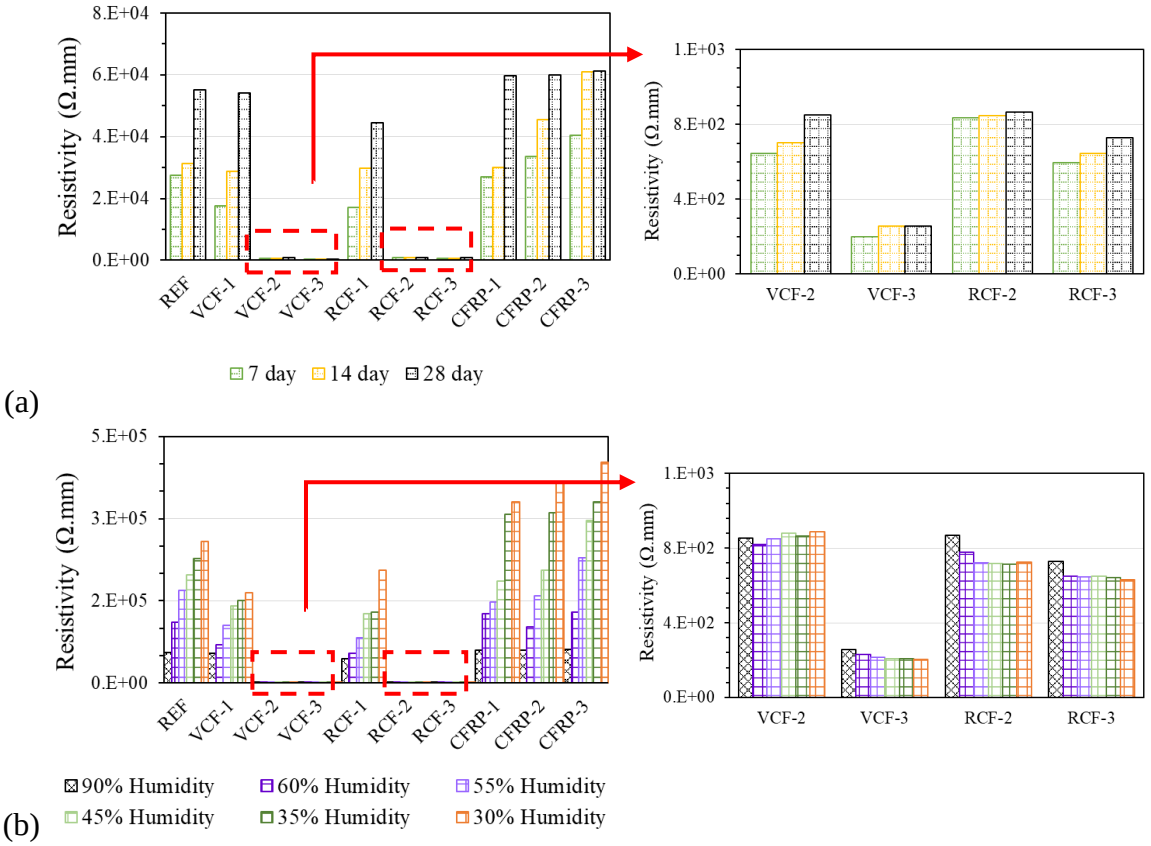

Figure 6-18. The effect of (a) curing age and (b) humidity on the electrical resistivity of cementitious composites containing different carbon-based fillers.

The electrical resistivity of the cementitious composite was influenced by temperature variations, which caused expansion and shrinkage of the fibre-matrix interface and conductive network within the specimens, as well as affecting electron movement and ion mobility through the material. Five specimens (REF, VCF-1, VCF-3, RCF-1, CFRP-3) were selected in this experiment, altering their temperature from 22°C to 50°C, and simultaneously measuring their FCR. Figure 6-19 illustrates the variation in electrical resistivity in response to temperature changes. The moisture level remained constant during the temperature variation experiment, as changes in moisture may also affect FCR variations. The specimens were maintained at the same temperature for 15 to 20 minutes to ensure uniform temperature distribution throughout the specimens. The behaviours of four specimens were consistent, with FCR decreasing as temperature increased. This trend indicated a clear temperature dependency in these cementitious composites. At higher temperatures, the thermal energy of electrons and the kinetic energy of ions increase, thereby improving the overall conductivity. Notably, CFRP-3 containing 10 wt.% CFRP replacement exhibited the highest temperature dependency among the five specimens. However, RCF-1 containing 0.1 vol.% rCF exhibited a different behaviour, where FCR remained stable with a slight increase. While the rCF enhanced resistivity stability, which is beneficial for the consistency and reliability of the cementitious material's self-sensing capabilities, the underlying mechanisms behind this effect could be attributed to various factors, including rCF surface modifications, fibre-matrix interfacial properties and conduction mechanisms. This phenomenon suggests that the rCF-incorporated specimens exhibited less dependence on thermal energy for charge carrier mobility. rCF might be degraded due to the sulfuric recycling process, which involves physical etching, a decreased degree of graphitisation, and surface chemical changes, consequently affecting the electrical properties. The rCF might enhance interaction with the cementitious matrix due to the oxygen-containing functional groups present on the surface, thus improving the bonding strength and potentially decreasing the resistivity of the fibre-matrix interface. However, the results suggest that there might be fewer direct fibre-to-fibre contacts in RCF-1, causing a loss of the primary conductive pathways present in the other specimens.

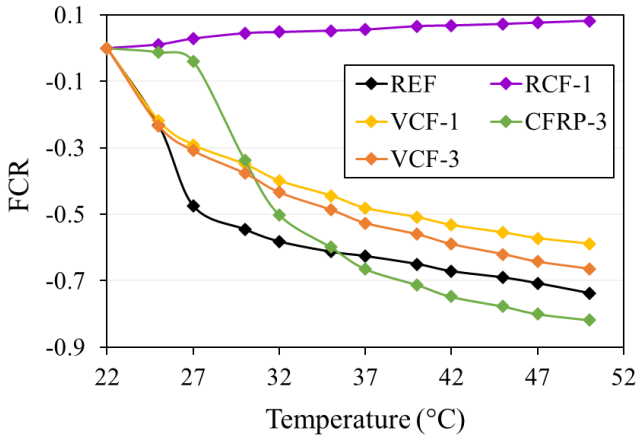

Figure 6-19. Effect of temperature variation on FCR.

6.3.4.5 Piezoresistive response with humidity levels

Based on our preliminary trial test, four mixes (REF, VCF-3, RCF-2, and CFRP-3) were selected for continuous piezoresistivity/self-sensing testing under different humidity and corrosion conditions [71]. For simplification, they were also labelled as REF, VCF, RCF, and CFRP to represent each type. Figure 6-20 displays the piezoresistive performance of these specimens at two different humidity levels, each subjected to five loading and unloading cycles. The left axis represents the cyclic stress, which is approximately 30% of the ultimate strength, indicating it is within the elastic range. The right axis shows the FCR%, representing the measured resistivity compared to the initial resistivity in percentage.

In each mix, the transmission of both ions and electrons can induce piezoresistive changes in plain mortar and those with carbon-based fillers. During each loading cycle, electrical resistivity decreases as the load increases and behaves oppositely during unloading. It is also known that plain cement paste is inherently self-sensing without the addition of conductive fillers [46]. The interconnected pores contain ionic liquid, which facilitates ionic conduction within the cementitious matrix. Besides the major ionic conduction, electrical conduction also takes place through the gel, gel-water, and unreacted cement particles. As shown in Figure 6-20 (a), the cyclic loading altered the microstructure of plain mortar. During loading, the micro voids in the matrix were compressed, narrowing the ionic pathways and reducing the air gaps, which enhanced ion transport and improved electrical conductivity. The opposite behaviour occurs during unloading. The resistivity change of REF was less sensitive at lower humidity (30%) compared to the higher humidity environment (90%). As the plain mortar without conductive fillers largely depended on ionic conduction, the lack of moisture significantly limited its self-sensing ability. Apart from this general pattern, some fluctuations were also observed during maximum compression and zero load, as circled in yellow. It is also possible

that initial bond microcracks formed at the interface between the fibre and matrix, or between the aggregate and matrix, under maximum compressive force, potentially disrupting existing conductive pathways [72]. This disruption hinders the flow of ions, leading to an increase in resistivity [73]. Shoulder peaks were observed during the unloading process, indicating a reduction in resistivity. This phenomenon suggests a competition between network breakdown and reconstruction within the conductive network during deformation, which is related to the material's viscoelasticity [74]. Similar behaviour was also observed in the other four cementitious composite specimens.

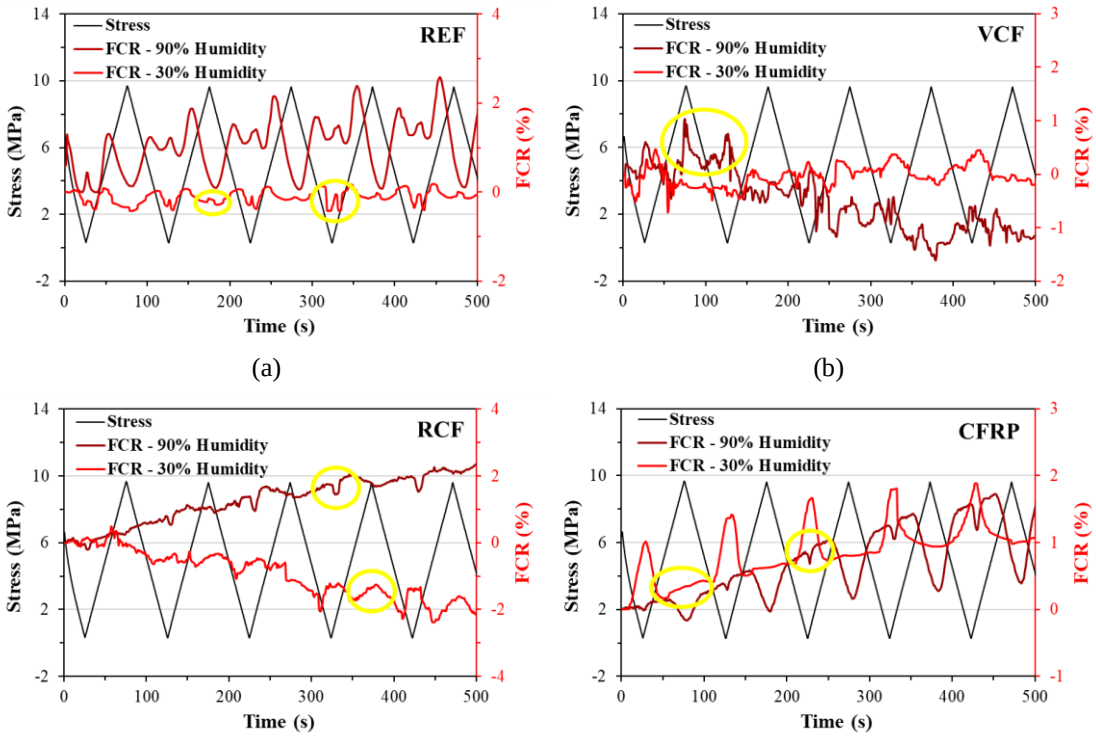

Figure 6-20. Piezoresistive behaviour of plain mortar and cementitious composites with varying fillers under 90% and 30% humidity conditions.

Due to the electronic nature of conduction in CFs, changes in the electrical resistivity of these cementitious composites containing conductive carbon-based fillers were primarily attributed to variations in electronic conduction [75]. These changes were related to the contact interface between CF and the cementitious matrix, as well as the spatial proximity between the CFs. When the specimen was subjected to a compression load, the distance between adjacent fibres decreased, thus reducing the resistivity. Conversely, the slight pullout of crack-bridging fibres during crack opening led to an increase in contact electrical resistivity at the fibre-matrix interface [76]. VCF and RCF displayed certain piezoresistive properties, but their electrical resistivity response to the cyclic load was not stable (Figure 6-20 (b) & (c)). Although the FCR

under 30% humidity exhibited some repetitiveness compared to the 90% humidity condition, the impact of free water ions on the microstructure was evident. These ions interfered with electronic conduction across the CF and matrix interface during the dynamic process. As previously reported by the authors [11], fibre-reinforced cementitious composites exhibited higher porosity compared to plain mortar. This can be attributed to the presence of additional interfacial transition zones between the fibre and matrix, as well as the increased occurrence of air entrainment during the mixing process. Higher porosity and small void channels along the fibre direction within the matrix created more opportunities for water ions to penetrate. In addition, it also allows for nearby pore solutions to come into contact and separate, leading to more frequent and noticeable changes in conductivity [77]. The fluctuations in resistivity over time when a DC current is applied can also be attributed to the polarisation effect in pore solutions, where ions move within the electric field until the electrical potential balance is achieved [77, 78]. Higher porosity in fibre-reinforced cementitious composites generally amplifies these effects. In addition, as circled in yellow, when the maximum compressive stress was reached, the buckling (reduction in straightness) of CFs resulted in an irreversible increase in resistivity [79].

In contrast, CFRP containing CFRP composite powder exhibited a stable electrical resistivity response under dynamic cyclic loading (Figure 6-20 (d)). The sensitivity of this type of cementitious composite strongly relied on a stable conductive network formed by mechanically recycled short CFs instead of ionic conductive pathways, making it much less sensitive to ionic interference. This characteristic is unique and beneficial to the self-sensing ability, enhancing the reliability of the structure's monitoring system. Environmental factors such as relative humidity can affect the concrete or cementitious composite structure, which impacts ionic conduction within the interconnected pores. For self-sensing materials, conductivity should be stable and insensitive to the change of internal pore solution to reduce any interference and enhance their ability to detect changes in stress and strain.

Among the four specimens, it is evident that the plain mortar and the cementitious composite containing CFRP recyclates exhibited a more stable and consistent resistivity change in response to cyclic stress under both high and low humidity conditions, as shown in Figure 6-20. To compare REF and CFRP and quantify their stress and strain sensing capacities, the average gauge factor (GF) and stress sensitivity (SS) were calculated using the middle four completed loading-unloading cycles, excluding any uncertain behaviour at the start and end of the test. The strain was measured from the central surface area using DIC detection, which

provides a more precise measurement of length changes compared to the crosshead movement of the loading machine. Figure 6-21 shows the FCR per stress and strain at 90% humidity. REF exhibited both higher stress sensitivity of 0.4%/MPa and a gauge factor of 12.75 compared to CFRP (average SS = 0.29%/MPa and GF = 9.20). After drying, as shown in Figure 6-22, REF's stress and strain sensitivities significantly decreased, while the piezoresistive response of the CFRP specimen strengthened. Previous research has demonstrated that incorporating different carbon-based conductive fillers into cementitious composites could lead to distinct piezoresistive behaviours. For instance, the cement pastes incorporating graphene oxide could have a maximum SS of 0.31%/MPa and a GF of 21.86 [80]. The addition of carbon black particles also showed promise for the sensing purposes of cement-based composites, with an SS of 0.29%/MPa and GF of 30 [81]. In some cases, the highest piezoresistive parameters, with a GF of 1415 and an SS of 0.68%/MPa, were reported in a combination mix containing 4 wt.% gasification char and 0.2 vol.% rCF [12]. The review study by Chung [82] stated that in the dry state, the GF of cement-based materials containing CFs ranges from 265 to 285. In this study, the cementitious composite containing CFRP recyclates demonstrated comparable self-sensing ability for both strain and stress, particularly in a low humidity environment (an average SS of 0.42%/MPa and an average GF of 17.50). Peak values reached 5.69%/MPa for SS and 395.80 for GF. It also exhibited repeatability and high accuracy, with a higher coefficient of determination, as shown in Figure 6-22 (b) and (d).

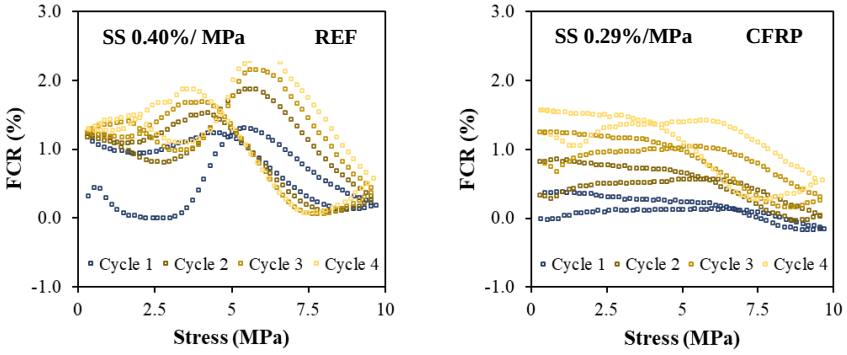

(a) (b)

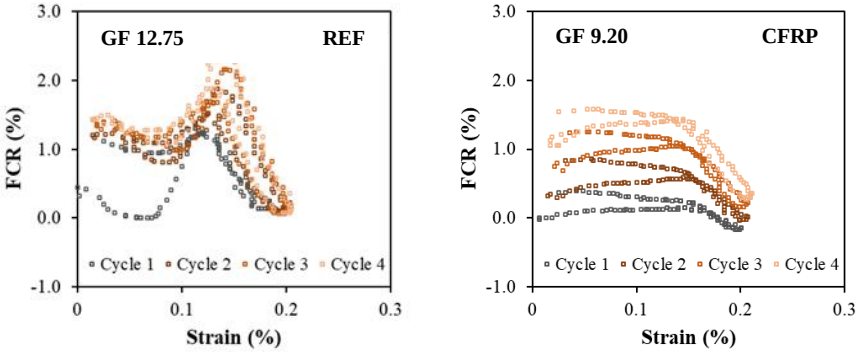

(c) (d)

Figure 6-21. Stress sensitivity and gauge factor of REF and CFRP under 90% humidity.

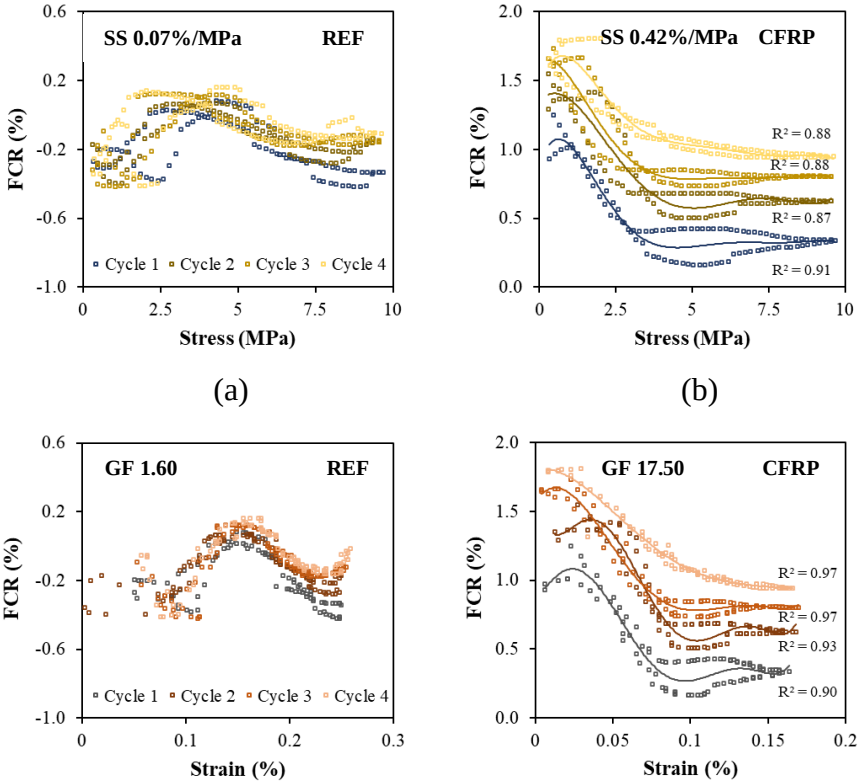

(a) (b)

(c) (d)

Figure 6-22. Stress sensitivity and gauge factor of REF and CFRP under 30% humidity.

6.3.4.6 Piezoresistive response after corrosion

To evaluate the impact of chloride ingress and corrosion on the piezoresistive performance of these composites, the same specimens were subjected to an accelerated corrosion process. Their resistivity change response to loading was then investigated after simulating 15 years of corrosion in a marine environment. Corrosion significantly alters the microstructure of steel-embedded cementitious composites, both chemically and physically. As illustrated in Figure 6-23, immersion of specimens in NaCl solution can lead to a reduction in calcium hydroxide ($Ca(OH)_2$) content. Once the $Ca(OH)_2$ is depleted, portlandite leaching

occurs, causing decalcification of the calcium silicate hydrate (CSH) gel [83, 84]. Moreover, NaCl and soluble $CaCl_2$ can react with tricalcium aluminate (C_3A) in the cement paste to form chloroaluminate crystals. These crystalline formations may induce micro-cracks, potentially reducing the material's mechanical strength [85, 86]. On the other hand, if chloride ions penetrate and reach the steel mesh, they disrupt the passive oxide layer, initiating corrosion and rust formation. The resulting rust expands, which can further cause internal pressure and cracks in the cementitious matrix. Corrosion products observed in Figure 6-23 were initiated from the embedded steel mesh and progressively expanded onto the specimen surface, further assisting the understanding of the actual corrosion status. Due to the higher pore volume, the void channels in VCF and RCF provided more pathways and opportunities for aggressive ions and moisture to reach the steel mesh. The inclusion of CFs also reduced electron transfer resistance by forming a conductive network. Besides, the galvanic coupling between CFs and steel may have accelerated corrosion. In comparison, CFRP with a denser microstructure demonstrated long-term corrosion resistance with stable performance, followed by REF.

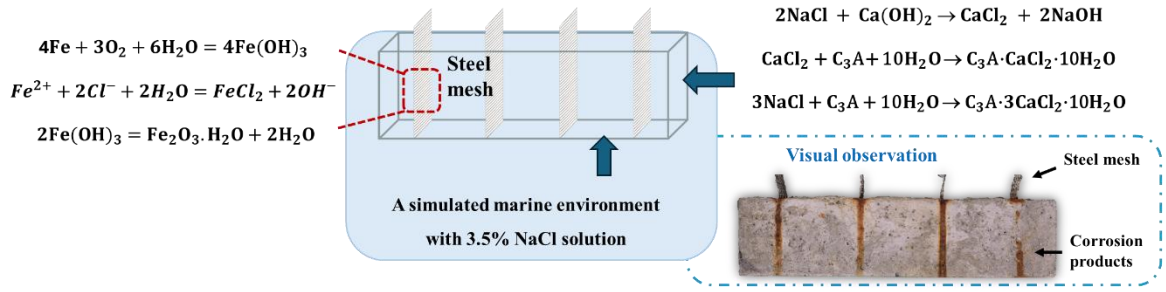

Figure 6-23. Corrosion process of steel embedded in cementitious composite immersed in NaCl solution.

The piezoresistive behaviour of plain mortar and cementitious composites after corrosion is shown in Figure 6-24. To prevent specimen failure during dynamic testing, the maximum load was limited to 20% of the ultimate compressive strength of the uncorroded specimens. This precaution was taken to account for potential decreases in strength due to corrosion impacts. After immersion in the 3.5% NaCl solution and the application of a constant imposed current for acceleration, the penetrated water and NaCl significantly enhanced ionic conduction. In the plain mortar, ionic conductivity was the primary electrical conduction mechanism, which contributed to its inherent piezoresistive response, as shown in Figure 6-24 (a). The VCF specimen exhibited a clear resistivity change in response to load variations, with a higher FCR amplitude observed, due to the introduction of more free ions. On the other hand, the presence of solution at the fibre-matrix interface potentially reduced the effective contact area between

fibres and the cementitious matrix. These solution-filled regions might not contribute to the overall piezoresistive behaviour of the cementitious composite. After corrosion, more cracks might occur in the matrix simultaneously. Thus, the piezoresistive performance of VCF was noticeable but not stable after immersion in the NaCl solution (Figure 6-24 (b)). As discussed in the sections above, acid recycling might adversely impact the rCF's surface and electrical properties. Additionally, fewer primary CF-to-CF conductive pathways might be present. Consequently, the piezoresistive behaviour of RCF after corrosion was worse than that of VCF (Figure 6-24 (c)). As expected, the specimen containing CFRP recyclates exhibited consistent and reproducible piezoresistive performance, primarily due to conductive pathways formed by CFs and its denser microstructure, although the maximum FCR value was reduced (Figure 6-24 (d)). The higher volume of micro-CFs contributed to maintaining a more stable electrical network, free from ion interruptions, and effectively bridging cracks.

The cement-based sensor incorporated with conductive fillers can be considered as a mixed conductor with both electronic and ionic conductivity [82, 87]. The primary tunnelling effect enables self-sensing in piezoresistive cement-based sensors [88]. Mechanical strain changes the distance between conductive phases, directly affecting tunnelling conductivity. Under uniaxial compressive loading, the conductive fillers in the cement-based composite move closer together. This proximity facilitates electrical current flow, thereby reducing the material's resistivity [87]. Slight fibre pullout may also contribute to the rise in resistivity due to increased interfacial resistance [82]. Nevertheless, piezoresistivity can be affected by various factors, such as the types of matrix and fillers, their interactions, and environmental conditions. In this work, the piezoresistivity of cementitious composites incorporating rCF and rCFRP under different humidity and chloride-induced corrosion environments was explored. The higher porosity in the cementitious composites introduces void channels that allow more water ions to migrate and interfere with electronic conduction at the fibre-matrix interface, especially in high humidity environments. It was also reported that moisture significantly degrades strain sensing performance and affects the repeatability and stability of piezoresistivity [82]. This is attributed to the polarisation effects related to ion movement, which result in fluctuations in resistivity. Additionally, chloride-induced corrosion introduces mechanisms that influence piezoresistivity, including microstructural changes and steel corrosion impacts. Although the introduction of free ions enhances the magnitude of the resistivity change, the chlorides reacting with hydration products lead to the degradation of the cement matrix, where microcracks can disrupt conductive pathways. Overall, the cementitious composite with CFRP recyclates and a

denser microstructure showed more stable electronically conductive networks with minimised effects from ionic interference.

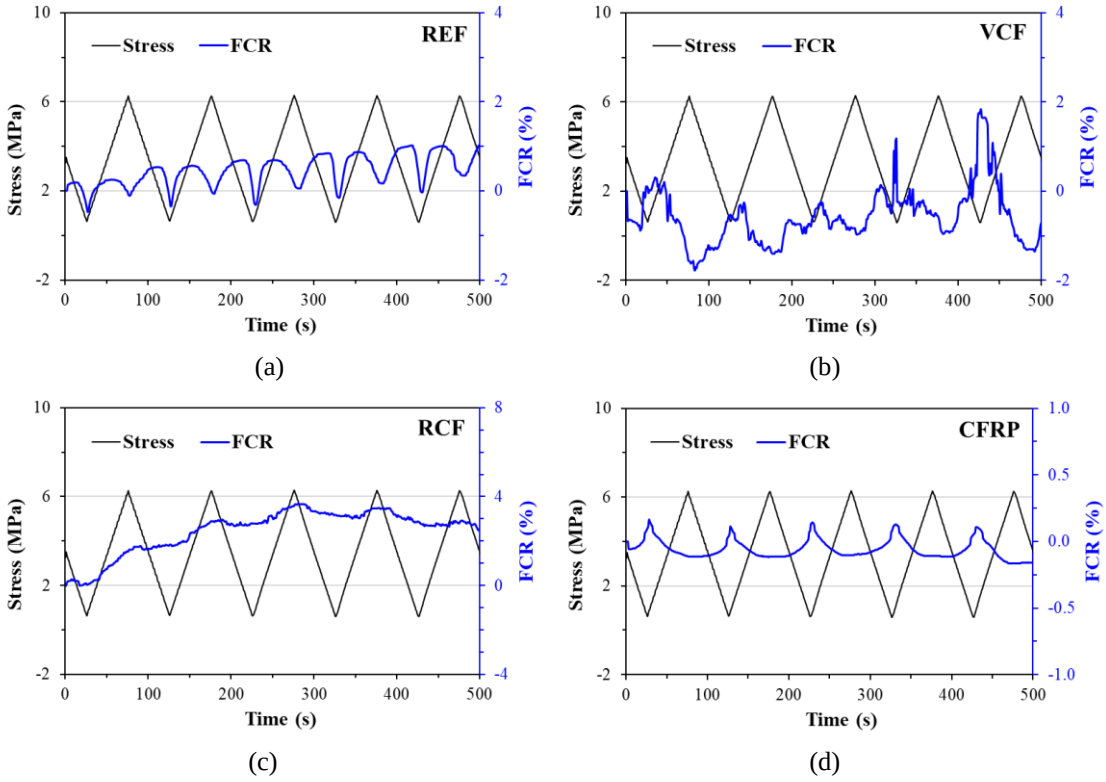

Figure 6-24. Piezoresistive behaviour of plain mortar and cementitious composites with carbon-based fillers after corrosion (under 90% humidity).

6.3.5 Summary of key findings from Section 6.3

This study experimentally investigated the electrical properties and piezoresistivity of cementitious composites incorporating rCF and rCFRP by examining parameters including filler dosages, curing age, temperature, humidity, and chloride-induced corrosion environment. The surface morphology, roughness, and chemical composition of these carbon-based recyclates were characterised using microstructural analysis techniques prior to incorporation. Meanwhile, the fresh properties, compressive strength, and water absorption of the resulting composites were evaluated to better understand the material properties. Based on the experimental results and microstructural evidence, the main conclusions and findings are summarised as follows:

- Both the flow table measurements and virtual observation indicated that the addition of CFs to the cementitious matrix caused fibre conglomeration and air entrapment, leading to void formation. This was further evidenced by the higher percentage of water absorption compared to plain mortar. While CF-incorporated cementitious composites reduced electrical resistivity and exhibited certain piezoresistive properties, their

electrical resistivity response to cyclic loading remained unstable. Ion interference with electronic conduction at the fibre-matrix interface, combined with higher porosity in these composites, contributed to the observed instability in resistivity under dynamic conditions.

- In comparison, incorporating rCFRP further improved flowability and reduced water absorption through optimised particle packing density and minimised inter-particle friction. Although this slightly increased the electrical resistivity of cementitious composite, rCFRP-incorporated cementitious composites demonstrated consistent and repeatable piezoresistive behaviour in both high and low-humidity environments. Notably, they achieved an average stress sensitivity of 0.42%/MPa and a gauge factor of 17.50, with peak values of 5.69%/MPa (SS) and 395.80 (GF) under a 30% humidity condition.
- Cementitious composites with a higher dosage of CFs (0.5 vol.% and 1.0 vol.%) showed less sensitivity to humidity changes, as their conductivity was primarily governed by CF contact networks. In terms of temperature effects, cementitious composites with rCFRP exhibited the highest temperature dependency, whereas those with rCF remained stable, showing only a slight resistivity increase.
- Although the maximum FCR of the rCFRP-incorporated specimen decreased after chloride-induced corrosion, its behaviour remained stable due to a well-distributed conductive network and dense microstructure. This minimised interference from chemicals and pore solutions, enhancing the material's ability to detect changes in stress and strain through electronic conduction.

This utilisation of CFRP waste into cementitious materials without further treatment highlights their potential as innovative cement-based sensors. The effectiveness of their self-sensing ability under various conditions, even in aggressive environments, was confirmed. In addition, recycling CF or CFRP waste into cementitious composites also provided promising mechanical properties. This approach offers a sustainable and efficient solution for SHM in the construction industry.

6.4 CONCLUSION

This chapter demonstrated the feasibility of repurposing CFRP and CF recyclates to enhance the self-sensing capabilities of cement-based sensors for SHM under varying environmental conditions, including chloride-induced corrosion. Both CFRP and CF recyclates enhanced electrical conductivity of CCs, forming conductive networks that facilitated strain and stress sensing. The experimental findings showed that CFRP recyclates allowed for a stable and responsive self-sensing mechanism. Furthermore, electrochemical analyses confirmed the long-term stability of rCFRP incorporated CCs in aggressive marine conditions. While CF offcuts enhanced conductivity, their higher porosity led to increased corrosion susceptibility. Chemically rCFs exhibited slightly better corrosion resistance than vCFs. Detailed key findings have been summarised in sections 6.2.6 and 6.3.5. This study underscores the potential of CFRP recyclates as a sustainable solution for developing durable and cement-based sensors. This incorporation offers a cost-effective and environmentally friendly approach to SHM even in diverse environment conditions.

6.5 REFERENCES

[1] H. Fatemi, S.A. Hadigheh, Y. Tao, G. Adam, Development of a novel and specialised cementitious matrix overlay for anode embedment in impressed current cathodic protection (ICCP) systems for reinforced concrete bridges, Case Stud. Constr. Mater. 20 (2024) e02908.

[2] A. Bentur, N. Berke, S. Diamond, Steel corrosion in concrete: fundamentals and civil engineering practice, CRC press1997.

[3] S.A. Hadigheh, K. Feihu, K. Sima, 3D acid diffusion model for FRP-strengthened reinforced concrete structures: Long-term durability prediction, Constr. Build. Mater. 261 (2020) 120548.

[4] S.A. Hadigheh, K. Feihu, F. Hamid, Durability design criteria for the hybrid carbon fibre reinforced polymer (CFRP)-reinforced geopolymer concrete bridges, Structures 35 (2022) 325-339.

[5] F. Bolzoni, A. Brenna, M. Ormellese, Recent advances in the use of inhibitors to prevent chloride-induced corrosion in reinforced concrete, Cem. Concr. Res. 154 (2022) 106719.

[6] M. Balonis, G. Sant, O. Burkan Isgor, Mitigating steel corrosion in reinforced concrete using functional coatings, corrosion inhibitors, and atomistic simulations, Cem. Concr. Compos. 101 (2019) 15-23.

[7] F. Wang, J. Xu, Y. Xu, L. Jiang, G. Ma, A comparative investigation on cathodic protections of three sacrificial anodes on chloride-contaminated reinforced concrete, Constr. Build. Mater. 246 (2020) 118476.

[8] B. Holland, P. Alapati, K.E. Kurtis, L.J.C.o.s.i.c.s. Kahn, Effect of different concrete materials on the corrosion of the embedded reinforcing steel, (2023) 199-218.

[9] K. Rajesh Kumar, G. Shyamala, A. Adesina, Structural performance of corroded reinforced concrete beams made with fiber-reinforced self-compacting concrete, Structures 32 (2021) 1145-1155.

[10] P. Garcés, L. G Andión, I. De la Varga, G. Catalá, E. Zornoza, Corrosion of steel reinforcement in structural concrete with carbon material addition, Corrosion Science 49(6) (2007) 2557-2566.

[11] Y. Tao, S.A. Hadigheh, Z. Wang, Void geometry analysis and multifaceted characterisation of cementitious mortar reinforced with short carbon and glass fibres – A comparative study, J. Build. Eng. 89 (2024) 109283.

[12] A. Belli, A. Mobili, T. Bellezze, P.B. Cachim, F. Tittarelli, Commercial and recycled carbon-based fillers and fibers for self-sensing cement-based composites: Comparison of mechanical strength, durability, and piezoresistive behavior, J. Build. Eng. 73 (2023) 106836.

[13] T.V. Muthukumarana, M.A.V.H.M. Arachchi, H.M.C.C. Somarathna, S.N. Raman, A review on the variation of mechanical properties of carbon fibre-reinforced concrete, Constr. Build. Mater. 366 (2023) 130173.

[14] J. Hou, D.D.L. Chung, Effect of admixtures in concrete on the corrosion resistance of steel reinforced concrete, Corrosion Science 42(9) (2000) 1489-1507.

[15] P. Garcés, J. Fraile, E. Vilaplana-Ortego, D. Cazorla-Amorós, E.G. Alcocel, L.G. Andión, Effect of carbon fibres on the mechanical properties and corrosion levels of reinforced portland cement mortars, Cem. Concr. Res. 35(2) (2005) 324-331.

[16] P. Garcés, E. Zornoza, E.G. Alcocel, Ó. Galao, L.G. Andión, Mechanical properties and corrosion of CAC mortars with carbon fibers, Constr. Build. Mater. 34 (2012) 91-96.

[17] A. Wei, M.Y. Tan, Y.-C. Koay, X. Hu, R. Al-Ameri, Effect of carbon fiber waste on steel corrosion of reinforced concrete structures exposed to the marine environment, J. Clean. Prod. 316 (2021) 128356.

[18] C. Bai, S. Liu, F. Ma, S. Lu, J. Wang, S. Liu, Electrochemical Behavior of Carbon Fiber - Coupled Steel in Concrete Environment, International Journal of Electrochemical Science 15(5) (2020) 4660-4670.

[19] Y. Tao, S.A. Hadigheh, Enhancing the strength, microstructural integrity, and shrinkage performance of cement-based mortar using pulverised carbon and glass FRP composite waste, J. Build. Eng. 94 (2024) 110053.

[20] A. Danish, M.A. Mosaberpanah, M.U. Salim, M. Amran, R. Fediuk, T. Ozbakkaloglu, M.F. Rashid, Utilization of recycled carbon fiber reinforced polymer in cementitious composites: A critical review, J. Build. Eng. 53 (2022) 104583.

[21] Y. Wei, S.A. Hadigheh, Development of an innovative hybrid thermo-chemical recycling method for CFRP waste recovery, Compos. B. Eng. 260 (2023) 110786.

[22] Y. Wei, S.A. Hadigheh, Cost benefit and life cycle analysis of CFRP and GFRP waste treatment methods, Constr. Build. Mater. 348 (2022) 128654.

[23] J. Zhao, L. Liu, N. Yang, C. Su, T. Zhang, J. Yue, X. Dong, H. Huan, K. Yang, G. Bi, S. Liu, Oxonium Poly(Ionic Liquids) Enabled Thermoset Fluidization and Intact Carbon Fiber Recycling, ACS Sustainable Chemistry & Engineering 10(30) (2022) 9969-9979.

[24] J. Zhao, P. Liu, J. Yue, H. Huan, G. Bi, L. Zhang, Recycling glass fibers from thermoset epoxy composites by in situ oxonium-type polyionic liquid formation and naphthalene-containing superplasticizer synthesis with the degradation solution of the epoxy resin, Compos. B. Eng. 254 (2023) 110435.

[25] Y. Tao, S. A. Hadigheh, S. Saha, Y. Wei, Smart Self-sensing Mortar with Recycled Fillers, Ninth Asia-Pacific Conference on FRP in Structures (APFIS 2024), Adelaide, Australia, 2024.

[26] NanoScope Analysis 3.00. Bruker Corporation, 2021.

[27] ASTM C948-81 Standard Test Method for Dry and Wet Bulk Density, Water Absorption, and Apparent Porosity of Thin Sections of Glass-Fiber Reinforced Concrete, ASTM International, West Conshohocken, United States, 2023.

[28] BS EN 1015-10 Methods of test for mortar for masonry — Part 10: Determination of dry bulk density of hardened mortar, British Standards Institution, UK, 1999.

[29] N.J. Laycock, R.C. Newman, Localised dissolution kinetics, salt films and pitting potentials, Corrosion Science 39(10) (1997) 1771-1790.

[30] F.A. Almuaili, Characterisation of 3D pitting corrosion kinetics of stainless steel in chloride containing environments, The University of Manchester (United Kingdom)2017.

[31] S. Piqueras, S. Füchtner, R. Rocha de Oliveira, A. Gómez-Sánchez, S. Jelavić, T. Keplinger, A. de Juan, L.G. Thygesen, Understanding the Formation of Heartwood in Larch Using Synchrotron Infrared Imaging Combined With Multivariate Analysis and Atomic Force Microscope Infrared Spectroscopy, Front. Plant Sci. 10 (2020).

[32] J. Coates, Interpretation of Infrared Spectra, A Practical Approach, Encyclopedia of Analytical Chemistry 2006.

[33] J. Zhang, A. Heath, H.M.T. Abdalgadir, R.J. Ball, K. Paine, Electrical impedance behaviour of carbon fibre reinforced cement-based sensors at different moisture contents, Constr. Build. Mater. 353 (2022) 129049.

[34] W. Li, Y. Guo, X. Zhang, W. Dong, X. Li, T. Yu, K. Wang, Development of self-sensing ultra-high-performance concrete using hybrid carbon black and carbon nanofibers, Cem. Concr. Compos. 148 (2024) 105466.

[35] G. Song, Equivalent circuit model for AC electrochemical impedance spectroscopy of concrete, Cem. Concr. Res. 30(11) (2000) 1723-1730.

[36] Y. Wang, L. Sun, A. Li, W. Li, B. Guo, Effect of modified recycled carbon fibers on the conductivity of cement-based materials, Constr. Build. Mater. 415 (2024) 135033.

[37] M. Mishra, P.B. Lourenço, G.V. Ramana, Structural health monitoring of civil engineering structures by using the internet of things: A review, J. Build. Eng. 48 (2022) 103954.

[38] P. Liu, W. Wang, Y. Chen, X. Feng, L. Miao, Concrete damage diagnosis using electromechanical impedance technique, Constr. Build. Mater. 136 (2017) 450-455.

[39] H.H. Pan, J.-C. Guan, Stress and strain behavior monitoring of concrete through electromechanical impedance using piezoelectric cement sensor and PZT sensor, Constr. Build. Mater. 324 (2022) 126685.

[40] S. Saha, S.A. Hadigheh, I. Rukhlenko, M. Valix, B. Uy, S. Fleming, Machine learning-augmented multi-arrayed fiber bragg grating sensors for enhanced structural health monitoring by discriminating strain and temperature variations, Journal of Civil Structural Health Monitoring (2024).

[41] T. Hielscher, S. Khalil, N. Virgona, S.A. Hadigheh, A neural network based digital twin model for the structural health monitoring of reinforced concrete bridges, Structures 57 (2023) 105248.

[42] D. A, S. D, M. Pichumani, Electro-mechanical investigations of steel fiber reinforced self-sensing cement composite and their implications for real-time structural health monitoring, J. Build. Eng. 51 (2022) 104343.

[43] D.L. Castañeda-Saldarriaga, J. Alvarez-Montoya, V. Martínez-Tejada, J. Sierra-Pérez, Toward Structural Health Monitoring of Civil Structures Based on Self-Sensing Concrete Nanocomposites: A Validation in a Reinforced-Concrete Beam, Int. J. Concr. Struct. Mater. 15(1) (2021) 3.

[44] L. Wang, F. Aslani, Self-sensing performance of cementitious composites with functional fillers at macro, micro and nano scales, Constr. Build. Mater. 314 (2022) 125679.

[45] B. Han, X. Yu, J. Ou, Chapter 1 - Structures of Self-Sensing Concrete, in: B. Han, X. Yu, J. Ou (Eds.), Self-Sensing Concrete in Smart Structures, Butterworth-Heinemann 2014, pp. 1-11.

[46] X. Wang, B. Cao, C. Vlachakis, A. Al-Tabbaa, S.K. Haigh, Characterization and piezo-resistivity studies on graphite-enabled self-sensing cementitious composites with high stress and strain sensitivity, Cem. Concr. Compos. 142 (2023) 105187.

[47] A.K. Thomoglou, M.G. Falara, M.E. Voutetaki, J.G. Fantidis, B.A. Tayeh, C.E. Chalioris, Electromechanical properties of multi-reinforced self-sensing cement-based mortar with MWCNTs, CFs, and PPs, Constr. Build. Mater. 400 (2023) 132566.

[48] L. Deng, Y. Ma, J. Hu, S. Yin, X. Ouyang, J. Fu, A. Liu, Z. Zhang, Preparation and piezoresistive properties of carbon fiber-reinforced alkali-activated fly ash/slag mortar, Constr. Build. Mater. 222 (2019) 738-749.

[49] H. Wang, A. Zhang, L. Zhang, Q. Wang, X.-h. Yang, X. Gao, F. Shi, Electrical and piezoresistive properties of carbon nanofiber cement mortar under different temperatures and water contents, Constr. Build. Mater. 265 (2020) 120740.

[50] D. Jang, H.N. Yoon, S.Z. Farooq, H.K. Lee, I.W. Nam, Influence of water ingress on the electrical properties and electromechanical sensing capabilities of CNT/cement composites, J. Build. Eng. 42 (2021) 103065.

[51] L. Zhang, S. Ding, B. Han, X. Yu, Y.-Q. Ni, Effect of water content on the piezoresistive property of smart cement-based materials with carbon nanotube/nanocarbon black composite filler, Compos. Part A Appl. Sci. Manuf. 119 (2019) 8-20.

[52] W. Dong, W. Li, Y. Guo, F. Qu, K. Wang, D. Sheng, Piezoresistive performance of hydrophobic cement-based sensors under moisture and chloride-rich environments, Cem. Concr. Compos. 126 (2022) 104379.

[53] W. Dong, W. Li, K. Vessalas, X. He, Z. Sun, D. Sheng, Piezoresistivity deterioration of smart graphene nanoplate/cement-based sensors subjected to sulphuric acid attack, Composites Communications 23 (2021) 100563.

[54] G. Faneca, I. Segura, J.M. Torrents, A. Aguado, Development of conductive cementitious materials using recycled carbon fibres, Cem. Concr. Compos. 92 (2018) 135-144.

[55] Y. Wei, S.A. Hadigheh, Enhancing carbon fibre recovery through optimised thermal recycling: Kinetic analysis and operational parameter investigation, Materials Today Sustainability 25 (2024) 100661.

[56] W. Dong, W. Li, Z. Tao, K. Wang, Piezoresistive properties of cement-based sensors: Review and perspective, Constr. Build. Mater. 203 (2019) 146-163.

[57] AS 3972 General purpose and blended cements, Standards Australia, Australia, 2021.

[58] AS 3700 Masonry Structures, Standards Australia, Australia, 2018.

[59] N. Angelidis, C.Y. Wei, P.E. Irving, The electrical resistance response of continuous carbon fibre composite laminates to mechanical strain, Compos. Part A Appl. Sci. Manuf. 35(10) (2004) 1135-1147.

[60] BS EN 1015-3 Methods of test for mortar masonry - Part 3: Determination of consistence of fresh mortar (by flow table), British Standards Institution, UK, 1999.

[61] BS EN 1015-6 Methods of test for mortar for masonry - Part 6: Determination of bulk density of fresh mortar, British Standards Institution, UK, 1999.

[62] C109/C109M Standard Test Method for Compressive Strength of Hydraulic Cement Mortars (Using 2-in. or [50 mm] Cube Specimens), ASTM International, West Conshohocken, United States, 2021.

[63] K. Ogi, T. Shinoda, M. Mizui, Strength in concrete reinforced with recycled CFRP pieces, Compos. Part A Appl. Sci. Manuf. 36(7) (2005) 893-902.

[64] M. Chiarello, R. Zinno, Electrical conductivity of self-monitoring CFRC, Cem. Concr. Compos. 27(4) (2005) 463-469.

[65] X.R. Zhu, G.Q. Huang, L.Y. Lin, D.Y. Liu, Long term corrosion characteristics of metallic materials in marine environments, Corrosion Engineering, Science and Technology 43(4) (2008) 328-334.

[66] S.A. Hadigheh, F. Ke, H. Fatemi, Durability design criteria for the hybrid carbon fibre reinforced polymer (CFRP)-reinforced geopolymer concrete bridges, Structures 35 (2022) 325-339.

[67] S.A. Hadigheh, R. McDougall, C. Wiseman, L. Reid, Evaluation of composite action in cross laminated timber-concrete composite beams with CFRP reinforcing bar and plate connectors using Digital Image Correlation (DIC), Eng. Struct. 232 (2021) 111791.

[68] H. Gao, Y. Xia, Research on the dispersion of carbon fiber and recycled carbon fiber in cement-based materials: a review, 10 (2023).

[69] L. Lavagna, S. Musso, G. Ferro, M. Pavese, Cement-based composites containing functionalized carbon fibers, Cem. Concr. Compos. 88 (2018) 165-171.

[70] Y. Tao, S.A. Hadigheh, Y. Wei, Recycling of glass fibre reinforced polymer (GFRP) composite wastes in concrete: A critical review and cost benefit analysis, Structures 53 (2023) 1540-1556.

[71] Y. Tao, S.A. Hadigheh, S. Saha, Y. Wei, Smart Self-sensing Mortar with Recycled Fillers, Ninth Asia-Pacific Conference on FRP in Structures (APFIS 2024), Adelaide, Australia, 2024.

[72] K. Derucher, Microcracking of concrete, Journal of the Washington Academy of Sciences (1977) 135-143.

[73] G. Cosoli, A. Mobili, F. Tittarelli, G.M. Revel, P. Chiariotti, Electrical Resistivity and Electrical Impedance Measurement in Mortar and Concrete Elements: A Systematic Review, Applied Sciences 10(24) (2020) 9152.

[74] H. Yang, X. Yao, L. Yuan, L. Gong, Y. Liu, Strain-sensitive electrical conductivity of carbon nanotube-graphene-filled rubber composites under cyclic loading, Nanoscale 11(2) (2019) 578-586.

[75] S. Wen, D. Chung, Effect of moisture on piezoresistivity of carbon fiber-reinforced cement paste, ACI Materials Journal 105 (2008) 274-280.

[76] S. Wen, D.D.L. Chung, Model of piezoresistivity in carbon fiber cement, Cem. Concr. Res. 36(10) (2006) 1879-1885.

[77] W. Dong, W. Li, N. Lu, F. Qu, K. Vessalas, D. Sheng, Piezoresistive behaviours of cement-based sensor with carbon black subjected to various temperature and water content, Compos. B. Eng. 178 (2019) 107488.

[78] L. Wang, F. Aslani, The Hybrid Effect of Micro Steel and Carbon Fibres on Mechanical, Electrical and Piezoresistive Properties of Cementitious Composites, 2021.

[79] H. Montazerian, A. Dalili, A.S. Milani, M. Hoorfar, Piezoresistive sensing in chopped carbon fiber embedded PDMS yarns, Compos. B. Eng. 164 (2019) 648-658.

[80] Y. Suo, H. Xia, R. Guo, Y. Yang, Study on self-sensing capabilities of smart cements filled with graphene oxide under dynamic cyclic loading, J. Build. Eng. 58 (2022) 104775.

[81] A.O. Monteiro, P.B. Cachim, P.M.F.J. Costa, Self-sensing piezoresistive cement composite loaded with carbon black particles, Cem. Concr. Compos. 81 (2017) 59-65.

[82] D.D.L. Chung, A critical review of electrical-resistance-based self-sensing in conductive cement-based materials, Carbon 203 (2023) 311-325.

[83] Y. Wang, T. Ueda, F. Gong, D. Zhang, Meso-scale mechanical deterioration of mortar due to sodium chloride attack, Cem. Concr. Compos. 96 (2019) 163-173.

[84] K. De Weerdt, B. Lothenbach, M.R. Geiker, Comparing chloride ingress from seawater and NaCl solution in Portland cement mortar, Cem. Concr. Res. 115 (2019) 80-89.

[85] L. Sutter, K. Peterson, G. Julio-Betancourt, D. Hooton, T.V. Dam, K. Smith, The deleterious chemical effects of concentrated deicing solutions on Portland cement concrete, South Dakota Department of Transportation, Office of Research Pierre, SD, USA 2008.

[86] F. Althoey, B. Wisner, A. Kontsos, Y. Farnam, Cementitious materials exposed to high concentration of sodium chloride solution: Formation of a deleterious chemical phase change, Constr. Build. Mater. 167 (2018) 543-552.

[87] D. Wenkui, L. Wengui, T. Zhong, W. Kejin, Piezoresistive properties of cement-based sensors: Review and perspective, Constr. Build. Mater. 203 (2019) 146-163.

[88] L. Wang, F. Aslani, Mechanical properties, electrical resistivity and piezoresistivity of carbon fibre-based self-sensing cementitious composites, Ceramics International 47(6) (2021) 7864-7879.

Chapter 7: Conclusions and Future Directions

7.1 CONCLUSIONS

Incorporating FRP composite waste into CCs provides an alternative pathway for managing wastes from the manufacturing process and EoL products. This approach addresses the significant waste management challenges posed by unsustainable practices, which can lead to negative environmental and ecosystem impacts. By recycling and incorporating FRP waste into the cementitious matrix, this approach delivers an effective, economical, and low-energy solution for resource repurposing. This thesis confirms the feasibility of repurposing various FRP wastes into cementitious matrices, evaluates their impact on the multifaceted performance of the resulting CCs, and proposes innovative strategies to enhance their functionality. These contributions collectively advance the field. This research work consists of literature reviews, experiments and numerical analyses. Based on the findings presented throughout this research, several key conclusions can be drawn from each chapter.

Chapter 2 laid the foundation through a comprehensive review of current FRP recycling methods and the feasibility of incorporating FRP waste into CCs. It focused on summarising existing research on the recycling and repurposing of GFRP and CFRP wastes in CCs, highlighting both the opportunities and challenges in this emerging field. The review began by introducing current FRP composite recycling methods and highlighted the need for developing sustainable waste management strategies. Repurposing FRP waste into CCs was then introduced as a promising alternative. Given that the optimum size and dosage of different forms of FRP waste incorporation are still under investigation, comprehensive analyses were conducted on the influences of various FRP waste on CCs with respect to fresh, mechanical and durability properties. Then the effects of different dosages of FRP recyclates with various replacement forms and sizes on CC performance were discussed and analysed. These investigations provided insights from past studies and offered valuable conclusions and recommendations for this research. While fresh and mechanical properties were primarily studied, limited research has been conducted on durability and internal structural characteristics. In addition, the effects of incorporating different types of FRP waste might vary depending on the specific case, while the practical challenges of repurposing real industrial FRP waste should be addressed. The review also presented the outcomes of CBA and BCR evaluations comparing commonly used FRP recycling methods, using GFRP as a case study.

The results demonstrated that repurposing rGFRP in concrete could reduce total investment requirements while increasing net profit. It highlighted that with proper design, the repurposing approach could benefit from sustainable practices, economic advantages, and improved performance of the resulting CCs.

To address the limitations of the conventional NDT methods, self-sensing concrete, also known as smart concrete, has emerged as an innovative SHM solution for civil infrastructure. To provide a better understanding of cement-based sensors, this chapter provides a systematic review with a focus on their mechanisms, materials, fabrication and measurement methods, as well as functional properties. The electrical resistivity and piezoresistivity of CCs with short CFs were discussed. While previous research has investigated the self-sensing capacities of cement-based sensors with various carbon-based fillers, few studies have incorporated CFRP and CF recyclates for this purpose. Through detailed examination, the influences of CF and CFRP recyclates on the self-sensing capacities of CCs were evaluated. Their effectiveness largely depended on various factors, including but not limited to the properties and concentrations of the fillers, filler dispersion, curing conditions, and external environmental conditions. Furthermore, this chapter also provided a comprehensive review of current fibre surface modification strategies aiming at enhancing FRCC performance. To achieve this, the interface and bonding mechanisms between CF and the cementitious matrix were first examined, as this is fundamental for developing and optimising modification strategies. Based on this understanding, different surface modification strategies were introduced, along with the evaluation techniques used to assess their effectiveness in improving the overall performance of FRCC. The limitations of conventional methods including cost, complexity, environmental impact, and compatibility issues, were then discussed. To overcome these challenges, this review underscored the need for more efficient, cost-effective, and sustainable alternatives. Through the literature review in Chapter 2, critical research gaps were identified, and the subsequent chapters addressed these challenges by conducting numerical and experimental research.

This thesis explored the repurposing of both fibre offcuts and FRP composite product waste into CCs, with materials sourced from both manufacturing processes and the end of their service life. Chapter 3 primarily focused on the incorporation of short CFs and GFs into CCs, commonly referred to as FRCCs. To address the research gap of limited examination on the durability and internal structural characterisations, the study first employed micro-CT analysis to analyse void geometry and distribution of FRCCs with 0.1 vol% to 0.5 vol% CFs and GFs,

and evaluated their impacts on multifaceted properties, including mechanical, durability, and electrical performance. The study also evaluated the effects of acid diffusion on these CCs through both experiments and finite element simulations. The findings demonstrated that the inclusion of short fibres increased air void content in the matrix, ranging from 6.26% to 8.94%, leading to reduced mechanical strength and durability performance. As fibres were incorporated, elongated voids formed around them, with a higher occurrence of elongated voids observed in specimens with CFs. The incorporation of both fibres remarkably limited drying shrinkage, primarily attributed to the bridging and bonding effects of fibres within the matrix. The addition of 1.0 vol% CFs significantly decreased the electrical resistivity and improved acid resistance performance, demonstrating the potential multifunctional benefits of CF offcuts incorporation.

To further enhance the NDT approach for examining the internal structure of FRCCs for quality assurance, the study in Chapter 3 also investigated the capacities of both micro-CT and UT to characterise CF and void features in the FRCCs. While Isotropic Gaussian blur and smoothing were successfully utilised for void detection, an Anisotropic Gaussian filtering technique was developed specifically for CF detection within the cementitious matrix. This new method was proposed to overcome the challenges of low-contrast and noisy images. A comparative study was conducted to quantitatively evaluate the segmentation accuracy among conventional methods using various performance metrics. The results consistently showed that the proposed approach achieved high accuracy and sharp boundary detection between CF and matrix, and a greater alignment with the ground truth, compared to the other methods. Despite the high-resolution 3D imaging capabilities of micro-CT, which include examining the spatial positions and dimensions of features, its limitations - such as high cost and unsuitability for field applications - were acknowledged. Instead, the application of the TFM ultrasonic technique provides an efficient and fast alternative for detecting these features in the cementitious matrix using the 1D ultrasonic phased array. Through a comparative analysis of these two NDT methods in characterising CF distribution and voids across various scales, the post-processed TFM image demonstrated high accuracy in detecting CF features embedded deeper within the matrix. The best performance was observed with a 3.26% error for the CF bundle and a 0% error for the CF strip. Additionally, void features located at mid-depth were detected with greater reliability.

As demonstrated in Chapter 3, incorporating short CFs into cementitious composites CCs enhanced multiple properties, including flexural strength and acid resistance. The study also

employed advanced NDT methods to assess internal structures, which are critical to FRCC performance and quality assurance. However, characterisation revealed the formation of elongated voids and heterogeneous internal structures, which potentially compromised mechanical integrity and long-term durability. These issues were primarily linked to the hydrophobicity and chemical inertness of CFs, resulting in poor dispersion and weak fibre-matrix bonding.

To overcome the hydrophobic nature of the CF surface and facilitate better fibre dispersion and stronger fibre-matrix interfacial bonding, novel fibre surface modification techniques were proposed in Chapter 4 to improve FRCC performance. These treatments aimed to overcome CF hydrophobicity, improve dispersion, and strengthen fibre-matrix bonding, ultimately enhancing the overall performance of FRCCs. Bio-based surface treatments have been developed as sustainable alternatives to conventional aggressive chemical treatments. Electrochemical grafting methods demonstrated in-situ efficacy and suitability for industrial continuous processing. To characterise CF alterations after treatment, surface morphology analysis, chemical characterisation, and single-fibre tensile testing were conducted. The improved compressive and flexural strength and interaction mechanisms of treated CFs within the cementitious matrix were assessed through mechanical testing, complemented by SEM and EDS analysis. The outcomes showed that both treatments were effective in introducing additional functional groups to the CF surface, increasing surface roughness and maintaining high tensile properties of CFs. For bio-based surface modifications, the co-deposition of tannic acid (TA) with ethanolamine formed a polymeric layer, while citric acid (CA) treatment created an irregular surface texture with ester groups through esterification reactions. During the in situ electrochemical grafting treatments, CFs were modified with hydroxyl (OH) and amine (NH_2) groups. Functional groups on the CF surface enhanced chemical adhesion through calcium and aluminium ion chemisorption, hydrogen bonding, and covalent interactions with C-S-H gels. The increased surface roughness improved mechanical interlocking and provided nucleation sites for hydration product deposition, further strengthening the CF-cementitious matrix interface. As a result, all treatments demonstrated their potential for improving FRCC performance, with the best results observed in the FRCC specimens incorporating OH-functionalised CFs and TA-modified CFs. Using the optimised combination of 0.1 vol% and 12mm CFs, OH-functionalised CFs improved FRCC compressive and flexural strengths by 32.30% and 21.04%, while TA-modified CFs enhanced these properties by 30.11% and 32.11%, respectively, compared to plain mortar.

Chapter 5 extended the scope of this research by shifting from laboratory-prepared fibre offcuts to real-world FRP composite waste sourced from local industries. While Chapter 3 demonstrated the potential of short CFs and GFs as viable reinforcements in CCs, this chapter successfully addressed the practical challenges of managing and repurposing actual industrial FRP waste. To this end, a two-step mechanical recycling process was developed to convert these waste materials into usable forms for CCs, offering a scalable and sustainable solution for composite waste management. Previous studies on the performance of CCs with FRP recyclates have shown contradictory results due to size effects and the diverse composition of waste composites from different sources. To address this, the current experimental work investigated the feasibility of repurposing waste GFRP EoL electrical crossarms and CFRP offcut panels from aerospace manufacturing on a case-by-case basis and determined the optimised combination. Firstly, in order to understand the properties of waste materials before incorporation, particle size distribution, chemical and mineralogical composition, and mechanical performance of the FRP composite were analysed. Subsequently, without resin removal, pulverised FRP recyclates were used as partial cement replacements in mortar at levels ranging from 1 wt.% to 10 wt.%. From the physical and mechanical evaluations of CCs, fresh and bulk densities decreased in all specimens with FRP recyclates due to their lightweight nature, while GFRP recyclates with lower surface area increased flow values. Compressive strength showed an inverse relationship with increasing FRP content, while flexural strength and ductility improved with higher FRP replacement. At 28 days, the incorporation of FRP recyclates reduced water absorption by 19% and significantly improved mechanical performance, with compressive strength increasing by up to 67% and flexural strength by up to 43%. Tiny FRP particles enhanced microstructural density and reduced porosity through the filling effect. The microstructural analysis also confirmed the fibre-reinforcing effect, which enhanced CC's mechanical performance. In addition, microfibres also mitigated drying shrinkage, with the greatest reduction observed at 5 wt.% recyclates. Although the reduction in electrical resistivity of CC with rCFRP incorporation was less significant than with CFs, CFRP recyclates still offer potential for applications in SHM, as further explored in Chapter 6.

Building on the material innovations and repurposing strategies developed in Chapters 3 to 5, Chapter 6 explored the functionalisation of CCs for SHM applications. The successful integration of recycled fibres and FRP waste into cementitious composites laid the groundwork for investigating their added value in functional roles. This chapter shifts attention to the self-sensing potential of cement-based composites incorporating conductive fillers derived from

FRP waste. For the first time, the viability of using CFRP and CF recyclates to enhance electrical and piezoresistive performance under varying environmental conditions, including temperature, humidity, and chloride-induced corrosion, is assessed. Various forms of recyclates, including vCF, chemically treated rCF offcuts, and pulverised CFRP waste, were characterised and integrated into cement-based sensors. Based on the previous findings, these recyclates were incorporated as additional reinforcement or partial cement replacement, with the design considering both mechanical strength and electrical properties. To address the research gap in self-sensing performance under aggressive environments and provide a better understanding of the corrosion behaviour of CCs with embedded reinforcement, a simulated marine environment with an impressed current was designed to accelerate corrosion and examine the electrochemical performance of the specimens. The corrosion of stainless-steel mesh was both observed visually and monitored using linear polarisation resistance (LPR) and Electrochemical Impedance Spectroscopy (EIS) techniques, with equivalent circuits developed to model the electrochemical system. The results confirmed that the optimal mix design for corrosion resistance incorporated 10 wt.% CFRP recyclates. This mix resulted in a 43% reduction in corrosion rate and a 32% increase in polarisation resistance compared to control specimens without additives, after 15 simulated years. EIS investigations also confirmed its enhanced long-term stability in corrosion resistance. The inclusion of CF offcuts improved conductivity but increased corrosion rates due to higher porosity, which facilitated ion penetration and reduced electron transfer resistance. Specimens with chemically rCFs exhibited slightly better corrosion resistance than those with vCFs. The findings confirmed that the incorporation of CFRP recyclates was effective and sustainable for CCs even in harsh marine environments.

Based on the understanding of the impact of different FRP recyclates on the corrosion behaviours of CCs, the study in Chapter 6 then evaluated their effect on the electrical resistivity and piezoresistivity under varying conditions, including temperatures ranging from 22°C to 50°C, humidity levels between 30% and 90%, and accelerated chloride-induced corrosion exposure. Experiments were conducted under cyclic loading, with resistivity simultaneously measured using a multimetre. The results showed that while CFRP recyclates increased CC's electrical resistivity compared to CFs, they provided more consistent and repeatable piezoresistive behaviour under varying humidity conditions. Specimens with CFRP recyclates achieved an average stress sensitivity of 0.42%/MPa and a gauge factor of 17.50, with peak values reaching 5.69%/MPa and 395.80 under 30% humidity. Higher CF dosages (0.5–1.0

vol.%) reduced humidity sensitivity due to conductivity governed by CF contact networks. Regarding temperature effects, CCs incorporated with CFRP recyclates exhibited the highest temperature dependency, whereas the specimens with rCFs remained stable with minimal resistivity changes. Despite a decrease in maximum FCR after chloride-induced corrosion, specimens with CFRP recyclates maintained stability due to a well-distributed conductive network and dense microstructure which minimised chemical interference and enhanced stress and strain detection. This research further confirmed that incorporating CFRP waste into CCs offers a promising approach for developing innovative self-sensing sensors with effective and stable piezoresistivity, even in aggressive environments, while preserving desirable mechanical properties.

To this end, this thesis explores innovative repurposing strategies for incorporating various FRP composite wastes into CCs. By integrating both fibre offcuts and EoL product wastes from different stages of the composite life cycle, this research presents a sustainable solution for waste management while enhancing the performance of the resulting CCs. The proposed approach also offers an economical and energy-efficient alternative to conventional resource utilisation, promoting circularity in construction materials. The findings highlight the benefits of incorporating these recyclates to improve the physical, mechanical and durability performance of CCs under diverse environmental conditions. Beyond structural enhancements, this research also contributes to the advancement of multifunctional CCs using FRP recyclates, in the development of self-sensing sensors for SHM. It not only promotes greener infrastructure but also paves the way for the development of smart and sustainable building systems. The outcomes of this thesis provide valuable insights, serving as a foundational study for future research while also offering a practical guideline for the adoption of FRP waste in the construction industry.

7.2 FUTURE DIRECTIONS

The following recommendations can be made for future research:

- This research utilised micro-CT to analyse air void dimensions and eccentricity distribution in FRCCs. However, resolution limitations and sample size constraints prevented the detection of sub-micron or smaller voids. Future studies should use higher-resolution micro-CT systems or optimise sample size to provide a more detailed and accurate characterisation of the entire pore system. Additionally, future

research could conduct porosity analysis during and after acid attack to understand its degradation progression, as well as investigate the local stress distribution around elongated voids and its impact on FRCC's mechanical performance.

- This research confirmed the effectiveness of the newly developed Anisotropic Gaussian filtering in detecting the orientation, dimensions, and spatial location of CF features within the cementitious matrix. Ongoing research should continue working on enhancing the detection of discrete CFs using this technique, as accurate fibre distribution analysis is crucial for evaluating FRCC performance.
- The feasibility of the TFM ultrasonic technique for detecting internal features in FRCCs using a 1D phased array was evaluated. However, challenges remained, such as limited resolution for small defects, interference from direct waves, and a low signal-to-noise ratio for deeper features. This application requires further refinement, including advancements in signal processing, deep learning integration, and improved focusing or signal compensation techniques to enhance imaging quality and the detection of deep defects. Continued exploration should focus on adopting a 3D TFM approach to achieve more comprehensive and accurate internal feature identification in cementitious materials.
- Both bio-based and electrochemical CF surface modifications represent innovative and sustainable ways for enhancing the performance of FRCCs. Current experiments utilising bio-based chemicals for CF surface modification have been conducted primarily at laboratory scale. Future research should focus on scaling bio-based methods for industrial applications and quantifying their sustainability benefits in construction contexts. In terms of in situ electrochemical grafting techniques, it is recommended to perform life cycle and cost benefit analyses to further emphasise their sustainability benefits, economic advantages, and market competitiveness compared to the other CF surface modification methods for construction industry.
- Repurposing FRP composite waste from diverse industrial sectors remains an ongoing research priority for developing greener construction materials. Future examination of CCs incorporating FRP recyclates is necessary to conduct more durability studies, such as sulfate attack resistance and carbonation resistance, to assess their long-term performance. Additionally, optimising rFRP content and mix design for various

applications can further enhance material performance and maximise repurposing efficiency.